Atomized Liquid Nitrogen Spray Assisted Machining of Al-TiC$_p$ Metal Matrix Composites with Different Tool Geometry

THESIS

Submitted in partial fulfilment
of the requirements for the degree of

DOCTOR OF PHILOSOPHY

by

SRAVAN KUMAR J

ID. No. 2012PHXF0504H

Under the Supervision of

Prof. SURESH KUMAR REDDY NARALA

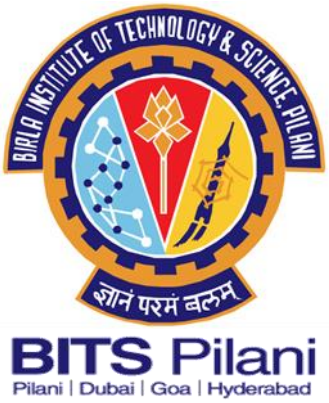

BIRLA INSTITUTE OF TECHNOLOGY AND SCIENCE, PILANI

2018

BIRLA INSTITUTE OF TECHNOLOGY AND SCIENCE, PILANI

CERTIFICATE

This is to certify that the thesis entitled "**Atomized Liquid Nitrogen Spray Assisted Machining of Al-TiCp Metal Matrix Composites with Different Tool Geometry**" and submitted by **Sravan Kumar J**, ID No. **2012PHXF0504H** for award of Ph.D. of the Institute embodies original work done by him under my supervision.

Signature of the Supervisor:

Name in capital letters: **SURESH KUMAR REDDY NARALA**

Designation: **Associate Professor**
Department of Mechanical Engineering
BITS-Pilani Hyderabad Campus,
Jawahar Nagar, Shameerpet (Mandal),
Hyderabad – 500078

Date:

I take this opportunity to sincerely acknowledge the ***Council of Scientific & Industrial Research (CSIR)****, Government of India, New Delhi, for providing financial assistance (sponsored project* ***22(0567)/12/EMR-II****) in the form of Senior Research Fellowship (SRF) which buttressed me to perform my work comfortably.*

ACKNOWLEDGEMENTS

This thesis is the final destination of my journey in obtaining my doctoral degree. Despite several ups and downs, the journey of conducting my research was kept well on track with the constant support and encouragement of my friends, my well-wishers and colleagues. It is a pleasant task to express my thanks to all those who contributed in many ways to the success of this study and made it an unforgettable experience for me.

First of all, I praise and thank God, the 'almighty' for blessing me with an opportunity to undertake this research and granting me the strength and confidence to proceed successfully.

I am extremely indebted to my supervisor **Prof. Suresh Kumar Reddy Narala**, for giving me a lifetime opportunity to work under him. His exceptional guidance and immense patience accompanied by valuable advices throughout my tenure helped to complete this research. I highly admire the constant motivation received from his end which always helped me to develop myself both professionally and personally.

I would like to express my gratitude to **Doctoral Research Committee (DRC) members** for providing valuable support during this research work. I am sincerely grateful to **Prof. Amit Kumar Gupta** and **Prof. Y V Daseswara Rao** as my **Doctoral Advisory Committee (DAC) members** for their valuable comment and insightful suggestions at various stages of this research work.

My deep sense of regards to **Prof. Amit Kumar Gupta,** current head, **Prof. S P Regella** and **Prof. Y V Daseswara Rao,** former heads**,** Department Mechanical Engineering, BITS-Pilani, Hyderabad campus for providing an amiable ambience leading to successful completion of my research.

Prof. G Sundar, current Director, and **Prof. V Sambasiva Rao**, former Director, BITS-Pilani, Hyderabad Campus, deserve my sincere expression of thanks for providing me all resources and state of the art facilities at the campus to carry out my research.

My special thanks to **Prof. Souvik Bhattacharyya** current Vice-Chancellor and **Prof. Bijendra Nath Jain**, former Vice-Chancellor, BITS-Pilani, for providing me an excellent platform for carrying my doctorial work at the institute.

I heartily thank **Prof. Vidya Rajesh**, Associate Dean, ARD and **Prof. P Yogeeswari**, Associate Dean, SRCD, BITS-Pilani, Hyderabad campus for their support throughout the research work.

I warmly thank **Prof. M Srinivas,** Associate Dean, ARD and **Prof. S S Deshmukh,** Associate Dean, SWD, BITS Pilani, Hyderabad Campus for their constant support during the period of Ph.D.

I extend my warm gratitude to all the **Faculty Members,** Department of Mechanical Engineering, BITS-Pilani, Hyderabad Campus for their support and encouragement to carry out my research work. **Dr. R Parameshwaran** for discussions regarding my project deserves special mention here.

Most of the results presented in this thesis would not have been obtained without the facilities provided by few of the laboratories. I owe a great deal of appreciation and gratitude to **Prof. Suresh Kumar Reddy Narala**, faculty in-charge for central workshop, **Prof. Amit Kumar Gupta** and **Dr. C Phaneendra Kiran,** the former and current faculty in charge for material testing lab respectively and **Prof. S P Regella,** faculty in charge for CPDR lab.

I thank **Dr. Arkhamitra Kar** for providing stereo microscope facility and **Prof. A. Ramesh Babu** for providing liquid nitrogen container to complete my experiments.

I expand my thanks to all the **technicians** of various laboratories at BITS Pilani Hyderabad Campus for their timely help and advice during my research tenure. My thanks go in particular to **Mr. P Sreedhar** and **Mr. B Chandrashekar** laboratory staff and technicians of Department Mechanical Engineering, for providing me experimental hands-on-training and their warm hearted assistance and support during my machining studies in central work shop.

I take this opportunity to say heartful thanks to **Mr. Prakash Marimuthu** for providing me an insight to simulation and building confidence in me to carry the same.

I would also like to thank some people from early days of my research tenure. **Dr. Appa Rao**, DMRL Hyderabad, **Dr. Nandhi**, DMRL Hyderabad**, Mr. C Vinay Choudary,** Innomet Powder**, Mr. K Vinay Kumar,** Kennametal, **Mr. Gulshan Varma**, Sandvik were among those who kept me going at the beginning. **Dr. S M Hussaini, Dr. K Suresh** and **Dr. K. Nithin R Kotkunde** for their moral support deserve special mention here. This list is incomplete without acknowledge **Dr. P Umamaheswera Reddy** who was the source of inspiration for me in early days and who thought me many things.

I am thankful to many student colleagues, in particular to **Mr. E Guru Charan** with whom I started this work and many rounds of discussion on my project helped me a lot. I am also thankful to **Mr. Rajat Bansal, Mr. Parth Gupta, Mr. Sanchay. B, Ms. M Meghana., Mr. Sai Kiran** and **Mr. Dheeraj Verma** for providing a stimulating and fun filled environment.

Thanks to all my PhD colleagues at BITS Pilani Hyderabad campus who shared many unforgettable moments during my stay at the campus. I would like to thank specially **Mr. G Rakesh Kumar, Mr. Amar S D** and **Mr. Pavandatta M Jadhav** for their friendship, co-operation and encouragement throughout the Ph.D. tenure and I admire them

for their distinguished helping nature. I am also thankful to **Mr. V R Shanmukhasundaram, Mr. Karthik Teja M, Ms. Swagatika Mohanty, Mr. A Uday Kumar, Mr. V V N Satya Suresh** and **Mr. Madhan Mohan Reddy**, and my fellow research scholars, Department of Mechanical Engineering, BITS Pilani Hyderabad Campus for sharing their research ideas in a health way.

It's my fortune to gratefully acknowledge the support of some special individuals. I feel my vocabulary is inadequate to express my special thanks to **Ms. Vemula Swathi**. She always stood by my side and has always been a constant source of motivation during the hardest moments of my life. Thank you doesn't seem sufficient but it is said with appreciation and respect her for support, encouragement, care, understanding and precious friendship. I convey my special gratitude to **Ms. Shubhmita Bhatnagar**. I can see the good shape of my thesis because of her help and suggestions in formatting the entire thesis.

I would also like to extend huge, warm thanks to my roommates, **Mr. V. Avinash, Mr. P. Sai Phaneedra, and Mr. Ganesh** for their love, care, support and creating a pleasant atmosphere. **Mr. Vishnu Kiran** deserves special mention for his valuable friendship, constant encouragement and helping nature. I am grateful to some of my good friends **Mr. M. Gowtham, Mr. N. Ramchandra, Mr. Pavan Kumar, Mr. V Chethan Kumar, Mr. Kaushik, Mr. Himanshu and Ms. Rimpy** for their love, care and moral support.

Last but not least, I would like to pay high regards to my family **Mr. Suryanarayana** (Father)**, Mrs. Radha Kumari** (Mother), **Mr. Pavan Kumar** (Brother)**, Mrs. Phani Shree** (Sister-in-law) **and Ms. Anagha Shree** (Brother's daughter) for their unconditional love, encouragement and support throughout my tenure of my Ph.D. I doubt that I will ever be able to convey my appreciation fully, but I owe them my eternal gratitude. I convey special acknowledge to **Mr. Ramkumar** (uncle) for his valuable advice

in language, spending his precious times to read my article and gave his valuable suggestions.

Besides this, I thank each and every individual who knowingly and unknowingly helped me in the successful completion of my research.

Sravan Kumar Josyula

ABSTRACT

The ever-growing need for advanced materials in manufacturing industries has always been a constant motivating force for materials scientists and engineers that has led to the development of one of the most prominent classes of engineering materials, the Metal Matrix Composites (MMCs), which offer numerous outstanding properties in contrast to traditional metals and alloys. Among various MMCs, Aluminum matrix reinforced with Titanium Carbide particulate (Al-TiC_p) MMCs has gained more attention owing to its excellent thermo-mechanical characteristics and high grain structure refinement properties. Several methods exist to produce Al-TiC_p MMCs ranging from solid to liquid state processing techniques. Over the past two decades, in-situ and ex-situ, based casting techniques have been practiced to produce high quality Al-TiC_p MMCs. However, these techniques fail to provide effective control over volume fraction, size and distribution of TiC particles and formation of intermetallic particles in composites. An ideal solution is to directly incorporate TiC particles into Al melt in order to produce high-quality Al-TiC_p composites without any interfacial reactions. Therefore, in the current research work a systemized inert atmospheric stir casting facility has been developed to produce cluster and reaction free Al-TiC_p composites. Flux and additive agents are used to reduce the thermo-mechanical barriers and improve the wettability of TiC_p with Al matrix. The quality of produced composites was tested using X-ray diffraction (XRD), metallography and Energy-dispersive X-ray spectroscopy (EDX) analysis and its performance was evaluated in terms of mechanical properties such as density, hardness, tensile test.

Although TiC particles significantly improve the performance characteristics, their abrasive and intermittent nature makes machining complex and thus reduces the machinability of Al-TiCp MMCs. During machining of MMCs, high strain and

temperatures arise at localized area (tool/work piece interface) leading to severe edge chipping and plastic deformation via seizure of chips. Studies reveal the potential of cryogenic technology for facilitating enhanced machinability of composites. However, this technology employs a large quantity of cryogenic fluid which not only increases the machining cost but also undesirably affect the surface integrity of work material. These adverse effects can be avoided by minimizing the quantity of cryogenic liquid and maximizing its capability to penetrate into the machining zone improves the machinability performance. Therefore, in the present study, an Atomized Liquid Nitrogen (ALN) spray system has been design and developed to enhance the machining performance of Al-TiC_p MMCs. The spray system is aimed to diffuse Liquid Nitrogen (LN_2) in the form of micro droplets effectively into the tool/chip/workpiece interface and minimize the undesirable cooling effect by delivering LN_2 at a controlled flow through a micro nozzle. The performance of developed ALN spray system has been analysed experimentally by studying the characteristics like, spray angle, spay pattern, spray velocity, droplet diameter and temperature. Preliminary machining experiments were also conducted to determine the optimum spray parameters.

In order to assess the performance of developed ALN spray discharge system and ascertain the cryogenic tribological behaviour of Al-TiC_p MMCs, friction and wear behaviour were studied using a customized cryogenic tribometer developed by attaching ALN spray system to pin-on-disc configuration. Wear studies have been carried out under different loading and sliding velocities under ALN, cryogenic chilled argon (CCA) gas and dry environments. The analysis under ALN spray condition reveals that presence of LN_2 in sliding contact offers significant reduction in friction and wear values of Al-TiC_p MMCs when compared to other environments.

Further, efforts have been made to investigate the impact of ALN spray assisted machining on tool performance and surface finish of the machined Al-TiC_p MMCs by using coated carbide tool of different tool geometry (rake angle, nose radius and approach angle) and cutting parameters (cutting speed and feed) as per industrial requirements. A series of experiments were carried out to analyze the performance of ALN spray assisted machining over dry, wet and CCA gas assisted machining conditions. The study yielded some interesting facts about influence of tool geometry on machinability performance of Al-TiC_p MMCs.

To mend the machinability characteristics, efforts should be made to follow a judicious selection of optimal cutting parameters in turning of Al-TiC_p MMC. In the present study, the significant machining parameters such as speed, feed, rake angle, nose radius and approach angle were determined by Analysis of Variance (ANOVA). These machining parameters were employed to establish a predictive mathematical model based on experimental results using Response Surface Methodology (RSM). This model was used to formulate an objective functions of the genetic algorithm (GA), to determine optimal machining conditions and helps to minimize the surface roughness, cutting force and tool wear simultaneously through multi-objective optimization technique.

Modeling of MMC machining is difficult due to its unique composition and structure which is inhomogeneous and anisotropic. Therefore, in the current study a Finite Element (FE) model of machining MMCs is developed to analyze the effect of particle distribution in matrix, cutting parameters and tool geometry on machining process. In FE analysis, the main phases of MMC workpiece, namely the matrix phase and the particle phase are modeled. The developed 2D FE models are successful in predicting the cutting performance variables like chip morphology, cutting forces, temperature, and stress distributions. Two different strategies (model A and B) are utilized to arrange the particles

in the matrix. Model B with angular distribution of particles shows better performance than the linear distribution of particles in model A. The performance of developed model at different machining conditions are successfully performed and minor deviation were observed with experimental results. Further, heat transfer properties are incorporated in the FE code of model B to perform the cryogenic machining simulation. The improved FE model was validated with experimental results to test the authenticity and the simulation outcome has an acceptable agreement with experimental results. The success of the developed model establishes a platform for MMC machining simulation and helps to comprehend the machinability characteristics of Al-TiC MMCs for productive improvement.

TABLE OF CONTENTS

CERTIFICATE i
ACKNOWLEDGEMENTS iii
ABSTRACT viii
TABLE OF CONTENTS xii
LIST OF TABLES xvi
LIST OF FIGURES xix
Chapter 1 Introduction 1
1.1 Introduction 1
1.2 Research motivation and scope 4
1.3 Objectives of the current research work 6
1.4 Thesis outline 7
Chapter 2 Literature Survey 11
2.1 Introduction 11
2.2 Processing of Al-MMCs 12
2.2.1 Solid phase process 12
2.2.2 Two phase processes 13
2.2.3 Liquid phase process 14
2.3 Machinability analysis of Al-MMCs 19
2.3.1 Influence of cutting parameters 20
2.3.2 Influence of cutting tool 24
2.3.3 Influence of cutting environments 25
2.4 Statistical tools for modelling and optimization 30
2.5 FEM of machining metal matrix composites 31
2.6 Identified gaps in the literature and proposed solution 35
2.7 Summary 36
Chapter 3 Processing of Al-TiC_p MMCs and its Characterization 37
3.1 Introduction 37
3.2 Development of stir casting setup 38
3.2.1 Matrix and reinforcement material 40
3.2.2 Production of Al-TiC_p composites 41

3.2.3 Characterization analysis of MMCs....43
3.3 Results and discussion....47
3.3.1 X ray diffraction analysis....47
3.3.2 Microstructural analysis of Al-TiC_p composites....49
3.3.3 Analysis of microhardness....51
3.3.4 Analysis of density....53
3.3.5 Analysis of tensile test....55
3.4 Summary....57
Chapter 4 Design, Development and Evaluation of Atomized Liquid Nitrogen Spray System....59
4.1 Introduction....59
4.2 Methodology....60
4.2.1 Design and development of Atomized Liquid Nitrogen (ALN) spray system....61
4.2.2 Evaluation of Argon to Liquid Nitrogen mass Ratio (ALNR)....64
4.2.3 Examination of spray characteristics....65
4.2.4 Evaluation of cryogenically chilled argon gas and droplet temperature....66
4.2.5 Machining tests....67
4.3 Results and discussion....69
4.3.1 Argon to Liquid Nitrogen mass Ratio (ALNR)....70
4.3.2 Spray characteristics analysis....74
4.3.3 Cryogenically chilled argon gas temperature and droplet temperature....80
4.3.4 Machining performance....81
4.4 Summary....85
Chapter 5 Tribological Behaviour of Al TiC_p MMCs....87
5.1 Introduction....87
5.2 Experimental details....88
5.2.1 Linear wear test....89
5.2.2 Sliding wear test....90
5.3 Results and discussion....93
5.3.1 Linear wear test....93
5.3.2 Sliding wear test....95

5.3.3 Analysis of worn surface using metallurgical microscope 99
5.3.4 Wear mechanism 100
5.3.5 Microscopic observation of wear debris 101
5.4 Summary 102
Chapter 6 Machinability Aspects of Turning Al-TiC$_p$ MMCs 103
6.1 Introduction 103
6.2 Experimental details 104
6.2.1 Design of experiments 107
6.2.2 Cutting tool 108
6.2.3 Selection of environmental conditions 109
6.2.4 Cutting forces 109
6.2.5 Surface roughness 110
6.2.6 Tool wear 111
6.3 Results and discussion 112
6.3.1 Analysis of cutting force 112
6.3.2 Analysis of surface quality 118
6.3.3 Analysis of tool performance 127
6.3.4 Analysis of chip formation 138
6.4 Summary 142
Chapter 7 Statistical Analysis and Optimization of Machining Parameters during Turning of Al-TiC MMCs 144
7.1 Introduction 144
7.2 Methodology 145
7.2.1 Analysis of experimental results 145
7.2.2 Modeling using Response Surface Methodology (RSM) 146
7.2.3 Optimization using Genetic Algorithm (GA) 147
7.3 Results and discussion 152
7.3.1 Statistical analysis 152
7.3.2 Optimization using GA 177
7.4 Summary 191
Chapter 8 Finite Element Modelling of Machining Al-TiC$_p$ MMCs 193
8.1 Introduction 193
8.2 Methodology 194
8.2.1 Workpiece and tool modeling (Part module) 195

8.2.2 Material flow modeling (Properties module)....196
8.2.3 Material flow....196
8.2.4 Chip separation criteria....197
8.2.5 Damage evolution....198
8.2.6 Explicit dynamic analysis (Step module)....199
8.2.7 Tool chip interface modeling (Interaction module)....200
8.2.8 Boundary condition modeling (Load module)....202
8.2.9 Meshing (Mesh module)....202
8.2.10 Analysis (Job module)....203
8.2.11 Post processing (Visualization module)....203
8.2.12 Machining experiments....204
8.3 Results and discussion....205
8.3.1 Phase-I: Analysis of plastic deformation of matrix with respect to particle distribution....205
8.3.2 Phase-II: Performance under different cutting conditions....212
8.3.3 Phase-III Cryogenic machining based on FE approach....218
8.4 Summary....228
Chapter 9 Conclusions and Future work....230
9.1 Summary....230
9.2 Conclusions....230
9.3 Future scope....238
REFERENCES....240
APPENDIX - A....255
APPENDIX - B....287
APPENDIX - C....323
LIST OF PUBLICATIONS AND CONFERENCES....327
BIOGRAPHY OF THE CANDIDATE....329
BIOGRAPHY OF THE SUPERVISOR....330

LIST OF TABLES

Table No.	Title	Page No.
Table 3.1	Work material details.	40
Table 3.2	Grain size before and after particle addition.	50
Table 3.3	Composite experimental density (g/cm^3).	53
Table 3.4	Composite density (g/cm^3), volume fraction and yields.	54
Table 4.1	Spray parameters.	68
Table 4.2	Machining conditions for finding optimum feeding pressure.	83
Table 4.3	Machining conditions for finding optimum impingement angle and spray distance.	84
Table 6.1	Process variables and their levels.	107
Table 7.1	Significance level of cutting parameters on machinability performance of characteristics.	154
Table 7.2.	Statistical inference for cutting force under different machining environments.	154
Table. 7.3	Output values of responses from GA program with respect to input machining parameters.	182
Table 7.4	Optimum value of machining parameters predicted by GA correspondent to minimized responses.	184
Table 7.5	Optimal combinations of machining parameters for machining of Al-TiC_p composites under ALN and CCA gas assisted machining.	189
Table 7.6	Optimal combinations of machining parameters for machining of Al-TiC_p composites under wet and dry machining.	190
Table 8.1	Thermal and mechanical properties of the workpiece and the cutting tool materials.	196
Table 8.2	Johnson-Cook material properties for Al-6061 aluminum matrix.	197
Table 8.3	Johnson-Cook failure constants.	198
Table 8.4	Experimental settings and conditions.	204

Table 8.5	Percentage differences between experimental and simulated results for machining of Al-TiC_p composites at different cutting condition.	212
Table A.1	Specifications of HMT PTC 200 CNC lathe machine.	255
Table A.2	Box-Behnken design for experimentation.	256
Table A.3	Specifications of 3-axis piezoelectric lathe tool dynamometer.	257
Table A.4	Specifications of Surtronic S25 surface profilometer.	258
Table A.5	Specifications of Olympus STM 6 optical microscope.	259
Table B.1	Sequential of adequate model sum of squares for cutting force.	287
Table B.2	Lack of fit tests for cutting force.	288
Table B.3	Model summary statistics for cutting force.	289
Table B.4	Sequential of adequate model sum of squares for surface roughness.	290
Table B.5	Lack of fit tests for surface roughness.	291
Table B.6	Model summary statistics for surface roughness.	292
Table B.7	Sequential of adequate model sum of squares for tool wear.	293
Table B.8	Lack of fit tests for tool wear.	294
Table B.9	Model summary statistics for tool wear.	295
Table B.10	ANOVA for cutting force under ALN spray assisted machining condition.	296
Table B.11	ANOVA for cutting force under CCA gas assisted machining condition.	297
Table B.12	ANOVA for cutting force under wet machining condition.	298
Table B.13	ANOVA for cutting force under dry machining condition.	299
Table B.14	ANOVA for surface roughness under ALN spray assisted machining condition.	300
Table B.15	ANOVA for surface roughness under CCA gas assisted machining condition.	301
Table B.16	ANOVA for surface roughness under wet machining condition.	302
Table B.17	ANOVA for surface roughness under dry machining condition.	303
Table B.18	ANOVA for tool wear under ALN spray assisted machining condition.	304

Table B.19	ANOVA for tool wear under CCA gas assisted machining condition.	305
Table B.20	ANOVA for tool wear under wet machining condition.	306
Table B.21	ANOVA for tool wear under dry machining condition.	307
Table B.22	Optimum values of machining conditions predicted by GA for corresponding minimum value of cutting force under ALN spray and CCA gas assisted machining.	317
Table B.23	Optimum values of machining conditions predicted by GA for corresponding minimum value of cutting force under wet and dry machining.	318
Table B.24	Optimum values of machining conditions predicted by GA for corresponding minimum value of surface roughness under ALN spray and CCA gas assisted machining.	319
Table B.25	Optimum values of machining conditions predicted by GA for corresponding minimum value of surface roughness under wet and dry machining.	320
Table B.26	Optimum values of machining conditions predicted by GA for corresponding minimum value of tool wear under ALN and CCA gas assisted machining	321
Table B.27	Optimum values of machining conditions predicted by GA for corresponding minimum value of tool wear under wet and dry machining.	322

LIST OF FIGURES

Fig. No.	Title	Page No
Fig. 1.1	Structure of thesis.	10
Fig. 2.1.	Micro mechanism of reaction synthesis TiC.	14
Fig. 2.2.	Optical micrographs of powder blends processed at (a) 700°C (b) 800°C (c) 900°C (d) 1000°C.	16
Fig. 2.3.	Fish bone diagram showing the influence of cutting parameters on machining performance parameters.	20
Fig. 2.4	Techniques to deliver Liquid nitrogen into the machining zone (a) Hong et al [19]; (b) Venugopal et al. [17]; (c) Ahmed et al. [16]; (d) Bermingham et al. [98]; (e) Pusavec et al. [23]; (f) Dhananchezian et al. [99].	28
Fig. 3.1.	Schematic design of stir casting facility used for the production of Al–TiC_p composites.	39
Fig. 3.2.	Process flow chart of stir casting technique for Al-TiC_p composites production.	41
Fig. 3.3.	Photographic image of developed stir casting facility.	42
Fig. 3.4.	X-ray diffractometer.	44
Fig. 3.5.	Microscope integrated with camera and measuring software setup.	45
Fig. 3.6.	Micro Vickers hardness test rig.	45
Fig. 3.7.	Density measuring setup.	46
Fig. 3.8.	Universal testing machine.	47
Fig. 3.9.	XRD pattern (a) Non-reinforced Al; (b) Al - 5wt%TiC_p (c) Al - 10wt%TiC_p.	48
Fig. 3.10.	Microscopic images of particle distribution in Al-TiC_p composites.	49
Fig. 3.11.	Microscopic image of segregated grain structure for (a) Non-reinforced Al, (b) Al-5wt%TiC_p castings.	50
Fig. 3.12.	EDX results of Al-5wt%TiC_p composites.	51
Fig. 3.13.	Microhardness of casted Al-TiC_p composite.	52
Fig. 3.14.	Density of casted composite.	54

Fig. 3.15.	Strain Vs strain of casted composites.	55
Fig. 3.16.	Variation of tensile properties of the composites with the TiC particle content at room temperature.	56
Fig. 3.17.	Fracture morphology of the tensile tested specimens.	57
Fig. 4.1.	Schematic view of atomized liquid nitrogen spray system.	61
Fig. 4.2.	Cross-sectional view of proposed nozzle unit. (All dimensions are in mm.)	63
Fig. 4.3.	Schematic (a) Arrangement of fluid flow through nozzle unit and (b) Photographic view at the nozzle unit.	64
Fig. 4.4.	Schematic view of spray characterization test rig.	66
Fig. 4.5.	Droplet temperature measurement test rig.	67
Fig. 4.6.	Arrangement of spray impingement angle w.r.t to cutting tool at (a) 0°and (b) 30°.	68
Fig. 4.7	Variation of mass flow rate of CCA gas and ALNR with supply pressure.	71
Fig. 4.8.	The measured value of LN_2 mass flow rate and air pressure with ALNR.	72
Fig. 4.9.	Variation of discharge coefficient with ALNR.	73
Fig. 4.10.	Observations of a spray generated by developed nozzle.	74
Fig. 4.11.	Flow in the vicinity of the nozzle (a) 0.5 bar (b) 1 bar (c) 2 bar (d) 3 bar (e) 4 bar.	75
Fig. 4.12.	The variation of spray angle as a function of ALNR.	77
Fig. 4.13.	Variation of velocity as a function of ALNR at various distances.	78
Fig. 4.14.	Droplets image acquired for 150 mm downstream from discharge orifice.	79
Fig. 4.15.	Variation of SMD as a function of ALNR at various distances.	79
Fig. 4.16.	Variation of temperature as a function of ALNR at various distances.	80
Fig. 4.17.	Effect of machinability performance parameters with respect feeding Pressure.	83
Fig. 4.18.	Effect of variation in spray impingement angle and spray distance on tool wear and surface roughness.	85

Fig. 5.1.	Schematic view of linear wear test.	89
Fig. 5.2.	Block diagram of sliding wear test setup.	90
Fig. 5.3.	Schematic view of nozzle setup for atomized cryogenic tribometer system.	91
Fig. 5.4.	(a) Traction force with a constant load of 25N under different environments. (b) Average friction coefficient (vs) load.	94
Fig. 5.5.	Variation of apparent friction coefficient: (a) 50 m/min; (b) 150 m/min; (c) 250 m/min.	96
Fig. 5.6.	Variation of wear rate with respect to load: (a) 50 m/min; (b) 150 m/min; (c) 250 m/min.	98
Fig. 5.7.	Microscopic images of wear tracks of Al-TiC_p at a load of 5 N and a sliding velocity of 150 m/min under (a) Dry (b) LN_2 (c) CCA gas.	100
Fig. 5.8.	Microscopic images of wear debris of Al-TiC_p at a load of 5 N and sliding velocity of 150 m/min under (a) Dry (b) LN_2 (c) CCA gas.	101
Fig. 6.1.	Photograph of complete arrangement of atomized liquid nitrogen spray system.	105
Fig. 6.2.	Three-axis piezoelectric lathe tool dynamometer.	110
Fig. 6.3.	Surface profilometer to measure surface roughness value.	111
Fig. 6.4.	Optical microscope (Olympus STM 6) to measure flank wear value.	111
Fig. 6.5.	Variation of cutting force at cutting speed of 50 m/min for different rake angle with various levels of nose radii, approach angles and feed under dry, wet, CCA gas and ALN spray assisted machining conditions (cryo).	113
Fig. 6.6.	Variation of cutting force at cutting speed of 100 m/min for different rake angle with various levels of nose radii, approach angles and feed under dry, wet, CCA gas and ALN spray assisted machining conditions (cryo).	114
Fig. 6.7.	Variation of cutting force at cutting speed of 150 m/min for different rake angle with various levels of nose radii, approach	115

angles and feed under dry, wet, CCA gas and ALN spray assisted machining conditions (cryo).

Fig. 6.8. Variation of surface roughness at cutting speed of 50 m/min for different rake angle with various levels of nose radii, approach angles and feed under dry, wet, CCA gas and ALN spray assisted machining conditions (cryo). 119

Fig. 6.9. Variation of surface roughness at cutting speed of 100 m/min for different rake angle with various levels of nose radii, approach angles and feed under dry, wet, CCA gas and ALN spray assisted machining conditions (cryo). 120

Fig. 6.10. Variation of surface roughness at cutting speed of 150 m/min for different rake angle with various levels of nose radii, approach angles and feed under dry, wet, CCA gas and ALN spray assisted machining conditions (cryo). 121

Fig. 6.11. (a) Micro cracks on Al-5wt%TiC_p MMC; (b) Voids around the TiC particles (c) Pulled-out TiC particles. 125

Fig. 6.12. Microscopic images of surface topography of machined Al-5wt%TiC_p MMC under (a) ALN spray (Cryo spray) (b) CCA
(c) Dry (d) Wet conditions. 126

Fig. 6.13. Variation of tool wear at cutting speed of 50 m/min for different rake angle with various levels of nose radii, approach angles and feed under dry, wet, CCA gas and ALN spray assisted machining conditions (cryo). 128

Fig. 6.14. Variation of tool wear at cutting speed of 100 m/min for different rake angle with various levels of nose radii, approach angles and feed under dry, wet, CCA gas and ALN spray assisted machining conditions (cryo). 129

Fig. 6.15. Variation of tool wear at cutting speed of 150 m/min for different rake angle with various levels of nose radii, approach angles and feed under dry, wet, CCA gas and ALN spray assisted machining conditions (cryo). 130

Fig. 6.16. SEM observation of worn tool under 16° rake angle 1.2 mm nose radius and 90° approach angle at (a) Dry (b) Wet (c) CCA gas and (d) ALN spray assisted machining. 135
Fig. 6.17. Microscopic observation of worn tool under150 m/min cutting speed, 0.2 mm/rev feed 1.2mm nose radius and 90° approach angle at (a) 0° (b) 4° (c) 8° and (d) 16° rake angles under dry machining conditions. 136
Fig. 6.18. SEM observation of worn tool surface and type of wear mechanism observed during dry condition. 137
Fig. 6.19. Comparison of chip samples formed during machining of Al-5wt%TiC_P under various environments at 100 m/min cutting speed, 0.1 mm/rev feed, 8° rake angle and 1.2 mm nose radius. 139
Fig. 6.20. Comparison of chip samples formed during machining of Al-5wt%TiC_p under various environments at 100 m/min cutting speed, 0.1 mm/rev feed, 30° approach angle and 8° rake angle. 139
Fig. 6.21. Comparison of chip samples formed during machining of Al-5wt%TiC_p under various environments at 100 m/min cutting speed, 0.1 mm/rev feed, 30° approach angle and 0.4 nose radius. 140
Fig. 6.22. Microscopic image of chip surface formed during machining of Al- 5wt%TiC_p under (a) ALN spray (b) CCA gas (c) Wet (d) Dry machining conditions. 142
Fig. 7.1. The flowchart of a simple GA. 149
Fig. 7.2. Percentage contribution of cutting parameter on cutting force in selected model (a) ALN spray (b) CCA gas (c) Wet and (d) Dry machining. 155
Fig. 7.3. Percentage contribution cutting parameter on surface roughness in selected model (a) ALN spray (b) CCA gas (c) Wet and (d) Dry machining. 157

Fig. 7.4. Percentage contribution of cutting parameters on tool wear in selected in the model (a) ALN spray (b) CCA gas (c) Wet and (d) Dry machining. 159
Fig. 7.5. Normal probability plot of residuals (a-d) and Predicted vs. actual values (i-iv) for cutting force under ALN (cryo) [a & i], CCA gas [b & ii], wet [c & iii] and dry [d & iv]. 161
Fig. 7.6. Perturbation plot shows the effect of cutting process parameters on cutting force (CF). 163
Fig. 7.7. Combined effect of approach angle and rake angle on cutting force (CF) at a cutting speed of 100 m/min, feed of 0.15 mm/rev and nose radius of 0.8 mm under (a) ALN spray (cryo) (b) CCA gas (c) Wet machining (d) Dry machining conditions. 164
Fig. 7.8. Combined effect of rake angle and nose radius on cutting force (CF) at a cutting speed of 100 m/min, feed of 0.15 mm/rev and approach angle of 60° under (a) ALN spray (cryo) (b) CCA gas (c) Wet machining (d) Dry machining conditions. 165
Fig. 7.9. Combined effect of approach angle and nose radius on cutting force (CF) at a speed of 100 m/min, feed of 0.15 mm/rev and rake angle of 8° under (a) ALN spray (cryo) (b) CCA gas (c) Wet machining (d) Dry machining conditions. 166
Fig. 7.10. Combined effect of cutting speed and feed on cutting force (CF) at rake angle of 8°, nose radius of 0.8 mm and approach angle of 60° under (a) ALN spray (cryo) (b) CCA gas (c) Wet machining (d) Dry machining conditions. 167
Fig. 7.11. Perturbation plot shows the effect of cutting parameters on surface roughness (SR). 168
Fig. 7.12. Combined effect of rake angle and nose radius on surface roughness (SR) at a cutting speed of 100 m/min, feed of 0.15 mm/rev and approach angle of 60° under (a) ALN spray (cryo) (b) CCA gas (c) Wet machining (d) Dry machining conditions. 169

Fig. 7.13. Combined effect of approach angle and nose radius on surface roughness (SR) at a cutting speed of 100 m/min, feed of 0.15 mm/rev and rake angle of 8° under (a) ALN spray (cryo) (b) CCA gas (c) Wet machining (d) Dry machining conditions. 170

Fig. 7.14. Combined effect approach angle and rake angle on surface roughness (SR) at a cutting speed of 100 m/min, feed of 0.15mm/rev and nose radius of 0.8 mm under (a) ALN spray (cryo) (b) CCA gas (c) Wet machining (d) Dry machining conditions. 171

Fig. 7.15. combined effect of cutting speed and feed on surface roughness (SR) at rake angle of 8°, nose radius of 0.8 mm and approach angle of 60° under (a) ALN spray (cryo) (b) CCA gas (c) Wet machining (d) Dry machining conditions. 172

Fig. 7.16. Perturbation plot shows the effect of cutting process parameters on tool wear (TW). 173

Fig. 7.17. Combined effect approach angle and rake angle on tool wear (TW) at a cutting speed of 100 m/min, feed of 0.15 mm/rev and nose radius of 0.8 mm under (a) ALN spray (cryo) (b) CCA gas (c) Wet machining (d) Dry machining conditions. 174

Fig. 7.18. Combined effect of rake angle and nose radius on tool wear (TW) at a cutting speed of 100 m/min, feed of 0.15 mm/rev and approach angle of 60° under (a) ALN spray (cryo) (b) CCA gas (c) Wet machining (d) Dry machining conditions. 175

Fig. 7.19. combined effect of approach angle and nose radius on tool wear at a cutting speed of 100 m/min, feed of 0.15 mm/rev and rake angle of 8° under (a) ALN spray (cryo) (b) CCA gas (c) Wet machining (d) Dry machining conditions. 176

Fig. 7.20. combined effect of cutting speed and feed on tool wear at rake angle of 8°, nose radius of 0.8 mm and approach angle of 60° under (a) ALN spray (cryo) (b) CCA gas (c) Wet machining (d) Dry machining conditions. 177

Fig. 7.21. Plot function of cutting force for best fitness under (a) ALN spray (b) CCA gas (C) Wet machining and (d) Dry machining. 184
Fig. 7.22. Plot function of surface roughness for best fitness under (a) ALN spray (b) CCA gas (C) Wet machining and (d) Dry machining. 185
Fig. 7.23. Plot function of tool wear for best fitness under (a) ALN spray (b) CCA gas (C) Wet machining and (d) Dry machining. 186
Fig. 7.24. 3D paretor front graph for cutting force surface roughness and tool wear under (a) ALN spray, (b) CCA gas, (c) Wet and (d) Dry machining condition. 188
Fig. 8.1. Model of MMCs and its dimensions used for cutting simulations. 195
Fig. 8.2. Contact interaction between tool and workpiece. 200
Fig. 8.3. Boundary condition setup for machining of MMCs. 202
Fig. 8.4. Initial mesh configurations. 203
Fig. 8.5. FEA modeling of microscale MMC workpiece with different strategies in arrangement of particles. 205
Fig. 8.6. Stress distribution at first step during machining of Al-TiC_p MMCs at cutting speed (V_c) = 50 m/min, uncut chip thickness (f) = 0.1 mm, rake angle (γ) = 0°. 206
Fig. 8.7. Deterioration of mesh quality around the particles during machining of Al-TiC_p MMCs at cutting speed (V_c) = 50 m/min, uncut chip thickness (f) = 0.1 mm rake angle (γ) = 0°. 207
Fig. 8.8. Equivalent plastic strain during Al-TiC_p MMC cutting (Al 6061/5 wt% 20 μm TiC_p, cutting speed (V_c) = 50 m/min, rake angle (γ) = 0°, uncut chip thickness (f) = 0.1 mm. 207
Fig. 8.9. Stress distribution, chip topography and thickness and shear angle measurement during machining Al-TiC_p MMC at cutting speed (V_c) = 50 m/min, rake angle (γ) = 0°, uncut chip thickness (f) = 0.1 mm. 208
Fig. 8.10. Comparison between experimental and simulated cutting forces when machining the Al-TiC_p MMC with cutting

speed (V_c) = 50 m/min, rake angle (γ) = 0°, uncut chip thickness (f) = 0.1 mm. 209

Fig. 8.11. Comparison between experimental and simulated temperature when machining the Al-TiC_p MMC with cutting speed (Vc) = 50 m/min, uncut chip thickness (f) = 0.1 mm, rake angle (γ) = 0°. 210

Fig. 8.12. Comparison of simulated with experiment at Test-I. 213

Fig. 8.13. Effect of uncut chip thickness during machining of Al-TiC_p MMCs at a cutting speed (V_c) of 50 m/min and a rake angle (γ) of 0°. 214

Fig. 8.14. Effect of rake angle during machining of Al-TiC_p MMCs at cutting speed (V_c) of 50 m/min and uncut chip thickness (f) of 0.1mm. 216

Fig. 8.15. Effect of cutting speed during machining of Al-TiC_p MMCs at rake angle (γ) of 16° and uncut chip thickness (f) of 0.2 mm. 217

Fig. 8.16. Shows the thermal boundary conditions considered for cryogenic machining. 219

Fig. 8.17. Effect of rake angle during machining of Al-TiC_p MMCs at cutting speed (V_c) of 50 m/min and uncut chip thickness (f) of 0.1mm. 220

Fig. 8.18. Comparison of temperature obtained at different rake angle by the use of present model and the experimental results in both cryogenic and dry machining conditions. 221

Fig. 8.19. Comparison of cutting force obtained at different rake angle by the use of present model and the experimental results in both cryogenic and dry machining conditions. 222

Fig. 8.20. Effect of cutting speed during machining of Al-TiC_p MMCs at rake angle (γ) of 16° and uncut chip thickness (f) of 0.2mm. 223

Fig. 8.21. Comparison of the temperature obtained at different cutting speed by the use of present model and the experimental results in both cryogenic and dry machining conditions. 224

Fig. 8.22 Comparison of the cutting force obtained at different cutting speed by the use of present model and the experimental results in both cryogenic and dry machining conditions. 225

Fig. 8.23. Effect of uncut chip thickness during machining of Al-TiC_p MMCs at a speed (V_c) of 50 m/min and rake angle (γ) of 0°. 226

Fig. 8.24. Comparison of the temperature obtained at different uncut chip thickness by the use of present model and the experimental results in both cryogenic and dry machining conditions. 227

Fig. 8.25. Comparison of the cutting force obtained at different uncut chip thickness by the use of present model and the experimental results in both cryogenic and dry machining conditions. 227

Fig. A.1. Variation of cutting force at cutting speed of 50 m/min and feed of 0.1 mm/rev for different rake angle with various levels of nose radii and approach angle under dry, wet, CCA gas and ALN spray machining conditions (cryo). 260

Fig. A.2. Variation of cutting force at cutting speed of 50 m/min and feed of 0.15 mm/rev for different rake angle with various levels of nose radii and approach angles under dry, wet, CCA gas and ALN spray assisted machining conditions(cryo). 261

Fig. A.3. Variation of cutting force at cutting speed of 50 m/min and feed of 0.2 mm/rev for different rake angle with various levels of nose radii and approach angles under dry, wet, CCA gas and ALN spray assisted machining conditions(cryo). 262

Fig. A.4. Variation of cutting force at cutting speed of 100 m/min and feed of 0.1 mm/rev for different rake angle with various levels of nose radii and approach angles under dry, wet, CCA gas and ALN spray assisted machining conditions(cryo). 263

Fig. A.5. Variation of cutting force at cutting speed of 100 m/min and feed of 0.15 mm/rev for different rake angle with various levels of nose radii and approach angles under dry, wet, CCA gas and ALN spray assisted machining conditions(cryo). 264

Fig. A.6. Variation of cutting force at cutting speed of 100 m/min and feed of 0.2 mm/rev for different rake angle with various levels of nose radii and approach angles under dry, wet, CCA gas and ALN spray assisted machining conditions (cryo). 265

Fig. A.7. Variation of cutting force at cutting speed of 150 m/min and feed of 0.1 mm/rev for different rake angle with various levels of nose radii and approach angles under dry, wet, CCA gas and ALN spray assisted machining conditions (cryo). 266

Fig. A.8. Variation of cutting force at cutting speed of 150 m/min and feed of 0.15 mm/rev for different rake angle with various levels of nose radii and approach angles under dry, wet, CCA gas and ALN spray assisted machining conditions (cryo). 267

Fig. A.9. Variation of cutting force at cutting speed of 150 m/min and feed of 0.2 mm/rev for different rake angle with various levels of nose radii and approach angles under dry, wet, CCA gas and ALN spray assisted machining conditions (cryo). 268

Fig. A.10. Variation of Surface roughness at cutting speed of 50 m/min and feed of 0.1 mm/rev for different rake angle with various levels of nose radii and approach angles under dry, wet, CCA gas and ALN spray assisted machining conditions (cryo). 269

Fig. A.11. Variation of Surface roughness at cutting speed of 50 m/min and feed of 0.15 mm/rev for different rake angle with various levels of nose radii and approach angles under dry, wet, CCA gas and ALN spray assisted machining conditions (cryo). 270

Fig. A.12. Variation of Surface roughness at cutting speed of 50 m/min and feed of 0.2 mm/rev for different rake angle with various levels of nose radii and approach angles under dry, wet, CCA gas and ALN spray assisted machining conditions(cryo). 271

Fig. A.13. Variation of Surface roughness at cutting speed of 100 m/min and feed of 0.1 mm/rev for different rake angle with various levels of nose radii and approach angles under dry, wet, CCA gas and ALN spray assisted machining conditions (cryo). 272

Fig. A.14. Variation of Surface roughness at cutting speed of 100 m/min and feed of 0.15 mm/rev for different rake angle with various levels of nose radii and approach angles under dry, wet, CCA gas and ALN spray assisted machining conditions (cryo). 273
Fig. A.15. Variation of Surface roughness at cutting speed of 100 m/min and feed of 0.2 mm/rev for different rake angle with various levels of nose radii and approach angles under dry, wet, CCA gas and ALN spray assisted machining conditions (cryo). 274
Fig. A.16. Variation of Surface roughness at cutting speed of 150 m/min and feed of 0.1 mm/rev for different rake angle with various levels of nose radii and approach angles under dry, wet, CCA gas and ALN spray assisted machining conditions (cryo). 275
Fig. A.17. Variation of Surface roughness at cutting speed of 150 m/min and feed of 0.15 mm/rev for different rake angle with various levels of nose radii and approach angles under dry, wet, CCA gas and ALN spray assisted machining conditions (cryo). 276
Fig. A.18. Variation of Surface roughness at cutting speed of 150 m/min and feed of 0.2 mm/rev for different rake angle with various levels of nose radii and approach angles under dry, wet, CCA gas and ALN spray assisted machining conditions (cryo). 277
Fig. A.19. Variation of tool wear at cutting speed of 50 m/min and feed of 0.1 mm/rev for different rake angle with various levels of nose radii and approach angles under dry, wet, CCA gas and ALN spray assisted machining conditions (cryo). 278
Fig. A.20. Variation of tool wear at cutting speed of 50 m/min and feed of 0.15 mm/rev for different rake angle with various levels of nose radii and approach angles under dry, wet, CCA gas and ALN spray assisted machining conditions (cryo). 279
Fig. A.21. Variation of tool wear at cutting speed of 50 m/min and feed of 0.2 mm/rev for different rake angle with various levels of nose radii and approach angles under dry, wet, CCA gas and ALN spray assisted machining conditions (cryo). 280

Fig. A.22. Variation of tool wear at cutting speed of 100 m/min and feed of 0.1 mm/rev for different rake angle with various levels of nose radii and approach angles under dry, wet, CCA gas and ALN spray assisted machining conditions (cryo). 281
Fig. A.23. Variation of tool wear at cutting speed of 100 m/min and feed of 0.15 mm/rev for different rake angle with various levels of nose radii and approach angles under dry, wet, CCA gas and ALN spray assisted machining conditions (cryo). 282
Fig. A.24. Variation of tool wear at cutting speed of 100 m/min and feed of 0.2 mm/rev for different rake angle with various levels of nose radii and approach angles under dry, wet, CCA gas and ALN spray assisted machining conditions (cryo). 283
Fig. A.25. Variation of tool wear at cutting speed of 150 m/min and feed of 0.1 mm/rev for different rake angle with various levels of nose radii and approach angles under dry, wet, CCA gas and ALN spray assisted machining conditions (cryo). 284
Fig. A.26. Variation of tool wear at cutting speed of 150 m/min and feed of 0.15 mm/rev for different rake angle with various levels of nose radii and approach angles under dry, wet, CCA gas and ALN spray assisted machining conditions (cryo). 285
Fig. A.27. Variation of tool wear at cutting speed of 150 m/min and feed of 0.2 mm/rev for different rake angle with various levels of nose radii and approach angles under dry, wet, CCA gas and ALN spray assisted machining conditions (cryo). 286
Fig. B.1. Normal probability plot of residuals for cutting force under different machining conditions. 311
Fig. B.2. Predicted vs. actual values for cutting force under different machining conditions. 312
Fig. B.3. Normal probability plot of residuals for surface roughness under different machining conditions. 313
Fig. B.4. Predicted vs. actual values for surface roughness under different machining conditions. 314

Fig. B.5. Normal probability plot of residuals for tool wear under different machining conditions. 315
Fig. B.6. Predicted vs actual values for tool wear under different machining conditions. 316
Fig. C.1. Comparison of simulated with experiment at Test-II. 323
Fig. C.2. Comparison of simulated with experiment at Test-III. 323
Fig. C.3. Comparison of simulated with experiment at Test-IV. 324
Fig. C.4. Comparison of simulated with experiment at Test-V. 324
Fig. C.5. Comparison of simulated with experiment at Test-VI. 325
Fig. C.6. Comparison of simulated data with experimental data at Test-VII. 325
Fig. C.7. Comparison of simulated with experiment at Test-VIII. 326
Fig. C.8. Comparison of simulated with experiment at Test-I.

LIST OF ABBREVIATIONS

Abbreviation	*Description*
2D	Two Dimensions
ACF	Atomized Cutting Fluid
Al	Aluminium
ALE	Arbitrary Lagrangian Eulerian
ALNR	Argon to Liquid Nitrogen Mass Ratio
AMC	Aluminum Matrix Composite
ANN	Artificial Neural Network
ANOVA	Analysis of Variance
BBD	Box-Behnken design
BUE	Built-Up-Edge
CCA	Cryogenically Chilled Argon
CCD	Central Composite Design
CF	Cutting force
CFM	Cutting Force Measurement
CLA	Center Line average
CNC	Computer Numerical Control
DAQ	Data Acquisition
DoE	Design of Experiments
EDM	Electric Discharge machining
EDX	Energy-dispersive X-ray spectroscopy
EFM	Finite Element Method
EHM	Equivalent Homogenous Material
FE	Finite Element
fps	Frames per sec
FSP	Friction Stir Processing
GA	Genetic Algorithm
J-C	Johnson Cook
LN_2	Liquid Nitrogen
LVDT	Linear Variable Differential Transformer
MD	Mean Diameter

MMCs	Metal Matrix Composites
PCBN	Polycrystalline Cubic Boron Nitride
PCD	Poly-Crystalline Diamond
PID	Proportional–Integral–Derivative
PIV	Particle Image Velocimetry
PMMC	Particulate Metal Matrix Composites
PVD	Physical Vapor Deposition
RSM	Response Surface Methodology
SEM	Scanning Electron Microscope
SiC	Silicon Carbide
SR	Surface Roughness
STM	Stereo Microscope
TiC_p	Titanium Carbide particulate
TW	Tool wear
wt%	Weight percentage
XRD	X-ray diffraction

LIST OF SYMBOLS

Symbol	*Definition*	*Units*
A, B, C, m and n	Material constants for J-C model	
A_{glo}	Area of liquid discharge orifice	mm^2
A_{go}	Area of the Argon gas discharge holes	mm^2
A_{lo}	Area of liquid orifices	mm^2
a_p	Depth of Cut	mm
A_t	True contact area	mm^2
b	Equivalent length	m
C_D	Discharge coefficient	
C_p	Specific heat capacity	J/kg˚C
D	Damage parameter	
D_1, D_2, D_3, D_4, *and* D_5	Material damage constants	
d_{gi}	Diameter air inlet port	mm
d_{glo}	Diameter of discharge orifice	mm
d_{go}	Diameter aerated port	mm
d_{li}	Diameter liquid inlet port	mm
d_{lo}	Diameter liquid injected port	mm
d_{lo}	Diameter of liquid orifices	mm
D_s	Sliding distance	mm
E	Young's modulus	GPa
F	Frictional force	N
F_c	Cutting force	N
F_f	Feed force	N
F_n	Normal force	N
F_t	Tangential force	N
f	Feed	mm/rev
G_f	Fracture energy	J/cm^2
g	Acceleration due to gravity	m/sec^2
h_{cryo}	Cryogenic heat transfer coefficient	$W/(m^2K)$.
K	Thermal conductivity	W/m˚C
K_C	Fracture toughness	$MPa\text{-}m^{1/2}$

K_f	Thermal conductivity of liquid	W/m˚C
L_c	Liquid core	mm
L_e	Length of element	
l_N	Discharge orifice extended length	mm
M_{Ar}	Molecular weight of argon	
M_L	Mass loss	mg
N	Normal load	N
N_0	Natural variable for 0-level	
N_1	Natural variable for 1-level	
N_i	Natural variable for ith level	
P_{CCA}	Feeding pressure	kPa
P_l	Liquid supply pressure	kPa
Q_g	Volumetric air flow rate of gas	m^3/min
Q_l	Volumetric flow rate of liquid	m^3/min
R	Universal gas constant	j/mol/K
R_a	Surface roughness	µm
r_e	Nose radius	mm
T	Temperature	°C
T_g	CCA gas temperature	°C
$\bar{u}^p$	Plastic displacement	mm
$\bar{u}^p{}_f$	Plastic displacement at failure	mm
V_b	Flank wear	µm
V_c	Cutting speed	m/min
V_f	Velocity of liquid	m/sec
v_f	Viscosity	cP
w_m	Weight fraction of matrix	
w_r	Weight fraction of reinforcement	
z	Impingement distance	mm
Greek letters		
µ	Apparent friction coefficient	
ψ	Approach angle	deg
α	Coefficient of thermal expansion	µm.m/˚C
ρ	Density	Kg/m^3

ρ_c	Density of composite	Kg/m^3
P_g	Density of gas	Kg/m^3
ρ_l	Density of liquid	Kg/m^3
ρ_m	Density of matrix	Kg/m^3
ρ_r	Density of reinforcement	Kg/m^3
$\bar{\varepsilon}$	Equivalent plastic strain	
τ_{max}	Equivalent shear stress	MPa
$\bar{\varepsilon}_f$	Equivalent stain at failure	
ρ_{exp}	Experimental density	Kg/m^3
τ_f	Friction stress	MPa
$\theta_s/2$	Half cone angle	deg
θ_m	Impingement angle	deg
λ	Inclination angle	deg
$\Delta\bar{\varepsilon}$	Increment of the equivalent plastic strain	
$\dot{m}_g$	Mass flow rate of gas	Kg/sec
$\dot{m}_l$	Mass flow rate of liquid	Kg/sec
θ_{melt}	Melting temperature of the material	°C
σ_n	Normal stress	MPa
α_o	Orthogonal clearance angle	deg
$\dot{\bar{\varepsilon}}$	Plastic strain rate	
ν	Poisson's ratio	
θ	Process temperature	°C
γ	Rake angle	deg
$\frac{P}{\bar{\sigma}}$	Ratio of pressure stress to von Mises stress	
$\theta_{transition}$	Reference room ambient temperature	°C
$\dot{\bar{\varepsilon}}_0$	Reference strain rate	
τ	Shear strength	MPa
γ_{cl}	Specific weight	kN/m^3
$\bar{\sigma}$	Von Mises stress	MPa
σ_y	Yield stress	MPa

Chapter 1
Introduction

In the current chapter, Section 1.1 presents a brief background to machining of metal matrix composites, the fundamental process of lubrication in machining and the research developments in the field. Motivation for this research work and research scope is explained in Section 1.2. Overall research objectives are presented in Section 1.3. Finally, Section 1.4 provides a complete organization of this dissertation.

1.1 Introduction

Metal Matrix Composites (MMCs) are one of the most advanced and adaptable class of engineering materials that give countless possibilities for the development of unique designs and high-performance products. Over the years, MMCs have replaced the conventional metals and alloys in various applications across manufacturing industries. These engineering materials consist of a hard-ceramic reinforcing phase introduced/created into a relatively softer metal matrix phase. The matrix phase transfers load and supports the integrity of the structure while the reinforcement phase enhances the material properties of the matrix metal. MMCs encompass a broad range of materials, which enable the designers to tailor the material properties by suitably varying the concentration of constituent phases as per the requirements to satisfy the ever-growing demands of manufacturing industries.

MMCs offers exceptional features such as significant strength-weight ratio, higher modulus, stiffness, high wear resistance and impact damage, lower thermal expansion coefficient, and sufficient thermal conductivity. These traits make MMCs an excellent choice for a wide range of applications including defense, aviation, automobile and medical fields. Particulate metal matrix composites (PMMCs) have gained special attention due to their superior ductility and lower anisotropy than reinforced fiber MMCs. Among various

PMMCs, Aluminum metal matrix composites (Al-MMCs) find a large number of application in various specific fields due to its unrivaled properties like high specific strength ratio (strength per unit weight), excellent wear resistance, high thermal conductivity and specific modulus (modulus per unit weight). A few ceramic reinforcements are recognized for Al-MMCs, of which Titanium Carbide (TiC) has received focus owing to its high stiffness, specific strength, thermal stability, hardness, and wear resistance [1-3]. In addition, grain refinement properties of TiC particles (TiC_p) make Al-TiC_p MMCs suitable material for the production of several high performance components in various applications [4, 5].

Two decades of intensive research on Al-TiC_p MMCs has provided new insights on its production, thermo-mechanical [6] and tribological properties [7]. Studies identify Al-TiC_p MMCs as one of the extremely difficult-to-machine materials which restricts their usage despite the various potential advantages they offer. To overcome the challenges encountered during machining of Al-TiC_p MMCs, optimal combination of process parameters need to be determined to achieve the desired tool life, surface finish, and metal removal rate.

During machining, MMCs are subjected to high strain and temperatures due to presence of intermittent reinforcements in matrix. High heat and intense pressure generation in a highly-localized area results in severe edge chipping and plastic deformation via seizure of chips. This ultimately shortens the tool life and affects the surface finish [8]. The direct contact between the particles and the cutting edge and their relative motion on chip direction results in deep grooves on rake and clearance faces of the tool [9]. Two body and three body rupture of tool/chip/workpieces cause tool failure during machining of MMCs. This creates friction between workpiece/cutting tool/chip interfaces leading to high temperature causing poor surface finish, higher cutting forces and built up

edge on the cutting tool. The tool life decreases while the surface finish improves only slightly with an increase in cutting speed [10]. On the other hand, feed tends to have less influence on tool wear but affects the surface integrity significantly. An increase in depth of cut decreases the quality of surface finish and has a stronger effect on tool wear [11]. Since the tool temperature increases with cutting speed, feed and depth of cut, the tool material softens and consequently diffusion wear accelerates.

Coolants are traditionally used to reduce heat generation and friction to minimize the tool wear. Conventional coolants include several disadvantages such as chances of workpiece contamination, enormous disposal cost and environmental hazards. The use of cryogenic coolants is aimed to overcome the aforementioned disadvantages associated with conventional coolants. Efforts on implementation of cryogenic technology in machining started early in 1950's. However, this technique could not gain significant attention in manufacturing industries as the ineffective cryogenic supply unit caused an early evaporation of the cryogenic liquid before it reached the machining zone. This required an excess quantity of cryogenic liquid to be supplied at the machining zone that eventually increased the production cost and hindered the workpiece integrity.

For the purpose of improving machinability of advanced materials, research on effective supply of cryogenic liquid to the machining zone has attained more focus in the recent years [12, 13]. Various cryogenic machining approaches such as i) pre-cooling of tool/workpiece cryogenically [14, 15] ii) Indirect cryogenic cooling[16, 17] iii) Jet based cooling and cryogenic based spraying (by delivering the cryogenic liquid to the tool/chip or tool/work interfaces) have been applied to machining operations [18, 19]. Cooling effect has been observed in all of the three strategies. Cryogenic spray and jet cooling strategies have shown both cooling as well as lubrication effect [20]. These new methods have

demonstrated good efficiency in terms of heat removal from the tool/workpiece interaction zone laying a path for high-productivity machining of Al-TiC_p MMCs.

Adequate knowledge is required on tool/work interface, failure modes and wear mechanisms for successful applications of Al-TiC_p MMCs in manufacturing industries. A laboratory based machining and tribological experimental tests provide quick and accurate prediction of optimal cutting conditions. In order to improve the efficiency and quality of machining process before going for expensive and lengthy experimental trials, it is necessary to model and simulate the metal cutting process by using finite element method (FEM). FEM uses an approach based on science where the entire process can be simulated as well as optimized to understand the physical cutting process variables such as cutting force, cutting temperature, tool wear and to relate the same with practical conditions of machining process. It is clear that a comprehensive and general understanding of MMCs during the machining operation is considered as an asset in achieving the best parameters.

1.2 Research motivation and scope

Due to difficulties encountered during machining, the implementation of Al-TiC_p MMCs in practical application is not translated as expected. While most engineering parts and tools made out of Al-TiC_p MMCs are usually produced using near to the final dimension by various manufacturing techniques, the necessity for machining cannot be eliminated completely. Machining of Al-TiC_p MMCs presents a significant challenge to industries due to the high abrasiveness of the TiC reinforcing particles and its anisotropic and non-homogenous structure. These intermittent TiC particles get removed or fractured due to high cutting temperature and pressure which are forced into rubbing with the cutting tool, thus, greatly damaging the tool surface leading to surplus wear of tool. Fractured TiC particles pass to cutting zone and form indentation, grooves, cracks and voids on machined surface, further triggering two body and three body abrasive wear leading to

premature failure of the tool. This, in turn, creates friction between workpiece-cutting tool/chip interfaces leading to high temperature. This can cause poor surface finish, higher cutting forces and built up edge on the cutting tool further attributing to the larger tool wear.

The negative effects due to tool/workpiece/chip interaction affect can be minimized by using optimal tool geometry, ideal machining parameters and proper lubrication/coolant applications. Conventional coolants have been used as a supplementary choice in order to reduce cutting temperature, formation of built up edge (BUE), flushing of the chip and preventing the tool from re-cutting the abrasive chips and further reducing the friction between tool/chip interfaces. Conventional coolants have no beneficial effect as a proposed alternative in terms of decreased cutting temperature. It can be clearly understood that conventional coolants fail to provide improvement in machinability of MMCs [21, 22]. Moreover, they add to the cost of machining and cause environmental problems.

The global focus is towards achieving sustainable manufacturing in the interest of ecological and environmental safety. To that end, ecofriendly Liquid nitrogen (LN_2) offers an excellent replacement for the traditionally used coolants for the desirable control of cutting temperature and enhancement of the tool life [23]. It also reduces power consumption and friction force, improves dimensional accuracy, surface quality, chip breakability and chip removal required for precision machining [18]. Further, it reduces production cost and time by facilitating high speed machining. Heat generated during machining results in shearing on primary shear plane and friction on tool/chip and tool/workpiece interfaces. This intensely elevates the temperature which is limited to a millimetric area on the face of tool only [15]. Supply of liquid nitrogen in large quantities often cools unwanted area causing a negative effect on characteristics of the work material [24]. Therefore, it is important that liquid nitrogen is applied in selectively identified areas to enhance cooling effect during machining.

The presence of hard TiC particles in Al matrix intensifies the mechanical properties of MMCs and influences the machinability characteristics using traditional machining methods. The main thrust of research in Al-TiC_p MMC has been on their production, properties and physical metallurgy. Focus on the machinability of MMC has been somewhat limited with relatively limited number of published literature available. Therefore, the current research aims to identify the effect of various methods to improve the machinability of Al-TiC_p composites.

1.3 Objectives of the current research work

The primary focus of the current research is to envisage an atomized liquid nitrogen spray assisted machining system for effective and minimum supply of liquid nitrogen into the machining zone based upon the concept that cryogenic air blast atomization processes. Investigations will be carried out to study performance of the developed spray system and to thoroughly analyse the effect of combined tool geometry and cutting conditions to improve the machinability characteristics of Al-TiC_p MMCs. The study is expected to help practising and manufacturing engineers in selecting the optimum range of tool geometry and machining environments for turning of Al-TiC_p MMCs effectively to reduce manufacturing cost. The following specific objectives will be pursued in the foregoing sections of this thesis.

*The **main objectives*** of the proposed study cover the following:

1. Fabrication of Al-TiC_p MMCs through liquid processing route (stir casting process) under inert atmosphere and evaluation of mechanical characteristics of developed composites.
2. To envisage an Atomized Liquid Nitrogen (ALN) spray assisted machining experimental system for effective and minimum supply of liquid nitrogen into the machining zone based upon the concept of cryogenic air blast atomization

processes. Further, determining the optimal flow parameters such as feeding pressure, impingement angle and spray distance.

3. To investigate the lubrication effect of liquid nitrogen and asses the performance of developed ALN spray discharge system in terms of friction and wear characteristics using pin on disc tribometer and comparatively study the efficiency in dry and cryogenic chilled argon (CCA) environment.
4. The present study aims to incorporate three parameters of tool geometry by considering rake angle, approach angle and nose radius along with cutting conditions to get the combined influence of these parameters on surface finish, cutting forces, and tool wear during machining of Al-TiC_p MMCs under ALN spray, CCA gas, wet and dry conditions, so that machining can be made environmental friendly.
5. To find the significance of machining parameters on the machining response using ANOVA and characterize the influence of cutting parameters on machining performance. Development of predictive model using response surface methodology (to develop a predictive capability in order to facilitate effective planning). Further use of Genetic Algorithm (GA) optimization techniques to determine the optimal conditions for machining of Al-TiC_p MMCs.
6. Finite element modelling for machining of MMCs will be developed to simulate and predict accurate chip morphology, cutting force and temperature while machining under varied cutting conditions. The results of finite element analysis will be validated through comparison with experimental data.

1.4 Thesis outline

The *first chapter* of this dissertation provides a background of cryogenic machining and MMCs. The importance of machining in current industrial practice is also discussed.

This sets the stage for motivation scope and research objectives to be carried out for the current research work.

Chapter 2 includes an extensive review of various national and international scientific journals in the area of production and machining of composites to understand the research developments on a global level. It also presents the existing research gaps and a framework to established a platform to overcome these gaps.

Chapter 3 describes the fabrication of Al-TiC_p composite work material. Further, it also describes the material and mechanical characterization of the synthesized composite.

Design and development of atomized liquid nitrogen spray setup is described in *Chapter 4*. Flow conditions and spray characteristics which were scientifically studied to evaluate the efficiency of the developed system is presented. Further, optimization of spray characterises is also discussed.

After arriving at the optimal conditions, the developed atomized liquid nitrogen spray discharge system efficiency was evaluated by friction and wear characteristics using pin on disc tribometer. The same is discussed in *chapter 5*. This chapter also entails influence of load and sliding velocities on tribological characteristics of Al-TiC_p composite. Comparative studies made with dry and cryogenic chilled argon (CCA) gas environment are also discussed.

The machining performance of atomized liquid nitrogen spray assisted machining is discussed in *chapter 6*. The influence of cutting parameters and tool geometry on cutting force tool wear formation and surface finish of machined work material surface in comparison to dry, wet and cryogenically chilled argon gas machining is presented in this chapter.

The significant parameters associated with machining process that are determined using statistical tools like ANOVA are presented in *chapter 7*. Details of predictive model

developed using RSM along with genetic algorithm optimization techniques used to determine the optimal machining condition for machining of Al-TiC_p MMCs are also discussed.

The proposed FEM is utilized for analysis of various unique aspects of MMC cutting, including interactions between tool geometry and the consequences of cutting parameters on MMC machining process (cutting), and plastic deformations during MMC machining. Finite element model results are presented and validated against experimental data in *chapter 8*.

Finally, *chapter 9* gives a detailed summary of the studies carried out, findings obtained and contribution to the research. It also proposes scope for future work in the field.

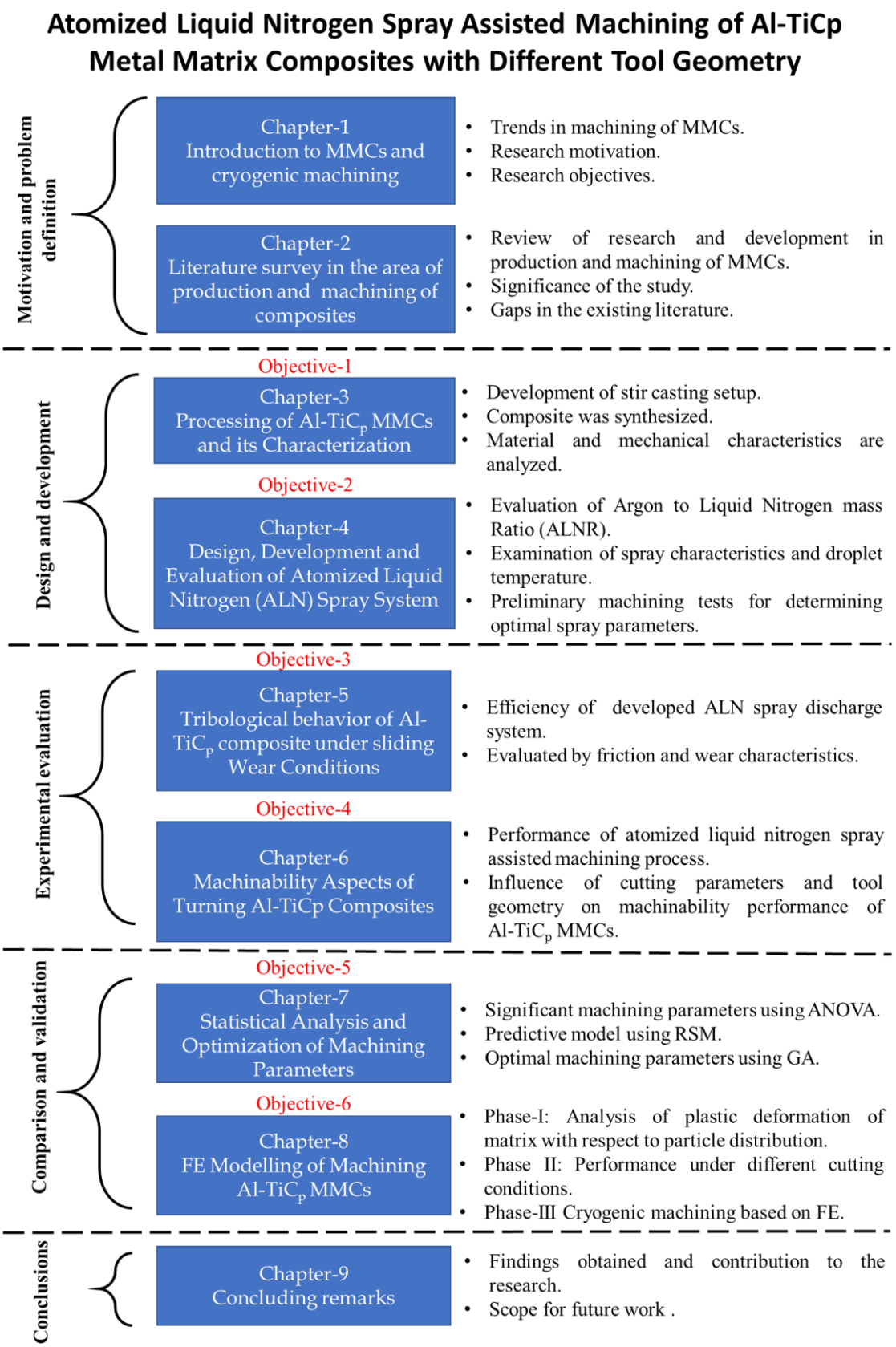

Fig. 1.1. Structure of thesis.

Chapter 2
Literature Survey

The current chapter consists of a broad literature survey on production and machinability of Al-MMCs from highly rated national and international scientific journals/conferences. The chapter begins with brief background (section 2.1) on particulate reinforced Al-MMCs and its applications. Section 2.2 covers the existing literature on methods of production and evolution of mechanical characteristics of particulate reinforced Al-MMCs. Section 2.3 explores various attempts made by scholars across the research community to overcome the characteristic difficulties encountered while machining of Al-MMCs. Section 2.4 describes the FE modelling of machining particulate reinforced Al-MMCs and fundamental aspects of metal cutting simulation with existing modelling. Section 2.5 focuses on the existing research gaps in current machining technologies and creates an outline that was used to carry the current research work. Finally, Section 2.6 presents the overall summary of this chapter.

2.1 Introduction

MMCs are composed of a metal matrix as the base and a reinforcement as the minor constituent. Common base metals are alloys with known characteristics-light weight, or high temperature resistance such as aluminum, magnesium or titanium [25]. Aluminum metal matrix composites (Al-MMCs) have greater advantages in a wide number of specific fields such as automobile, aerospace and defense. Al-MMCs are commonly reinforced with high strength, high modulus and brittle ceramic phases, which may be in the form of fibers, whiskers and particulates. Among them, particulate reinforced composites have gained more attention due to their improved anisotropy, ease of fabrication and low cost. Titanium carbide particulate (TiC_p) reinforced Al-MMCs (Al-TiC_p MMCs) belong to the new

generation of MMCs which is to expected to be used in higher commercial & industrial applications due to its low cost and improved properties [26]. Despite its superior properties, its applications are limited owing to the complexity in its manufacturing and poor machinability. For better understanding of Al-MMCs and their limitations, a detailed survey on the relevant literature has been carried out and is presented in this chapter.

2.2 Processing of Al-MMCs

Particulate reinforced MMCs (PMMC) are of particular interest because of their easy manufacturing and low production cost [26]. Over the past few decades, several processing methods have been developed by various researchers to optimize the microstructural integrity and properties of Al-MMCs. Accordingly, the process can be classifying into three categories, (i) solid state process, (ii) two phase solid and liquid process and (iii) liquid phase process.

2.2.1 Solid phase process

Powder metallurgy is a highly-evolved method for fabrication of particulate reinforced Al-MMC to very close dimensional tolerances, with minimum scrap and fewer secondary machining operations. It involves numerous steps prior to final consolidation. Optimal proportions of TiC (sized and wt%) and Al were mixed in powder for a long duration to achieve uniform distribution of TiC particle. The mixed powder was compacted at a pressure of 300 - 500 MPa with zinc stearate as a lubricant. This compacted product was sintered at 500–550^{o}C with a socking time of 2-3hr under argon atmosphere and then subjected to furnace cooling [27]. Hashimoto et al. [28] have fabricated TiC/Al composites by powder metallurgy route i.e. heating the powder mixture compacts consisting of Al and TiC in argon atmosphere at 1000-1500 °C for 1 hour and reported that the relative density of the composites was 95 - 97%. V Senthil Kumar et al. [29] & M Ali et al. [6] have found that mechanical properties like hardness and strength increase with increase in % of TiC

content in composite. Further studies revealed that with the increase in sintering temperature, the number of pores decreases and the rate of grain growth apparently increases. However, this method requires alloy powders that are generally more expensive than bulk material, and involves complicated processes during the material fabrication. Thus, powder metallurgy may not be an ideal processing technique for mass production.

2.2.2 Two phase processes

In a two phase process, the particulate reinforced Al-MMCs are produced by spray deposition process [30], rheocasting [31] and friction stir method [32]. In spray disposition method, reinforcement particles are introduced into the steam of molten alloy which is subsequently atomized by high pressure jet of inert gas. This spray mixture is collected on a substrate in the form of a reinforced metal matrix billet. MMC manufactured by this technique reduces the interfacial reaction possibilities [30].

Mehrabian et al. [31] used rheocasting, to produced 30wt% of Al_2O_3, SiC, and 21 wt% glass particles in Al alloy. In rheocasting, the ceramic particles are added into the metallic alloy at a temperature at the solid – liquid range of the alloy, followed by vigorous agitation to form a low viscosity slurry. The slurry characteristics of the matrix during solidification makes the ceramics particles mechanically entrapped and prevented from agglomeration. The particulates subsequently interact with the liquid matrix affecting the bonding. It was observed that a majority of the particulates were found to be homogeneously distributed in the matrix, except for coarser, 340 μm size, particulates which settled during solidification. Thangarasu et al. [32] used Friction Stir Processing (FSP) to fabricate TiC particulate (~2 μm) reinforced aluminum matrix composite (AMC). The TiC powders were compacted into a groove of 0.5 mm × 5.5 mm. A single pass FSP was carried out using HCHCr steel tool rotational speed of 1600 rpm, processing cutting speed of 60 mm/min and axial force of 10 kN. Friction between the rotating tool and the

workpiece raised the local temperature till the material plastically deformed. All these techniques are complicated and require high cost processing equipment, hence, may not be ideal to produce Al-MMCs.

2.2.3 Liquid phase process

In this technique, ceramic particles are incorporated into the molten metal using various proprietary techniques, followed by mixing and casting of the resulting MMCs. (i) in situ synthesis process, (ii) melt infiltration and (iii) stir casting techniques are the various methods used to develop Al-TiC_p composites.

2.2.3.1 In situ synthesis process

In situ techniques involve a chemical reaction resulting in the formation of a very fine and thermodynamically stable reinforcing ceramic phase within a metal matrix. As a result, this provides thermodynamic compatibility at the matrix-reinforcement interface. This procedure takes place in both *solid* and *liquid phase processes*. Both phases produce very fine reinforcements in the matrix which are clean and semi coherent in some cases.

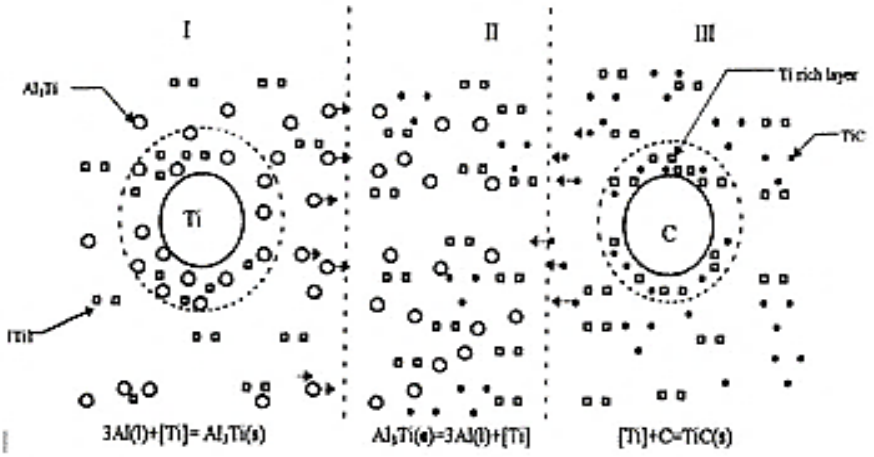

Fig. 2.1. Micro mechanism of reaction synthesis TiC. [33]

In solid synthesis processes, high purity powders of titanium (Ti), carbon (C) and aluminium were together mixed, compacted and heated from top to begin the formation of

reinforcements. EL Zhang et al. [33] successfully fabricated Al-TiC composite using this process. The whole process of synthesis was started by diffusion of partially molten aluminium around the Ti and C powders. When concentration of Ti powder around aluminium reaches 0.15wt%, a precipitate reaction happens and Al_3Ti phase is formed around the Ti powder. Titanium concentrated around carbon and a Ti-rich layer is high enough, an exothermic reaction to synthesize TiC. The micro-mechanism of the reaction synthesis TiC is shown in Fig. 2.1.

In liquid synthesis process, TiC particles are formed by addition of gaseous phase (Carbonaceous gas) and precipitates phase (K_2TiF_6 or Ti and C) into a liquid metal/alloy. Shyu et al. [2] used Al–5.1Cu–6.2Ti as a matrix material in this process of fabrication of Al-TiC composite. The in-situ reaction was carried out by diffusion of carbonaceous gas in vacuum induction furnace for 4hrs at a constant temperature of 1400°K. The diffused C gas reacts with Ti substrate in the molten matrix and forms TiC particles. Sahoo and Koczak [34] studied the in-situ formed TiC in aluminum alloys (Al-4.4wt.%Cu) by injection of a carbonaceous gas, methane (CH_4), into the melt. They reported that highly exothermic reaction is moderated by means of a carrier gas that leads to a fine (0.1 - 2.0 μm) and homogeneous distribution of the stoichiometric carbides. They also suggested that nucleation of carbide occurs via titanium diffusion to the carbon and precipitates out as a carbide via a solid-liquid chemical reaction.

In reaction synthesis by precipitation, Ti dissolves and wets the graphite particles which leads to the formation of TiC reinforcement. Bauri [35] successfully fabricated Al-TiC_p MMCs by reaction synthesis of K_2TiF_6 and graphite powder in molten Al matrix. The results show that at lowest temperature there is no sign of formation of TiC_p and only blocky type Al_3Ti particles are observed. When temperature increases above 900°C, the blocky

Al_3Ti particles become unstable and Ti dissolves and wets the graphite particles to form TiC according to the following reaction.

$$3K_2TiF_6 + 4Al = 3Ti + 3KAlF_4 + K_3AlF_6$$

$$Ti + 3Al = Al_3Ti$$

$$Al_3Ti + C = TiC + 3Al$$

Effect of temperature on reaction process is shown in Fig. 2.2. These observations also provide some insights into the reaction mechanism of TiC formation. Composites manufactured via in-situ processes have better properties over the conventional composites. This is due to formation of fine and dispersed TiC particles in the composite. The reaction kinetics for formation of TiC particles in-situ in the Al melt depend on various factors like temperature, reaction time, Ti:C ratio and TiC particle formation during process.

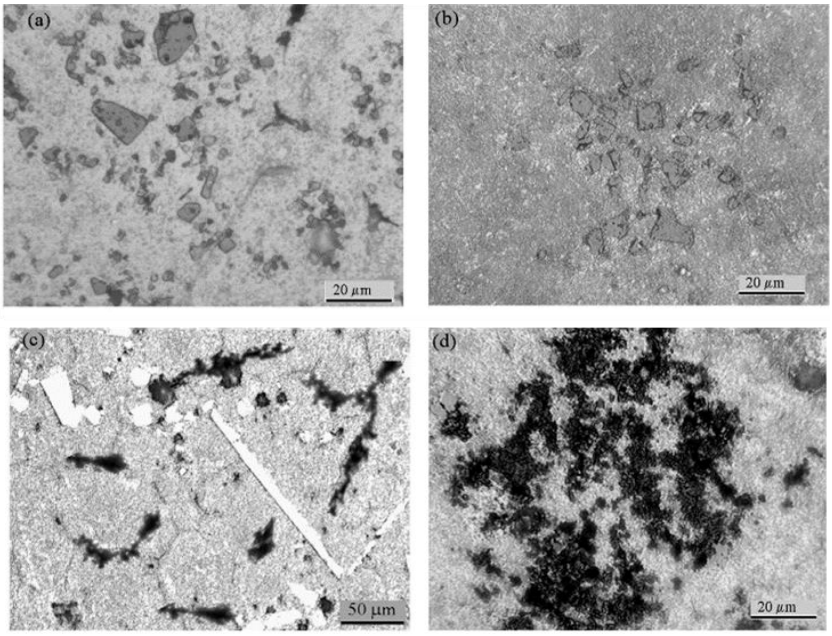

Fig. 2.2. Optical micrographs of powder blends processed at (a) 700°C (b) 800°C (c) 900°C (d) 1000°C. [35]

Lee et al. [3] have observed Al_4C_3, $Al_{18}Ti_2Mg_3$, Ti_2AlC, Al_3Ti, and TiAl interfacial reaction products in Al-Mg/TiC composite, which was fabricated by the pressure less infiltration process, whereas Mitra et al. [3] have reported Al_3Ti, Al_4C_3, Ti_2AlC, and TiAl

phases in Al/TiC composite, which was fabricated by the exothermic dispersion process. This interfacial reaction product will cause disturbance in mechanical and thermal properties of composites. Extensive interfacial reaction causes degradation of composite mechanical properties. Therefore, in course of reaction synthesis, system must be carefully screened in order to obtain optimum mechanical properties and appropriate interfacial reaction.

2.2.3.2 Melt infiltration technique

Muscat et al. [36]developed Al-TiC composite using melt infiltration technique. In this process, TiC particles are uniaxially compressed to 70 MN/m^2 and are sintered in argon furnace at 1200 to 1500°C for 30 min. The bars are placed with molten aluminium in furnace at 850 to 1350°C. It was observed that after infiltration, all the Al/TiC composites reached 98% of theoretical density and the elastic modulus of the composites increases with increase in TiC content. Studies by Mortensen et al. [37] revealed that that during metal infiltration, interfacial reaction occurs which deceases the mechanical properties of the developed composites. Further damage in reinforcements and micro structural non-uniformities are also observed during this process.

2.2.3.3 Stir casting (SC) technique

In stir casting process, powder form reinforcements are distributed into molten metal by the means of mechanical stirring. Over the past two decades, in-situ, ex-situ, reaction synthesis based casting techniques have been developed to produce high quality Al-TiC_p. But these processes use carbonaceous gas and reaction synthesis agents that require complicated apparatus and are associated with problems like no control on volume fraction, size, distribution of TiC_p and formation of intermetallic particles in composites. Gopala Krishnan et al. [38] used stir casting process to fabricate Al-TiC_p MMCs under

argon atmosphere to prevent reaction of molten aluminium during casting process. It was observed that wear loss in terms of volume was very less when compared with composite manufacture in in-situ reaction process. Mandal et al. [39] fabricated Al-MMCs using stir casting route. They preheated the reinforcement to 475°K and added to the center of the vortex formed by stirring. The preheating temperature of the die was maintained at 825°K. It was observed that volumetric wear during wear test increased with increasing applied load.

Direct incorporation of particles into melt is an ideal solution but the contact angle for Al on TiC is roughly 118° at 700°C on an oxidized melt surface [40, 41]. This suggests that spontaneous entry is impossible without fluxing agents. Ramachandra et al. [42] fabricated aluminium composites reinforced with fly ash particles using liquid metallurgy route. They added flux to the melt in order to minimize the oxidation of molten metal. The super-heated molten metal was degassed at a temperature of 1025°K. The reinforcement particles were preheated to 875°K.

Homogenous dispersion of particles and particles cluster during solidification process are the major difficulties encountered during direct casting of composites. To minimize these difficulties, many studies have been conducted aiming to achieve defect free composites [5, 7]. Improvement of wettability of TiC particles with Al melt will improve the particle incorporation. This can be achieved by reduction in mechanical and thermodynamic barriers. Additions of fluxes and performing the casting process in a controlled environment will reduce the formation oxide layers. Usage of magnesium helps to overcome the thermodynamic barriers. By removing oxide layer and reducing thermodynamic barrier, Muthu Krishnan et al. [9] adopted stir casting route for fabricating Al/SiC composites with the addition of hexachloroethane tablets to the molten aluminium for effective degassing. The preheating temperature of SiC particles was maintained at

875°K. They also added magnesium chips in order to reduce thermodynamic barrier as well as to improve wetting.

Naidich stated that the contact angle of TiC gets reduced by approximately 10° at a temperature of 990°C [41]. Particle incorporation can be improved by dissolving the oxide layer on the surface of the melt by using cryolite-type flux (K-Al-F). To achieve homogenous dispersion and reduce particle cluster, melts are often vigorously stirred to add reinforcements below the melt surface. The high shear induced by stirring also affects wetting and thereby the particles are retained in the melt after solidification takes place. This wetting will improve the homogeneity and decrease particle cluster. Incorporation of flux and stirring action in casting helps to produce high quality Al-TiC_p composites.

The above literature discusses several techniques that have evolved for manufacturing of Al-TiC_p MMCs. Among all, stir casting is generally accepted, and is the most economical of all the available techniques for fabrication of particulate reinforced Al-MMCs. It is attractive because of simplicity, flexibility, and is most economical for large sized components to be fabricated [43]. The advantage of stir casting lies in lower processing temperature, leading to a longer die life and high production cycle time [44]. Therefore, employing of flux and stirring action in casting will help to produce high quality Al-TiCp composites.

2.3 Machinability analysis of Al-MMCs

Al-TiC_p MMCs are also preferred as engineering materials for various high-performance components being used for varieties of applications due to the grain refinery properties of TiC particles (TiC_p) as reinforcement [45, 46]. During machining of Al-TiC_p MMCs, tough abrasive and intermittent nature of TiC_p gets unattached or fractured at high pressure and cutting temperature. Reinforcements in MMCs are usually harder than conventional tool materials, hence cutting tool endures premature failure. Both coated and

uncoated carbide tool can withstand significant level of tool wear subsequently in a short period [5, 47]. This section focuses on the effect of cutting parameters on machining performance parameters are mentioned in Fig. 2.3.

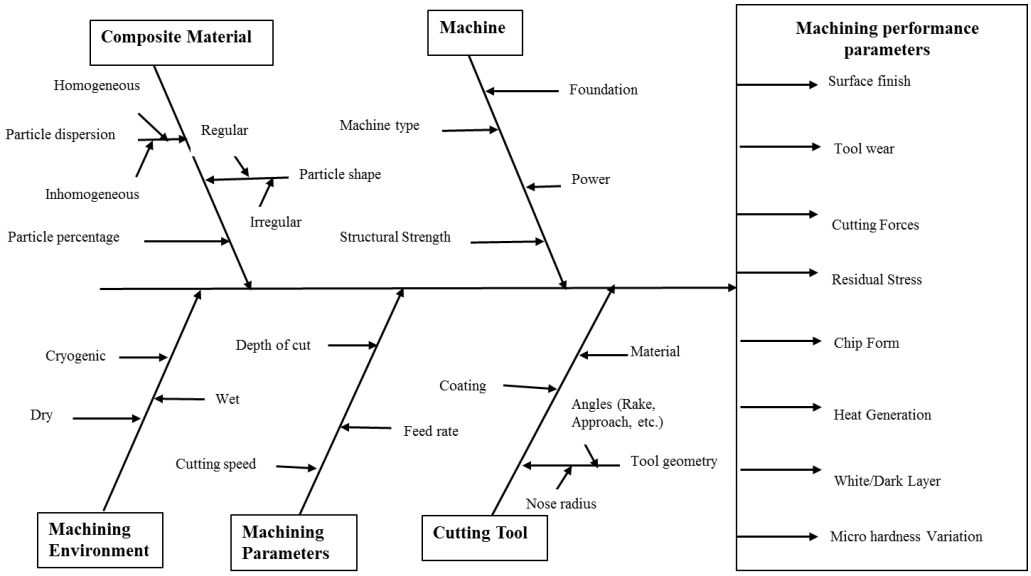

Fig. 2.3. Fish bone diagram showing the influence of cutting parameters on machining performance parameters.

2.3.1 Influence of cutting parameters

Generally cutting forces, tool performance, surface finish etc., are considered as various measures of machinability. Machinability performance is dependent upon large number of variables such as work material, tool geometry, cutting conditions, machine tool rigidity etc. Three decades of intensive research has provided a wealth of scientific knowledge on machinability of particulate reinforced Al-MMCs.

Understanding chip formation is very important to comprehend the cutting forces. The incorporation of hard particles into the soft ductile metallic matrix alters the deformation behavior of the soft matrix. This change affects chip formation and hence the cutting forces. From the literature, it is understood that the tool geometry (rake angle, clearance angle), cutting speed and feed have been identified as the major process variables

[48, 49]. The particle sizes and volume fractions have been cited as the dominant factors affecting the machinability of MMCs [50].

Manna et al. [51] and Altinkok et al. [52] observed built-up edge (BUE) at low cutting speeds causing lower cutting forces at lower cutting speeds than cutting force observed at higher cutting speeds. The presence of a BUE increases the actual rake angle of the tool resulting in a lower cutting force. Wang et al. [53] and Manna et al. [54] have shown a decrease in the cutting forces with an increase in the cutting speed. In the study conducted by Manna, the effect of the cutting speed on the feed force and cutting force during turning of an Al/SiC composite was measured. It was observed that the feed force and the cutting force decreased with an increase in the cutting speed. Feed has considerable effect on the cutting forces as the cutting forces rise considerably with an increase in the feed [55, 56].

During machining, the particulates have been found to align themselves along the shear plane and initiate micro cracks and voids due to particle pull-outs [57]. The abrasiveness of these particles causes premature failure of the tool. Improper tooling and machining conditions not only escalate the component cost, but also induce sub-surface damage to the machined product. The hard reinforcements in MMC provide the preferred high wear resistance, but are detrimental to cutting tools and forming dies. The particle size and weight fraction are factors responsible for tool wear [58, 59]. Published literature on the machinability of particulate MMCs indicates that only diamond tools (PCD & SCD) provide a useful tool life [60]. However, due to the extremely high cost of PCD tools, other tools like cemented carbides ware preferred for machining at low cutting speeds and high feed rates [61].

During machining, coated carbide tools ensure higher wear resistance, lower heat generation and lower cutting forces than their uncoated counterparts [50]. It has also been

shown that the wear acceleration varies with the densities of the reinforcement and the matrix [62]. Chambers and Stephens [63] found that a triple-coated carbide, having a top layer of TiN performed best in terms of flank wear but gave the poorest surface finish when machining the SiC particulate-reinforced composite. Yanming and Zehna [64] investigated the tool wear and its mechanism for cutting A356 Al/SiC composites. Their results showed that the major damage mechanism was abrasive wear for conventional tools and edge chipping for high hardness cutting tools. The work carried out by Tomac and Tonnesson [65], attributed the increase in tool life at higher feed rates to thermal softening of the composite. However, El-Gallab et al. [66] attributed the reduction in tool wear at higher feed rates to reduction in contact between the hard ceramic particles and the cutting tool edge.

Lin et al. [49] observed flank wear as a primary mode of tool failure in machining Al-SiC MMC with two body and three-body abrasion between the tool and workpiece playing a dominant role in causing the flank wear land. In their experiments, at high cutting speed turning with PCD tools (cutting speeds 300 to 700 m/min), tool wear was found to increase with increasing cutting speed and feed. Within the cutting conditions of the experiments, the surface finish was observed to be independent of cutting speed and a slightly worn tool was observed to give better surface finish. The presence of uniformly dispersed SiC particles resulted in discontinuous chip formation.

Ding et al. [67] found that flank wear incrementing with cutting speed directly. They explained this occurrence on the basis of thermal weakening of binder in the tool. Furthermore, there was no significant difference in flank wear at high cutting speeds under dry and wet machining conditions. This important conclusion was attributed to the inability of coolant to reach flank face during high cutting speeds, hindered by the high flow rate of the work material past the tool.

Since it is well known that machining causes various geometrical and metallurgical defects in the surface region, one cannot draw conclusive decisions about the machinability of any material by just looking at the tool wear and tool wear rates. Mechanical properties such as creep and fatigue are greatly influenced by the condition of the surface. Hence, the effect of machining on the type of surface defects, as well as on their distribution, has a major impact on the performance of the machined component. Previous literature shows that in MMCs machining, cutting parameters and cutting geometry are also significant factors influencing the surface quality [68, 69]. It is also found that cooling conditions, particle reinforcement size and volume fraction have significant effect on surface integrity [70]. Severe damage to the machined surface can be caused due to high temperature gradients developed during the plastic deformation in the chip formation process [66]. This imposes residual stresses along with micro and macro cracks on the metal matrix [71].

Bhushan et al. [61] investigated the effect of cutting speed, depth of cut and feed rate on surface roughness and tool wear rate during machining of Al-7075 alloy and 10 wt.% SiC particulate metal-matrix composites. Tungsten carbide and PCD inserts were used as cutting tools. It was found that surface roughness of Al alloy decreased with increase in cutting speed at all cutting conditions. Feed rate decreased from 0.4 to 0.1 mm/rev while surface roughness is decreased from 6 µm to 4 µm at cutting speed of 180 m\min. Surface roughness obtained by PCD tool insert were less in comparison with carbide insert for the same cutting conditions.

Quan et al. [71] investigated the hardness and residual stress of SiC/Al composites in the surface layer affected by machining. SiC/Al composites are composed of a soft matrix and hard reinforcing particles. Under cutting force, Al matrix and the SiC particles do not deform uniformly. Thus, it is expected that there will remain work-hardening and stress in the machined surface layer.

2.3.2 Influence of cutting tool

The back-rake angle in a single point cutting tool affects its ability to shear the work material and form the chip. It can be positive or negative. Positive rake angles reduce the cutting forces resulting in smaller deflections of the workpiece, tool holder, and machine. If the back-rake angle is too large, the strength of the tool, as well as its capacity to conduct heat is reduced. When machining hard to cut materials, the back-rake angle must be small and can be even negative for carbide, PCBN and diamond tools. The higher the hardness, the smaller the back rake [72]. The magnitude of rake angle has significant effects on the performance of the cutting tool and the surface integrity generated during machining [73].

El-Gallab et al. [66] observed that negative rake angles led to greater surface roughness, this being attributed to the clogging of the hot chips between the tool and the machined surface causing severe damage to the workpiece surface. Also, with reduction in tool nose radius, excessive chipping and crater wear was seen. This tool chipping led to an increase in cutting forces and flank wear. The most practical and effective way to enhance the machining performance in cutting difficult-to-cut materials is to reduce cutting temperature.

A larger nose radius produces a smoother surface at lower feed rates and a higher cutting speed. Large nose radius tools have, along the whole cutting period, slightly better surface finish than small nose radius tools [74, 75]. During cutting with a tool of a larger nose radius, a large part of the chip will have a thickness less than the minimum value. In addition, increasing the nose radius has a direct effect on cutting forces, leading to a significant increase in the ploughing effect in the cutting zone. Increasing the ploughing effect leads to more material side flow on the machined surface.

Sahoo et al. [76] observed improved machinability of Al/SiC composites due to multi-layer coated inserts of TiN, TiCN and Al_2O_3. The lubricating effect of the TiN

coating reduced chip tool interface temperature and eliminated BUE formation as well. Thus, tool wear was subdued. Al_2O_3 provided thermal barrier coating, TiN gave diffusion barrier coating and TiCN endowed a wear resistant coating for longer tool hardness retention.

Kilickap et al. [77] reported the effect of machining parameters such as cutting speed, feed and depth of cut on tool wear and surface roughness while machining $AlSiC_p$ MMC. Two types of K10 cutting tool (uncoated and TiN-coated) were used at different cutting speeds (50, 100 and 150 m/min), feed rates (0.1, 0.2 and 0.3 mm/rev) and depths of cut (0.5, 1 and 1.5 mm). In dry turning conditions, tool wear was mainly affected by cutting speed and increased with increasing cutting speed. Surface roughness influenced the cutting speed and feed rate. Based on their results, the higher cutting speeds and lower feed rates produced better surface quality.

2.3.3 Influence of cutting environments

Proper selection of process parameters, tool geometry and cutting environments will wisely reduce temperature rise and strain hardening during machining of composites. Application of cutting fluid during machining process is one of the alternatives to reduce the temperature and friction between tool/chip workpiece interfaces (lack of build-up-edge) and flush away the chip (preventing the tool from re-cutting the abrasive chips). Narahari et al. reported that a lower tool life was experienced in machining aluminium MMCs in the presence of cutting fluid, which is 10 to 20% of that under dry condition [78]. Hence, aluminium MMCs with SiC_p reinforcement need to be machined under dry conditions for rough and semi-finished machining.

Shetty et al. [79] utilized high-pressure steam as a coolant and lubricant during machining of Al/SiC_p composites. High-pressure steam condition yielded lower cutting forces and temperatures of about 25% and 30% respectively when compared with oil in

water emulsion. However, studies by Hung et al. [21] and Kannan et al. [22] reported that conventional application of pressurized and copious cutting fluid did not have much impact on improvement of tool life. Conventional coolants and cooling methods are not sufficiently effective to enhance the machining performance of metal matrix composites. Therefore, it is still desirable to compel various researchers to discover alternative coolants to achieve economical and eco-friendly manufacturing processes [13, 80]. Inherent environmental benefits, reduction in disposal cost and its efficiency in controlling heat generation from the cutting zone are few of the benefits that made liquid nitrogen gain popularity as an effective coolant [81]. Effective coolants like LN_2 lower cutting temperature, modify the frictional characteristics at the tool/chip, and enhance the tool life during machining [82]. Moreover, they also minimize friction force power consumption; maximize surface quality, dimensional accuracy, chip removal and chip breakability for precision machining [12].

During machining of MMCs, the plastic deformation of the layer being cut results in heat generation. Studies by Heigel et al. [83] and Kamruzzaman et al. [84] indicate that maximum temperature generation is observes at tool/chip contact on tool rake face. Therefore, application of coolant into the tool chip interface diminishes the heat generation drastically. Hong and Din [85] supplied LN_2 jet on flank and rake face of tool simultaneously and observed that heat generation in machining zone was reduced extensively over dry machining. Pu, Z. et al. [86] observed that heat generation was reduced by 60% under cryogenic machining. Wang et al. [87] realized that considerable reduction of heat generation by cryogenic cooling implies decrease in stress at tool flank face substantially. Hence, lowering the cutting temperature and stress on tool face tends to improve the tool life successfully.

Tool wear is one of the prominent factor to analyze the tool life and machinability performance of the workpiece. Lin et al. [88] witnessed smaller flank wear, decrease in chip size and improved surface finish under cryogenic machining condition than dry machining conditions during turning of metal matrix composites. Kalyan et al. [89] attained a 37% decrease in tool flank wear under LN_2 machining when compared to dry condition. Introduction of LN_2 at the flank surface, remarkably reduces flank wear under cryogenic machining [90]. The authors also attributed lowering of flank wear to the intensive cooling condition under LN_2 resulting in steady hardness and sharpness of the tool cutting edge. Studies by Paul et al. [91] revealed that LN_2 jet cooling helps to reduce flank wear by retaining tool hardness, thus, improving quality of the machined surface.

Surface roughness is one of the most commonly studied surface quality factors since it remarkably affects the life of the workpiece. Pusavec et al. [92] using cryogenic machining observed that an increase in micro hardness and compressive residual stress in work material resulted in enhanced machined surface quality. Application of cryogenic cooling by liquid nitrogen jet substantially improves the surface quality over dry conditions [93]. Hong et al. [20] developed a sliding contact test rig, which was fitted on CNC lathe, by mounting an LN_2 cooling jet between tool and workpiece. The results indicated that jet cooling between the workpiece and the cutting tool generated hydrodynamic film, which led to lower friction. This reduction was observed due to the combination of both cooling and lubrication effect of a high pressure LN_2 which absorbs heat swiftly and creates fluid/gas cushion between tool/chip interfaces. Dhar et al. [94] observed a significant decrease in cutting forces by favorable chip formation in turning with LN_2 jets under cryogenically cooled machining condition.

In addition, position of nozzle on rake face and flank face reduced friction coefficient drastically and improved tool life and surface quality [95]. Nozzle position

influences the penetration of LN_2 in machining zone [85]. Studies performed by Khan et al. [96] revealed that nozzle position significantly affects tool wear, and influences surface quality. Lo´pez de Lacalle et al. [97] indicated that the nozzle position in relation to the feed direction is crucial for improving the machinability performance. The use of cutting fluid reduces the cutting temperature, tool wear and surface roughness, if applied in optimum amount. Hence, various researches are looking toward to develop effective ways of supplying optimum amount of LN_2 into the tool/chip interface. Hong et al. [85] developed a modified chip breaker technique by integrating chip breaker with cryogenic micro nozzle. Ahmed et al. [16] modified the standard tool holder by making a counter bore hole in the surface of the tool holder on which the insert is mounted.

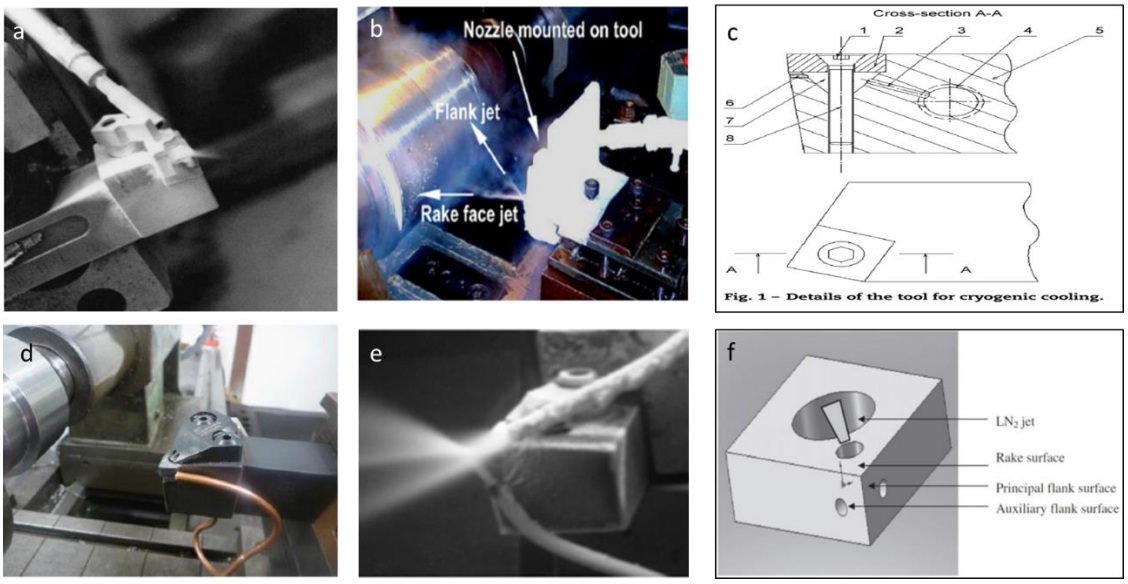

Fig. 2.4. Techniques to deliver Liquid nitrogen into the machining zone (a) Hong et al [19]; (b) Venugopal et al. [17]; (c) Ahmed et al. [16]; (d) Bermingham et al. [98]; (e) Pusavec et al. [23]; (f) Dhananchezian et al. [99].

Venugopal et al. [17] designed a special nozzle to direct the LN_2 on rake and flank face. The experimental results yielded a significant improvement in tool life and surface quality than dry machining conditions. However, these techniques require a considerable quantity of LN_2 to be delivered, for example, 45–250 l/hr. Studies have shown that usage

of large quantity of liquid nitrogen creates adverse effects during machining, altering work material characteristic, premature failure of tool and poor surface finish [24].

As highlighted by Hong et al. [85], high heat generation is limited to only a millimetric area of the tool face. Applying LN_2 in the selective area will enhance cooling effect during machining. Heisel et al. [100] supplied minimum quantity of cutting fluid into machining based on the concept of atomization. A venturi-based system was developed by Machado and Wallbank [101] in which a small quantity of fluid was mixed with compressed air. Jun et al. [102] used an atomization-based cutting fluid (ACF) spray system to deliver cutting fluid in the form of small separated droplets. A considerable reduction in cutting force and cutting temperature, along with an extended tool life by three times over flood cooling was observed. Rukosuyev et al. [103] proposed ACF spray system equipped with a nozzle to produce more focused flow in the cutting zone, as it is desired to have a narrow and targeted spray for effective penetration into the cutting zone. The authors also state that focus height and focus length are the two relevant parameters which affect the machinability characteristics. It was observed that an increase in the mist velocity leads to an increase in the focus length and height and also increase in the spray velocity which further leads to a decrease in the focus length and height. Studies by Ghai et al. [104, 105] revealed that atomization-based cutting fluid spray is an alternative solution to achieve better cooling and lubrication of the cutting tool/chip interface.

Therefore, application of liquid nitrogen in atomized form may maximize the penetration into the tool/chip interface and simultaneously minimize the usage of liquid nitrogen, thereby diminishing difficulties associated with machinability performance. Cutting speed and feed are major machining parameters and, rake angle, nose radius and approach angle in tool geometry significantly affect the performance of the cutting tool and the surface integrity generated during machining.

2.4 Statistical tools for modelling and optimization

Manufacturing processes are characterized by a multiplicity of dynamically interacting process variables. Surface finish has been an important factor in predicting the performance of any machining operation. Machining involves large number of parameters; combined influence of the significant parameters can only be obtained by modeling [105]. Since the turn of century, quite a large number of attempts have been made to develop surface roughness model and tool wear models using statistical regression models, response surface methodology, Artificial Neural Network (ANN) and fuzzy set theory [106]. The first and second order models were constructed along with contour graphs for the selection of the proper combination of machining to predict the response [107, 108]. Analysis of variance was used to validate the developed model [109].

Muthukrishnan et al. [110] used two modelling techniques used to predict the surface roughness namely ANOVA and ANN. In ANOVA, it was revealed that the feed rate has the highest physical as well as statistical influence on the surface roughness right after the depth of cut and the cutting speed. ANN methodology consumed lesser time giving accuracy. Hence, optimization using ANN is the most effective method compared with ANOVA. Basheer et al. [111] developed an ANN based model to predict surface roughness of machined surface of Al/SiC_p composites. The predicted roughness of machined surfaces was found to be in very good agreement with the unexposed experimental data set.

Dabade et al. [112] considered tool/chip interface friction to predict cutting forces in oblique cutting. They provided an analytical model to compute the machining force components in three directions during oblique cutting. Unfortunately, the authors did not consider the effect of particle debonding and ploughing force.

A systematic approach of modelling and determination of optimal or near-optimal cutting conditions has shown an interesting potential in both product and process quality

improvement in machining operation. The generic framework for process parameter optimization in cutting operation attempts to provide a single, unified, and systematic approach to determine optimal or near-optimal cutting conditions in various kinds of machining process optimization problems. It incorporates the use of one or more of the existing modelling and optimization techniques, making the framework unified and effective [113].

Many researchers have attempted to obtain optimum machining condition while machining of MMCs by minimizing the surface roughness and tool wear using different approaches [114, 115]. Among various techniques, Taguchi and RSM are widely used in research and industrial applications. These techniques are excellent to predict responses in machining applications with fewer experimental runs, and are less sensitive to variation due to uncontrolled or noise variables [116, 117]. Considering the limitations of these techniques, there is a need to concentrate on other methods like genetic algorithm, which are being successfully used to find the optimum machining conditions for validation [118].

2.5 FEM of machining metal matrix composites

Researchers and engineers mainly adopt two approaches namely experimental and finite element simulation techniques to adequately understand the machining process [119]. Finite element simulation (FEM) is advantageous over experimental technique due to its ability to comprehensively provide adequate knowledge about the machining process within shorter processing time. Finite element (FE) techniques like element-separation for chip formation modelling, material and geometrical non-linear analysis, element separation criteria etc. are widely preferred for modelling machining of MMCs with better accuracy. However, due to the association of various complexities, only a very few attempts have been made by researchers to simulate the machining of MMCs [48, 120, 121]. The advantage of FE analysis lies in its ability to provide a better prediction of deformations,

stress-strain relationships, temperature profile, and the cutting forces involved during a particular cutting operation.

Osakada et al. [122] simulated orthogonal machining process based on rigid-plastic material model with taking no temperature effects into consideration. Tay et al. [123] and chow et al. [124] performed FEM simulations taking temperature effects into consideration. Lajczok [125] proposed utilization of plane strain analysis for FE simulation of cutting. Ceretti et al. [126] studied segmental chip formation using FEM while Marusich and Ortiz [127] used adaptive remeshing techniques for simulation of transition from continuous to segmented chip during high cutting speed machining.

FE simulations are carried out based on Lagrangian or Eulerian formulations of material behavior. In Lagrangian formulation based FE simulations, nodes on the mesh follow the points on the underlying the material to update the element geometry in accordance with material deformation during simulation. This model enables to simulate more realistic chip formation; however, fracture modeling using this approach requires removal of elements from the model, which leads to decrease in accuracy of results due to reduction in the material mass. Also, this technique may result in severe mesh distortion [128, 129]. Unlike Lagrangian method, in Eulerian formulation, the underlying material flows inside the FE mesh in a fixed space. In this formulation, the variables of the conservation equations are significant for an instant in a specific position in space. Thus, each variable is expressed for a position on the fixed mesh, which is independent of material's previous configuration or coordinates. This technique overcomes the mesh distortion phenomena, however, it cannot simulate initiation of chip formation unless chip shape is predetermined [130].

To overcome the significant shortcomings associated with both Lagrangian and Eulerian formulation methods, an Arbitrary Lagrangian Eulerian (ALE) method was

developed [131-134]. In this technique, some finite element mesh nodes are attached to the underlying material and follow the continuum while others are fixed in space. This technique minimizes mess distortion and provides a more realistic chip formation simulation in contrast with Lagrangian and Eulerian technique.

Monaghan and Brazil [120] carried a two stage simulation FE modelling of particulate MMCs; in the first stage, steady state cutting process was simulated by employing the single-phase global machining model while in the second stage, the loading history recorded in the previous stage is applied to a micro-mechanical model of a square section of the MMC material. With the help of this technique, they successfully managed to simulate particle debonding in MMCs and contact stresses on the tool surface during the cutting process.

Zhu and Kishawy [135] simulated a thermo-elastic-plastic plain strain workpiece model along with elastic particles and a particle-matrix interface with the same hardness as the particles. This technique helps to model plastic behavior of the material by considering the temperature effect in the simulation and to predict cutting forces, stress and temperature distribution in the workpiece material. Study by Pramanik et al. [55] suggested that the main reasons for particle fracture and interfacial debonding during machining MMC are the tool/particle interactions and the distribution of stress in the material.

Zhou et al. [136] provided a two-dimensional thermo-mechanical model of orthogonal cutting which was used to analyze the removal mechanism of the particle from the matrix. This analysis provided an understanding of the relation between von Mises equivalent stress distribution in the particle and matrix, and the removal mechanism of the particle. Hence, the removal mechanism of the particle based on the location of the cutting tool with respect to the particle can be investigated.

Further advancements in FEM led Dandekar and Shin [121] to develop a multi-step 3D model to predict sub-surface damage in MMC during the machining. They initially simulated the process using a single-phase Equivalent Homogenous Material (EHM) model to obtain the stress and temperature distribution in the workpiece material. Then, they applied the obtained data to a local multi-phase model consisting of a thermo-elastic-plastic matrix, linearly-elastic particles, and particle-matrix interface modeled using cohesive zone elements. This model was successful in providing a better prediction of debonding and particle fracture as well as the depth of damage during machining of MMCs.

FEM employs constitutive models to simulate the behavior of workpiece material during machining in terms of flow stress, strain, strain rate, and temperature which help to provide a correlation between stress and strain based on strain rate, temperature, and work hardening. In order to understand the chip separation criterion in FE analysis, fracture models are employed to model the initiation and evolution of damage in material during machining. The effects of strain rate and temperature should also be incorporated in the fracture models that are to be used for the cutting process. Johnson and Cook constitutive and damage model are the most commonly used for simulating the behavior of materials subjected to large strain, high strain rate, and high temperature [137-139].

Based on the literature survey, the performance of machining simulation of MMCs using microscopic approach in terms of chip formation is mainly reliant on the distribution of reinforcements in the matrix, machining parameters and tool geometry. In addition, the simulation of a microscopic model is challenging due to the severe mesh distortion and large simulation time. Limited studies have been performed using microscopic model without considering the effect of particle distribution, machining parameters and cryogenic technology during machining simulation of MMCs.

2.6 Identified gaps in the literature and proposed solution

The literature review summarizes the key gaps in existing literature and the proposed solution as follows.

Gaps	Proposed solution
Gap-1: Homogeneous dispersion and particle clustering during solidification process during casting.	**Sol-1:** Need to fabricate of Al-TiC_p MMC using stir casting metallurgical route.
Gap-2: Usage of large quantity of liquid nitrogen leading to adverse effects during machining including altering of work material characteristics, premature failure of tool and poor surface finish.	**Sol-2:** It is necessary to design and development of atomized Cryogenic liquid spray discharge system.
Gap-3: Limited studies reported on combined influence of tool geometry and cutting parameters during machining of Al-TiC_p composites	**Sol-3:** Need to perform Machinability studies of Al-TiC_p composite with different tool geometry and cutting conditions.
Gap-4: Very limited research on tribological performance of MMCs under cryogenic environment.	**Sol-4:** It is required to Investigate the efficiency of developed cryogenic experimental on tribological characteristics of Al-TiC_p composites.
Gap-5: No reliable model incorporating both the aspects of tool geometry and cutting parameters	**Sol-5:** There is a need for development of predictive model to facilitate effective planning.
Gap-6: No single guideline or criterion to choose the best parameters and judge the performance of optimization technique in metal cutting	**Sol-6:** Need for identification of optimal parameters for specified machining conditions under different environments.
Gap-7: Limited studies carried out using microscopic model without considering the effect of particle distribution, machining parameters and cryogenic technology during machining simulation of MMCs	**Sol-7:** Need to develop Finite element modeling & Validation of machining results of MMCs.

2.7 Summary

A review of the literature indicates that conventional machining of MMC leads to excessive tool wear and possible subsurface damage, thereby resulting in an increased machining cost and production time. These limitations are caused due to the extremely abrasive nature of the reinforcements used in MMCs.

Therefore, the present research work focuses on various issues of machining and tribology studies of particulate reinforced Al-MMC. By building on the work of previous studies conducted in the industrialized countries, this study helps to provide a better understanding and enhancing the performance of turning MMC, and consequently improving productivity, through optimization of machining process by proper selection of machining parameters. The present study further aims to improve the performance of turning MMC by introducing cryogenic coolant. It also provides an insight of development of FE Modeling using Abaqus to have a more understanding of the turning MMCs.

Chapter 3
Processing of Al-TiC_p MMCs and its Characterization

This chapter deals with the processing methods used for the fabrication of aluminium reinforced titanium carbide particulate metal matrix composites (Al-TiC_p MMCs). The current chapter is divided as, section 3.1 presents a brief information about MMCs and their production methods. Section 3.2, explains the development of stir casted Al-TiC MMCs. The developed composite samples were analyzed to determine the material and mechanical characteristics and the same is discussed in section 3.3. Finally, section 3.4 provides the remarks on developed Al-TiC_p composites and their performance.

3.1 Introduction

Al-TiC MMCs are preferred as engineering materials for various high-performance components and are used for varieties of applications due to the grain refinery properties of TiC reinforcement particles (TiC_p) [46]. Al-TiC_p composites are remeltable and manufatured in large quantites at lesser costs. Casting is the most economical and effective technique to produce high quality composites. In-situ, ex-situ and reaction synthesis based casting techniques are used to produce high quality Al-TiC_p. However, these methods involve carbonaceous gas and reaction synthesis agents requiring complicated apparatus. Moreover, they suffer from problems like control on volume fraction and size, distribution of TiC_p and formation of intermetallic particles in composites. Direct incorporation of particles into melt is an ideal solution, however, contact angle for Al on TiC is roughly 118° at 700°C on an oxidized melt surface [41]. This means that spontaneous entry is impossible without fluxing agents. Difficulty in obtaining a homogenous dispersion of particles and formation of particles clusters during solidification process are the major

difficulties during direct casting of composites. Many studies have been conducted previously to achieve defect free composites [40, 140].

Enhancing the wettability of TiC particles with Al melt will improve the particle incorporation. Fluxes, performing the casting process in a controlled environment will reduce the formation of oxide layers and magnesium helps to overcome the thermodynamic barriers. To achieve homogenous dispersion and reduce particle cluster, melts are often vigorously stirred to add reinforcements below the melt surface. This induces wetting and thereby the particles are retained in the metal after solidification occurs. By introducing flux agent and stirring action in casting will help to produce high quality Al-TiC_p composites.

3.2 Development of stir casting setup

Liquid stirring is one of the important techniques having versatility to cast MMCs without compromising the quality of cast product. A systemized inert atmospheric stir casting setup has been developed to produce high quality Al-TiC_p composites. A schematic line diagram of developed stir casting setup is shown in Fig. 3.1. The complete stir casting facility comprises of gas furnace, mechanical motor with speed regulator, stir arrangement, K type thermocouple, and a metal chamber filled with argon gas. K type thermocouple with digital temperature recorder was attached to the furnace and the stainless-steel stirrer is coated with alumina to avoid migration of ferrous ions from stirrer to molten metal. stirrer was attached to mechanical motor. Pneumatic hose was connected to copper tube in metal chamber to help supply argon gas. A gas furnace of capacity of 900 – 1150°C was used to melt the aluminium matrix and preheat the reinforcement particles. A micro-processor based PID digital temperature recorder was attached to K type thermocouple of accuracy ±2°C and fitted to the furnace to record the temperature during preheating and melting of

aluminium matrix. Doubled layer fire bricks were used for furnace walls which ensure uniform maintenance of heat.

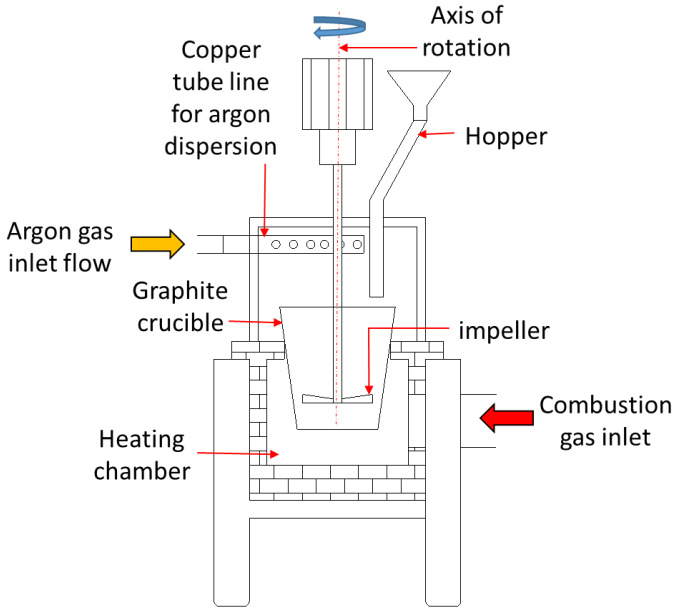

Fig. 3.1. Schematic design of stir casting facility used for the production of Al–TiC_p composites.

Graphite crucible of 5 kg capacity was used to melt the metal. After melting of aluminium, hard-reinforced particulates were added to melt and immediately mixed properly for proper homogenizing of reinforced particulate in the molten metal matrix. To serve this purpose, a stirring mechanism has been design and fabricated. An electric motor of 0.092 KW, of maximum speed 4000 rpm was used to rotate the stirrer. A speed regulator with tachometer was also fitted to the system to regulate the stirring speed during mixing of hard reinforced particulate and matrix. A stainless-steel stirring rod coated with alumina was used with an impeller having 3 blades (see Fig. 3.1). A metal chamber was placed on the top of crucible to maintain argon blanket over the surface of the melt. Argon gas was supplied through flow line into the chamber to avoid reaction of molten metal with atmosphere. Melt stirring technique for production of composite has some important advantages like better bonding of metal matrix and hard particles, easier control of matrix structure, simplicity and low cost of processing.

3.2.1 Matrix and reinforcement material

The main driving force for development of particulate reinforced composites is to produce a material with desirable structures and characteristic. Al-TiC_p composite specimens of size 150 mm length and 32 mm diameter were fabricated using developed stir casting system. Al-TiC_p composite is extensively preferred as an engineering material for various high-performance components due to the grain refinery properties of TiC reinforcement particles.

Table 3.1 Work material details.

Titanium carbide (*TiC*)	*Source:* Himedia labs Pvt Ltd *Density:* 4900 Kg m^{-3} *Average particle size:* 40 microns *Coefficient of thermal expansion:* 4.7 x10^{-6}/°C *Thermal conductivity:* 200W/mK *Young's modulus:* 415 GPa, *Poisson ratio:* 0.18
Aluminium (*Al*)	Composition of Al 6061(by weight %) Si, 0.15; Fe, 0.15; Cu, 0.021; Ti, 0.053; Mg, 0.92; Mn, 0.044; Zn, 0.072; Cr, 0.005; Al remaining *Density:* 2700 Kg m^{-3} *Coefficient of thermal expansion:* 22 x10^{-6}/°C *Thermal conductive:* 72 GPa *Poisson's ratio:* 0.33

In the present investigation, Al6061 was selected as a matrix material. This alloy was chosen as matrix based on the literature survey as it exhibits high strength with the option of modifying the strength of the composites by adopting optimal heat treatment. This alloy is commonly used for making automobile and aircraft components. The chemical composition of the matrix material was obtained through chemical characterization test conducted using a spectrometer (Table 3.1). TiC particles were considered as reinforcement to achieve high wear resistance, specific strength to weight ratio, thermal conductivity and low thermal coefficient. The particle morphology study reveals that shape of the TiC particles has been angular –irregular. The mean size, density and source of TiC_p are given in table 3.1.

3.2.2 Production of Al-TiC_p composites

Al-TiC_p composites were produced with stir casting process using mechanical mixing of the molten aluminium. Al ingots were placed inside the graphite crucible and heated to a temperature 200°C above the melting point of Al alloy. The process involved in production of composite is shown in Fig. 3.2.

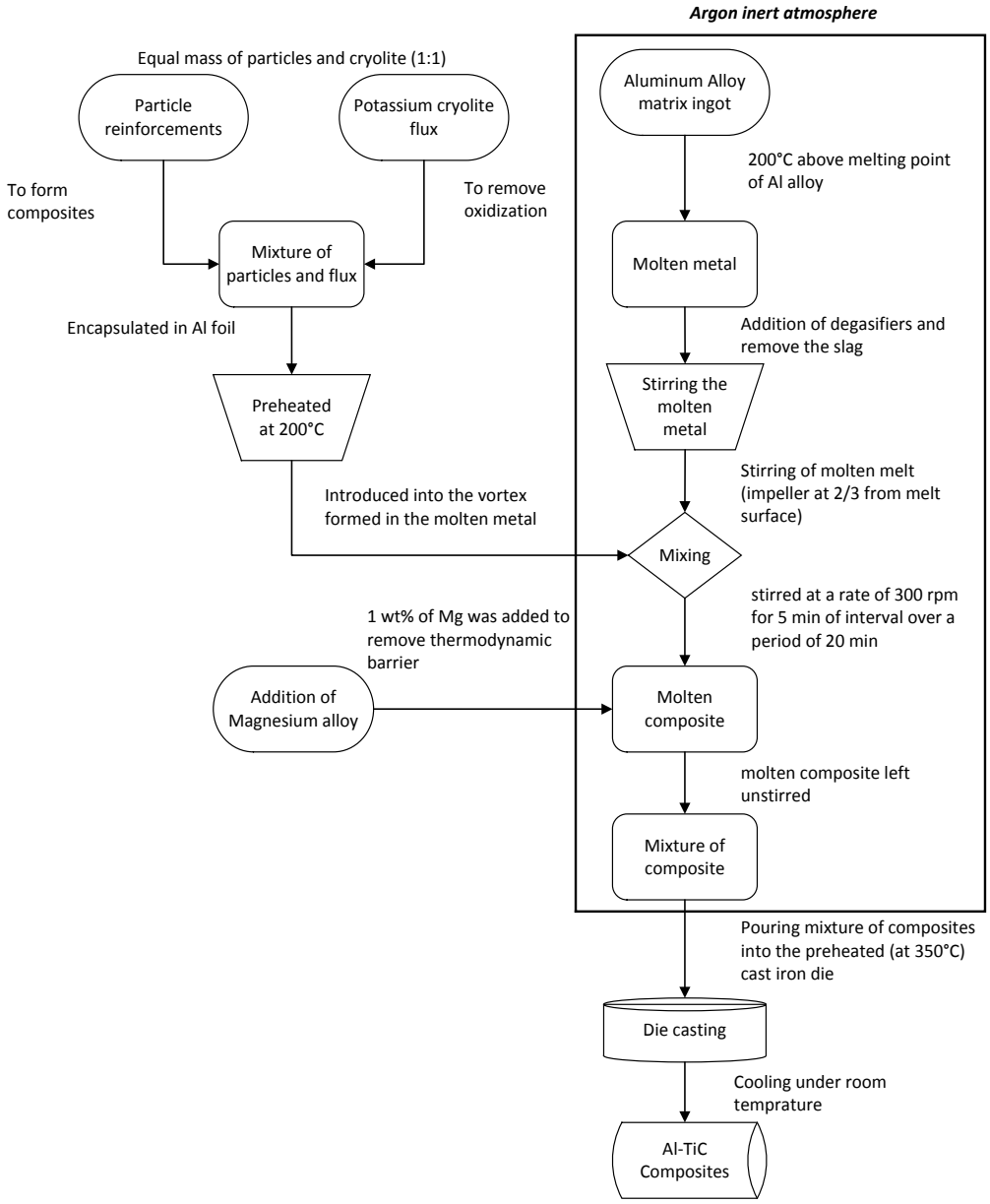

Fig. 3.2. Process flow chart of stir casting technique for Al-TiC_p composites production.

After complete melting, degasifies were added to remove the gas pockets and slag was removed if any. After release of gas pockets, the impeller was introduced immediately at 2/3 from the surface of the melt into the crucible and stirring was carried out. The molten

metal was stirred at a speed of 400 rpm for 20 min to create a vortex. Equal mass proportion of TiC_p and $KAlF_6$ flux were mixed uniformly. This mixture was wrapped inside aluminium foil in the form of capsules and heated up to 300°C before introducing into the molten melt. These preheated capsules were introduced into the vortex of molten metal and mixture was continuously stirred at a rate of 300 rpm for 5 min of interval over a period of 20 min. 1% of magnesium (weight of composite) was added during stirring to improve wettability of TiC_p with molten aluminium. This whole process was carried out under inert environment to achieve better bonding between reinforcements and matrix and also to reduce reaction of matrix with the atmosphere. Argon gas was supplied into the metal chamber at a uniform flow rate to form a gas blanket over the molten metal inside the crucible. The process of composites was performed at 850-950°C temperature and 300- 400 rpm stirring speed.

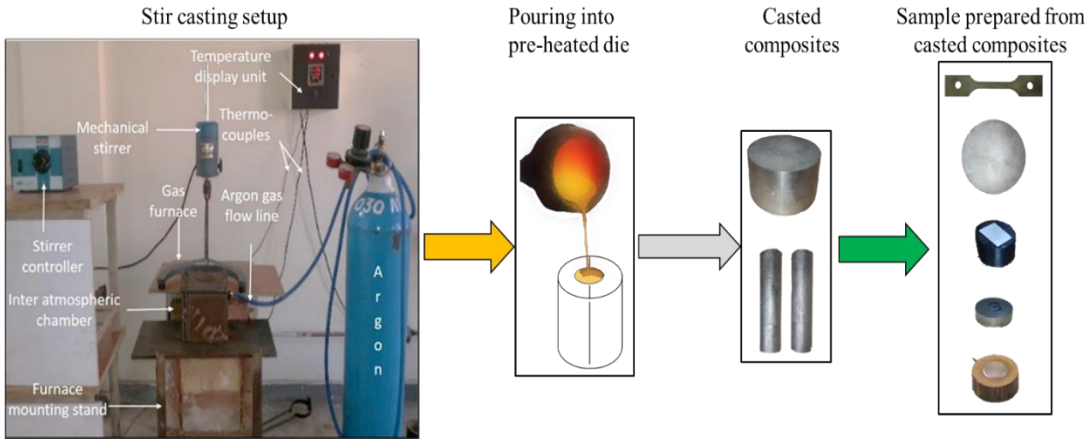

Fig. 3.3. Photographic image of developed stir casting facility.

A photographic image of developed stir casting setup is shown in Fig. 3.3. The molten metal temperature variation is measured with the help of K-type thermocouples. After complete stirring, the molten MMC mixture was ported into the preheated cast iron mould to form a test material in bar. The die was preheated to 300°C to remove the moisture. Finally, the molten mixture was allowed to cool down to room temperature and

solidify in the die to obtain the required Al/TiC specimens of 150 mm length, 30 mm diameter, 50 mm height and 120 mm diameter. This process ensured that the structure of the composite would be homogenous. The Al/TiC specimens in the 'as-cast' conditions are shown in Fig. 3.3.

Two composite samples of different weight fractions, Al-5%TiC_p and Al-10%TiC_p were produced. These test samples were subjected to heat treatment process (T6 condition) in a carbolite oven at 540°C for about 6 hr to ensure homogenized cast structure and minimized segregation of alloy elements. These heat-treated sample were then quenched in water between 25 and 100°C to obtain maximum strength. These quenched samples were artificially aged at 160°C for about 6 hr to precipitate constituents which were dissolved during the solution treatment for pronounced improvement in properties. Heat treatment (T6 condition) processes are carried on the test samples prior to the characterization.

3.2.3 Characterization analysis of MMCs

In the present study 5 and 10 wt% of TiC particles were added in Al-6061 matrix to form Al-TiC composites. Characterization was performed on casted Al-TiC_p composites and Al-6061 alloy was used as base material. The specimens were sectioned from the mid plane along the full length of the casted material and machined precisely to require dimensions as per the standards (see Fig. 3.3).

3.2.3.1 X-ray diffraction

A Rigaku X-ray diffractometer (shown in 3.4) was used in order to identify the phases present in casted Al-TiC_p composite and TiC particles. X-ray diffraction was carried out at a scanning rate of 0.01º 2θ/sec using Cu k (α) radiation. The source voltage and current were maintained at 40 kV and 40 mA. Peaks obtained in the diagram were analyzed. In order to get an idea of the relative volume fraction of TiC, the ratio of the peak intensities

of the most intense peaks of TiC and Al has been calculated. The samples were scrapped through filler and powder was collected and loaded into the XRD unit.

Fig. 3.4. X-ray diffractometer.

3.2.3.2 Microstructure

Microstructural characterization of the specimens was carried out under optical microscope (STM6, Olympus; accuracy 0.1 μm) shown in Fig. 3.5. The specimens were prepared from sectioned cylindrical components. Cross section surfaces were polished with 400, 800, 1200, 1600 and 2000 grit papers for fine finished surface. The disk polishing was carried out in a rotating wheel fixed with velvet cloth (around 300 rpm) and diamond paste of varying size ranging from 6, 3, 1 and 0.25 μm with a gentle applied pressure to get final finish. Then, these samples were etched with Keller's reagent to observe the effect of TiC_p addition on the grain structure and particle distribution. Optical micrographs of the polished specimens were recorded at different magnifications. Scanning electron microscopic (SEM) analysis was performed to ascertain the particle distribution. EDX analysis was performed to confirm the presence of TiC_p reinforcements. Further, these metallographic finished samples are used for micro hardness studies.

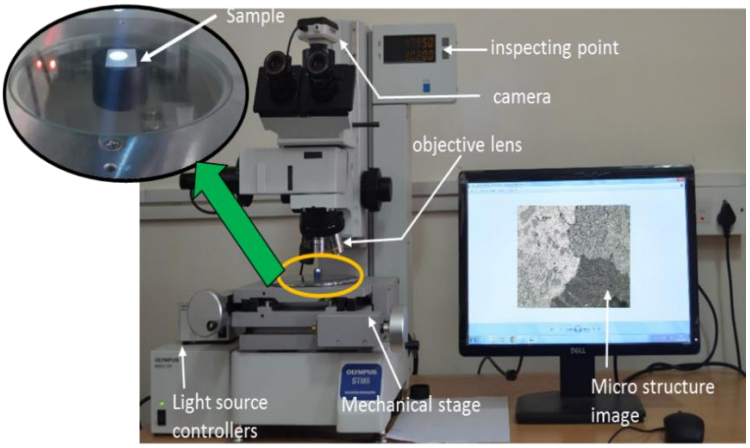

Fig. 3.5. Microscope integrated with camera and measuring software setup.

3.2.3.3 Micro hardness

Micro-hardness of the casted composites was determined using micro Vicker's hardness tester (HM 220A - Mitutoyo make) integrated with diamond pyramid indenter (Fig. 3.6.). A 100-gf load with a dwell time of 30 s was employed for each test to estimate the hardness value. For measuring the micro-hardness, distance between the diagonals of the rhombus is measured. In order to eliminate the segregation effect, readings were taken at three different locations for each specimen.

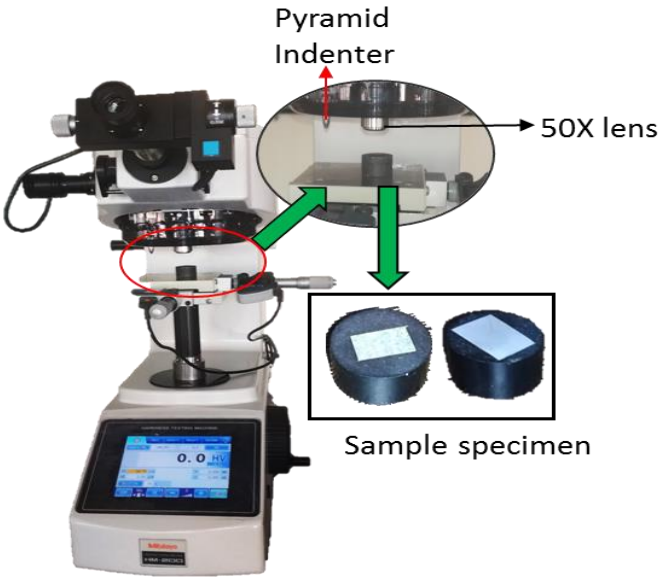

Fig. 3.6. Micro Vickers hardness test rig.

3.2.3.4 Density

The density of the base material and composite were measured using an Archimedean technique in order to determine the particle volume fraction and the particle yield. Density was measured on top loading electronic balance (ViBRA make HT/HTR series) of precision 0.1 mg in water and air was as shown in Fig. 3.7. Standard cylindrical specimens of 14 mm diameter and 20 mm length were used for these tests. Average readings of three random specimens for each composition were taken as the density of the composite specimen.

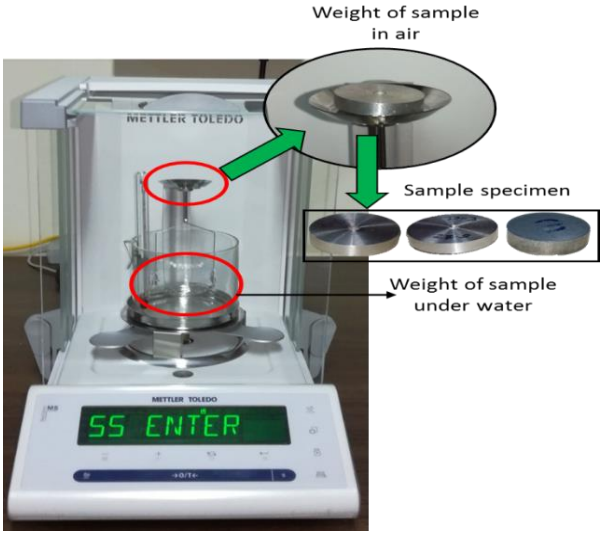

Fig. 3.7. Density measuring setup.

3.2.3.5 Tensile test

Tensile testing is one of the most widely used testing method to quantify several important mechanical properties of a material. As per the ASTM E08-08-11 (sub size), samples of gauge length 30.8 mm, 25.7 mm grip distance and thickness of 2.8 mm were machined from casted composite by wire cutting electro-discharge machining process. Tensile tests were carried out on casted composites and base material on a computer controlled universal testing machining under room temperature as shown in Fig. 3.8. These tests help to determine the Young's modulus (elastic deformation), yield strength, ultimate

tensile strength and percentage elongation (ductility properties) of the casted materials. Tests were conducted in triplicate and average of three random samples was taken as material properties of casted components.

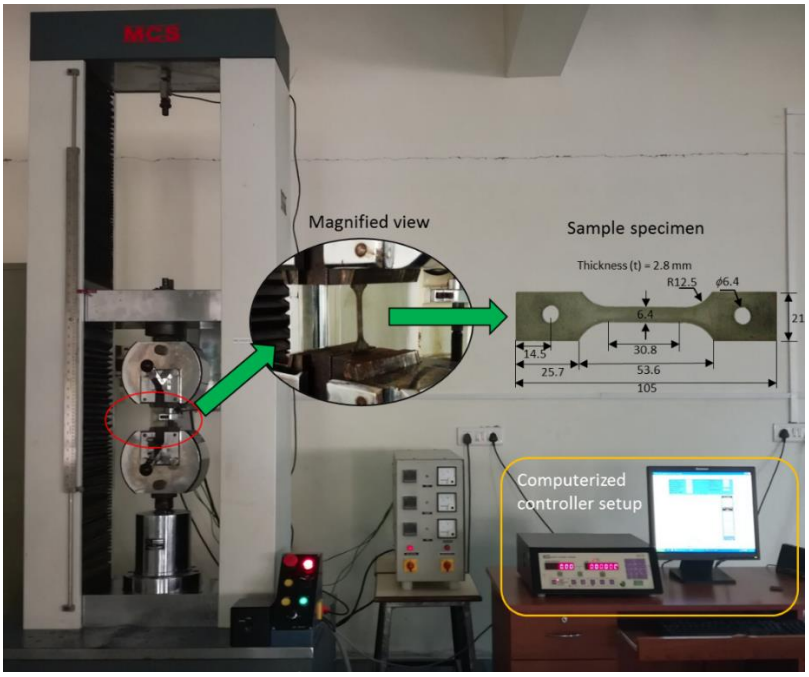

Fig. 3.8. Universal testing machine.

3.3 Results and discussion

The quality and performance of produced Al-TiC_p composites were needed to be analysed. Therefore, in the following sections, particle incorporation capability of the developed process by metallographic and EDX analysis which explain the effect of TiC_p on Al matrix are discussed. Further, to understand the effect of reinforcements on casted composites (casted Al-6061, Al-5wt%TiC_p and Al-10wt%TiC_p), mechanical testing was performed to determined mechanical properties like density, hardness, tensile strength, yield strength and elongation.

3.3.1 X ray diffraction analysis

In order to identify the different phases, XRD analysis was performed on developed Al-TiC_p composites and TiC particles. The XRD patterns are shown in Fig. 3.9. (a-c). The

XRD spectrum of developed Al-TiC_p composites shows that no extra peaks due to any impurity phases were present.

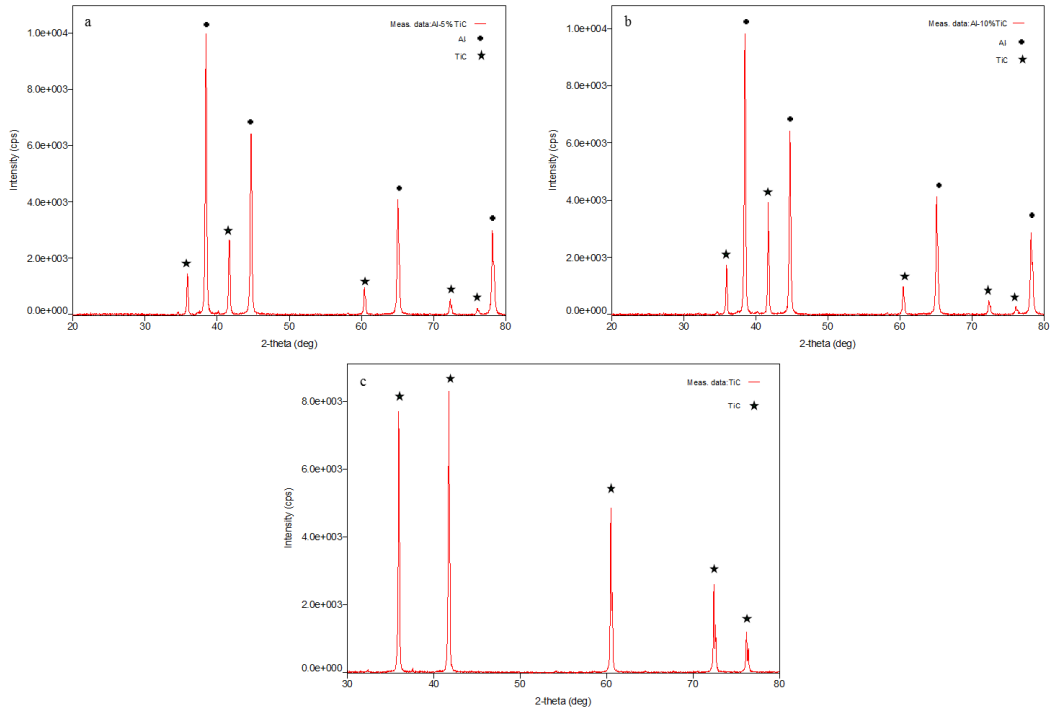

Fig. 3.9. XRD pattern (a) Non-reinforced Al; (b) Al - 5wt% TiC_p (c) Al - 10wt% TiC_p.

The peak intensity of TiC particle increases with increase in wt%. It is evident from Fig. 3.9. that diffraction peaks of other elements except Al, and TiC were not detected. This observation led to a conclusion that the integrity of TiC_p was preserved during casting. TiC_p are thermodynamically stable at the applied casting temperature. There is no interfacial reaction between TiC particles and aluminum matrix during casting. Such interfacial reactions would often result in the formation of brittle intermetallic compounds in the composite and degrade the mechanical and tribological properties. The absence of those intermetallic compounds in the XRD patterns of the prepared composites confirms that the utilized systemized inert atmospheric stir casting facility for production of high quality Al-TiC_p composites is successful. However, its quality and performance were needed to be analysed. Therefore, in the following section, results from microstructural analysis of the

TiC particle distribution and its grain refinement characteristics under different weight percentages are discussed.

3.3.2 Microstructural analysis of Al-TiC_p composites

Microscopic observations of cast Al-TiC_p composites at different weight percentages are shown in Fig. 3.10. TiC_p are distributed partially uniform over the composite and are mostly segregation in the Al grain boundary. The micrograph shows fine distribution of TiC reinforcements with fewer clusters. Extensive agglomeration may occur due to the possibility of inter-particle collisions at higher number of particles present. Studies by Kennedy et al. confirm that cooling condition does not affect the homogeneity of the particle distribution significantly [140]. At higher volume fraction, a smaller percentage of the particle simulate grain refinement and hence smaller proportion of them are located at the center of the matrix grain. The microstructure of non-reinforced Al alloy varied strongly with TiC_p reinforcement in Al alloy composite. Grain size measurements presented in Table 3.2 indicate that addition of TiC_p forms 50 times smaller grain size compared to non-reinforced Al alloy.

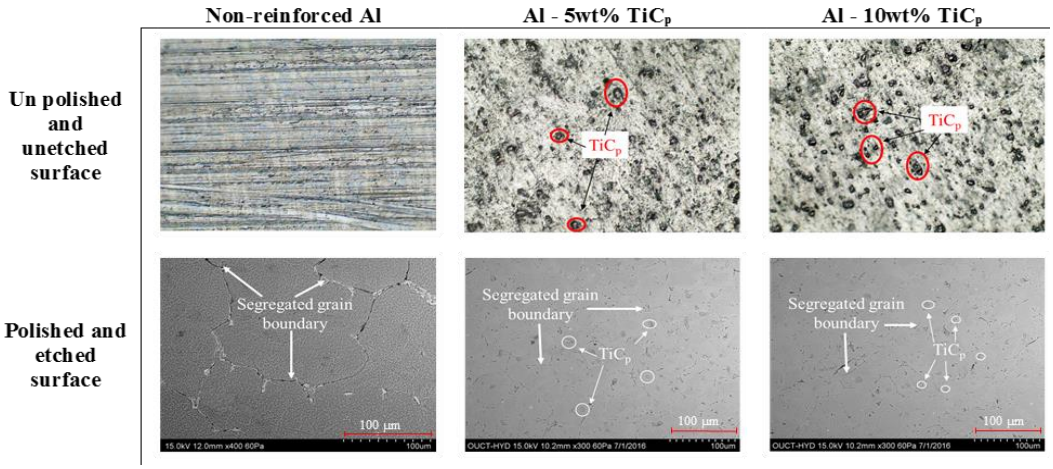

Fig. 3.10. Microscopic images of particle distribution in Al-TiC_p composites.

The grain structure of non-reinforced Al alloy is shown in Fig. 3.10. and 3.11. (a). The presence of TiC particles results in significant grain refinement. The micro structure

observed in Al-5%TiC_p composite shows highly refined grain structure as shown in Fig. 3.11. (b). This may be due to sufficient lattice matching for direct nucleation of solid aluminium on the particle's surface [141, 142]. This refinement occurs along the full length of the casting and a significant portion of TiC particles are positioned within the Al grains.

Table 3.2 Grain size before and after particle addition.

	Non-reinforced Al	Al - 5wt% TiC_p	Al - 10wt% TiC_p
Grain Size (microns)	> 4000	80	92

Table 3.2 illustrates that as the weight fraction increases, the grain size of composite decreases. The grain size refinement in Al-10wt% TiC_p is only slightly higher than Al-5wt% TiC_p. This suggests that at higher particle fraction, a smaller proportion of the particles act as grain nucleation site. Homogenous distribution of the TiC and un-clustered spatial distribution of TiC reinforcement particles being located mainly at the center of Al grain, and also at the grain boundary (see Fig. 3.10 (b, d, f) and.6 (b)) was observed. This is obvious because it is easier for atoms to adhere to a growing crystal than a nucleation site to get activated [141].

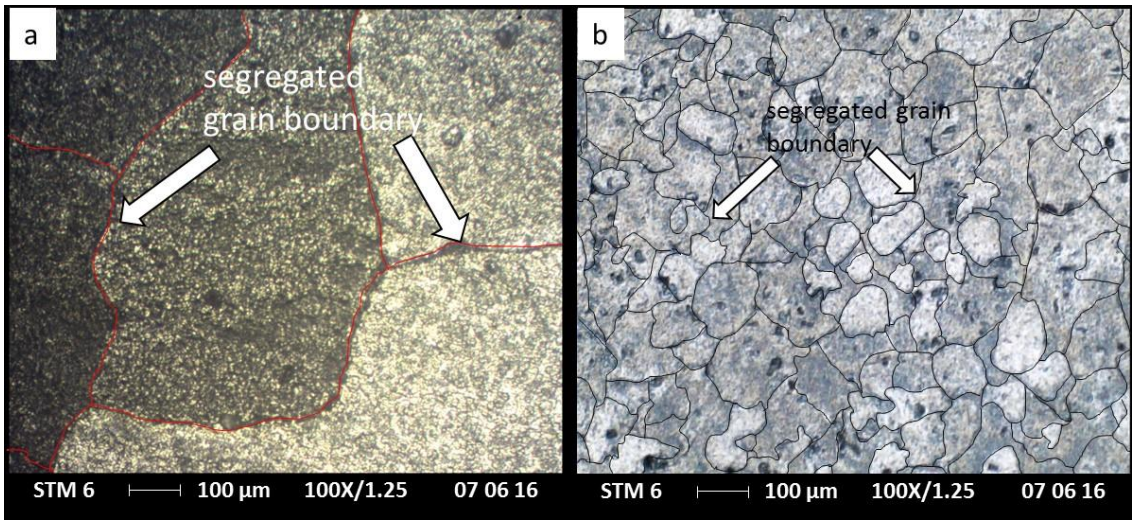

Fig. 3.11. Microscopic image of segregated grain structure for (a) Non-reinforced Al, (b) Al-5 wt% TiC castings.

TiC particles act as grain nucleation sites and form small gain structures. Similar fashion in grain refinement was observed by other researchers [143, 144]. The resultant grain size is equi-axed and small, to achieve homogenous distribution. The interfacial energy between the particles and the solid metal plays a major role for engulfment of TiC_p in Al matrix. EDX analysis confirms the presence of TiC particle reinforcements as shown in Fig. 3.12. The peak confirms the presence of aluminium and TiC_p in the sample. Metallic reaction has not occurred throughout the observation; this can be confirmed as the graph shows no extra peaks. Hence the prepared composite was good to perform machining studies.

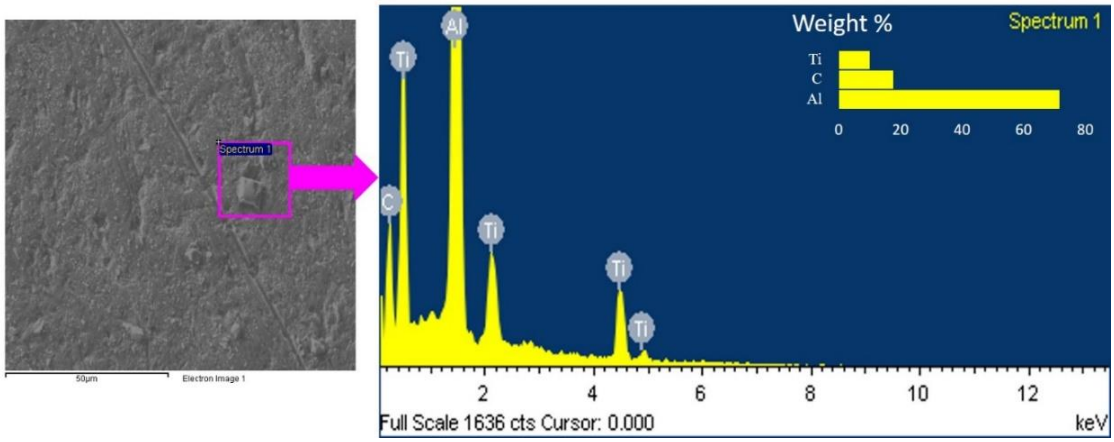

Fig. 3.12. EDX results of Al-5wt% TiC_p composites.

3.3.3 Analysis of microhardness

Hardness is defined as the resistance offered by the material to surface indentation. It is the function of the stress required to produce some specific types of surface deformation. The hardness of the fabricated samples made by the stir casting processes is measured using Vicker's micro hardness measuring machine with a load of 0.4903 kgf. The load is applied for 30 seconds. In order to eliminate a possible segregation effect, a minimum of five hardness readings are taken for each specimen at different locations of the test samples.

From Fig. 3.13, it is evident that, as the percentage of TiC particles is increased from 0 to 10wt.%, the hardness of the composite increases monotonically and significantly. It is also reported by other researchers, that the addition of ceramic particles to aluminium alloys leads to the improvement in their strength, wear resistance, and hardness [145]. According to Christy et al. [146] and Sahin [147], the increased hardness is also attributed to the fact that the hard TiC particles act as barriers to the movement of the dislocations within the matrix. The other reason for the increase in hardness is due to the effect of the increase in the interfacial contact area between the matrix and the reinforcement.

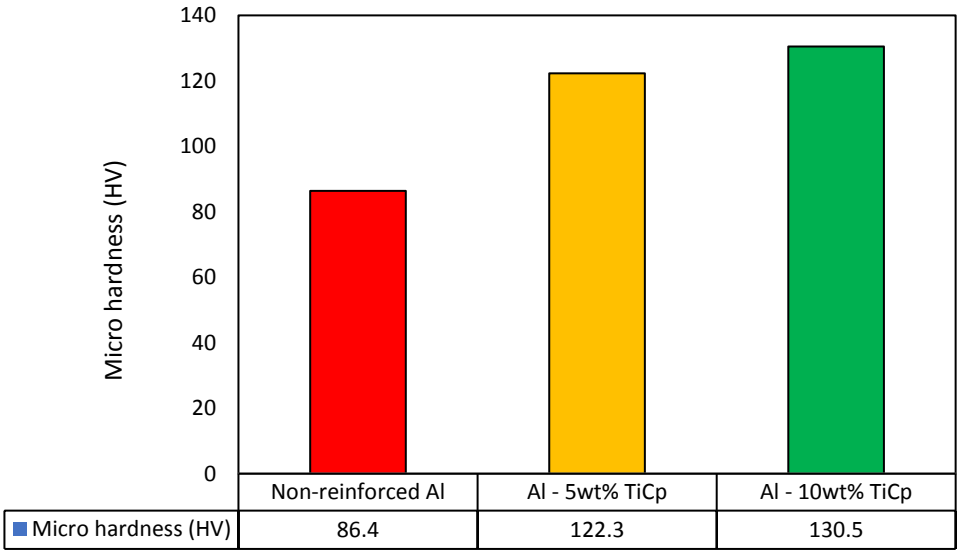

Fig. 3.13. Microhardness of casted Al-TiC_p composite.

Further, hardness is decreased as reinforcement content increases. Sample with 10wt% TiC_p shows slightly higher hardness as compared to 5wt% of TiC_p. Thus, 5wt% TiC_p can be considered as the optimum weight percentage of the particulate for the desired application. This is due to the effect of the decrease in the cohesive strength or debonding between the particles and the matrix. The hardness of the composites was significantly higher than that of the matrix material due to the increased strain energy the hardness of the composites is increased at the peripheral of the particles dispersed in the matrix [148].

3.3.4 Analysis of density

Density is a physical property that reflects the characteristics of the composites. Experimentally, density of composites as well as matrix alloy was determined by immersing solid body in a liquid. The solid apparently loses as much of its own weight of the liquid it has displaced. The density of the solid body was determined by using a liquid of known density (water). The mean, standard deviation, standard error and upper and lower limits of confidence interval of density of Al-6061, Al-5wt%TiC_p and Al-10wt%TiC_p are presented in table 3.3. In all the conditions, average of density lines with in the respective upper and lower limits of confidence for both alloy and composites. It is well known that the density of Al-TiC_p composite marginally increases due to the weight percentage of TiC particles.

Table 3.3 Composite experimental density (g/cm^3).

Material	Density (ρ_{exp}) g/cm^3			Mean density (M) g/cm^3	Standard Deviation (SD)	Standard Error (SE)	95% Confidence Interval (CI)	
	1	2	3				Min	Max
Al-6061	2.699	2.694	2.689	2.694	0.005	0.0029	2.688	2.699
Al-5wt%TiC_p	2.758	2.748	2.75	2.752	0.005	0.0031	2.746	2.757
Al-10wt%TiC_p	2.801	2.803	2.802	2.802	0.001	0.0006	2.800	2.803

In a composite, the proportion of the matrix and the reinforcement have been expressed either as the weight fraction (w) which is relevant to fabrication or volume fraction (ϑ) which is commonly used in properties calculation. By relating weight and volume fraction via density (ρ), the following expression has been obtained and its general form has been known as rule of mixture.

$$\rho_c = \frac{\rho_r \cdot \rho_m}{\rho_r \cdot w_m + \rho_m \cdot w_r} \tag{3.1}$$

Where,

ρ_c, ρ_m, ρ_r - Density of the composites, the matrix and the reinforcements (particulates) respectively.

w_m, w_r -weight fraction of the matrix and the reinforcement (particulates) respectively.

Table 3.4 Composite density (g/cm^3), volume fraction and yields.

System	Vol fraction of TiC_p	Experimental density g/m^3	Calculated vol. fraction	Approx. yield (%)	Theoretical density g/m^3
Non-reinforced Al	0	2.694	0	0	2.700
Al - 5wt% TiC_p	2.82	2.752	0.0273	97	2.762
Al - 10wt% TiC_p	5.77	2.802	0.0538	93	2.829

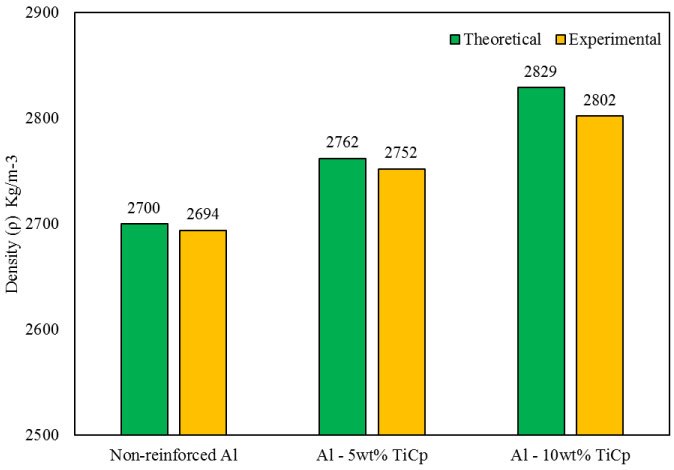

Fig. 3.14. Density of casted composite.

The mean density of unreinforced and reinforced Al alloy is calculated theoretically by rule of mixture concept. Both the theoretical and experimental values are presented in Fig. 3.14. Table 3.4 shows that the developed composites yield 97% closer to the theoretical density. It is observed that the experimental and the theoretical density have been in line with each other and confirms that the developed stir casting method is successful for preparation Al-TiC_p composites

3.3.5 Analysis of tensile test

To evaluate further the mechanical properties of the composites, tensile tests were conducted and stress-strain graph is shown in Fig. 3.15. Tensile properties of developed composites have been examined and is presented in Fig. 3.16. The ultimate tensile strength is improved with increase in TiC particles. This increase of ultimate tensile strength is a result of much higher work hardening rate at lower strain during tensile loading, resulting from the constraint exerted by TiC particles on plastic flow matrix. This further leads to reduction in percentage of elongation. It is observed from the tensile results that the percentage elongation is reduced from 8.4 to 7.3% with addition of TiC particles from 0 to 10 wt%. TiC particles commonly deform elastically, considerably higher local matrix strain is required to accommodate any plastic deformation in composites than the non-reinforced Al.

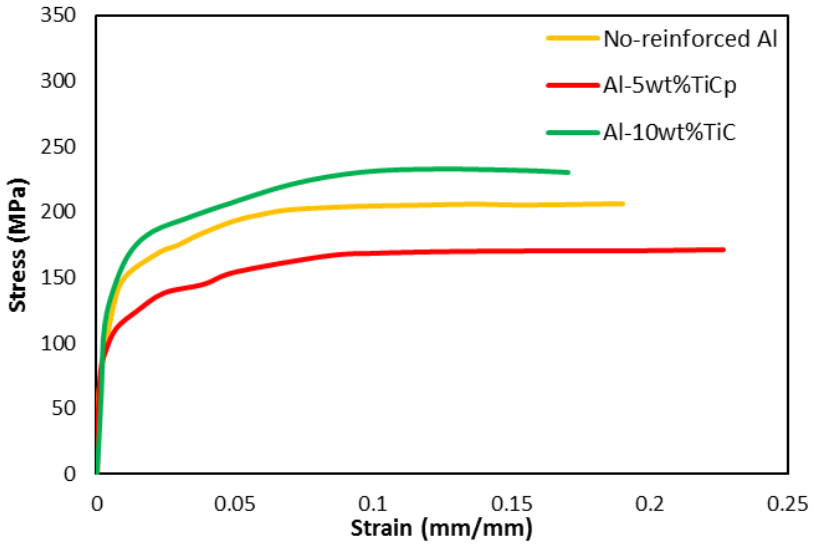

Fig. 3.15. Strain Vs strain of casted composites.

The ultimate tensile strengths of Al-5wt% TiC_p and Al-10wt% TiC_p were found to be 25% and 41.4% higher than the non-reinforced Al alloy respectively. The addition of TiC particles improves the mechanical properties mainly by stress transference from the aluminum matrix to the reinforced particles TiC. This is because of Orowan mechanism by

which a dislocation bypasses impenetrable obstacle where a dislocation bows out considerably to leave a dislocation loop around a particle. The interaction between the dislocations and TiC results in an improvement in strength [149]. The increase in strength is (i) due to grain refinement effect, (ii) solid solution strengthening and (iii) the presence of reinforcement and other phases hinders the dislocation movement and sliding of grain boundary.

Further the developed composites give 25.3% and 45.4% larger yield strength value for Al-5wt% TiC and Al-10wt% TiC respectively than non-reinforced Al. The increase in the yield strength with increase in addition of TiC particles is due to reduction in the interspatial distance between the TiC_p particles. Because of this, there is restriction in the plastic flow due to the random distribution of the particles in the matrix. This action provides an increase in material properties of the developed composites. Unlu et al. [150] also made similar observations in his experiment during the testing of the aluminium-alumina oxide composites.

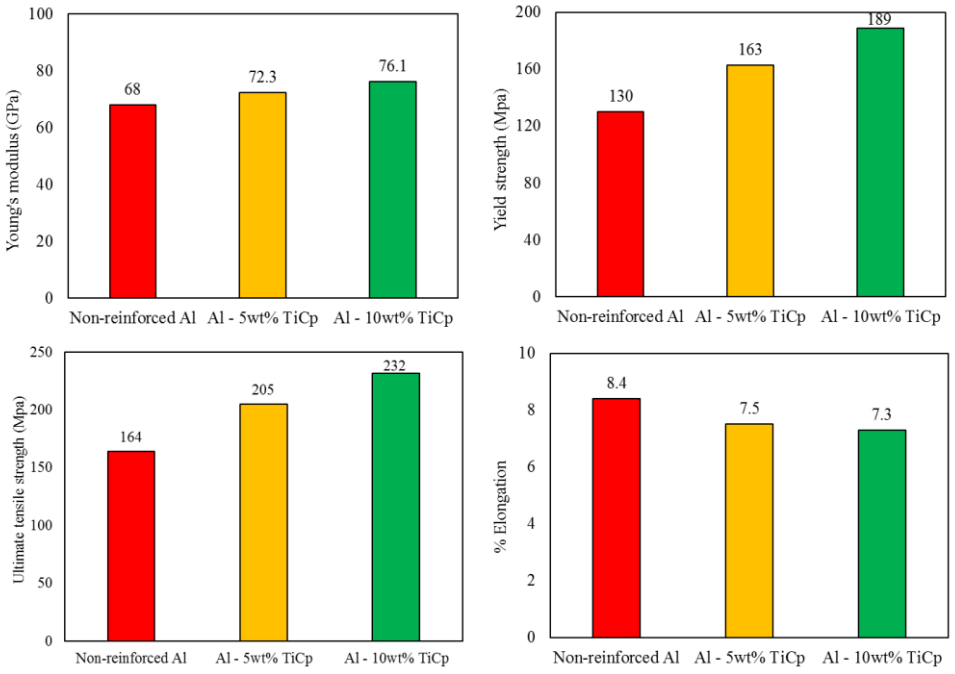

Fig. 3.16. Variation of tensile properties of the composites with the TiC particle content at room temperature.

The fracture morphology of the tensile tested specimens is shown in Fig. 3.16 which presents the effect of weight percentage of TiC particles. The fracture morphology of the non-reinforced Al in Fig. 3.17. (a) shows bigger and uniformly distributed voids which indicate a ductile fracture. The fracture morphology of the prepared composites shows smaller size voids as TiC content increases. It is also observed that composites present smaller void than the non-reinforced alloy which indicates macroscopically brittle fracture and microscopically ductile fracture. This is due to presence of TiC particles, which refined the grain size of aluminum and reduced ductility resulting in smaller voids. It has also been observed that TiC particles remain well located in the dimple contouring even after fracture, suggesting that there exists a strong bond between the reinforcements and the matrix.

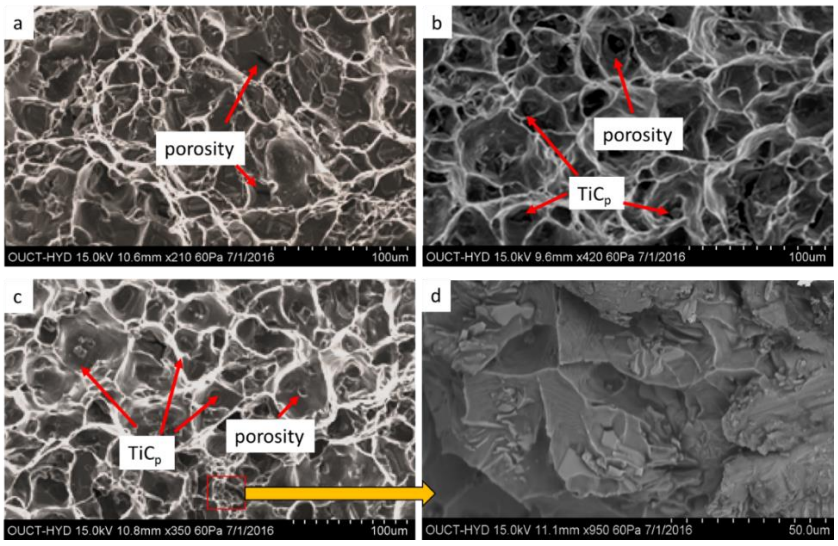

Fig. 3.17. Fracture morphology of the tensile tested specimens.

3.4 Summary

In the current chapter, Al-TiC_p composites were successfully produced by using systemized inert atmospheric stir casting facility. Its quality and performance was analysed by studying the microstructural and mechanical properties of the material. From the XRD analysis, it is clearly understood that, no intermittent phases are formed in the production. The microstructural analysis reveals that TiC particles significantly refined the grain

structure of aluminium matrix. It is also observed that TiC particles are engulfed into the growing solid which reduces particle solid interface energy leading to reduction in agglomeration. Density analysis presents that 5wt% composites yields 97% closer density to the theoretical value. These results confirm that production of Al-TiC composite produced by the purposed methodology helps to produce high quality composites. Further mechanical testing studies are performed to analyse the performance of the developed composites. From the experimental results, it is inferred that the percentage increase in mechanical properties is reduced beyond a certain increase in wt% of TiC particles. 20% increase in micro hardness was found for 0 to 5wt%, while it was just 11.6% for 5 to 10wt% of TiC particles as reinforcements. Similar trend was observed in tensile test results. Therefore, a composition consisting of 5wt% TiC particles in aluminium 6061 alloy is used for the further machining studies. In order to overcome the inherent difficulties associated with machining of Al-TiC composites, an experimental setup has been developed based on the concept of cryogenic air blast atomization process. The subsequent chapter deals with design and development of the cryogenic experimental setup along with scientific analysis of flow conditions and spray characteristics.

Chapter 4
Design, Development and Evaluation of Atomized Liquid Nitrogen Spray System

The set objective of current research (objective 2 listed in Chapter 1) and impetus to overcome the research gap in the existing literature (gap 4 listed in Chapter 2) to design and develop an atomized liquid nitrogen spray system. This system supplies liquid nitrogen (LN_2) at high velocity jet and constant flow rate into the machining zone during machining of Al-5%TiC_p composites. The LN_2 spray discharge technique used combines atomization process with cryogenic technology. This chapter is organized as follows: Section 3.1 presents brief information about cryogenic technology and atomization based cutting fluid. In section 3.2 design and development of atomized liquid nitrogen (ALN) spray assisted machining setup is presented. Section 3.3 explains the spray characteristics of developed ALN spray system. Section 3.4 presents the optimal ALN spray discharge parameters during machining process. Finally, Section 3.5 presents the overall summary of this chapter.

4.1 Introduction

During machining, heat is generated as a result of shearing on the primary shear plane and friction on tool/chip and tool/workpiece interfaces. Supply of cryogenic liquid (i.e., Liquid Nitrogen: LN_2) at constant pressure and a minimum flow rate into the tool/chip/workpiece interface will enhance cooling effect during machining. Previous studies [16, 17, 19] have revealed various techniques such as high-pressure jet, modified tool holder and cooling by means of modified chip breaker to maximize the effectiveness of cryogenic machining. These techniques show the promising results than techniques

utilizing conventional coolants, however, they need large quantities of LN_2 (0.625-0.814 L/min) [17, 19, 151]. Studies portray a potential in the use of atomized technique for effective penetration of cutting fluid and cryogenic machining to achieve better cooling and lubrication. Combining of atomization process with cryogenic technology will improve machining performance. Pressurized cryogenic jet interacts with high velocity gas producing focused jet droplets which will help to improve the cooling at the selective area and achieve better penetration into the machining zones. Improved penetration with pressurized LN_2 has been suggested by Hong et al. [19, 20]. This study is an attempt to develop an innovative cooling approach based on cryogenic air blast atomization process to minimize the use of LN_2 and maximize its cooling effect on the cutting tool edge. The work is also extended to design and develop a micro nozzle to improve the supply of LN_2 effectively into the machining zone.

4.2 Methodology

The aim of the current research work is to develop and evaluate the Atomized Liquid Nitrogen (ALN) spray diffusion system by combining atomization process with cryogenic technology. This technique helps to produce 50 μm liquid droplets, which impinges as a jet of 45 m/s high-velocity droplets directed towards tool/chip interface which will help to improve the cooling at the selective area and achieve better penetration into the machining zones and minimize the usage of LN_2. To evaluate the developed spray diffusion system spray characteristics such as spray pattern, angle, spray velocity, droplet diameter and droplet temperature were experimentally determined and performance was analyzed by machining test at different spray parameters such as feeding pressure, spay distance and impingement angle. Tool wear and surface roughness were considered as performance indices to evaluate the machinability of Al-TiC_p Composites.

4.2.1 Design and development of Atomized Liquid Nitrogen (ALN) spray system

Atomized Liquid Nitrogen (ALN) spray system is developed by combining atomization process with cryogenic technology. A schematic view of proposed ALN spray system is illustrated in Fig. 4.1. Liquid nitrogen is drawn along with high velocity cryogenic chilled air in the form of droplets. Cryogenic liquid droplets are sprayed through a nozzle, achieving effective penetration of the suspended droplets into the tool/chip/workpiece interface. LN_2 at -196 ºC was used as cryogenic liquid in this process. This technique reduces the amount of LN_2 used while improving lubrication effect at the cutting edge.

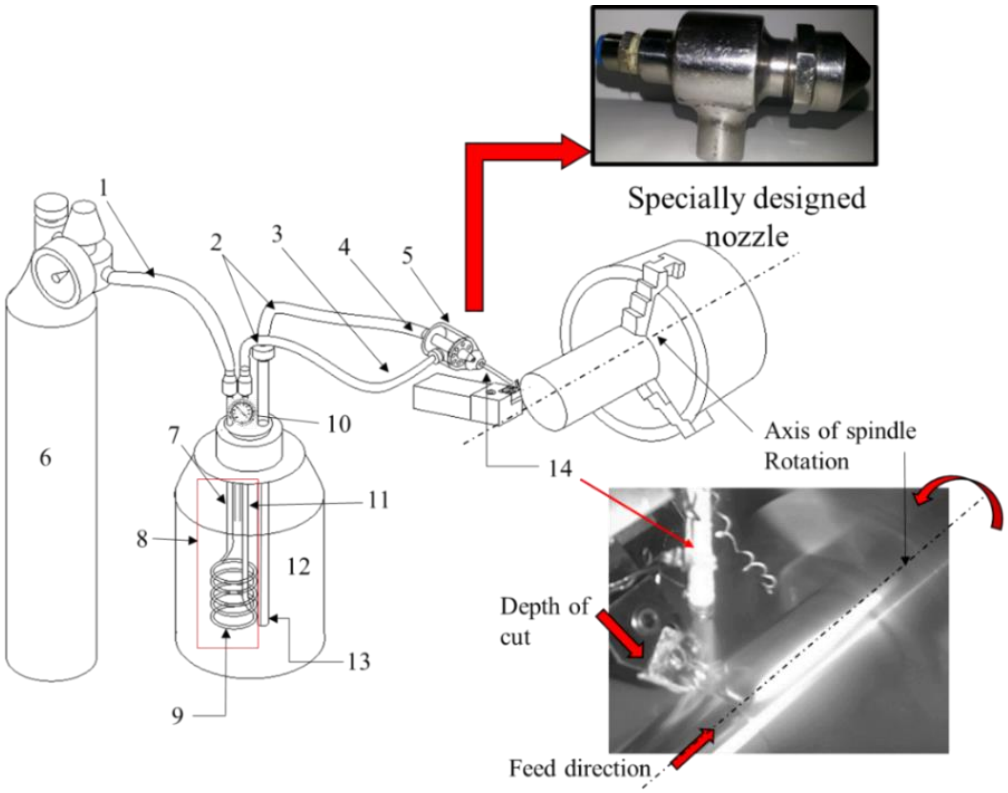

1. Pneumatic hose
2. Insulated stainless steel hose
3. CCA inlet
4. LN_2 inlet
5. Nozzle unit
6. Argon
7. CCA inlet flow line
8. CAC unit
9. Copper coiled pipe
10. Pressure gauge
11. CCA outlet flow line
12. Dewar flask
13. Liquid flow line
14. Nozzle exit

Fig. 4.1. Schematic view of atomized liquid nitrogen spray system.

Atomized liquid nitrogen spray system consists of (i) cryogenic air cooling (CAC) unit, (ii) nozzle unit, (iii) cryo- liquid reservoir with the delivery tube, (iv) highly insulated

delivery tube to the nozzle spray unit. In the cryogenically air cooling unit, argon gas is precooled to cryogenic temperature (-196 ºC, the temperature of LN_2) by running it through a stainless-steel pipe connected to the copper coil (overall length: 3 ft.) immersed in the cryogenic liquid bath. Cryogenically Chilled Argon (CCA) gas is sent to air setting chamber of atomizer through the insulated hose. Argon gas is precooled to minimize the evaporation rate of LN_2 droplets during the spray process. The flow rate of argon gas is measured using the calibrated rotameter before supplying to the nozzle unit. The supply pressure of the cryogenically chilled argon gas for atomization is closely monitored using a pressure controller.

4.2.1.1 Cryogenic air cooling unit

LN_2 was stored in dewar flask well sealed by a rubber stopper. A stainless-steel pipe (1.5 ft. length) was immersed in the liquid. The other end of the pipe protruded out through the rubber stopper. The flow of liquid takes place through the immersed pipe which was connected to the liquid inlet port of nozzle unit through an insulated flexible stainless-steel hose of 6 ft. length to maintain uniform flow process. All the hoses and pipes used in this system have 4 mm inner diameter and 6 mm outer diameter. For safety purpose, pressure relief value was connected and the pressure inside the dewar flask was closely monitored using a pressure gauge.

4.2.1.2 Nozzle unit design and development

The nozzle in this study was formed by two different pieces, an inner part (Fig. 4.2 (a)) and an outer part (Fig. 4.2 (b)), which forms an internal mixing chamber when assembled. The inner part consists of a combination of two nozzles (air and liquid) of different sizes that were coaxially assembled. A sketch of the nozzle and the cross-sectional view of the atomizer is shown in Fig. 4.2.

CCA gas was supplied to air setting chamber of atomizer from the air inlet port (d_{gi}) of 4 mm diameter. The LN_2 is supplied to liquid flow chambers of atomizer from the inlet port (d_{li}) of 4 mm diameter. The chamber maintains the uniform distribution of air in the circular tube. CCA gas is then introduced into the LN_2 stream through six radial 2 mm diameter aerated holes (d_{go}) on the circular wall of inner chamber. LN_2 jet (d_{lo}) of 2 mm diameter was injected into the axis of a high-velocity coaxial CCA gas jet, where the kinetic energy of the CCA gas stream initiates the transformation of the initial continuous medium of LN_2 phase into discrete ligaments and droplets. This energy transfer is more in the internal mixing atomizer.

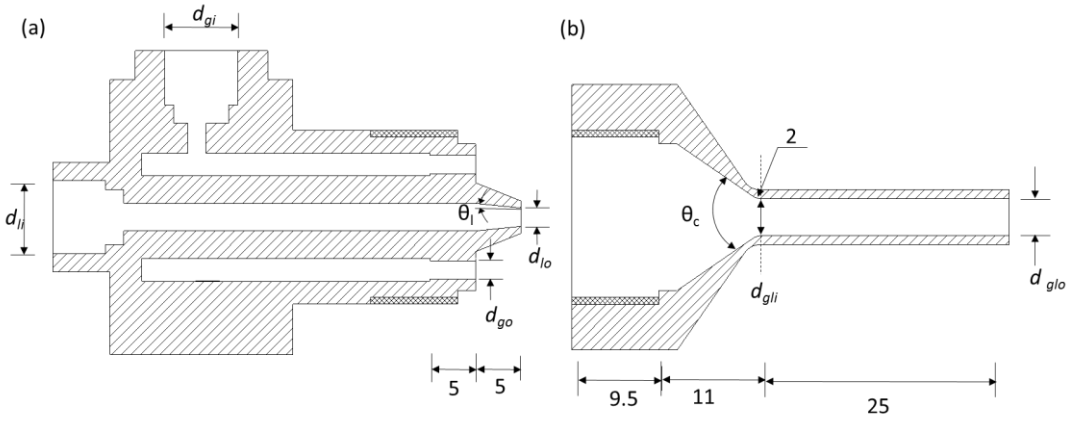

Fig. 4.2. Cross-sectional view of proposed nozzle unit. (All dimensions are in mm.)

Mean drop size highly depends upon the ratio of area of discharge orifice to the total area of the aerator holes (A_{glo}/A_{go}) and the location of aerator holes relative to the diameter of discharge orifice (l_N/d_{glo}). Smaller ratios lead to formation of bubble flow regime inside the nozzle resulting in fine sprays. Therefore, discharge orifice was extended to a length (l_N) of 35 mm from the aerator holes to reduce the mean drop size. Fig. 4.3. shows the photographic and schematic arrangement of fluid flow through the nozzle unit. The two-phase flow leaves the atomizer through 3 mm orifices in the form of micro-sized droplets that are carried by air stream. The LN_2 droplets follow the argon gas flow or develop their own trajectory depending on their size and relative velocity. In order to secure

maximum LN_2 droplets coming with pressurized CCA gas, liquid outlet port should have a convergent slope [5,10]. The outlet diameters of the liquid nozzles are designed to have a convergence slope ($\theta_l = 6^o$). The outer part is a conical hollow piece, where the interface of this piece forms the base of the mixing chamber and has a conical shape with $\theta_c = 69^o$.

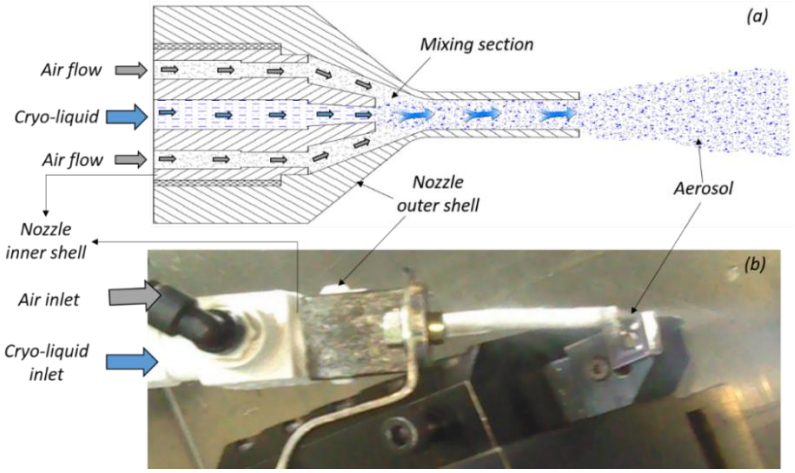

Fig. 4.3. Schematic (a) Arrangement of fluid flow through nozzle unit and (b) Photographic view at the nozzle unit.

4.2.2 Evaluation of Argon to Liquid Nitrogen mass Ratio (ALNR)

ALNR is determined to estimate the mass fraction of gas and liquid in the mixture developed in the spray system. The performance of developed system mainly depends on precooling of argon gas, which will minimize the heat loss during atomization of liquid nitrogen in the spray discharge system. Pressure in Dewar flask (thermally insulated vessel) was maintained to 14 psi as a safety measure and also sufficient to drive liquid from container to liquid nozzle inlet. The chilled argon gas interacts with liquid nitrogen in mixing chamber and creates a two-phase Argon liquid nitrogen mixture. The efficiency of spray is mainly dependent on mass ratio of argon and LN_2 in the mixture. To measure the mass consumption of liquid nitrogen, the complete assembly of Dewar flask that stores LN_2 is positioned on a digital-type electronic weighing balance with the precision of 0.1g. Change in mass of flask over a period was converted into the mass flow rate of liquid

nitrogen. Change in mass of flask over a period was converted into the mass flow rate of liquid nitrogen. The flow rate of the atomizing air was controlled and measured using the air pressure regulating valve.

For the sake of corrections in density variation, the feeding pressure of the atomizing air was closely monitored and measured. To achieve the desired operating condition variation in the air feeding pressure was also monitored and has been discussed along with the results. The liquid supply pressure was kept constant throughout the experiments and the air flow rate through the atomizer was varied over a range by changing the air feeding pressure to obtain the variation in Argon to LN_2 Mass Ratio (ALNR).

4.2.3 Examination of spray characteristics

Spray visualization was conducted by using videography technique to assess the spray characteristics. Fig. 4.4. illustrates the schematic image of spray characterization test rig consists of (i) developed ALN spray discharge system, (ii) digital cameras with light source, (iii) computer (iv) measuring tape. The cryogenic - nozzle unit was mounted vertically on a stand. The nozzle unit discharges LN_2 in the form of droplets at room temperature and atmospheric pressure. The complete process has been captured by Canon EOS 5D Mark III camera and automatic flash with exposure times of 1/8000 s and a high speed camera with a with a frame rate of 240 frames per sec (fps) and minimum exposer time of 4 ms. The light source was placed along with the diffuser glass at a distance of 3ft from the nozzle end. The flash lamp and the camera are placed in the same horizontal level, with the camera inspecting perpendicularly to the spray axis and all pictures are taken under same lighting conditions.

Pictures and videos of the sprays were captured by placing the cameras 20 cm away from the nozzle tip and directing the flashlight towards the nozzle tip at an angle of 30°

with respect to camera axis. The spray characteristics were analyzed by averaging the values of 5 photographs for each experimental condition, which were taken below the nozzle. The photographs were analyzed using Motic image plus 2.0^{ML} analyzer delivered by Motic China Group. Co. LTD, which provides in-depth and precise measurement analysis of the parameters of spray characteristics: the spray angle, spray pattern and droplet diameter. Particle Image Velocimetry (PIV) analysis was performed by using the open source code PIV lab developed by Thielicke and Stamhuis [152].

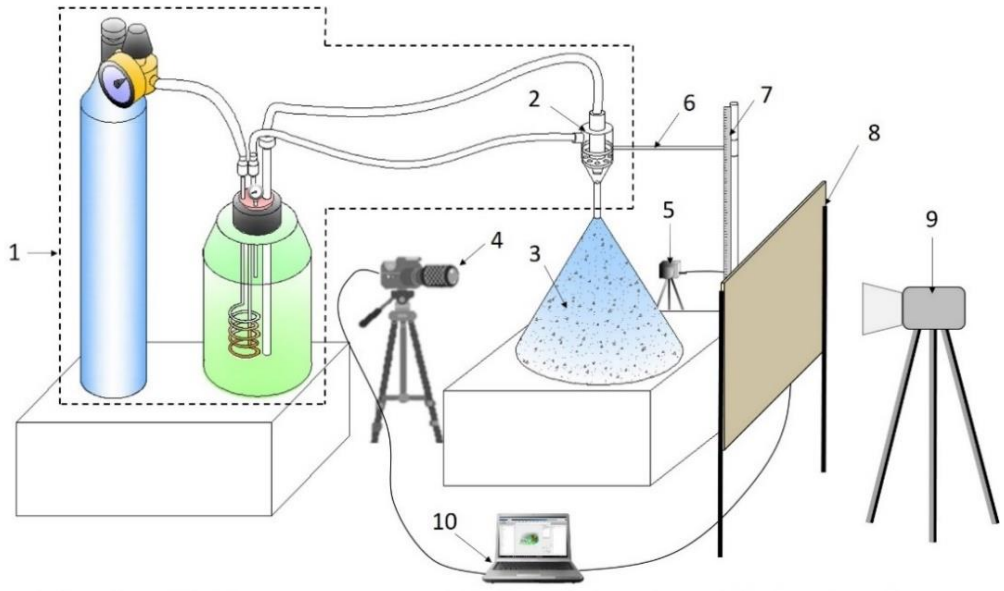

Fig. 4.4. Schematic view of spray characterization test rig.

4.2.4 Evaluation of cryogenically chilled argon gas and droplet temperature

Performance of developed spray system is highly depending upon the cryogenically chilled argon gas temperature and droplet temperature. Therefore, an experimental setup was devolved to determine the Argon gas temperature at the exit of the CAC unit, nozzle tip and droplet temperature at the tip of the nozzle. Fig. 4.5. shows the droplet temperature test rig using bare thermocouple. Three K type thermocouples of wire diameter 1mm

(National Instruments) were used to measure temperatures. The response time of the thermocouple was about 40 ms in still water at 100ºC, and error is below ±2.2ºC for the range of temperatures measured. Two thermocouples were inserted into the flow pipe, one in inlet pipe and another is in the outlet pipe of the cryogenic air cooling unit through a micro-hole and it was completely sealed. The third thermocouple place into the center of the spray cone at the tip of nozzle and measurements were taken. Measurements were conducted taken under dry air condition (relative humidity below 5%) to minimize the condensation and freezing effect.

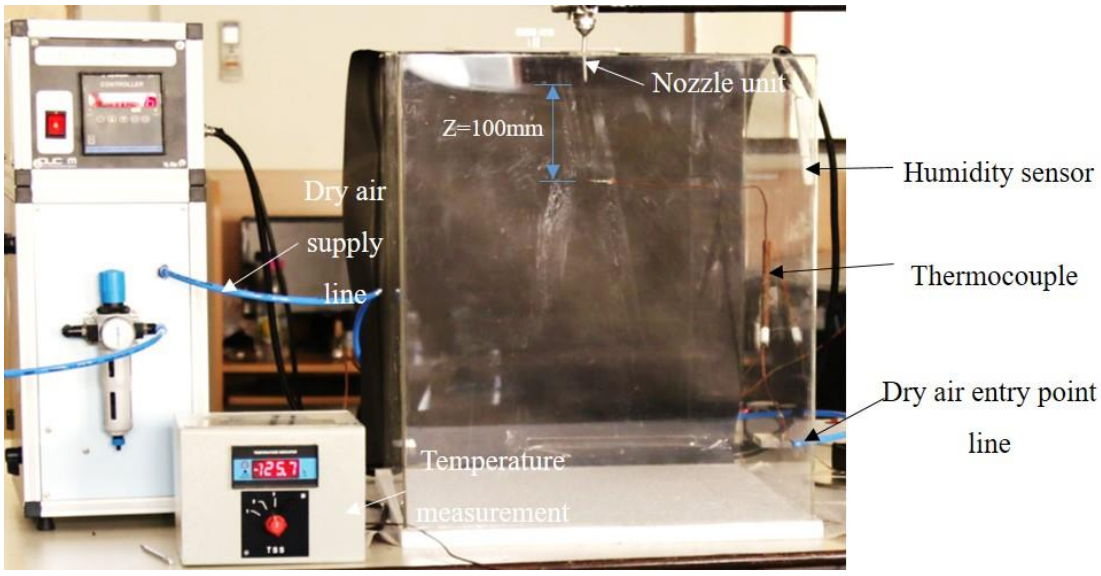

Fig. 4.5. Droplet temperature measurement test rig.

4.2.5 Machining tests

Developed atomized liquid nitrogen spray system shown in Fig. 4.1. was fitted to the HMT PTC 200 CNC machine using a metal frame which is fastened to the lathe turret as shown in Fig. 4.6. The frame can be easily adjusted to achieve different spray distance, nozzle orientation and spray impingement angle. The spray unit is directed on the tool rake and auxiliary flank face for impinging the spray droplets in direction of cutting edge. Two different types of secondary nozzles were used for impingement of spray on both the faces.

A cylindrical Al-TiC_p composites bar with an initial size of Ø30 mm and 150 mm length was used as workpiece. It was selected as it is extensively preferred as an engineering material for various high-performance components due to the grain refinery possessions of TiC reinforcement particles.

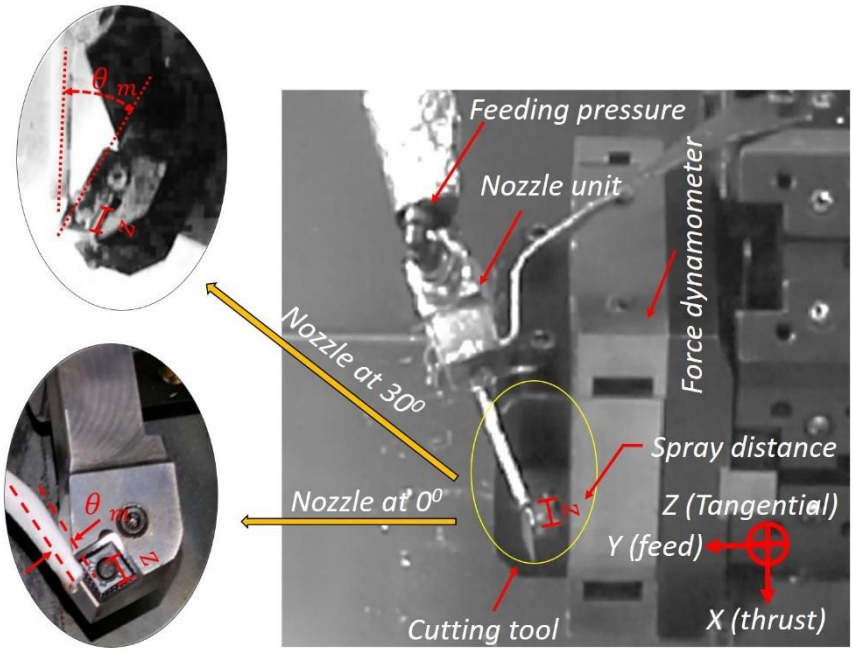

Fig. 4.6. Arrangement of spray impingement angle w.r.t to cutting tool at (a) 0° and (b) 30°.

Table 4.1 Spray parameters.

Parameters	Values
Cutting speed (V_c)	100 m/min
Feed (f)	0.1 mm/rev
Depth of cut (a_p)	0.25 mm/rev
Tool holder	P-type tool holder with Inclination angle (λ): -6^0, orthogonal rake angle (γ): -6^0, orthogonal clearance angle (α_o): 6^0, approach angles (ψ): 90^0.
Cutting insert	CNMG1204 in grade of KCU10; Rake angles γ: 0^0, Nose radius (r_e): 0.8 mm.
Feeding pressure (P_{CCA})	50, 100, 150, 200, 250, 300, 350, 400 kPa
Impingement distance (z)	5, 10,15 mm
Impingement angle (θ_m)	0^0 and 30^0

In machining tests, carbide CNMG inserts were used and mounted on a commercially available ISO standard tool holder. Table 4.1, gives a brief explanation of experimental conditions under which machining tests were performed. All the turning test were carried out to a length of cut 90 mm in the axial direction at constant cutting speed, feed and depth of cut. Each experiment was repeated three times at every cutting condition, and the average of three measurements was used to represent the performance parameters such as surface roughness and flank wear. After finishing of each trial under determined machining conditions, surface roughness of machined composites was measured by using Taylor Hobson Surtronic 25 Profilometer of 8mm sampling length, speed of 1 mm/sec with 5 μm diamond tip. Four readings are taken at the middle of machined surface at 90° angle for each measurement on the sample. Tool performance was analyzed to understand the pragmatic nature of wear modes that are formed during machining of Al-TiC_p under different environmental conditions. Tool wear of cutting tool was inspected using tool maker's microscope Olympus STM 6 to measure the flank wear. The flank wear on tool was measured by the width of wear land that forms along the major and minor cutting edge of the tool.

4.3 Results and discussion

Supply of LN_2 in large quantities often cools unwanted area causing an adverse effect on characteristics of the work material. Therefore, in the present work cryogenic air blast atomization process has been developed to minimize the use of LN_2 and maximize the cooling effect at the cutting tool edge. The effectiveness, efficiency and overall economy of developed spray stem was mainly depending on the concentration of air and liquid of spray characterizes of the jet.

4.3.1 Argon to Liquid Nitrogen mass Ratio (ALNR)

As a preliminary study, a dry test was carried out by closing the cryo-liquid line in order to assess the performance of developed system with fundamental air driving performances such as CCA gas temperature ('T_g') and liquid supply pressure ('P_l') in nozzle unit. The performance of developed system mainly depends on precooling of argon gas which will minimize the heat loss during atomization of LN_2 in the cryo spray discharge system.

Three K type thermocouples of wire diameter 1mm (National Instruments) were used to measure temperature of CCA gas in CAC unit. The response time of the thermocouple was about 40 ms in still water at 100ºC and error below ±2.2ºC for the range of temperatures measured. For temperature measurements, two thermocouples were inserted into the flow pipe, one in inlet pipe and other in the outlet pipe of the CAC unit through a microhole which was completely sealed. The third thermocouple was placed at the tip of the nozzle. To minimize the error due to condensation, all measurements were taken under dry air condition. The inlet temperature of gas was recorded as 22ºC to 25ºC for all flow rates, and outlet temperature from CAC unit was recorded to be -190ºC to -160ºC. For lower flows (i.e., 9.459 L/min to 14.9 L/min) the stabilization temperature (-190ºC to -174ºC) reached within 30 s, whereas for high flow rates (i.e., 6.859 to 23.65 L/min), the stabilization temperature (-174ºC to -160ºC) reaching time was reduced to approximately 15 s. The third thermocouple is placed exactly at the exit of the tip recorded a range of -140ºC to -120ºC. It was observed that difference in temperature of inlet to outlet of CAC unit decreased with increase in mass flow rate of CCA gas. At the same time, it was observed that exit temperature at the nozzle tip was increased. If the supply temperature of CCA gas is much higher than the boiling point of LN_2, the LN_2 evaporates instantaneously.

During this energy transfer, LN_2 in contact with coiled pipe starts evaporating. As expansion ratio of LN_2 from liquid-to-gas is high i.e., 1:694 at 20°C, it creates sufficient pressure to feed LN_2 into nozzle unit. Due to the rapid phase change in LN_2, pressure accumulates inside the Dewar flask. The built-up pressure acts as a feeding pressure for LN_2 i.e., in a range of 4 to 17 psi. A control valve is placed to release the excess pressure built up inside the flask. To measure the mass consumption of liquid nitrogen, the complete assembly of Dewar flask that stores LN_2 was positioned on a digital-type electronic weighing with the precision of 0.01 g. Change in mass of the Dewar flask over a period of time was converted into the mass flow rate of liquid nitrogen. Air flow rate was varied over a range by changing the air supply pressure to obtain the variation in Argon to Liquid Nitrogen Mass Ratio (ALNR). ALNR ratio can be easily determined by Eq. (4.1).

$$ALR = \frac{\dot{m}_g}{\dot{m}_l} \tag{4.1}$$

Where, $\dot{m}_l(mass\ flow) = \rho_l Q_l$, where '$Q_l$' is the measured volumetric flow rate for the LN_2 and 'ρ_l' is its density, apparently considered constant for all the calculations. The mass flow '$\dot{m}_g$' is defined as $\dot{m}_g = \rho_g Q_g$, where is 'Q_g' is the inlet volumetric air flow rate of CCA gas.

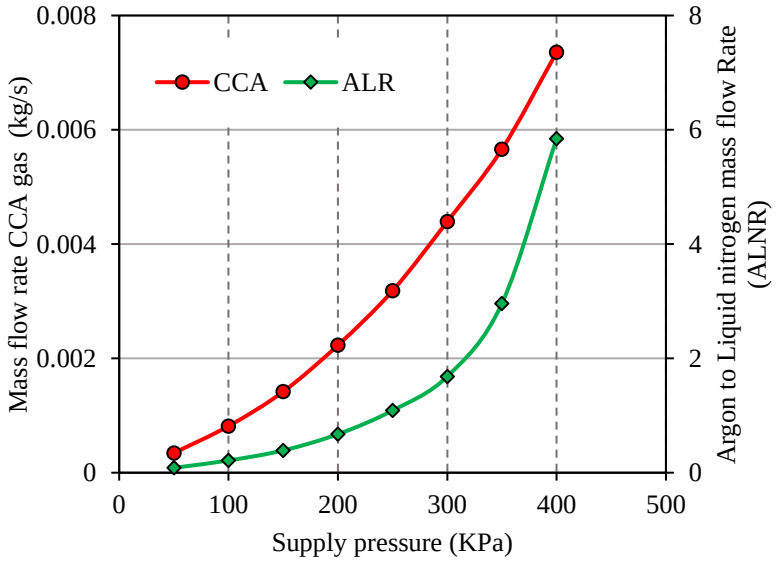

Fig. 4.7 Variation of mass flow rate of CCA gas and ALNR with supply pressure.

The gas volumetric flow is measured using flow meter and is considered compressible. Its density is calculated using ideal gas relation $\rho_g = \frac{P_g}{M_{Ar} R\, T_g}$, where 'R' is the universal gas constant (8.314 j/mol/K), 'M_{Ar}' is the molecular weight of argon and 'P_g' and 'T_g' are the CCA gas flow pressure and temperature respectively.

The mass flow rate of CCA gas with respect to supply pressure is shown in Fig. 4.7. The variation of liquid mass flow rate as a function of ALNR is shown in Fig. 4.8. The figures reveal that the LN_2 flow rate decreases with an increase of ALNR. This is in agreement with the results reported by various researchers [153-155]. Further, at lower values of ALNR, the decrease of flow rate is quite rapid. But, at higher values of ALNR, the change in LN_2 flow rate is minimal with an increase in ALNR. The liquid flow rate was varied between 0.094 L/min to 0.299 L/min.

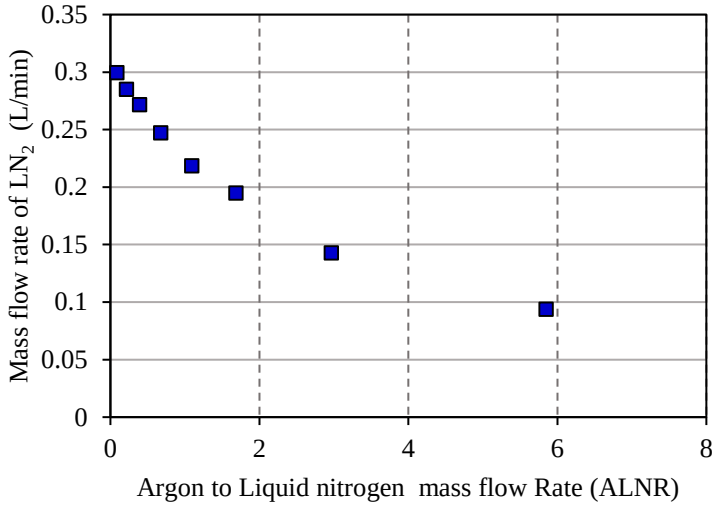

Fig. 4.8. The measured value of LN_2 mass flow rate and air pressure with ALNR.

In order to create a functional correlation between the LN_2 flow rate, ALNR and the liquid supply pressure, the variation of discharge coefficient (C_D) with respect to ALNR was estimated using Eq. (4.2) and the results plotted in Fig. 4.9.

$$C_D = \frac{m_l}{A_{lo}\left(2\rho_g P_l\right)^{1/2}} \qquad (4.2)$$

Where, $A_{lo} = \pi \left(\frac{d_{lo}}{2}\right)^2$ is the area of liquid orifices and 'P_l' is the liquid supply pressure. The functional relationship between the discharge coefficient and ALN*R* is given by Eq. (4.3)

$$C_D = 0.0239e^{-0.202\ ALNR} \qquad R^2 = 0.9771 \qquad (4.3)$$

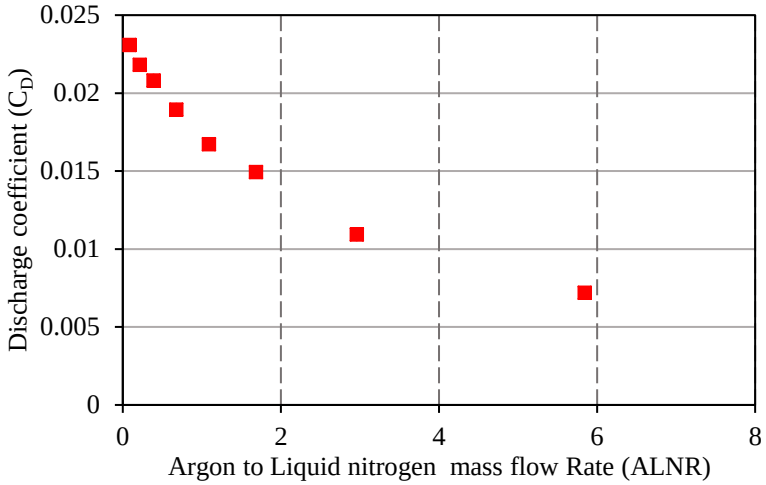

Fig. 4.9. Variation of discharge coefficient with ALNR.

The discharge coefficient decreases with an increase in ALNR (Fig 4.9). Lefebvre [156] has defined the discharge coefficient to be a measure of the extent the liquid flows through a final discharge orifice while making full use of the flow area available. Therefore, the decrease in C_D w.r.t ALNR reveals that the accessible liquid flow area decreases with an increase in ALNR resulting in decrease of LN_2 flow rate (see Fig. 4.8). According to Eq. 4.3, the rate of change of 'C_D' is inversely proportional to ALNR, which is accountable for slower rate of diminishing LN_2 flow rate at higher values of ALNR (see Fig 4.8). This can be safely attributed to the change in two-phase flow regime with ALNR. This two-phase flow is expected to be annual or dispersed at higher values of ALNR, which is less sensitive to external forces.

4.3.2 Spray characteristics analysis

Efficiency of the discharge systems is mainly dependent on the spray characteristics, including (i) spray pattern, (ii) spray angle, (iii) spray velocity, (iv) spray droplet diameter and (v) droplet temperature. A detailed discussion of all these characteristics are studied in this section. Study on spray pattern and angle will help in analyzing the impact of impingement on the target surface. The penetration and cooling action of the liquid depends on the velocity and the droplet diameter of the spray.

4.3.2.1 Spray pattern

Spray generated by proposed nozzle unit was photographed and its observations are shown in Fig. 4.10. It was observed that the solid cone spray pattern was formed for all the considered pressure conditions. LN_2 introduced into a CCA gas environment through nozzle interacts with the adjacent gas thereafter disintegrating into droplets. Aerodynamic interaction of LN_2 with CCA gas may cause waviness. Spray begins with detaching of droplets from the outer surface of a continuous liquid core extending from the outlet of the injection nozzle (see Fig. 4.10).

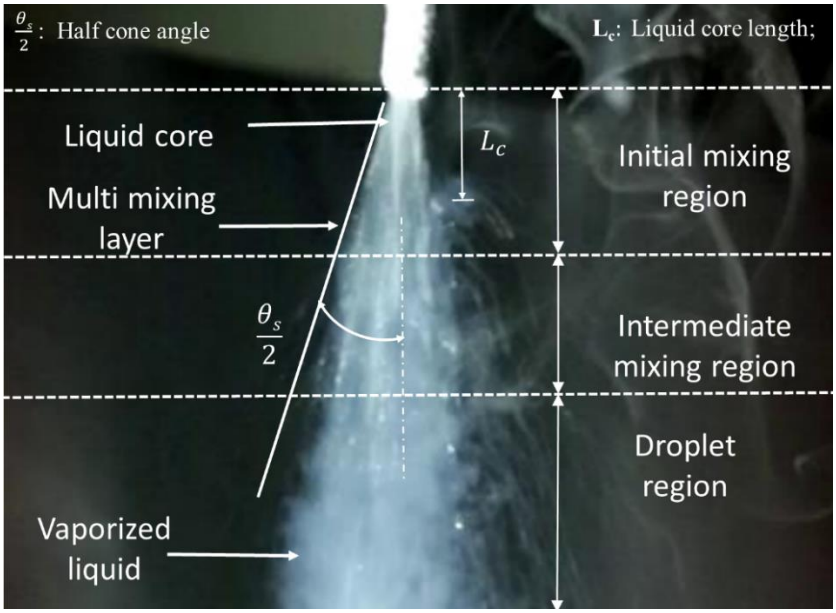

Fig. 4.10. Observations of a spray generated by developed nozzle.

Initially, the LN_2 core disintegrates into ligaments or large droplets called primary breakup region. At this stage, the instability of the liquid was instigated in the internal mixing chamber due to the interaction between the high-velocity CCA gas and LN_2. Thus, liquid in the primary region was more unstable than that in a single-fluid atomizer. The liquid ligaments and large droplets further fragment into small spurts due to constant interactions between the CCA gas and LN_2 or droplet collisions. The region where further fragmentation occurs is the secondary break-up region. Dense spray region was formed in the vicinity of the nozzle region due to larger volume fraction of the LN_2 than that of the CCA gas.

Fig. 4.11 shows LN_2 jet flow in the vicinity of the nozzle for different supply pressure conditions. As supply pressure increases, the length of the LN_2 liquid core (L_c) from the nozzle decreases. Review of complete set of experiments revealed that LN_2 liquid core is formed to a range of 5-10 mm. The disintegration into droplets was formed at a longer distance from the nozzle at lower pressure for all the cases considered in this study. Also, half spay cone angles ($\theta_s/2$) are indicated in Fig. 4.11.

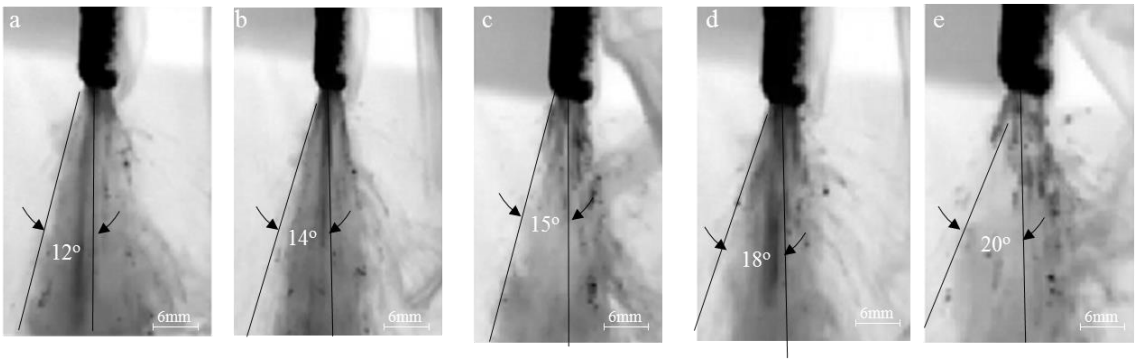

Fig. 4.11. Flow in the vicinity of the nozzle (a) 0.5 bar (b) 1 bar (c) 2 bar (d) 3 bar (e) 4 bar.

The LN_2 stream interacts with high-velocity CCA gas disintegrating promptly into large ligaments and non-spherical droplets (seen Fig. 4.11). As the supply pressure increases, liquid core decreases and ligaments become shorter and prompt atomization was

observed as seen in Fig. 4.10. The image showed densely existing particles which were not spherical. This can be attributed to two main factors (i) aerodynamic forces and (ii) droplet collision. When the atomized flow was sparse, effects of the interaction between droplets was observed to be small [157, 158]. These findings are in correlation with the results obtained by Faeth et al. [159].

4.3.2.2 Spray divergence angle

Spray cone edges were identified by image processing using MATLAB results and their angle was measured using Motic plus 2.0 image processing software. Fig. 4.12 shows the variation of spray angle as a function of ALNR. It is clear from the Fig. 4.12 that the spray cone angle increased with the elevation in ALNR of the spray. With further increases of ALNR, the difference between the angles gets slightly elevated. The increase in cone angle with ALNR enhances turbulence level in the spray delivered out of the nozzle which could probably influence spray cone angle. Higher turbulence levels cause an increase in the ratio of radial to axial velocity of the spray leading to larger cone angles ($\frac{\theta_s}{2}$) [160].

The functional relationship between half spray cone angle and ALNR is given by Eq. (4.4)

$$\frac{\theta_s}{2} = 16.436\, ALNR^{0.122} \qquad R^2 = 0.9799 \qquad (4.4)$$

At lower ALNR, LN_2 jet maintains its merger for a longer distance from the nozzle before breaking up. As the air flow rate is increased, the initial filaments become shorter and breaking up of the filament into droplets happen closer to the nozzle. Thus, as the CCA gas flow rate is decreased, the point of initial breakup is moved away from the nozzle exit. In general, at low CCA gas flow rates, the droplets are not disintegrated quickly and larger droplets are produced. This means that there are a smaller number of larger diameter

droplets, some of which may not follow the CCA gas flow as accurately as the smaller particles.

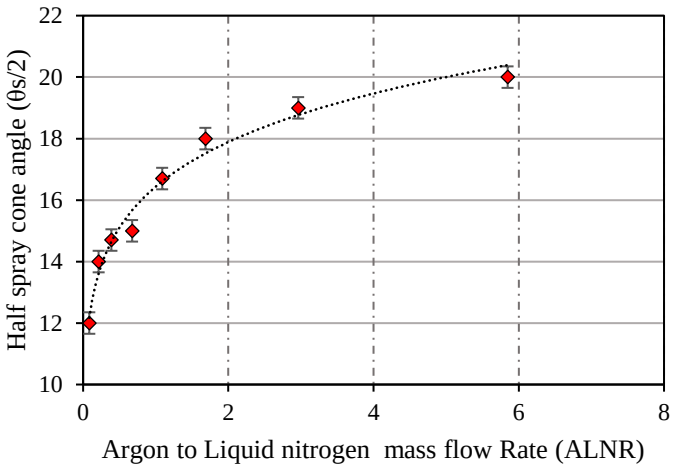

Fig. 4.12**.** The variation of spray angle as a function of ALNR.

As ALNR increases, the atomizing CCA gas is injected with a greater velocity into the LN_2 stream inside the nozzle enhancing turbulence levels leading to wider spray cones. The secondary nozzle is longer than the final discharge orifice diameter the ratio being l_N /d_{glo} = 5. Further, it should be noted that the present nozzle could produce a smaller diameter droplet at higher injection pressure. Therefore, the spray angle is relatively small which is advantageous in machining application as concentrated flow can be obtained using the developed nozzle even at lower flow rates.

4.3.2.3 Spray velocity

Spray droplet velocity is a dominant parameter in spray cooling studies. With the size of impinging droplets, the cooling performance of the spray is affected. In this study, spray droplet velocities were determined using the videography method. The spray flow was recorded at 240 fps and the successive images recorded were analyzed using PIV lab, an open source MATLAB application used for determining the particle velocity. The droplet images taken at two different instants of time (about 4 ms) were coupled manually

and analyzed. The coordinates of the coupled droplets were measured by pixels to calculate the approximate droplets velocity. The direction of the velocity vector can also be determined directly from the image as an angle of flight with respect to the central axis of spray.

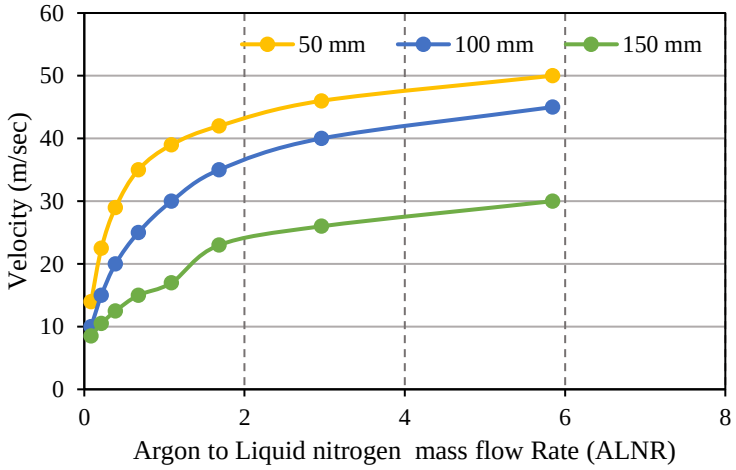

Fig. 4.13. Variation of velocity as a function of ALNR at various distances.

Fig. 4.13 shows a typical plot of droplet velocities measured as a function of ALNR for various points from the nozzle exit. It is observed that droplet velocity increases with increase in ALNR. It was also found that the velocity decreases with an increase in spray distance. Cooling action in turn increases with increase in spray velocity. From the developed experimental setup, droplet velocities are found to be in the range of 8 to 50 m/s for all the values of ALNR. But, after a certain value of ALNR, mean velocity will have an impact on cooling time. This may be due to the fact that the residing time of droplet on hot surface decreases with increase in droplet velocity. Other factors that affect the cooling efficiency are splashing and rebounding of droplet from the surface due to higher pressure and droplet velocity, which in turn has negative impact on the residing time of the droplet on the surface.

4.3.2.4 Droplet diameter

The spray structure at 150 mm downstream from the discharge is shown in Fig. 4.14. Secondary atomization occurs at this location, where ligaments and droplets are present. The relatively large initial droplets obtained from the primary breakup process further disintegrate into smaller droplets and may evaporate finally. Optical visualization was carried out by videography method. Images were taken at an exposure time of 1/8000 s and processed in MATLAB with edge detection. These images were further processed using Image J software to determine the average diameter of droplets.

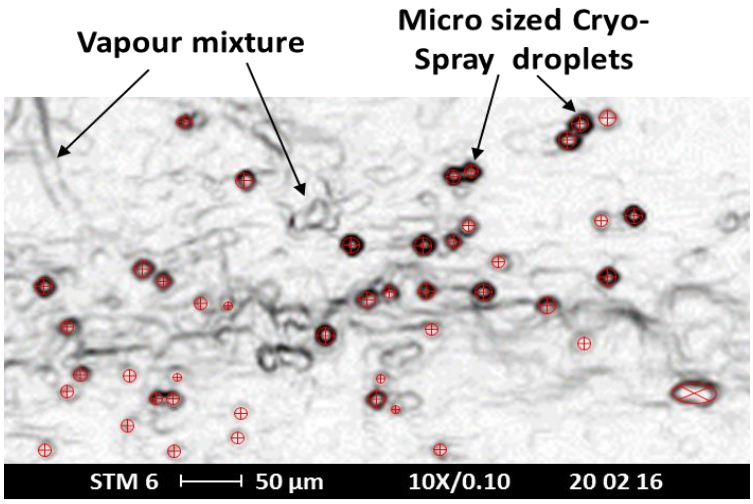

Fig. 4.14. Droplets image acquired for 150 mm downstream from discharge orifice.

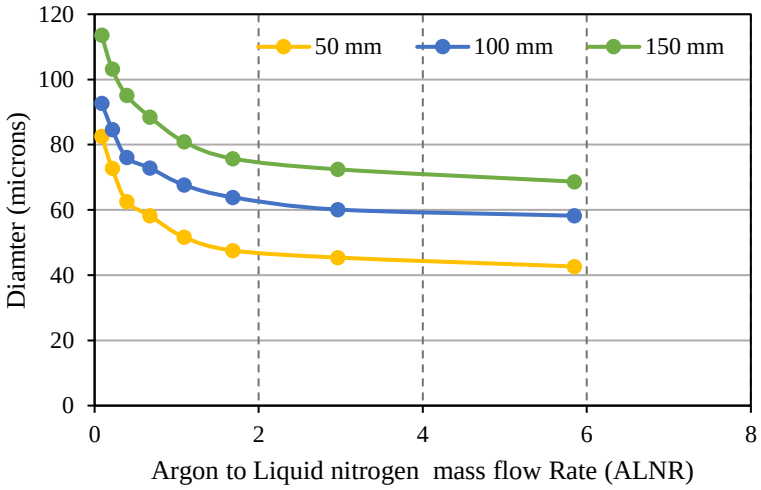

Fig. 4.15. Variation of MD as a function of ALNR at various distances.

The dependence of droplet Mean Diameter (MD) on ALNR for different axial locations from the nozzle exit is shown in Fig. 4.15, which is seen that the MD of the spray decreases with increasing ALNR. It was observed that MD varies between 120 to 40 μm over the entire operating range reported in this paper. The increase in supply pressure of CCA gas is accompanied by increase in air flow rate, accelerating the LN_2 at the nozzle exit. This in turn increases the kinetic energy of LN_2, resulting in an improved atomization.

The increase in air flow rate is accompanied by an increase in air velocity, exerting shear force upon LN_2. Consequently, the number of droplets being stripped from the water filament increases, resulting in finer atomization. An increase in flow rate will increase the pressure drop and decrease the drop size. The results obtained agree fairly well with those obtained by other investigators. In fact, smaller droplets evaporate as it moves along the downstream direction. Further it was observed that as the spray distance increases, the reduced cooling action results in finer droplets.

4.3.3 Cryogenically chilled argon gas temperature and droplet temperature

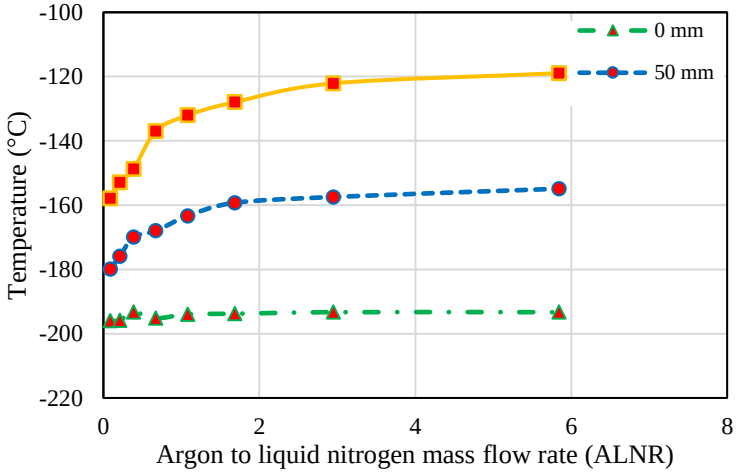

Fig. 4.16. Variation of temperature as a function of ALNR at various distances.

The inlet temperature of Argon gas was recorded as 22 to 25°C for all flow rates, and outlet temperature from CAC unit has been recorded to be -190 to-160°C. For lower

flow rates (i.e., 9.459 L/min to 14.9 L/min) the stabilization temperature -190 to -72°C was reached in 30 s. whereas for high flow rates (i.e., 16.859 L/min to 23.65 L/min) the stabilization temperature -172 to -145°C reaching time was reduced to approximately 15 s. The third thermocouple was placed exactly at the exit of the tip, giving a range of -140 to -120°C. By the experimental results, it can be observed that droplet temperature variation is in the range of -190 to -150°C. As ALNR increases, the droplet temperature has been increased. Fig. 4.16 provides the droplet temperature as a function of ALNR at various distance from nozzle tip. These results are correlating with other researchers and support the normal heat transfer phenomenon i.e. as the velocity of drop increases there is more heat transfer between the drop and surrounding air and thereby increasing the droplet temperature.

4.3.4 Machining performance

The air blast atomizer produces micro-sized LN_2 droplets, which impinges as a jet of high-velocity droplets at the machining zone. Since the heat in machining results from shearing of the metal by the cutting edge on the primary shear plane, and resulting in friction at the tool/chip interaction, effective penetration of the LN_2 in the cutting zone is essential for longer tool life. These high-velocity LN_2 droplets penetrate effectively into the machining zone and produce hydrostatic lubrication effect as the liquid evaporates between the mating zones. Effective penetration of the LN_2 is necessary in order to achieve improved cooling and lubrication.

The cooling and lubrication characteristics of atomized liquid nitrogen spray system are influenced by three main parameters viz. feed pressure of the gas atomizer, droplet impingement angle, and spray distance. In cryogenic machining, quantity of liquid used as one of the important factor to avoid adverse effect on machinability characteristics. Therefore, the optimum flow concentration of air and liquid has to be determined to achieve

both cooling and lubrication. The wetting of the entire tool/chip contact zone directly depends on the ALNR. The variation of ALNR ratio i.e., 0.0848 to 4.396 in developed atomized liquid nitrogen spray system depends on the feeding pressure (50 kPa to 400 kPa). Increase in feeding pressure, there will be faster penetration of droplets resulting in higher lift force. The impingement angle with respect to tool rake face defines the regime for cooling function, 0° and 30° as shown in Fig 4.6. The spray distance controls the diffusive nature of the spray over the travel distance, chip breaking, and quantity of droplets penetration into the interface [161]. Nozzle has been positioned in such a way that the spray was directed towards both rake and auxiliary flank surface of the tool with different nozzle tips. Experiments are performed after ensuring the setup for proper lubrication. An investigation was carried out to determine the optimum argon gas to liquid nitrogen concentration i.e., depends on feeding pressure used in atomized liquid nitrogen Spray system for cooling action. At this stage, it also required to find the ideal spray impingement angle and spray distance to improve the penetration capability there by lubrication effect., in the present study the proposed atomized liquid nitrogen spray system shown in Fig.4.1, equipped with a nozzle used to yield more micro-sized liquid nitrogen droplets of 45 – 120 μm. These atomized liquid nitrogen droplets are impinged as a focused jet in the machining zone with the help of high velocity cryogenically chilled argon gas of 8 - 50 m/sec. This will help to feed liquid nitrogen effective between the tool chip interfaces and reduces friction by creating a micro hydrostatics lubrication effect as the liquid evaporates between the mating zones there by resulting lower heat generation.

4.3.4.1 Machinability behavior under different feeding pressure

To determine the appropriate feeding pressure for turning experiments, according to Table 4.2 turning test are performed for five different feeding pressures and for each test surface roughness on machined surface and tool wear was measured. At 200 kPa feeding

pressure (ALNR = 0.666) provides 10.35% to 26.6 % and 3.48% to 27.09% lower flank wear and Surface roughness respectively when compared with other feeding pressures.

Table 4.2 Machining conditions for finding optimum feeding pressure.

Cutting speed V_c (*m/min*)	100
Feed *f* (*mm/rev*)	0.1
Depth of cut a_p (*mm*)	0.25
Feeding pressure P_{CCA} (*kPa*)	50, 100, 150, 200, 250, 300, 350, 400

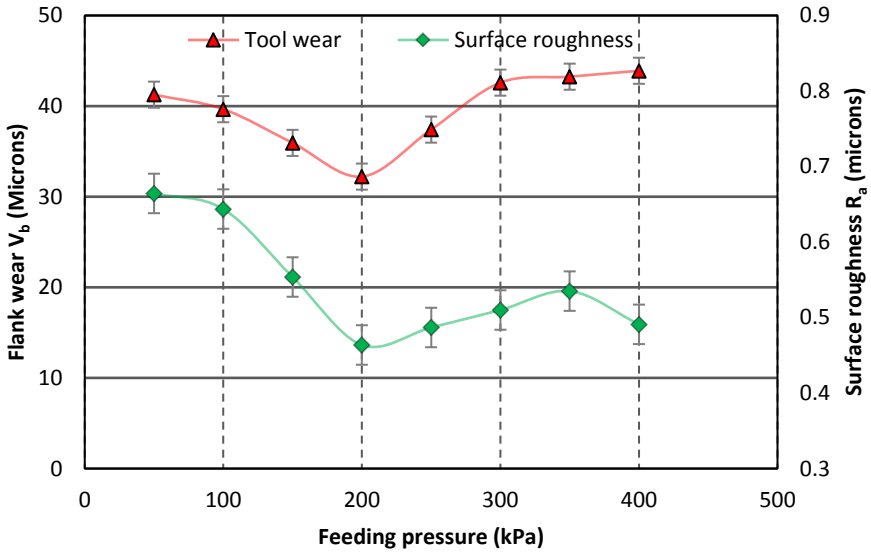

Fig. 4.17. Effect of machinability performance parameters with respect feeding Pressure.

Fig. 4.17 shows the variation of surface roughness and flank wear as a function of feeding pressure under atomized liquid nitrogen spray machining. It can be observed from the graph that tool wear and surface roughness decreases as feeding pressure increases from 50 to 200 kPa and the increases from 200 to 350 kPa. This improvement can be attributed due to the fact that the atomized liquid nitrogen spray technique can significantly enhance the penetrability by improved velocity (30 - 40 m/sec) and wettability of the lubricant droplet as well decrease the drop size by (50 – 60 µm) varying the feeding pressure. However, at high feeding pressure (250 - 400 kPa), the tool wear and surface finish increase. According to Hong [20], this may be attributed to the fact that larger ALNR ration lower mass rate of LN_2 in the mixture there by leads to higher flank wear and larger surface

roughness value. It has been revealed from Fig. 4.17, the optimum feeding pressure is, 200 kPa (ALNR = 0.666) by reducing flank wear and surface roughness. Therefore, further machining tests are carried out under same feeding pressure.

4.3.4.2 Machining behavior under different spray impingement angle and distance

Increase in supply pressure, causes faster penetration of droplets resulting effective transfer of fluid along with diffusion of spray over spray distance. Cooling function and direction of lubricant that flows depend on impingement angle on tools rake face. At this stage, it also required to find the ideal spray impingement angle and spray distance to improve the penetration capability there by lubrication effect. An experimental analysis has been conducted to determine the optimal impingement angle and spray distance using developed atomized spray system under 200 kPa feeding pressure. Machining test conditions and spray parameters are given in Table 4.3.

Table 4.3 Machining conditions for finding optimum impingement angle and spray distance

Cutting speed V_c (*m/min*)	100
Feed *f* (*mm/rev*)	0.1
Depth of cut a_p (*mm*)	0.25
Feeding pressure P_{CCA} (*kPa*)	200
Spray impingement angle θ_m (deg)	0 and 30
Spray distance *z* (*mm*)	5, 10, 15

The nozzles were arranged in such a way that the spray was directed towards both rake and auxiliary flank surface of the tool. Fig. 4.18 shows the variation in the tool wear 4.18 (a) and surface roughness 4.18 (b) as a function of spray distance and impingement angle. Higher impingement angle in combination with lower spot distance tend to provide relatively lower flank wear, though the effect was not very significant. At 10 mm spray distance and 30° impingement angle, minimal tool wear and better surface finish were obtained. It was observed that 10 mm at 30° condition provides 9.25% to 34.22% and 5% to 24.72% decrease of flank wear and surface roughness respectively when

compared with other selected conditions. This can be attributed to better penetration and cooling action of the LN_2 on both rake and auxiliary flank face at moderate distance and higher angle. During the machining process, the droplet distribution, which associated with the wetting area by LN_2, can affect the lubrication performance. In addition, the LN_2 droplet with high velocity can provide better penetration into the contacting surface.

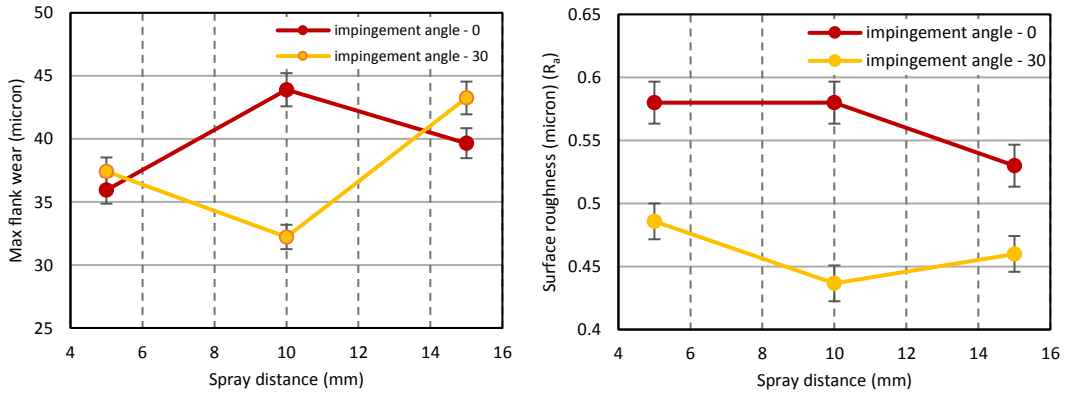

Fig. 4.18. Effect of variation in spray impingement angle and spray distance on tool wear and surface roughness.

It can be concluded from the above experimentation that, moderate feeding pressure 200 kPa with the combination of larger impingement angle (30°) and adequate spray distance (10 mm) provide better performance for selected too/work combination and cutting condition. This may be observed due to the possible formation of thick fluid film which helps in providing cooling and lubrication effect in the entire zone, there by leading to lower flank wear and surface roughness. Therefore, in subsequent section the analysis of experimental results in atomized liquid nitrogen spray assisted machining are carried out with a combination of 200 kPa feeding pressure, 30° impingement angle and 10 mm spray distance.

4.4 Summary

In this chapter, the fundamental aspects of spray and important operational parameters such as feeding pressure, spray angle and spray distance from nozzle to tool tip

have been explained. The design and fabrication of atomized liquid nitrogen spray discharge system has been built. It was observed that half spray cone angle increases slightly with increase in ALNR. As a result, ligaments become shorter and prompt atomization was observed. Spray droplet velocity increased and droplet size decreased with increase in ALNR. Smaller droplets get evaporated as they move along the downstream direction resulting in reduced cooling action. This further confirms that droplet temperature varies in the range of -160 to -120°C away from nozzle spray centre axis. As ALNR increases, the droplet temperature was seen to increase. As the velocity of drop increases there is more heat transfer between the drop and surrounding air and thereby increasing the droplet temperature. To comprehend the optimal process parameters of atomized liquid nitrogen spray discharge system, turning experiments were performed. From the experimental results, it was noticed that moderate feeding pressure (200 kPa), larger spray angle (30°) and adequate spray distance (10 mm) could be the best plausible conditions for better atomized liquid nitrogen spray machining performance. Before utilizing the developed atomized liquid nitrogen spray system in machining analysis of the penetration capability under sliding wear condition is needed to be studied. Therefore, the performance of atomized liquid nitrogen spray system on tribological characteristics is comprehensively studied and presented in chapter 5.

Chapter 5
Tribological Behaviour of Al TiC_p MMCs

The current chapter investigates the tribological behavior of developed Al-TiC_p composites by pin-on-disc tribometer over a wide range of sliding velocities and applied loads. Further, to understand the effect of cryogenic technology on wear behavior of Al-TiC_p composites, sliding wear studies are carried out under Atomized Liquid Nitrogen (ALN) spray condition, cryogenically chilled argon (CCA) gas and dry conditions. The current chapter is organized as follows: Section 5.1 presents a brief background about effect of atomized cryogenic technology on tribological performance. Section 5.2 deals with the material and test condition used in sliding experiments. Section 5.3 presents the friction and wear behavior of Al-TiC_p composites. Finally, Section 5.4 presents the summary of this chapter.

5.1 Introduction

Over the last few decades, application of Liquid Nitrogen (LN_2) has been widely reported for reduction of wear and frictional forces. These reports mainly attribute by the super cooling effect of LN_2 [12] and on heat resistance super alloys [162]. Although there are several findings in this field, an important uncertainty is the action of cryogenic fluid (a) especially regarding its cooling and /or lubrication capabilities (b) tribological characteristics of MMCs. To our knowledge, it appears that most of literature has been investigated on wear behavior of Al-MMCs at room temperature. The studies on cryogenic tribological performance of MMCs has limited literature [163] [164].

Cryogenic tribological studies are performed by immersing the material into LN_2 which affects the mechanical properties of material by changing durability and elastic parameters. Additionally, in cryogenic applications, it is still uncertain whether the

lubrication effect is responsible for reduction in friction coefficient or by its cooling effect at the contact interface. Therefore, in the current research work, an ALN spray system was attached to pin on disc tribometer to minimize the effect on mechanical properties of material. This method of introducing LN_2 at the interface zone has strong potential to control the tribological and mechanical behavior of sliding surfaces. Sliding wear experiments were carried out on developed atomized cryogenic tribometer system to obtain the cryogenic tribological behavior of Al-5wt%TiC_p composite at different loads and sliding velocities. The experimental results of this research work are very promising and will be useful for tribology designers to implement and promote the usage of Al-TiC_p composites for high performance components in aerospace, automobile and defense sectors for process enhancement.

5.2 Experimental details

To investigate the cryogenic tribological behavior of MMCs and the lubricity of LN_2, sliding wear tests were performed under three different environments i.e. dry, cryogenically chilled argon (CCA) gas and Atomized Liquid Nitrogen (ALN) spray (LN_2) conditions. In dry condition, experiments were conducted at ambient conditions of 25°C and 40 – 60% relative humidity approximately. In ALN spray condition, atomized LN_2 jet was directed towards the interface between the mating surfaces using nozzle arrangement. Finally, in cryogenically chilled argon gas condition, pressurized argon gas is passed through a coil immersed in LN_2 and is cooled down to cryogenic temperature (-190 to -160°C). It is then supplied to the pin and disc interface zone to provide cryogenic cooling effect. Further, effect of variable loads and sliding velocity were also considered to study the tribological characteristics of Al-5wt%TiC_p MMC for the above conditions.

5.2.1 Linear wear test

Linear wear tests were conducted by using modified atomized cryogenic scratch tester where ALN spray system was attached to the scratch tester to feed the LN_2 with a continuous flow rate (10-12 L/hr) and constant pressure (200 kPa) between the interfaces of diamond indenter and developed composite. Fig. 5.1 illustrates the schematic view of atomized cryogenic scratch testing setup. Wear tests were performed by moving the diamond indenter linearly over the surface of Al-TiC_p composite to form a scratch. A reference line was drawn over the surface of the sample and the displacement of the indenter is parallel to the reference line. The indenter was allowed to touch the surface at the beginning and end of the specified scratch length. All the tests were carried out at a constant load. The tests were also carried at constant loads under dry, cryogenically chilled argon gas and ALN spray environments.

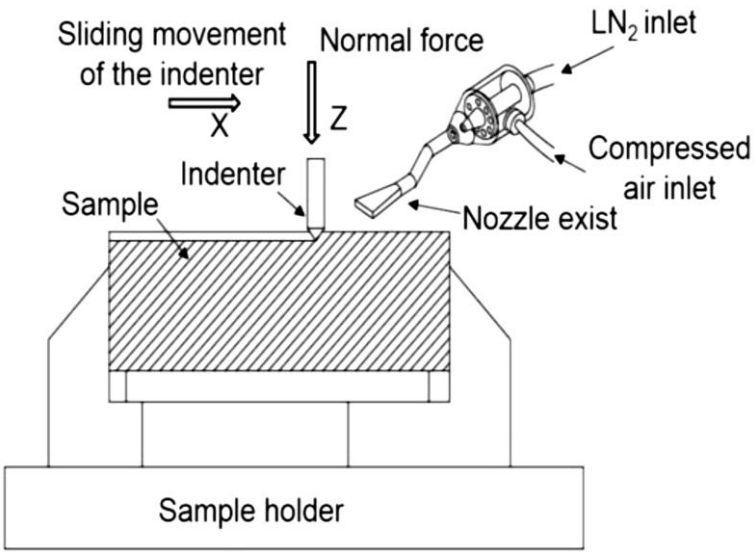

Fig. 5.1. Schematic view of linear wear test.

For linear wear test, billet of size 20 mm × 20 mm × 20 mm was sliced from the cast rod using EDM wired cut. The faces of the sample were ground and lapped with SiC abrasives, 80 and 600 mesh respectively. Finally, the faces were polished with 6µm diamond paste to get the polished finish. The scratch tests were performed with a diamond

indenter at an attack angle of 22°, a scratch speed of 2 mm/s, and a scratch test length of 15 mm at an acquisition rate of 300 Hz. The above tests were conducted under three different loads, ranging from 5-25 N maintaining constant load throughout the scratch. The sample was rigidly held in a customized holder with LN_2 supplied over the surface to be scratched.

The system automatically maintains the normal load and sliding velocities at the adjusted value. The scratch depth was kept constant during the test. Tangential force was measured and recorded at any instance during the scratching process. These forces were used to measure the apparent friction coefficient (μ), defined by Eq (5.1).

$$\mu = \frac{F_t}{F_n} \tag{5.1}$$

where, 'F_t' is the tangential force and 'F_n' is the normal force.

5.2.2 Sliding wear test

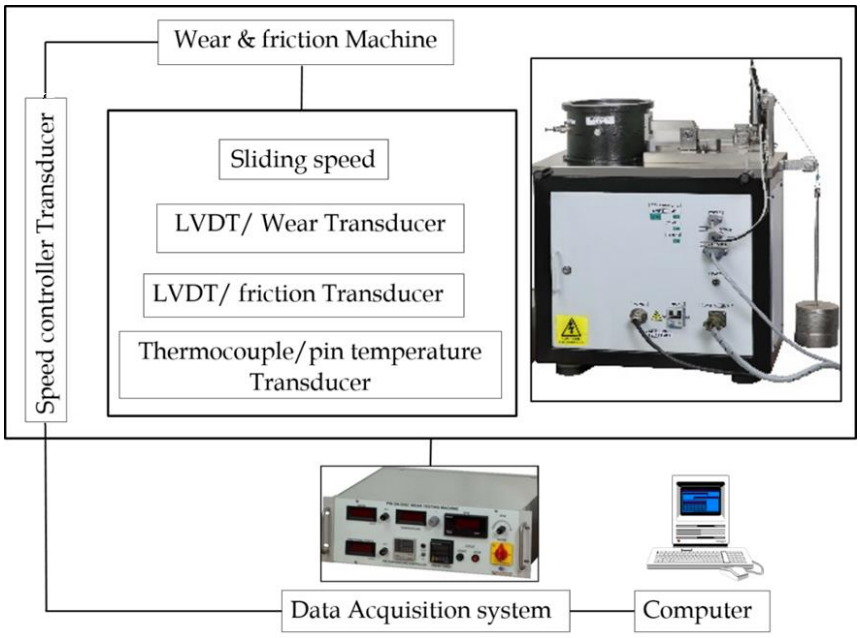

Fig. 5.2. Block diagram of sliding wear test setup.

Sliding wear tests were performed using modified pin-on-disc tribometer. The block view of sliding wear system is shown in Fig. 5.2. Experiments were performed as per

ASTM G99-95 standard sliding wear test [165]. atomized cryogenic tribometer system was developed by connecting an ALN spray system to the pin-on-disc configuration to feed the LN_2 exactly into the matting zone with a continuous flow rate (10-12 L/hr) and constant pressure (200 kPa). Experiments were conducted by sliding Al-TiC_p composite pin of 6 mm diameter and 25 mm length (with surface roughness of 0.3 mm center line average (CLA), and hardness of 95 HB) against EN31 steel disc of 165 mm diameter, 12 mm thickness (with surface roughness of 0.3 mm CLA, and hardness of 57 HRC) under dry, cryogenically chilled argon gas and atomized liquid nitrogen spray (LN_2) conditions. Sliding wear experiments were carried out on the developed atomized cryogenic tribometer system to obtain the cryogenic tribological behavior of Al-TiC_p composite at five different applied loads ranging from 5–25 N and three different sliding velocities ranging from 50–250 m/min. Load cell and linear variable differential transformer (LVDT) were used to measure the wear. The ratio of frictional force to normal force provides the apparent friction coefficient value (μ). Wear rate was measured by mass loss of pin per unit sliding time.

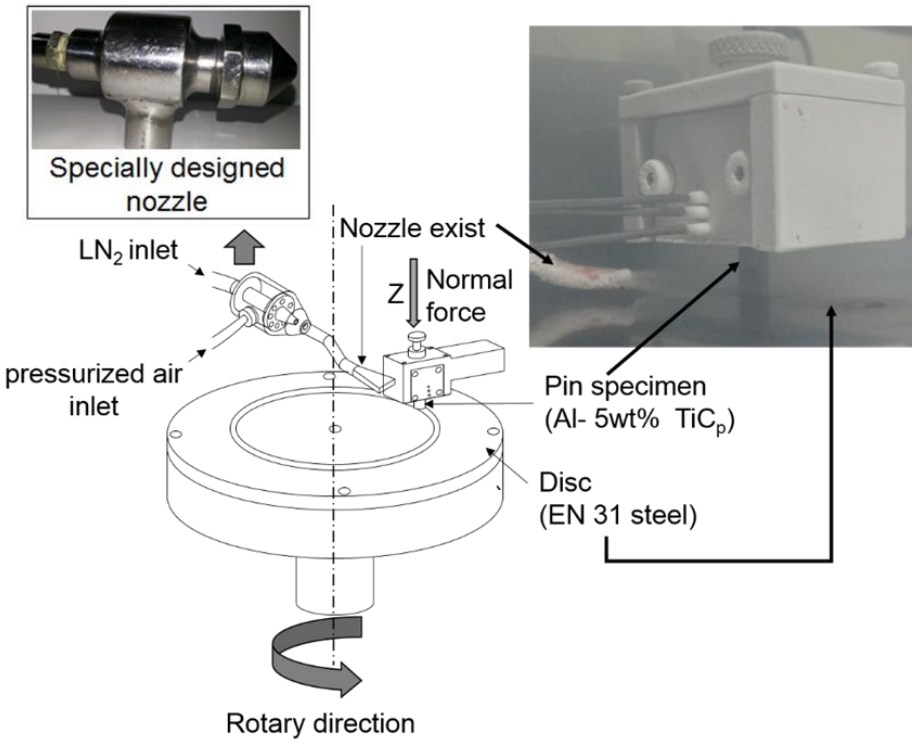

Fig. 5.3. Schematic view of nozzle setup for atomized cryogenic tribometer system.

To obtain a relative comparison under each specific condition, experiments were repeated thrice and average value was considered. Fig. 5.3. depicts the supply of LN_2 between the contact interfaces of composite pin and counter face (EN 31 steel) disc. Similarly, in chilled argon gas condition, instead of LN_2, pressurized cryogenically cooled air was passed through the mating zone. This gave the same cooling effect as LN_2 but fluidization effect varied. This variation is due to lack of liquid state in chilled argon gas condition unlike in LN_2, where both liquid and gas states help to reduce the friction force and wear between the mating surfaces.

Due to the lubrication effect of the fluid, wear and friction force of sliding contact reduces. Apparent frictional coefficient provides an understanding on how LN_2 influences the interaction of the contacting surfaces. Effective shear strength (τ) of the contacting materials multiplied by the true contact area (A_t) represents the frictional force (F). Contact area is dependent on the resultant normal load (N). The above mentioned is described by Eq. (5.2) [81].

$$F = \tau \times A_t = \tau \times m \times N^m = k \times N^m \tag{5.2}$$

where, 'm' and 'k' are constants. These constants are independent of the normal load. For most metallic materials, the parameter n is usually less than 1.0 and is also constant. However, it is dependent on the specific load range [166].

Therefore, apparent friction coefficient ('μ') can be obtained as below Eq. (5.3).

$$\mu = \frac{F}{N} = \frac{kN^m}{N} = kN^{m-1} \tag{5.3}$$

Equations (5.2) and (5.3) have not taken into account the shearing resistance of liquid which fills the valley around the contacting asperities, therefore they are applicable only to sliding contact which is soaked by fluid of low viscosity such as air and LN_2. Before each experiment, the Al-TiC_p pin is cleaned with acetone, dried and the mass measured

using an electronic weighing balance (least count: 0.0001 g). The loss in mass of pin was taken to evaluate the volumetric wear loss during wear tests. Each test was repeated for three times and the average values of volume wear was considered for wear behavior analysis. The wear rate ('W') was calculated by Eq. (5.4) where, 'M_L' is the mass loss, 'ρ' is the density and 'D_s' is the sliding distance.

$$W\left(\frac{mm^3}{m}\right) = \left(\frac{M_L/\rho}{c}\right) \tag{5.4}$$

Coefficient of friction (COF) was calculated from tangential force measured during wear tests. Tribological behavior of Al-TiC_p MMCs pin was analyzed and compared under three different environments. Further, in order to elucidate the lubrication effect of LN_2, coefficient of friction was analyzed. Worn surface of the pin and wear debris of all experiments were examined by using metallurgical microscope.

5.3 Results and discussion

In this research work, an attempt has been made to understand the lubrication effect of LN_2 during sliding condition. The following section explains the lubrication effectiveness of LN_2 by the friction coefficient value and sliding wear obtained using linear scratch tester and pin on disc tribometer. Finally, detailed explanation about the microscopic observations performed on worn surface and debris are collected to understand the wear mechanism of the Al-TiC_p composite under LN_2 environment are discussed.

5.3.1 Linear wear test

The intent behind the linear wear test is to identify the accessibility of the fluid to the indenter–chip interface. An attempt has been made, to estimate the apparent frictional coefficient under various fluid conditions: dry, cryogenically chilled argon (CCA) gas and atomized liquid nitrogen spray (cryogenic) environments. A very marginal deviation in force was observed among all the three conditions. Atomized liquid nitrogen spray

(cryogenic) condition recorded the least average traction force, followed by cryogenically chilled argon gas and dry condition. Fig. 5.4. (a) depicts plots of the traction force for the various media conditions investigated at a load of 25 N.

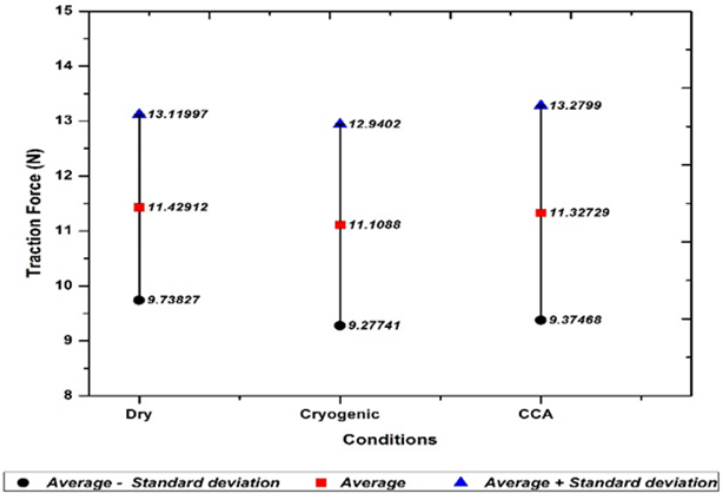

Fig. 5.4. (a) Traction force with a constant load of 25N under different environments.

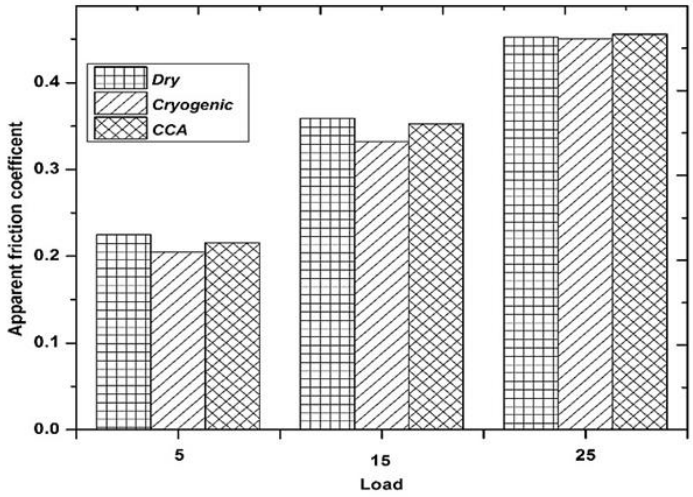

Fig. 5.4 (b) Average friction coefficient (vs) load.

As part of the experiment, friction coefficients for all three media conditions namely dry, atomized liquid nitrogen spray (cryogenic) and cryogenically chilled argon (CCA) gas, were observed under three different load conditions. The results are depicted in Fig. 5.4 (b). The results reveal that the coefficient of friction is directly proportional to load. It can be seen that there is minimum variation in the apparent friction coefficient (μ) for all the three conditions investigated.

The transition of material from elastic deformation to plastic deformation mainly depends upon the variation in contact area and hence the critical load regime will vary accordingly. For the applied normal load (5-25 N), the frictional force increases much more than the applied normal load. Due to this fact, coefficient of friction value increases. The technique involves generating a controlled scratch with a diamond tip (200 µm diameter) on the sample. The tip is drawn linearly across the surface under constant load causing ploughing of stylus in the sample resulting in scratch. As the load increases, the depression of indent will increase, resulting in increase in pulling force during scratch. In this phase, work done for overcoming friction is considered. The increasing pulling force (frictional force) results in increase of coefficient of friction. However, due to measurement variability, a true statement cannot be made on the relative lubricity of the various fluids evaluated.

5.3.2 Sliding wear test

Since no significant friction coefficient deviations were observed in the linear wear test, sliding wear tests were conducted on developed atomized cryogenic tribometer system for further analysis. The test results revealed that wear rate for cryogenic technique system offers lower wear rate due to both cooling as well as lubrication effect of LN_2. The apparent friction coefficient gives an understanding on how LN_2 influences the interaction of the mating surfaces. By lowering the interfacial temperature at the contact point, the coefficient of friction is reduced [167].

5.3.2.1 Apparent coefficient of friction

The variation of apparent friction coefficients at different sliding velocities (50 m/min, 150 m/min and 250 m/ min) and normal loads (5 N, 10 N, 15N and 25 N) under three environmental conditions i.e. dry, atomized liquid nitrogen spray (LN_2) and

cryogenically chilled argon gas environments are shown in Fig. 5.5 (a) to (c). It was observed that with an increase in sliding velocity there was an increase in apparent friction coefficient under all three environmental conditions.

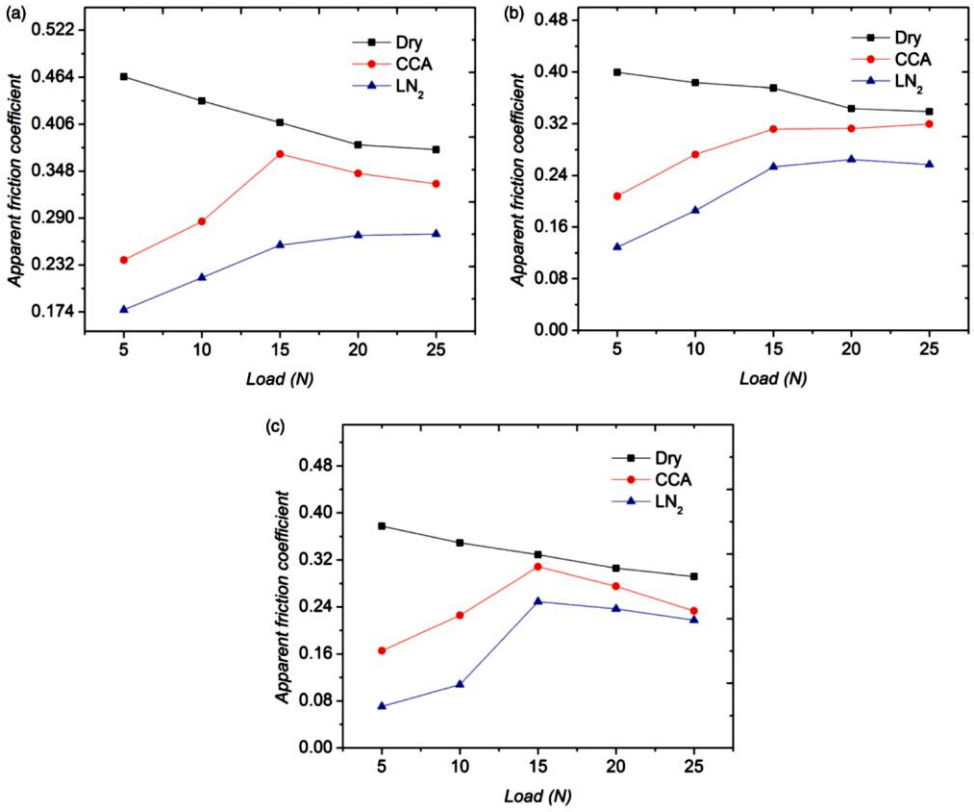

Fig. 5.5. Variation of apparent friction coefficient: (a) 50 m/min; (b) 150 m/min; (c) 250 m/min.

Further, with increase in load, a decrease in apparent frictional coefficient is also observed. A reduction of 38.45% and 22% in frictional coefficient was observed under LN_2 and cryogenically chilled argon gas respectively when compared to dry condition. Friction coefficient decreased drastically with increase in load for dry condition. Results followed the same trend as empirical observations described in equations (5.2) and (5.3), which describe that with increase in normal load, values of coefficient of friction decreases. By considering the fact that LN_2 is chemically inert, physically volatile and low viscous, no LN_2 film or LN_2 derived chemical are expected to survive between the contact asperities of the mating surfaces [168]. Cooling action and micro-hydrostatic lubrication effect may

cause this type of friction mechanism. LN_2 penetrates into valleys of collective asperities and reduces the true contact area and changes the effective shear strength, eventually affecting the friction coefficient [169].

Since atomized LN_2 is applied with a pressure of 2 bar at close proximity to the contact area, the trapped nitrogen should be partly in liquid state while supply pressure is maintained. Formation of thin gaseous film between the mating surfaces enhances the hydraulic pressure of trapped nitrogen. However, atomized LN_2 applied with a 2 bar pressure is not capable enough to fully separate the sliding surfaces, but the hydraulic pressure of the trapped LN_2 can reduce the true contact area, therefore reducing the resultant friction force. This microscale hydrostatic fluid film plays a predominant role in reducing the apparent friction coefficient at low normal load condition than high normal loads. Microscale hydrostatic lubrication becomes less effective with increase in normal loads [168]. Therefore, the sliding conditions play a significant role in developing a micro-LN_2 fluidized gas film. Auxiliary observation from Fig. 5.5 reveals that micro-hydrostatic thin film was effectively formed at low load i.e. 5, 10 and 15 N load at all sliding velocities. Further change in friction coefficient value of the composite was due to a thin adherent solid lubricating film formed by fractured brittle reinforcement particles squeezed out from matrix alloy [170, 171]. This thin solid lubricating film resulted in decrease in coefficient of friction.

5.3.2.2 Wear studies

The influence of sliding velocity and load on the wear rates of Al-TiC_p composites at different environmental conditions is shown in Fig. 5.6. It was observed that with increase in applied normal load, there was increase in wear rate of composites. This can be attributed to the higher extent of plastic deformation which further increases the probability of sub surface cracking and delamination [172]. Also, with increase in sliding velocity, an

increase in wear rate was noted. This can be attributed to high strain rate subsurface damage leading to increase in contact area by fracture and fragmentation enhancing the delamination contributing to higher wear loss [170].

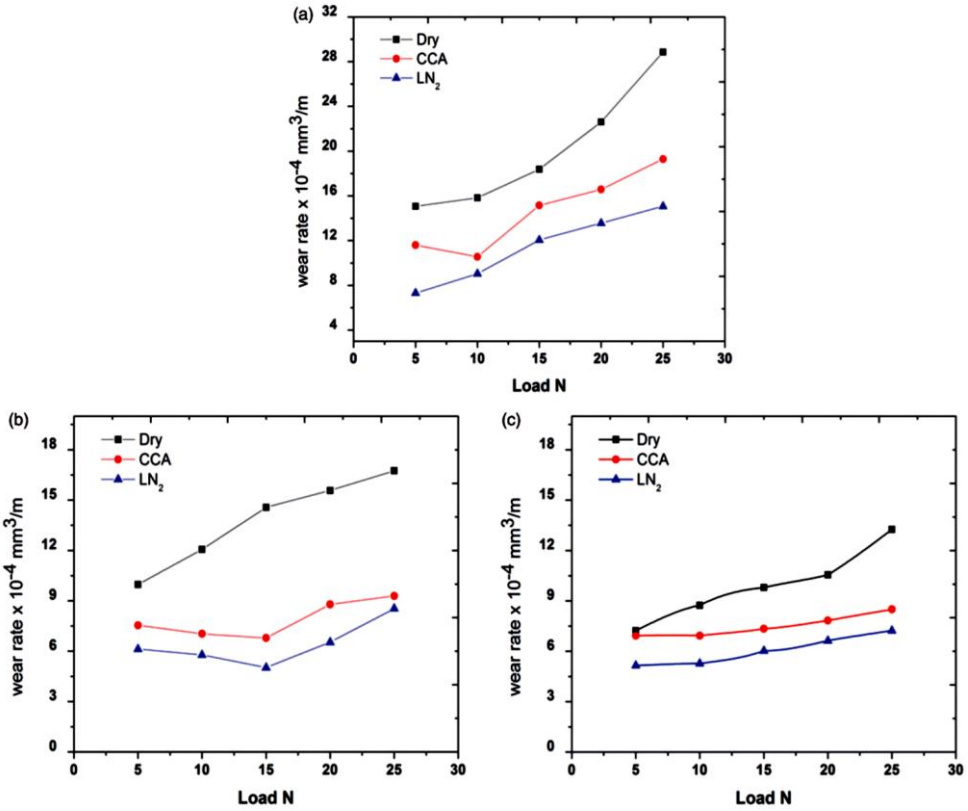

Fig. 5.6. Variation of wear rate with respect to load: (a) 50 m/min; (b) 150 m/min; (c) 250 m/min.

A reduction of 46.68% and 37.56% in wear rate was observed under LN_2 and cryogenically chilled argon gas condition respectively in comparison to dry condition. Micro-hardness of Al-TiC_p composite increases under cryogenic environment, thus, reducing the wear intensity. There is experimental data and practical evidence to show that the wear rate increases up to 200–300 s during LN_2 condition, lowers to 10–15% at a period of 250–350 s and then marginally improvs till the end i.e. 600 s. Further cooling action of LN_2 and microscale lubricating film were also major causes in reduction of wear under atomized LN_2 spray environment. With application of atomized LN_2 spray and cryogenically chilled argon gas condition with a pressure of 2 bar between the mating

surfaces, leading to reduction of contact temperature. Lowering the interfacial temperature substantially reduces the diffusive and adhesive wear without causing any chemical reaction.

5.3.3 Analysis of worn surface using metallurgical microscope

Microscopic photographs of worn surfaces of Al-TiC_p composites under dry, atomized LN_2 spray and cryogenically chilled argon gas conditions are shown in Fig. 5.7. It is observed that the morphology of worn surfaces of composites was different from environmental conditions. Atomized LN_2 spray condition shows crater wear and small cracks such as dry shallow groves with delamination of materials along with ploughing action. Fine grooves with delamination were observed under cryogenically chilled argon gas condition. These observations support that lower wear rate resulted at atomized LN_2 spray condition followed by cryogenically chilled argon gas and then dry condition. Sliding velocity and normal loading are two important conditions which affect the morphology of worn surface. As load increases, worn surface progressively changes from fine scratches to distinct grooves under all environmental conditions. A mixed abrasion plastic deformation was observed at low loads under dry condition. Scoring grooves were observed in direction of sliding which is evident from abrasion. These are formed due to the action of wear hardened deposits on track. At high loads, cracks and local damage were observed which resulted in a high wear rate. Highest sliding velocity of 250 m/min exhibited severe grooving and plastic flow. It is reported that at low sliding velocity, LN_2 forms a fluidized thin film between the mating surfaces which forms a protective layer. At low velocities, fluid film was found to be stable whereas at higher velocities it was too difficult to maintain thin fluid film, which in turn lead to delamination. Delaminated particles get entrapped between the mating surfaces resulting in three body abrasive wear. Thus, delamination and abrasive wear subsequently form cracks and cause excessive wear [173].

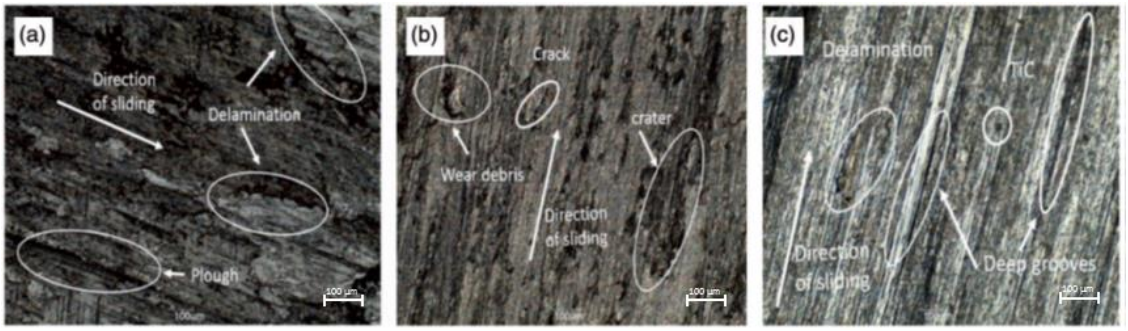

Fig. 5.7. Microscopic images of wear tracks of Al-TiC_p at a load of 5 N and a sliding velocity of 150 m/min under (a) Dry (b) LN_2 (c) CCA gas.

5.3.4 Wear mechanism

Different wear mechanisms were observed when developed composites were subjected to various sliding velocities under dry and cryogenic conditions (Fig. 5.7 (a)). Under dry condition, at low sliding velocities, flake structured wear debris and shallow grooves can be seen while the worn surface showed signs of three body abrasion. Under cryogenic sliding (atomized LN_2 spray and cryogenically chilled argon gas condition), relatively smooth wear tracks were produced at shorter distances. The hardening effect was evident due to interposing of LN_2 on Al-TiC_p composite when subjected to a longer sliding speed. This confirms that developed composite becomes harder and brittle leading to cracks and crater wear as can be seen in Fig. 5.7 (b).

It is clear that different wear mechanisms occur at different environmental and sliding conditions. During sliding motion, heat is generated between the mating surfaces of composite pin and EN 31 steel disc. An adiabatic shear band is likely formed between these contact surfaces under all sliding conditions which further causes void nucleation with the shear bands [174]. As a result, delamination occurs and flake-like debris particles are formed in sliding tests. These flake-like debris conducive to adiabatic type shear localization phenomena. Besides this, high interface temperature also may cause changes in microstructure and thermal softening [175]. In sliding under atomized LN_2 spray

condition, interface temperature decreased drastically by interposing liquid nitrogen proximately between the mating surfaces. Thus, LN_2 prevents the formation of adiabatic shear band and delamination wear. Moreover, intense cooling effect of LN_2 hardens the surface of specimen and counter body [176]. This resulted in abrasion wear by micro-cutting of composite on the worn surfaces.

5.3.5 Microscopic observation of wear debris

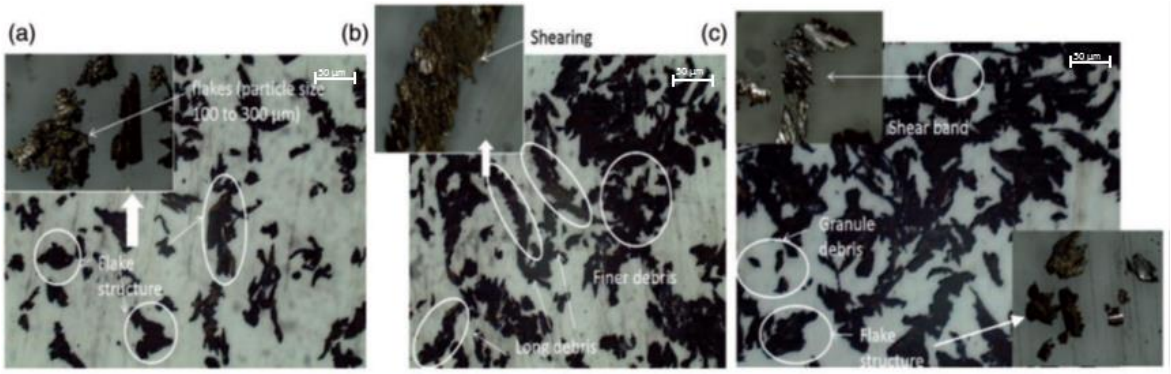

Fig. 5.8. Microscopic images of wear debris of Al-TiC_p at a load of 5 N and sliding velocity of 150 m/min under (a) Dry (b) LN_2 (c) CCA gas.

Micrographic images of wear debris of Al-TiC_p MMC alloy were collected and are presented in Fig. 5.8. Metallic flake form of debris was formed in developed composite at all the three conditions. It was observed that thin sheets/plates-like structured debris were formed with an average particle range of 100 –300 microns under dry condition. Whereas in both atomized LN_2 spray and cryogenically chilled argon gas conditions, wear debris in the form of long flakes with an average length of 300 microns and width of 40 microns were seen. Further, it was also observed that with the increase of load and sliding velocities, there was an increase in granules size of debris particles collected which explains the severity of wear rate. This will support the results of wear rate discussed earlier. It was observed that at high load and low sliding velocity, the debris produced were fine and coarse in structure. This supports the increased wear rate at higher loads and

speeds [177, 178]. Since severity of surface contact is very high at high loads and velocities, the stress on reinforced particle leads to fracture [179]. Additionally, some irregular and grain-shaped debris particles were also observed because of continuous plastic flow and orientation in the direction of sliding [173]. This is due to abrasive action of TiC particles by ploughing into the hard steel counter face. In addition, composite debris also consisted of TiC particles. This was due to sternness of surface contact causing cracks in TiC particles. Similar results were obtained by Ramesh et al.. [170] while studying the sliding wear behavior of Al-TiB_2 in-situ composite.

5.4 Summary

The cryogenic tribological behavior of Al-TiC_p composite using sliding wear tests were studied successfully on customized atomized cryogenic tribometer. Nozzle arrangement to the atomized cryogenic tribometer setup feeds LN_2 exactly into sliding contact with a restricted flow rate and constant pressure for better cooling and lubrication. The observations reveal that presence of LN_2 in sliding contact offers significant reduction in friction and wear values when compared to other environments. The performance improvement with LN_2 could be due to the hydraulic pressure of trapped LN_2 into the sliding contact which takes away a part of normal load resulting in reduced apparent friction coefficient and wear rate.

It can be inferred from the above results that the developed atomized LN_2 spray system has shown to be advantageous in improvement of the tribological characteristics of Al-TiC_p MMC over dry condition. To analyze the performance of ALN spray system, cutting experiments need to be performed apart from the tribological studies. The performance of atomized liquid nitrogen spray assisted machining on machinability parameters like cutting force, tool wear, and quality of machined surface during machining process is comprehensively studied and presented in chapter 6.

Chapter 6
Machinability Aspects of Turning Al-TiC_p MMCs

As discussed in the preceding chapter, atomized cryogenic technology has proven its advantages in improving tribological behavior of developed Al-TiC_p composites over the selected experimental domains. The current chapter describes the comprehensive experimental investigation carried to enhance the machinability performance of Al-TiC_p composites with different industrial cutting speed-feed combination and tool geometry (rake angle, nose radius and approach angle) under atomized liquid nitrogen spray assisted machining condition. This chapter is organized as follows: Section 6.1 gives a brief information about machining of metal matrix composites. Section 6.2 presents the experimental details of turning experiments. Section 6.3 presents the machining performance of atomized liquid nitrogen (ALN) spray system in terms of cutting forces, tool wear and surface finish of machined work material over a broad experimental domain. Finally, Section 6.4 presents the overall summary of this chapter.

6.1 Introduction

During machining, tool temperature increases with increase in cutting speed, feed and depth of cut which softens the tool material and consequently accelerates the diffusion wear. Conventional coolants have been used as supplementary choices to reduce the heat generation (lack of build-up-edge) and flush away the chip (avoids re-cutting) reducing the friction between tool and chip interfaces. However, incompatibilities have been reported in relation to conventional coolants in machining of composite materials [21, 22]. Researchers are focusing on alternatives coolant to achieve economical and eco-friendly manufacturing process. Achieving green machining with cost effective cryogenic cooling is gaining popularity. Among various cryogenic liquids, liquid nitrogen (LN_2) is an eco-friendly

coolant used for the desirable control of machining temperature and enrichment of tool life [23].

Although cryogenic technology brings promising advancement in machinability of MMC materials, it has not been investigated in detail towards improving the performance in machining of Al-TiC_p MMCs. As an attempt to fill this gap in existing research, atomized liquid nitrogen (ALN) spray jets directed towards the tool/chip interface will penetrate effectively and minimize the supply of LN_2 leading to performance improvement of machining. To endorse the performance of developed ALN spray system, turning experiments were conducted under different tool geometry, i.e., rake angle, nose radius and approach angle. The quality of machined surface, machining force and tool performance are considered as machinability performance parameters to evaluate the combined influence of cryogenic technology and tool geometry. Detailed understanding of their influence on machining performance will help to overcome the machining barrier of Al-TiC_p MMCs.

6.2 Experimental details

In the present investigation, Al-5wt%TiC_p composite specimens of size 150 mm length 32 mm diameter were used for turning. The rationale behind selection of these specimens was their extensive preferability as engineering material for various high-performance components due to the grain refinery properties of TiC_p reinforcement particles. Machinability analysis was performed under dry, wet and atomized liquid nitrogen spray machining conditions on CNC lathe with carbide inserts of various tool geometry. The developed atomized liquid nitrogen spray system was fitted to the CNC machine using a metal frame which was fastened to the lathe turret as shown in Fig. 6.1. The ALN spray setup was developed based on the concept of cryogenic air blast atomization process which enhances the process efficiency on turning operation.

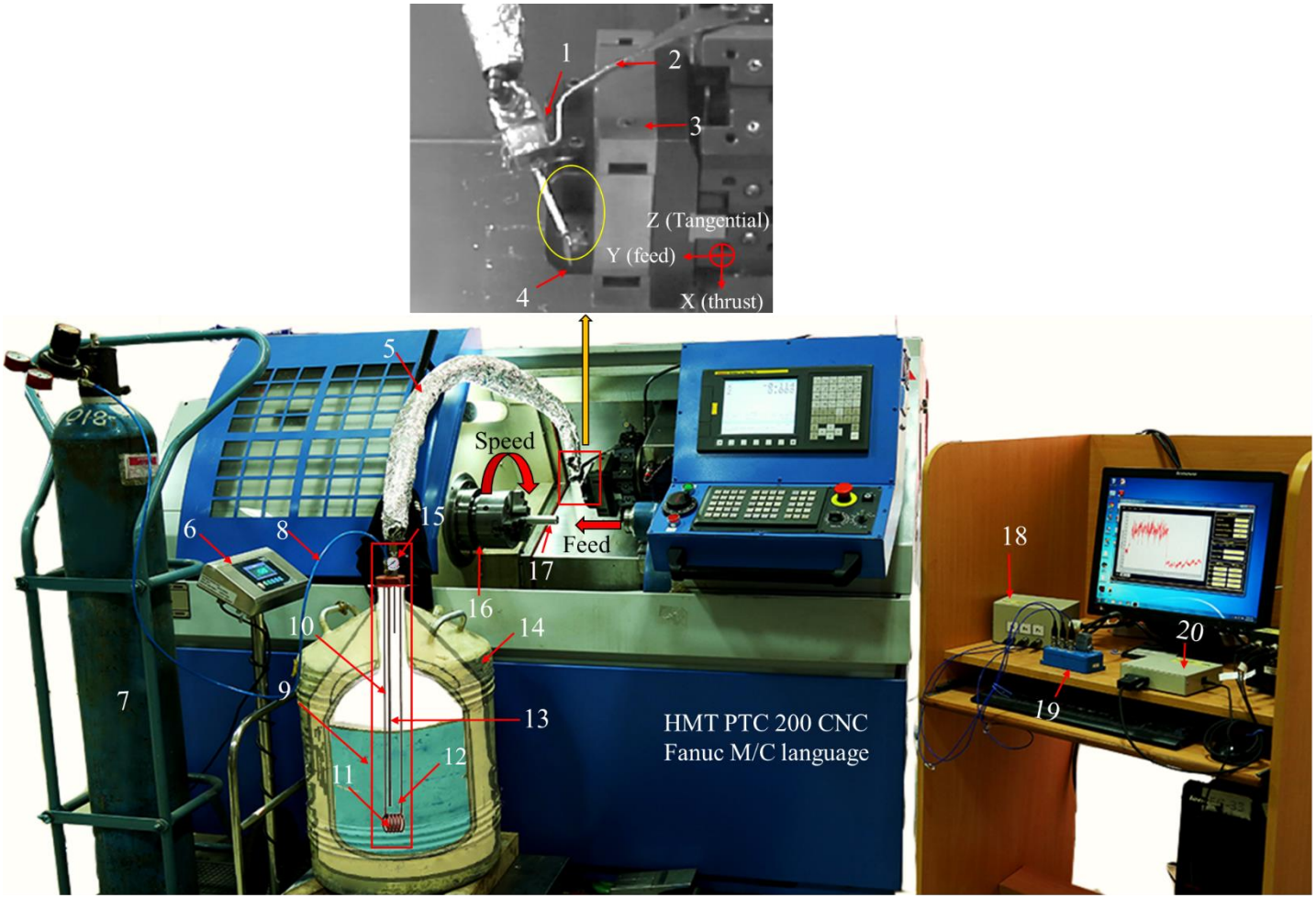

1. Nozzle unit
2. metallic frame to adjust the nozzle unit
3. Force dynamometer
4. Cutting tool
5. Insulated stainless steel hose
6. Weighing balance
7. Argon cylinder
8. Pneumatic hose
9. CAC unit
10. CCA inlet flow line
11. Copper coiled pipe
12. CCA outlet flow line
13. Liquid flow line
14. Dewar flask
15. Pressure gauge
16. 3 jaw chuck
17. Al-5% TiC_p
18. Signal conditioner
19. DAC
20. Charge amplifier

Fig. 6.1. Photograph of complete arrangement of atomized liquid nitrogen spray system.

Cryogenic air blast atomization process was used to produce uniform liquid droplets the size of about 50 μm at the peak flow rate of 0.299 L/min. As previously explained in Chapter 4, optimal spray conditions have been determined to ensure the setup for proper cooling and lubrication performance. It can be inferred from the preliminary experimental results, moderate feeding pressure (200 kPa) in combination with larger impingement angle (30°) and adequate spray distance (10 mm) provided better performance for selected tool/work combination and cutting condition. This was possibly due to formation of thick fluid film which provides cooling and lubrication effect in the entire zone, leading in turn to lower flank wear and surface roughness. In the following section, the study of experimental results in ALN spray assisted machining conducted with a combination of 200 kPa feeding pressure, 30° impingement angle and 10 mm spray distance are discussed.

Machining tests were performed on HMT PTC 200 high precision CNC lathe machine with the specifications provided in Table A.1 (APPENDIX-A). There are numerous variables that affect the performance of machining; the important parameters include the type of lubricant, tool geometry and cutting conditions. However, to facilitate the data collection, only five dominant factors were considered in the planning of experimentation. Based on review of existing literature, influence of cutting conditions (cutting speed and feed) and tool geometry (rake angle, nose radius and approach angle) on the tool wear, surface finish, and cutting forces was investigated. The range of each factor was selected based on the present day industrial requirements. On the basis of availability and widespread use, coated carbide inserts (varying rake angle and nose radius) and tool holders (approach angle) were used in the current research work. Experiments were carried out keeping these factors at three different levels.

6.2.1 Design of experiments

A well-designed series of experiments can substantially reduce the total number of experiments often carried out randomly. In order to determine equation of the response surface, several experimental designs have been developed which attempt to approximate the equation using the smallest number of experiments possible. In this work, Box-Behnken design (BBD) developed by George E. P. Box and Donald Behnken [180] has been implemented. Box-Behnken design (BBD) is a response surface methodology (RSM) design with a class of rotatable or nearly rotatable second order design based on three-level design for fitting response surfaces. Ferreira et al.[181] suggested that BBD is slightly more efficient than central composite design (CCD) and much more efficient than the three-level full factorial designs. The number of experiments (N) required for development of BBD is defined as, $N = 2k(k-1) + C_0$, where, k is number of variables and $C_0$is number of central points.

Table 6.1 Process variables and their levels.

S no	Parameter	units	Level-I (-1)	Level-II (0)	Level-III (1)
1	Cutting speed (V_c)	m/min	50	100	150
2	Feed (f)	mm/rev	0.1	0.15	0.2
3	Rake angle (γ)	deg	0	8	16
4	Nose radius (r_e)	mm	0.4	0.8	1.2
5	Approach angle (ψ)	deg	30	60	95

In the present study, five independent variables considered for experimental investigation are cutting speed, feed, rake angle, nose radius and approach angle. Table 6.1 represents selected factors and their levels for current research work. The range of input variables and their initial setting values are coded for simplification of experimental data analysis. The central point i.e. the 0-level is chosen as the approximate point of optimality. Then, a range of points are selected within the vicinity of the central point.

For the easy simplification of the input parameters, the standard relation [181] was used to determine the coded parametric values as $X_i = \frac{N_i - N_0}{N_1 - N_0}$where, '$N_i$'=actual parametric value corresponding to the level of interest i.e. natural variable for i^{th} level, 'N_1'= actual value of the parameter corresponding to the level 1 i.e. natural variable for 1-level and 'N_0' = actual value corresponding to the 0 level i.e. natural variable for 0-level. The surface roughness, cutting forces and tool wear were considered as machining performance measures. BBD requires fewer treatments combinations than a CCD in a problem involving five factors. A five factors BBD with one block consisting of 46 experiments (40 base runs and 6 central points) was carried out. This design allows for efficient estimation of the first and second-order coefficients. Table A.2 (APPENDIX-A) shows the chosen design of experiments each having a combination of different levels of process variables.

6.2.2 Cutting tool

Machining of MMCs with triple coated tools with a top layer of TiN are best option among carbide tools [147]. Therefore, in the in the present research work, KCU10 coated carbide inserts of different geometry were used to perform experimental investigations. KCU10 is an advanced multilayer PVD coated cutting tool featured in dual layer coating applications. A top layer of AlSiTiN atop a second layer of AlTiN is used to perform machining of super alloys at wide range of cutting speed and feed capability. ISO geometry (CNMG 1204) tools were used in the current research work to machine Al-TiC_p MMCs. Twelve different tools were used to achieve variations in rake angle and nose radius. Three different P-type tool holders were used to achieve different approach angles. The tools and tool holders were supplied by Kennametal Widia India Ltd, Hyderabad.

6.2.3 Selection of environmental conditions

Machinability analysis of developed Al-TiC_p composite cylindrical specimen was performed on CNC lathe with carbide inserts of various tool geometry under dry, wet, chilled argon (CCA) gas and ALN spray assisted machining conditions. Under dry condition, experiments were conducted at ambient conditions of 25°C and 40-60% relative humidity. In wet conditions, emulsion (AmulKart 4C) was mixed with water at a ratio of 1:10 and supplied into the tool/chip/workpiece contact zone through a nozzle arrangement. Preliminary machining experiments are carried out using free flow of liquid nitrogen and results show a larger adverse effect on surface integrity and tool performance when compared with CCA gas and ALN spray condition. Therefore, the study was continued with CCA gas and ALN spray conditions. In ALN spray condition, atomized jet of LN_2 was directed towards the interface between the mating surfaces using specially designed nozzle arrangement. Finally, in chilled argon gas condition, argon gas was cooled down to -190 to -160°C and then supplied to the interface zone to give cryogenic cooling effect. However, fluidization effect will vary due to lack of liquid state in chilled argon gas condition. Machining tests were conducted under constant depth of cut of 0.25 mm throughout the investigation. The important selected process parameters are presented in Table 6.1. Turning test was carried with a fixed cutting length of 90 mm and all the tests were done thrice at individual condition to minimize error. The mean of three quantities was used to depict the machining performance.

6.2.4 Cutting forces

A 3-component piezo-electric force sensor was employed to measure the dynamic forces formed on the tool during turning tests. A proportional charge signal is produced in the measuring element and fed to charge amplifier. These signals are amplified by charge

amplifier, then, converted by signal conditioner and recorded in computer by national instruments DAQ. CFM software was developed on basis of Lab View to log the data at a sampling rate of 10 KHz. Fig. 6.2 shows the complete arrangement of Fig. 6.2. Three-axis piezoelectric lathe tool dynamometers on the lathe turret. Specifications of 3-axis piezoelectric lathe tool dynamometer are tabulated in Table A.3 (APPENDIX-A).

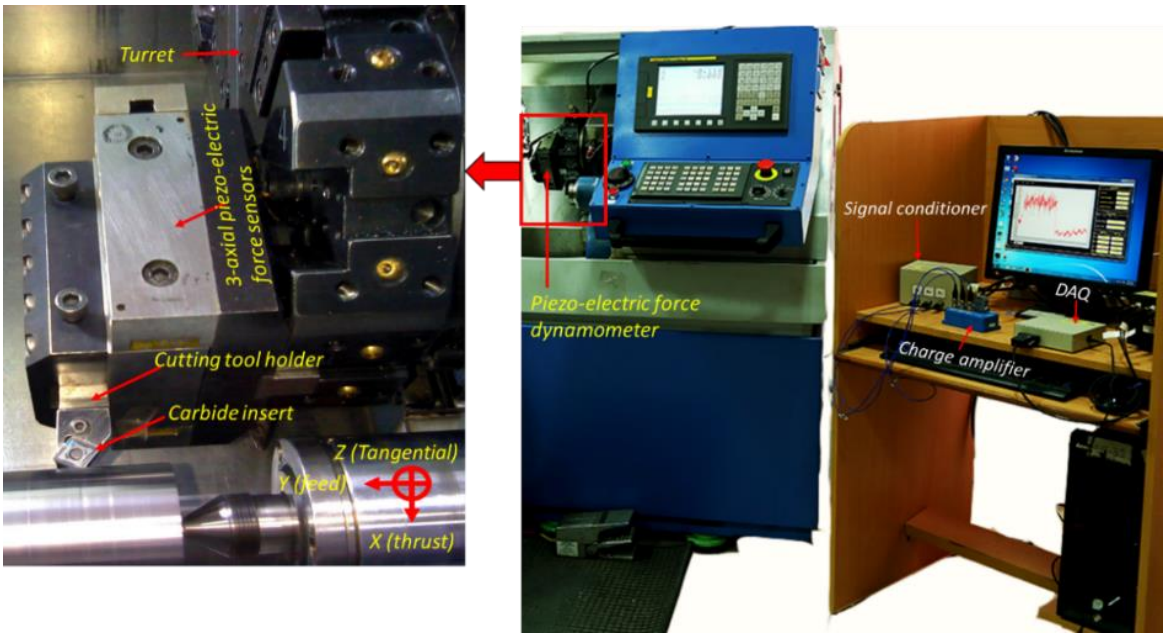

Fig. 6.2. Three-axis piezoelectric lathe tool dynamometer.

6.2.5 Surface roughness

After finishing of each trial under determined cutting conditions, surface roughness of machined composites was measured by using Taylor Hobson Surtronic 25 Profilometer (Fig. 6.2) with 8 mm sampling length, speed of 1 mm/sec with 5 μm diamond tip. The specifications of surface profilometer are shown in Table A.4 (APPENDIX-A). Four readings were taken at the middle of machined surface at 90° angle for each measurement on the sample. Surface topography of machined composites was examined and analyzed using optical microscope (Olympus STM 6) and ZETA-20 3D optical profilometer.

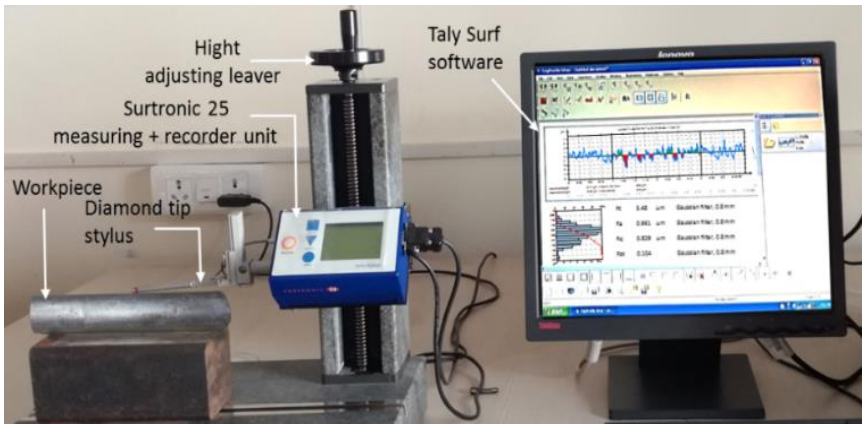

Fig. 6.3. Surface profilometer to measure surface roughness value.

6.2.6 Tool wear

Tool performance was analyzed to understand the pragmatic nature of wear modes that occur while machining of Al-TiC_p MMCs under various environmental conditions. Tool performance significantly alters the machinability behavior of MMCs. This was analyzed by measuring and examining the wear occurring on tool surface.

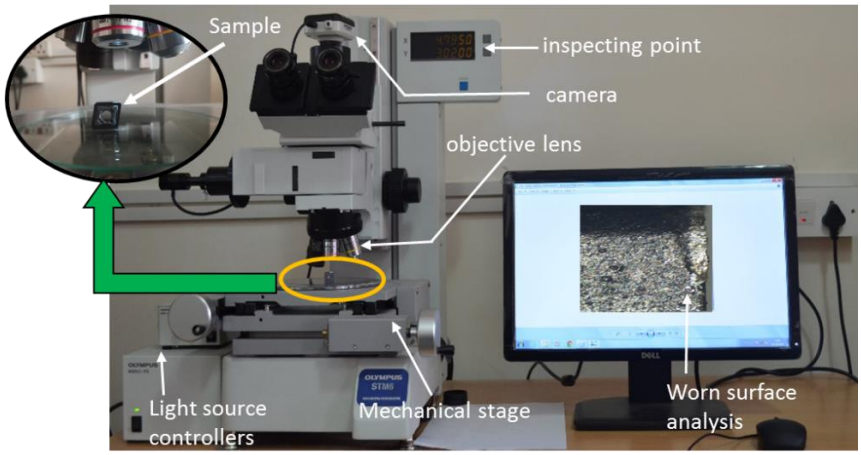

Fig. 6.4. Optical microscope (Olympus STM 6) to measure flank wear value.

Measuring of tool wear helps in determining the life of the tool while examination of wear on tool surface helps in determining the type of wear mechanism observed during machining. Flank wear which occurs on the flank or relief face of the tool below the cutting

edge is the primary mode of tool failure in machining of composites. The extent of flank wear (V_b) can be measured as the distance between the top of the cutting edge and the bottom of the area where flank wear occurs. An optical microscope (Olympus STM 6,) was used to measure the flank wear (Fig. 6.4). The specifications of the microscope are tabulated in Table A.5 (Appendix-A).

6.3 Results and discussion

ALN spray system has been attached to the CNC lathe to improve the machinability performance of Al-TiC_p composite. The system is equipped with a nozzle which yields micro-sized LN_2 droplets of 45–120 μm. These atomized LN_2 droplets are impinged as a focused jet in the machining zone with the help of high velocity CCA gas of 8–50 m/sec. This helps to feed LN_2 effectively between the tool chip interfaces. The conducted research indicates that the tool geometry (radial rake angle and nose radius) and cutting conditions (cutting speed and feed) also play an important role in machinability performance of MMCs.

6.3.1 Analysis of cutting force

Cutting force is directly influenced by tool geometry, tool and workpiece, cutting and environmental conditions. It also influences the specific energy and power requirement of the machining process [182]. Some of the variations in cutting force with respect to various machining parameters are shown in Fig. 6.5-6.7. The comparative advantages of LN_2 over other machining conditions can be clearly seen from the curves. It was observed that at all selected machining parameters, lower cutting force values were observed under ALN spray system. This can be attributed to the presence of LN_2 in the contact zone which reduces frictional force at the tool/workpiece interface over rake face. This is achieved due to the effective penetration capability of atomized LN_2 droplets into interaction zone within a short

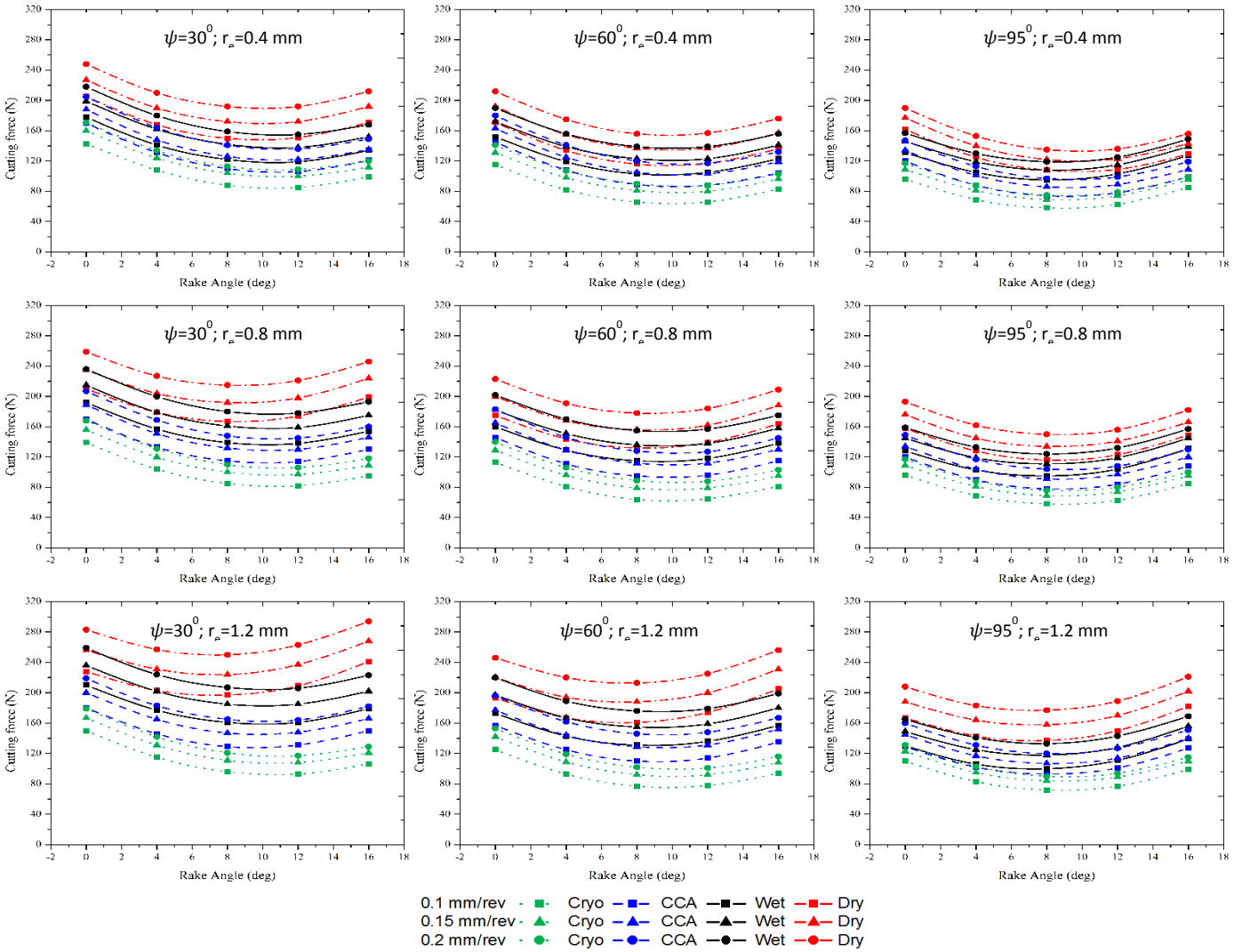

Fig. 6.5. Variation of cutting force at cutting speed of 50 m/min for different rake angle with various levels of nose radii, approach angles and feed under dry, wet, CCA gas and ALN spray assisted machining conditions (cryo).

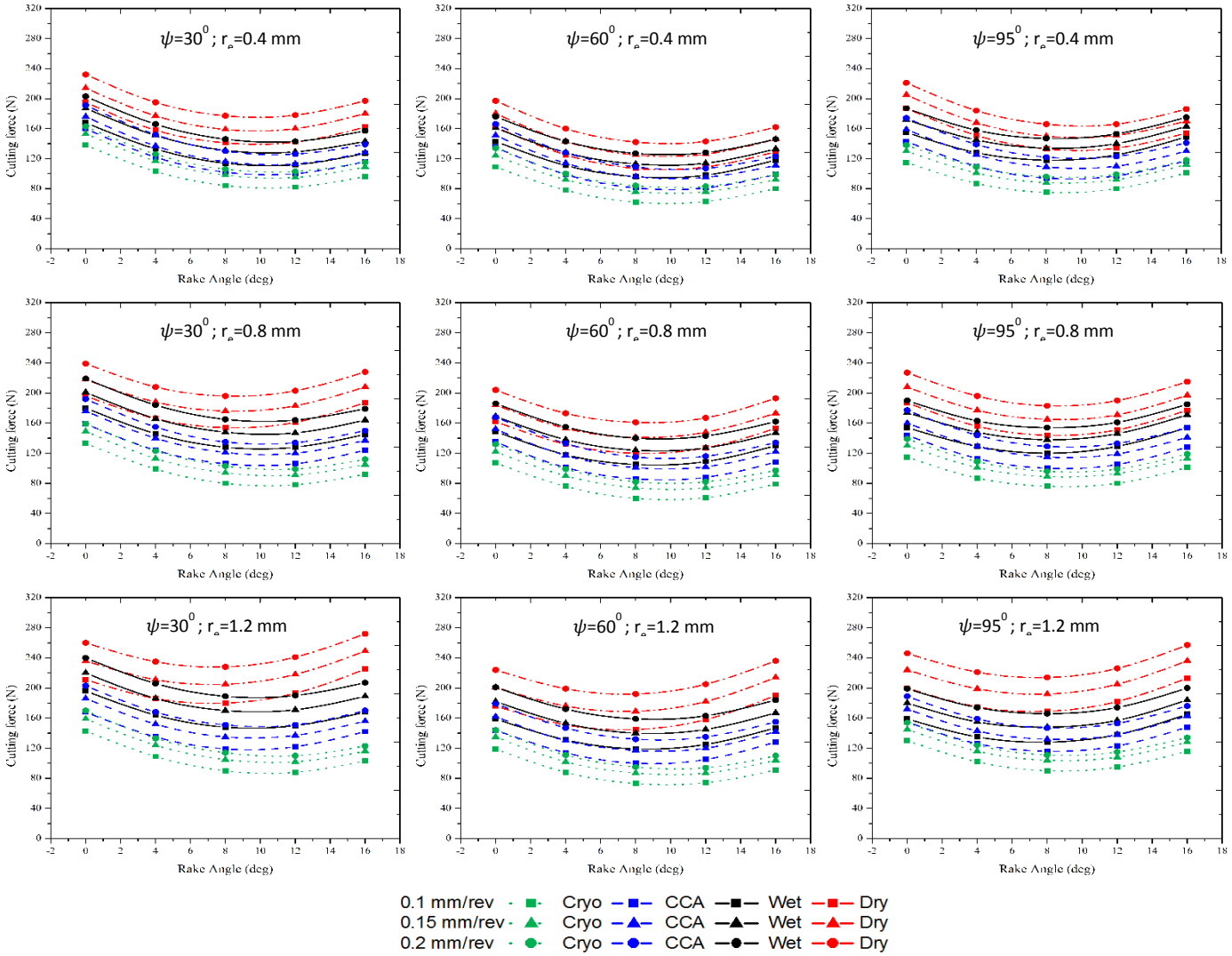

Fig. 6.6. Variation of cutting force at cutting speed of 100 m/min for different rake angle with various levels of nose radii, approach angles and feed under dry, wet, CCA gas and ALN spray assisted machining conditions (cryo).

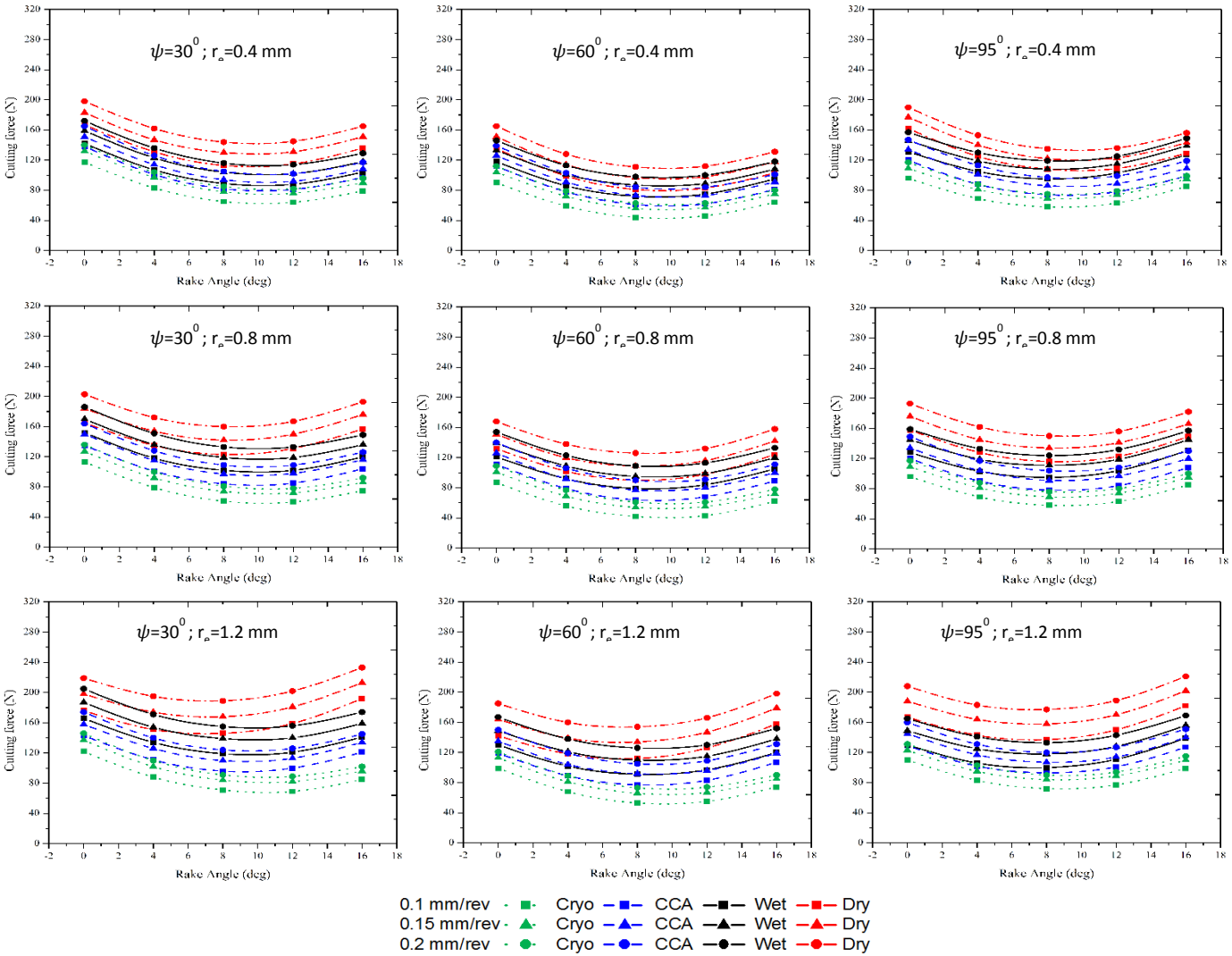

Fig. 6.7. Variation of cutting force at cutting speed of 150 m/min for different rake angle with various levels of nose radii, approach angles and feed under dry, wet, CCA gas and ALN spray assisted machining conditions (cryo).

period of time. Similar observations have been reported by Kalyan Kumar & Choudhury [89]. Further, the penetrated LN_2 evaporates swiftly between the interfaces forming a nitrogen cushion leading to reduction in coefficient of friction values which in turn reduces the cutting force. It was observed that ALN spray system gave 56%, 48% and 36% lower cutting force values in comparison with dry, wet and CCA gas assisted machining conditions respectively. The maximum variation of cutting force was less than 14% under wet condition over dry machining condition for all selected machining parameters. The possible reason for this is the rapid abrasion of cutting tool by the particles even under wet cutting condition [21]. Though the coolant used in wet condition was efficient in reducing heat generation, it did not form any protective film to reduce the frictional conditions existing at the tool flank face. However, under ALN spray and CCA gas condition, the variation in cutting force was more than 30% and 50% respectively due the effective penetration of LN_2 as droplets into the tool/chip interface.

Further analysis of Fig. 6.5 - 6.7. reveals that under all selected machining conditions, cutting force values decrease and then increase with increase in rake angle. This is due to the fact that as rake angle increases from 0 to 8°, cutting forces decrease due the increase in sharpness. Beyond 8° rake angle, the cutting force increases due to increase in contact area of tool/workpiece. 8° rake angle produces maximum of 53%, 47%, 39% and 40% lower cutting force value over 0° rake angle at selected machining conditions under ALN spray system, CCA gas, wet and dry machining conditions respectively. A similar trend has also been observed with approach angle. This can be attributed to the fact that at low approach angles, the effective cutting edge is increased. As a result, the chip thickness becomes smaller and favors low cutting force. Upon further increase in approach angle, the cutting forces are distributed over

a shorter section of the cutting edge since the main cutting edge enters and leaves the cutting zone suddenly at 90° approach angle, thus subjecting the workpiece to maximum loading and unloading. Nose radius is another important tool geometry parameter which affects the force obtained during machining. As nose radius increases from 0.4 mm to 0.8 mm, the cutting force increases due to higher contact area between tool/workpiece. With further increase in nose radius from 0.8 mm to 1.2 mm, the cutting force decreases.

Additionally, it can also be observed that as cutting speed increases, the cutting force decreases. This trend was expected because as cutting speed increases, machining becomes more adiabatic and the heat generated in the shear zone cannot be conducted away during the very short time in which the metal passes through this zone. So, the rise in temperature softens the material aiding grain boundary dislocation and thus reducing the cutting forces [183]. It can also be observed from Fig. 6.5-6.7 that as the feed value increases, cutting force increases. This is due to the fact that as feed value is increased, more material will have to be cut per tooth per revolution, requiring more energy leading to increase in the cutting force. From the performed studies, conclusion can be drawn that the change in magnitude of the force component with increase in feed are affected by hard reinforcements.

While machining of Al-TiC_p composites, tool face is not greatly restricted by built-up edge or friction at the tool/chip interface. Al-TiC_p composite material contains TiC reinforced particles which have globular and polyhedral morphology and are hard in nature. Hence, sudden increase in cutting force is observed when tool comes into contact with TiC particle. Similar trend was observed for all machining conditions. This effect is lesser in ALN spray system due to the lubrication and cooling effect of LN_2. It has been observed from experimental results that the maximum cutting force was observed at a cutting speed of 150 m/min,

0.1 mm/rev feed, 8° rake angle, nose radius of 0.8 mm and 60° approach angle in ALN spray assisted machining conditions at 40 N cutting force. The lowering of cutting force under ALN spray system clearly establishes the improvement of machinability performance of Al-TiC_p MMCs. In order to further warrant the improvement of machinability, additional analyses are needed. Analysis of tool wear and surface roughness under selected machining conditions is presented in the foregoing sections.

6.3.2 Analysis of surface quality

In addition to the cutting force, surface roughness also plays an important role in the assessment of machinability performance since durability and service life of a machined part depends mainly on the surface finish. Nam et al. stated that the surface quality is a very important factor to be considered in manufacturing [184]. To evaluate the process quality, surface finish was evaluated by measuring surface roughness values and studying the topography of machined surface.

6.3.2.1 Analysis of surface roughness

The measured surface roughness values at different levels of tool geometries and cutting conditions are shown in Fig. 6.8 - 6.10. An average of 65%, 64% and 36% lower surface roughness was observed during atomized LN_2 spray assisted machining in comparison to dry, wet and CCA gas assisted machining conditions respectively. Lowest surface roughness value of machined surface in turning of Al-TiC_p composite under ALN spray system was approximately 0.25 µm at high cutting speed, low feed value, 4° rake angle, high nose radius and moderate approach angle. The average roughness value was observed to be 0.63 µm under ALN spray system. In the case of other condition like CCA gas, wet and dry machining, average roughness values were 0.84 µm, 1.08 µm and 1.13 µm respectively. This can be

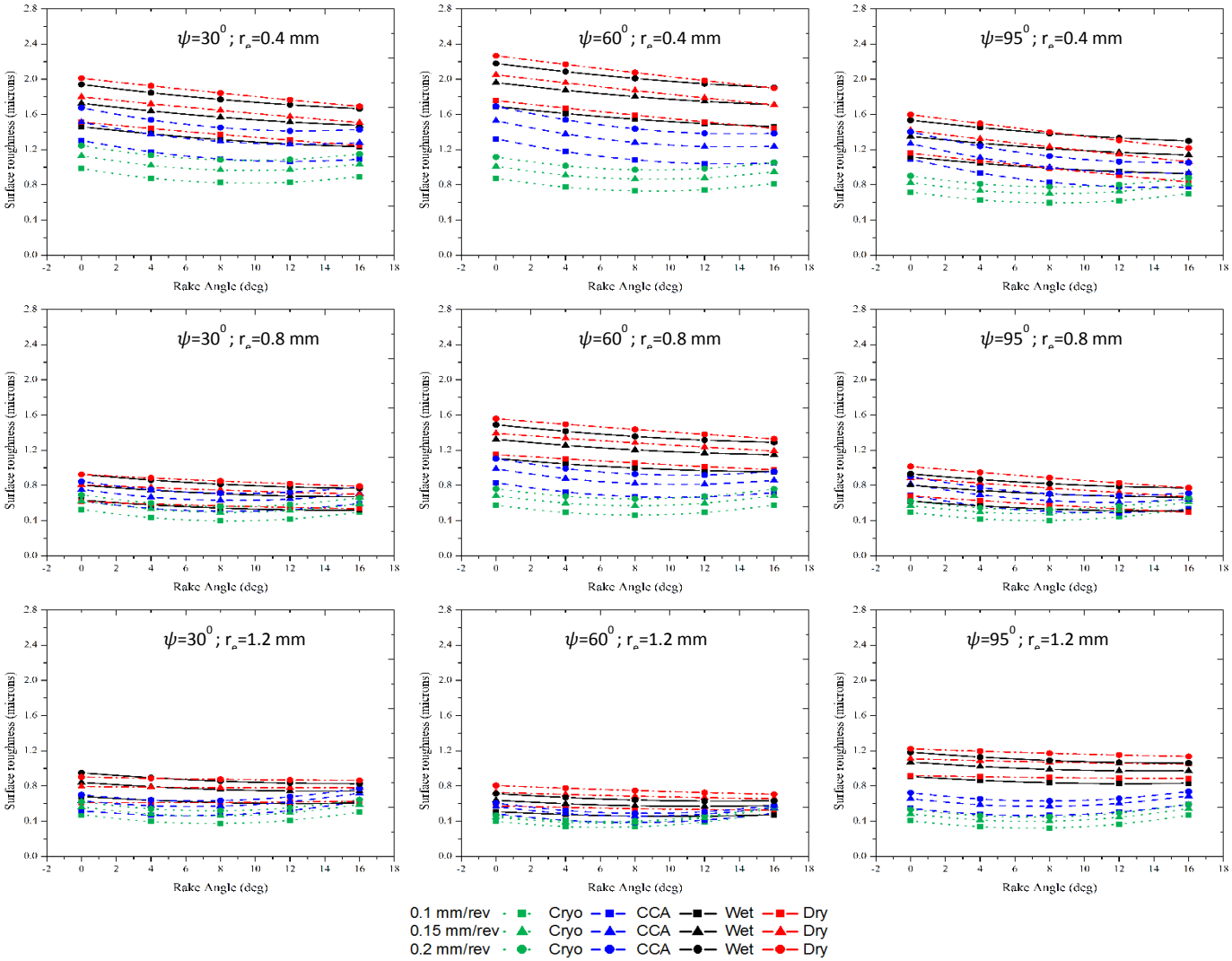

Fig. 6.8. Variation of surface roughness at cutting speed of 50 m/min for different rake angle with various levels of nose radii, approach angles and feed under dry, wet, CCA gas and ALN spray assisted machining conditions (cryo).

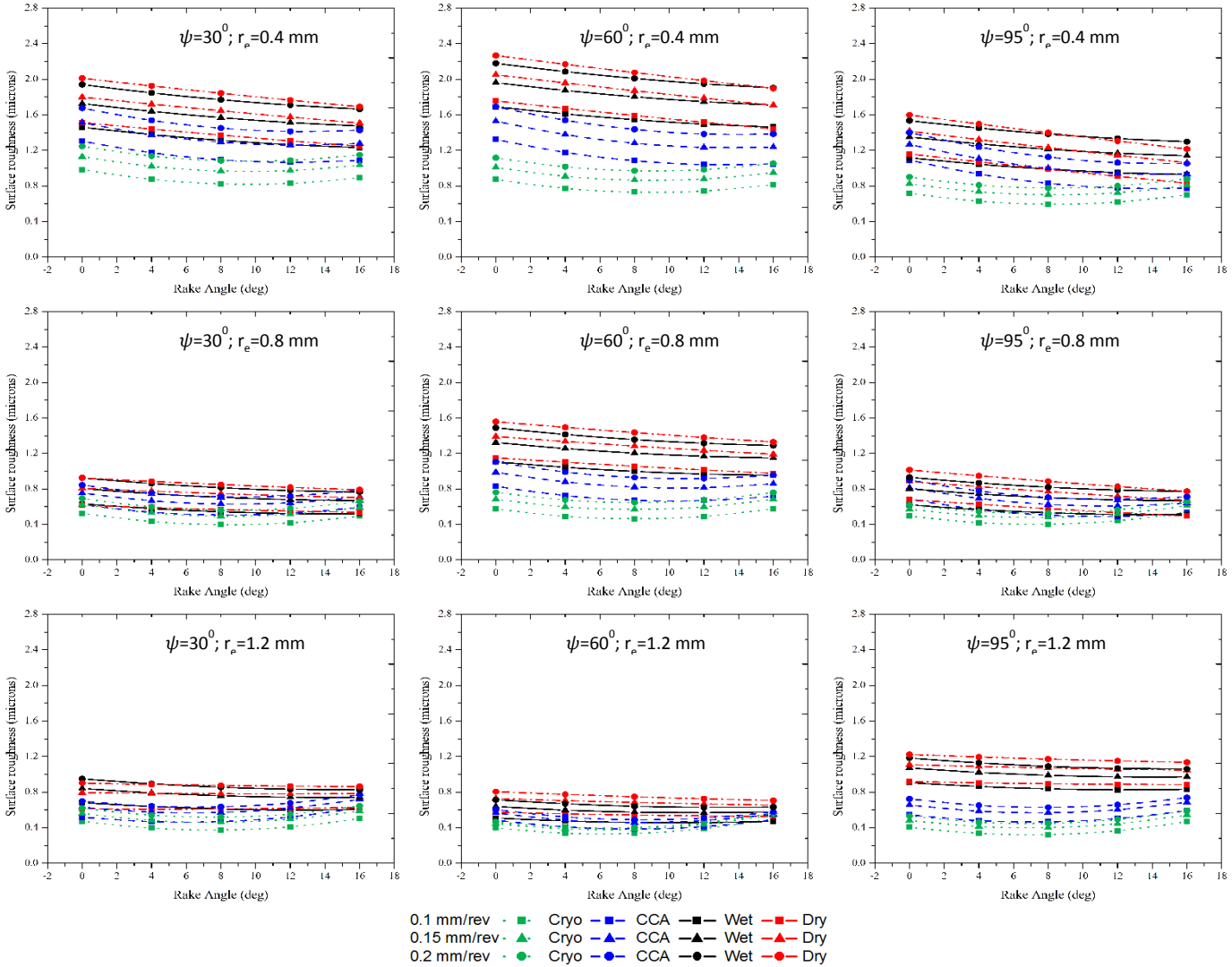

Fig. 6.9. Variation of surface roughness at cutting speed of 100 m/min for different rake angle with various levels of nose radii, approach angles and feed under dry, wet, CCA gas and ALN spray assisted machining conditions (cryo).

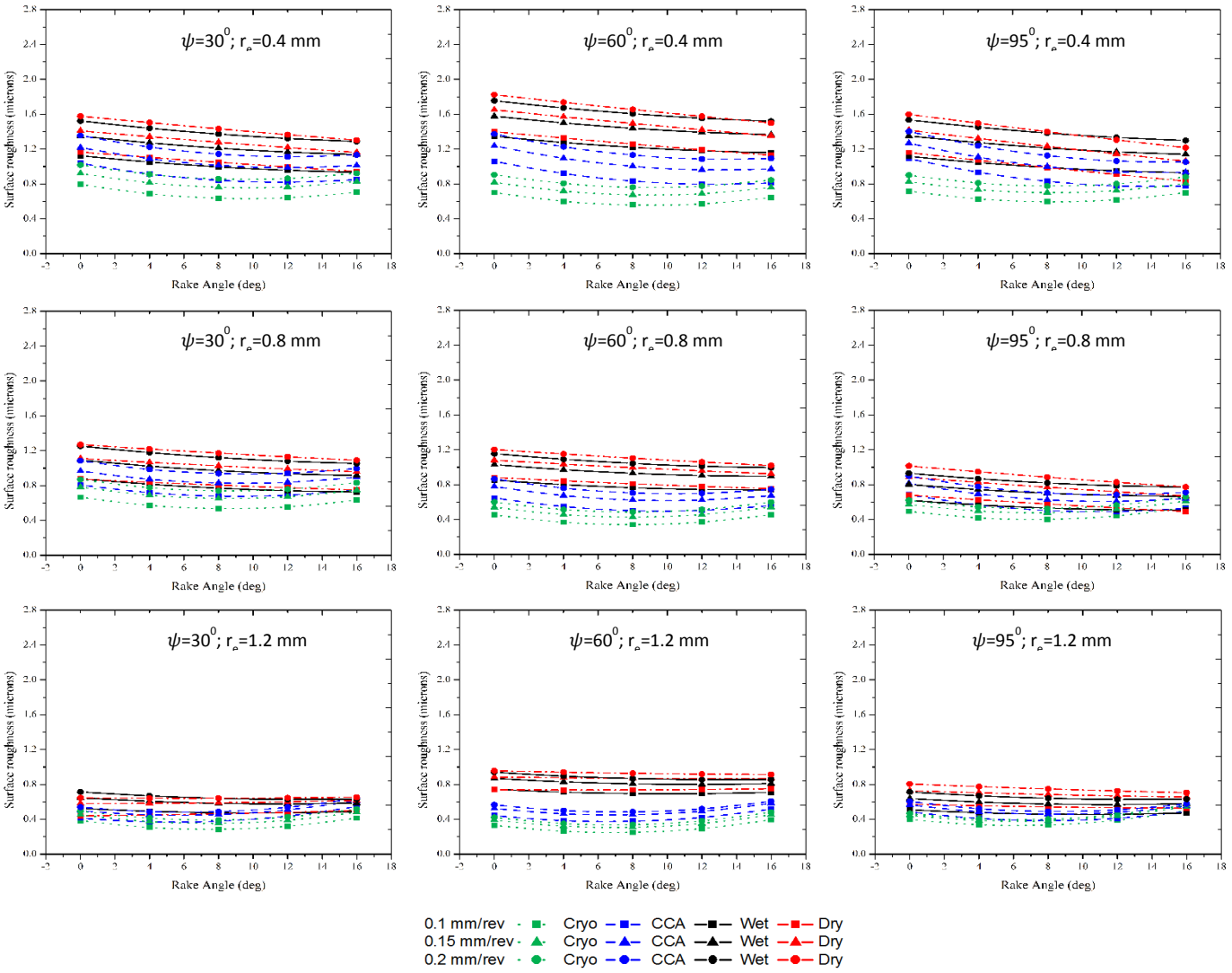

Fig. 6.10. Variation of surface roughness at cutting speed of 150 m/min for different rake angle with various levels of nose radii, approach angles and feed under dry, wet, CCA gas and ALN spray assisted machining conditions (cryo).

attributed to the micro hydrostatic lubrication effect of LN_2 which diminishes the frictional force between tool/workpiece resulting in development of lower temperatures, ultimately minimizing the tool wear and improving surface finish. Similar results have been observed with utilization of the same system in tribological analysis on pin on disc tribometer [185]. The developed ALN spray system helps in reduction of friction by creating a thin film of lubrication at the interface which in turn helps to achieve better tribological conditions. The recorded surface roughness showed maximum percentage difference of about 19% under wet and dry machining conditions. The possible reason for this is the rapid abrasion of the cutting tool by the particles even under wet cutting conditions. Although, ALN spray system and CCA gas show the same cooling effect, the former shows 25% lower surface roughness value than latter. This is due to the variation in fluidization effect. This further confirms that LN_2 droplets reach the tool/chip interface due to effective penetration capability of developed atomized spray system.

Further evaluation of Fig. 6.8 - 6.10 reveals that surface roughness decreases with increase in rake angle. Minimum surface roughness value of 0.25 µm and 0.37 µm were observed at 4° rake angle under LN_2 and CCA gas condition respectively. However, under dry and wet condition, lower surface roughness values of 0.47 µm and 0.44 µm were observed at 8° rake angle. Analyzing the overall effect of rake angle on surface roughness reveals that as rake angle increases, surface roughness value decreases up to 8° rake angle beyond which a slight increase in surface roughness is observed. This can be attributed to the fact that increase in rake angle till 10° causes reduction in tool/chip contact length which lowers cutting force and favors low surface roughness. Further increase in rake angle makes the tool sharper which may cause premature failure of the tool and thus resulting in higher surface roughness [186].

8° rake angle provides a maximum of 27.24%, 26%, 15.87% and 16.86% lower surface roughness value over other selected rake angles under ALN spray assisted machining, CCA gas, wet and dry machining conditions respectively. As nose radius increases, surface roughness decreases rapidly from 0.4 mm to 0.8 mm. This can be attributed to breakage of tool tip due to chipping of tool caused by maximum load applied at smaller tip, which results in higher surface roughness [187]. As nose radius increases from 0.8 to 1.2 mm, a gradual decrease in surface roughness values has been observed at low feed value and high cutting speed [188]. Under dry condition, progression of surface roughness is more as nose radius increases due to larger contact of tool to workpiece which tends to plough a larger portion of chip rather than shearing. Results suggest that higher abrasive wear leads to severe surface damage. Similar trend was observed in case of approach angle as well where for all the selected machining conditions, surface roughness first decreased and then increased with increase in approach angle [189]. This could be attributed to the fact that at smaller approach angle, the effective cutting edge is increased. As a result, the chip thickness becomes lesser and favors low surface roughness.

Upon further increase in approach angle, the cutting forces are distributed over a shorter section of the cutting edge, thus subjecting the workpiece to maximum loading and unloading. This explanation confirms the experiments results revealed in analysis of cutting force section. It was observed that 60° approach angle provided lower surface roughness values under ALN spray and CCA gas assisted machining conditions. In case of dry and wet machining conditions, 90° approach angle was seen to provide lower surface roughness values. It is clear that the lower values of surface roughness were observed during ALN spray and CCA gas assisted machining conditions due to the greater penetration capability of high velocity gas jet

which carried the LN_2 droplet. This in turn lowers the cutting force and improves surface quality.

Further analysis also reveals that the surface roughness decreases with increase in cutting speed and increases with increase in feed value (Fig. 6.8 - 6.10). An increase in cutting speed causes increase in temperature in the major deformation zone which softens the cutting tool. With increase in cutting speed, build-up edge (BUE) formation reduces. Therefore, deposition of BUE material on the tool surface will be minimized. Under selected conditions, workpiece undergo plastic deformation thereby easy removal of particles occurs which increases cracks, voids and dimples. This lead to larger surface roughness value at lower cutting speeds. Heat generation in shear zone at higher cutting speeds cannot be conducted away in a short period of time in which the material passes the machining zone. This aids grain boundary dislocation and thus reduces surface roughness value. Increase in feed value raises thermodynamic loading on the cutting tool thereby accelerating the surface defect.

At low feed value, the distance between two successive tool paths is less, thus, a higher number of tool/particle interactions occur compared to the number at higher feed value. Relatively high particle fracture/debonding force at lower feed value also indicates higher tool/particle interactions. This will cause higher surface damage at low feed value than higher feed value. It is noticed that at lower feed value (0.1 to 0.15 mm/rev), the magnitude of surface roughness value varies from 2.05 to 0.44 µm under dry machining. Application of LN_2 in machining of MMCs will enhance the machinability by providing cooling effect and improve the lubrication effect (due to atomized spray). This would reduce the thermodynamic load on tool and improve the surface finish. ALN spray system produced 27%, 42% and 44% lower surface roughness value than CCA gas, wet and dry machining condition respectively at lower

feed value. Though the surface roughness value provides information about surface quality, further study of the topography of machined surface is needed to comprehend the complete nature of surface quality under different machining environments.

6.3.2.2 Analysis of machined surface topography

Topographic observations of machined Al-TiC_p composites surface is shown through microscopic images in Fig. 6.11 and 6.12. Examinations of machined surface reveal feed marks in dry and wet conditions due to high ductility (Fig. 6.11). In the case of ALN spray and CCA gas assisted machining conditions, visibility of feed marks is negligible to zero due to slightly lower ductility of metal after cooling of the workpiece to subzero temperatures. Particle pullouts, shearing of matrix and formation of grooves was observed due to dragging of pullout TiC particle on the machined surface. The chips are diffused to the tool surface and then abraded against the work surface itself (Fig. 6.11 (a)).

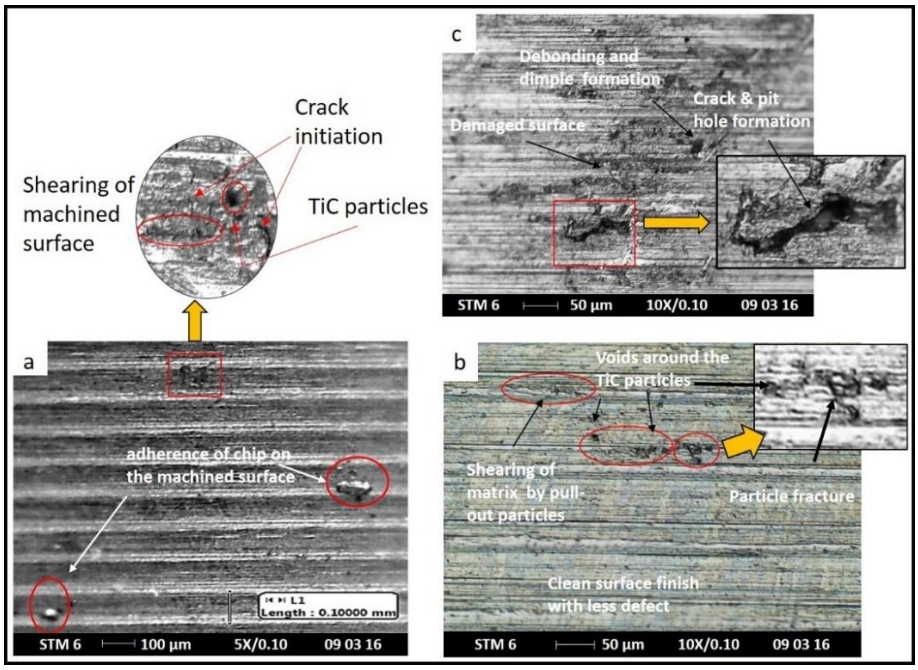

Fig. 6.11. (a) Micro cracks on Al-5wt%TiC_p MMC; (b) Voids around the TiC particles (c) Pulled-out TiC particles.

Fracture of crushed TiC particles and void formation without cracks (Fig. 6.11 (c)) was observed under ALN spray assisted machining. This confirms that ALN spray assisted machining provides better surface finish in comparison with other conditions. Strain hardening of materials leads to formation of microcracks and voids around the TiC_p. Pull-out is seen due to cohesion present between the aluminium matrix and TiC particles which makes small grooves and causes scratches and thus influencing the quality and rate of the production (Fig.6.11. (a) & (c)). In Al-TiC_p MMCs, deformation occurs along the shear plane and stress concentration takes place around the TiC particles resulting in the formation of micro-cracks. These micro-cracks propagate at particle/matrix interface leading to the fracture through the chip cross-section. This feature reduces the chip sticking period and the cutting force for machining, thereby producing better surface finish.

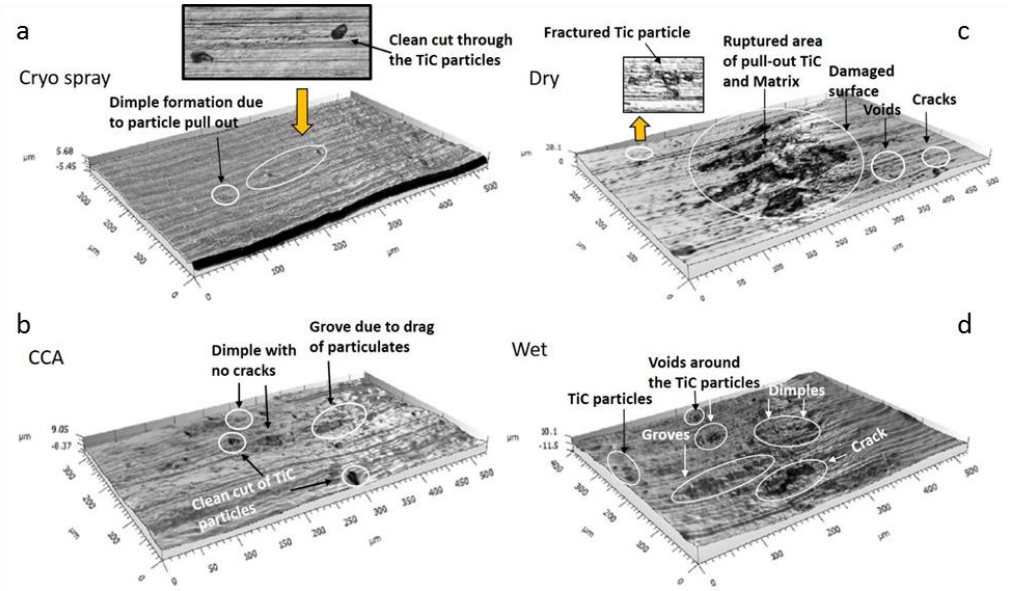

Fig. 6.12. Microscopic images of surface topography of machined Al-5wt%TiC_p MMC under (a) ALN spray (Cryo spray) (b) CCA gas (c) Dry (d) Wet conditions.

More or less defect-free surface was observed in ALN spray assisted machining condition. This could have occurred due to cooling action provided by LN_2 on the

reinforcement which makes it brittle and breaks easily but TiC particles are crushed. This confirms that ALN spray assisted machining provides better surface finish when compared to other conditions. In Fig. 6.12 (b), under chilled argon gas condition, groves and cracks around the TiC particles and voids can also be observed. Fig. 6.12 (d) & (c) shows topography under wet and dry machining respectively. Dry condition provides large quantity of surface defect than wet machining while CCA gas assisted machining has lower defect when compared with dry machining. The flushing effect of pressurized air and lubricant in the machining zone helps to flush away the intermittent particle and reduces the holes and scars on the machined surface. A complete assessment of topography of machined surface gives a clear idea that surface defects like voids, dimple and pull out of particles are common in all the environments. ALN spray assisted machining provides less defects as compared to other environments due to the reduction of friction between the tool and workpiece.

6.3.3 Analysis of tool performance

Estimation of tool performance is one of the most important criteria to assess machinability behavior. Increasing of tool performance will reduce the manufacturing cost and improve the quality of the product significantly. Flank wear, is the predominant reason for tool failure during composite machining. Two body and three-body abrasion causing flank wear is commonly observed in machining of composites, since softening of matrix easily leads to removal of particles at high cutting temperature [9]. Microscopic analysis of the worn tool helps to determine the wear mechanism that occurs during machining of Al-TiC_p composite in selected machining conditions. Intensity of heat generation and surface quality of machined surface profoundly depends on type of tool wear. Understanding of the wear mechanism is vital as far as the surface quality and production cost are concerned.

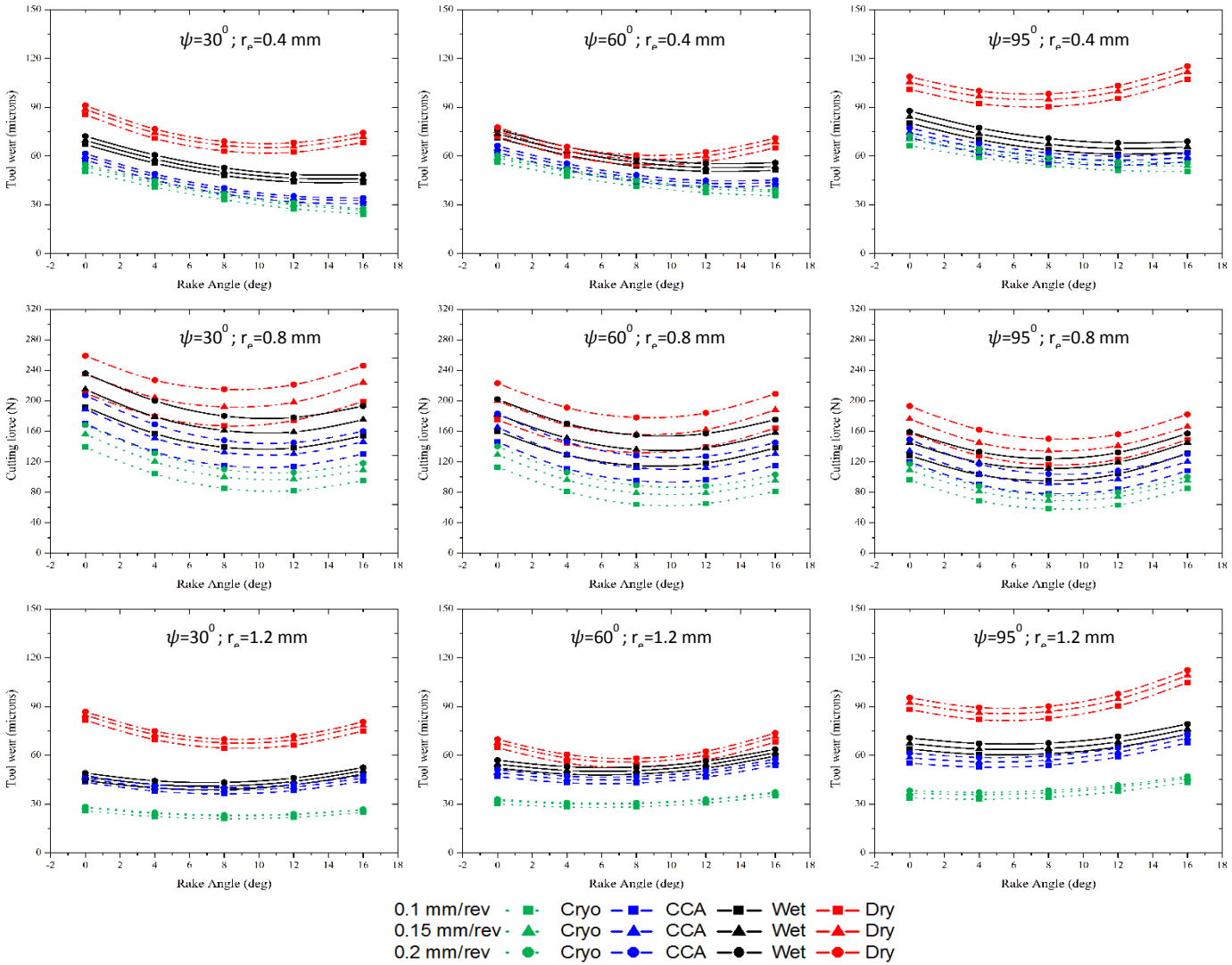

Fig. 6.13. Variation of tool wear at cutting speed of 50 m/min for different rake angle with various levels of nose radii, approach angles and feed under dry, wet, CCA gas and ALN spray assisted machining conditions (cryo).

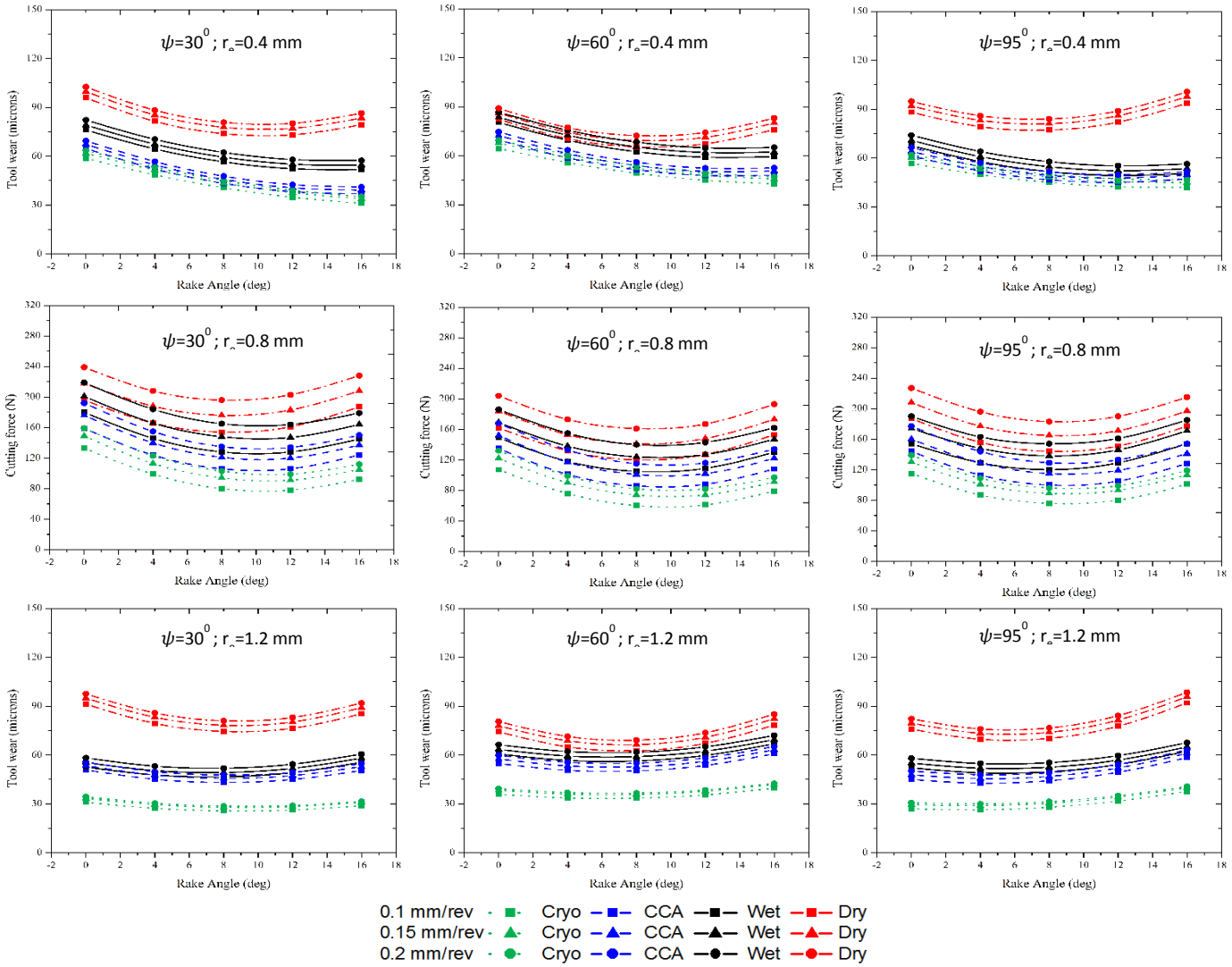

Fig. 6.14. Variation of tool wear at cutting speed of 100 m/min for different rake angle with various levels of nose radii, approach angles and feed under dry, wet, CCA gas and ALN spray assisted machining conditions (cryo).

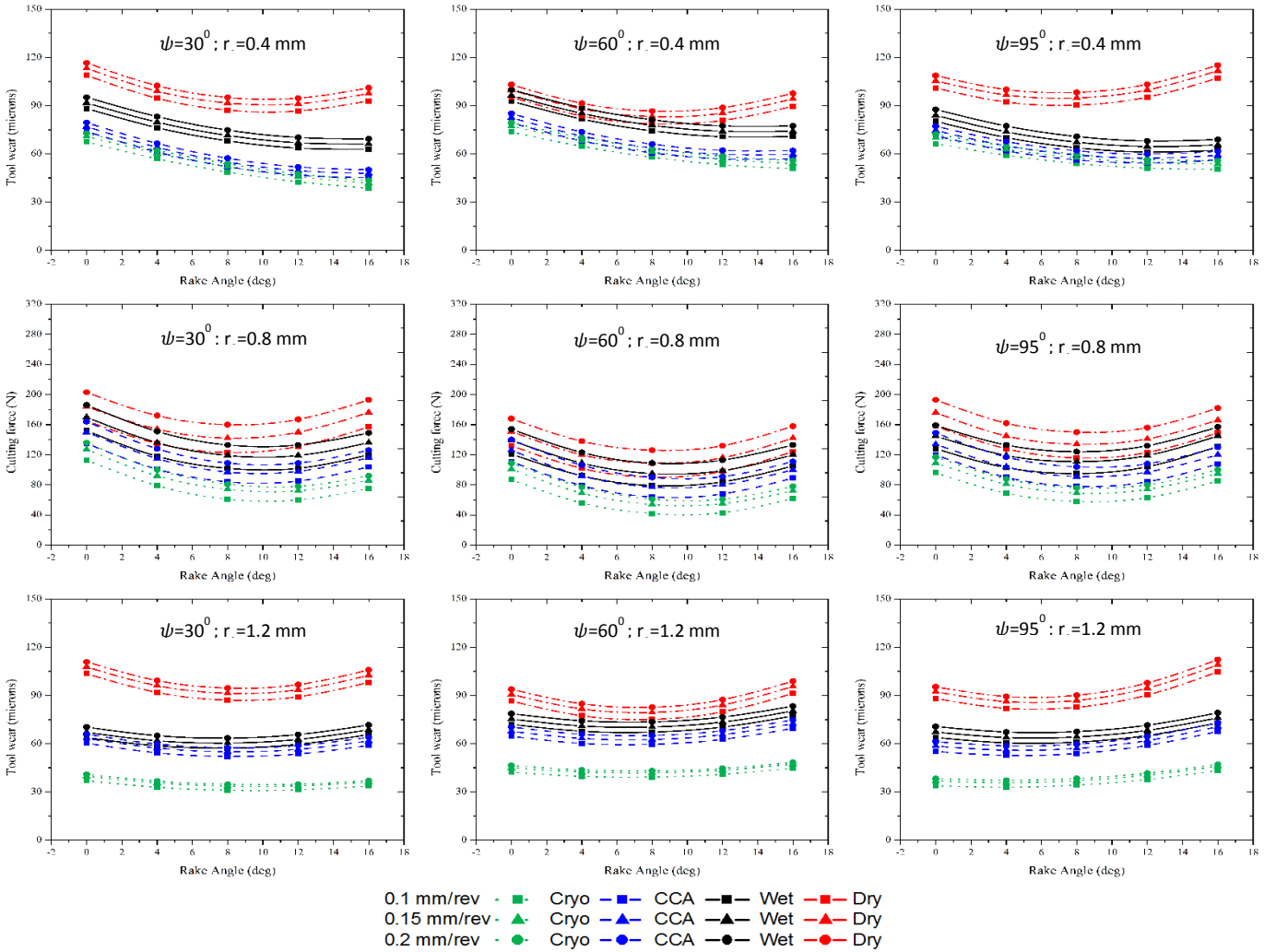

Fig. 6.15. Variation of tool wear at cutting speed of 150 m/min for different rake angle with various levels of nose radii, approach angles and feed under dry, wet, CCA gas and ALN spray assisted machining conditions (cryo).

6.3.3.1 Analysis of flank wear

Average flank wear was measured at different levels of rake angle, nose radius and approach angle. The results are shown in Fig. 6.13 - 6.15. The curves show variation in flank wear under dry, wet, CCA gas, and ALN spray assisted machining conditions. A quick analysis of these curves reveals that ALN spray assisted machining is advantageous over other selected machining methods due to the lower flank wear during machining of Al-TiC_p composites. This can be attributed to smaller droplet size and high velocity LN_2 jet attained while using the developed atomization system that improves penetration capability of LN_2 significantly. It was observed that tool wear values reduced by 68%, 50% and 44% under ALN spray assisted machining over dry, wet and CCA gas assisted machining conditions respectively. ALN spray condition provided an average flank wear of 41 µm whereas dry, wet and CCA gas assisted machining conditions attained 52 µm, 61 µm and 79 µm respectively. The variation of average flank wear between ALN and CCA gas was approximately 20%.

These results prove that the application of lubricant causes reduction in the progression of flank wear. The cooling effect of LN_2 reduces thermal load on the cutting edge to a greater extent and thus leads to lower adhesive and diffusive wear. Further comparison between ALN spray and CCA gas assisted machining reveals that the presence of liquid phase in the ALN spray assisted machining is expected to build a protective and lubrication layer at the contact area between tool/ chip/ workpiece. This might be a reason for low flank wear in ALN spray than CCA gas condition. CCA gas provides the same cooling effect as LN_2 but the fluidization effect varies. Similar trend has been reported in previous works [20], where higher pressure LN_2 enters effectively into interface zone and results in relatively lower frictional forces, leading to lower cutting temperatures. Fig. 6.13-6.15 reveals that tool wear decreases as rake angle increases from 0 to 8°. Beyond 8°, slight

increment in tool wear was observed at all selected machining conditions. Increase in rake angle over an optimal angle makes the tool sharper which may cause premature failure of the tool [186]. Rake angle of 8° provides 41%, 38%, 32% and 27% reduction in flank wear compared to other rake angles under ALN spray, CCA gas, wet and dry machining conditions respectively. It is observed that reduction is lower in dry condition due to larger contact length between tool and workpiece leading to larger tool wear. The magnitude of average tool wear measures at 10° rake angle are 38.3 µm, 47.6 µm, 56.6 µm and 73.3 µm under ALN spray, CCA gas, wet and dry machining conditions respectively. This could be due to lower loads at 10° confirmed by previous results. Fig 6.13–6.15 where the average cutting force at 8° rake angle provides approximately 38.5%, 13.4%, and 14% cut down over 0°, 4° and 16° rake angle respectively. By increasing positive rake angle, the cutting forces were decreased as the tool can plunge into the workpiece easily. Therefore, percentage variation reduces as rake angle increases.

At lower values of nose radii and approach angles, the reduction in tool wear with respect to rake angle is steeper than over higher nose radii and approach angles. This can be credited to increasing contact lengths with increase in nose radius [190]. However, during machining of Al-TiC_p composite, smaller nose radii gives higher tool wear value over larger nose radii because of chipping of cutting tool, leading to higher heat generation between tool/workpiece interface over a period of time. Hence, lower average tool wear under dry, wet and CCA gas assisted machining condition was observed for 0.8 mm nose radius. In ALN spray assisted machining condition, it was observed for 1.2 mm nose radius. Higher nose radius gives larger contact area, thus, higher volume of LN_2 can stay between the machining interfaces. Whereas under dry, wet and CCA gas assisted machining conditions, smaller nose radius attains higher temperature over larger nose radius due to edge chipping, leading to higher surface roughness. This has been confirmed by the

observation made in surface roughness section. It was also observed that under dry condition, as approach angle increases, tool wear decreases up to 60°. Beyond 60°, increase in tool wear was observed for all selected machining conditions. Reversed effect was observed in wet, CCA gas and ALN spay assisted machining conditions. For large approach angles, the cutting forces are distributed over a shorter section of the cutting edge. Since the main cutting edge enters and leaves the cutting zone suddenly at 90° of entering angle, it is subjected to maximum loading and unloading. This has been confirmed by the results presented in previous sections. Therefore, under dry condition, 60° approach angle gives lower tool wear of 49.83 µm. In the presence of lubricants, smaller approach angle of 30° gives lower average tool wear of 38.3 µm, 29.6 µm and 21.4 µm under wet, CCA gas and ALN spray assisted machining condition respectively over other selected approach angles. This is observed due to increase of effective cutting edge which reduces chip thickness thereby reducing tool/workpiece contact area.

It can also be observed that as feed value increases, tool wear increases. This is due to the fact that as feed value increases, large quantity of material approaches the tool leading to a higher thermodynamic load on the tool. This causes increase in tool wear. Thermal softening effect was not observed while increasing feed value from 0.1 to 0.2 mm/rev. However, as cutting speed increased, the tool wear value variation with respect to feed value decreased. It can be concluded that cutting speed is the dominant process parameter which affects the progression of tool wear. The curves in Fig 6.13-6.15 clearly suggest that the cutting tool encounters higher flank wear at all cutting speeds. As cutting speed increases, tool wear increases. An increase in cutting speed causes high heat generation in machining zone, which softens the tool material [191]. This causes severe wear. While machining of MMCs, abrasive wear is the major type of tool wear by which abrasive reinforcement particles plough over the tool rapidly at higher sliding velocities. This

ploughing process results in increased stresses and deformation of the tool, consequently causes rise in temperature. The length of the active part of the cutting edge and volume of the tool edge in contact with the material increases. This results in a greater number of abrasive particles coming into contact with cutting tool and abrading it. This also leads to severe wear. At higher cutting speeds, average tool wear was recorded as 48.9 µm, 61.11 µm, 71.9 µm and 91.9 µm for ALN spray, CCA gas, wet and dry machining conditions respectively. At lower cutting speeds, the heat generated is lower and higher mechanical stresses are imposed on the tool surface due to the higher cutting forces generated. As a result, the effect of work hardening of the tool material dominates the loss of strength due to thermal softening of both tool and work material. This thermal softening can be minimized by using coolants. ALN spray assisted machining produces 47.5% lower average tool wear over dry machining condition. Similarly, for wet and CCA gas conditions, 23.2% and 34.2% lower tool wear respectively over dry machining condition were observed.

ALN spray assisted machining outperforms the other machining environments under selected machining conditions. This can be due to lowering of machining temperature by ALN spray setup, which helps in minimizing abrasion wear by maintaining apparent tool hardness. Further, the adhesive wear and diffusive wear are also reduced significantly (which are profoundly sensitive to temperature). The tool wear figures give a clear idea about combined effect of tool geometry and machining parameters on tool wear. However, there is a need to study the worn surface of the tool to understand the type of wear mechanism.

6.3.3.2 Analysis of worn tool surface

The microscopic inspection on cutting edge revealed edge chipping at higher rake angle, nose radius and approach angle as shown in Fig. 6.16. ALN spray assisted machining

exhibits improved performance in terms of lower tool wear at all selected machining conditions. Microscopic observations revealed that there was some sign of adhesive wear suggesting a strong bonding between tool and workpiece.

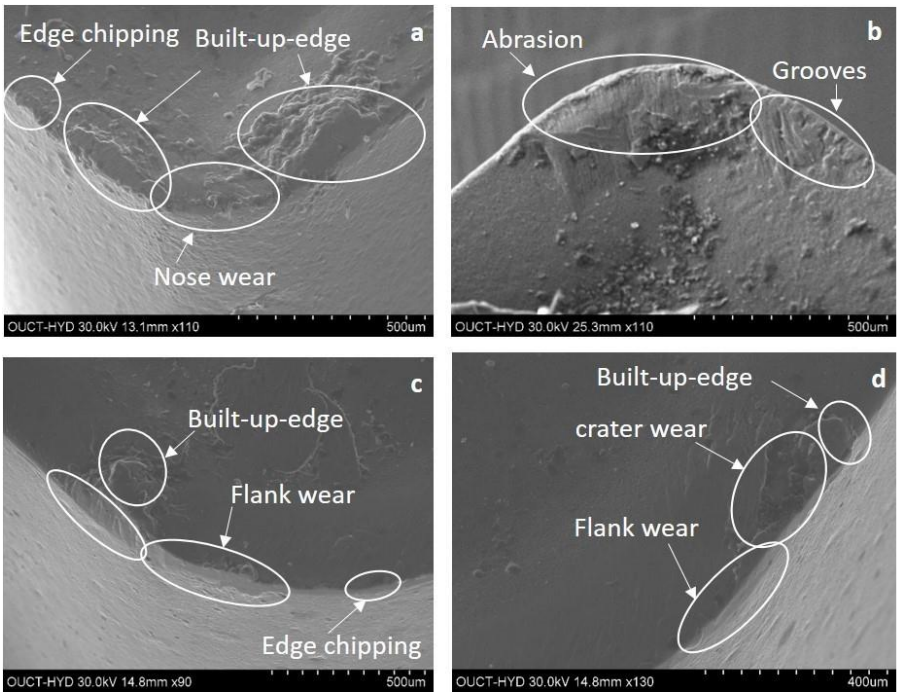

Fig. 6.16. SEM observation of worn tool under 16° rake angle 1.2 mm nose radius and 90° approach angle at (a) Dry (b) Wet (c) CCA gas and (d) ALN spray assisted machining.

Though the application of LN_2 into the machining zone reduces the heat generation occurring in the principle region of plastic deformation drastically, some indications of BUE formation were still observed. Large amount of edge chipping and plastic deformation was found in dry machining than wet, CCA gas, and ALN spray assisted machining. The texture of worn tool flank surface appeared with parallel grooves indicating the dominance of a two-body abrasive wear mechanism. The worn tool surface remains similar in both dry and wet condition with two body wear mechanisms. The three-body abrasion decreased to some extent while turning with wet, CCA gas and ALN spray coolant. Reduction of three body abrasion under lubrication condition is due to the geometric structure of CNMG tool

having deep grooves parallel to the cutting edge, which assists large fraction of lubricant (emulsion, liquid nitrogen and CCA gas) to enter effectively into tool/chip interface.

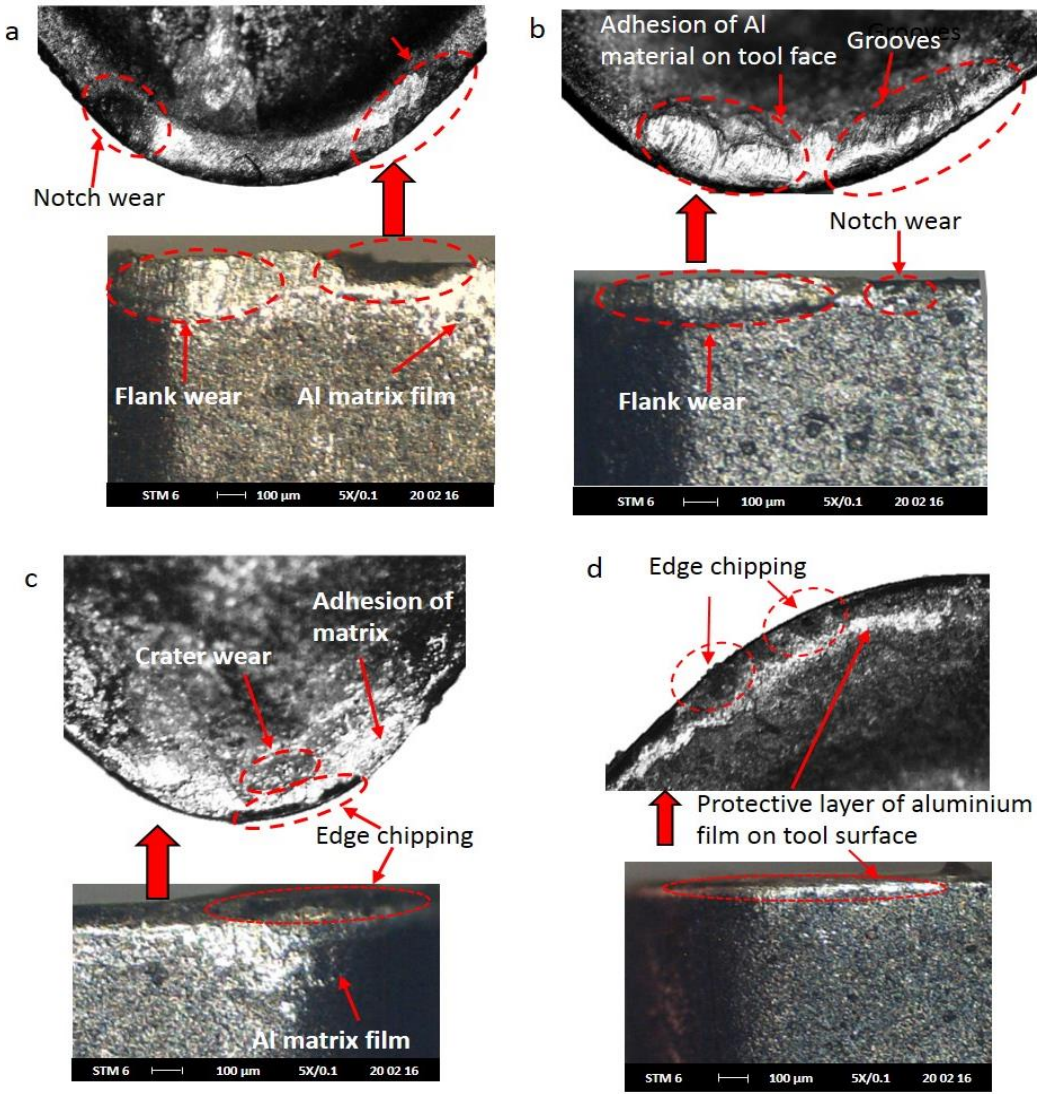

Fig. 6.17. Microscopic observation of worn tool under150 m/min cutting speed, 0.2 mm/rev feed, 1.2 mm nose radius and 90° approach angle at (a) 0° (b) 4° (c) 8° and (d) 16° rake angles under dry machining conditions.

Further, supplying of lubrication at high velocity helps it to penetrate quickly and effectively in a short period of time. This quick penetration helps in creating a lubrication action. The high velocity jet aids in flushing away the unattached particles from the interface thereby reduction in abrasion wear was observed under wet, CCA gas and ALN spray lubrication environments. Stable BUE formation during ALN spray assisted

machining process could be a possible explanation for better performance over other machining conditions. El-Gallab et al [66] explained that BUE forms as a strain hardened the two-phase material under high pressure and temperature. It was also observed that BUE increases with increase in rake angle, leading to tool edge chipping.

Higher rake angles cause pitting on tool while lower rake angles cause high pressure and temperature which increase adhesion wear mode (shown in Fig. 6.17). Therefore, higher rake angle of 8° gives lower flank wear in all the machining conditions in comparison with 0° and 4° rake angles. A BUE of 200 µm long and more than 100 µm height was formed on rake face of the tool under dry environment. ALN spray assisted machining provided lower BUE, adhesion and chipping in comparison with other environments. This can be attributed to reduced friction between the tool/workpiece which further minimizes the temperature at the contact interface. Abrasion wear is due to existence of hard particles in matrix which are known to indent into the tool forming grooves on the tool surface [192].

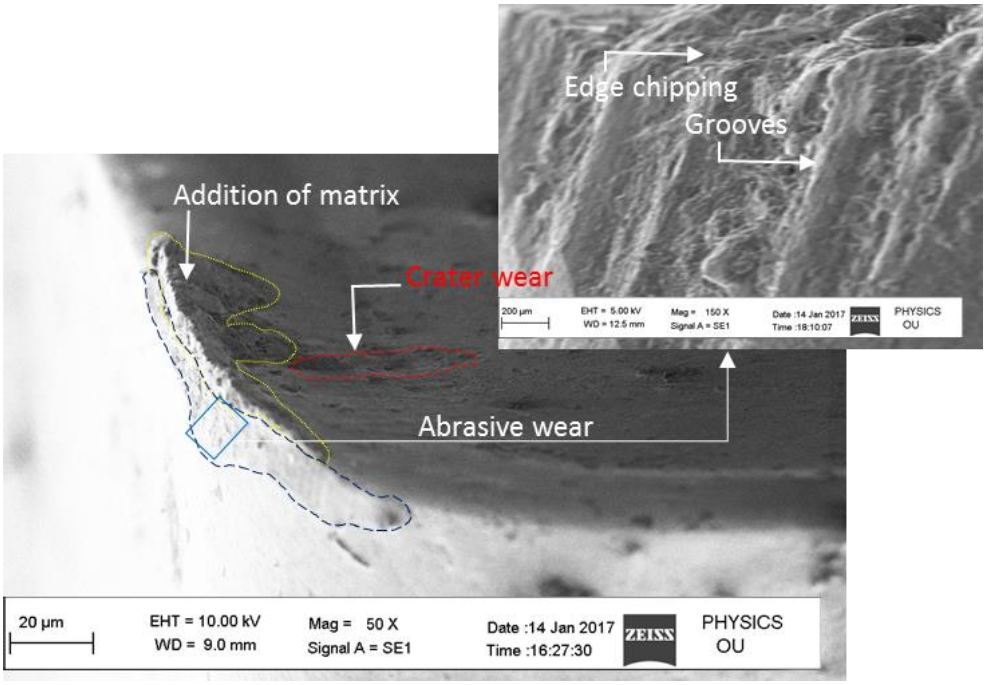

Fig. 6.18. SEM observation of worn tool surface and type of wear mechanism observed during dry condition.

Examination of topographies of the worn cutting edge led to the conclusion that the main wear mechanism was abrasion. The hardness of TiC particles is higher than the carbide grains of the tool. Therefore, the carbide is abraded by micro-cutting, which is indicated by the grooves at the clearance face (seen in Fig. 6.18). The tool wear was substantially reduced in atomized LN_2 spray machining in comparison with dry, wet and CCA gas assisted machining. This is due to the fact that LN_2 was applied directly to the cutting area in the form of small droplet of 50 µm at a velocity of 50 m/sec, which helped it to penetrate efficiently into the machining zone, cooling the cutting edges effectively and providing less adhesion between the tool/chip/workpiece interacting surfaces. Further, to understand the nature of cutting process during machining Al-TiC_p composites, chip morphological studies were conducted.

6.3.4 Analysis of chip formation

The form of chip produced in a machining process is one of the most important parameters that not only influences the surface finish, but also the accuracy of workpiece and the tool life, thus, affecting productivity and product quality [193]. Hence, in metal cutting process, production of an acceptable form of chip is vital. According to ISO 3685 standards, chip shapes during a machining process can be classified into several types, which can be in either acceptable form or unacceptable form. Acceptable chip forms (short tubular, washer type, spiral and arc shape) can move easily from the machining zone and do not interfere with the machined surface quality. Contrarily, unacceptable chips (ribbon, tangled and needle type) can not only influence the quality of the machined surface but also tend to pose safety problems to the operator, as they tend to tangle around the tool and the workpiece. Fig. 6.19 - 6.21 shows some of the chip shapes obtained during machining of Al-TiC_p MMCs under different cutting conditions. Chip formation begins with chip curving. This process is highly influenced by tool geometry and cutting process parameters.

It can be seen that the chip shapes formed during ALN spray assisted machining of Al-TiC_p composite are short tubular and helical.

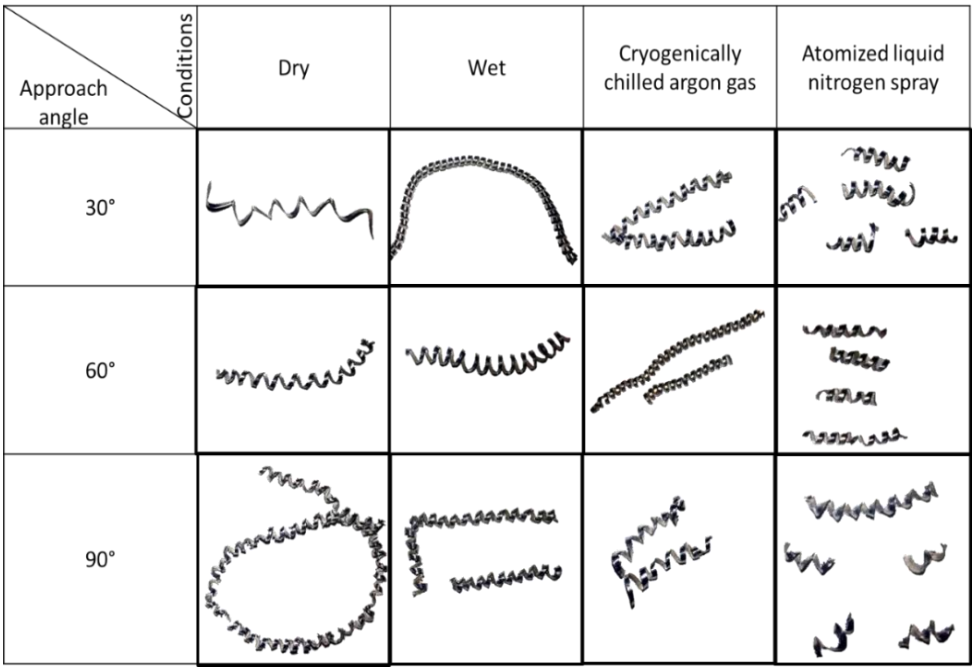

Fig. 6.19. Comparison of chip samples formed during machining of Al-5wt%TiC_P under various environments at 100 m/min cutting speed, 0.1 mm/rev feed, 8° rake angle and 1.2 mm nose radius.

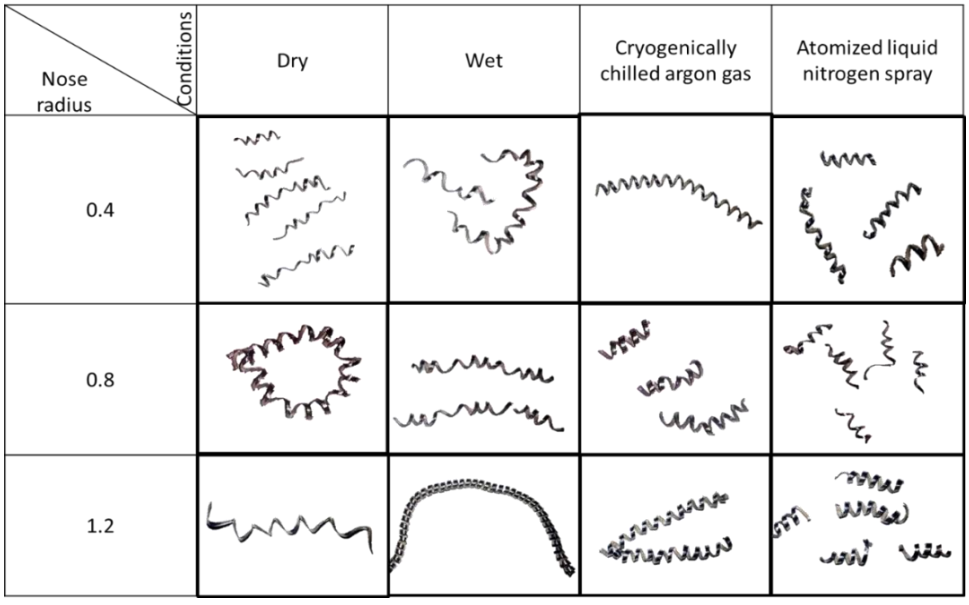

Fig. 6.20. Comparison of chip samples formed during machining of Al-5wt%TiC_P under various environments at 100 m/min cutting speed, 0.1 mm/rev feed, 30° approach angle and 8° rake angle.

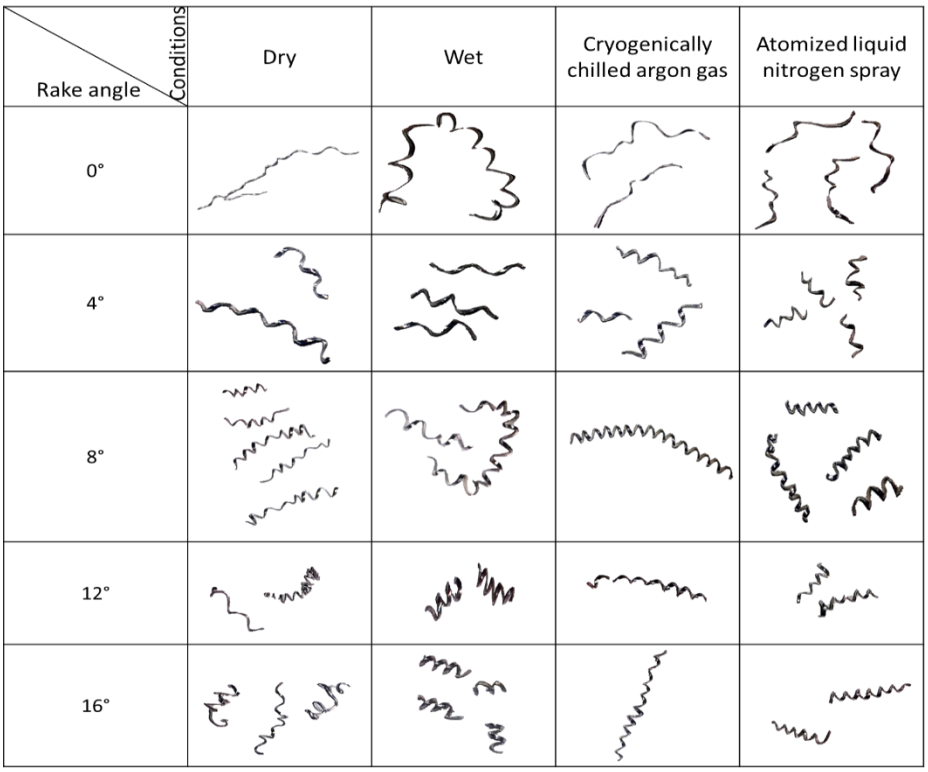

Fig. 6.21. Comparison of chip samples formed during machining of Al-5wt%TiC_P under various environments at 100 m/min cutting speed, 0.1 mm/rev feed, 30° approach angle and 0.4 mm nose radius.

It is observed that as approach angle increases, the chip curving diameter increases. Tubular type chip was commonly formed under all approach angles, but under different cutting environments, different types of tubular chips were formed. At 30° approach angle, under dry condition, tubular snarled chips were observed (refer Fig. 6.19). Whereas under coolant machining condition, pure tubular (long or short) chips were observed. Under 60° and 90° approach angle, tubular long and short chips were observed in all the environments.

The machining of Al-TiC_p MMCs resulted in different types of chip formation. When the tool cutting edge cuts only the matrix but not the reinforcement particles, plastic deformation occurs. If the shear deformation of the matrix is hindered by reinforcing particles, squeeze-break and collapse cutting will occur [194]. This significantly depends upon nose radius. Nose radius is another dominant tool geometry parameter which

influences the point of contact between tool and workpiece leading to significant effect on chip formation. From Fig. 6.20, it can be understood that as nose radius decreases, thinner chips are formed (0.4 mm nose radius provides thinner chips). Under dry condition, all nose radii produced snarled tubular chips. Whereas in wet condition, for 0.4 mm and 0.8 mm nose radius, snarled chips were formed but for 1.2 mm nose radius, long tubular chips were formed. In both cryogenic chilled argon gas and ALN spray assisted machining condition, tubular type chips were observed.

Chip formation during machining is accompanied by very severe plastic deformation at the shear zone owing to the lack of sufficient ductility of work material. This deformation creates cracks on the chip surface. Cracks on chips are highly influenced by rake angle. As rake angle increases, chip compression and self-breaking of chip is easily observed. This is due to effect of rake angle on chip curving tendency. From Fig. 6.21 it is observed that tubular type chips were formed at 8° and 16° rake angles while washer type snarled helical chips were found at 0° rake angles under all environments. Rake angle of 4° provided snarled chips under dry and wet condition, whereas in CCA gas and ALN spray condition, helical chips were formed. In ALN spray condition, however, comparatively shorter chips were formed at all conditions. At 0° rake angle, snarled type of chips was formed which tangled with the workpiece and caused surface damage. This observation provides the proof for sudden increase in surface roughness value in the earlier section.

Microscopic observation of chip formed reveals that cracks and voids were frequently formed on outer surface of the chip (Fig 6.22). This is due to the matrix material undergoing shear by the movement of cutting. Once the material was sheared, the amalgamation of voids forms cracks and they propagate in a zig-zag manner along the shear plane throughout the thickness of the chip. Segmented chips are formed due to fracture. Propagation of fracture through the matrix material seems to develop along the stress

concentration zone, i.e. at the boundary of the TiC particles within the matrix. More continuous chips were formed under dry condition due to high plastic strain experienced by matrix. under wet condition, tubular chips with serrations were formed at all cutting parameters. The reason for this type of chip morphology is due to constraints imposed on the uniform plastic deformation of the aluminum matrix by the preferential alignment of brittle ceramic particulates along the shear zones.

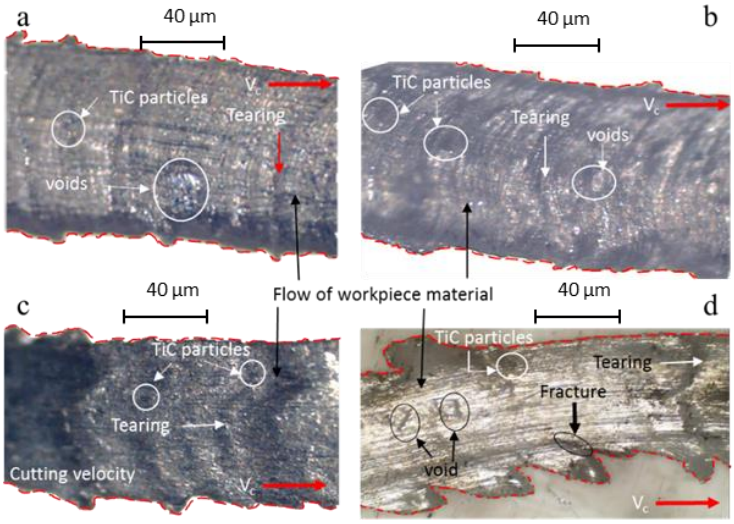

Fig. 6.22. Microscopic image of chip surface formed during machining of Al- 5wt%TiCp under (a) ALN spray (b) CCA gas (c) Wet (d) Dry machining conditions.

Upon comparing with various conditions, ALN spray condition chips were found to be more brittle. Chip breakage occurred more easily than other conditions (refer Fig. 6.22). Application of LN_2 affects the heat distribution pattern in aluminium matrix on the top and bottom surfaces of the chip. Because of the cryogenic temperature of LN_2, the matrix material properties will vary, thereby weakening the interface between the matrix and particulates creating cracks in chip. Consequently, the interface is subjected to tensile stresses that are high enough to cause brittle cracking.

6.4 Summary

Investigations were carried out on the machinability aspects in turning of Al-TiC_p composites with atomized liquid nitrogen spray assisted machining. Turning test results

revealed that the ALN spray assisted machining can endow superior benefits on machinability performance of Al-TiC_p MMCs in comparison to dry, wet and CCA gas machining. The experimental results show that at all selected machining parameters and tool geometry, lower cutting force, surface roughness and tool wear was observed under atomized LN_2 spray system. As a result of lesser cutting forces and cutting temperature, average flank wear in ALN spray system is reduced by 47%, 32% and 20% over dry, wet and CCA gas assisted machining conditions respectively. Formation of nitrogen cushion improves the surface quality of the machined material thereby average surface roughness in ALN spray system is reduced by 44%, 41% and 25% over dry, wet and CCA gas assisted machining conditions respectively. In addition, topographical analysis of machined surface reveals that surface defects like voids, dimple and pull out of particles are common in all the environments and further ALN spray assisted machining provides less defects over other environments. Application of pressurized coolant will flush away the intermittent particles and reduce the holes and scars on the machined surface. Therefore, the surface roughness under coolant condition is less than dry condition. The results also suggest that the rake angle directly influences the temperature on the tool/chip interface, which in turn effects the surface quality and tool performance. It was observed that as rake angle increases, cutting temperature decreases under all selected environments.

To understand the machining processes better, sufficient experimentation needs to be conducted due to the complex nature of the process. A more prudent approach would be to model the process, for assessing its performance without conducting laborious experiments. The subsequent chapter deals with the aspects of theoretical modeling of the machining process.

Chapter 7
Statistical Analysis and Optimization of Machining Parameters during Turning of Al-TiC MMCs

The current chapter deals with the optimal selection of various factors that have significant influence on machinability performance based on statistical analysis. The current chapter is organized into four sections. Section 7.1 describes brief background of optimization techniques while section 7.2 presents the methodology adopted to implement these techniques. Section 7.3 explains the analysis of single objective and multi objective optimization using genetic algorithm approach. The procedure evaluates the optimal machining conditions subjected to the given constraints. Finally, Section 7.4 summarizes the overall chapter.

7.1 Introduction

Response surface methodology is a mathematical and statistical approach for modelling analysis the machining performance without conducting several turning tests. It is an effective tool as constructing optimization model for selecting the levels or values of the process variables that produce optimum values of the response outputs [77]. Compared to traditional optimization paradigms, Genetic algorithms (GA) is a robust and global approach which may be applied generally without recourse to domain-specific heuristics [195]. It is a derivative free approach for near-optimal point(s) search direction and provides an automatic search for the non-linear connection between the inputs and outputs. Hence, GA provides a faster and simpler optimizing technique to achieve more significant results compared to experimental techniques.

Based on the experimental data obtained in previous chapter, a mathematical surface model was built using response surface methodology approach. This model would

be utilized as the objective function for optimization of process parameters in turning using GAs. This methodology helps to obtain the best possible tool geometry and cutting conditions for turning of Al-TiC_p composites. The current chapter also provides the statistical analysis of design parameters and uses desirability functional approach to determine optimization parameters.

7.2 Methodology

Initially, statistical analysis of experimental results was carried out using analysis of variance (ANOVA) to determine the significant parameters affecting the performance effectively. This was followed by development of empirical relation between machining responses and their factors to enable the optimization of cutting process. Further optimization process has been carried out using genetic algorithm. Genetic algorithm is a well-known technique for determining the global optimum solution in a complex multi model search space.

7.2.1 Analysis of experimental results

ANOVA is a computational technique that enables the estimation of relative contributions of each of control factors that makes to the overall measured response and expresses it as a percentage. ANOVA uses a mathematical technique known as sum of squares to quantitatively examine the deviation of the control factor response average from the overall experimental mean response, which is referred to as the variation between the control factors. The significance of the individual and interaction effects is quantified by comparing the variance between the control factors effects against the variance in the experimental variability. The ANOVA process helps to gain insight into which factors have main effects, interaction effects, less significant effects or noise. These will also be useful to predict the target parameters.

7.2.2 Modeling using Response Surface Methodology (RSM)

In this work, mathematical models were developed using experimental results using Response Surface Methodology (RSM). RSM has been utilized for developing tool wear, surface roughness and cutting force prediction. It is a combination of mathematical and statistical techniques useful for modeling and analyzing the problems in which several independent variables influence a dependent variable or response and the objective is to optimize the response. Though RSM is an optimization tool, it does not provide any explicit strategy for searching. This methodology has been used successfully in variety of applications, such as tool-life testing, surface roughness analysis, friction damping characteristics of machine structures, and design and control of cellular manufacturing system [196-198].

By conducting experiments and applying regression analysis, a model of the response with independent input variables can be obtained. The second order polynomial mathematical models commonly used are represented by:

$$Y_2 = Y - \in = b_0x_0 + b_1x_1 + b_2x_2 + b_3x_3 + b_4x_4 + b_5x_5 + b_{12}x_1x_2 + b_{13}x_1x_3 + b_{14}x_1x_4 + b_{15}x_1x_5 + b_{23}x_2x_3 + b_{24}x_2x_4 + b_{25}x_2x_5 + b_{34}x_3x_4 + b_{35}x_3x_5 + b_{45}x_4x_5 + b_{11}{x_1}^2 + b_{22}{x_2}^2 + b_{33}{x_3}^2 + b_{44}{x_4}^2 + b_{55}{x_5}^2 \quad (7.1)$$

Where 'Y_2' is the estimated response based on second order equation. The parameters i.e. $b_0, b_1, b_2, b_3, b_4, b_{12}, b_{23}, b_{14}$, etc. are to be estimated by the method of least squares.

R^2, also called multiple correlation or the coefficient of multiple determination, is the percent of the variance in the dependent explained uniquely or jointly by the independents. R^2 can also be interpreted as the proportionate reduction in error while estimating the dependent when knowing the independents. That is, R^2 reflects the number of errors made when using the regression model to guess the value of the dependent, in

ratio to the total errors made when using only the dependent means as the basis for estimating all cases.

7.2.3 Optimization using Genetic Algorithm (GA)

Optimization of machining parameters not only increases the utility for machining economics, but also improves the product quality to a great extent. The main objective of the present work is to optimize the machining process in order to achieve lower cutting force, lower tool wear and good surface finish, as these factors affect the functionality of the manufacturing process. In this context, an effort has been made to optimize the machining process within the constraints using optimization technique.

Traditional techniques are not efficient when practical search space is too large. These algorithms are not robust. They are inclined to obtain a local optimal solution. Numerous constraints and number of passes make the machining optimization problem more complicated. So, it was decided to employ GAs as the optimization technique. GA comes under the class of non-traditional search and optimization techniques. GA different from traditional optimization techniques in the following ways:

1. GA works with a coding of the parameter set, not the parameter themselves
2. GA searches from a population of points and not a single point
3. GA uses information of fitness function, not derivatives or other auxiliary knowledge
4. GA uses probabilistic transition rules not deterministic rules
5. It is very likely that the expected GA solution will be global solution

7.2.3.1 Coding

Generally, in GA, the variables are represented as strings which can be thought of as a gene of a chromosome. The length of the string is usually chosen according to the

desired accuracy of the optimal solution. These artificial chromosome (or) bit string is called genotype.

7.2.3.2 Population

Unlike conventional methods of optimization, GAs start with a group of randomly created initial solutions. This group of solutions is called “population”.

7.2.3.3 Population size

It is the number of the solutions present in the populations in form of strings. This population size is one of the control parameters, which will have enormous bearing on the accuracy of the optimal solutions. This depends on the nature and domain of the problem for which GAs are used.

7.2.3.4 Decoding

Decoding is the process of finding the equivalent value of the parameters sets from their string representations for use in evaluating the objective function value. This decoded parameter x is called phenotype.

7.2.3.5 Fitness

Fitness is suitably transformed value of the objective function for a particular set of parameter values. For a maximization problem, the objective function value can be used.

7.2.3.6 Working principal of GA

The basic working principle of GA is described with the help of a flow chart shown in Fig. 7.1.

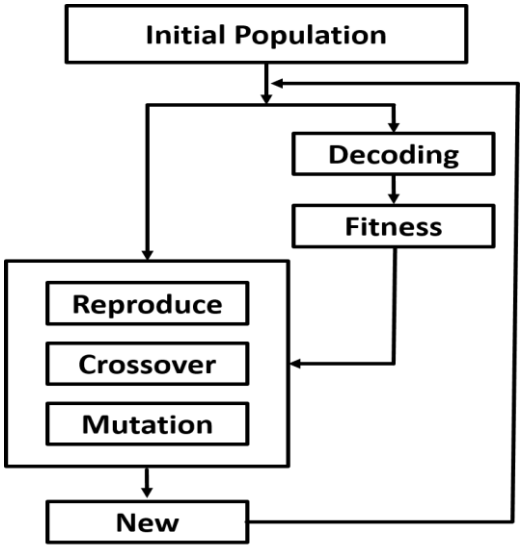

Fig. 7.1. The flowchart of a simple GA.

Step 1 – Initialize population

GA is started by initializing a number of solutions (N) at random. Instances of the problem variables are created randomly within the specified lower and upper bounds. Binary strings representing the problem variables are initialized.

Step 2 – Evaluate solutions

Each solution in the population is evaluated to compute the objective function value. In the case of constrained problems, each solution is checked for constraint violation and an appropriate penalty is added to the objective function value. The bracket-operator and parabolic penalty terms are commonly used [199]. The resulting penalized function value is transformed to compute the fitness $(F(x))$ of the solution,

x: $$F(x) = \frac{1}{1 + f(x) + R\left(\sum_{j=1}^{J}\left(\bar{g}_j(x)\right)^2\right) + \sum_{k=1}^{k}\left(\bar{h}_k(x)\right)^2} \qquad (7.2)$$

Here, a constant penalty parameter 'R' is used with the normalized constraints $\bar{g}$ *and* $\bar{h}$. The above transformation function converts the minimization problem into a maximization problem. Thus, solutions having larger fitness value are better than solutions having smaller fitness value.

Step 3 – Reproduction

Reproduction operator selects good solutions in the population (the solutions having large fitness values) stochastically and places in a temporary population called the mating pool. There exist lot of reproduction operators of GA literature, but widely used reproduction operator is Roulette wheel selection, since the string is selected for the mating pool with a probability proportional to its fitness in this method [200].

The probability of a particular string being copied into the mating pool is proportional its fitness value and is being given by the following expression:

$$P_i = \frac{f_i}{\sum_{i=1}^{m} f_i} \tag{7.3}$$

Where P_i = Probability of string i being selected

f_i = fitness of string i

m = Population size

Roulette wheel selection:

This method can be implemented as follows:

1. Sum the fitness of all members in the population (say ' m '). Call this sum 'T'.
2. Generate a maximum of ' m ' random numbers $r_i (i = 1,2,3,.....m)$ between $0 \& T$
3. Select the population member 'i' whose cumulative fitness obtained by adding its fitness to those of previous members is greater than or equal to $r_i (i = 1,2,3,.....m)$

The effect of Roulette wheel parent selection is to return a randomly selected parent. Although this parent selection is random, each parent's choice of being selected is directly proportional to its fitness value. Selection of population member to be a parent can then be viewed as spin of the wheel. This parent selection technique has the advantage that it

directly promotes the reproduction of the fittest population members by biasing each member's chance of being selected in accordance with its fitness.

Step 4 – Crossover

Crossover operator creates new solutions from good solutions in the mating pool. Two solutions (called parent solutions) are picked randomly from the mating pool and some information about the problem variables are exchanged between the solutions to create two new children solutions. The crossover probability is a control parameter, which is usually kept around 0.8. However, it can be changed depending on the problem domain and the stage of the search.

Step 5 – Mutation

Mutation operator chooses a child solution from the mating pool and perturbs the problem variables probabilistically (with a mutation Probability, P_m) to create a new solution. The need for using the mutation operator is to introduce diversity in the population. A very low value for mutation probability (Usually in the range of 0.01) is used, and if it were higher, the probability of the good strings getting destroyed will be more.

Step 6 – Termination

Reproduction, crossover and mutation operators create a new (and hopefully better) population. The successive operation of these operators is known as generation in GA terminology. In order to check the termination of GA, usually one or more of the following aspects are calculated.

1. The best solution in the population has not been improved in the last few generations
2. The average fitness of the solutions in the population is very close to the maximum fitness in the population

3. The best solution is close to the desired (Previously- known) solution
4. Total number of function evaluations has expected a pre-specified number

The three GA operators are simple and straight forward. Reproduction operator selects good strings and cross over operator recombines good substrings from two good strings together to hopefully form a better substring. Mutation operator alters a string locally to hopefully create a better string. Even though none of these claims are guaranteed and/ or tested while creating a population, it is expected that if bad strings are created they will be eliminated by the reproduction operator in the next generation and if good strings are created, they will be emphasized.

7.3 Results and discussion

The current section describes various statistical analysis techniques and optimization tools adopted to develop and optimize regression models for different response characteristics. It also explains the investigations made to understand the effect of process variables on response characteristics.

7.3.1 Statistical analysis

Statistical analysis has been carried using Analysis of variance (ANOVA). The experimental results were analyzed with the help of commercial software Design-Expert (DX-10) which has been specially used for DoE and statistical analysis of experiment appliances. The influence of control parameters such as cutting speed, feed, rake angle, nose radius and approach angle on machinability performance parameters has been analyzed. The response surfaces graphs are plotted to investigate the effect of input process parameters together with their second order interactions on response characteristics. The Tables B.1-B.9 (APPENDIX-B) depict the three-different statistical tests viz. sequential model sum of squares, lack of fit test and model summary statistics performed to select the most adequate models that fit cutting force, surface roughness and tool wear under all

selected machining environments. The sequential model sum of squares test (Table B.1; B.4 and B.7 (APPENDIX-B)) shows, the pattern in which the terms of increasing complexity contribute to the model. It can be observed that for all the responses/characteristics, the quadratic model is appropriate (Prob> F values are less than 0.05 in all the cases). The lack of fit test compares the residual error to pure error from the replicated design points. Lack of fit tables (Table B.2; B.5 and B.8 (APPENDIX-B)) indicate that the quadratic model in all the response characteristics does not show a significant lack of fit confirming the adequacy of quadratic model. Another test model summary statistics (Table B.3, B.6 and B.9 (APPENDIX-B)) further confirms that quadratic model is the best to fit as it exhibits low standard deviation, high "R-squared values", and a low "PRESS" (Adequate precision).

7.3.1.1 ANOVA for Response Surface Quadratic model

ANOVA test has been performed to test the adequacy of the developed models for establishing the mathematical link between the machinability performance parameters (cutting force, tool wear and surface roughness) and the cutting parameters (cutting speed, feed, rake angle, nose radius and approach angle) of turning process. The ANOVA test module has been designed to estimate the sum of squares of the response into the contribution due to the second order and a lack of fit component which measures the deviations of the responses from the fitted surface as well as a measure of the experimental errors. Process variables having p-value <0.05 are considered significant terms for the requisite response characteristics. ANOAVA for cutting force, surface roughness and tool wear under all selected machining environments has been presented in Tables B.10 – B.21 (APPENDIX-B). The analysis has been carried out at a level of 5% implication, specifically up to a confidence level of 95%. This has been further confirmed from the results, as the error in the results of percentage contribution values has been less than 5%. The influence

of each cutting parameter on the machinability performance of characteristics is determined using ANOVA and their significance level is as presented in Table.7.1.

Table. 7.1. Significance level of cutting parameters on machinability performance of characteristics.

Cutting parameters	Cutting force (N)				Surface roughness (µm)				Tool wear (µm)			
	ALN	CCA	Wet	Dry	ALN	CCA	Wet	Dry	ALN	CCA	Wet	Dry
Speed (m/min)	HS*	HS	HS	HS	LS	LS	LS	LS	HS	HS	HS	HS
Feed (mm/rev)	HS	HS	HS	HS	LS	LS	LS	LS	LS	LS	LS	LS
Rake angle (deg)	HS	HS	LS	NS	NS	LS	LS	LS	LS	LS	LS	NS
Nose radius (mm)	NS+	LS#	HS	HS	HS	HS	HS	HS	HS	NS	LS	NS
Approach angle (deg)	NS	NS	NS	NS	NS	NS	NS	LS	LS	LS	LS	NS

***HS: High Significance; +NS: No Significance; #LS: Low Significance**

Table 7.2. Statistical inference for cutting force under different machining environments.

Cutting parameters	Machining environments	Lack-of-fit p value	Correlation coefficient R^2	Pred R^2	Adj R^2
Cutting force (N)	ALN	0.119	0.956	0.832	0.921
	CCA	0.756	0.944	0.814	0.899
	Wet	0.707	0.957	0.857	0.923
	Dry	0.508	0.919	0.717	0.856
Surface roughness (µm)	ALN	0.241	0.961	0.856	0.931
	CCA	0.241	0.986	0.955	0.978
	Wet	0.626	0.992	0.974	0.986
	Dry	0.107	0.992	0.971	0.986
Tool wear (µm)	ALN	0.602	0.967	0.887	0.941
	CCA	0.896	0.985	0.954	0.973
	Wet	0.919	0.963	0.888	0.934
	Dry	0.375	0.933	0.758	0.879

Further, the lack-of-fit p value, correlation coefficient R^2, Pred $R^2$and Adj R^2 were evaluated for each of the machining environments individually and are found to be as given in Table 7.2. The values of lack-of-fit ‘p’ for all the machining environment were found to be greater than 0.05 which implies that the regression models successfully explain the functional relationships between the experimental factors and the response. Further, for

each of the machining environment, the correlation coefficient 'R^2' was found to be very strong. It represents the proportion of variation in the response which is explained by the model. The 'Pred R^2' for all the machining environment have reasonable agreement with the 'Adj R^2'.

7.3.1.1.1 Percentage contribution of cutting parameters on cutting force:

The percentage contribution of each cutting parameter on cutting force under all selected machining environments are determined and presented in Fig. 7.2. It is observed that cutting speed (A), feed (B), and rake angle (C) show a statistical significance on cutting force with contributions of 14.04, 10.37 and 17.88% respectively under atomized LN_2 (ALN) spray condition (Fig. 7.2 (a)). On the other hand, nose radius (D) and approach angle (E) do not present any statistical significance. Rake angle and approach angle quadratic terms C^2 and E^2 are significant with contribution of 41.86 and 7.75 %.

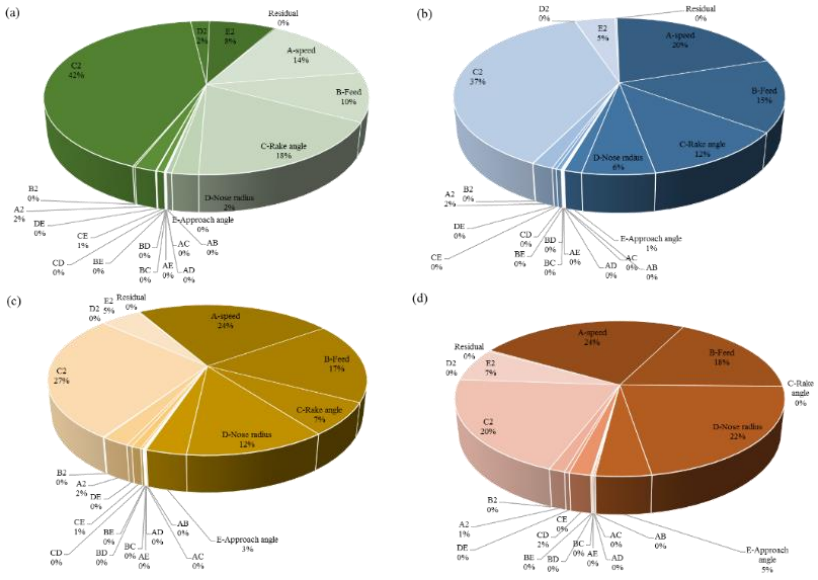

Fig. 7.2. Percentage contribution of cutting parameter on cutting force in selected model (a) ALN spray (b) CCA gas (c) Wet and (d) Dry machining.

Under cryogenically chilled argon (CCA) gas condition (Fig. 7.2 (b)), cutting speed (A), feed (B) and rake angle (C) represent the higher statistical significance on cutting force with contributions of 20.29, 14.98 and 12.04% respectively. The term nose radius (D) is

also significant with smaller contribution of 6.01%. On the other hand, approach angle (E) does not present any statistical significance. Rake angle quadratic terms C^2 is significant with a highest contribution of 37.44%.

Cutting speed (A), feed (B), and nose radius (D) demonstrated a higher statistical significance on cutting force with contributions of 23.56, 17.38 and 12.02% respectively under wet condition (Fig. 7.2 (c)). The term rake angle (C) was also significant although with a smaller contribution of 7%. The term approach angle (E) does not present any statistical significance. The quadratic term of rake angle and approach angle quadratic terms C^2 and E^2 were significant with contributions of 27.1 and 4.822% respectively.

It is also observed that, cutting speed (A), feed (B) and nose radius (D) showed a higher statistical significance on cutting force with contributions of 24.133, 17.78 and 22.11% respectively under dry condition (Fig. 7.2 (d)). The quadratic terms of rake angle (C^2), is also significant with contribution of 20.25%. On the other hand, rake angle (C) and approach angle (E) do not present any statistical significance.

7.3.1.1.2 Percentage contribution of cutting parameters on surface roughness:

Concerning surface roughness, the adopted model which fits well with the experimental data. The percentage contribution of cutting parameter on surface roughness under all selected machining environments are presented in Fig. 7.3. The most significant term, nose radius (D) contributed 65.04% on surface roughness under ALN condition (Fig. 7.3 (a)). Previously, Meng observed that nose radius had a notable effect on surface roughness [187]. The term cutting speed (A) and feed (B) are also significant with smaller contribution of 7.54 and10.36 %, respectively. On the other hand, the rake angle (C) and approach angle (E) does not present any statistical significance. The quadratic term of rake angle i.e., C^2 showed significance with a contribution of 9%.

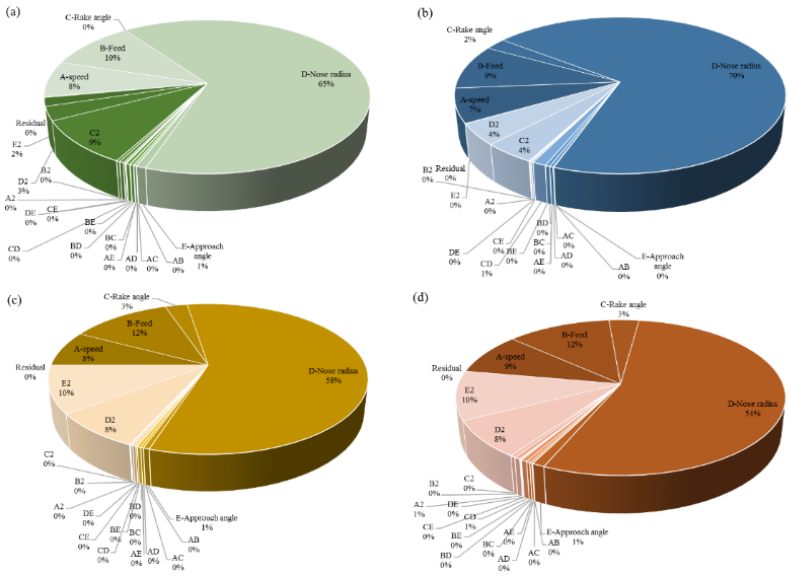

Fig. 7.3. Percentage contribution cutting parameter on surface roughness in selected model (a) ALN spray (b) CCA gas (c) Wet and (d) Dry machining.

Under CCA gas condition (Fig. 7.3 (b)), it was found that nose radius (D) is the most dominating significant factor with a contribution of 70.11 %. The terms cutting speed (A), feed (B), and rake angle (C) also showed significant effect on surface roughness, although with smaller contributions of 7.05, 9.26 and 2.42%, respectively. The interaction between rake angle and nose radius (CD) showed a smaller contribution of 1.14%. The quadratic terms of rake angle and nose radius i.e., C^2 and D^2 are significant with a contribution of 4.36 and 4.40% respectively.

It is inferred that the terms cutting speed (A), feed (B), rake angle (C) and nose radius (D) shows significant effect on surface roughness under wet condition (Fig. 7.3 (c)). In those, the most significant term, nose radius (D) had a contribution of 57.51%, followed by cutting speed (A), feed (B), rake angle (C) and approach angle (D) with lower contribution of 7.7, 12.1 and 2.669% respectively. The term approach angle does not show any statistical significance. On the other hand, the selected interaction does not show any significance, whereas, quadratic terms of nose radius and approach angle i.e., D^2 and E^2 are significant with a contribution of 7.97 and 10.18%, respectively.

As observed for wet machining, all linear terms showed significant on surface roughness under dry machining. Nose radius (D) shows significance with highest contribution of 54.33% under dry condition (Fig. 7.3 (d)). The next terms which influence the surface roughness under dry machining are cutting speed (A), feed (B), rake angle (C) and approach angle (D) with respective contributions of 8.83, 12.04, 3.47 and 1.07% respectively. The selected interactions do not show any significant influence, quadratic terms of nose radius and approach angle i.e., D^2 and E^2 are significant with a smaller contribution of 7.76 and 10.17%, respectively.

7.3.1.1.3 Percentage contribution of cutting parameters on tool wear

A quadratic model is implemented to fit well with the experimental data related to tool wear for all the machining environments under consideration and the percentage of contribution of each cutting parameter is presented in Fig. 7.4. Under ALN spray condition (Fig. 7.4 (a)), Nose radius (D) and cutting speed (A) are the most significant terms with contribution of 32.23and 27.78%, respectively. The terms feed (B), rake angle (C) and approach angle (D) are also significant with smaller contribution of 4.63, 7.21 and 4.47%, respectively. The interaction terms between rake angle and nose radius and rake angle and approach angle i.e., CD and CE shows significance with a contribution of 4.94 and 3.38% respectively. The quadratic terms of rake angle and approach angle i.e., C^2 and E^2 are significant with a contribution of 5.38 and 8.4%, respectively.

It was seen that cutting speed (A) is the most dominating significant factor with a contribution of 40.70 % on tool wear under CCA gas condition (Fig. 7.4 (b)). The other linear terms feed (B), rake angle (C) and approach angle (E) are significant with a smaller contribution of 6.78, 7.28 and 1.75%, respectively. The nose radius (D) in linear term does not show significance. The interaction term s, rake and nose radius are significant with a

contribution of 4.65%. The quadratic terms of rake angle, nose radius and approach angle i.e., C^2, D^2 are E^2, are significant with contributions of 17.47, 10.47 and 8.21% respectively.

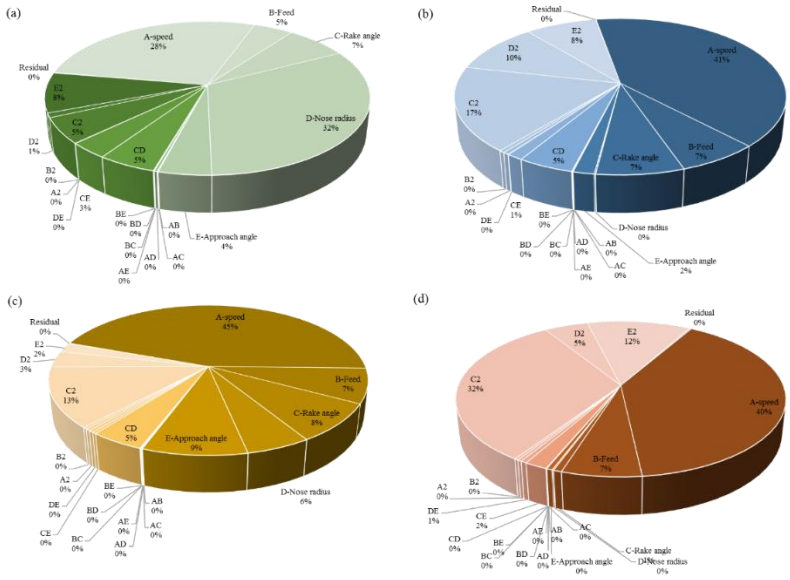

Fig. 7.4. Percentage contribution of cutting parameters on tool wear in selected in the model (a) ALN spray (b) CCA gas (c) Wet and (d) Dry machining.

Results indicate that cutting speed (A) is significant with largest contribution of 44.8%. The linear terms feed (B), rake angle (C), nose radius (D) and approach angle (E) are significant with a contribution of 7.46, 8.344, 5.51 and 8.96%, respectively under wet condition (Fig. 7.4 (c)). The interaction terms of rake and nose radius i.e., CD and quadratic terms of rake angle and nose radius i.e., C^2 and D^2 are significant with a contribution of 4.62, 12.86 and 3.47%, respectively.

From Fig. 7.4 (d) the term cutting speed (A) had the major statistical significance on tool wear with a contribution of 39.92% under dry condition. This was followed by feed with a contribution 6.65%. The quadratic terms of rake angle and approach angel i.e., C^2 and E^2 are significant with a contribution of 31.71 and 11.92%, respectively.

From the ANOVA analysis, it can be observed that the model F value for cutting force, surface roughness and tool wear under selected machining conditions are significant. There is only a 0.01% chance that an F-value this large could occur due to noise. The "Lack

of Fit F-value" for all the responses is not significant relative to the pure error. Non-significant lack of fit is an ideal model to fit. Values of "Prob > F" less than 0.0500 indicate that model terms are significant in all the selected conditions. In other words, most of interaction and quadratic terms do not show significant effect. When there are many insignificant terms (not counting those required to support hierarchy), reduction of these terms may improve the overall model to a better fit. Hence, the insignificant parameters were pooled using backward elimination method and regression models were created and used for further analysis.

7.3.1.2 Multiple linear regression models

A multiple linear regression analysis attempts to model the relation between two or more predictor variables and a response variable by fitting a linear equation to the observed data. The statistical software Design Expert DX-10 has been employed to obtain the correlation between the selected machining parameters. The cutting force, surface roughness and tool wear have been calculated based on multi linear regression models. To improve the model fit P-value, backward selection method is selected. P value is the standard method looking for significant terms to keep and or insignificant terms to remove from the model and the backward selection seeks to remove terms from a model that are detrimental to the criterion. This will help to decide the terms that form the best model. The regression coefficients of the second order equation are obtained by using the experimental data. The insignificant coefficient terms (identified from ANOVA) have been omitted from the equations. The final regression equation in terms of real factor of cutting force, surface roughness and tool wear as an individual function of input process variables are given as Eq. B.1 to B.12 (APENDIX-B).

The suitability of adopted model must be checked by appropriate statistical analysis. There are several residual graphs to test the model assumptions. The primary analysis is to examine a normal probability plot of the residuals, that is, the number of standard

deviations of actual values based on predicted values. The normal probability plots of the residuals versus the predicted response cutting force under selected machining conditions are shown in Fig. 7.5 (a-d). It reveals that the residuals generally fall on a straight line, implying that the errors are normally distributed. This suggests that the models proposed are adequate and there is no reason to suspect any violation of the independence or constant variance assumption [197]. It can be seen from Fig. 7.5 (i-iv) that the predicted values and the actual values of cutting force under all selected machining conditions are varying linearly. Similar observations were made during the analysis of surface roughness and tool wear. The normal probability plot of residuals and Predicted vs. actual graphs of surface roughness and tool wear are presented in Figure B.1 and B.6 (APENDIX-B) respectively.

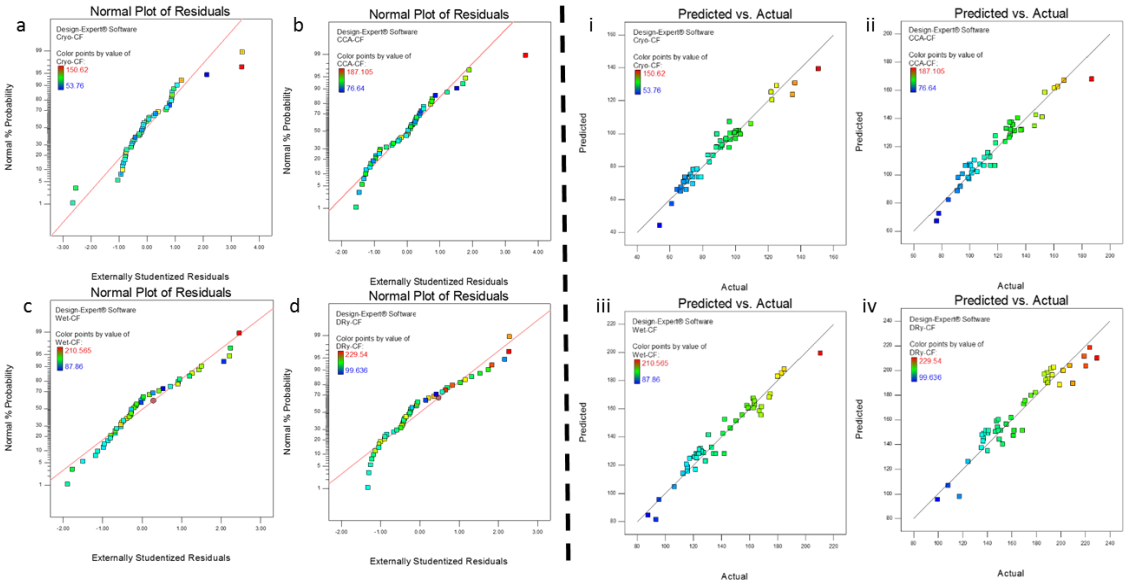

Fig. 7.5. Normal probability plot of residuals (a-d) and Predicted vs. actual values (i-iv) for cutting force under ALN (cryo) [a & i]; CCA gas [b & ii]; wet [c & iii] and dry [d & iv].

Further, to check the usefulness of the developed models, R^2, Adj-R^2 and Pre-R^2 values are analyzed. R^2 is a measure of the amount of variation around the mean explained by the model. R^2 value should be close to 1. From the pooled ANOVA analysis for cutting force, surface roughness and tool wear under various machining conditions, R^2 was seen to be more than 0.9, which represents 90% of the data is closest to the line of best fit. Adj-R^2 measures

the amount of variation around the mean of the model. The Adj-R^2 decreases as the number of insignificant terms increases. The Adj-R^2 value for cutting force, surface roughness and tool wear under all selected machining environments in the current models is higher than 0.9 which represents more number of significant terms in the model. The Pre-R^2 helps to determine the amount of variation in new data by the selected model. The difference between pre-R^2 and Adj-R^2 should be less than 0.2 for the selected model fitting the data to be reliably to interpolate. It is observed that the pre-R^2 for the selected model is reasonably in agreement with the Adj-R^2 under all selected machining conditions. A strong statistical correlation was observed between the selected model and the experimental data. Further analysis is carried out with the same model to predict the cutting force, surface roughness and tool wear with respect to selected range of machining parameters. Influence of machining process parameters on cutting force was studied by perturbation plot and 3D response surface graphs.

7.3.1.2.1 Effect on cutting force

Perturbation plot helps to compare the effects of cutting speed, feed rake angle nose radius and approach angle with the cutting force at a particular point in the design space as shown in Fig. 7.6. The response is plotted by changing only one factor over its range while keeping all the other factors constant. A steep slope or curvature in a factor shows that the response is sensitive to that factor. From Fig. 7.6, rake angle (C) curve appears steeper from 0° to 8° followed by cutting speed (A) at a range of 100 to 150 m/min range. This phenomenon was observed under all machining conditions. Significant increase in cutting force was observed by increase the feed (B) from 0.1 to 0.15 mm/rev and nose radius (D) from 0.4 to 0.8 mm. Beyond these feed (0.15 to 0.2 mm/rev) and nose radius (0.8-1.2 mm) values, increase in cutting force was smaller under all selected machining conditions. Approach angle (E) has shown similar effect as rake angle under dry machining condition (as seen in Fig. 7.6). Tool geometry factor C, D and E have shown more curve feature

whereas cutting parameters A and B vary linearly under all machining conditions. Therefore, tool geometry factors are good choice for the axes on surface plots.

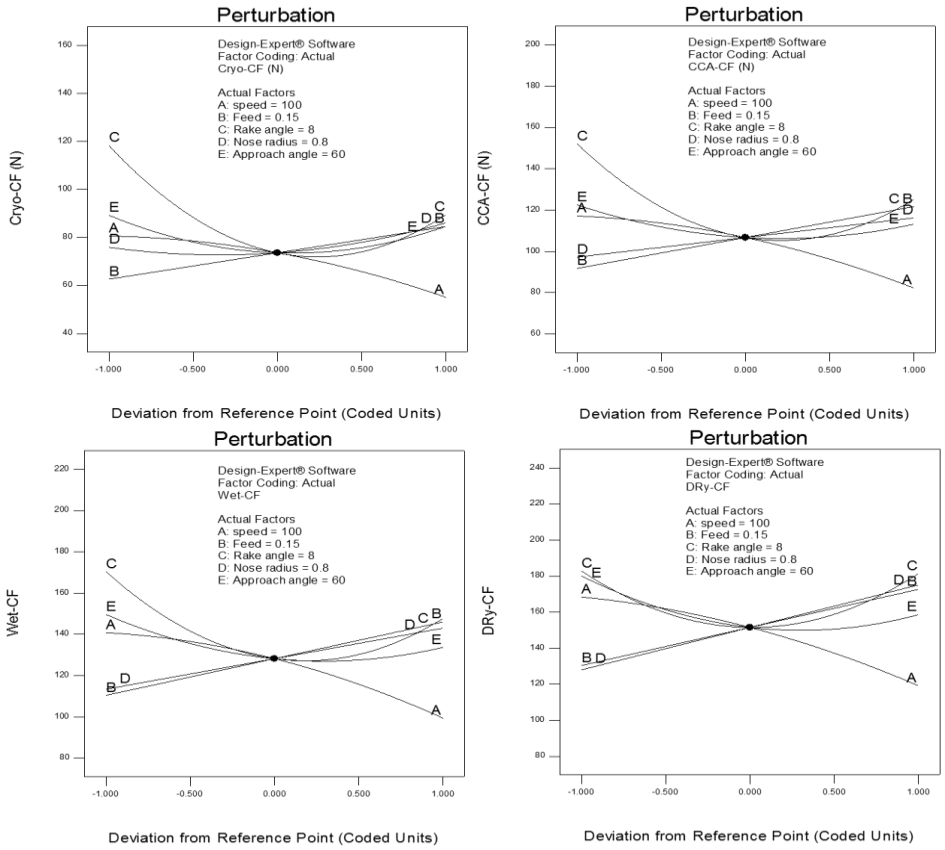

Fig. 7.6. Perturbation plot shows the effect of cutting process parameters on cutting force (CF).

3D surface plots are drawn to study the effect of process variables on the cutting force and is shown in Fig. 7.7-7.10. It is observed that the cutting force decreases with 0 to 8° rake angle, beyond which increase in cutting force was observed under all machining conditions. A probable reason for it may be that with increase in rake angle, tool/chip contact area increases causing higher cutting force. As approach angle increases from 30° to 60°, cutting force decreases and thereafter increase in cutting force was observed. At 90° approach angle, the main cutting edge enters and leaves the cutting zone suddenly, thus workpiece undergoes to maximum loading and unloading. This could be a plausible reason to increase in cutting force beyond 60° approach angle. As nose radius from

0.4 to 0.8 mm increases the cutting force increases due to higher contact area between tool and workpiece and then decreases from0.8 to 1.2 mm as a consequence energy variation occurred during turning. The variation in cutting force from 0.4 to 0.8 mm is less as compared to variation observed between 0.8 to 1.2 mm. As cutting speed increases and feed decreases, cutting force decreases significantly but when nose radius decreases, this influence is reduced.

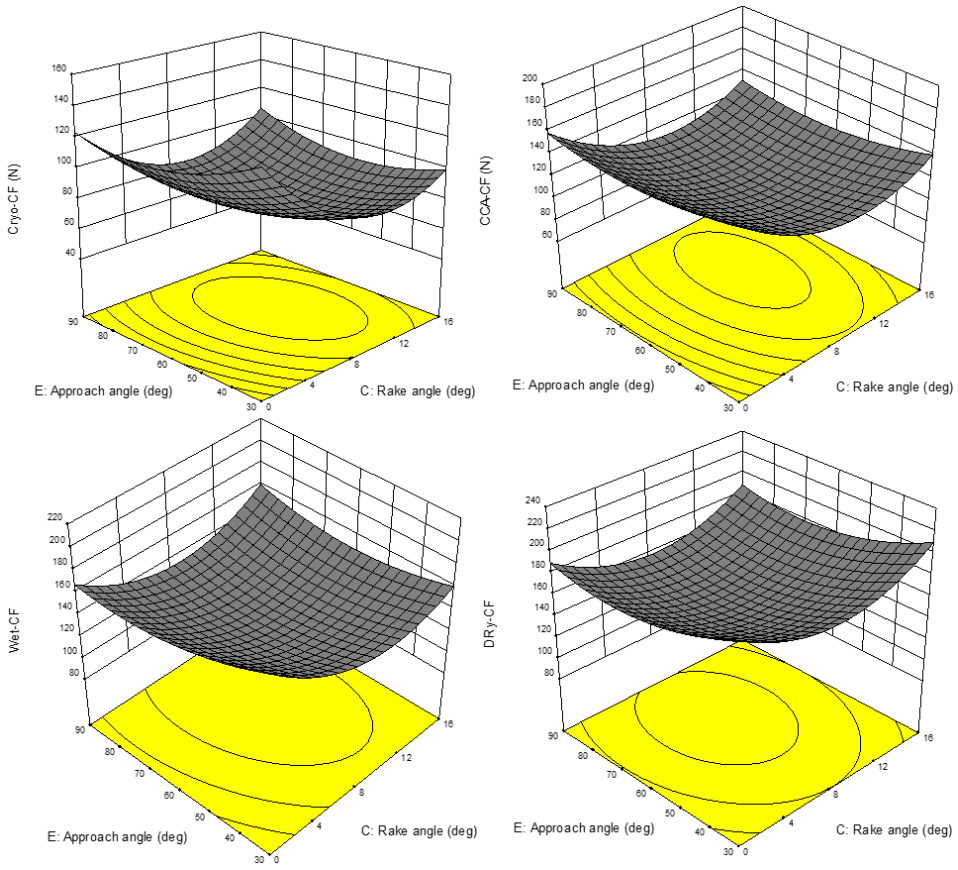

Fig. 7.7. Combined effect of approach angle and rake angle on cutting force (CF) at a cutting speed of 100 m/min, feed of 0.15 mm/rev and nose radius of 0.8 mm under (a) ALN spray (cryo) (b) CCA gas (c) Wet machining (d) Dry machining conditions.

Fig. 7.7. represents the surface plot of cutting force with respect to varying approach angle and rake angle. It shows that cutting force initialy decreases and later increases after certain rake angle under all aproach angles. Similar phenomenon has been observed with varying nose radius in all the machining conditions which is represented in Fig. 7.8. The

variation of cutting force with respect to rake angle under different nose radius is more in comparison with approach angle.

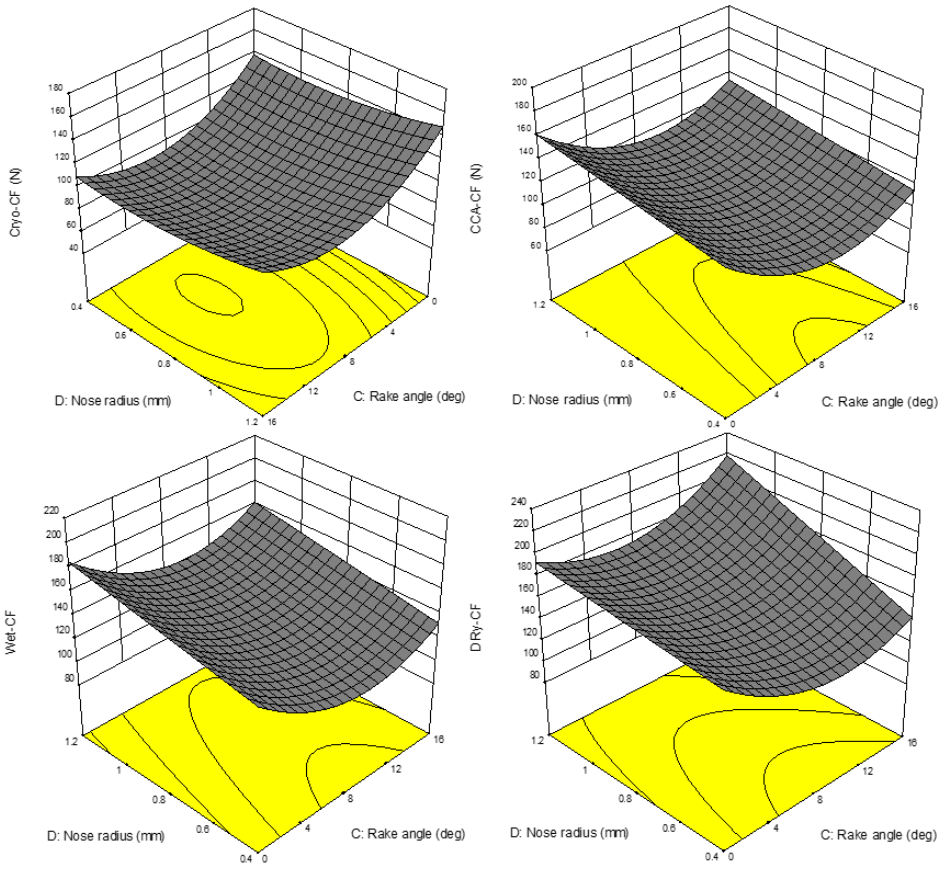

Fig. 7.8. Combined effect of rake angle and nose radius on cutting force (CF) at a cutting speed of 100 m/min, feed of 0.15 mm/rev and approach angle of 60° under (a) ALN spray (cryo) (b) CCA gas (c) Wet machining (d) Dry machining conditions.

Fig. 7.9 indicates the influence of approach angle and nose radius on cutting force. It is observed that nose radius is the most significant factor. As nose radius increases, cutting force decreases under all machining condition due increases in contact length. In addition, the effect of approach angle on cutting force with respect to nose radius is also shown in figure. Cutting force decreases as approach angle increases from 30° to 60°. Beyond 60° approach angle, cutting force shows an increasing trend under all nose radius.

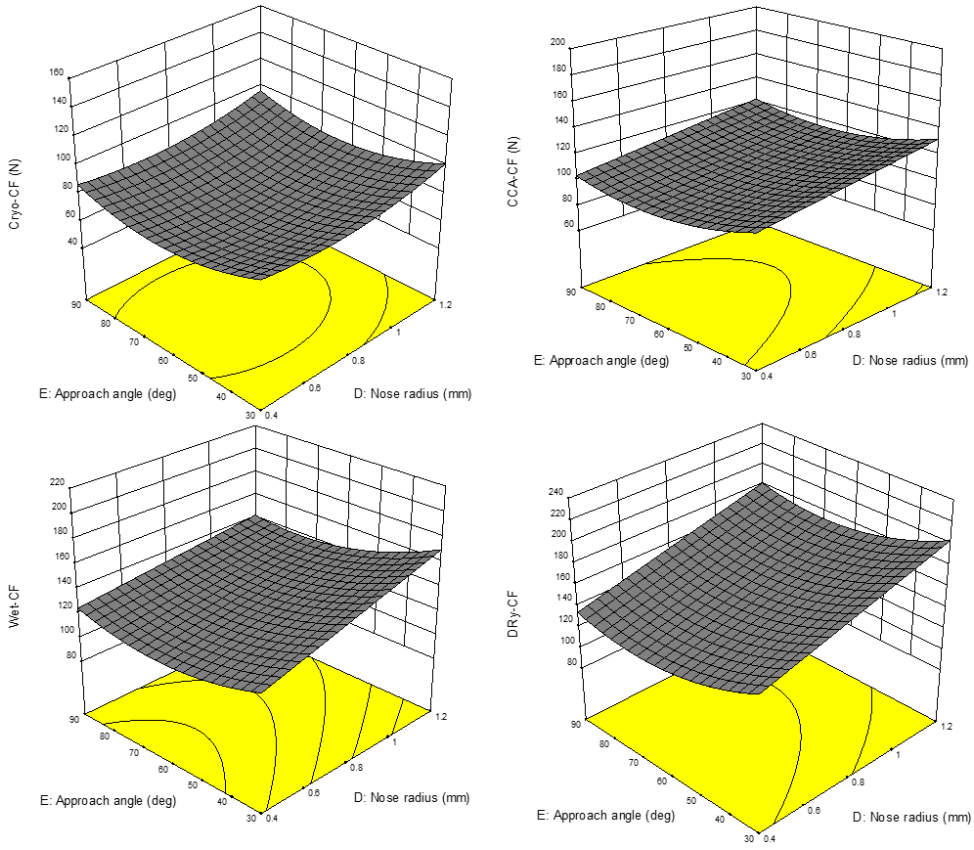

Fig. 7.9. Combined effect of approach angle and nose radius on cutting force (CF) at a speed of 100 m/min, feed of 0.15 mm/rev and rake angle of 8° under (a) ALN spray (cryo) (b) CCA gas (c) Wet machining (d) Dry machining conditions.

Fig. 7.10 indicates the combined influence of cutting speed and feed on cutting force. It is observed that as cutting speed increases, cutting force decreases. The reduction in cutting force with increase in feed may be attributed to thermal softening effects. Higher cutting force was observed at higher feed and smaller cutting force at smaller feed. Under lesser cutting speed condition, the tool cutting edge will impact the reinforcement particles, which will then either be dislodged from the matrix, without harming the tool, or be embedded into the matrix, ploughing on the tool flank, resulting in a higher cutting force. As the cutting speed increases, the tool would cut better without ploughing, resulting in a drop in cutting force.

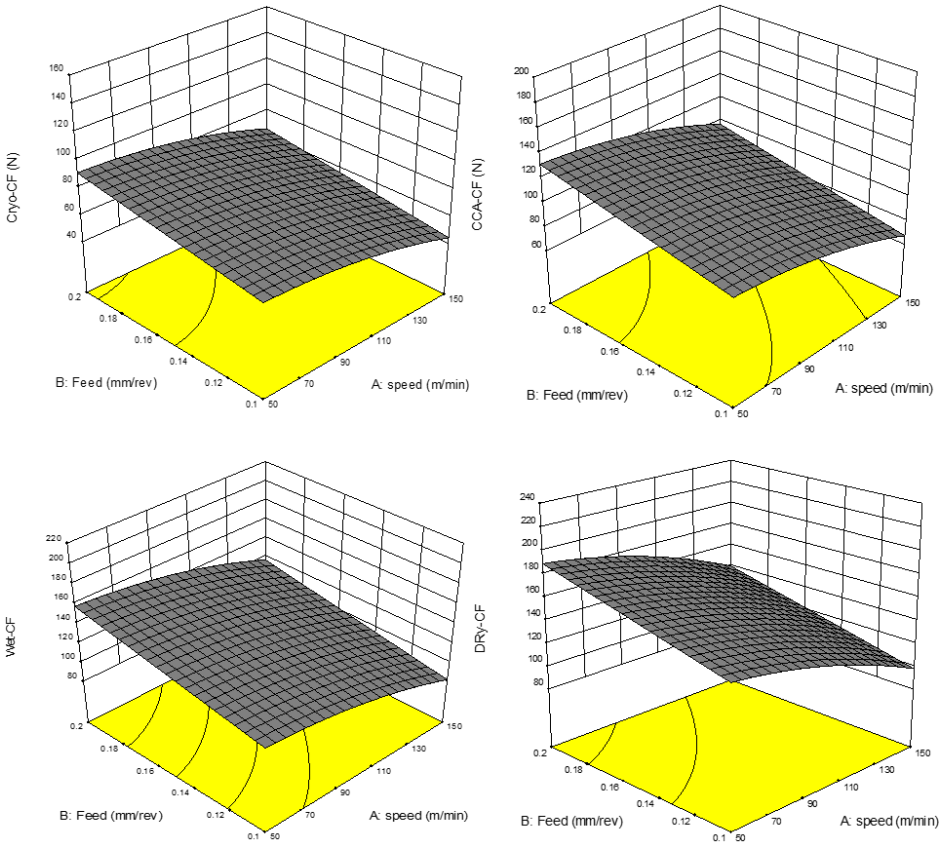

Fig. 7.10. Combined effect of cutting speed and feed on cutting force (CF) at rake angle of 8°, nose radius of 0.8 mm and approach angle of 60° under (a) ALN spray (cryo) (b) CCA gas (c) Wet machining (d) Dry machining conditions.

7.3.1.2.2 Effect on surface roughness:

From Fig. 7.11, it appears that as nose radius increases, surface roughness decreases. Approach angle (E) does not show significant effect under ALN spray and CCA gas assisted machining (seen in Fig. 7.11), however under wet and dry machining, effect of approach angle is high between 30° and 60°, beyond which its influence is less. Cutting speed (A) and rake angle (C) have low effect on surface roughness at both lower bounds under ALN spray and CCA gas assisted machining, but their influence increased at higher bounds. Surface roughness value decreases with increase in rake angle from 0° to 8°. This trend was inversed by increase in rake angle from 8° to 16°. Under dry and wet machining, the surface roughness varied linearly with increases in rake angle from 0° to 16°.

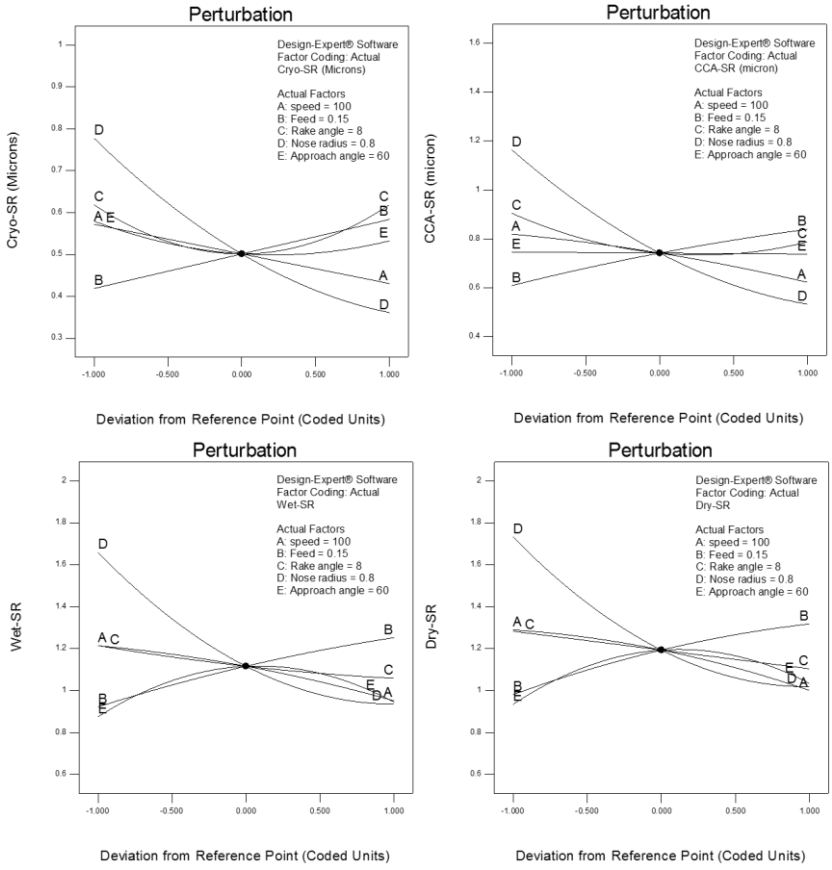

Fig. 7.11. Perturbation plot shows the effect of cutting parameters on surface roughness (SR).

Cutting speed (A) at higher bound i.e., 100 to 150 m/min has larger significant effect than the lower bounds from 50 to 100 m/min under all machining conditions. It is observed that in tool geometry factor, C, D and E factors formed more curved graphs meaning that the variation is not linear, however, cutting parameters A and B fluctuated in a roughly linear fashion under all machining conditions.

The response surface is plotted to study the effect of process variables on the surface roughness and is shown in Fig. 7.12-7.15. The effect of approach angle on surface roughness with respect to rake angle is shown in Fig. 7.12. It is observed that, as approach angle increases from 30° to 60°, surface roughness decreases. Further increase in approach angle leads to increase in surface roughness. This type of deviation was observed in ALN spray assisted machining condition. On the contrary, the surface roughness decreases with

increase in approach angle during wet and dry machining. This can be due to significant reduction of cutting temperature under ALN spray assisted machining. The surface roughness value varies almost linearly under CCA gas assisted machining condition, i.e., as approach angle increased, surface roughness value decreased.

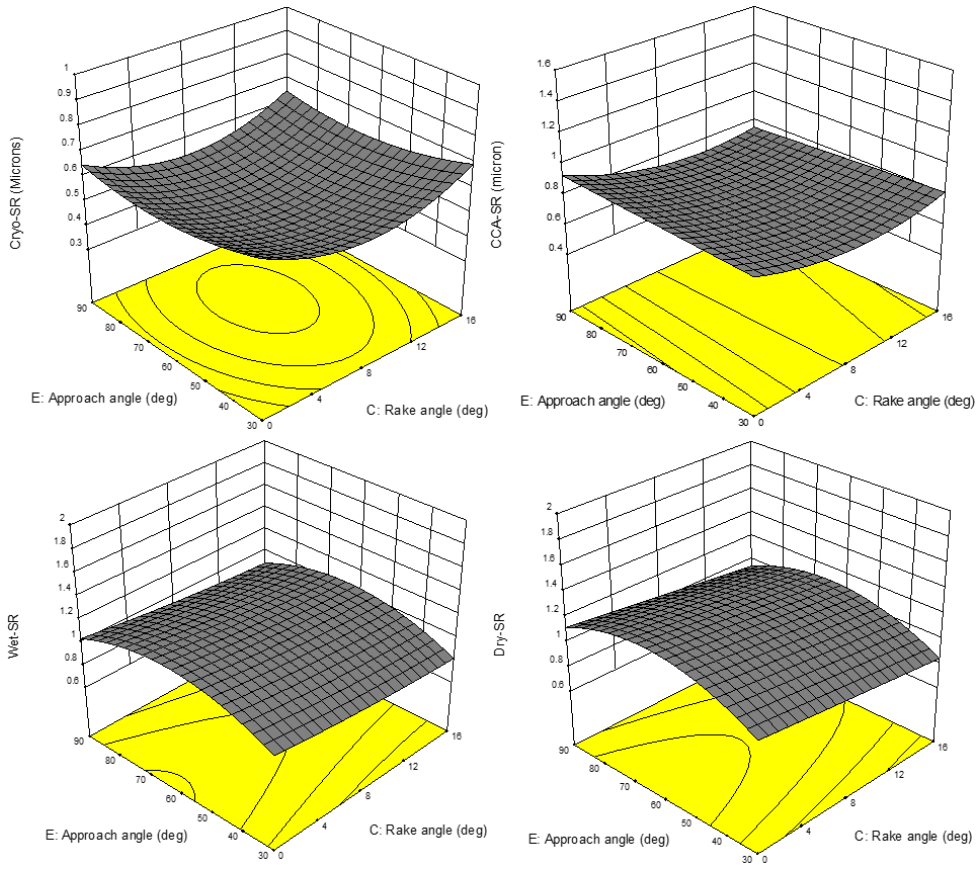

Fig. 7.12. Combined effect approach angle and rake angle on surface roughness (SR) at a cutting speed of 100 m/min, feed of 0.15mm/rev and nose radius of 0.8 mm under (a) ALN spray (cryo) (b) CCA gas (c) Wet machining (d) Dry machining conditions.

Surface roughness first decreases and then increases with rake angle. This could be due to the easy entry of tool in workpiece. As nose radius increases, surface roughness value decreases. The effect of nose radius and rake angle on surface roughness can be observed in Fig. 7.13 surface plot. Similar trend was observed in all the machining environments. Under dry condition, at larger nose radius (1.2 mm) the variation of surface

roughness is linear with respect to rake angle, where as in other environments surface roughness decreases and then increases with increase in rake angle.

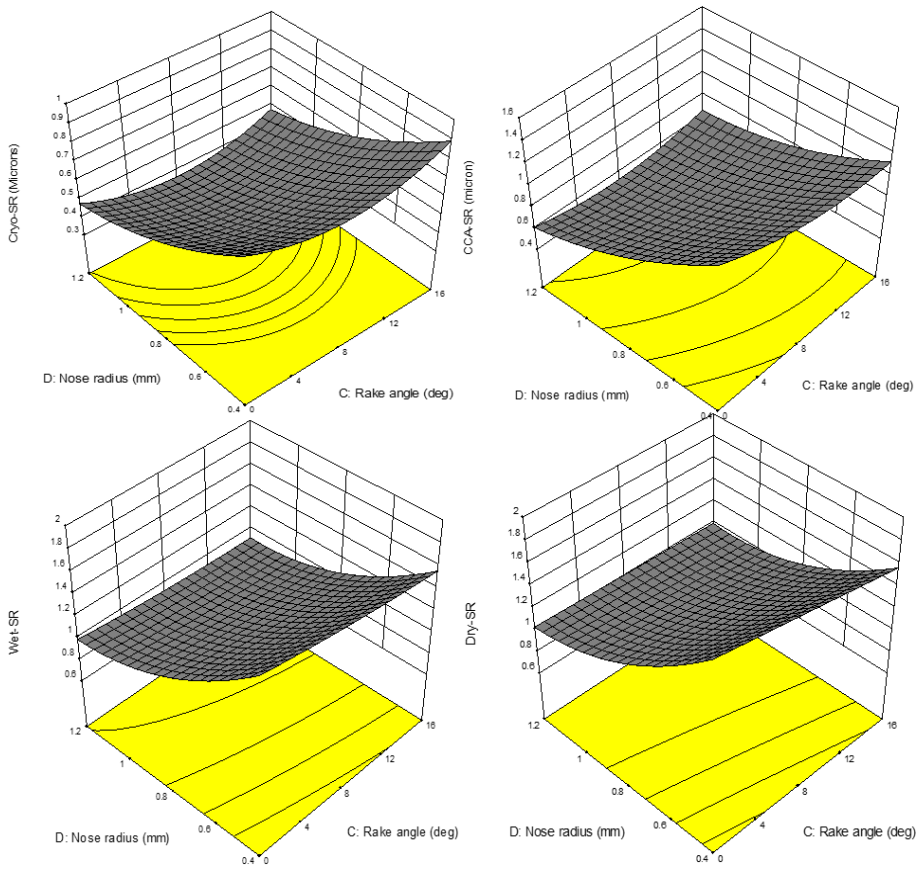

Fig. 7.13. Combined effect of nose radius and rake angle on surface roughness (SR) at a cutting speed of 100 m/min, feed of 0.15 mm/rev and approach angle of 60° under (a) ALN spray (cryo) (b) CCA gas (c) Wet machining (d) Dry machining conditions.

Fig. 7.14 represents the combined influence of nose radius and approach angle. As approach angle increases, surface roughness values first increase and then decrease under dry and wet machining, whereas under ALN spray and CCA gas assisted machining, it was nearly linear. The variation of approach angle is high at smaller nose radius. Larger approach angle and larger nose radius produce smaller surface roughness. As nose radius increases surface roughness decreases under all machining environments.

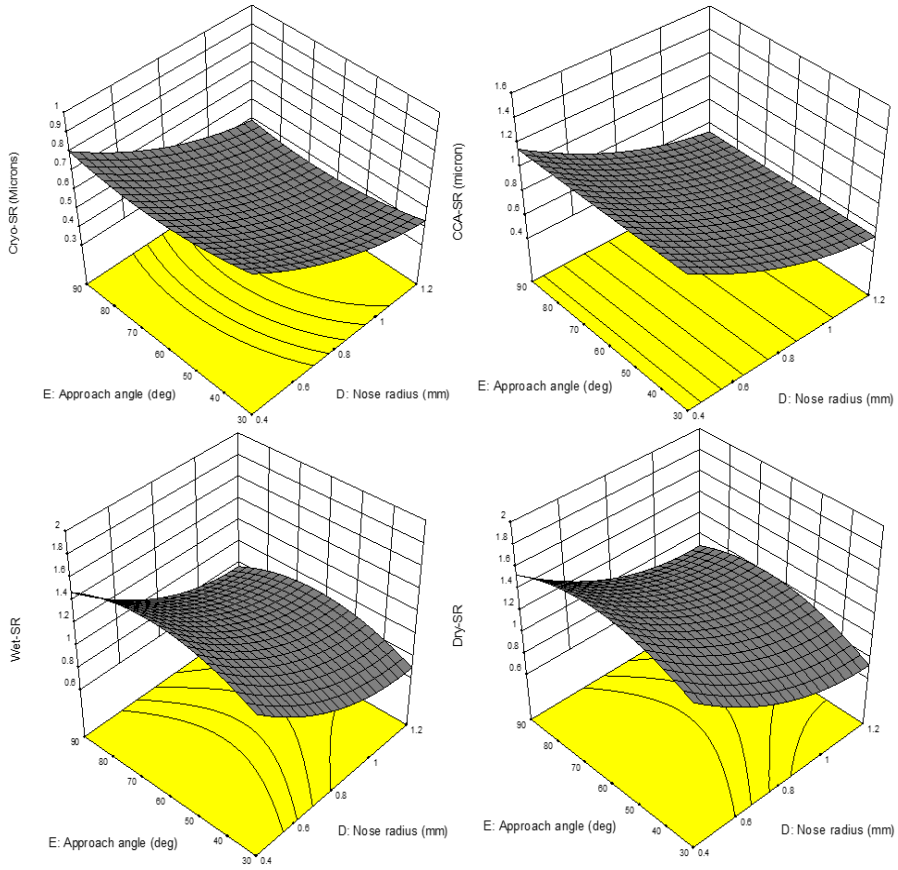

Fig. 7.14. Combined effect of approach angle and nose radius on surface roughness (SR) at a cutting speed of 100 m/min, feed of 0.15 mm/rev and rake angle of 8° under (a) ALN spray (cryo) (b) CCA gas (c) Wet machining (d) Dry machining conditions.

Cutting speed and feed are two important parameters in machining process of these, feed is most significant factor which affects the surface roughness value. The combined influence of speed and feed surface plots is presented in Fig. 7.15. It can be inferred that low cutting speed conditions produced a better surface finish for all machining conditions. The surface roughness increased with increase in feed in all machining conditions. This was attributed to high heat generation in the cutting zone at higher feed values. Increases in temperature softens the Al matrix material and decreases the bonding effect between TiCp and Al matrix. The influence of feed on surface roughness was affected by cutting speed, but the application of the higher cutting speed with the larger feed provided a little change. However, the trend was similar and was almost a straight line.

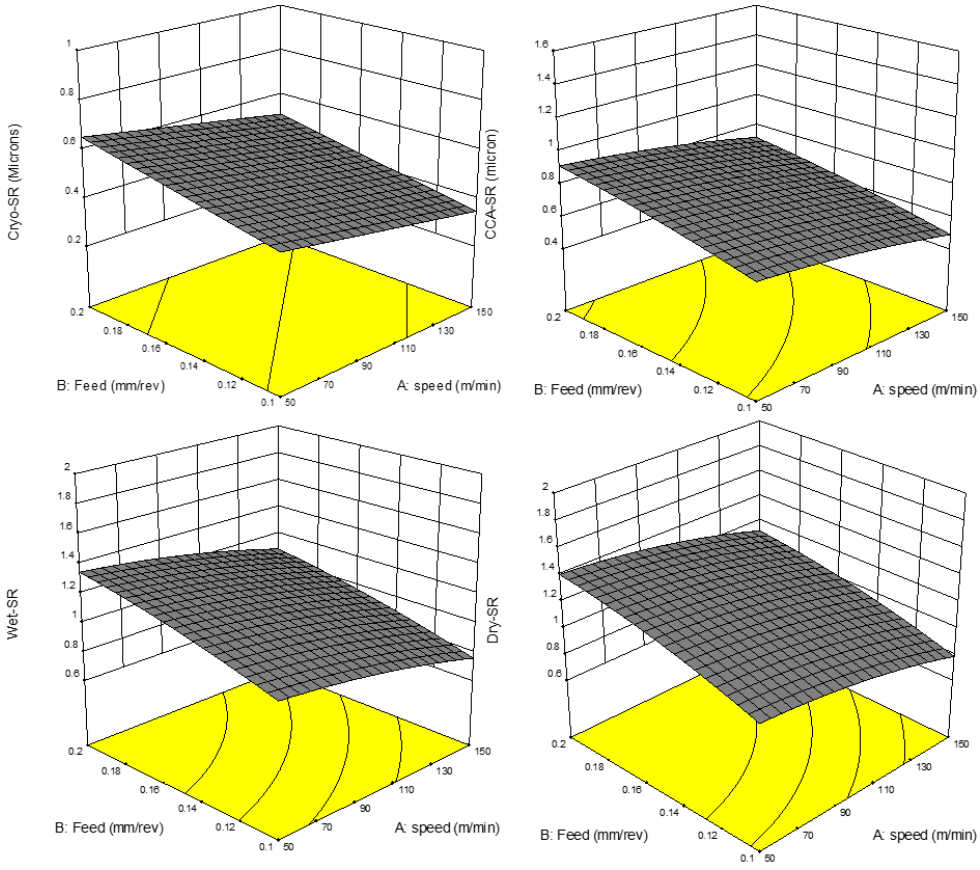

Fig. 7.15. combined effect of cutting speed and feed on surface roughness (SR) at rake angle of 8°, nose radius of 0.8 mm and approach angle of 60° under (a) ALN spray (cryo) (b) CCA gas (c) Wet machining (d) Dry machining conditions.

7.3.1.2.3 Effect on tool wear

The comparison between the effect of cutting speed, feed, rake angle, nose radius and approach angle on tool wear at a particular point in design space is determined by perturbation plot as shown in Fig. 7.16. It is observed that as rake angle (C) increases, tool wear first decreases and then increases. Similar trend was observed in nose radius (D) and approach angle (E) as well. During wet machining, the variation of tool wear with respect to rake angle, nose radius and approach angle at higher bounds does not show significant variation over the lower bounds. The machining parameters, cutting speed (A) and feed (B) also showed significant influence on tool wear by formation of steeper lines in perturbation

plots and it is observed that as cutting speed and feed increase, tool wear increases. While cutting, as cutting speed increased from 50 to 150 m/min, tool wear value nearly doubled. From this, it can be inferred that cutting speed is the dominant factor among all the machining parameters. Similar observations have been made under all selected machining environments where the cutting tool did wear out faster when higher cutting speeds were employed. It is observed that tool geometry factor C, D and E have shown more curve feature whereas cutting parameters A and B vary linearly under all machining conditions. Thus, tool geometry factors are good choice for the axes on surface plots.

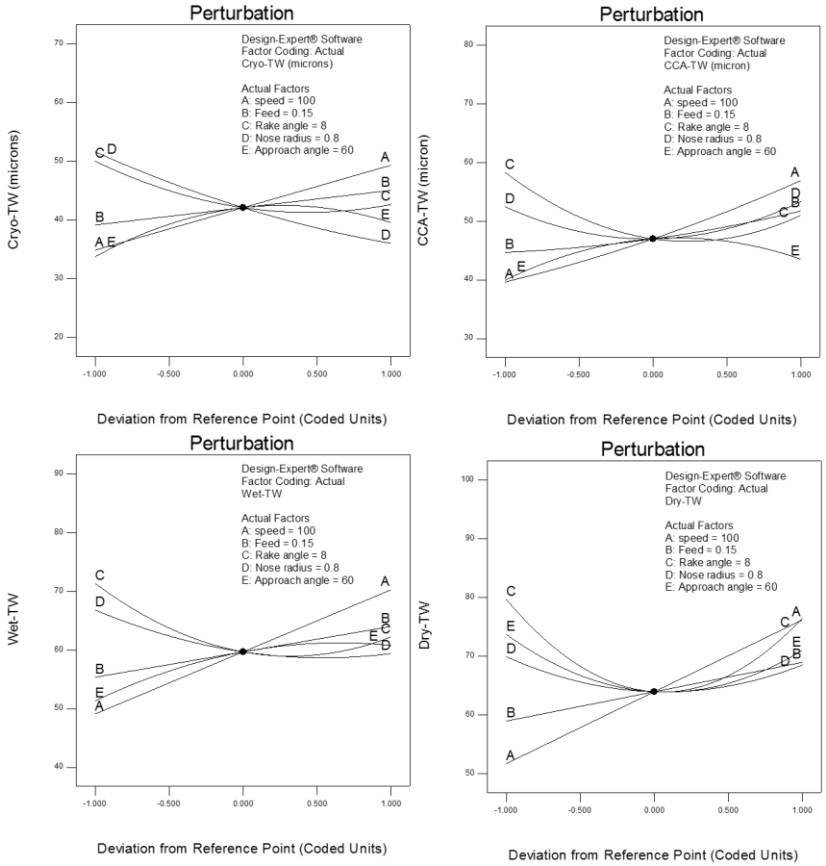

Fig. 7.16. Perturbation plot shows the effect of cutting process parameters on tool wear (TW).

The response surface is plotted to study the effect of process variables on the tool wear and is shown in Fig. 7.17-7.20. It is observed that under ALN spray assisted machining, the tool wear first decreases and then increases with rake angle. This tool wear

fluctuation is less at smaller approach angle i.e., 30°, than larger approach angle i.e., 90°. This can be observed in Fig. 7.17. Similar effect was observed under all machining conditions.

Under dry machining, as approach angle increases from 30° to 90°, tool wear first decreases and then increases, whereas in ALN spray and CCA gas assisted machining condition, inverse effect was observed. This can be attributed to cryogenic cooling effect. The variation in tool wear under CCA gas assisted condition is less as compared to ALN spray assisted machining due to difference in fluidization effect in the machining zone. Under wet machining, as approach angle increases from 30° to 60°, the tool wear increases. Beyond 60°, increase in tool wear is less as observed in Fig. 7.17.

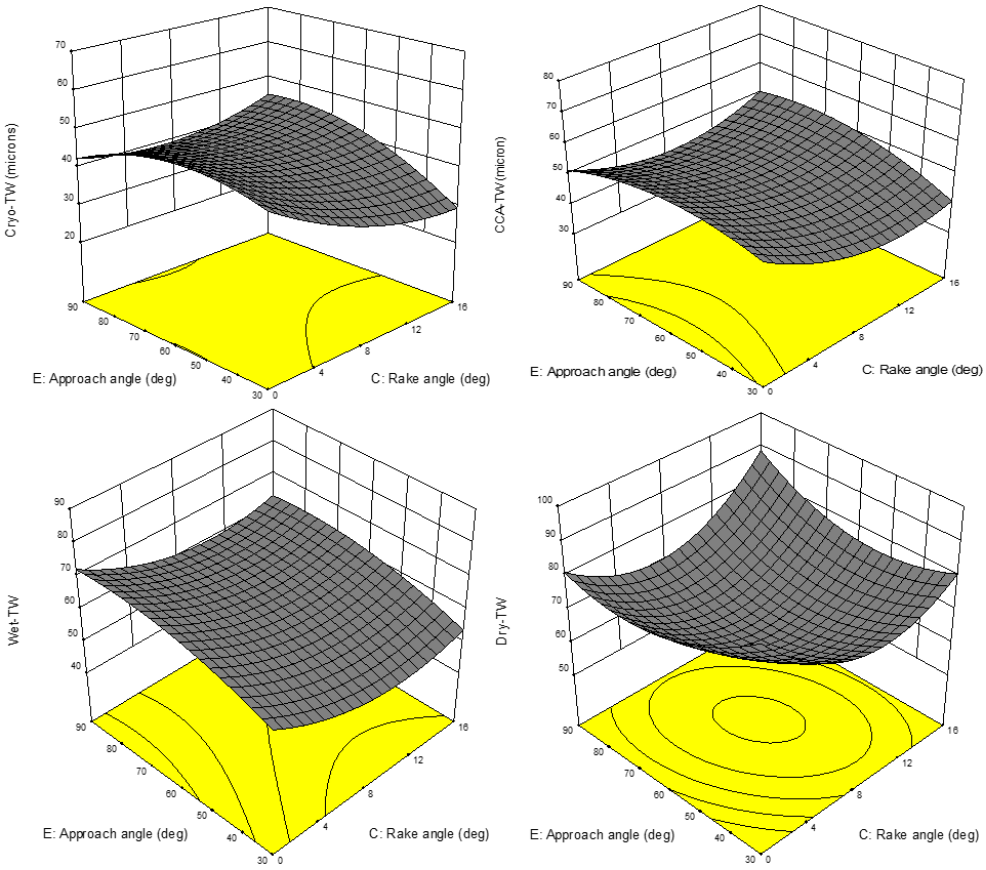

Fig. 7.17. Combined effect approach angle and rake angle on tool wear (TW) at a cutting speed of 100 m/min, feed of 0.15 mm/rev and nose radius of 0.8 mm under (a) ALN spray (cryo) (b) CCA gas (c) Wet machining (d) Dry machining conditions.

Fig. 7.18 depicts the effect of rake angle and nose radius on tool wear. It is observed that a rake angle of 0° and nose radius of 0.4 mm give higher tool wear under all machining environments. As rake angle increase from 0° to 16°, tool wear decreases and then increases under CCA gas, wet and dry machining environments, where as in ALN spray assisted machining condition increase in tool wear was observed. As nose radius increases from 0.4 to 1.2 mm tool wear decreases and then increases under dry condition. Under wet and CCA gas assisted condition tool wear increases with increase in nose radius. This fluctuation is higher at lower rake angles than compared to higher rake angles.

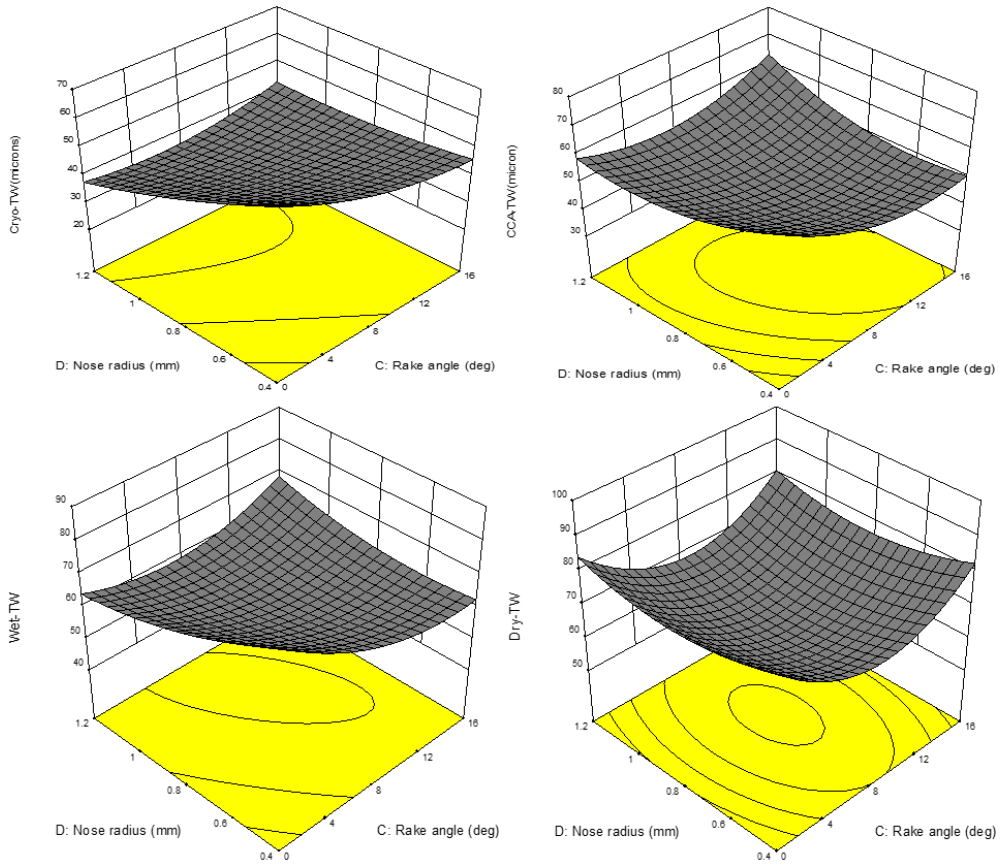

Fig. 7.18. Combined effect of rake angle and nose radius on tool wear (TW) at a cutting speed of 100 m/min, feed of 0.15 mm/rev and approach angle of 60° under (a) ALN spray (cryo) (b) CCA gas (c) Wet machining (d) Dry machining conditions.

Fig. 7.19 represents the combined influence of approach angle and nose radius. It is observed that as nose radius increases, tool wear decreases for all approach angles under ALN

spray assisted machining environment, where as in wet, CCA gas and dry condition tool wear decreases and then increases with increase in nose radius. Under dry machining, tool wear first decreases and then increases with increase in approach angle. Under ALN spray, CCA gas and wet conditions, tool wear increases with increase in approach angle under all nose radius.

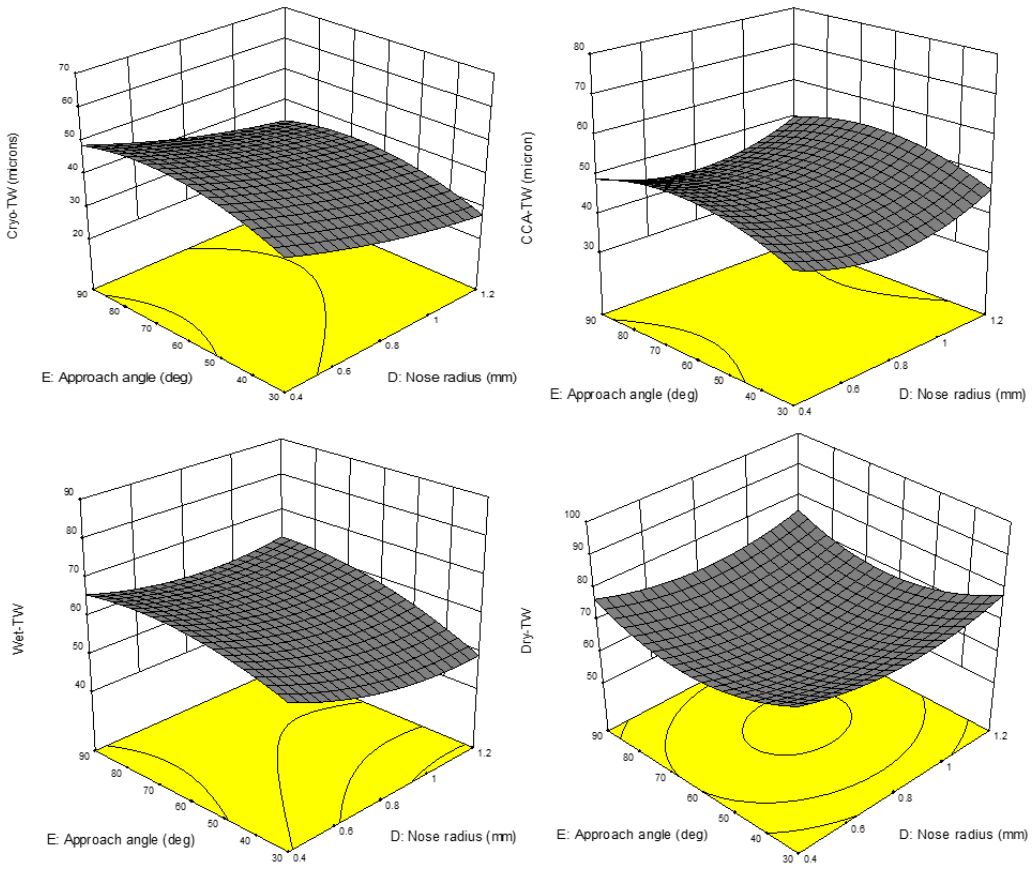

Fig. 7.19. combined effect of approach angle and nose radius on tool wear at a cutting speed of 100 m/min, feed of 0.15 mm/rev and rake angle of 8° under (a) ALN spray (cryo) (b) CCA gas (c) Wet machining (d) Dry machining conditions.

Cutting speed is the most significant factor which affects the tool wear. Fig. 7.20 represents the surface plot on effect of cutting speed and feed on tool wear. It is observed that as cutting speed increases, an increase in tool wear is observed due to high heat generation associated with thermal softening and deterioration of stability of the cutting wedge [201]. Also, the flank wear increases with increase in feed. At lower cutting speeds, the effect of feed on tool wear was found to be very little; tool wear was slightly higher when higher feeds were used.

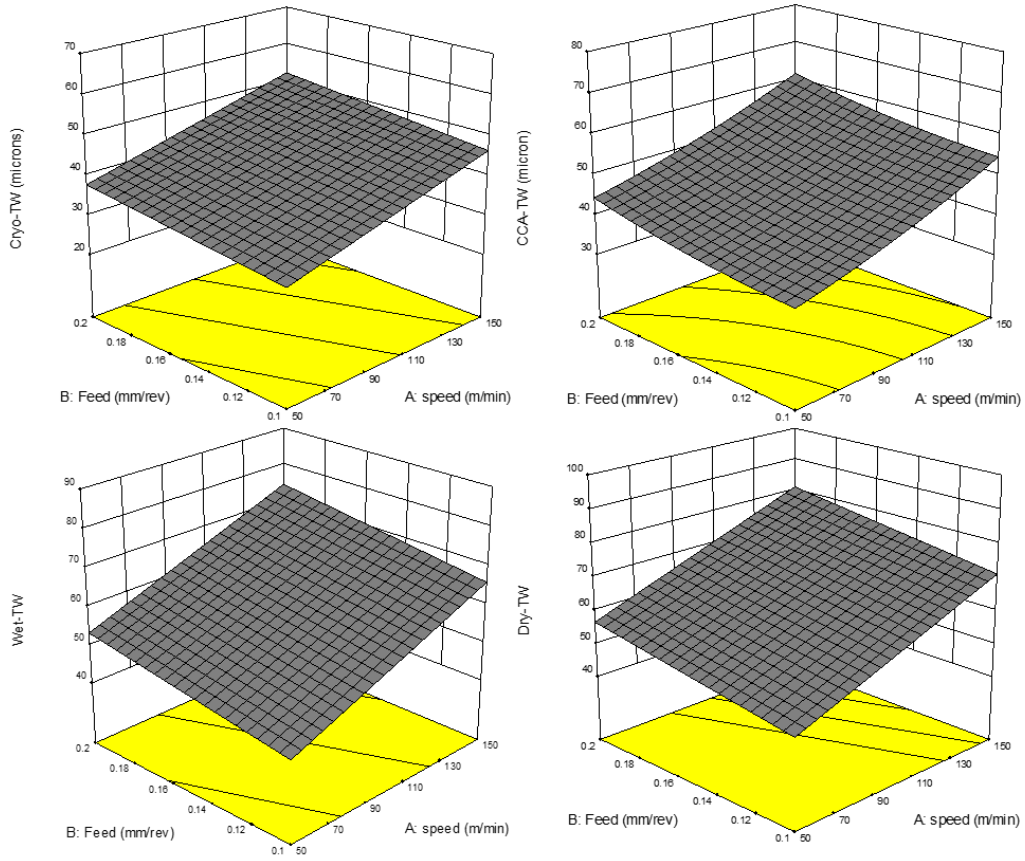

Fig. 7.20. combined effect of cutting speed and feed on tool wear at rake angle of 8°, nose radius of 0.8 mm and approach angle of 60° under (a) ALN spray (cryo) (b) CCA gas (c) Wet machining (d) Dry machining conditions.

7.3.2 Optimization using GA

A simple GA code was used in the present study to optimize the turning process using the experimental results and subsequently developed models as previously explained in section 7.3.1. The main objective of the current optimization can be described as minimization of surface roughness (SR), cutting force (CF) and tool wear (TW) individually to a criterion set of constraints (input variables). For effective results in the optimization of machining parameters, it is better to provide the actual values of the process parameters and for this purpose experimental machining study was carried out.

The constrained optimization problem is stated as follows:

(a) Atomized liquid nitrogen (ALN) spray assisted machining condition

$$\boldsymbol{ALN-CF} = +176.30994 + 0.20662 \times v_c + 218.91750 \times f - 10.74727 \times \gamma - 61.27431 \times r_e - 2.03894 \times \psi + 0.022990 \times \gamma \times \psi - 2.30636E-003 \times {v_f}^2 + 0.47325 \times \gamma^2 + 46.22403 \times {r_e}^2 + 0.014815 \times \psi^2 \quad (7.16)$$

$$\boldsymbol{ALN-SR} = +1.46609 - 1.41500E-003 \times v_c + 1.64875 \times f - 0.029323 \times \gamma - 1.19871 \times r_e - 8.07728E-003 \times \psi + 1.83417E-003 \times \gamma^2 + 0.42429 \times {r_e}^2 + 6.08003E-005 \times \psi^2 \quad (7.17)$$

$$\boldsymbol{ALN-TW} = +43.83004 + 0.14461 \times v_f + 59.04347 \times f - 4.30606 \times \gamma - 51.90842 \times r_e + 0.65669 \times \psi + 1.90723 \times \gamma \times r_e + 0.021044 \times \gamma \times \psi + 0.066085 \times \gamma^2 + 10.73708 \times {r_e}^2 - 6.06914E-003 \times \psi^2 \quad (7.18)$$

(b) Cryogenically chilled argon gas assisted machining

$$\boldsymbol{CCA-CF} = +148.78853 + 0.21449 \times v_f + 299.78250 \times f - 9.67980 \times \gamma + 23.74570 \times r_e - 1.63884 \times \psi - 2.81687E-003 \times {v_f}^2 + 0.50001 \times \gamma^2 + 0.012355 \times \psi^2 \quad (7.19)$$

$$\boldsymbol{CCA-SR} = +1.55415 - 1.89989E-003 \times v_f + 6.36891 \times f - 0.046164 \times \gamma - 1.90145 \times r_e + 8.58333E-004 \times \psi + 2.02500E-003 \times v_f \times r_e - 2.38750 \times f \times r_e + 0.025156 \times \gamma \times r_e - 1.22917E-004 \times \gamma \times \psi - 8.46303E-006 \times {v_f}^2 - 7.19636 \times f^2 + 1.63035E-003\gamma^2 + 0.66672 \times {r_e}^2 \quad (7.20)$$

$$\boldsymbol{CCA-TW} = +62.98600 + 0.069582 \times v_f - 77.46059 \times f - 4.63344 \times \gamma - 72.94812 \times r_e + 0.65581 \times \psi + 1.82953 \times \gamma \times r_e + 0.013212 \times \gamma \times \psi + 5.17402E-004 \times {v_f}^2 + 493.72854 \times f^2 + 0.11996 \times \gamma^2 + 37.15243 \times {r_e}^2 - 5.84613E-003 \times \psi^2 \quad (7.21)$$

(c) Wet machining condition

$$\boldsymbol{Wet - CF} = +157.72905 + 0.23452 \times v_f + 355.87875 \times f - 11.05438 \times \gamma + 66.75570 \times r_e - 1.91757 \times \psi + 0.032104 \times \gamma \times \psi - 0.49594 \times r_e \times \psi - 3.24409E - 003 \times {v_f}^2 + 0.48176 \times \gamma^2 + 0.014934 \times \psi^2 \quad (7.22)$$

$$\boldsymbol{Wet - SR} = +1.08190 - 1.76033E - 003 \times v_f + 8.87825 \times f - 0.024366 \times \gamma - 2.63916 \times r_e + 0.028651 \times \psi + 2.27500E - 003 \times v_f \times r_e - 2.65000 \times f \times r_e + 0.011953 \times \gamma \times r_e - 1.34233E - 005 \times {v_f}^2 - 11.52333 \times f^2 + 3.16797E - 004 \times \gamma^2 + 1.13141 \times {r_e}^2 - 2.29139E - 004 \times \psi^2 \quad (7.23)$$

$$\boldsymbol{Wet - TW} = +56.21556 + 0.21176 \times v_f + 86.45859 \times f - 4.05060 \times \gamma - 70.82567 \times r_e + 0.50425 \times \psi + 2.12625 \times \gamma \times r_e + 0.17128 \times r_e \times \psi + 0.11115 \times \gamma^2 + 21.40958 \times {r_e}^2 - 4.02886E - 003 \times \psi^2 \quad (7.24)$$

(d) Dry machining condition

$$\boldsymbol{Dry - CF} = +210.36932 + 0.12639 \times v_f + 422.67375 \times f - 11.12246 \times \gamma + 25.20836 \times r_e - 2.73124 \times \psi + 4.21367 \times \gamma \times \psi - 3.09396E - 003 \times {v_f}^2 + 0.47853 \times \gamma^2 + 0.019772 \times \psi^2 \quad (7.25)$$

$$\boldsymbol{Dry - SR} = +1.12029 - 7.84924E - 004 \times v_f + 10.68386 \times f - 0.028813 \times \gamma - 2.87780 \times r_e + 0.027371 \times \psi + 2.21250E - 003 v_f \times r_e - 2.57500 \times f \times r_e + 0.022031 \times \gamma \times r_e + 2.68750E - 003 \times r_e \times \psi - 1.93879E - 005 \times {v_f}^2 - 17.52121 \times f^2 + 1.13456 \times {r_e}^2 - 2.32189E - 004 \times \psi^2 \quad (7.26)$$

$$\boldsymbol{Dry - TW} = +109.71139 + 0.24447 \times v_f + 99.80962 \times f - 5.06283 \times \gamma - 54.31664 \times r_e - 1.34372 \times \psi + 0.022247 \times \gamma \times \psi + 0.22043 \times \gamma^2 + 32.84945 \times {r_e}^2 + 9.33812E - 003 \times \psi^2 \quad (7.27)$$

Subjected to

$$\begin{aligned} 50\ m/min \leq \quad & v_c \quad \leq 50\ m/min \\ 0.1mm/rev \leq \quad & f \quad \leq 0.2\ mm/rev \\ 0° \quad \leq \quad & \gamma \quad \leq \quad 16° \\ 0.4\ mm \quad \leq \quad & r_e \quad \leq \quad 1.2\ mm \\ 30° \quad \leq \quad & \psi \quad \leq \quad 95° \end{aligned}$$

$$x_{il} \leq x_i \leq x_{iu}$$

Where x_{il} and x_{iu} are the upper and lower bounds of process variables x_i. Where, x_1, x_2, x_3, x_4, x_5, are logarithmic transformation of cutting speed (v_c), feed (f), rake angle(γ), nose radius (r_e) and approach angle (ψ).

The following parameters have been selected to obtain optimal solutions with less computational efforts:

Population size	= 50
Population type	= Double vector
Creation function	= constrain dependent
Scaling function	= Rank
Selection operator	= Roulette wheel
Elite count	= 0.05*population size
Cross over fraction	= 0.8
Mutation function	= constrain dependent
Crossover function	= Single point operator
Maximum number of generations	= 500

The GA code was developed using MATLAB. This approach makes a binary coding system to represent the variables: cutting speed (v_c), feed (f), rake angle (γ), nose radius (r_e) and approach angle (ψ), i.e. each of these variables is represented by a ten-bit binary equivalent, limiting the total string length to forty. It is known as chromosome. The variables are represented as genes (substrings) in the chromosome. The randomly generated twenty such chromosomes (population size is 20), fulfilling the constraints on the variables,

are taken in each generation. The first generation is called initial population. Once the coding of variables has been done, then the actual decoded values for the variables are estimated.

Using the present generation of fifty chromosomes, fitness values are calculated by using the transformation equation. Out of these fifty fitness values, four are chosen using Roulette-Wheel selection scheme. The chromosomes corresponding to these four fitness values are taken as parents. Then the crossover and mutation reproduction methods are applied to generate fifty new chromosomes for next generation. This process of generating new population from the old population is called generation. Many such generations are run till the maximum number of generations is met or the average of four selected fitness values in each generation becomes steady. This ensures that the optimization of all the variables (cutting speed, feed, rake angle, nose radius and approach angle) is carried out simultaneously. The statistics is displayed at the end of all iterations.

7.3.2.1 Single objective optimization using GA

Optimization is carried out to optimize single response for each time. Minimization of cutting force, surface roughness and tool wear is performed. Table 7.3 shows some of the minimum values of various responses with respect to input machining ranges. It has been observed that 22^{nd} run i.e., cutting speed (100 m/min -150 m/min) feed (0.1 mm/rev -0.15 mm/rev), rake angle (8°-16°), nose radius (0.4 mm - 0.8 mm) and approach angle (60°- 90°) gives the lower cutting force value of 41.62 N under ALN spray condition. This confirms that higher cutting speed and lower feed give the lower cutting force value. It can be inferred that the optimum machining parameters slightly vary but they fall within the range under all machining conditions.

Table. 7.3. Output values of responses from GA program with respect to input machining parameters.

Runs	V_c	f	γ	r_e	ψ	ALN			CCA			Wet			Dry		
						CF	SR	TW	CF	SR	TW	CF	SR	TW	CF	SR	TW
	(m/min)	(mm/rev)	(deg)	(mm)	(deg)	(N)	(microns)	(microns)	(N)	(microns)	(microns)	(N)	(microns)	(microns)	(N)	(microns)	(microns)
1	50-100	0.1-0.15	0-8	0.4-0.8	30-60	61.84	0.4191	23.58	82.26	0.5995	30.26	95.64	0.6822	36.42	106.85	0.7231	46.76
2	50-100	0.1-0.15	0-8	0.4-0.8	60-90	61.74	0.4166	29.28	81.76	0.5958	33.86	95.57	0.7514	44.78	105.23	0.8226	46.71
3	***50-100***	***0.1-0.15***	***0-8***	***0.8-1.2***	***30-60***	62.71	0.2791	17.51	91.75	0.4358	30.27	110.44	0.5509	***33.91***	130.42	0.5669	46.74
4	50-100	0.1-0.15	0-8	0.8-1.2	60-90	62.61	0.2766	20.02	91.26	0.4346	33.87	109.26	0.6201	43.77	128.8	0.7205	46.68
5	***50-100***	***0.1-0.15***	***8-16***	***0.4-0.8***	***30-60***	60.13	0.4191	19.08	80.84	0.5913	***28.26***	94.6	0.6246	35.68	105.2	0.6336	46.71
6	50-100	0.1-0.15	8-16	0.4-0.8	60-90	60.11	0.4166	29.39	80.35	0.5772	33.84	94.59	0.6938	44.05	103.57	0.7331	46.68
7	***50-100***	***0.1-0.15***	***8-16***	***0.8-1.2***	***30-60***	61	0.2791	***17.11***	90.34	0.4383	28.75	109.4	0.5238	33.99	130.42	0.536	46.69
8	***50-100***	***0.1-0.15***	***8-16***	***0.8-1.2***	***60-90***	60.99	0.2766	25.88	89.85	0.4344	33.86	108.57	0.5931	43.72	128.8	0.6771	***46.65***
9	50-100	0.15-0.2	0-8	0.4-0.8	30-60	72.78	0.5015	26.53	97.24	0.7325	32.56	113.44	0.876	40.74	127.99	0.9353	51.75
10	50-100	0.15-0.2	0-8	0.4-0.8	60-90	72.68	0.499	32.23	96.75	0.7288	36.15	113.36	0.9453	49.11	126.36	1.0348	51.69
11	50-100	0.15-0.2	0-8	0.8-1.2	30-60	73.65	0.3615	20.46	106.74	0.521	32.57	128.24	0.6957	38.22	151.56	0.7286	51.73
12	50-100	0.15-0.2	0-8	0.8-1.2	60-90	73.56	0.359	22.97	106.25	0.5198	36.16	127.06	0.765	48.09	149.93	0.8905	51.67
13	50-100	0.15-0.2	8-16	0.4-0.8	30-60	71.08	0.5015	22.03	95.83	0.7243	30.57	112.39	0.8184	40.01	126.33	0.8458	51.71
14	50-100	0.15-0.2	8-16	0.4-0.8	60-90	71.06	0.499	32.34	95.34	0.7102	36.13	112.38	0.8877	48.36	124.71	0.9453	51.67
15	50-100	0.15-0.2	8-16	0.8-1.2	30-60	71.95	0.3615	20.06	105.33	0.5236	31.05	127.19	0.6743	38.31	151.55	0.7068	51.68
16	50-100	0.15-0.2	8-16	0.8-1.2	60-90	71.93	0.359	26.27	104.84	0.5197	36.16	126.37	0.7435	48.04	149.92	0.857	51.65
17	100-150	0.1-0.15	0-8	0.4-0.8	30-60	43.34	0.3484	30.81	57.77	0.4797	37.62	66.82	0.5173	47.01	74.5	0.53	58.98
18	***100-150***	***0.1-0.15***	***0-8***	***0.4-0.8***	***60-90***	43.24	0.3459	36.51	57.27	0.476	41.22	66.74	0.5866	55.36	***72.87***	0.6295	58.93
19	100-150	0.1-0.15	0-8	0.8-1.2	30-60	44.21	0.2083	24.74	67.27	0.3565	37.63	81.62	0.422	44.49	98.07	0.4122	58.96
20	100-150	0.1-0.15	0-8	0.8-1.2	60-90	44.11	0.2058	27.25	66.77	0.3553	41.23	80.44	0.4912	54.36	96.44	0.5579	58.91
21	***100-150***	***0.1-0.15***	***8-16***	***0.4-0.8***	***30-60***	41.64	0.3484	26.31	56.36	0.4715	35.63	***65.77***	0.4598	46.27	72.84	0.4405	58.94
22	***100-150***	***0.1-0.15***	***8-16***	***0.4-0.8***	***60-90***	***41.62***	0.3458	36.62	***55.86***	0.4574	41.21	***65.77***	0.529	54.63	71.22	0.54	58.91
23	***100-150***	***0.1-0.15***	***8-16***	***0.8-1.2***	***30-60***	42.5	0.2083	24.33	65.86	0.359	36.11	80.57	***0.3901***	44.58	98.06	***0.3726***	58.91
24	***100-150***	***0.1-0.15***	***8-16***	***0.8-1.2***	***60-90***	42.49	***0.2058***	30.55	65.36	***0.3552***	41.22	79.75	0.4594	54.31	96.44	0.5059	58.88
25	100-150	0.15-0.2	0-8	0.4-0.8	30-60	54.28	0.4308	33.76	72.76	0.6127	39.92	84.61	0.7112	51.33	95.63	0.7422	63.97
26	100-150	0.15-0.2	0-8	0.4-0.8	60-90	54.18	0.4283	39.46	72.26	0.609	43.51	84.54	0.7805	59.69	94.01	0.8417	63.92
27	100-150	0.15-0.2	0-8	0.8-1.2	30-60	55.16	0.2907	27.69	82.26	0.4417	39.93	99.41	0.5735	48.81	119.2	0.5792	63.95
28	100-150	0.15-0.2	0-8	0.8-1.2	60-90	55.06	0.2882	30.21	81.76	0.4405	43.53	98.23	0.6427	58.69	117.57	0.7341	63.91
29	100-150	0.15-0.2	8-16	0.4-0.8	30-60	52.58	0.4308	29.26	71.35	0.6045	37.92	83.57	0.6536	50.59	93.98	0.6527	63.93
30	100-150	0.15-0.2	8-16	0.4-0.8	60-90	52.56	0.4283	39.57	70.85	0.5904	43.49	83.56	0.7229	58.95	92.36	0.7522	63.89
31	100-150	0.15-0.2	8-16	0.8-1.2	30-60	53.45	0.2907	27.29	80.85	0.4443	38.41	98.37	0.5472	48.91	119.2	0.5497	63.91
32	100-150	0.15-0.2	8-16	0.8-1.2	60-90	53.43	0.2882	33.51	80.35	0.4404	43.52	97.54	0.6165	58.63	117.57	0.692	63.873

The minimum value of surface roughness was observed at 24th run (i.e., cutting speed (100 m/min -150 m/min), feed (0.1 mm/rev -0.15 mm/rev), rake angle (8° -16°), nose radius (0.8 mm-1.2 mm), approach angle (60° - 90°) under ALN spray and CCA gas assisted machining condition whereas under wet and dry machining, optimum value of surface roughness has been observed at 23rd run at same cutting speed, feed, rake angle and nose radius ranges as ALN spray and CCA gas but approach angle range has varied to 30° - 60°. Further, analysis discloses that the minimized values of tool wear were observed at 7th, 5th, 3rd, and 8th run under ALN spray, CCA gas, wet and dry machining environments respectively. At the same range of cutting speed 50 -100 m/min, feed 0.1 - 0.15 mm/rev, lower tool wear was observed under all machining conditions. This optimization methodology could obtain the minimum possible response with the given constraints and also identify the conditions at which this minimum occurs. The optimum combination of input parameters at which the turning operation has to be carried out in order to get minimum values of cutting force. surface roughness and tool wear under all selected machining environments is present in Table B.22 – B.27 (APENDIX-B).

The above results determine the range of input machining parameters that provide minimum response value. This helps to crosscheck global minimum values obtained in GA. The optimization process with GA has been carried out for all the fitness functions. The obtained global minimum value along with optimum machining parameters for each objective is tabulated in Table 7.4. The best fitness plot for cutting force under various environments is presented in Fig. 7.21. Optimal solution is obtained at 189th generation for ALN spray, 214th generation for CCA gas, 176th generation for wet and 228th generation for dry (iteration) of GA algorithm.

Table 7.4. Optimum value of machining parameters predicted by GA correspondent to minimized responses.

Machining conditions	machining parameters (lower bound-upper bound)					Minimum response	optimum machining parameters				
	V_c (m/min)	f (mm/rev)	γ (deg)	r_e (mm)	ψ (deg)		V_c (m/min)	f (mm/rev)	γ (deg)	r_e (mm)	ψ (deg)
ALN-SR	50-150	0.1-0.2	0-16	0.4-1.2	30-90	0.206	150	0.1	7.99	1.2	66.4
CCA-SR	50-150	0.1-0.2	0-16	0.4-1.2	30-90	0.355	150	0.1	8.29	1.2	90
Wet-SR	50-150	0.1-0.2	0-16	0.4-1.2	30-90	0.373	150	0.1	16	1.05	30
Dry-SR	50-150	0.1-0.2	0-16	0.4-1.2	30-90	0.390	150	0.1	16	1.05	30
ALN-TW	50-150	0.1-0.2	0-16	0.4-1.2	30-90	17.11	50	0.1	10.46	1.2	30
CCA-TW	50-150	0.1-0.2	0-16	0.4-1.2	30-90	28.26	50	0.1	12.5	0.67	30
Wet-TW	50-150	0.1-0.2	0-16	0.4-1.2	30-90	33.91	50	0.1	6.76	1.19	30
Dry-TW	50-150	0.1-0.2	0-16	0.4-1.2	30-90	46.66	50	0.1	8.36	0.83	61.9
ALN-CF	50-150	0.1-0.2	0-16	0.4-1.2	30-90	46.15	150	0.1	9.87	0.66	61.2
CCA-CF	50-150	0.1-0.2	0-16	0.4-1.2	30-90	55.86	150	0.1	9.86	0.4	66.3
Wet-CF	50-150	0.1-0.2	0-16	0.4-1.2	30-90	65.76	150	0.1	9.451	0.4	60.7
Dry-CF	50-150	0.1-0.2	0-16	0.4-1.2	30-90	71.21	150	0.1	9.861	0.4	69.1

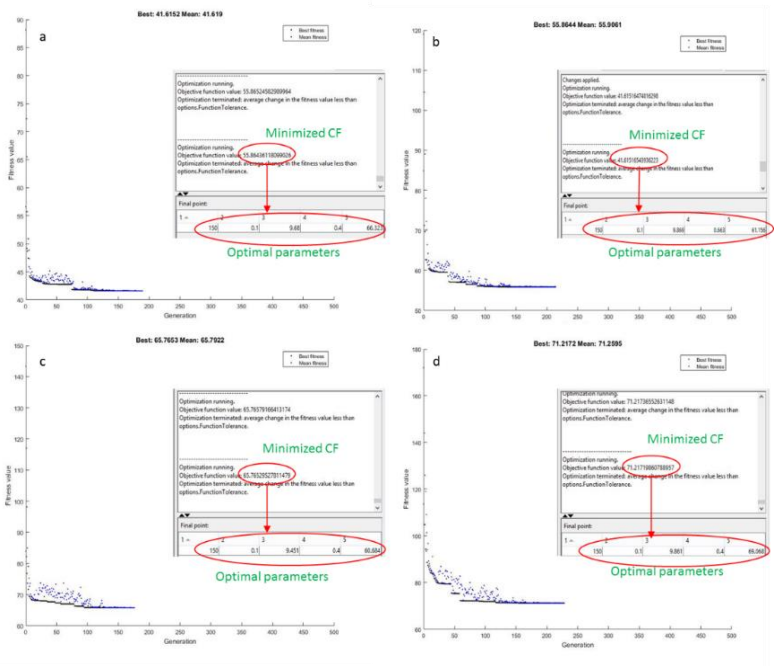

Fig. 7.21. Plot function of cutting force for best fitness under (a) ALN spray (b) CCA gas (C) Wet machining and (d) Dry machining.

The set of machining parameters that led to minimum surface roughness value are given in Table 7.4. The best fitness plot for surface roughness under various environments has been presented in Fig. 7.22. Optimal solution was obtained at 173rd generation for ALN spray, 169th generation for CCA gas, 161th generation for wet and 105th generation for dry (iteration) of GA algorithm.

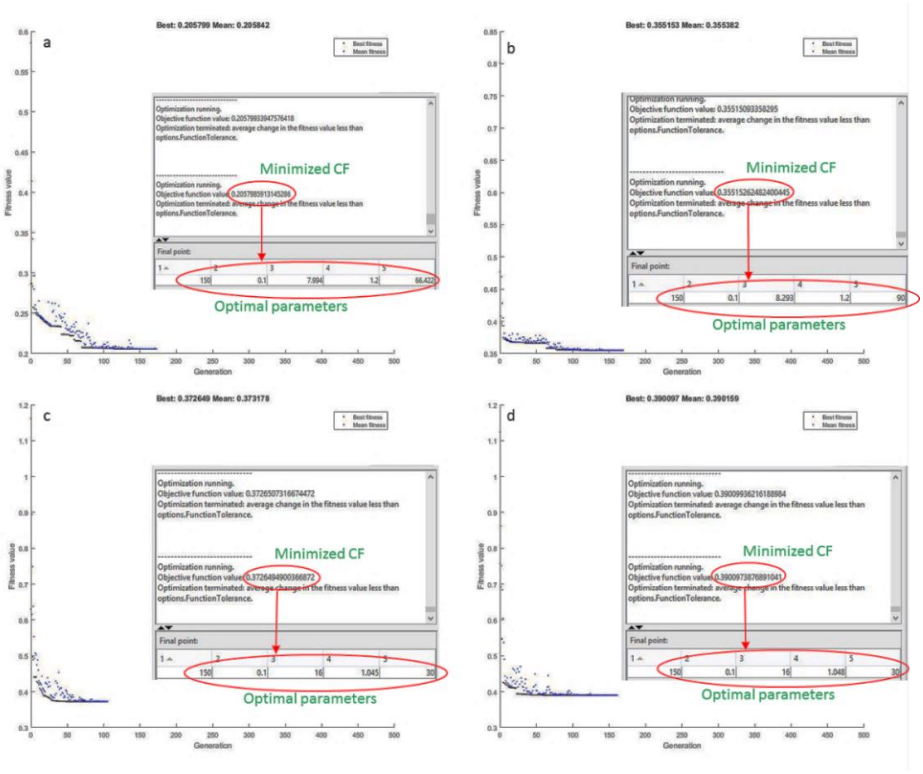

Fig. 7.22. Plot function of surface roughness for best fitness under (a) ALN spray (b) CCA gas (C) Wet machining and (d) Dry machining.

The set of machining parameters that led to minimum tool wear value are given in Table 7.4. The best fitness plot for tool wear under various environments is presented in Fig. 7.23. Optimal solution is obtained at 172nd generation for atomized LN_2 spray, 181th generation for CCA gas, 194th generation for wet and 168th generation for dry (iteration) of GA algorithm.

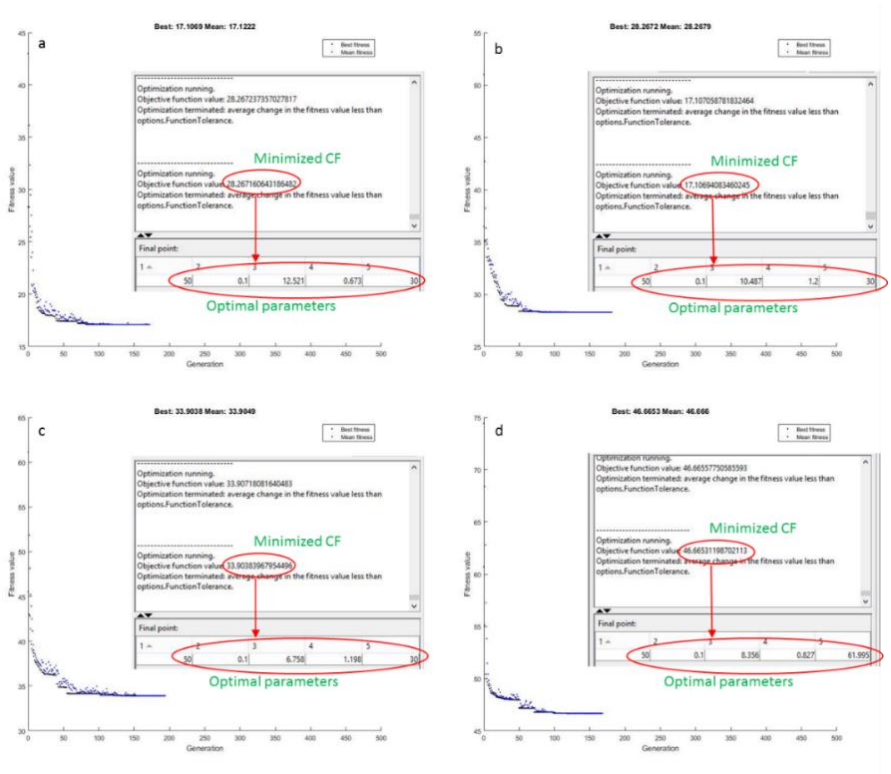

Fig. 7.23. Plot function of tool wear for best fitness under (a) ALN spray (b) CCA gas (C) Wet machining and (d) Dry machining.

7.3.2.2 Multi objective optimization using GA

The optimization results of GA program presented in previous section suggest that it is possible to select a combination of cutting speed, feed, rake angle, nose radius and approach angle for achieving the required response value. But when equal importance is given to all the three responses, the above analysis is not adequate to arrive at an optimum value. Hence multi objective optimization technique has been carried out to determine the optimal machining parameters at which minimized responses are obtained. Multi objective optimization using GA in MATLAB uses a controlled, elitist genetic algorithm (a variant of NSGA-II [202]). An elitist GA always favors individuals with better fitness value (rank). A controlled elitist GA also favors individuals that can help increase the diversity of the population even if they have a

lower fitness value. It always attempts to create a set of pareto optima for a multi objective minimization. The aim of the present study is to minimize cutting force, surface roughness and tool wear to determine the optimum machining conditions. The multi objective optimization process was carried out with same regression equations which has been used to study each objective independently at each machining condition. The following parameters have been selected to obtain optimal solution with less computation efforts:

Population size	=	50
Population type	=	Double vector
Selection function	=	tournament
Tournament size	=	4
Cross over probability (P_c)	=	0.8
Mutation function	=	constrain dependent
Crossover function	=	heuristic
Cross over function ratio	=	1.2
Migration	=	Forward
Maximum number of generations	=	500

GA multi objective helps to find the local pareto front for multiple objective functions. It works on a population using a set of operators that are applied to the population. Initial population has been generated randomly and the generations of the population are computed using the non-dominated rank and a distance measure of the individual in current generation. The non-dominated rank is assigned to each individual using the relative fitness and the distance measure of an individual is used to compare the individual with equal rank. This forces the GA to uniformly cover the frontier rather than bunching up at several good points by trying to keep population diversity. The algorithm stops if the spread, a measure of movement of the praetor front is small.

The procedure was repeated ten times to get a greater number in pareto solution set. The corresponding objective function values and decision variables of this GA solution set are given in Table 7.5 and 7.6. The 20 out of 50 sets were presented since none of the solutions in the GA set is absolutely better than any other; any one of them is an acceptable solution. The choice of one solution over the other depends on the requirement of the process engineer. If a better surface finish or a lower tool wear is required, a suitable combination of variables can be selected under each machining environments. The GA solution set obtained over the entire optimization process under various machining environments is shown in Fig. 7.24 This shows the formation of the Pareto front leading to the final set of solutions.

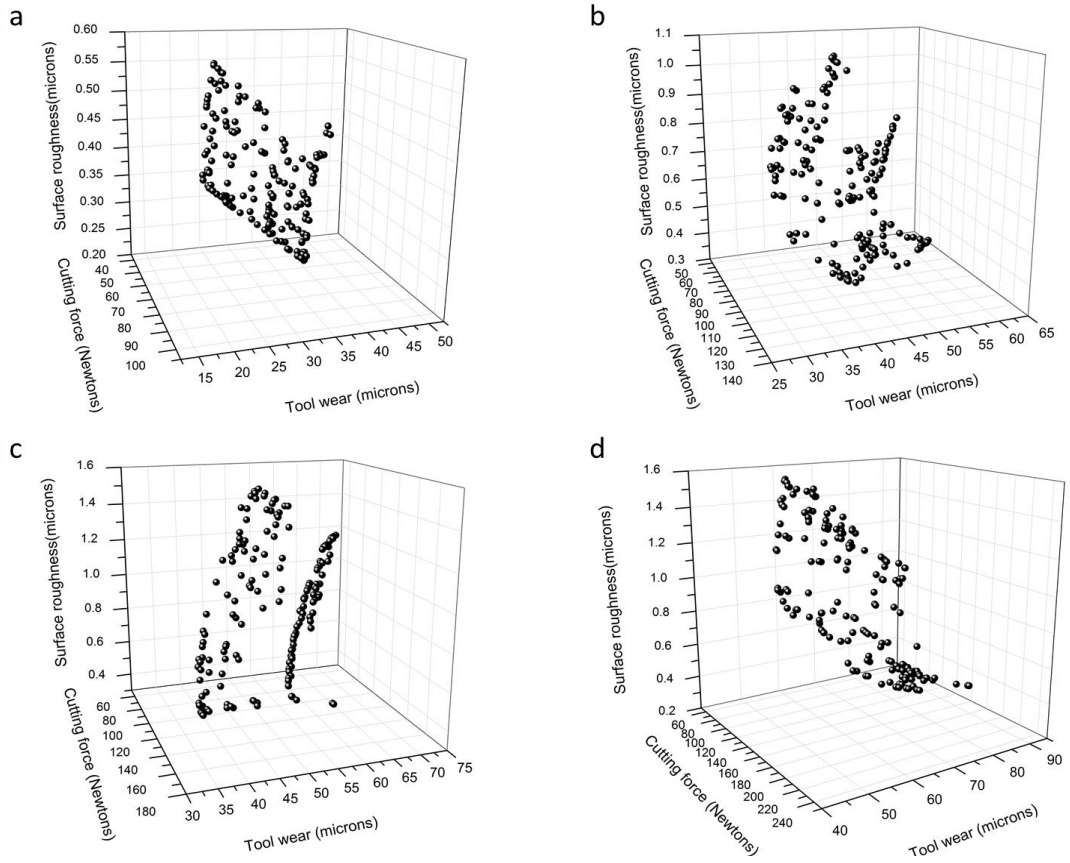

Fig. 7.24. 3D paretor front graph for cutting force surface roughness and tool wear under (a) ALN spray, (b) CCA gas, (c) Wet and (d) Dry machining condition.

Table 7.5 Optimal combinations of machining parameters for machining of Al-TiC_p composites under ALN spray and CCA gas assisted machining.

	ALN								CCA							
S.no	CF	TW	SR	V_c	f	γ	r_e	ψ	CF	TW	SR	V_c	f	γ	r_e	ψ
	N	µm	µm	m/min	mm/rev	deg	mm	deg	N	µm	µm	m/min	mm/rev	deg	mm	deg
1	94.56	17.12	0.439	50.04	0.1	10.41	1.2	30	118.42	28.29	0.787	50.01	0.1	12.74	0.68	30.01
2	94.93	17.16	0.433	50.04	0.1	9.72	1.2	30	118.41	28.29	0.787	50.01	0.1	12.74	0.68	30.02
3	94.15	17.29	0.436	50.10	0.1	9.72	1.18	30.01	115.05	28.62	0.746	50.01	0.1	10.68	0.72	30.03
4	97.78	17.53	0.428	50.08	0.1	8.01	1.2	30	113.18	28.86	0.815	50.01	0.1	10.67	0.64	30.02
5	94.07	17.68	0.432	52.78	0.1	9.72	1.18	30.01	112.06	29.21	0.866	50.01	0.1	10.91	0.58	30.15
6	91.26	17.86	0.455	50.07	0.1	11.18	1.14	30.75	111.78	29.37	0.866	50.01	0.1	10.65	0.58	30.15
7	93.40	17.94	0.428	50.08	0.1	9.87	1.2	31.61	111.49	29.49	0.885	50.01	0.1	10.67	0.57	30.02
8	97.42	17.99	0.425	52.78	0.1	8.01	1.19	30	112.69	29.82	0.793	58.18	0.1	10.68	0.65	30.02
9	96.82	18.04	0.423	50.06	0.1	7.97	1.2	31.11	112.45	29.89	0.802	58.23	0.1	10.67	0.64	30.02
10	96.82	18.05	0.423	50.11	0.1	7.97	1.2	31.11	113.72	30.01	0.736	58.19	0.1	9.96	0.71	30.11
11	92.66	18.22	0.426	50.13	0.1	9.74	1.19	32.02	110.38	30.08	0.932	50.01	0.1	10.67	0.52	30.02
12	90.77	18.28	0.442	50.13	0.1	10.39	1.15	31.61	110.72	30.52	0.871	58.23	0.1	10.67	0.57	30.02
13	95.81	18.42	0.419	50.04	0.1	8.04	1.2	32.02	109.53	30.67	0.97	50.01	0.1	10.65	0.49	30.03
14	91.62	18.67	0.424	50.10	0.1	9.72	1.18	32.88	112.94	30.90	0.728	64.18	0.1	9.72	0.71	30.03
15	95.12	18.81	0.416	50.13	0.1	8.01	1.2	32.88	108.96	31.14	1.012	50.01	0.1	10.91	0.45	30.03
16	89.17	19.02	0.437	50.11	0.1	10.20	1.14	32.91	116.03	31.21	0.618	50.01	0.1	10.18	0.89	33.39
17	84.66	19.38	0.537	50.11	0.1	12.05	0.92	30.72	108.00	31.24	0.91	50.01	0.1	10.67	0.54	33.39
18	84.30	19.52	0.544	50.10	0.1	12.03	0.91	30.72	108.61	31.64	0.852	58.23	0.1	10.91	0.58	33.39
19	90.12	19.63	0.414	50.06	0.1	9.87	1.19	35.21	117.37	31.77	0.599	50.01	0.1	10.68	0.93	33.39
20	86.22	19.81	0.462	52.78	0.1	10.20	1.05	32.03	120.58	31.96	0.588	58.19	0.104	8.74	0.94	30.12

Table 7.6 Optimal combinations of machining parameters for machining of Al-TiC_p composites under wet and dry machining.

S.no	Wet								Dry							
	CF	TW	SR	V_c	f	γ	r_e	ψ	CF	TW	SR	V_c	f	γ	r_e	ψ
	N	µm	µm	m/min	mm/rev	deg	mm	deg	N	µm	µm	m/min	mm/rev	deg	mm	deg
1	118.42	28.29	0.787	50.01	0.1	12.74	0.68	30.01	147.91	46.70	1.063	50.01	0.1	8.34	0.82	30.02
2	118.41	28.29	0.787	50.01	0.1	12.74	0.68	30.02	147.99	47.56	1.043	50.99	0.1	9.30	0.83	30.06
3	115.05	28.62	0.746	50.01	0.1	10.68	0.72	30.03	137.97	47.86	1.204	50.01	0.1	8.34	0.67	30.01
4	113.18	28.86	0.815	50.01	0.1	10.67	0.64	30.02	154.48	48.12	1.008	50.01	0.1	10.87	0.86	30.02
5	112.06	29.21	0.866	50.01	0.1	10.91	0.58	30.15	141.13	48.17	1.157	50.01	0.101	9.83	0.70	30.52
6	111.78	29.37	0.866	50.01	0.1	10.65	0.58	30.15	135.52	48.39	1.293	50.01	0.101	8.32	0.61	30.52
7	111.49	29.49	0.885	50.01	0.1	10.67	0.57	30.02	133.50	48.77	1.307	50.26	0.1	8.09	0.59	30.20
8	112.69	29.82	0.793	58.18	0.1	10.68	0.65	30.02	130.53	49.57	1.367	50.01	0.101	8.44	0.54	30.02
9	112.45	29.89	0.802	58.23	0.1	10.67	0.64	30.02	146.19	49.61	1.034	59.37	0.1	9.30	0.83	30.02
10	113.72	30.01	0.736	58.19	0.1	9.96	0.71	30.11	166.37	49.93	0.92	50.51	0.101	9.30	1.11	30.12
11	110.38	30.08	0.932	50.01	0.1	10.67	0.52	30.02	129.48	50.09	1.416	50.01	0.101	8.84	0.51	30.21
12	110.72	30.52	0.871	58.23	0.1	10.67	0.57	30.02	166.98	50.18	0.919	50.01	0.1	8.57	1.14	30.42
13	109.53	30.67	0.97	50.01	0.1	10.65	0.49	30.03	132.90	50.63	1.277	59.37	0.1	8.32	0.60	30.53
14	112.94	30.90	0.728	64.18	0.1	9.72	0.71	30.03	132.77	50.64	1.274	59.37	0.1	8.57	0.60	30.53
15	108.96	31.14	1.012	50.01	0.1	10.91	0.45	30.03	126.80	50.90	1.461	50.01	0.101	8.34	0.48	30.23
16	116.03	31.21	0.618	50.01	0.1	10.18	0.89	33.39	145.44	51.00	1.019	64.67	0.1	9.34	0.83	33.09
17	108.00	31.24	0.91	50.01	0.1	10.67	0.54	33.39	126.27	51.23	1.433	50.01	0.1	9.32	0.49	33.09
18	108.61	31.64	0.852	58.23	0.1	10.91	0.58	33.39	132.14	51.24	1.25	59.12	0.1	9.30	0.61	33.09
19	117.37	31.77	0.599	50.01	0.1	10.68	0.93	33.39	123.84	52.16	1.571	50.01	0.1	8.34	0.42	33.09
20	120.58	31.96	0.588	58.19	0.104	8.74	0.94	30.12	128.25	52.35	1.387	50.01	0.1	10.96	0.50	30.02

By using GA, minimized tool wear values were found to be 17.1175, 28.2850, 33.921 and 46.669 μm, under, ALN spray, CCA gas, wet and dry machining conditions respectively. The corresponding cutting forces are at higher side and surface roughness values at lower side. However, the values of rake angle, nose radius approach angle in the optimal solution are not standard and thus cannot be practically implemented. So, the values of rake angle nose radius and approach angle are updated to the nearest standard values and accordingly the optimization has been carried out for cutting speed and feed in order to achieve minimum surface finish.

It can be concluded from the GA optimization results that it is possible to select a combination of cutting speed, feed, rake angle, nose radius and approach angle for achieving the lower cutting force, minimized surface roughness and lower tool wear under various machining environments. This GA program provides optimum machining conditions for corresponding minimum values of responses. With the known boundaries of responses and machining conditions, machining could be performed with a relatively high rate of success under all the selected machining environments. This has validated the trends available in the literature, and extended the data range to the present operating conditions, apart from improving the accuracy and modelling by involving the most recent modelling method. The application of the GA approach to obtain optimal machining conditions will be quite useful at the Computer Aided Process Planning (CAPP) stages in the production of high quality goods with tight tolerances by a variety of machining operations, and in adaptive control of automated machine tools. Predictive capability of this methodology using GA could also be employed for automatic monitoring of machining processes.

7.4 Summary

Statistical analysis of experimental results was carried out using ANOVA to determine the significant parameters which affect the performance effectively. Further,

ANOVA helps to test the adequacy of the developed models for establishing the mathematical link between the machinability performance parameters and the cutting parameters of turning process. A regression equation was developed with the help of experimental results based of the selected model. The satisfactoriness of the selected model was tested statistically by studying normal probability and residual plots. Further, effect of machining parameters on response is studied by perturbation plots and 3D surface plots. The above developed mathematical relation was used as an objective function for optimization of process parameters in turning using GA which help to determine the optimum conditions for machining under each response. But in real time, optimum conditions for multiple responses are needed for manufacturing to achieve certain surface finish. Therefore, multi objective optimization process has been performed using GA. Optimum values of cutting speed, feed rake angle nose radius and approach angle were found out to simultaneously minimize the surface roughness, cutting force and tool wear. Optimization of this model by GAs has resulted in a fairly useful method of obtaining process parameters in order to attain to improve the machinability performance of Al-TiC_p composites.

In order to understand the turning of Al-TiC_p composite, modelling and optimization study has been performed successfully. In order to improve the efficiency and quality of machining process before resorting to costly and time consuming experimental trials, simulation of metal cutting process was performed using finite element method (FEM). However, modeling of composite machining is difficult due to its unique composition and structure which is inhomogeneous and anisotropic. Therefore, in the following chapter an attempt has been made to perform machining of composites using ABAQUS.

Chapter 8
Finite Element Modelling of Machining Al-TiC_p MMCs

Finite element (FE) analysis in manufacturing field reduces both manufacturing cost and time. In the current research work, a microscopic finite element analysis has been carried to simulate the machining of particulate-reinforced MMC. The results of this analysis have been validated by comparing with experimental data. The current chapter is organized as follows: Section 8.1 presents a brief introduction to importance of FE modelling. Section 8.2 gives detailed information about modeling of particulate-reinforced MMC and various steps involved in simulation of its machining using ABAQUS 6.14. The developed FE modeling approach has been validated with the cutting experiments and the same is discussed in section 8.3. Finally, Section 8.4 presents outcome of this chapter in brief.

8.1 Introduction

Finite element modeling is a most powerful numerical technique applied by various researchers to comprehend the mechanics of machining process. FE analysis gives more importance to material properties and non-linearity than analytical models, thereby, predicting results with higher accuracy. FE modeling of machining MMCs can be performed using two different approaches, namely equivalent homogenous approach and microscopic approach [11]. Equivalent homogenous approach does not predict the local damages at the particle-matrix interface, whereas microscopic finite element analysis captures the behavior of the composite material during machining [203, 204]. However, simulation of a microscopic model is still challenging due to the severe mesh distortion, and is also very time-consuming. To overcome the above-mentioned challenges, a finite

element model for machining of MMCs has been developed to simulate and predict the accurate chip morphology, cutting force and temperature while machining of MMC under varied cutting conditions.

A 2D FE modeling approach was used to perform orthogonal machining of metal matrix using ABAQUS commercial FEM software [205]. The workpiece material MMC has been modeled at a microscopic level consisting of matrix and particles. A dynamic temperature-displacement type model has been employed to study the effect of stress, strain and machining temperature on material behavior. Various studies have been performed to investigate the effect of mesh size, damage evolution energy, coefficient of friction and other input parameters on the numerical results. The results of finite element analysis will be validated through comparison with experimental data. The developed FE model helps to comprehend the actual behavior of MMCs during machining process with the interactions between the tool/particles, the tool/matrix, and particles/matrix. Chip morphology, cutting force and machining temperature are considered as measuring indices to validate the developed model.

8.2 Methodology

Finite element code for modeling of machining MMCs was developed using ABAQUS. ABAQUS is a general-purpose FE software, hence, designer has to model the tool and the workpiece separately and also specify the process parameters, material properties, boundary conditions and mesh geometry for simulation controls. This certainly requires more skill, effort and time to setup the simulation. However, this feature provides flexibility for the designer to have a complete control over simulation and ensures a thorough analysis. FE modeling takes place in three stages – preprocessing, analysis and post processing. In ABAQUS, these three stages are divided into functional units called modules, with each module designed to serve a specific task.

8.2.1 Workpiece and tool modeling (Part module)

In the present study, a two-dimensional deformable microscale MMC and tool were modeled in part module. Matrix and reinforcement phases of MMC are modeled separately in the workpiece with distinct boundary geometries, as shown in Fig. 8.1. Lagrangian technique was employed to model the MMC as it helps to simulate the nature of non-plastic reinforcements and its interaction behavior with plastic matrix. Shared node method was employed to model the interface of matrix and reinforcements. It was assumed that particles are perfectly bonded and fracture of the matrix material surrounding the reinforcement is responsible for the debonding and failure of particles. Chip is formed by element deletion method using two approaches i.e., with and without separation layer. In model without separation layer, damage failure criteria were assigned to whole workpiece whereas for model with separated layer, damage failure criteria were assigned to the elements in the scarifying layer.

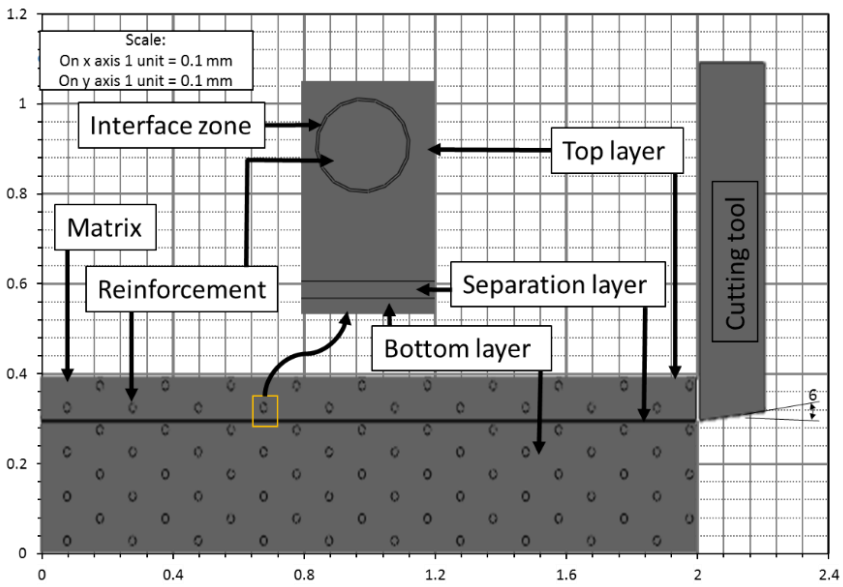

Fig. 8.1. Model of MMCs and its dimensions used for cutting simulations.

A separation layer of elements is defined along the cutting path in order to simulate chip separation using progressive damage model. This layer consists of elements which will be deleted as soon as damage accumulation in the material reaches the maximum value

and material fracture occurs. Fig. 8.1. shows the damage zone of thickness 0.01 mm, which is computationally acceptable. It is assumed that TiC particles are round in shape, are perfectly bonded and uniformly distributed throughout the matrix. Chip separation criteria has been incorporated in the FEM machining process to analysis chip formation.

Table 8.1. Thermal and mechanical properties of the workpiece and the cutting tool materials. [139]

Physical properties	**Matrix Al 6061**	**Reinforcement TiC particles**	**Tool (Tungsten Carbide)**
Density (ρ) (kg/m3)	2700	4900	11900
Young's modulus (E) (GPa)	68.9	439.4	534
Poisson ratio (ν)	0.33	0.191	0.22
Coefficient of thermal expansion (α) (μm.m/˚C)	2.34E-5	7.6E-6	
Thermal conductivity (k) (W/m˚C)	167	21	40.15
Specific heat (C_p) (J/kg˚C)	896	565	346

8.2.2 Material flow modeling (Properties module)

In order to attain the actual behavior of MMCs during machining simulation, the material properties for matrix, reinforcements are included in the model separately. The mechanical and thermal properties of the workpiece and cutting tool material are included in Table 8.1. For problem simplification, tool and TiC particles are assumed to be isotropic elastic material without considering failure. Matrix material was modeled as elastic–plastic model in ABAQUS/Explicit.

8.2.3 Material flow

Matrix material is modeled using Johnson-Cook (J-C) thermal- elastic-plastic constitutive model to predict the post-yield of Al6061-T6 matrix [139]. This model is frequently adopted for dynamic problems with high strain rates and temperature effects which are common characteristics of the cutting process. The equivalent plastic flow stress

is presented in Eq. 8.1. The basic form of J-C model for Von-Mises flow stress $\bar{\sigma}$, is provided by

$$\bar{\sigma} = (A + B\bar{\varepsilon}^{n})\left[1 + C\ln\left(\frac{\dot{\bar{\varepsilon}}}{\dot{\bar{\varepsilon}}_0}\right)\right]\left[1 - \left(\frac{\theta-\theta_{transition}}{\theta_{melt}-\theta_{transition}}\right)^{m}\right] \quad (8.1)$$

Where, 'A', 'B' and 'n' are material constants for strain hardening; 'C' is the material constant for strain-rate hardening; m is the material constant for thermal softening effect; '$\theta_{transition}$' is the reference room ambient temperature; 'θ_{melt}' is the melting temperature of the workpiece material and 'θ' is the current process temperature; $\bar{\varepsilon}$ is equivalent plastic strain; '$\dot{\bar{\varepsilon}}$' is plastic strain rate; '$\dot{\bar{\varepsilon}}_0$' is reference strain rate.

The material constants are determined using torsion test, static tensile tests, and dynamic Hopkinson bar tensile tests over a wide range of strain rates and temperatures. The J-C flow model parameters for Al6061-T6 is presented in Table 8.2

Table 8.2. Johnson-Cook material properties for Al6061 aluminum matrix. [139] [206].

A	B	n	C	m	$\theta_{transition}$	θ_{melt}	$\dot{\bar{\varepsilon}}$
324	114	0.42	0.002	1.34	582	25	1

8.2.4 Chip separation criteria

A failure model is also incorporated as a chip separation criterion along with the material model in the damage zone in order to simulate the chip formation in FEA cutting process. Johnson- Cook's model for progressive damage and fracture is used to model the Element deletion in scarifying layer [137, 207]. The damage criterion was modeled in ABAQUS/Explicit for each element and is defined by

$$D = \sum\left(\frac{\Delta\bar{\varepsilon}}{\bar{\varepsilon}_f}\right) \quad (8.2)$$

Where, '$\Delta\bar{\varepsilon}$' is increment of the equivalent plastic strain and '$\bar{\varepsilon}_f$' is equivalent stain at failure. 'D' is the damage parameter in the element [137]. Fractured element will be

deleted when the damage parameter exceeds unity. As per J-C damage model, $\Delta\bar{\varepsilon}$ updated at every load step and equivalent strain failure $\bar{\varepsilon}_f$ is stated by following expression

$$\bar{\varepsilon}_f = \left[D_1 + D_2 exp\left(D_3 \frac{P}{\bar{\sigma}}\right)\right]\left[1 + D_4 \ln\left(\frac{\dot{\bar{\varepsilon}}}{\dot{\bar{\varepsilon}}_0}\right)\right]\left[1 - D_5\left(\frac{\theta - \theta_{transition}}{\theta_{melt} - \theta_{transition}}\right)\right] \quad (8.3)$$

Where, 'D_1', 'D_2', 'D_3', 'D_4', and 'D_5', are material damage constants, '$\theta_{transition}$' is the reference room ambient temperature, 'θ_{melt}' is the melting temperature of the workpiece material and 'θ' is the current process temperature. '$\frac{P}{\bar{\sigma}}$' is ratio of pressure stress to von Mises stress, '$\dot{\bar{\varepsilon}}$' is plastic strain rate and '$\dot{\bar{\varepsilon}}_0$' is the reference strain rate.

The material damage constants were determined by tensile and torsion tests. It is known that front of the cutting tool experiences maximum stress and strain during machining. Since damage model is defined particularly in the damage zone, as the plastic strain increases, 'D' of the elements in the damage zone gradually reaches the damage initiation criterion threshold. J-C damage model constants for Al 6061 are provided in Table 8.3

Table 8.3. Johnson-Cook failure constants. [113]

D_1	D_2	D_3	D_4	D_5	$\theta_{transition}$	θ_{melt}
-0.77	1.45	-0.47	0.0	1.60	582	25

8.2.5 Damage evolution

J-C failure model is used here as a damage initiation criterion, instead of as a failure criterion in a Pure J-C model. Namely, the damage in a given element is initiated when a scalar damage parameter (similar to 'D' in Equation (2)) exceeds unity, based on a cumulative evolution law and is defined by Eq. 8.4.

$$\bar{u}^p = L_e \bar{\varepsilon} \quad (8.4)$$

Where, 'L_e' is length of element and '$\bar{\varepsilon}$' is equivalent plastic strain.

If a linear evolution of the damage variable with plastic displacement is assumed, then the damage variable increases as follows:

$$D = \frac{L_e \bar{\varepsilon}}{\bar{u}^p{}_f} = \frac{\bar{u}^p}{\bar{u}^p{}_f} \tag{8.5}$$

$$\bar{u}^p{}_f = \frac{2G_f}{\bar{\sigma}} \tag{8.6}$$

Where, '$\bar{u}^p{}_f$' is the plastic displacement at failure, 'G_f' is the fracture energy per unit area. and '$\bar{\sigma}$' is the von Mises stress.

The above model ensures that the energy dissipated during the damage evolution process is equal to 'G_f' only if the effective response of the material is perfectly plastic (constant yield stress) beyond the onset of damage by Eq 8.7. In this study, for the plane strain condition, 'G_f' is given as an input parameter which is a function of fracture toughness 'K_C', Young's modulus 'E' and Poisson's ratio 'ν'. The analysis is carried out with a damage evolution value of 10.87 MPa/mm^2.

$$G_f = \left[\frac{1-\upsilon^2}{E}\right] K_c^2 \tag{8.7}$$

The ELEMENT DELETION = YES module in ABAQUS 6.14–4 software along with the Johnson–Cook damage model of the software are used to delete the elements that failed. This produces the chip separation and allows the cutting tool to penetrate further into the workpiece through a predefined path (damage zone).

8.2.6 Explicit dynamic analysis (Step module)

In the present study, dynamic temperature-displacement procedure is used to simulate machining process. FE analysis causes larger computation cost due to severe deformation and dislocation of matrix elements resulting in smaller increments of time. Implementation of mass scaling option in ABAQUS Explicit can significantly reduce the computational time and retain the accuracy to a great extent. FE machining modeling was

carried out for period of 0.002 sec with a mass scaling factor of 3000. Excessive mesh distortion is higher during machining MMC simulation. In order to overcome this problem, Arbitrary Lagrangian-Eulerian (ALE) adaptive meshing technique is employed. As workpiece undergoes large deformation, the mesh is modified to prevent excessive element distortion and conserve the quality of the mesh. In this technique, the mesh in a region is allowed to move independently of the underlying material, but, ALE adaptive meshing technique does not alter the elements and connectivity between them (i.e. mesh topology).

In the present study volume, smoothing algorithm is used to perform meshing and smoothing. In volume smoothing, for each node, the new location is calculated by obtaining the volume-weighted average of the centers of the elements surrounding the node. Mesh predictors are determined by position from previous ALE adaptive mesh increments.

8.2.7 Tool chip interface modeling (Interaction module)

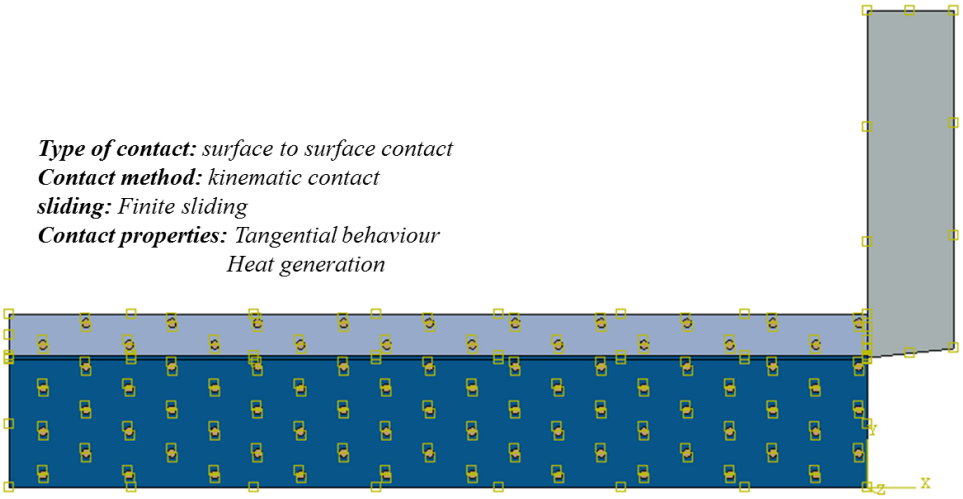

Fig. 8.2. Contact interaction between tool and workpiece.

Contact behavior between tool and workpiece was modeled in interaction module to specify mechanical and thermal interaction between the region and surrounding of the model. Surface to surface type of contact interaction has been used to describe contact between tool and workpiece in the present study as shown in Fig. 8.2.

A kinematic contact algorithm has been used to enforce contact constraints in master slave contact pair, where tool surface is defined as the master surface and the workpiece as slave (node based) surface. TANGENTIAL BEHAVIOR and gap HEAT GENERATION MODULES are considered during definition of contact of tool and workpiece. In tangential behavior, the contact between tool and workpiece is modeled using sliding-sticking friction model based on Coulomb's frictional law. The friction stress, τ_f in sliding and sticking regions is determined by Eq. 8.8 and 8.9

$$\tau_f = \mu\sigma_n \quad \text{when} \quad \mu\sigma_n \leq \tau_{max} \text{ (sliding friction)} \tag{8.8}$$

$$\tau_f = \tau_{max} \quad \text{when} \quad \mu\sigma_n \geq \tau_{max} \text{ (sticking friction)} \tag{8.9}$$

Where, 'τ_{max}' is equivalent shear stress, 'μ' is friction coefficient and 'σ_n' is normal stress along the tool rake face.

In this research, 'τ_{max}' is assumed to be equal to '$\frac{\sigma_y}{\sqrt{3}}$' where '$\sigma_y$' is the yield stress of the matrix material. This value is considered as a reasonable upper bound estimate for the maximum shear stress on the contact surface [205]. All the energy dissipated as a result of friction is transformed into heat and is distributed to the surfaces in contact. The estimation of friction coefficient (μ) in Eq. 8.10 along the tool–chip interface for each cutting condition is based on the experimental measurement of cutting force during orthogonal cutting as:

$$\mu = \frac{F_f \cos\gamma + F_c \sin\gamma}{F_c \cos\gamma - F_f \sin\gamma} \tag{8.10}$$

Where, 'F_c' is cutting force, 'F_f' is feed force and 'γ' is the rake angle.

During machining process, high heat generation is observed due to plastic deformation and friction between tool-chip and tool-workpiece interface. Most of the plastic deformation energy is converted into heat, which is usually between 85% to 95% of the heat fraction assumed to be '1' in ABAQUS. A small amount of heat J is remained in

the chip and heat fraction (1-J) conducted into the cutting tool. In the present work, heat generation caused by mechanical dissipation due to plastic strain is 90%. The value considered for the simulation is the default value in ABAQUS being 0.5 [205].

8.2.8 Boundary condition modeling (Load module)

Lagrangian formulation is adopted in which the workpiece is fixed and the tool moves with a constant cutting speed. To fix the workpiece, bottom edge nodes of the workpiece model were constrained both vertically and horizontally. Cutting tool was constrained against vertical displacement and rotation and allowed to move in only one direction with velocity input boundary condition. Boundary conditions used in the present study are demonstrated in Fig. 8.3.

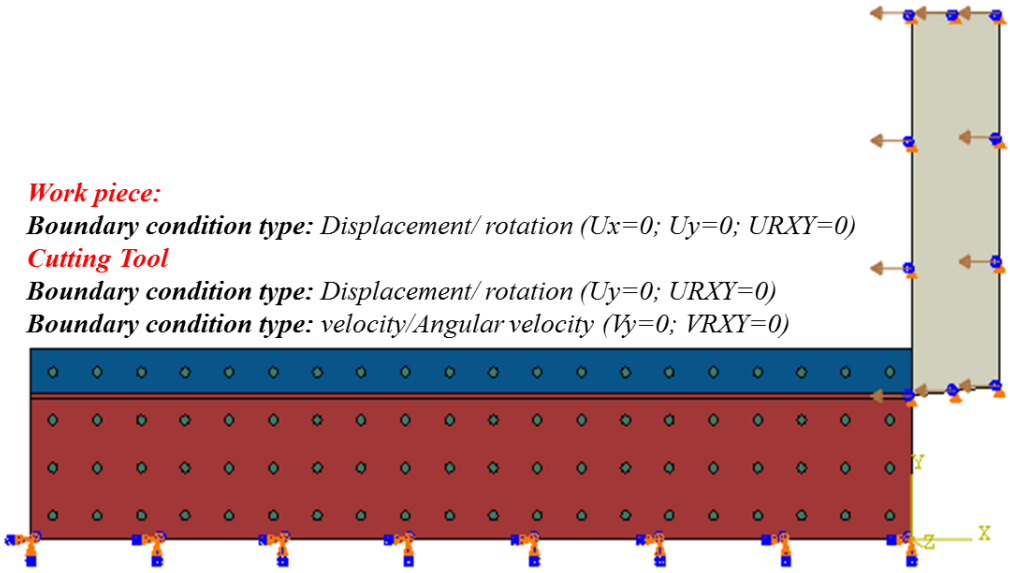

Fig. 8.3. Boundary condition setup for machining of MMCs.

8.2.9 Meshing (Mesh module)

In the preset study, a four-node plane strain thermally coupled quadrilateral element designed as CPE4RT was used for the bilinear displacement and temperature analysis with automatic hourglass control and distortion control integration was used for meshing the tool and the workpiece. Free mesh technique was used to mesh the workpiece and tool. A

higher mesh density was used in the potential chip region: top layer and separation layer, by edge seeding with 0.001 mm element size. The bottom layered was meshed with an element size to 0.02 mm. Advance front algorithm is used to mesh the workpiece and the tool. In the advancing front algorithm, elements are first generated at the region boundary and then mesh generation continues towards the interior of region using a systematic approach thereby generating elements of more uniform size with consistent aspect ratio. Meshed parts and the specifications are displayed in Fig. 8.4.

Fig. 8.4. Initial mesh configurations.

8.2.10 Analysis (Job module)

The created model was submitted to ABAQUS Explicit for analysis and its progress was monitored in the job module.

8.2.11 Post processing (Visualization module)

Post processing analysis is carried out in visualization module which provides graphical display of FEA model and results. It extracts the model and provides information from the output database.

All finite element simulations are run on a Del precision T1650 Workstation with intel xenon E3-1225 V2 3.2GHz process and 32 GB of RAM. The total simulation cutting

time was 0.2 ms with a length of cut of 2 mm. The average computation time was approximately 13 hours.

8.2.12 Machining experiments

Machinability analysis of developed Al-TiC_p composite rod was performed on HMT PTC 200 high precision lathe with carbide inserts of various cutting speed, feed and rake angles under dry condition. In dry machining, experiments were conducted at ambient conditions of approximately 25°C and 40-60% RH. The experiment conditions and tool parameters used in turning tests are present in Table 8.4. Each experiment was repeated three times for every cutting condition and the average of three measurements was used to represent the performance parameters such as cutting forces, machining temperature, chip thickness and shear angle. L_9 orthogonal array was employed to perform the machining test.

Table 8.4. Experimental settings and conditions.

Turning machine	
Machine tool	***Machine type:*** CNC lathe machine ***Model:*** HMT PTC 200 ***Control software:*** Fanuc
Work material Al-TiC_p composite	
Matrix material	Al-6061
Particle material	Titanium Carbide (TiC)
Average particle diameter	20μm
Particle weight fraction	5%
Particle size	20 μm diameter
Tool geometry	
Tool holder type	P-type tool holder in k20 grade (20×20×125);
Cutting insert	CNMG1204 in grade of K68
Approach angles ψ (degree)	90
Rake angles γ (degree)	0, 8, 16
clearance angle λ(degree)	6
Nose radius r_e (mm)	0.8
Process parameters	
Cutting speed V_c (m/min)	50, 100, 150
Feed f (mm/rev)	0.1, 0.15, 0.2
Depth of cut a_p (mm)	0.25
Environmental conditions	Dry, Cryogenic

8.3 Results and discussion

Finite element modeling of machining MMCs was performed by ABAQUS/ Explicit. The performance of the FEM simulation in terms of chip formation is highly dependent on the distribution of reinforcements in the matrix, the cutting parameters and tool geometry. The present study is divided into three phases. In first phase, different strategies are adopted to analyze chip formation and plastic deformation behavior of the matrix with respect to distribution of reinforcement particles. The obtained results are validated with experimental results to analyze the performance of the developed models.

In the second phase, the better performed model was adopted from the first phase and its performance was further analyzed under different cutting parameters and tool geometry combinations during machining of Al-TiC_p MMCs. After ensuring the accuracy of the developed model at different cutting parameters and tool geometry, cryogenic machining technology was introduced in the developed FEM machining model and its performance was analyzed in the third phase.

8.3.1 Phase-I: Analysis of plastic deformation of matrix with respect to particle distribution

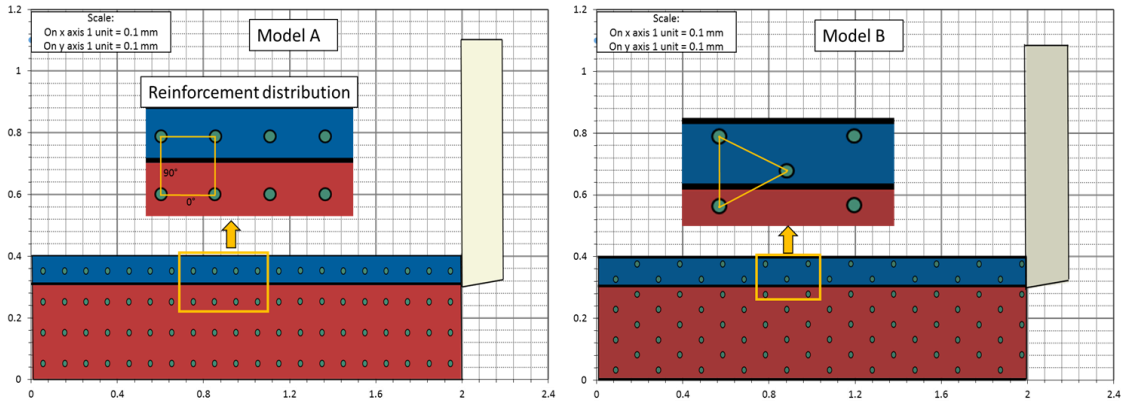

Fig. 8.5. FEA modeling of microscale MMC workpiece with different strategies in arrangement of particles.

Presence of TiC particles into Al matrix in the chip separation dictates the type of chip that has been formed and plastic deformation in matrix. Two different strategies (model A and B) are utilized to arrange the particles in the matrix as shows in Fig. 8.5. In the first strategy (model A), the TiC particles are arranged at 0° and 90° direct in the form of rows and columns whereas in second strategy (model B), they are arranged at 90° and 30° direction maintaining the particles at equal distance on both the strategies. This type of arrangement forms a single row and two rows of particles in chip formation layer by model A and model B respectively. Both models are developed with separation layer and shear failure is only applied to the separation layer. The use of separation layer along the cutting tool track in horizontal aids the penetration of tool and corresponding shear failure of the element before excessive distortion.

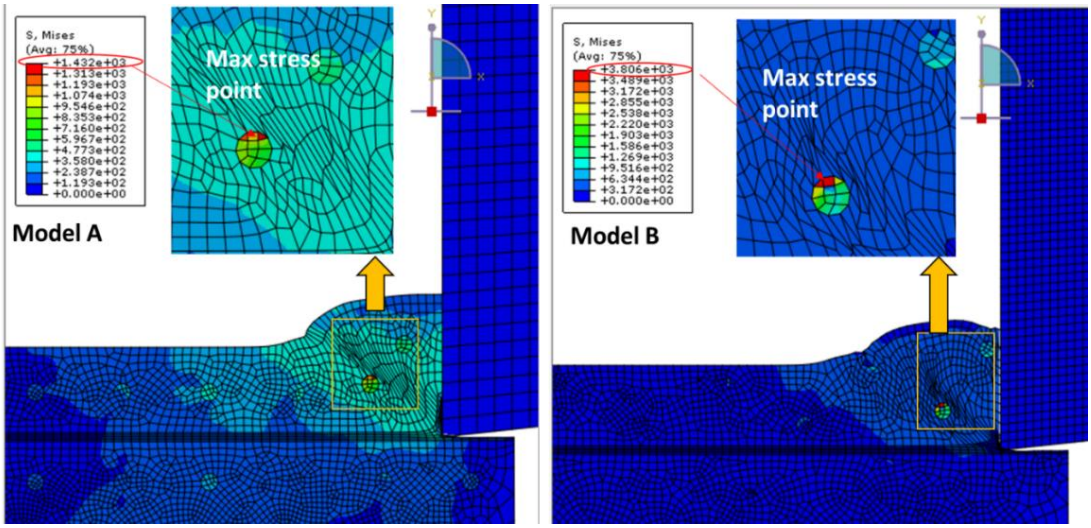

Fig. 8.6. Stress distribution at first step during machining of Al-TiC_p MMCs at cutting speed (V_c) = 50 m/min, uncut chip thickness (f) = 0.1 mm, rake angle (γ) = 0°.

It has been observed that in both the models, higher stress is observed at the top of second particle closer to the tool shown in Fig. 8.6. Topography of initial chip formation is more or less same in both models but the larger plastic deformation in matrix was observed in model B than model A. The large deformation leads to severe degradation of mesh quality in the chip area. From Fig. 8.7 it is revealed that largest mesh distortion is observed

around the reinforcement particles in both model A and model B. In model B, the reinforcements are arranged in two rows thereby distortion is formed along the shear bands of the chip, whereas in model A, the plastic deformation occurs around the reinforcements therefore the distortion is observed in between the particle.

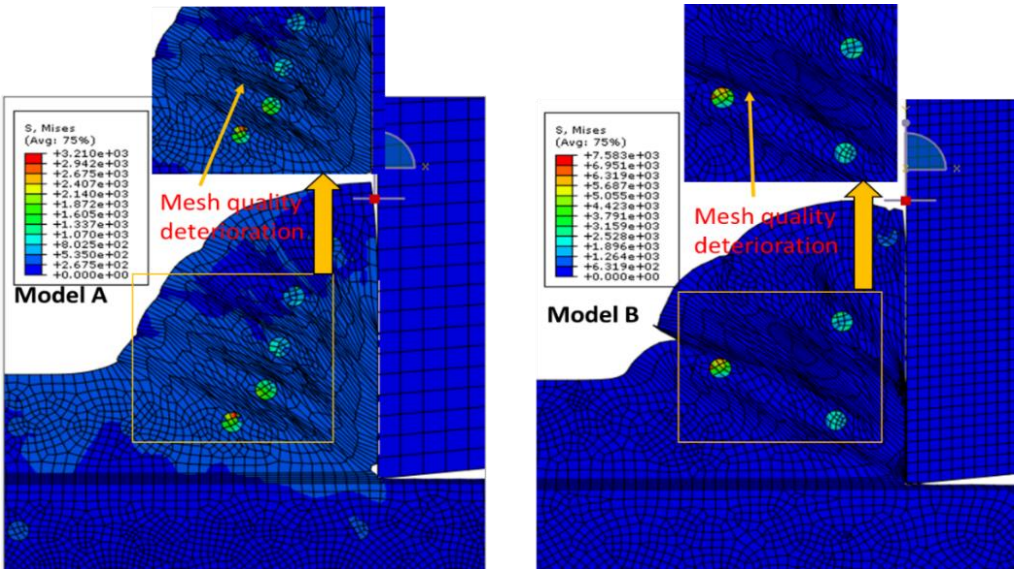

Fig. 8.7. Deterioration of mesh quality around the particles during machining of Al-TiC_p MMCs at cutting speed (V_c) = 50 m/min, uncut chip thickness (f) = 0.1 mm rake angle (γ) = 0°.

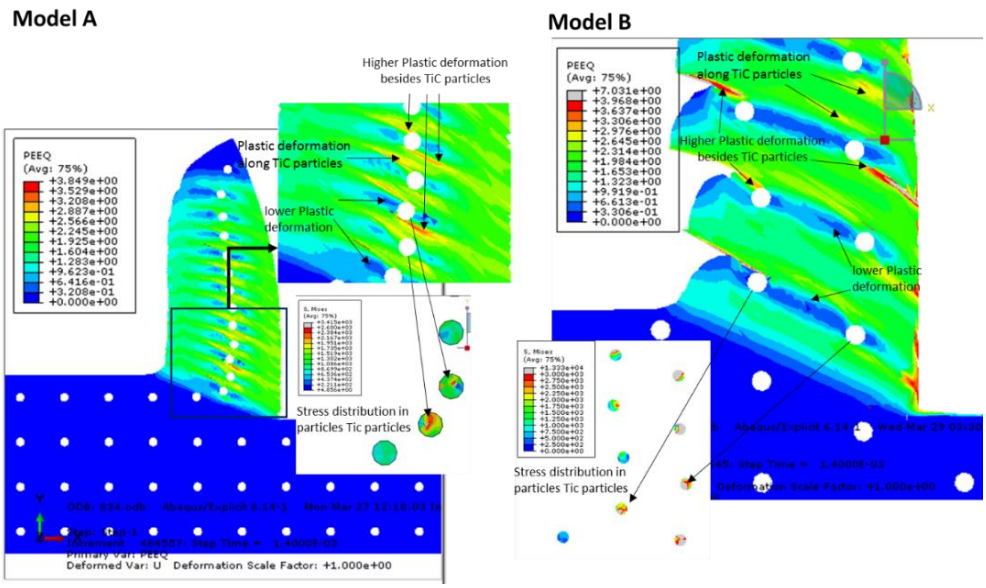

Fig. 8.8. Equivalent plastic strain during Al-TiC_p MMC cutting (cutting speed (v_c) = 50 m/min, rake angle (γ) = 0°, uncut chip thickness (f) = 0.1 mm.

Equivalent plastic strain is used to measure the plastic deformation in matrix phase of MMC, as shown in Fig. 8.8. Unique shape of plastic deformation was demonstrated while machining of MMCs which is different from the deformation observed in machining of monolithic materials. The zones of high deformation along the particles as well as the zones of low deformation between the particles in both the models. This figure also shows the high plastic strain in the matrix areas adjacent to the particles. The stress distribution in particles, shown in Fig. 8.8 proves that the large plastic strains in the matrix result in high stress concentration in the particles, which can cause particle fracture.

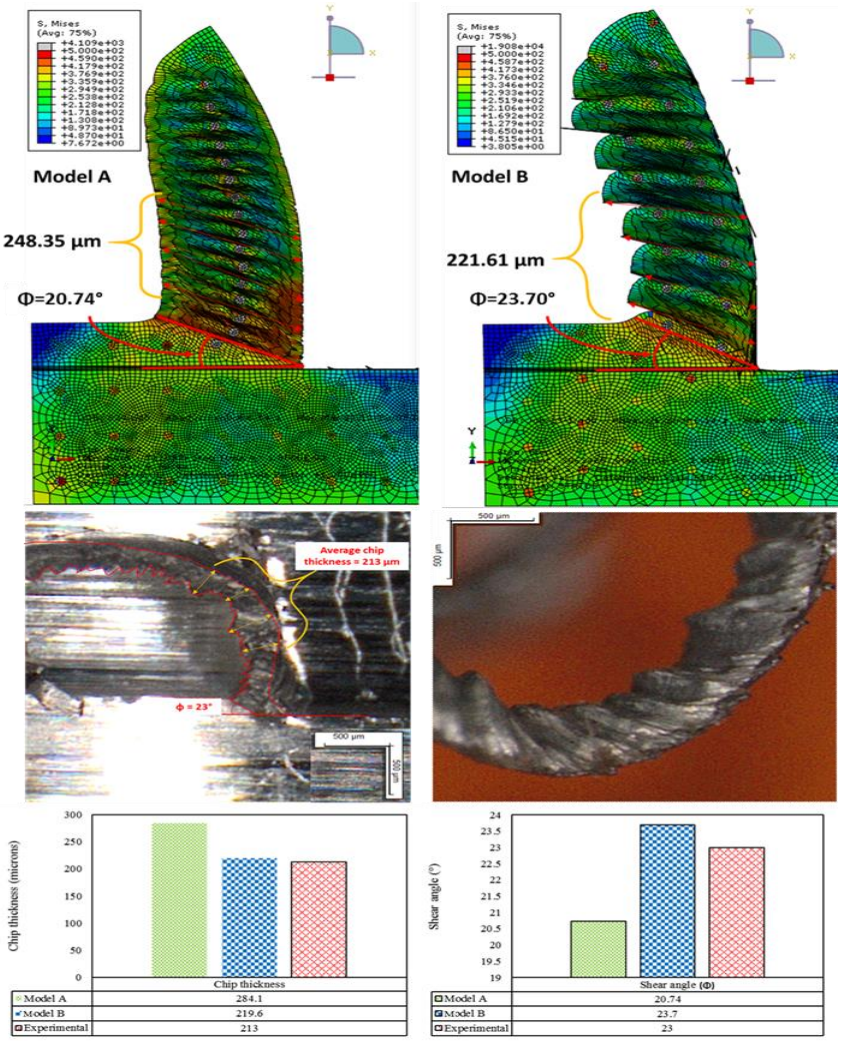

Fig. 8.9. Stress distribution, chip topography and thickness and shear angle measurement during machining Al-TiC_p MMC at cutting speed (V_c) = 50 m/min, rake angle (γ) = 0°, uncut chip thickness (f) = 0.1 mm.

Mises stresses are lowest for model A due to shear failure. The stress distribution in matrix is not visible due to huge difference in stress levels for reinforcement and matrix, therefore the maximum stress is set to 500 MPa to better visualize the stress variation in workpiece matrix for both models A and B. At step of 1.8 ms, model B has shown 78% higher value of stress than model A as shown in Fig. 8.9. From the chip morphology analysis presented in Fig. 8.9, continuous chip can be seen to be formed in both the models. In model A, plastic deformation chip with small damage to back and front of chip was observed, whereas in model B, saw type of chips were observed. This serration is mostly because of matrix element failure. No mechanism of debonding of reinforcement particles was observed until the complete material damage around the particle occurred.

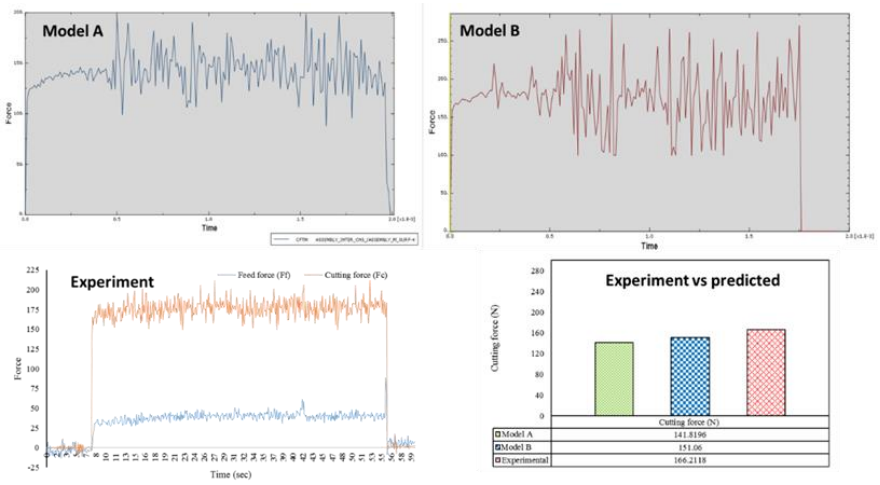

Fig. 8.10. Comparison between experimental and simulated cutting forces when machining the Al-TiC_p MMC with cutting speed (V_c) = 50 m/min, rake angle (γ) = 0°, uncut chip thickness (f) = 0.1 mm.

In order to validate the results of FE model, the obtained predicted values of chip thickness and shear angle were compared with experimental results performed under same conditions. The chip thickness and shear angle obtained from the experiments and FEA model is shown in Fig. 8.9 It is observed that Model A gave larger chip thicknesses and

smaller shear angles, whereas model B showed a minimal difference due to the optimal distribution of particles and separation layer along the cutting path.

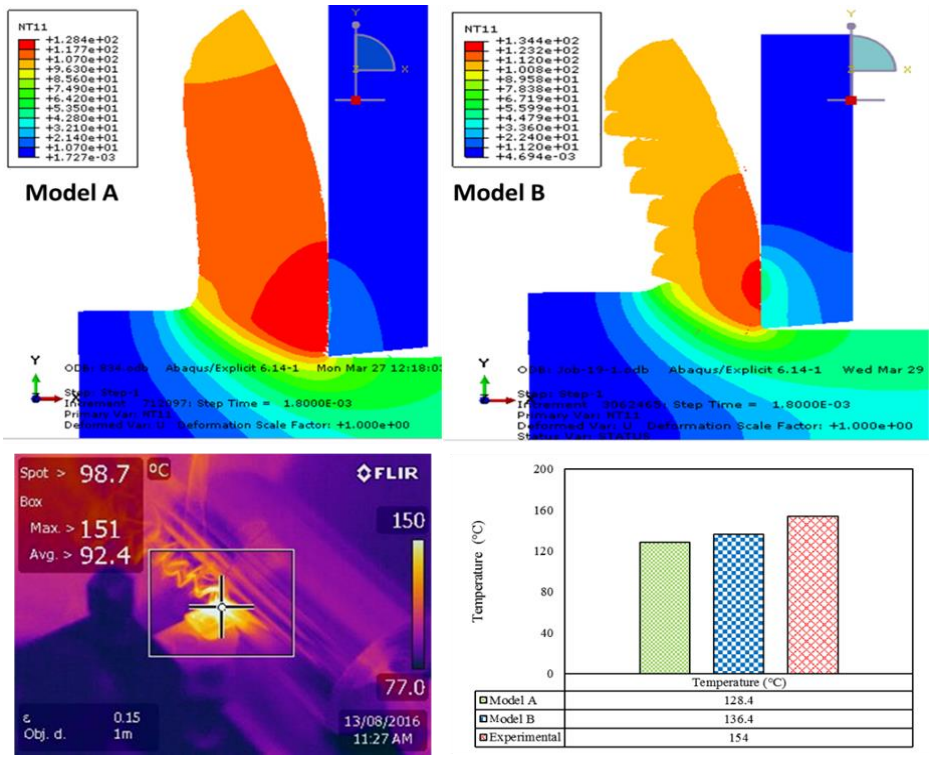

Fig. 8.11. Comparison between experimental and simulated temperature when machining the Al-TiC_p MMC with cutting speed (V_c) = 50 m/min, uncut chip thickness (f) = 0.1 mm, rake angle (γ) = 0°.

Cutting forces obtained from model A, model B and experiments are shown in Fig. 8.10. Both model give good agreement but it was seen that cutting force was lowest for model A due to poor distribution of particles in comparison to model B. Model B contains two rows of particles, thus, minimal difference in cutting force is observed. Further, temperature distribution of model A and B are shown in Fig. 8.11. As expected, temperatures are lower for model A due to deletion of highly distorted elements. The range of temperatures predicted by model B is in close agreement with experimental results for machining of Al-TiC_p MMCs at similar conditions. For both models, higher temperatures are predicted corresponding to the region of maximum deformation of the workpiece material around the hard reinforcement particle.

8.3.1.1 FEM analysis validation with the distribution of particles

As previously shown, distribution of particles in the matrix is the major factor affecting the chip formation in machining simulation. Further stress development, plastic deformation of the matrix, cutting force and temperature formation also depends upon the distribution of particles in the matrix during simulation. In the present study, 5wt% of TiC particles of 20 μm diameter are distributed inside the matrix uniformly in two different directions in model A and model B. Both the models showed acceptable agreement with experimental results. Model B gave values much closer to the experimental ones. It was observed that model B gave 80%, 60%, 70, 90% closer results in terms of chip thickness, shear angle, cutting force and cutting temperature respectively than model A. It confirms that model B performs better in regard to mesh distortion problem and shows a realistic deformation of chip. Also, shear localization can also be easily realized for model B. Therefore, model B type distribution gives closer results to experimental than model A type of distribution. It should be noted that the FE analysis of machining MMCs not only depends on distribution of particles but also upon other machining parameters like speed, uncut chip thickness and rake angle of the tool. As cutting speed increases, the movement of tool becomes faster and causes heavy mesh distortion. Improper meshing at higher cutting speed leads to errors like "The ratio of deformation speed to wave speed exceed 1.00". During machining simulation, larger uncut chip thickness and smaller rake angle causes excessive element distortion at the initial step terminating the simulation. To overcome these errors, mesh refinements and adjustment of the damage evolution value will improve the machining process. To analyze the performance of the developed FEA model, three different cutting speeds, uncut chip thicknesses and rake angle combinations are used for simulations with the help of model B. In this chapter, the obtained FEA results are compared with experimental results to validate the developed FEA model.

8.3.2 Phase-II: Performance under different cutting conditions

Performance of the developed FEA machining MMC model at different cutting speeds (50 m/min, 100m/min and 150m/min), feed (0.1 mm/rev, 0.15 mm/rev, 0.2 mm/rev) and rake angles (0°, 8°, 16°) are analyzed in the present subsection by comparing with experimental results. Total 9 experiments are performed as per Taguchi L9 orthogonal array. The test conditions are represented as test terms and shown in Table 8.5.

Table 8.5. Percentage differences between experimental and simulated results for machining of Al-TiC_p composites at different cutting condition.

Test terms	cutting Speed (V_c) (m/min)	Feed (f) (mm/rev)	Rake angle (γ) (°)	Cutting force (CF) (%)	Temperature (T) (%)	Chip thickness (CT) (%)	Shear angle (ϕ) (%)
Test-I	50	0.1	0	9.04	10.99	2.71	3.04
Test-II	50	0.15	8	3.18	2.83	6.34	1.92
Test-III	50	0.2	16	9.05	11.77	0.59	1.17
Test-IV	100	0.1	8	8.62	5.33	4.31	5.77
Test-V	100	0.15	16	6.12	8.09	15.54	3.87
Test-VI	100	0.2	0	11.06	13.83	3.76	3.33
Test-VII	150	0.1	16	3.57	12.28	23.98	10.56
Test-VIII	150	0.15	0	11.11	10.10	2.09	6.86
Test-IX	150	0.2	8	16.00	7.41	7.47	-5.00

The results of developed FEM model closely match the experimental results under similar conditions. Fig. 8.12 show the comparison between experimental and simulated results at Test-1 conditions. Remaining test images are presented Fig. C.1-C.8 (APPENDIX-C). It is observed that, as cutting speed and rake angle increases, the % difference between simulation and experimental results increases. The results were within the acceptable limit. Table 8.5 shows the percentage difference between the experimental and simulated results at selected test conditions in machining of Al-TiC_p MMCs.

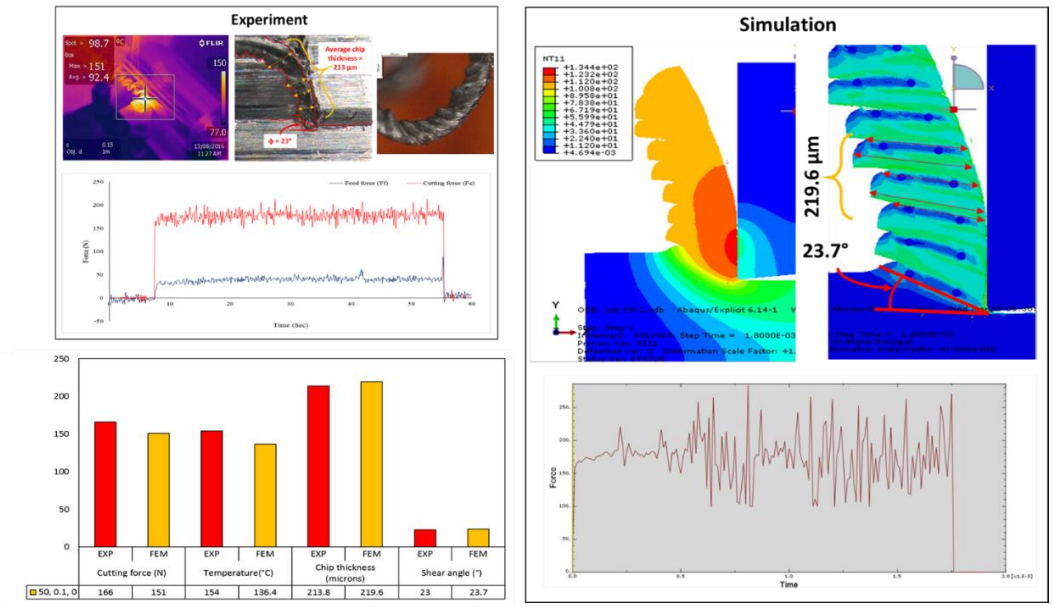

Fig. 8.12. Comparison of simulated with experiment at Test-I.

This variation is observed due to heat generation fraction value at higher cutting conditions. Test-V in terms of chip thickness; Test-IV, Test VII and Test-IX in terms of cutting force and Test-I, Test-III, Test VI and Test-VII and Test-VII in terms of temperature show more than 10% difference between experimental and simulation results. This is expected in FEA since the cutting tool was assumed to be ideally sharp in the analysis, which is not the case in actual machining tests. Even the corner radius of the cutting tool is an important factor which causes variation in simulated and experimental results. Higher corner radius makes tool blunt and increases the contact area, which causes requirement of larger forces to shear the material [208]. The evaluation of cutting force along the cutting time is presented in Fig. 8.12 and Fig. C.1-C.8 (APPENDIX-C). Sudden peak value was observed when the tool shears the reinforcement present matrix during machining of MMCs. Similar trend was observed in experimental results. However, the variation was limited as compared to simulation results.

The evolution of chip topography and shear angle at selected machining conditions are presented in above figures. It is observed that chip thickness is highly dependent upon the uncut chip thickness and shear angle is dependent upon the rake angle used. Similar

observations were made by other researches in terms of chip thickness and shear angle. Further, the cutting temperature increases as cutting time increases. Thereby it is confirmed that the chip is the major source of removal of generated heat in the shear zone during machining of MMCs.

8.3.2.1 Effect of uncut chip thickness

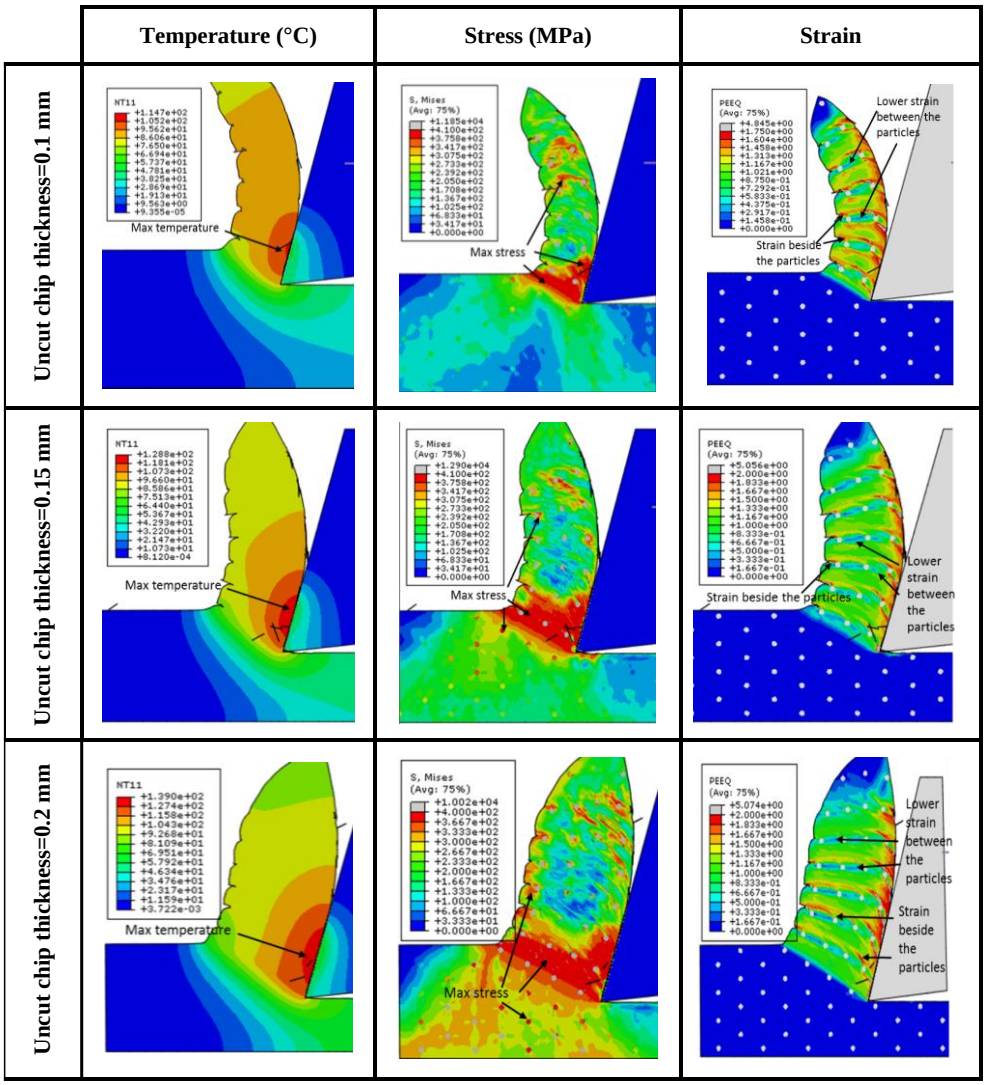

Fig. 8.13. Effect of uncut chip thickness during machining of Al-TiC_p MMCs at a cutting speed (V_c) of 50 m/min and a rake angle (γ) of 0°.

The detailed distribution of cutting temperature, stress and plastic strain in the tool, workpiece and chip is presented (the figure was taken at the end of the length of cut where

the temperature reaches its peak and steady state conditions are present). The thermal effects are bigger at larger feeds leading to more plastic deformation in matrix shown in Fig. 8.13. It can be observed that as uncut chip thickness increases, temperature increase leading to larger plastic strain matrix. The deformation has a trend to increase, a fact which can be explained by fact that maximum shear stress also shows an increase with the increase of the feed. The outside of the chip curling is obviously more affected by the plastic strain when compared to the inside zone. This leads to increase in tool/chip contact length causing crater wear in this region of the tool face, which in turn effects the rake angle. As uncut chip thickness increases, the decrease in stress value was observed which is a result of increase in plastic strain.

8.3.2.2 Effect of rake angle

To understand the performance of FEA model at different rake angles, three different rake angles were considered to perform the machining simulation. It is observed that as 0° rake angle gives a difficulty during the initial step, when the tool directly comes into contact with the workpiece, the elements in the workpiece distort excessively and the simulation terminates. To overcome this, the damage evolution energy value was reduced to 40% than the initial value given for rake angle 8° and 16°. The reduction in damage value helps to perform the simulation. Fig. 8.14. shows the detailed distribution of temperature, stress and strain in MMC at a constant cutting speed and feed conditions (taken at the end of length of cut due to reaching steady state cutting conditions). It is observed that as rake angle increases from 0° to 16°, temperature decreased. This can be a result of reduction in tool/chip contact length. This is confirmed by the stress results obtained at the same conditions. Further, the plastic strain in matrix is highly influenced by rake angle. As rake angle increases, plastic strain decreases. It is also observed that higher

plastic strain values are observed beside the reinforcement particles and lower plastic strain is observed in between the reinforcements.

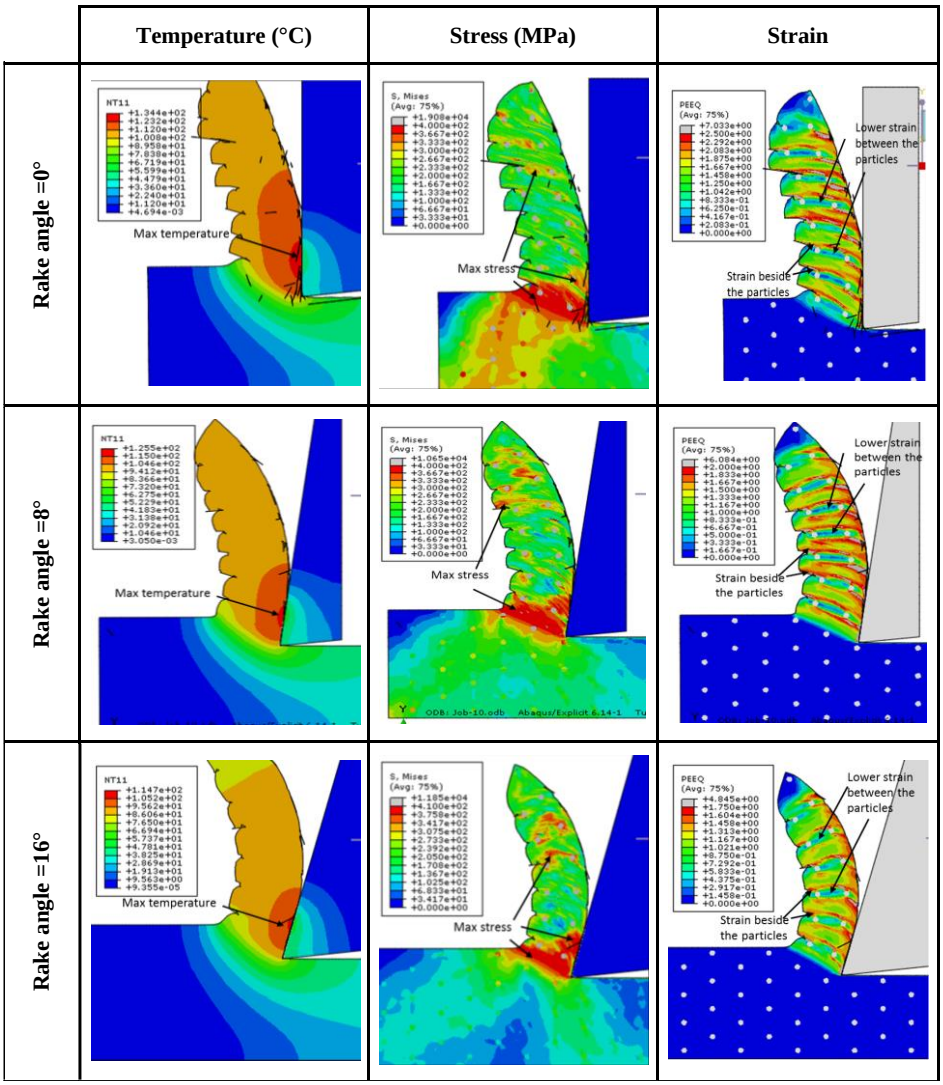

Fig. 8.14. Effect of rake angle during machining of Al-TiC_p MMCs at cutting speed (V_c) of 50 m/min and uncut chip thickness (f) of 0.1mm.

8.3.2.3 Effect of cutting speed

An increase in the temperature with an increase in cutting speed is apparent from Fig. 8.15. This increase in temperature softens the matrix material, which will in turn results in a decrease in cutting forces. The stress distribution and strain distribution at different cutting speeds is shown in Fig. 8.15. The larger stress distribution was located closer to the particles and at the primary and shear zone. It is observed that, stress decreases with

increase in cutting speed. This strain decrease is consistent with the decrease in stress in the matrix as a result of matrix material softening caused by higher temperature. The increase in temperature with the increase in cutting speed causes thermal softening of the workpiece material, leading to increase in the plastic strain rate. A detailed distribution of strain at different cutting speeds (taken at the end of length of cut due to reach steady state cutting conditions) is presented in Fig. 8.15. Higher plastic deformation occurred along the particles while lower deformation was observed between the particles. This is due to higher stress concentration in the particles.

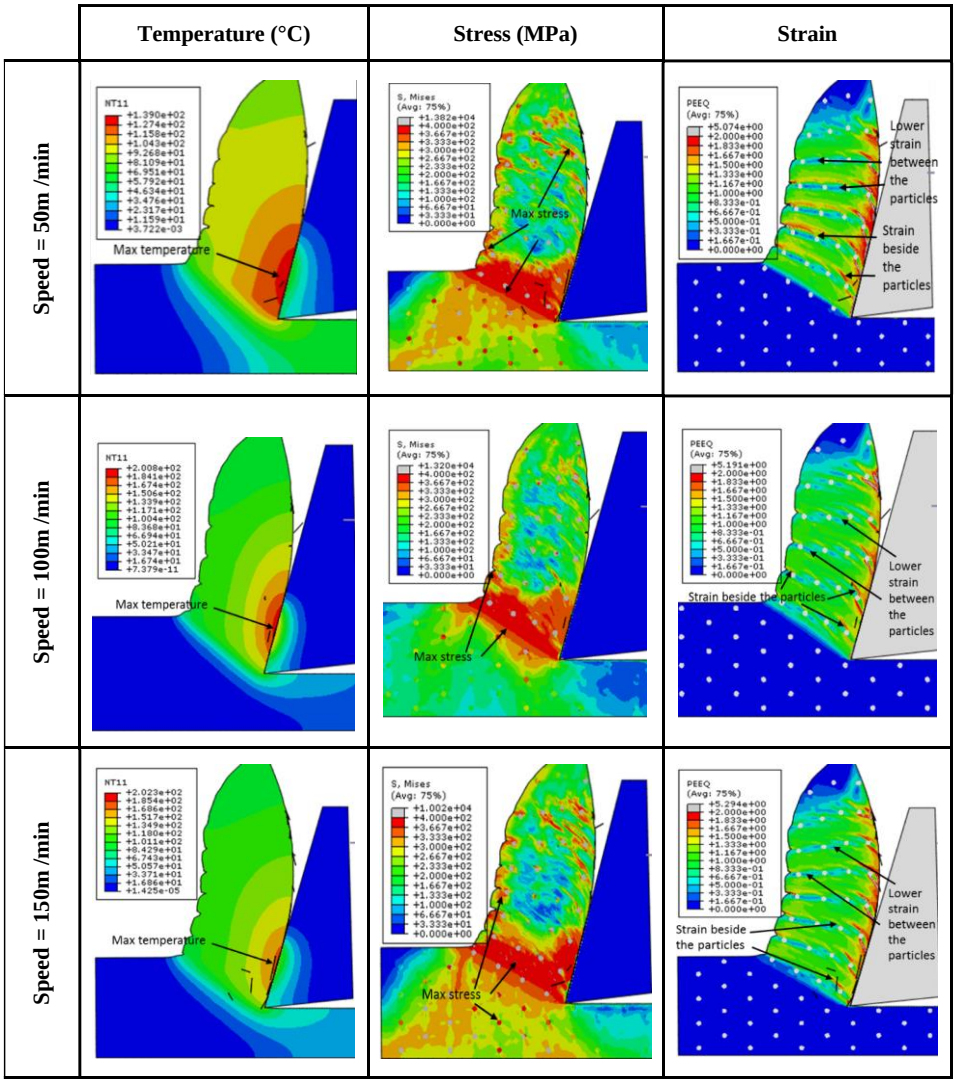

Fig. 8.15. Effect of cutting speed during machining of Al-TiC_p MMCs at rake angle (γ) of 16° and uncut chip thickness (f) of 0.2 mm.

The machinability performance is highly influenced by heat generation in cutting zone, especially in MMCs. In presence of hard reinforcement particles, MMCs are subjected to high strain and temperatures during machining. The generation of intense heat and pressure in a localized area results in severe edge chipping and plastic deformation via seizure of chips [134]. Cryogenic technology in machining has proven its capability in reducing the heat generation effectively. Therefore, in the present work, after ensuring the accuracy of the developed FE model for machining of MMCs at different cutting combinations, an improvised FEA model for cryogenic machining was developed in ABAQUS by applying the cryogenic cooling impact on the workpiece and tool using convention heat transfer. To analyze the performance of the developed FEA cryogenic machining model, a combination of three different cutting speeds, uncut chip thicknesses and rake angles is used for simulation using model B. The obtained FEA results are compared with experimental results to validate the developed FEA cryogenic machining model and presented in the current chapter.

8.3.3 Phase-III Cryogenic machining based on FE approach

In the current work, liquid nitrogen (LN_2) is sprayed by a nozzle at cutting area particularly at the contact surface of tool/workpiece. To simulate the effect of cryogenic cooling, the upper surface and right side of the workpiece same as rake and flank face of the cutting tool are kept under forced heat transferred surfaces by cryogenic cooling. The impact of cryogenic cooling is applied using conventional heat transfer. The temperature on force heat transfer surface was considered to be -196°C owing to the use of liquid nitrogen. Fig. 8.16 shows the thermal boundary conditions considered for cryogenic machining. The local conventional heat transfer coefficient is one of the major parameter which dictates the performance of the cryogenic cooling effect. Pashaki et al. [209]

measured the heat transfer coefficient for cryogenic machining of aluminum from the studies of Miranda [210]. The direct cooling of LN_2 is due to forced convection. Such heat transfer coefficient was considered by Eq. 8.11.

$$h_{cryo} = \frac{0.2}{b^{0.35} g^{0.33}} \frac{{V_f}^{0.65} {K_f}^{0.67} {C_p}^{0.33} {\gamma_{cl}}^{0.33}}{{v_f}^{0.32}} \quad (8.11)$$

Where, 'b' is the equivalent length, g is acceleration due to gravity, 'V_f' is velocity of liquid nitrogen flow (ms-1), 'K_f' is thermal conductivity of liquid nitrogen ($Wm^{-1}°C$), 'γ_{cl}' is Specific weight of liquid nitrogen, 'V_f' is dynamic viscosity of liquid nitrogen (Pa s) and 'C_p' is specific heat capacity of liquid nitrogen ($J\ kg^{-1}°C$).

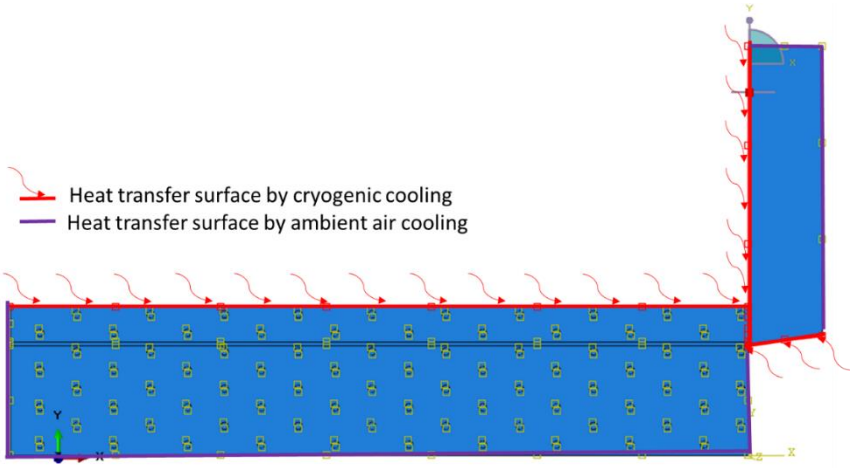

Fig. 8.16. Shows the thermal boundary conditions considered for cryogenic machining.

From the physical and thermal properties of liquid nitrogen, heat transfer coefficient is a function of temperature which is achieved by Eq. 8.12

$$h_{cryo} = -8 \times 10^{-6} T^3 - 0.0149 T^2 + 44.396 CT + 10162 \quad (8.12)$$

The surface film condition interaction properties are used to provide heat transfer coefficient for cryogenic machining in FE model. The local convectional heat transfer coefficient can be adjusted from the above equation to simulate the cryogenic cooling effect for the workpiece and tool shown in Fig. 8.16 and the remaining area of both tool and

workpieces are subjected to air convention at room temperature. Cryogenic machining simulation are carried out on Al-TiC_p MMCs using ABAQUS. The impact of different parameters like cutting speed, uncut chip thickness and rake angle are examined. The obtained simulated results are validated through cutting forces and temperatures measurements acquired under dry and cryogenic machining conditions.

8.3.3.1 Effect of rake angle under cryogenic machining

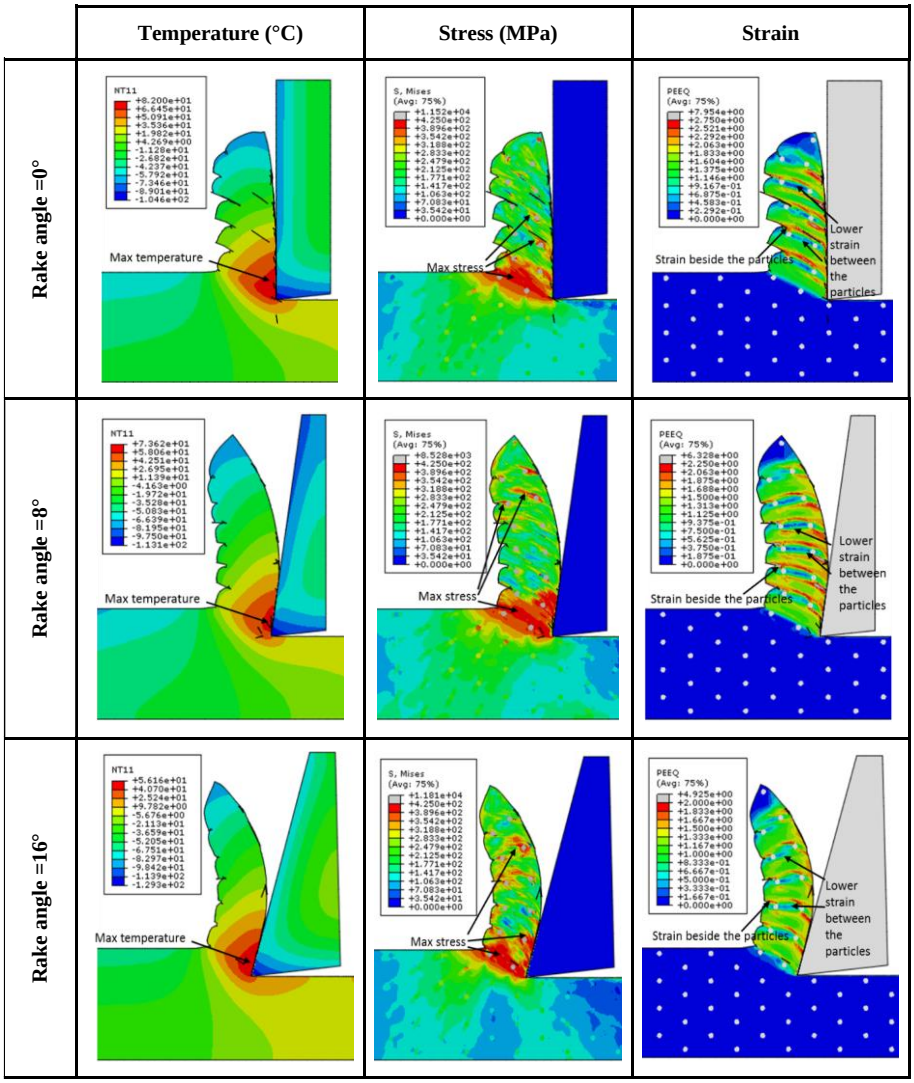

Fig. 8.17. Effect of rake angle during machining of Al-TiC_p MMCs at cutting speed (V_c) of 50 m/min and uncut chip thickness (f) of 0.1mm.

Rake angle is the major factor which influences the heat generation in the machining. As rake angle increases, tool/chip contact length increases leading to reduction in cutting temperature. Fig. 8.17 shows the effect of rake angle on distribution of temperature, stress and strain in MMCs at constant cutting speed and uncut chip thickness. The stress distribution and strain distribution shows same trend as dry conditions. Maximum stress is observed around the particles and primary shear zone while maximum strain is observed along the sides of the particles. Lower strain was observed between particles. As rake angle increases, the strain value decreases, where stress decreases initially and then increases.

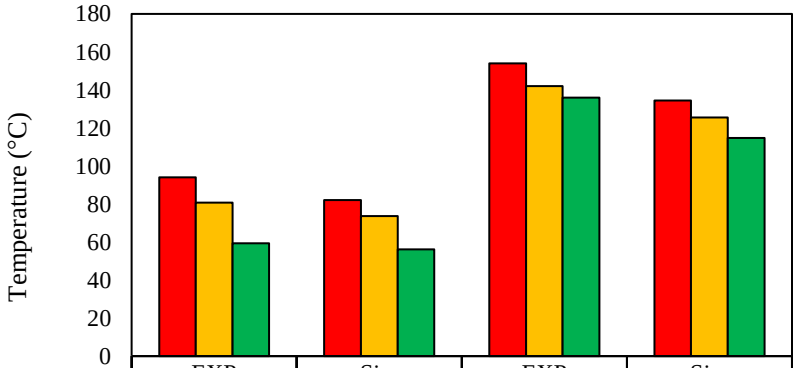

	Cryo		Dry	
	EXP	Sim	EXP	Sim
Vc = 50; f = 0.1; γ = 0	94	82	154	134.4
Vc = 50; f = 0.1; γ = 8	80.66	73.62	142	125.5
Vc = 50; f = 0.1; γ = 16	59.36	56.16	136	114.7

Fig. 8.18. Comparison of temperature obtained at different rake angle by the use of present model and the experimental results in both cryogenic and dry machining conditions.

To validate the developed model, simulated results are compared with experimental results. Fig. 8.18 and 8.19 shows the comparison of experimental and simulated results in both dry and cryogenic machining conditions. Fig. 8.18 compares the temperature results for both cryogenic machining and dry machining conditions. It is observed that simulated temperature values are 94% closer to the experimental cutting temperature under cryogenic

machining. During simulation, cryogenic machining gives a 43% average reduction in temperature than dry machining simulation whereas in actual experiments, the average reduction in temperature is about 46%. This variation is due to the heat transfer coefficient value selected. By fine tuning it, closer results can be achieved. These comparisons confirm that the developed FE model for cryogenic machining of MMC has given an acceptable correlation with experimental results under different rake angles. Similar analysis was performed in terms of cutting force under cryogenic and dry machining conditions.

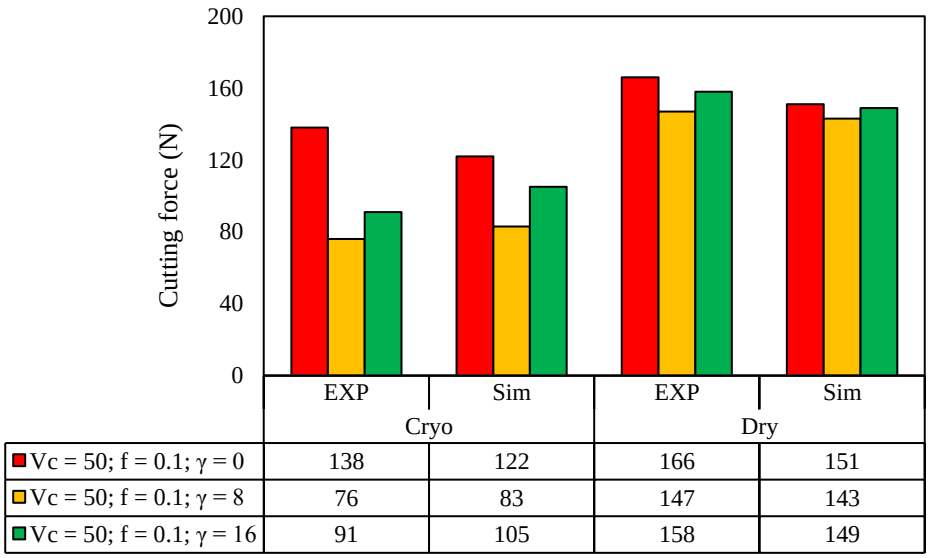

	Cryo		Dry	
	EXP	Sim	EXP	Sim
Vc = 50; f = 0.1; γ = 0	138	122	166	151
Vc = 50; f = 0.1; γ = 8	76	83	147	143
Vc = 50; f = 0.1; γ = 16	91	105	158	149

Fig. 8.19. Comparison of cutting force obtained at different rake angle by the use of present model and the experimental results in both cryogenic and dry machining conditions.

Fig. 8.19 compares the cutting force simulation results for both cryogenic machining and dry machining conditions. It is observed that cryogenic simulation provides an average of 87% closeness to the experimental values, where as in dry machining 94% closer values were observed. This variation in cutting force for dry and cryogenic machining simulation can be achieved by variation in friction coefficient. Friction coefficient calculated from the experimental analysis was given as an input for cryogenic machining. The percentage difference of cutting force from cryogenic to dry conditions

was observed to be an average of 30%. Cryogenic condition gave lower cutting force than dry condition due to the selection of actual friction value in cryogenic machining. As rake angle increases, the cutting force value initially decreases and the increases. Similar phenomenon is observed for experimental analysis as well. To understand the cryogenic machining effective in FE model, effect of cutting parameters in machining process are studied.

8.3.3.2 Effect of cutting speed under cryogenic machining

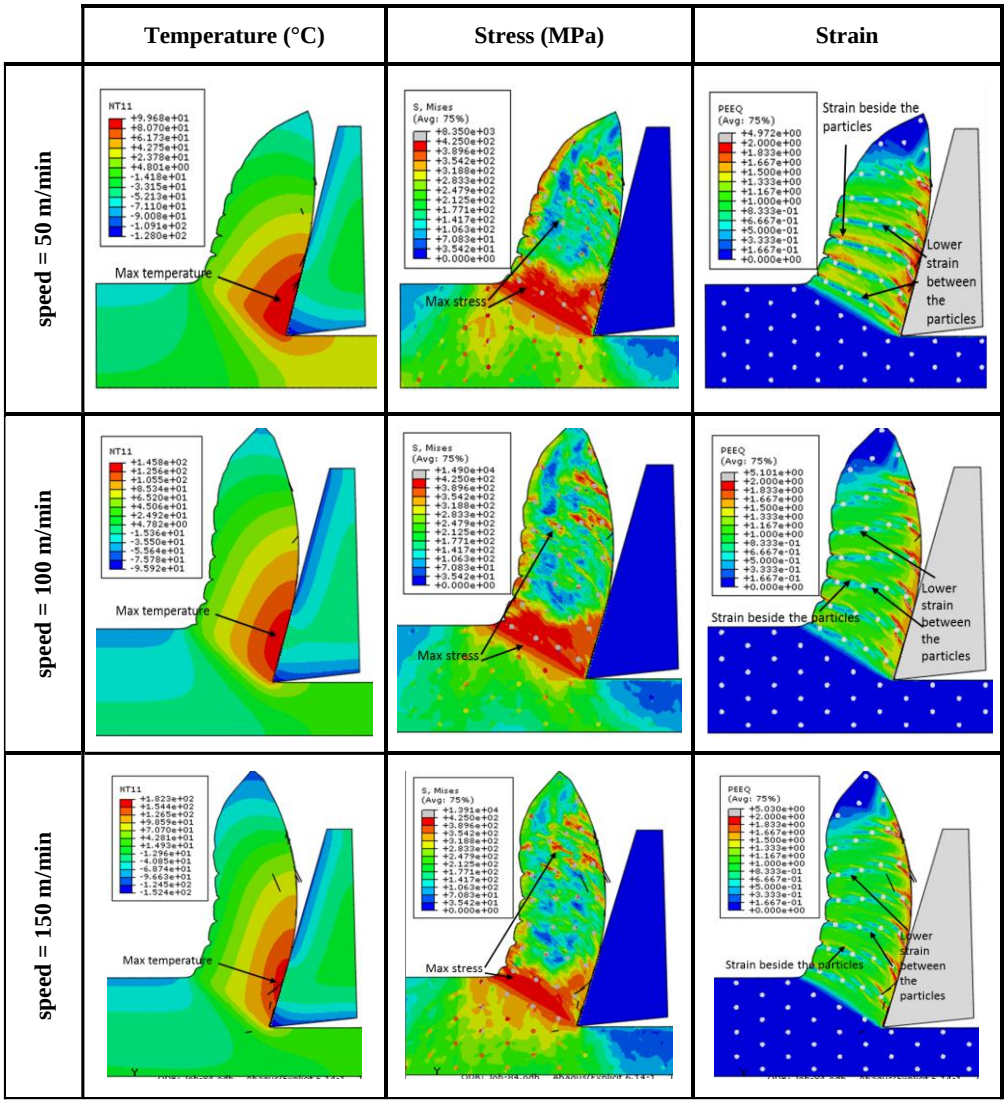

Fig. 8.20. Effect of cutting speed during machining of Al-TiC_p MMCs at rake angle (γ) of 16° and uncut chip thickness (f) of 0.2mm.

With the increase in cutting speed, the temperature in cutting zone increases. The distribution of temperature in machining workpiece and tool with respect to cutting speed is shown in Fig. 8.20. it can be seen that temperature rise in primary shear zone and the maximum temperature in contact surface of tool and chip is created. Results indicated that up to 46% rise in temperature was observed by increasing cutting speed from 50 m/min to 150 m/min. The stress and strain distribution in workpiece with respect to different cutting speed is also shown in Fig. 8.20. It is observed that as cutting speed increases, the stress increases. As temperature increases, matrix thermally softens and larger plastic deformation is observed. This phenomenon leads to larger plastic strain and lower cutting force. Similar observations are made with experimental tests as well.

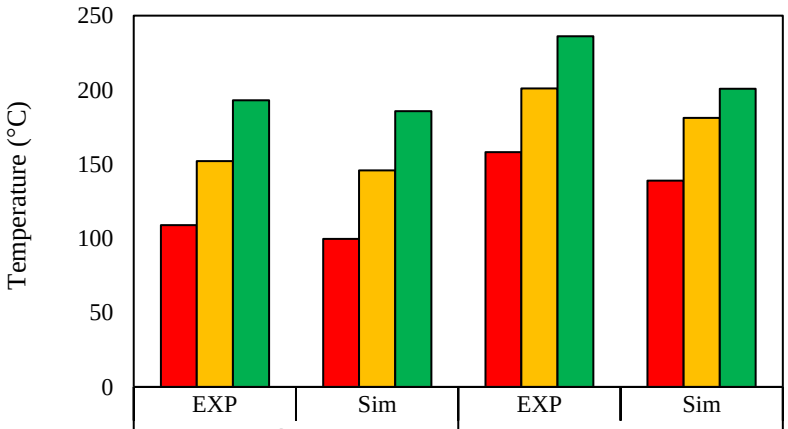

	Cryo		Dry	
	EXP	Sim	EXP	Sim
Vc = 50; f = 0.2; γ = 16	109	99.68	158	139
Vc = 100; f = 0.2; γ = 16	152	145.8	201	181.1
Vc = 150; f = 0.2; γ = 16	193	185.6	236	200.8

Fig. 8.21. Comparison of the temperature obtained at different cutting speed by the use of present model and the experimental results in both cryogenic and dry machining conditions.

Further it can also be observed from Fig. 8.20 that as cutting speed increases, the tool/chip contact length increases which further causes rise in temperature. Providing actual conventional heat transfer coefficient value to the workpiece and tool surface, improve the cooling effect in cryogenic machining. Fig. 8.21 and 8.22 provide the comparison of

experimental results with simulated results under dry and cryogenic machining conditions. It is observed that cryogenic simulation gives an average of 94% closer results to experimental results in terms of temperature and 96% in terms of cutting force at different cutting speeds. The percentage difference of cryogenic machining simulation with dry simulation is around 18% and 45 % in terms of temperature and cutting force respectively.

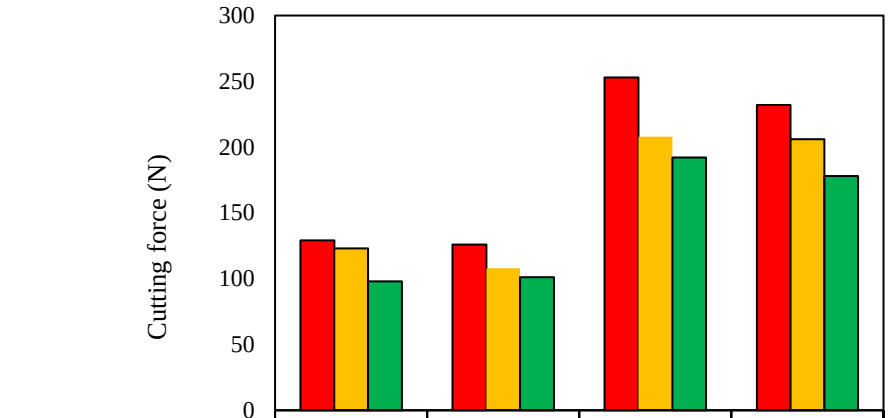

	Cryo		Dry	
Vc = 50; f = 0.2; γ = 16	129	126	253	232
Vc = 100; f = 0.2; γ = 16	123	108	208	206
Vc = 150; f = 0.2; γ = 16	98	101	192	178

Fig. 8.22 Comparison of the cutting force obtained at different cutting speed by the use of present model and the experimental results in both cryogenic and dry machining conditions.

8.3.3.3 Effect of uncut chip thickness under cryogenic machining

In 2D-Plane strain machining problem, feed is considered as uncut chip thickness. Fig. 8.23 shows the temperature, stress and strain distribution on workpiece and tool at different feeds. It is observed that as feed increases, the chip thickness increases leading to increase in contact area of tool with chip, further raising the temperature. As uncut chip thickness increases from 0.1 to 0.2, a 40% rise in temperature was observed. Further, the stress first increases and then decreases as uncut chip thickness increases. This is due to increase in plastic deformation of matrix resulting in larger plastic strains.

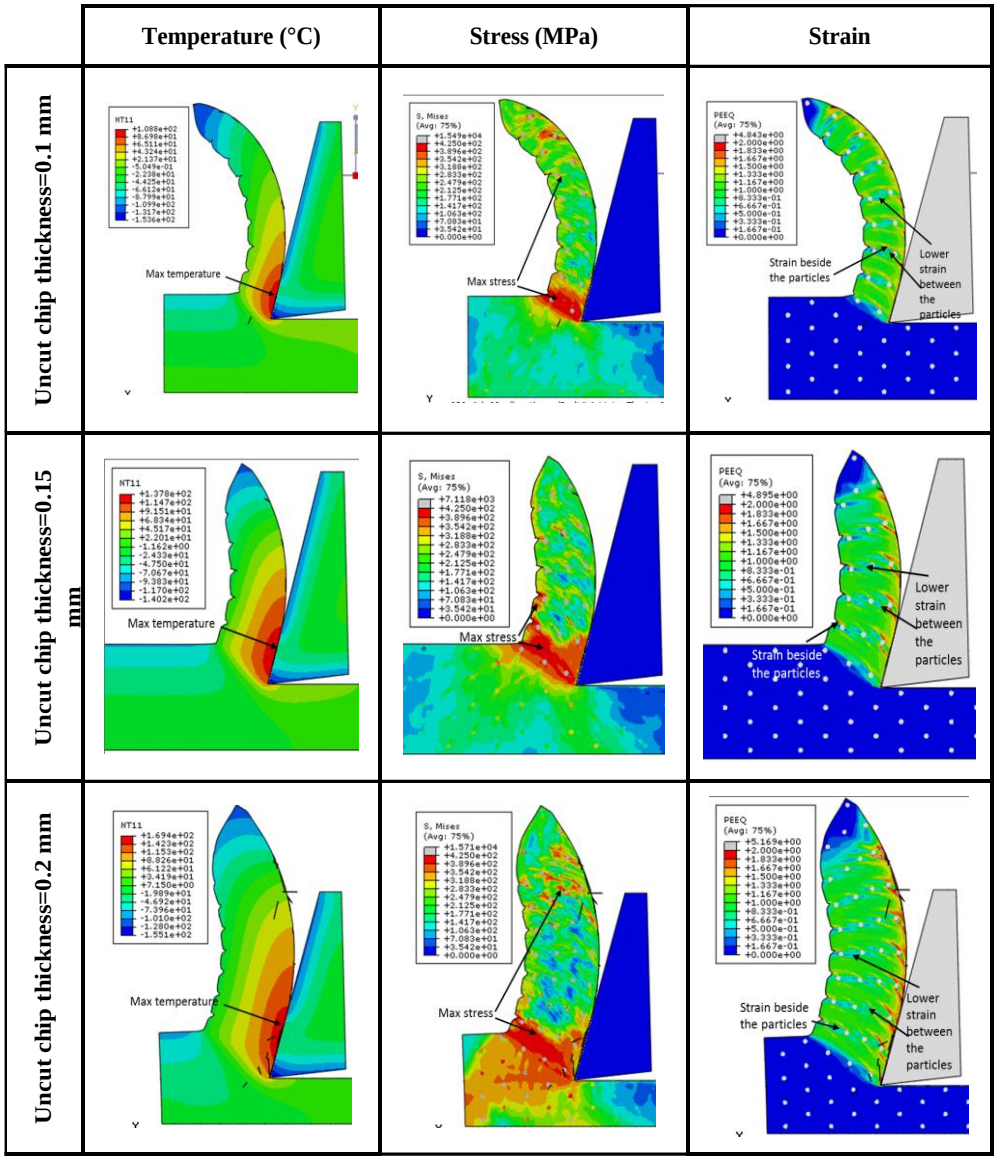

Fig. 8.23. Effect of uncut chip thickness during machining of Al-TiC_p MMCs at a speed (v_c) of 50 m/min and rake angle (γ) of 0°.

Further analysis reveals that cryogenic simulation results under different uncut chip thickness have shown good correlation with experimental results are shown in Fig. 8.24 and 8.25. Temperature reduction by an average of 26% was observed in comparison with dry machining. The simulation results demonstrated 92% closeness to experimental results for both temperature and cutting force.

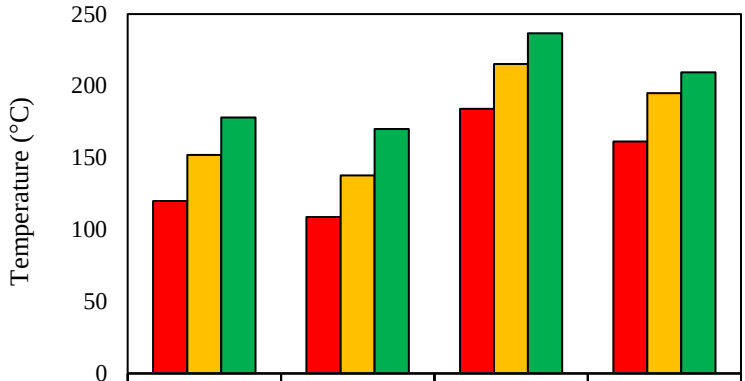

	Cryo		Dry	
	EXP	Sim	EXP	Sim
Vc = 150; f = 0.1; γ = 16	120	108.8	184	161.4
Vc = 150; f = 0.15; γ = 16	152	137.8	215.3	195
Vc = 150; f = 0.2; γ = 16	178	169.94	236.6	209.4

Fig. 8.24. Comparison of the temperature obtained at different uncut chip thickness by the use of present model and the experimental results in both cryogenic and dry machining conditions.

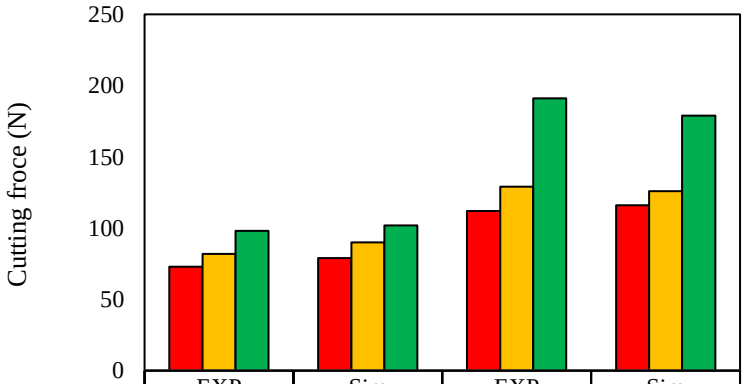

	Cryo		Dry	
	EXP	Sim	EXP	Sim
Vc = 150; f = 0.1; γ = 16	73	79	112	116
Vc = 150; f = 0.15; γ = 16	82	90	129	126
Vc = 150; f = 0.2; γ = 16	98	102	191	179

Fig. 8.25. Comparison of the cutting force obtained at different uncut chip thickness by the use of present model and the experimental results in both cryogenic and dry machining conditions.

It was also observed that the cutting force value with simulation is slightly on the higher side than the experimental results under cryogenic machining. Whereas for dry

machining, simulation gives an average of 93% closer cutting force value to the experimental results. In dry machining simulation, cutting force values are smaller than the experimental values. This variation is caused due to the difference in friction coefficient value in FEM machining and assumption in FE model. The authenticity of the developed model was successfully tested and the comparative analysis reveals that an acceptable correction was established between the simulation and experimental results in both dry and cryogenic machining.

8.4 Summary

. The current chapter presents utilization of FEM as a systematic numerical analysis tool employed to simulate machining behavior of Al-TiC MMCs. The constituent phases were separately modeled using microscopic approach to have a realistic understand the tool/matrix/particle interaction during machining. The mechanism of chip formation was constructed based on J-C material flow model and failure criteria. The scientific study was divided into three phases to analyze the plastic deformation of matrix with respect to particle distribution, influence of cutting conditions and effect of cryogenic machining based on FE approach. In the first phase, reinforcements are distributed within the matrix uniformly in two different directions in model A (linear distribution) and model B (angular distribution). Both the models showed acceptable agreement with experimental results. However, model B shows better performance than the model A in terms of chip formation. Further, to analyze the performance of the developed FEA machining model three different cutting speed, rake angle and uncut chip thickness (feed) combinations using model B type MMCs. The performance of developed model at different machining conditions was successfully performed with results close to the experimental results. Higher plastic deformation occurred along the particles while lower deformation was observed between the particles. This is due to higher stress concentration in the particles. This confirms that

presence of hard reinforcement particles, MMCs are subjected to high strain and temperatures during machining. To overcome the temperature effect cryogenic technology was introduced in the FE model by incorporating heat transfer properties tool and work material. During simulation, cryogenic machining gives a 43% average reduction in temperature than dry machining. This improved FEM model had an acceptable agreement with experimental results with an error being less than 15%. The success of the developed model establishes a platform for MMC machining simulation and helps to comprehend the machinability characteristics of Al-TiC MMCs to improve the productivity.

Chapter 9
Conclusions and Future work

9.1 Summary

The applicability of Al-TiCp MMCs has been limited to specific application despite their superior thermos-mechanical properties. Shortcomings such as complex processing techniques and difficulties associated with their machining increase the production cost and thus have become the greatest barrier to their proliferation. Improvement in production techniques and machining approaches are therefore pivotal for increasing their commercial applicability.

9.2 Conclusions

Chapter-3 describe the production of high quality Al-TiC_p composites with the developed systematic inert atmospheric stir casting facility. The results of the study reveal that potassium cryolite and magnesium successfully removed the oxide layer and promoted strong and perfect melt and particle contact. TiC particle addition significantly refined the grain structure and majority of TiC_p became engulfed into the growing solid which reduced particle solid interface energy leading to reduction in agglomeration.

- Metallographic studies revealed that TiC_p reinforced Al-MMc showed high grain refinement with average Al grain size being 50 times lesser than non-reinforced Al grains and suggest that a significant portion of the reinforcing TiC particles was situated within the metal grains. The process used to develop MMCs successfully removed the oxide layer and reduced the thermodynamic barrier by producing un-clustered and reaction free composites as confirmed by EDX analysis.
- Mechanical characterization has been performed to evaluate the performance of the developed composites. The mechanical properties enhanced due to the addition of

TiC reinforcement particles. The percentage increase in microhardness for Al-MMCs with 0 to 5 wt% of TiC particles was found to be 20% while it was just 11.6% in case of Al-MMcs with 5 to 10wt% of TiC particles. This suggests that beyond certain wt% of TiC particles in Al-MMCs, no considerable percentage increase in mechanical properties was observed. Similar trend was observed in tensile test results. Therefore, a composition consisting of 5wt% TiC particles in aluminium 6061 alloy was used for the further machining studies.

Chapter-4 deals with the design and development of an atomized liquid nitrogen spray discharge system by combining atomization process with cryogenic technology to improve the machinability of Al-MMCs. Pressurized LN_2 spray interacts with a high velocity stream of cryogenically chilled argon gas and produces a jet of droplets focused towards the tool/chip interface to improve cooling and penetration. This system significantly reduces the application of cutting fluid rate and also increases lubrication effect in the tool/chip interface simultaneously. To understand the performance of the developed system, spray characterization studies were performed. Also, optimal flow parameters were determined to understand the influence of LN_2 spray cooling during turning of Al-MMCs.

- An internally mixed spray nozzle was designed and developed to reduced the application of cutting fluid rate and to increase the lubrication effect at the tool/chip interface. The results obtained from characterization of an internal-mixing spray nozzle revealed that LN_2 flow rate decreases with an increase in ALNR, which is attributed to a decrease in available area for liquid flow with increasing air flow rate. It was observed that, when feeding pressure increased from 0.5 to 4 bar, the nozzle produces a mass ratio of argon to liquid nitrogen ranging between 0.85 and 5.844.

- The spray characteristics were investigated from spray images obtained at various ALNR. The spray half cone angle was found to be in the range of 12 to 20°. The spray half cone angle was found to be slightly increasing with ALNR which could probably be due to increase in turbulence level inside the mixing chamber.
- The solid cone spray with the LN_2 liquid core was formed in the range of 5 mm to 100 mm at various feeding pressures. As ALNR increased, liquid core decreased, ligaments became shorter and prompt atomization was observed. LN_2 stream interacted with high velocity CCA gas and disintegrated promptly into large ligaments with non-spherical droplets closer to the nozzle. The liquid ligaments and large droplets further fragmented into small spurts as it moved away from the nozzle tip.
- Spray velocity and direction were determined directly from the spray image as an angle of flight with respect to the central axis of spray. It is observed that, droplet velocity increased with increase in ALNR. It was also found that droplet velocity decreased with increase in spray distance. Velocities were found to be in the range of 8 to 50 m/s for all values of ALNR.
- Spray droplet size decreased significantly with increasing ALNR due to increase in inertial forces extended by air. With increase in ALNR, droplet diameter reduced from 120 μm to 40 μm over the entire operating range reported in current research work. Smaller droplets evaporated as they moved along the downstream resulting in reduced cooling action. This further confirms that droplet temperature varies in the range of -160 to -120^{o}C away from nozzle spray center axis. As ALNR increases, the droplet temperature increases. As the velocity of droplets increases, there is more heat transfer between the drop and surrounding air thereby increasing the droplet temperature.

- ❖ Feeding pressure, spray distance and impingement angle play a vital role in influencing the machining performance under ALN spray assisted machining process. For a feeding pressure of 200 kPa, spray distance of 10 mm and an impingement angle of 30°, tool wear showed a variation from 10.35% to 34.22% while the variation in surface roughness was found to be 5% to 24.713%. This can be due to possible formation of thick fluid film which helped in providing cooling and lubrication effect in the entire zone.

Chapter-5 describes various investigations carried to evaluate the cryogenic tribological behaviour of Al-TiC_p composite. An ALN spray system was attached to pin-on-disc configuration to facilitate cryogenic sliding wear tests. When compared to other environments, LN_2 conditions significantly lower friction and wear values. This performance improvement could be attributed to the hydraulic pressure generated by LN_2 droplets trapped in side the contact zone that helps to takes away a part of normal load. An intense cooling effect provided by LN_2 at the interface zone results in lower wear through preventing thermal softening and increasing the hardness of Al-TiC_p MMCs.

- ❖ For a maximum load of 25N under ALN spray system, Al-TiC_p composite showed a 10–20% reduction in wear rate when compared to CCA gas assisted condition. Microscopic analysis of worn surfaces confirms the dominance of abrasion wear with few evidences suggesting traces of three body abrasion under LN_2 condition. Further, it was found that debonding of TiC particles resulted in formation of cracks and subsequent fracture of the worn surface.
- ❖ Thin lengthy flake type wear debris were collected under LN_2 and CCA gas assisted condition. Thin flake structured debris were formed under dry sliding tests, which suggest predominance of delamination wear mode. Further it was also observed

that, with the increase of load and sliding velocities, there was an increase in granules size of debris particles collected, thus, explaining the severity of wear rate.

- ❖ Friction factor predominantly reflected the lubrication mechanism of LN_2. Lower friction factor was observed under LN_2 contact than dry and CCA sliding contact at all loads and sliding velocities. A maximum of 28.45% and 18.32% reduction in apparent frictional coefficient and wear rate was observed for LN_2 when compared to CCA gas assisted condition respectively.
- ❖ Friction coefficient for LN_2 lubricated contact attains a positive slope for lower loads i.e., 5N and 10N and negative slope for high loads, for i.e., 15N and 25 N, at all cutting speeds. This indicates that at low normal loads, the microscale hydrostatic lubrication film is formed between the contact surfaces.

Chapter-6 presents the turning studies carried out to revamp the machinability performance of Al-TiC_p composites with different industrial speed-feed combinations and tool geometry (rake angle, nose radius and approach angle) under ALN spray assisted machining conditions. The test results revealed that the use of atomized liquid nitrogen spray assisted machining has been successful during machining of Al-TiC composites by reducing cutting force, surface roughness and tool wear. It can be inferred from experimental findings that temperature generated between contact interfaces reduced at a significant rate in liquid nitrogen spray assisted machining.

- ❖ ALN spray assisted machining gives 84%, 70% and 33% reduction in surface roughness when compared with dry, wet and CCA gas assisted machining conditions respectively. Experimental results reveal that rake angle of 8° provides 16 to 28 % reduction in surface roughness compared to other selected rake angles under ALN spray assisted machining condition for all nose radii and approach angles. It is also observed that a nose radius of 1.2 mm and an approach angle of

30° provided lower surface roughness value of 0.193 to 0.471 µm at a rake angle of 8°under all operating environments.

- Although cryogenic technology reduced cutting temperature drastically, wear adhesion, and BUE wear modes were still observed. Chipping and delamination of wear were common in all environments. Higher rake angles caused pitting on tool while lower rake angles caused high pressure and temperature which increased adhesion wear mode. Furthermore, lower nose radius caused greater chipping and flank wear. An approach angle of 60° gave higher flank wear of 34.382% at all nose radii and rake angles.
- ALN spray assisted machining gave 36, 45 and 53% reduction in flank wear when compared to CCA gas, wet and dry machining conditions respectively. This lower tool wear was a result of prominent cooling and lubrication effect. The interface temperature decreased drastically and was essentially constant for all tool geometries. The hydraulic lubrication pressure by effective penetration plays a predominant role in tool wear mechanism. Under ALN spray assisted machining, a rake angle of 8° provided 16% to 28% reduction in flank wear compared to other rake angles.

Chapter-7 deals with determination of various significant parameters using ANOVA. Further, ANOVA also helped to test the adequacy of the developed models for establishing the mathematical link between the machinability performance parameters (cutting force, tool wear and surface roughness) and the cutting parameters (cutting speed, feed, rake angle, nose radius and approach angle) of turning process.

- ANOVA for surface roughness revealed that, nose radius, being the most significant factor influencing the surface roughness value, contributes upto 65%, 70%, 58% and 54% under ALN spray, CCA gas, wet and dry machining respectively. As nose

radius increased, the contact area between tool and workpiece increased, thereby affecting the surface roughness. ANOVA for tool wear revealed that cutting speed is the dominant factor affecting the tool wear. As cutting speed increased, tool wear increased due to generation of higher temperature at higher cutting speed and associated thermal softening and deterioration of form stability of the cutting wedge.

- Based on the results obtained from GA it was observed that lower surface roughness values were observed at an approach angle of 60° and 90° under ALN spray and CCA gas assisted conditions respectively for a cutting speed of 150 m/min, a feed of 0.1 mm/rev, a rake angle of 8° and a nose radius of 1.2 mm. Same speed and feed were maintained with a rake of 16°, a nose radius of 1mm and an approach angle of 30° to achieve lower surface roughness under dry and wet conditions.
- Lower cutting force was observed for a same cutting speed (150 m/min), a feed (0.1 mm/rev) and rake angle (10°) with varying nose radius and approach angle under all machining environments. During ALN spray assisted machining condition, nose radius of 0.6mm and approach angle of 60° were identified for lower tool wear.
- Lower tool wear values were observed for a same cutting speed (50 m/min) and feed (0.1 mm/rev) with varying tool geometry under all environments. Under ALN spray machining, a rake angle of 10°, a nose radius of 1.2 mm and an approach angle of 30° give lower tool wear.
- Further, the multi-objective optimization was carried out to identify optimum combination of cutting parameters and tool geometry that yield lower response.

Chapter-8 concentrates on the simulation of particle-reinforced MMC machining using ABAQUS. Microscale MMC models were developed to accurately simulate the machining

behavior of MMCs. FEM studies include three phases where chip-formation, plastic behavior of the matrix, cutting force and cutting force were analyzed at different reinforcement distribution, cutting parameters and tool geometry.

- Initially, the effect of particle distribution on machining of MMCs was simulated. The results revealed that the particles arranged at 90° and 30° direction (model B) gave more closer results to experimental than the particles arranged at 0° and 90° direction (model A). At 1.8 ms, model B showed 78% higher value of stress than model A. During machining simulation with Model B, saw type of chips were observed. This serration is mostly because of matrix element failure. Both the models showed acceptable agreement with experimental results.
- Model B exhibits much closer values to the experimental ones. It was observed that model B resulted in 80%, 60%, 70, 90% closer values in terms of chip thickness, shear angle, cutting force and cutting temperature respectively than model A. Hence further simulation studies were continued with model B.
- The performance of developed FE model was evaluated by simulating under three different cutting speeds, uncut chip thicknesses and rake angle combinations. The results of developed FE model closely match the experimental results under similar conditions. It was observed that as cutting speed and rake angle increased, the % difference between simulation and experimental results increased. Test VIII shows larger variation with experimental results. This is expected at higher cutting speed and feed in FEA cutting simulation, since the cutting tool was assumed to be ideally sharp in the analysis.
- FEA model for cryogenic machining was developed in ABAQUS by applying the cryogenic cooling impact on the workpiece and tool using convention heat transfer. It was observed that simulated temperature values are 94% closer to the

experimental cutting temperature under cryogenic machining. During simulation, cryogenic machining gave a 43% average reduction in temperature than dry machining simulation whereas in actual experiments, the average reduction in temperature was about 46%. This variation is due to the heat transfer coefficient value selected. These comparisons confirm that the developed FE model for cryogenic machining of MMC has given an acceptable correlation with experimental results under different rake angles.

The proposed methodology appears to offer considerable benefits over other methods of machining of Al-TiC composites. It can be inferred from the results that careful selection of these parameters could produce high quality components at a lower machining cost with minimum usage of liquid nitrogen. Therefore, the developed atomized liquid nitrogen spray assisted machining can be considered as a viable solution for improving machinability of composites. The details presented in this research work can be considered as a scientific basis for developing atomized liquid nitrogen spray discharge system to satisfying the present-day requirements of manufacturing industries.

9.3 Future scope

Future work demands adequate analysis of specific mechanisms and new proposals to develop improved techniques for sustainable machining. However, various studies have been left owing to time constraint. The below mentioned ideas further widen the scope of the current study.

- It would be interesting to extend the present study by developing Al-TiC MMCs using nano-size TiC particle. Nano sized TiC reinforcement can significantly improve the performance of Al-TiC_p composites owing to the fact that material properties enhance at nano level. A bottom pour mechanism and centrifugal die

casting process can be incorporated to the developed stir casting setup for further improvement in processing of composites.

- In order to analyze the performance of the developed atomized LN_2 spray system, surface integrity of the machined surface can be analyzed. Further analysis can be carried out by varying the nozzle design to vary the supply of LN_2 into the machining zone under micro machining which may improve the machinability performance of the material.
- A detailed analysis on the effect of volume percentage of TiC_p on machining under atomized liquid nitrogen spray system needs to be performe and effect of process parameters can be analyzed by studying the tool life.
- It would be quite interesting to develop FE model to understand the machining of MMCs with coated tools. A three-dimensional FE model can be simulated for studying the actual impact of oblique cutting process for MMCs. Further prediction of material flow of MMCs during machining can be analyzed by incorporating various flow stress models such as Zerilli-Armstrong model, Norton-Hoff model, etc. Finite element modeling can be performed on whisker-reinforced and fiber-reinforced MMCs.

REFERENCES

1. I. Gotman, M. Koczak, E. Shtessel, Fabrication of Al matrix in situ composites via self-propagating synthesis, Materials Science and Engineering: A 187(2) (1994) 189-199.
2. R. Shyu, C. Ho, In situ reacted titanium carbide-reinforced aluminum alloys composite, Journal of materials processing technology 171(3) (2006) 411-416.
3. K. Lee, H. Sim, H. Kwon, Reaction products of Al/TiC composites fabricated by the pressureless infiltration technique, Metallurgical and Materials Transactions A 36(9) (2005) 2517-2527.
4. W. Ding, W. Zhao, T. Xia, Grain refining action of Al–5Ti–C and Al–TiC master alloys with Al–5Ti master alloy addition for commercial purity aluminium, International Journal of Cast Metals Research 27(3) (2014) 187-192.
5. P.S. Bains, S.S. Sidhu, H. Payal, Fabrication and machining of metal matrix composites: A review, Materials and Manufacturing Processes 31(5) (2016) 553-573.
6. M. Ali, M. Fadhel, M. Alghoul, A. Zaharim, K. Sopian, Synthesis and characterization of aluminum matrix composites reinforced with various ratio of TiC for light devices, Models and Methods in Applied Sciences (2012) 169-174.
7. R. Tyagi, Synthesis and tribological characterization of in situ cast Al–TiC composites, Wear 259(1) (2005) 569-576.
8. Ibrahim, F. Mohamed, E. Lavernia, Particulate reinforced metal matrix composites—a review, Journal of materials science 26(5) (1991) 1137-1156.
9. N. Muthukrishnan, M. Murugan, K. Prahlada Rao, Machinability issues in turning of Al-SiC (10p) metal matrix composites, The International Journal of Advanced Manufacturing Technology 39(3) (2008) 211-218.
10. C.R. Dandekar, Multi-scale modeling and laser-assisted machining of metal matrix composites, Purdue University2010.
11. C.R. Dandekar, Y.C. Shin, Modeling of machining of composite materials: a review, International Journal of Machine tools and manufacture 57 (2012) 102-121.
12. Y. Yildiz, M. Nalbant, A review of cryogenic cooling in machining processes, International Journal of Machine Tools and Manufacture 48(9) (2008) 947-964.
13. Y. Kaynak, T. Lu, I. Jawahir, Cryogenic machining-induced surface integrity: a review and comparison with dry, MQL, and flood-cooled machining, Machining Science and Technology 18(2) (2014) 149-198.
14. A.Yong, K. Seah, M. Rahman, Performance evaluation of cryogenically treated tungsten carbide tools in turning, International Journal of Machine Tools and Manufacture 46(15) (2006) 2051-2056.

15. S.Y. Hong, Y. Ding, Micro-temperature manipulation in cryogenic machining of low carbon steel, Journal of Materials Processing Technology 116(1) (2001) 22-30.
16. M.I. Ahmed, A.F. Ismail, Y.A. Abakr, A.N. Amin, Effectiveness of cryogenic machining with modified tool holder, Journal of materials processing technology 185(1) (2007) 91-96.
17. K. Venugopal, S. Paul, A. Chattopadhyay, Tool wear in cryogenic turning of Ti-6Al-4V alloy, Cryogenics 47(1) (2007) 12-18.
18. N. Dhar, S. Paul, A. Chattopadhyay, The influence of cryogenic cooling on tool wear, dimensional accuracy and surface finish in turning AISI 1040 and E4340C steels, Wear 249(10) (2001) 932-942.
19. S.Y. Hong, I. Markus, W.-c. Jeong, New cooling approach and tool life improvement in cryogenic machining of titanium alloy Ti-6Al-4V, International Journal of Machine Tools and Manufacture 41(15) (2001) 2245-2260.
20. S.Y. Hong, Y. Ding, J. Jeong, Experimental evaluation of friction coefficient and liquid nitrogen lubrication effect in cryogenic machining, Machining Science and Technology 6(2) (2002) 235-250.
21. N. Hung, S. Yeo, B. Oon, Effect of cutting fluid on the machinability of metal matrix composites, Journal of Materials Processing Technology 67(1-3) (1997) 157-161.
22. S. Kannan, H. Kishawy, Tribological aspects of machining aluminium metal matrix composites, Journal of Materials Processing Technology 198(1) (2008) 399-406.
23. F. Pušavec, J. Kopač, Sustainability assessment: cryogenic machining of Inconel 718, Strojniški vestnik-Journal of Mechanical Engineering 57(9) (2011) 637-647.
24. Z. Zurecki, J. Frey, R. Ghosh, Finish-turning of hardened powder-metallurgy steel using cryogenic cooling, Advances in Powder Metallurgy and Particulate Materials (7) (2003) 7-185.
25. I.Batraev, S. Chaitanya, X. Cheng, D.V. Dudina, V. Krishnaraj, R. Kumar, Y. Li, W. Lu, A. Manna, J.M.M. Jordá, Metal Matrix Composites: Materials, Manufacturing and Engineering, Walter de Gruyter GmbH & Co KG2014.
26. M. Ali, P. Basu, M. Liwa, M. Fadhel, M. Souiyah, B. Abu Ziend, Comparison Between the Properties of Al-TiC and Al-(TiC+ FeC+ FeTi+ Fe) Composites, Arabian Journal for Science & Engineering (Springer Science & Business Media BV) 38(10) (2013).
27. A. Alpas, J. Zhang, Effect of microstructure (particulate size and volume fraction) and counter face material on the sliding wear resistance of particulate-reinforced aluminum matrix composites, Metallurgical and Materials Transactions A 25(5) (1994) 969-983.
28. S. Hashimoto, A. Yamaguchi, M. Koshino, Fabrication and characterization of TiC/Al composites, Materials Science and Engineering: A 265(1) (1999) 71-76.

29. V. Senthilkumar, A. Balaji, H. Ahamed, Effect of secondary processing and nanoscale reinforcement on the mechanical properties of Al-TiC composites, Journal of Minerals and Materials Characterization and Engineering 10(14) (2011) 1293.
30. D.L. Erich, Metal-matrix composites: problems, applications, and potential in the P/M industry, International journal of powder metallurgy (1986) 23(1) (1987) 45-54.
31. R. Mehrabian, R. Riek, M. Flemings, Preparation and casting of metal-particulate non-metal composites, Metallurgical and Materials Transactions B 5(8) (1974) 1899-1905.
32. A. Thangarasu, N. Murugan, I. Dinaharan, S. Vijay, Microstructure and microhardness of AA1050/TiC surface composite fabricated using friction stir processing, Sadhana 37(5) (2012) 579-586.
33. E. Zhang, B. Yang, S. Zeng, Q. Li, Experimental study on reaction synthesis of TiC in Al-Ti-C system, Acta Metallurgica Sinica (English letters) 11(4) (2009) 255-260.
34. P. Sahoo, M.J. Koczak, Analysis of in situ formation of titanium carbide in aluminum alloys, Materials Science and Engineering: A 144(1-2) (1991) 37-44.
35. R. Bauri, Synthesis of Al-TiC in-situ composites: Effect of processing temperature and Ti: C ratio, Transactions of the Indian Institute of Metals 62(4-5) (2009) 391-395.
36. D. Muscat, K. Shanker, R.A. Drew, Al/TiC composites produced by melt infiltration, Materials science and technology 8(11) (1992) 971-976.
37. A. Mortensen, J.A. Cornie, M.C. Flemings, Columnar dendritic solidification in a metal-matrix composite, Metallurgical Transactions A 19(3) (1988) 709-721.
38. S. Gopalakrishnan, N. Murugan, Prediction of tensile strength of friction stir welded aluminium matrix TiC p particulate reinforced composite, Materials & Design 32(1) (2011) 462-467.
39. D. Mandal, B. Dutta, S. Panigrahi, Wear and friction behavior of stir cast aluminium-base short steel fiber reinforced composites, Wear 257(7) (2004) 654-664.
40. Q. Lin, P. Shen, L. Yang, S. Jin, Q. Jiang, Wetting of TiC by molten Al at 1123–1323K, Acta materialia 59(5) (2011) 1898-1911.
41. J.V. Naidich, The wettability of solids by liquid metals, Progress in surface and membrane science 14 (1981) 353-484.
42. M. Ramachandra, K. Radhakrishna, Effect of reinforcement of flyash on sliding wear, slurry erosive wear and corrosive behavior of aluminium matrix composite, Wear 262(11) (2007) 1450-1462.
43. J. Hashim, L. Looney, M. Hashmi, Metal matrix composites: production by the stir casting method, Journal of Materials Processing Technology 92 (1999) 1-7.
44. M.P. Kenney and J.A. Courtois et al. Metal Handbooks. 15, Casting, ASM. International, OH,USA, 30th March 1998.

45. A. Kumar, R. Gautam, R. Tyagi, Dry sliding wear characteristics of in situ synthesized Al-TiC composites, Composite Interfaces 23(6) (2016) 469-480.
46. Y. Birol, Grain refining efficiency of Al–Ti–C alloys, Journal of alloys and compounds 422(1) (2006) 128-131.
47. H. Hocheng, Machining technology for composite materials: principles and practice, Elsevier2011.
48. A. Pramanik, L. Zhang, J. Arsecularatne, Prediction of cutting forces in machining of metal matrix composites, International Journal of Machine Tools and Manufacture 46(14) (2006) 1795-1803.
49. J. Lin, D. Bhattacharyya, C. Lane, Machinability of a silicon carbide reinforced aluminium metal matrix composite, Wear 181 (1995) 883-888.
50. M. Kök, A study on the machinability of Al2O3 particle reinforced aluminium alloy composite, Practical Metallography 46(11) (2009) 580-597.
51. A. Manna, B. Bhattacharayya, A study on machinability of Al/SiC-MMC, Journal of Materials Processing Technology 140(1) (2003) 711-716.
52. N. Altınkök, Investigation of mechanical and machinability properties of Al2O3/SiCp reinforced Al-based composite fabricated by stir cast technique, Journal of Porous Materials 22(6) (2015) 1643-1654.
53. J. Wang, C. Huang, W. Song, The effect of tool flank wear on the orthogonal cutting process and its practical implications, Journal of Materials Processing Technology 142(2) (2003) 338-346.
54. A. Manna, B. Bhattacharayya, Influence of machining parameters on the machinability of particulate reinforced Al/SiC–MMC, The International Journal of Advanced Manufacturing Technology 25(9) (2005) 850-856.
55. A. Pramanik, L. Zhang, J. Arsecularatne, An FEM investigation into the behavior of metal matrix composites: Tool–particle interaction during orthogonal cutting, International Journal of Machine Tools and Manufacture 47(10) (2007) 1497-1506.
56. A Pramanik, L. Zhang, J. Arsecularatne, Machining of metal matrix composites: effect of ceramic particles on residual stress, surface roughness and chip formation, International Journal of Machine Tools and Manufacture 48(15) (2008) 1613-1625.
57. J. Arsecularatne, L. Zhang, C. Montross, Wear and tool life of tungsten carbide, PCBN and PCD cutting tools, International Journal of Machine Tools and Manufacture 46(5) (2006) 482-491.
58. S.Z. Chavoshi, Tool flank wear prediction in CNC turning of 7075 AL alloy SiC composite, Production Engineering 5(1) (2011) 37-47.
59. I. Ciftci, M. Turker, U. Seker, Evaluation of tool wear when machining SiC p-reinforced Al-2014 alloy matrix composites, Materials & design 25(3) (2004) 251-255.

60. G. Yingfei, X. Jiuhua, Y. Hui, Diamond tools wear and their applicability when ultra-precision turning of SiC p/2009Al matrix composite, Wear 269(11) (2010) 699-708.
61. R.K. Bhushan, S. Kumar, S. Das, Effect of machining parameters on surface roughness and tool wear for 7075 Al alloy SiC composite, The International Journal of Advanced Manufacturing Technology 50(5) (2010) 459-469.
62. X. Li, W. Seah, Tool wear acceleration in relation to workpiece reinforcement percentage in cutting of metal matrix composites, Wear 247(2) (2001) 161-171.
63. A. Chambers, S. Stephens, Machining of Al□ 5Mg reinforced with 5 vol.% Saffil and 15 vol.% SiC, Materials Science and Engineering: A 135 (1991) 287-290.
64. Q. Yanming, Z. Zehua, Tool wear and its mechanism for cutting SiC particle-reinforced aluminium matrix composites, Journal of materials processing technology 100(1) (2000) 194-199.
65. N. Tomac, K. Tannessen, F.O. Rasch, Machinability of particulate aluminium matrix composites, CIRP Annals-Manufacturing Technology 41(1) (1992) 55-58.
66. M. El-Gallab, M. Sklad, Machining of Al/SiC particulate metal-matrix composites: Part I: Tool performance, Journal of Materials Processing Technology 83(1) (1998) 151-158.
67. X. Ding, W. Liew, X. Liu, Evaluation of machining performance of MMC with PCBN and PCD tools, Wear 259(7) (2005) 1225-1234.
68. R. Venkatesh, A. Hariharan, N. Muthukrishnan, Machinability studies of Al/SiC/(20p) MMC by using PCD insert (1300 grade), Proceedings of the World Congress on Engineering, 2009, pp. 1-3.
69. A. Di Ilio, A. Paoletti, V. Tagliaferri, F. Veniali, An experimental study on grinding of silicon carbide reinforced aluminium alloys, International journal of Machine tools and Manufacture 36(6) (1996) 673-685.
70. Y. Ge, J. Xu, H. Yang, S. Luo, Y. Fu, Workpiece surface quality when ultra-precision turning of SiC p/Al composites, Journal of materials processing technology 203(1) (2008) 166-175.
71. Y. Quan, B. Ye, The effect of machining on the surface properties of SiC/Al composites, Journal of Materials Processing Technology 138(1) (2003) 464-467.
72. E.M. Trent, P.K. Wright, Metal cutting, Butterworth-Heinemann2000.
73. A.J. Shih, Finite element analysis of the rake angle effects in orthogonal metal cutting, International Journal of Mechanical Sciences 38(1) (1995) 1-17.
74. Y. Beauchamp, M. Thomas, Y.A. Youssef, J. Masounave, Investigation of cutting parameter effects on surface roughness in lathe boring operation by use of a full factorial design, Computers & industrial engineering 31(3-4) (1996) 645-651.
75. H. Kishawy, M. Elbestawi, Effects of process parameters on material side flow during hard turning, International Journal of Machine Tools and Manufacture 39(7) (1999) 1017-1030.

76. A.K. Sahoo, S. Pradhan, A. Rout, Development and machinability assessment in turning Al/SiCp-metal matrix composite with multilayer coated carbide insert using Taguchi and statistical techniques, Archives of civil and mechanical engineering 13(1) (2013) 27-35.
77. E. Kılıckap, O. Cakır, M. Aksoy, A. Inan, Study of tool wear and surface roughness in machining of homogenised SiC-p reinforced aluminium metal matrix composite, Journal of Materials Processing Technology 164 (2005) 862-867.
78. P. Narahari, B. Pai, R. Pillai, Some aspects of machining cast Al-SiCp composites with conventional high-speed steel and tungsten carbide tools, Journal of materials engineering and performance 8(5) (1999) 538-542.
79. R. Shetty, R. Pai, V. Kamath, S.S. Rao, Steam as coolant and lubricant in turning of metal matrix composites, Journal of Zhejiang University-SCIENCE A 9(9) (2008) 1245-1250.
80. A. Shokrani, V. Dhokia, S.T. Newman, Comparative investigation on using cryogenic machining in CNC milling of Ti-6Al-4V titanium alloy, Machining Science and Technology 20(3) (2016) 475-494.
81. S.Y. Hong, Lubrication mechanisms of LN2 in ecological cryogenic machining, Machining science and technology 10(1) (2006) 133-155.
82. P. Sivaiah, D. Chakradhar, Influence of cryogenic coolant on turning performance characteristics: A comparison with wet machining, Materials and Manufacturing Processes (2017) 1-11.
83. J. Heigel, E. Whitenton, B. Lane, M. Donmez, V. Madhavan, W. Moscoso-Kingsley, Infrared measurement of the temperature at the tool–chip interface while machining Ti–6Al–4V, Journal of Materials Processing Technology 243 (2017) 123-130.
84. M. Kamruzzaman, S.S. Rahman, M.Z.I. Ashraf, N.R. Dhar, Modeling of chip–tool interface temperature using response surface methodology and artificial neural network in HPC-assisted turning and tool life investigation, The International Journal of Advanced Manufacturing Technology (2016) 1-22.
85. S.Y. Hong, Y. Ding, Cooling approaches and cutting temperatures in cryogenic machining of Ti-6Al-4V, International Journal of Machine Tools and Manufacture 41(10) (2001) 1417-1437.
86. Z. Pu, J. Outeiro, A. Batista, O. Dillon, D. Puleo, I. Jawahir, Surface integrity in dry and cryogenic machining of AZ31B Mg alloy with varying cutting edge radius tools, Procedia Engineering 19 (2011) 282-287.
87. Z. Wang, G. Petrescu, Stress analyses of CBN insert in hybrid machining of RBSN ceramic, Machining science and technology 8(1) (2004) 1-19.
88. I. Lin, Y. Hung, W.-C. Liu, S.-W. Kang, Machining and fluidity of 356Al/SiC (p) composites, Journal of Materials Processing Technology 110(2) (2001) 152-159.

89. K.K. Kumar, S. Choudhury, Investigation of tool wear and cutting force in cryogenic machining using design of experiments, Journal of Materials Processing Technology 203(1) (2008) 95-101.
90. Y. Kaynak, H. Karaca, R. Noebe, I. Jawahir, Tool-wear analysis in cryogenic machining of NiTi shape memory alloys: A comparison of tool-wear performance with dry and MQL machining, Wear 306(1) (2013) 51-63.
91. S. Paul, N. Dhar, A. Chattopadhyay, Beneficial effects of cryogenic cooling over dry and wet machining on tool wear and surface finish in turning AISI 1060 steel, Journal of Materials Processing Technology 116(1) (2001) 44-48.
92. F. Pusavec, T. Lu, C. Courbon, J. Rech, U. Aljancic, J. Kopac, I. Jawahir, Analysis of the influence of nitrogen phase and surface heat transfer coefficient on cryogenic machining performance, Journal of Materials Processing Technology 233 (2016) 19-28.
93. P.C. Priarone, F. Klocke, M.G. Faga, D. Lung, L. Settineri, Tool life and surface integrity when turning titanium aluminides with PCD tools under conventional wet cutting and cryogenic cooling, The International Journal of Advanced Manufacturing Technology 85(1-4) (2016) 807-816.
94. N. Dhar, N.S. Kishore, S. Paul, A. Chattopadhyay, The effects of cryogenic cooling on chips and cutting forces in turning AISI 1040 and AISI 4320 steels, Proceedings of the Institution of Mechanical Engineers, Part B: Journal of Engineering Manufacture 216(5) (2002) 713-724.
95. C .D. Wang, M. Chen, Q.-L. An, M. Wang, Y.-H. Zhu, Tool wear performance in face milling Inconel 182 using minimum quantity lubrication with different nozzle positions, International journal of precision engineering and manufacturing 15(3) (2014) 557-565.
96. A.A. Khan, M.Y. Ali, M. Haque, A new approach of applying cryogenic coolant in turning AISI 304 stainless steel, International Journal of Mechanical and Materials Engineering (IJMME) 5(2) (2010) 171-174.
97. L.L. De Lacalle, C. Angulo, A. Lamikiz, J. Sanchez, Experimental and numerical investigation of the effect of spray cutting fluids in high speed milling, Journal of Materials Processing Technology 172(1) (2006) 11-15.
98. Bermingham, M. J., J. Kirsch, S. Sun, S. Palanisamy, and M. S. Dargusch. "New observations on tool life, cutting forces and chip morphology in cryogenic machining Ti-6Al-4V." International Journal of Machine Tools and Manufacture 51, no. 6 (2011): 500-511.
99. Dhananchezian, M., and M. Pradeep Kumar. "Cryogenic turning of the Ti–6Al–4V alloy with modified cutting tool inserts." Cryogenics 51, no. 1 (2011): 34-40.
100. U. Heisel, M. Lutz, D. Spath, R.A. Wassmer, U. Walter, Application of minimum quantity cooling lubrication technology in cutting processes (1994).

101. A. R. Machado, J. Wallbank, The effect of extremely low lubricant volumes in machining, Wear 210(1-2) (1997) 76-82.
102. M.B. Jun, S.S. Joshi, R.E. DeVor, S.G. Kapoor, An experimental evaluation of an atomization-based cutting fluid application system for micromachining, Journal of manufacturing science and engineering 130(3) (2008) 031118.
103. M. Rukosuyev, C. Goo, M. Jun, S. Park, Design and development of cutting fluid system based on ultrasonic atomization for micro-machining, Trans. NAMRI/SME 38(1) (2010) 97-104.
104. I. Ghai, Analysis of droplet behavior on a rotating surface in atomization-based cutting fluid systems for micro-machining, University of Illinois at Urbana-Champaign, 2010.
105. D.M. Pendse, S.S. Joshi, Modeling and optimization of machining process in discontinuously reinforced aluminium matrix composites, Machining science and technology 8(1) (2004) 85-102.
106. J. S. Dureja, "Modelling and Optimization Methods for Hard Turning," 2nd International Conference on Production and Industrial Engineering, CPIE December 2010
107. A. Kremer, A. Devillez, S. Dominiak, D. Dudzinski, M. El Mansori, Machinability of AI/SiC particulate metal-matrix composites under dry conditions with CVD diamond-coated carbide tools, Machining Science and Technology 12(2) (2008) 214-233.
108. P. Sivasakthivel, V. Velmurugan, R. Sudhakaran, Prediction of vibration amplitude from machining parameters by response surface methodology in end milling, The International Journal of Advanced Manufacturing Technology 53(5) (2011) 453-461.
109. K. Palanikumar, Modeling and analysis for surface roughness in machining glass fibre reinforced plastics using response surface methodology, Materials & design 28(10) (2007) 2611-2618.
110. N. Muthukrishnan, J.P. Davim, Optimization of machining parameters of Al/SiC-MMC with ANOVA and ANN analysis, Journal of materials processing technology 209(1) (2009) 225-232.
111. A.C. Basheer, U.A. Dabade, S.S. Joshi, V. Bhanuprasad, V. Gadre, Modeling of surface roughness in precision machining of metal matrix composites using ANN, Journal of Materials Processing Technology 197(1) (2008) 439-444.
112. U.A. Dabade, D. Dapkekar, S.S. Joshi, Modeling of chip–tool interface friction to predict cutting forces in machining of Al/SiCp composites, International Journal of Machine Tools and Manufacture 49(9) (2009) 690-700.
113. S. Deepak, Applications of Different Optimization Methods for Metal Cutting Operation–A Review, Research Journal of Engineering Sciences ISSN 2278 (2012) 9472.

114. U.A. Dabade, H.A. Sonawane, S.S. Joshi, Cutting forces and surface roughness in machining Al/SiCp composites of varying composition, Machining Science and Technology 14(2) (2010) 258-279.
115. R.K. Jain, V.K. Jain, Optimum selection of machining conditions in abrasive flow machining using neural network, Journal of Materials Processing Technology 108(1) (2000) 62-67.
116. P. Suresh, P.V. Rao, S. Deshmukh, A genetic algorithmic approach for optimization of surface roughness prediction model, International Journal of Machine Tools and Manufacture 42(6) (2002) 675-680.
117. J.P. Davim, Design of optimisation of cutting parameters for turning metal matrix composites based on the orthogonal arrays, Journal of materials processing technology 132(1) (2003) 340-344.
118. R. Saravanan, M. Sachithanandam, Genetic algorithm (GA) for multivariable surface grinding process optimisation using a multi-objective function model, The International Journal of Advanced Manufacturing Technology 17(5) (2001) 330-338.
119. J. Mackerle, Finite-element analysis and simulation of machining: a bibliography (1976–1996), Journal of Materials Processing Technology 86(1) (1999) 17-44.
120. J. Monaghan, D. Brazil, Modelling the flow processes of a particle reinforced metal matrix composite during machining, Composites Part A: Applied Science and Manufacturing 29(1) (1998) 87-99.
121. C.R. Dandekar, Y.C. Shin, Multi-step 3-D finite element modeling of subsurface damage in machining particulate reinforced metal matrix composites, Composites Part A: Applied Science and Manufacturing 40(8) (2009) 1231-1239.
122. K. Osakada, Y. Terasaka, Process modeling of orthogonal cutting by the rigid-plastic finite element method, Journal of Engineering Materials and Technology 106 (1984) 133.
123. A. Tay, M. Stevenson, G. de Vahl Davis, Using the finite element method to determine temperature distributions in orthogonal machining, Proceedings of the institution of mechanical engineers 188(1) (1974) 627-638.
124. J. Chow, Further developments in applying the finite element method to the calculation of temperature distributions in machining and comparisons with experiment, Journal of engineering for industry 105 (1983) 149.
125. M. Lajczok, A Study of Some Aspects of Metal Machining Using the Finite-Element Method, Dissertation Abstracts International 41(12) (1981) 242.
126. I.Ceretti, P. Fallböhmer, W. Wu, T. Altan, Application of 2D FEM to chip formation in orthogonal cutting, Journal of Materials Processing Technology 59(1-2) (1996) 169-180.
127. T. Marusich, M. Ortiz, Modelling and simulation of high-speed machining, International Journal for Numerical Methods in Engineering 38(21) (1995) 3675-3694.

128. J.T. Carroll, J.S. Strenkowski, Finite element models of orthogonal cutting with application to single point diamond turning, International Journal of Mechanical Sciences 30(12) (1988) 899-920.
129. K.J. Moon, Finite element prediction of chip geometry and tool/workpiece temperature distributions in orthogonal metal cutting, Journal of Engineering for Industry 112 (1990) 313.
130. J.S. Strenkowski, J. Carol, An orthogonal metal cutting model based on an eulerian finite element method, Manufacturing Processes, Machines and Systems, Proceedings of the 13th NSF Conference on Production Research and Technology, 1986, pp. 261-264.
131. W.K. Liu, C. Herman, C. Jiun-Shyan, B. Ted, Arbitrary Lagrangian-Eulerian Petrov-Galerkin finite elements for nonlinear continua, Computer methods in applied mechanics and engineering 68(3) (1988) 259-310.
132. R. Rakotomalala, P. Joyot, M. Touratier, Arbitrary Lagrangian-Eulerian thermomechanical finite-element model of material cutting, International Journal for Numerical Methods in Biomedical Engineering 9(12) (1993) 975-987.
133. M. Movahhedy, M. Gadala, Y. Altintas, Simulation of the orthogonal metal cutting process using an arbitrary Lagrangian–Eulerian finite-element method, Journal of materials processing technology 103(2) (2000) 267-275.
134. M. Movahhedy, M. Gadala, Y. Altintas, Simulation of chip formation in orthogonal metal cutting process: an ALE finite element approach, Machining Science and Technology 4(1) (2000) 15-42.
135. Y. Zhu, H. Kishawy, Influence of alumina particles on the mechanics of machining metal matrix composites, International Journal of Machine Tools and Manufacture 45(4) (2005) 389-398.
136. L. Zhou, S. Huang, D. Wang, X. Yu, Finite element and experimental studies of the cutting process of SiCp/Al composites with PCD tools, The International Journal of Advanced Manufacturing Technology 52(5) (2011) 619-626.
137. G.R. Johnson, W.H. Cook, Fracture characteristics of three metals subjected to various strains, strain rates, temperatures and pressures, Engineering fracture mechanics 21(1) (1985) 31-48.
138. G.R. Johnson, Materials Characterization for computations involving severe dynamic loading, Proc. Army Symp. Of Solid Mechanics, DTIC Document, 1980, pp. 62-67.
139. G.R. Johnson, W.H. Cook, A constitutive model and data for metals subjected to large strains, high strain rates and high temperatures, Proceedings of the 7th International Symposium on Ballistics, The Hague, The Netherlands, 1983, pp. 541-547.

140. A. Kennedy, A. Karantzalis, S. Wyatt, The microstructure and mechanical properties of TiC and TiB2-reinforced cast metal matrix composites, Journal of materials science 34(5) (1999) 933-940.
141. Maxwell, A. Hellawell, A simple model for grain refinement during solidification, Acta Metallurgica 23(2) (1975) 229-237.
142. Q. Zhou, Y. Cao, L.P. Chen, Grain Refinement of 6061 Alloy by Low-Voltage Pulsed Magnetic Field Treatment, Advanced Materials Research, Trans Tech Publ, 2013, pp. 2413-2417.
143. N. Samer, J. Andrieux, B. Gardiola, N. Karnatak, O. Martin, H. Kurita, L. Chaffron, S. Gourdet, S. Lay, O. Dezellus, Microstructure and mechanical properties of an Al–TiC metal matrix composite obtained by reactive synthesis, Composites Part A: Applied Science and Manufacturing 72 (2015) 50-57.
144. R. Rai, S. Saha, G. Datta, M. Chakraborty, Studies on synthesis of in-situ Al-TiC metal matrix composites, IOP Conference Series: Materials Science and Engineering, IOP Publishing, 2016, p. 012042.
145. K. Mahadevan, K. Raghukandan, T. Senthilvelan, B. Pai, U. Pillai, Investigation on the influence of heat-treatment parameters on the hardness of AA6061-SiC p composite, Journal of materials processing technology 171(2) (2006) 314-318.
146. T. Christy, N. Murugan, S. Kumar, A comparative study on the microstructures and mechanical properties of Al 6061 alloy and the MMC Al 6061/TiB2/12p, Journal of Minerals and Materials Characterization and Engineering 9(01) (2010) 57.
147. Y. Şahin, Abrasive wear behaviour of SiC/2014 aluminium composite, Tribology International 43(5) (2010) 939-943.
148. R.R. Veeravalli, R. Nallu, S. Mohammed Moulana Mohiuddin, Mechanical and tribological properties of AA7075–TiC metal matrix composites under heat treated (T6) and cast conditions, Journal of Materials Research and Technology 5(4) (2016) 377-383.
149. Z. Xing, Y. Han, J. Guo, L. Yu, Microstructure and mechanical behavior of the NiAl-TiC in situ composite, Metallurgical and Materials Transactions A 28(4) (1997) 1079-1087.
150. B.S. Ünlü, Investigation of tribological and mechanical properties Al 2 O 3–SiC reinforced Al composites manufactured by casting or P/M method, Materials & Design 29(10) (2008) 2002-2008.
151. Z. Wang, K. Rajurkar, Cryogenic machining of hard-to-cut materials, Wear 239(2) (2000) 168-175.
152. W. Thielicke, E. Stamhuis, PIVlab–towards user-friendly, affordable and accurate digital particle image velocimetry in MATLAB, Journal of Open Research Software 2(1) (2014).

153. P. Mullinger, N. Chigier, DESIGN AND PERFORMANCE OF INTERNAL MIXING MULTIJET TWIN FLUID ATOMIZERS, Journal of the Institute of Fuel 47(393) (1974) 251-261.
154. T. Roesler, A. Lefebvre, Studies on aerated-liquid atomization, Int J Turbo Jet Engines 6(3-4) (1989) 221-230.
155. J. Chin, Effervescent atomization and internal mixing air assist atomization, International journal of turbo and jet engines 12(2) (1995) 119-128.
156. A. Lefebvre, Atomization and sprays, CRC press1988.
157. H. Hirahara, M. Kawahashi, Experimental investigation of viscous effects upon a breakup of droplets in high-speed air flow, Experiments in Fluids 13(6) (1992) 423-428.
158. Y. Zama, M. Kawahashi, H. Hirahara, Simultaneous measurement method of size and 3D velocity components of droplets in a spray field illuminated with a thin laser-light sheet, Measurement Science and Technology 16(10) (2005) 1977.
159. I. Faeth, L.-P. Hsiang, P.-K. Wu, Structure and breakup properties of sprays, International Journal of Multiphase Flow 21 (1995) 99-127.
160. Elbadawy, Ibrahim, Philip H. Gaskell, Malcolm Lawes, and Harvey M. Thompson. "Numerical investigation of the effect of ambient turbulence on pressure swirl spray characteristics." International Journal of Multiphase Flow 77 (2015): 271-284.
161. E.C. Blount, Effects of drop size and drop velocity on cooling characteristics of sprays, Texas Tech University, 1991.
162. A. Courbon, F. Pusavec, F. Dumont, J. Rech, J. Kopac, Tribological behaviour of Ti6Al4V and Inconel718 under dry and cryogenic conditions—Application to the context of machining with carbide tools, Tribology International 66 (2013) 72-82.
163. J. Hemanth, Tribological behavior of cryogenically treated B 4 Cp/Al–12% Si composites, Wear 258(11) (2005) 1732-1744.
164. K. Seah, J. Hemanth, Cryogenic effects during casting on the wear behavior of aluminum-alloy/glass MMCs, Composites Part A: Applied Science and Manufacturing 38(5) (2007) 1395-1402.
165. ASTM, G 99–95a Standard Test Method for Wear Testing with a Pin-on-Disk Apparatus, ASTM International (2000).
166. F. Bowden, D. Tabor, The Friction and Lubrication of Solids, Oxford, 1954.
167. W. Hübner, T. Gradt, T. Schneider, H. Börner, Tribological behaviour of materials at cryogenic temperatures, Wear 216(2) (1998) 150-159.
168. S.Y. Hong, Investigation of liquid nitrogen lubrication effect in cryogenic machining, World Tribology Congress III, American Society of Mechanical Engineers, 2005, pp. 801-802.

169. S. C. Jun, Lubrication effect of liquid nitrogen in cryogenic machining friction on the tool-chip interface, Journal of mechanical science and technology 19(4) (2005) 936-946.
170. C. Ramesh, A. Ahamed, Friction and wear behaviour of cast Al 6063 based in situ metal matrix composites, Wear 271(9) (2011) 1928-1939.
171. M. Kestursatya, J. Kim, P. Rohatgi, Friction and wear behavior of a centrifugally cast lead-free copper alloy containing graphite particles, Metallurgical and Materials transactions A 32(8) (2001) 2115-2125.
172. F. Akhtar, Microstructure evolution and wear properties of in situ synthesized TiB 2 and TiC reinforced steel matrix composites, Journal of Alloys and Compounds 459(1) (2008) 491-497.
173. A.A. Hamid, P. Ghosh, S. Jain, S. Ray, The influence of porosity and particles content on dry sliding wear of cast in situ Al (Ti)–Al 2 O 3 (TiO 2) composite, Wear 265(1) (2008) 14-26.
174. S. Wilson, A. Alpas, Wear mechanism maps for metal matrix composites, Wear 212(1) (1997) 41-49.
175. S. Wilson, A. Alpas, Thermal effects on mild wear transitions in dry sliding of an aluminum alloy, Wear 225 (1999) 440-449.
176. S.Y. Hong, Z. Zhao, Thermal aspects, material considerations and cooling strategies in cryogenic machining, Clean Technologies and Environmental Policy 1(2) (1999) 107-116.
177. M. Surappa, Dry sliding wear of fly ash particle reinforced A356 Al composites, Wear 265(3) (2008) 349-360.
178. A. Mandal, M. Chakraborty, B. Murty, Effect of TiB 2 particles on sliding wear behaviour of Al–4Cu alloy, Wear 262(1) (2007) 160-166.
179. I.M. Hutchings, Tribological properties of metal matrix composites, Materials science and technology 10(6) (1994) 513-517.
180. G.E. Box, D.W. Behnken, Some new three level designs for the study of quantitative variables, Technometrics 2(4) (1960) 455-475.
181. S.C. Ferreira, R. Bruns, H. Ferreira, G. Matos, J. David, G. Brandao, E.P. da Silva, L. Portugal, P. Dos Reis, A. Souza, Box-Behnken design: an alternative for the optimization of analytical methods, Analytica chimica acta 597(2) (2007) 179-186.
182. N.S.K. Reddy, P.V. Rao, Experimental investigation to study the effect of solid lubricants on cutting forces and surface quality in end milling, International Journal of Machine Tools and Manufacture 46(2) (2006) 189-198.
183. N.S.K. Reddy, S. Kwang-Sup, M. Yang, Experimental study of surface integrity during end milling of Al/SiC particulate metal–matrix composites, journal of materials processing technology 201(1) (2008) 574-579.

184. N.P. Suh, N. Saka, Surface Engineering, CIRP Annals - Manufacturing Technology 36(1) (1987) 403-408.
185. S.K. Josyula, S.K.R. Narala, Experimental investigation on tribological behaviour of Al-TiCp composite under sliding wear conditions, Proceedings of the Institution of Mechanical Engineers, Part J: Journal of Engineering Tribology 230(8) (2016) 919-929.
186. H. Saglam, F. Unsacar, S. Yaldiz, Investigation of the effect of rake angle and approaching angle on main cutting force and tool tip temperature, International Journal of machine tools and manufacture 46(2) (2006) 132-141.
187. M. Liu, J. I. Takagi, A. Tsukuda, Effect of tool nose radius and tool wear on residual stress distribution in hard turning of bearing steel, Journal of Materials Processing Technology 150(3) (2004) 234-241.
188. T. Özel, T.-K. Hsu, E. Zeren, Effects of cutting edge geometry, workpiece hardness, feed rate and cutting speed on surface roughness and forces in finish turning of hardened AISI H13 steel, The International Journal of Advanced Manufacturing Technology 25(3) (2005) 262-269.
189. F. Klocke, H. Kratz, Advanced tool edge geometry for high precision hard turning, CIRP Annals-Manufacturing Technology 54(1) (2005) 47-50.
190. A.K. Parida, K. Maity, Effect of nose radius on forces, and process parameters in hot machining of Inconel 718 using finite element analysis, Engineering Science and Technology, an International Journal (2016).
191. P. Suresh, K. Marimuthu, S. Ranganathan, T. Rajmohan, Optimization of machining parameters in turning of Al-SiC-Gr hybrid metal matrix composites using grey-fuzzy algorithm, Transactions of Nonferrous Metals Society of China 24(9) (2014) 2805-2814.
192. C. Cheung, K. Chan, S. To, W. Lee, Effect of reinforcement in ultra-precision machining of Al6061/SiC metal matrix composites, Scripta Materialia 47(2) (2002) 77-82.
193. U.M.R. Paturi, S.K.R. Narala, Experimental investigation to study the effect of electrostatic micro-solid lubricant–coated carbide tools on machinability parameters in turning, Proceedings of the Institution of Mechanical Engineers, Part B: Journal of Engineering Manufacture 229(5) (2015) 693-702.
194. Y. Quan, Z. Zhou, B. Ye, Cutting process and chip appearance of aluminum matrix composites reinforced by SiC particle, Journal of Materials Processing Technology 91(1) (1999) 231-235.
195. F. Cus, M. Milfelner, J. Balic, An intelligent system for monitoring and optimization of ball-end milling process, Journal of Materials Processing Technology 175(1) (2006) 90-97.

196. R.K. Bhushan, Optimization of cutting parameters for minimizing power consumption and maximizing tool life during machining of Al alloy SiC particle composites, Journal of Cleaner Production 39 (2013) 242-254.
197. M.K. Barua, J.S. Rao, S. Anbuudayasankar, T. Page, Measurement of Surface Roughness Through RSM: Effect of Coated Carbide Tool on 6061-T4 Aluminium, International Journal of Enterprise Network Management 4(2) (2010) 136-153.
198. S. Khamel, N. Ouelaa, K. Bouacha, Analysis and prediction of tool wear, surface roughness and cutting forces in hard turning with CBN tool, Journal of mechanical science and technology 26(11) (2012) 3605-3616.
199. K.N. Das, R.P. Parouha, Optimization of Engineering Design Problems via an Efficient Hybrid Meta-heuristic Algorithm, IFAC Proceedings Volumes 47(1) (2014) 692-699.
200. Y.-C. Chang, J.-K. Lin, M.-H. Chuang, Optimal chiller loading by genetic algorithm for reducing energy consumption, Energy and Buildings 37(2) (2005) 147-155.
201. N. Abukhshim, P. Mativenga, M. Sheikh, Heat generation and temperature prediction in metal cutting: A review and implications for high speed machining, International Journal of Machine Tools and Manufacture 46(7) (2006) 782-800.
202. K. Deb, A. Pratap, S. Agarwal, T. Meyarivan, A fast and elitist multiobjective genetic algorithm: NSGA-II, IEEE transactions on evolutionary computation 6(2) (2002) 182-197.
203. C.R. Dandekar, Y.C. Shin, Multiphase finite element modeling of machining unidirectional composites: prediction of debonding and fiber damage, Journal of Manufacturing Science and Engineering 130(5) (2008) 051016.
204. G. Camus, Modelling of the mechanical behavior and damage processes of fibrous ceramic matrix composites: application to a 2-D SiC/SiC, International Journal of solids and Structures 37(6) (2000) 919-942.
205. D. Systemes, I.(2007), Abaqus Analysis User Manual (v6. 7).
206. D.R. Lesuer, G. Kay, M. LeBlanc, Modeling large strain, high rate deformation in metals, Engineering research, development and technology (1999).
207. M. Sima, T. Özel, Modified material constitutive models for serrated chip formation simulations and experimental validation in machining of titanium alloy Ti–6Al–4V, International Journal of Machine Tools and Manufacture 50(11) (2010) 943-960.
208. Y. C. Yen, A. Jain, T. Altan, A finite element analysis of orthogonal machining using different tool edge geometries, Journal of Materials Processing Technology 146(1) (2004) 72-81.
209. P.V. Pashaki, M. Pouya, Investigation of High-Speed Cryogenic Machining Based on Finite Element Approach, Latin American Journal of Solids and Structures 13 (2017).
210. R. Miranda, Metalworking fluids (MWFs) for cutting and grinding–Fundamentals and recent advances, Taylor & Francis, 2013.

APPENDIX - A.

Table A.1 Specifications of HMT PTC 200 CNC lathe machine.

Specifications	Units	Details
Type of bed		Inclined 30° to vertical
Swing over cross slide	*mm*	200
Swing over bed	*mm*	ϕ 250
Distance between centers	*mm*	300
Chuck type	*mm*	Hydraulic operated 3 jaw self-centering chuck with hollow cylinder (ϕ165)
Power	*Std kW*	55/7
Spindle speed	*Std rpm*	100-4000
Turning tool size	*mm*	20 × 20
Feed rate	*mm/min*	1-5000
Positional X-axis	*mm*	±0.003 over 100mm length
Positional Z-axis	*mm*	±0.004 over 100mm length
Repeatability X-axis	*mm*	±0.003
Repeatability Z-axis	*mm*	±0.003

Table A.2 Box-Behnken design for experimentation.

Std	Run	Factor 1 A: Cutting speed m/min	Factor 2 B: Feed mm/rev	Factor 3 C: Rake angle deg	Factor 4 D: Nose radius mm	Factor 5 E: Approach angle deg	Std	Run	Factor 1 A: Cutting speed m/min	Factor 2 B: Feed mm/rev	Factor 3 C: Rake angle deg	Factor 4 D: Nose radius mm	Factor 5 E: Approach angle deg
44	1	0	0	0	0	0	22	24	0	1	-1	0	0
15	2	-1	0	1	0	0	19	25	0	0	0	-1	1
26	3	1	0	0	-1	0	45	26	0	0	0	0	0
27	4	-1	0	0	1	0	10	27	0	1	0	0	-1
46	5	0	0	0	0	0	17	28	0	0	0	-1	-1
12	6	0	1	0	0	1	23	29	0	-1	1	0	0
40	7	0	1	0	1	0	2	30	1	-1	0	0	0
18	8	0	0	0	1	-1	25	31	-1	0	0	-1	0
21	9	0	-1	-1	0	0	8	32	0	0	1	1	0
1	10	-1	-1	0	0	0	33	33	-1	0	0	0	-1
30	11	0	0	1	0	-1	34	34	1	0	0	0	-1
37	12	0	-1	0	-1	0	31	35	0	0	-1	0	1
29	13	0	0	-1	0	-1	28	36	1	0	0	1	0
6	14	0	0	1	-1	0	4	37	1	1	0	0	0
24	15	0	1	1	0	0	13	38	-1	0	-1	0	0
3	16	-1	1	0	0	0	39	39	0	-1	0	1	0
7	17	0	0	-1	1	0	42	40	0	0	0	0	0
9	18	0	-1	0	0	-1	36	41	1	0	0	0	1
43	19	0	0	0	0	0	20	42	0	0	0	1	1
14	20	1	0	-1	0	0	16	43	1	0	1	0	0
5	21	0	0	-1	-1	0	41	44	0	0	0	0	0
38	22	0	1	0	-1	0	11	45	0	-1	0	0	1
35	23	-1	0	0	0	1	32	46	0	0	1	0	1

Table A.3 Specifications of 3-axis piezoelectric lathe tool dynamometer.

Performance	Units	Specification		
Sensor		X	Y	Z
Measurement range	N	0 to 2200	0 to 2200	0 to 4450
Maximum force	N	2940	2940	5870
Sensitivity (±15%)	pC/N	7.19	7.19	3.37
linearity	%FS	≤1		
Capacitance	pF	18.1		
Temperature range	C	-73 to 177		
Frequency limit	KHz	90		
Charge amplifier				
Type		ICAM 5073A311 (4827454)		
No of channels		4		
Measuring range	pC	100 to 1000000		
Signal conditioner				
Type		PCB 482C54		
No of channels		4		
accuracy		±1% to ±5%		
Sensitivity (±1%)	mVpC	0.1/ 1.0/ 10.0		
Input range	pC	±100000		
Output range	Vpk	10		
Frequency range	Hz	0.05 to 100000		
Non-linearity	%FS	≤1		
DAQ				
Type		NI USB-6002		
Analogue to digital converter (ADC) resolution	bit	16		
Maximum Sample rate (aggregate)	KS/s	50		
Absolute Accuracy, typical, at full scale	mV	8.6		
Software				
Name		Cutting force measurement (CFM)		
Version		1.0.2		

Table A.4 Specifications of Surtronic S25 surface profilometer.

Performance	units	Specification
Model		Subtronic 25 Taylor Hobson
Gauge range	μm	300
Resolution	μm	0.01
Accuracy		2% of reading +LSDM um
Gauge force	mg	150-300
Stylus		Diamond tip
Diamond tip radius	μm	5
Transverse length	mm	0.25 to 25
Transverse speed	mm/sec	1
Filter		2CR or Gaussian
Software		Taly Profile silver

Table A.5 Specifications of Olympus STM 6 optical microscope.

Performance	Specification
Measuring accuracy	50mm stroke: (3+L/50) µm 100mm stroke: (3+2L/100) µm 150mm stroke: (3+3L/150) µm L=measuring length (mm)
Maximum acceptable sample height	155 mm
Coarse focusing speed	48 mm/sec
Fine focusing speed	800/400/200/50µm (full rotation of knob) 4steps
illumination	12V 100W halogen
Eyepiece	MM6-OCC 10X (with cross lie, F.N. 22)
Stage	X axis=100 mm; Y axis=50 mm
Counter display minimum readout	0.5 µm
Power consumption	100-120/220-240V~0.7 / 0.4A 50/60 Hz

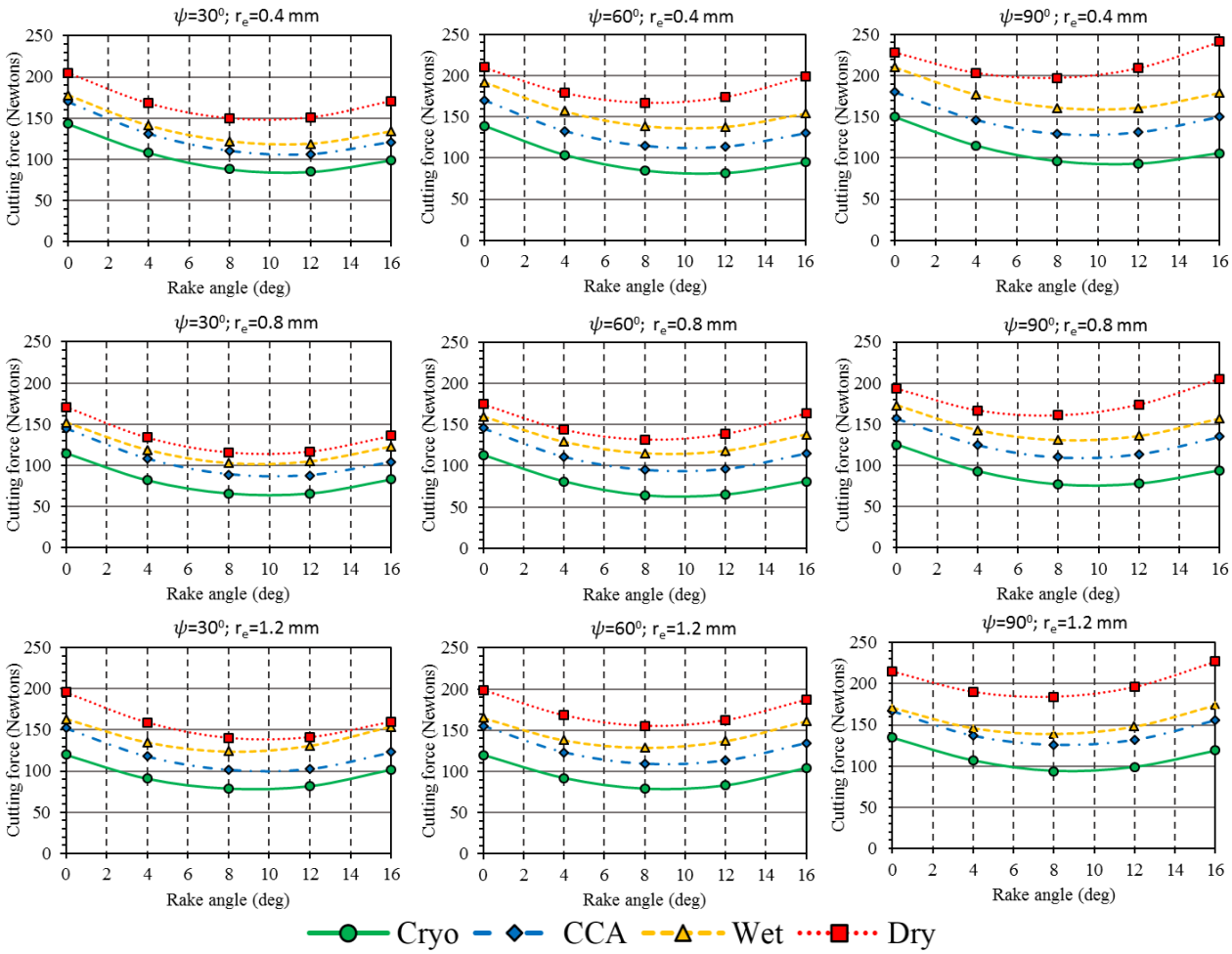

Fig. A.1. Variation of cutting force at cutting speed of 50 m/min and feed of 0.1 mm/rev for different rake angle with various levels of nose radii and approach angle under dry, wet, CCA gas and ALN spray assisted machining conditions (cryo).

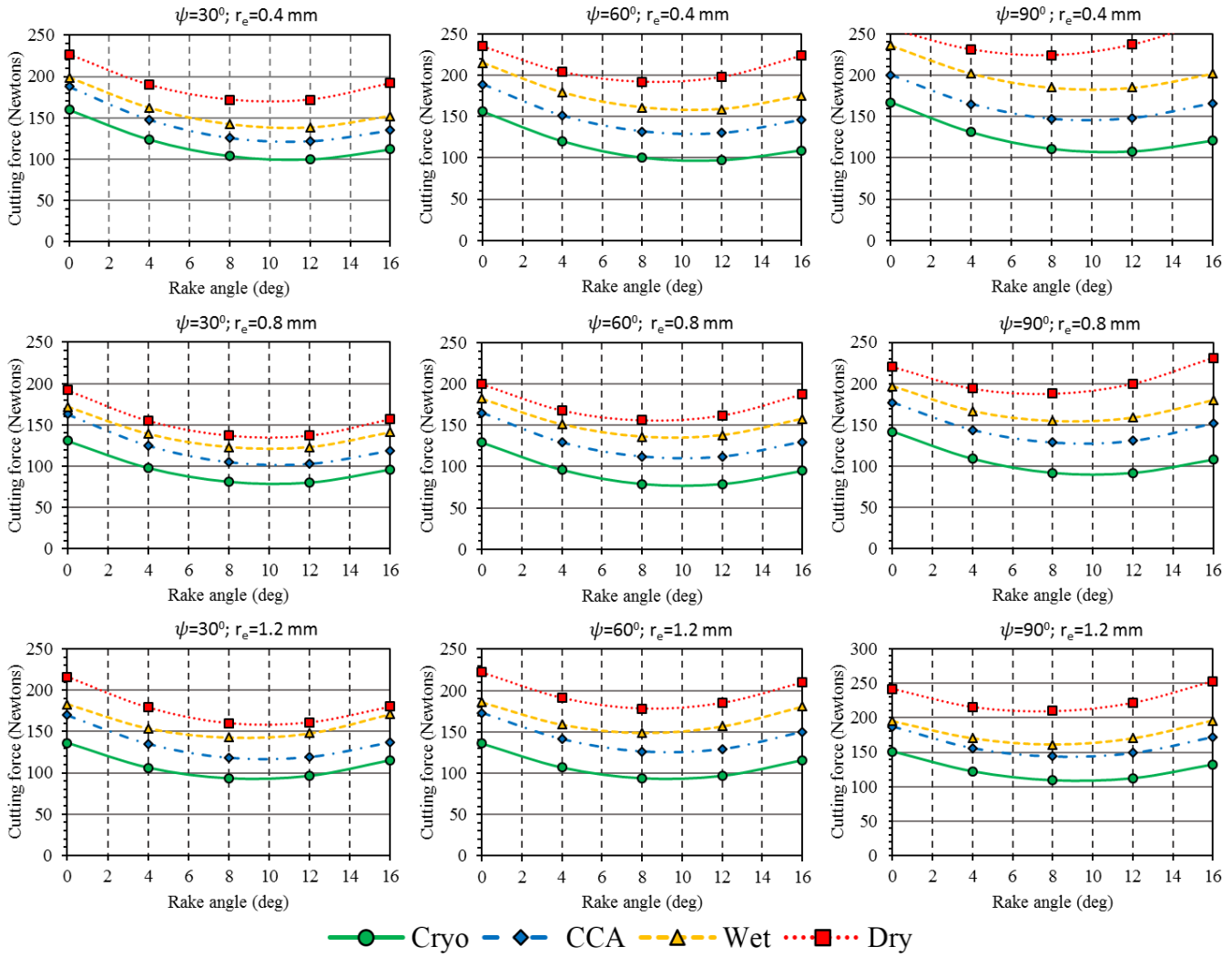

Fig. A.2. Variation of cutting force at cutting speed of 50 m/min and feed of 0.15 mm/rev for different rake angle with various levels of nose radii and approach angles under dry, wet, CCA gas and ALN spray assisted machining conditions (cryo).

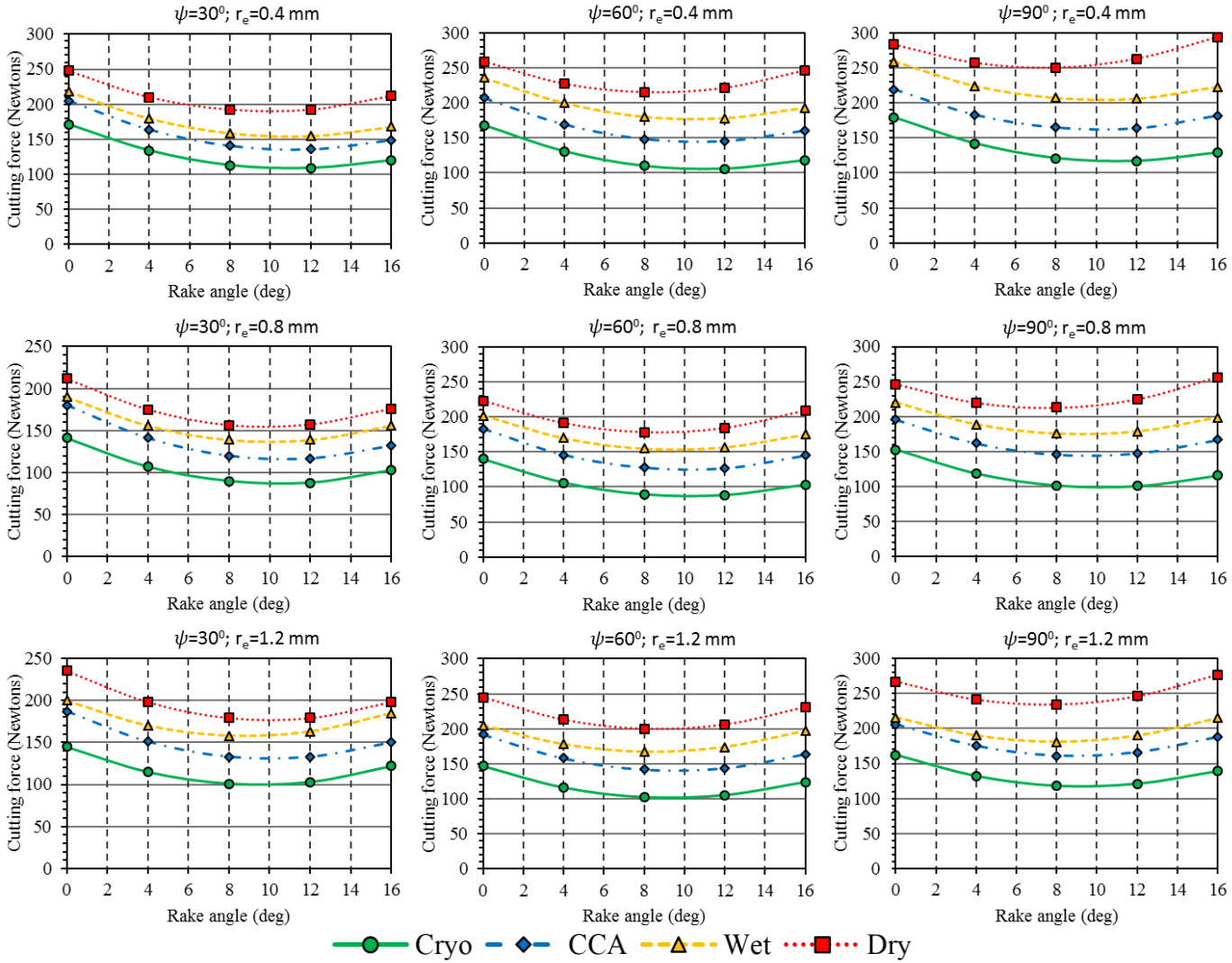

Fig. A.3. Variation of cutting force at cutting speed of 50 m/min and feed of 0.2 mm/rev for different rake angle with various levels of nose radii and approach angles under dry, wet, CCA gas and ALN spray assisted machining conditions (cryo).

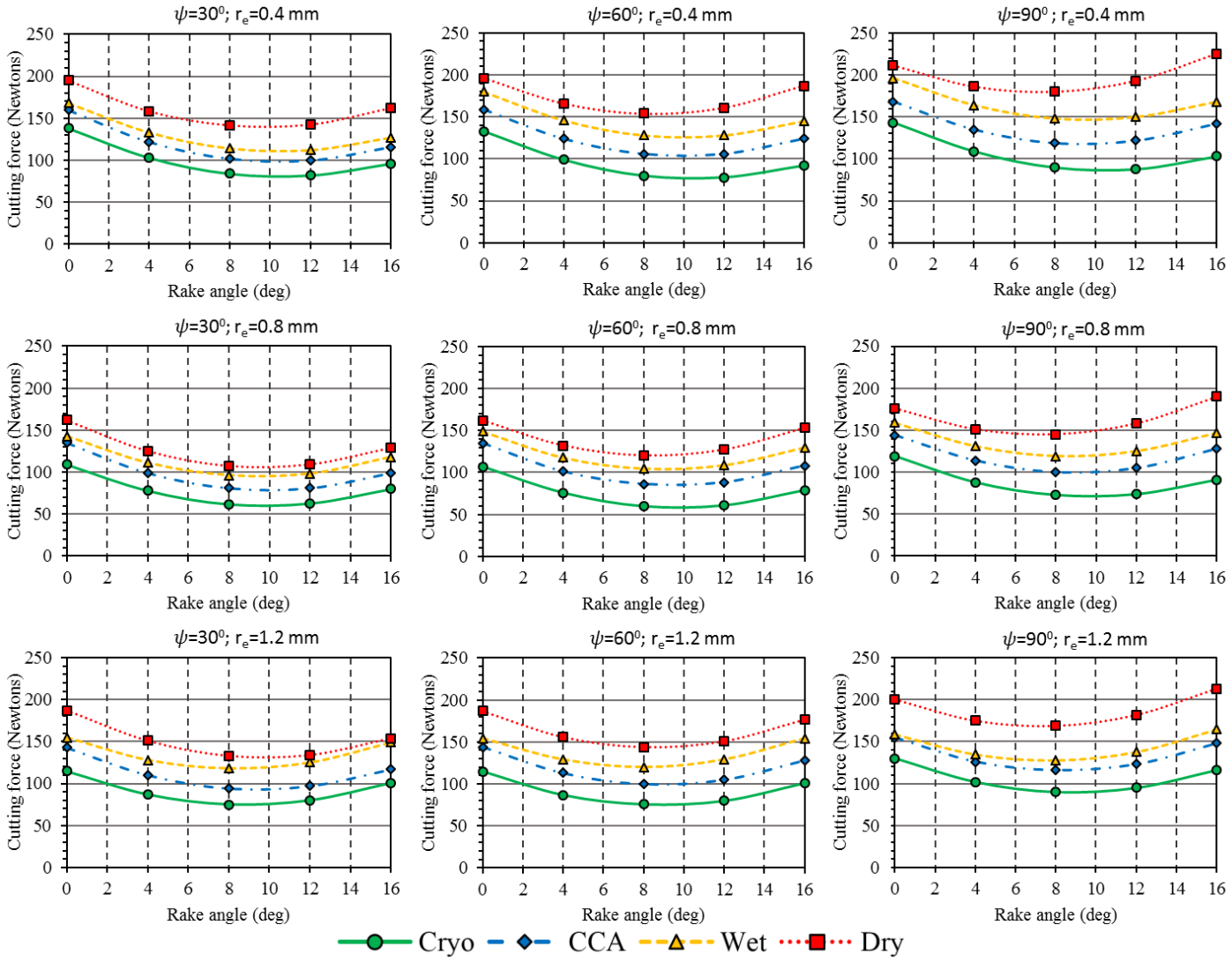

Fig. A.4. Variation of cutting force at cutting speed of 100 m/min and feed of 0.1 mm/rev for different rake angle with various levels of nose radii and approach angles under dry, wet, CCA gas and ALN spray assisted machining conditions (cryo).

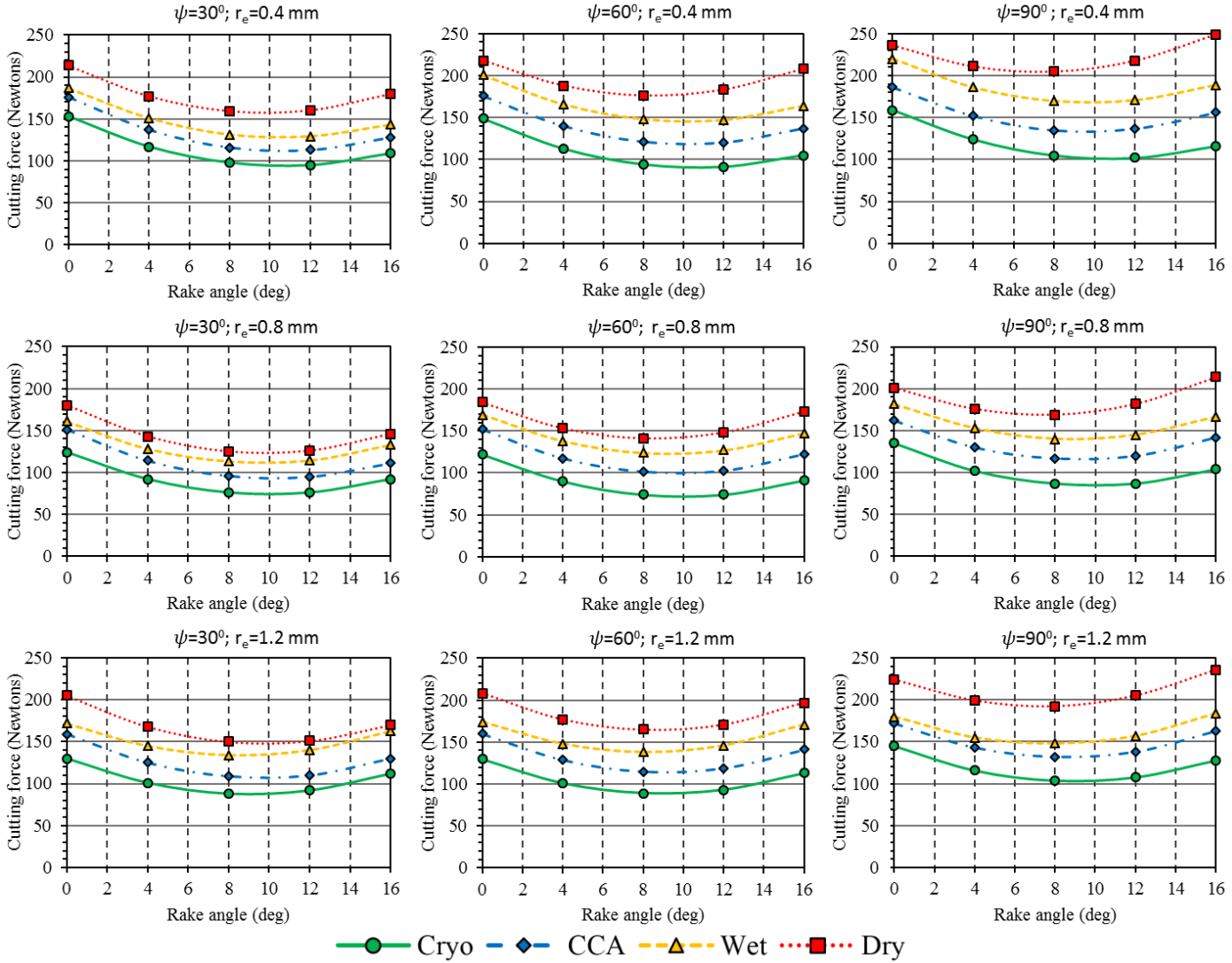

Fig. A.5. Variation of cutting force at cutting speed of 100 m/min and feed of 0.15 mm/rev for different rake angle with various levels of nose radii and approach angles under dry, wet, CCA gas and ALN spray assisted machining conditions (cryo).

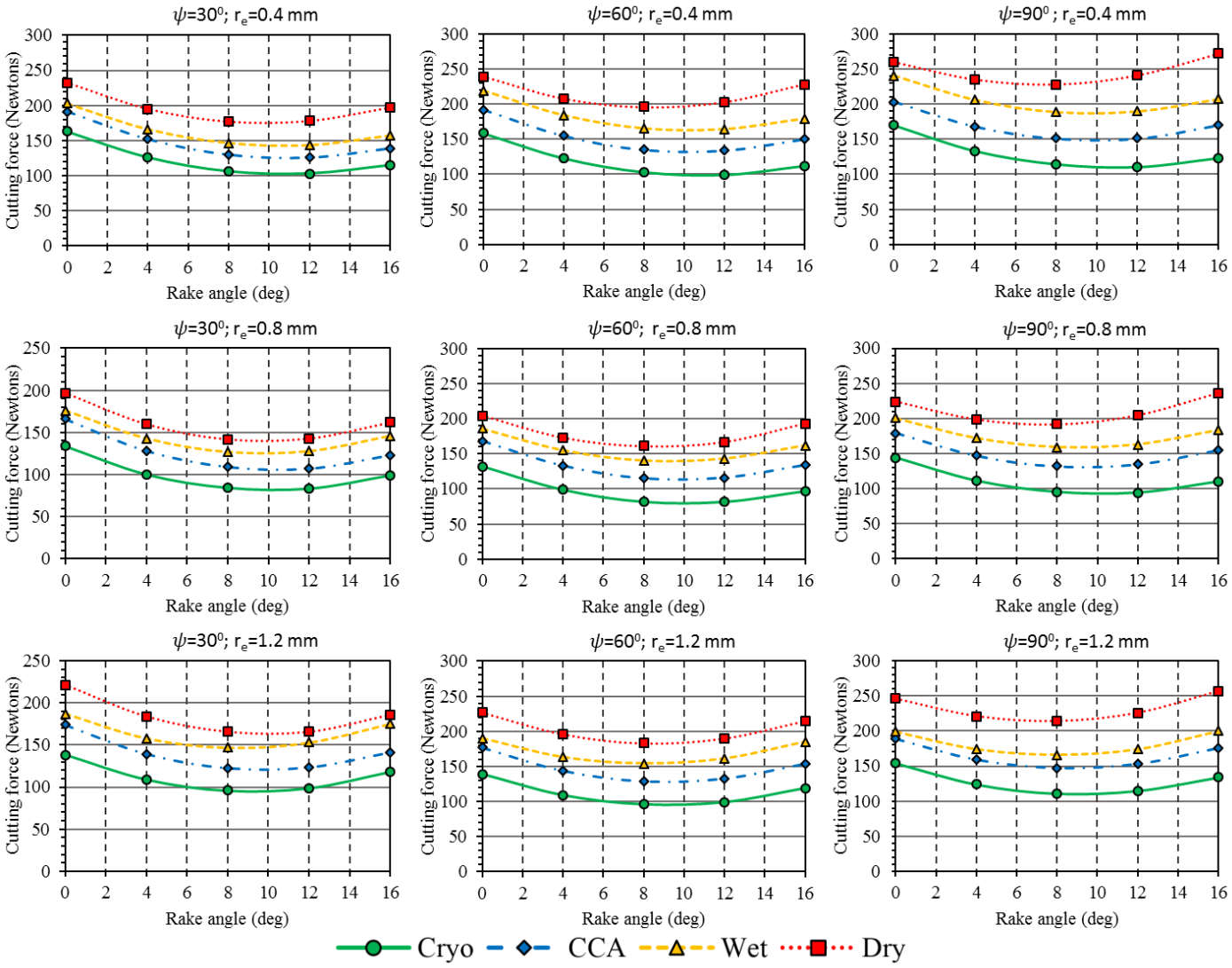

Fig. A.6. Variation of cutting force at cutting speed of 100 m/min and feed of 0.2 mm/rev for different rake angle with various levels of nose radii and approach angles under dry, wet, CCA gas and ALN spray assisted machining conditions (cryo).

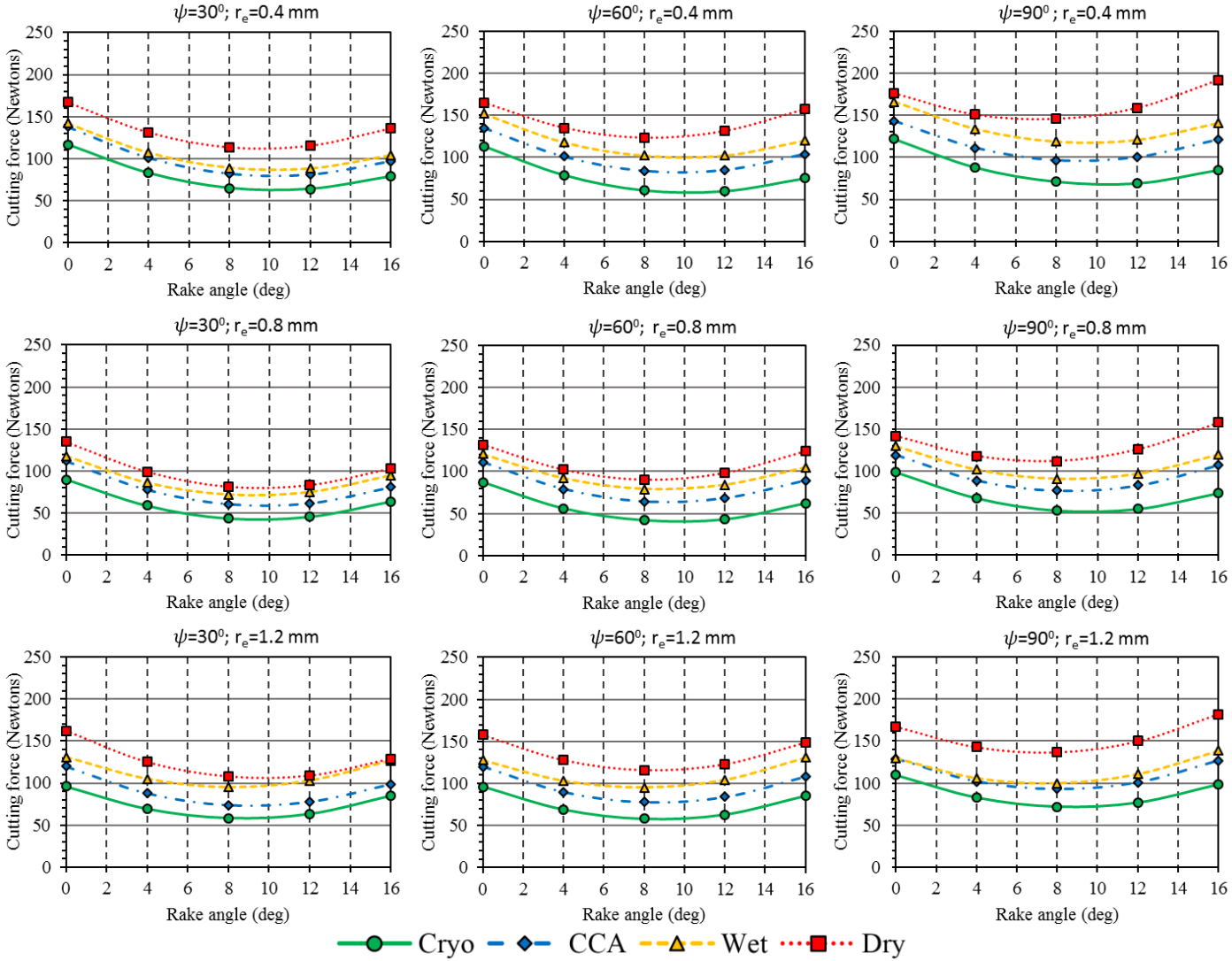

Fig. A.7. Variation of cutting force at cutting speed of 150 m/min and feed of 0.1 mm/rev for different rake angle with various levels of nose radii and approach angles under dry, wet, CCA gas and ALN spray assisted machining conditions (cryo).

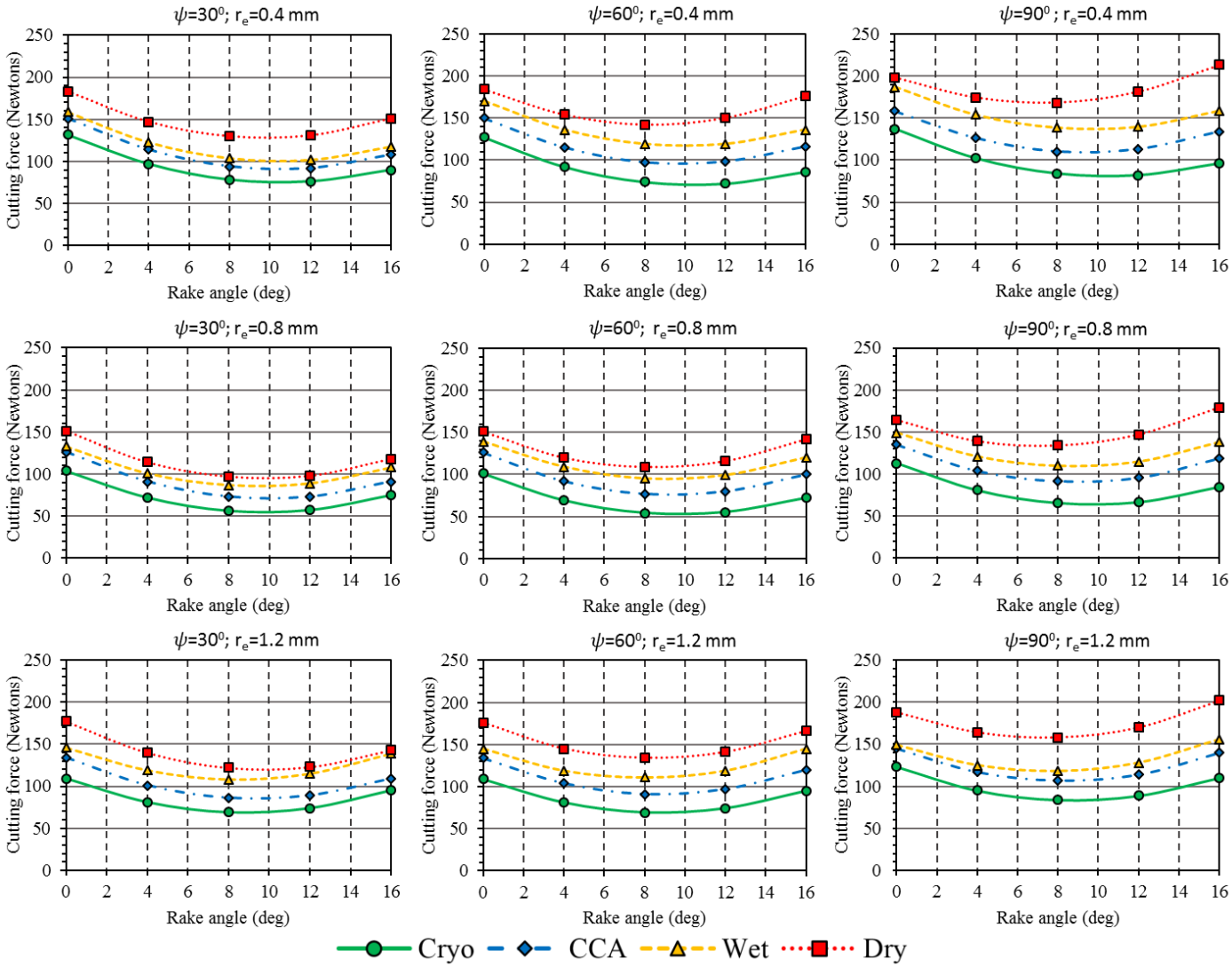

Fig. A.8. Variation of cutting force at cutting speed of 150 m/min and feed of 0.15 mm/rev for different rake angle with various levels of nose radii and approach angles under dry, wet, CCA gas and ALN spray assisted machining conditions (cryo).

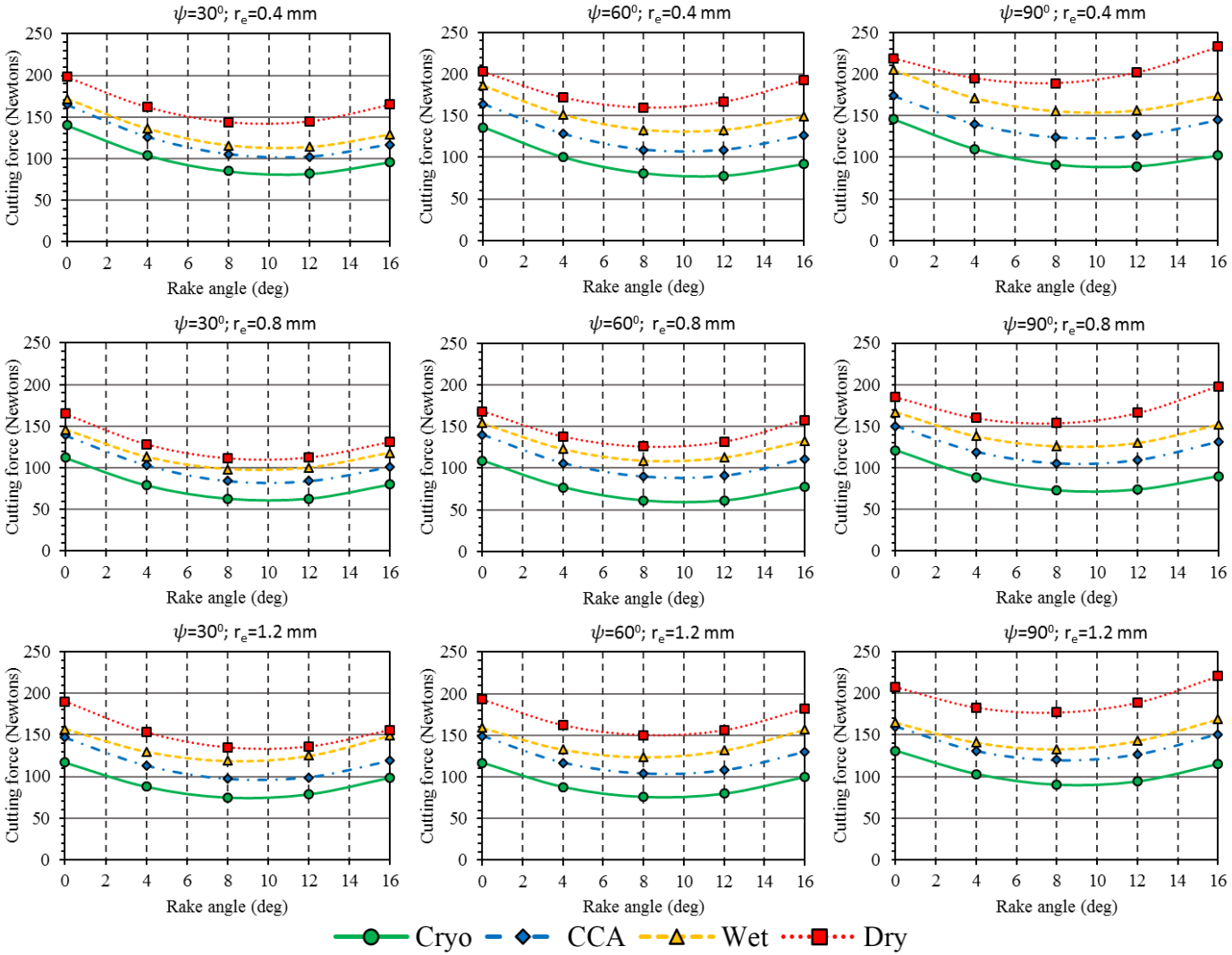

Fig. A.9. Variation of cutting force at cutting speed of 150 m/min and feed of 0.2 mm/rev for different rake angle with various levels of nose radii and approach angles under dry, wet, CCA gas and ALN spray assisted machining conditions (cryo).

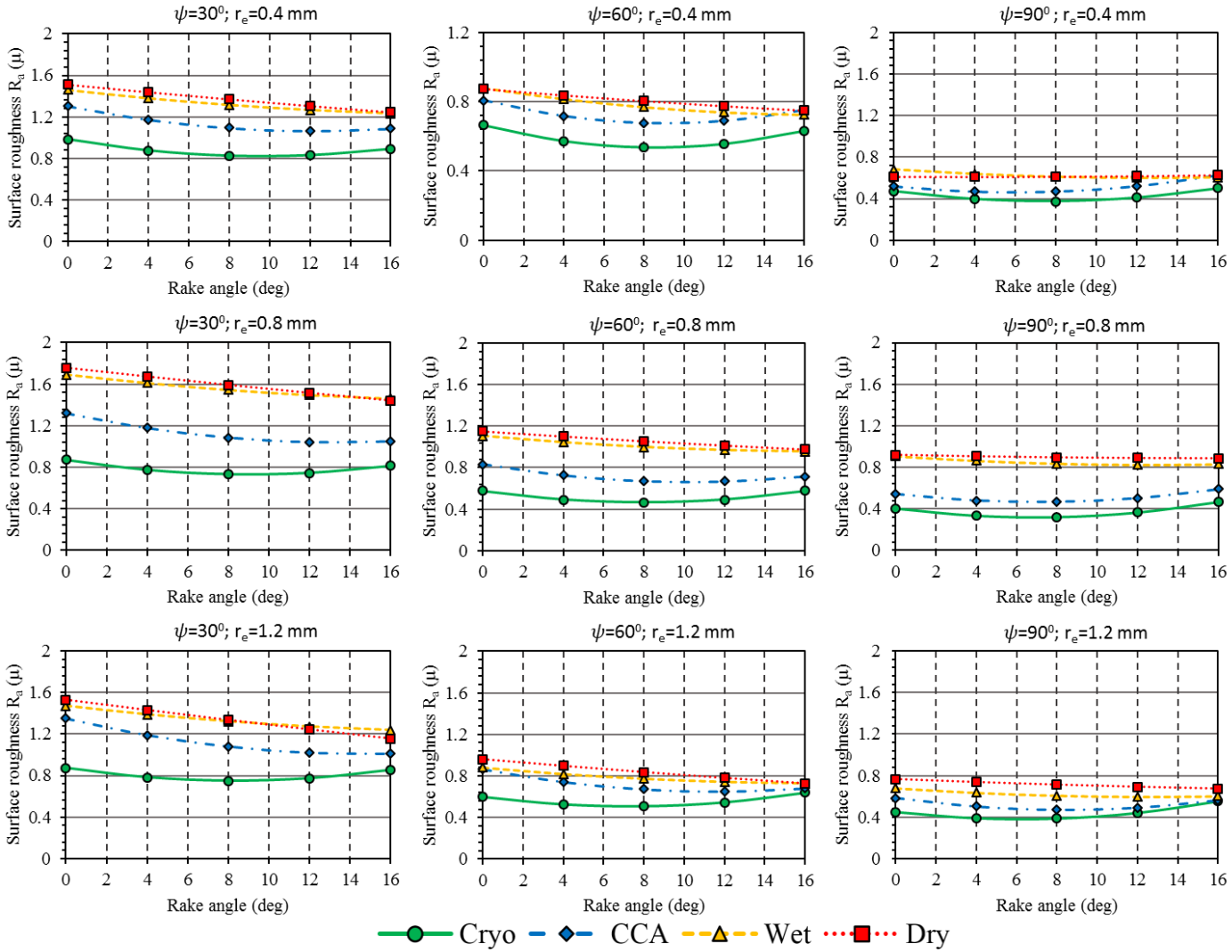

Fig. A.10. Variation of Surface roughness at cutting speed of 50 m/min and feed of 0.1 mm/rev for different rake angle with various levels of nose radii and approach angles under dry, wet, CCA gas and ALN spray assisted machining conditions (cryo).

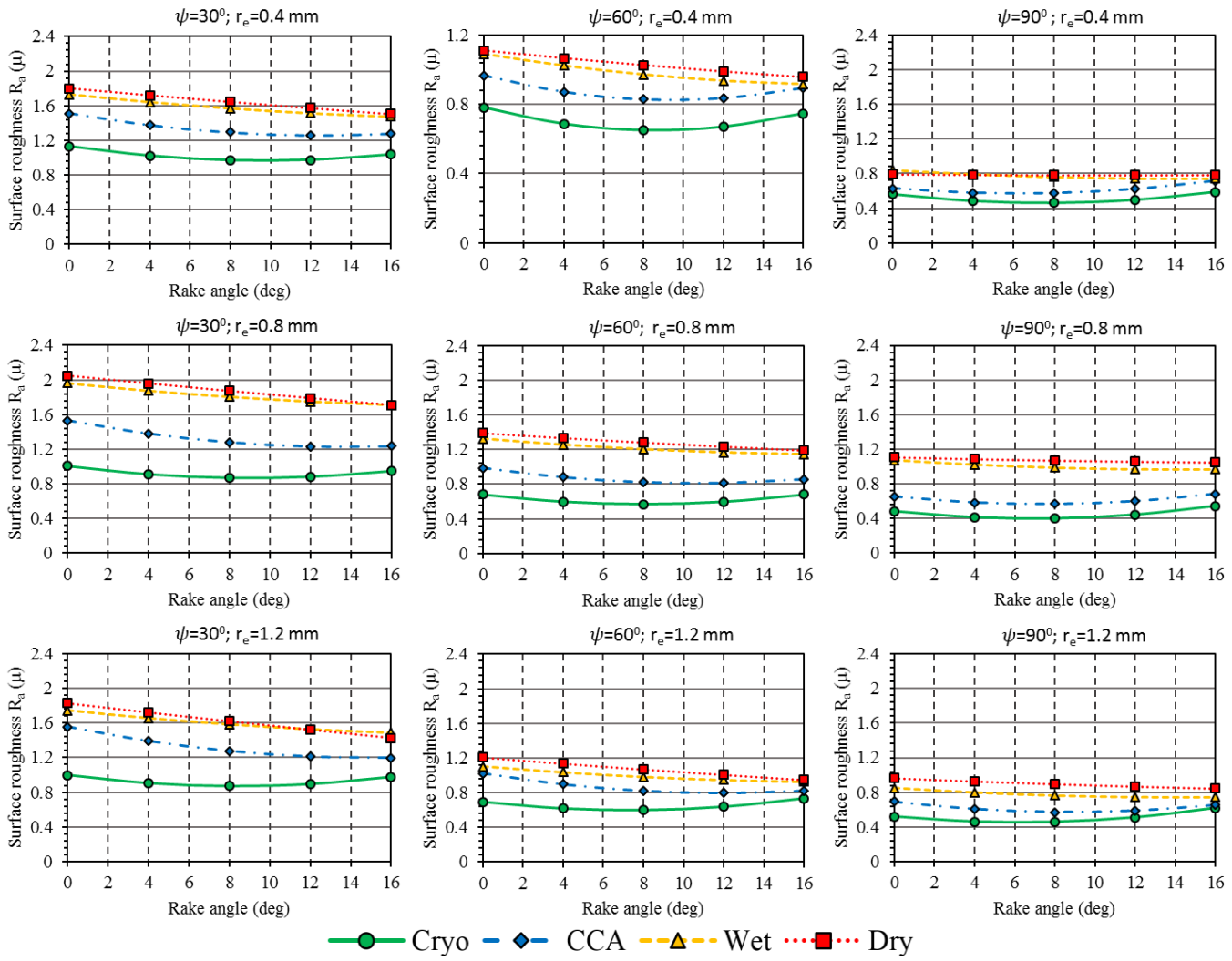

Fig. A.11. Variation of Surface roughness at cutting speed of 50 m/min and feed of 0.15 mm/rev for different rake angle with various levels of nose radii and approach angles under dry, wet, CCA gas and ALN spray assisted machining conditions (cryo).

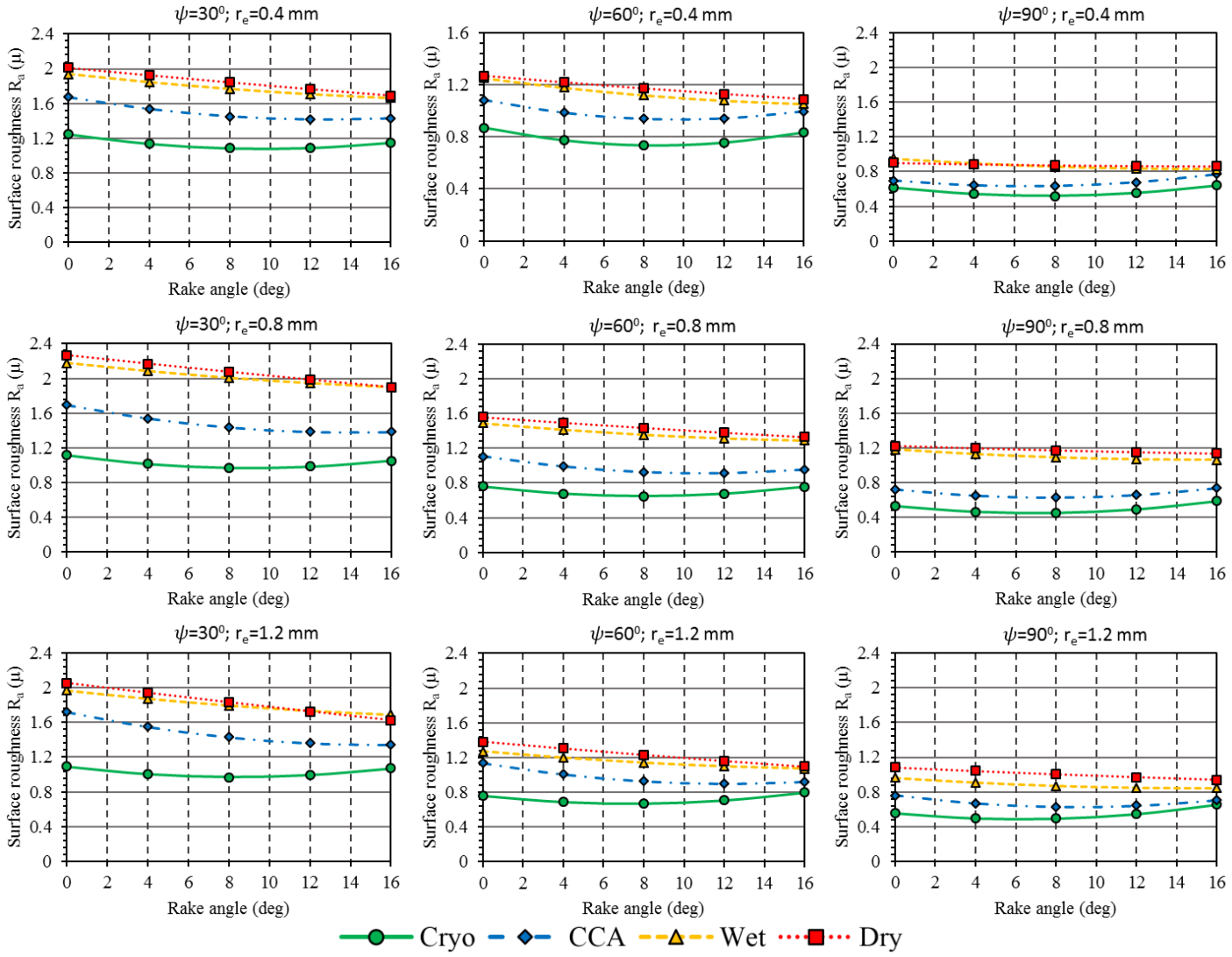

Fig. A.12. Variation of Surface roughness at cutting speed of 50 m/min and feed of 0.2 mm/rev for different rake angle with various levels of nose radii and approach angles under dry, wet, CCA gas and ALN spray assisted machining conditions(cryo).

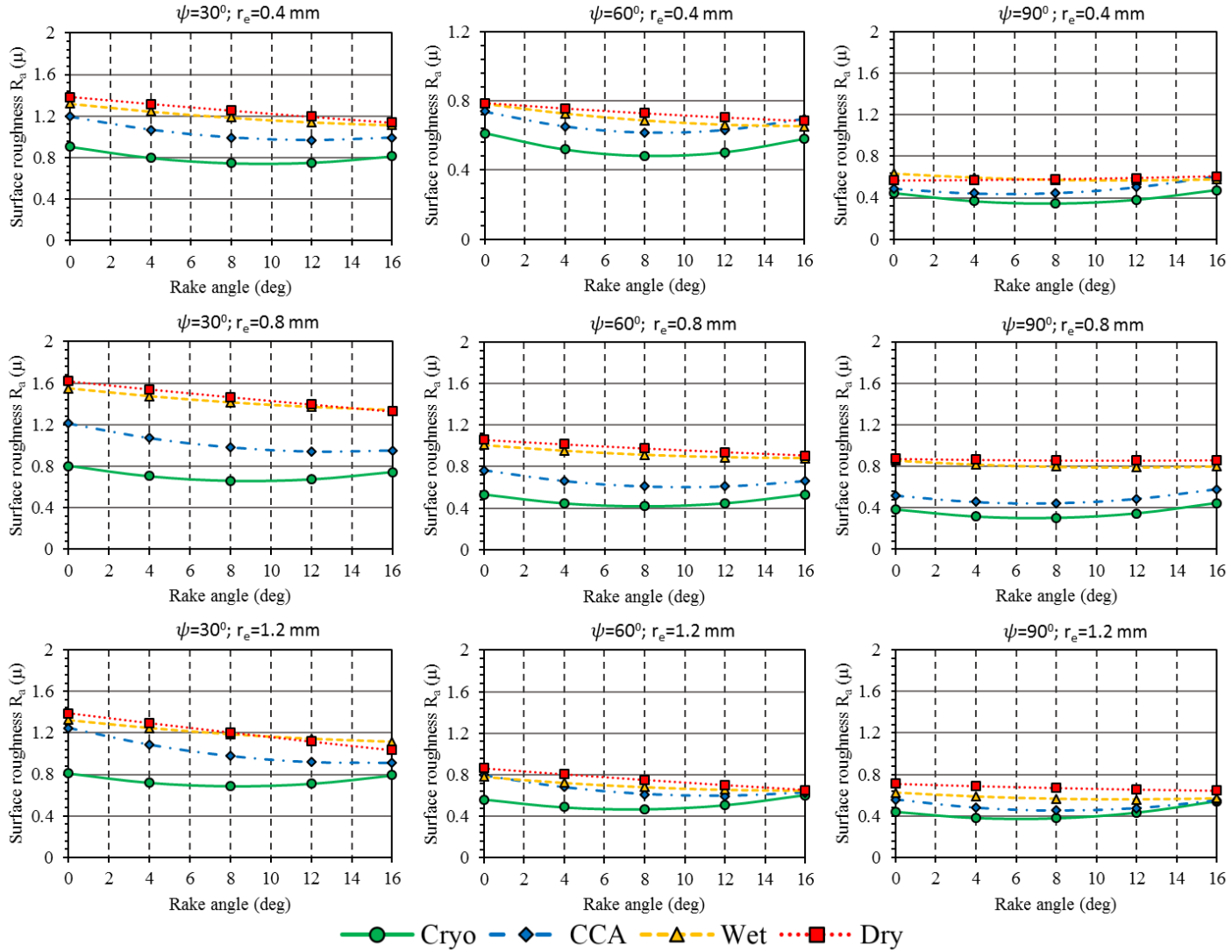

Fig. A.13. Variation of Surface roughness at cutting speed of 100 m/min and feed of 0.1 mm/rev for different rake angle with various levels of nose radii and approach angles under dry, wet, CCA gas and ALN spray assisted machining conditions (cryo).

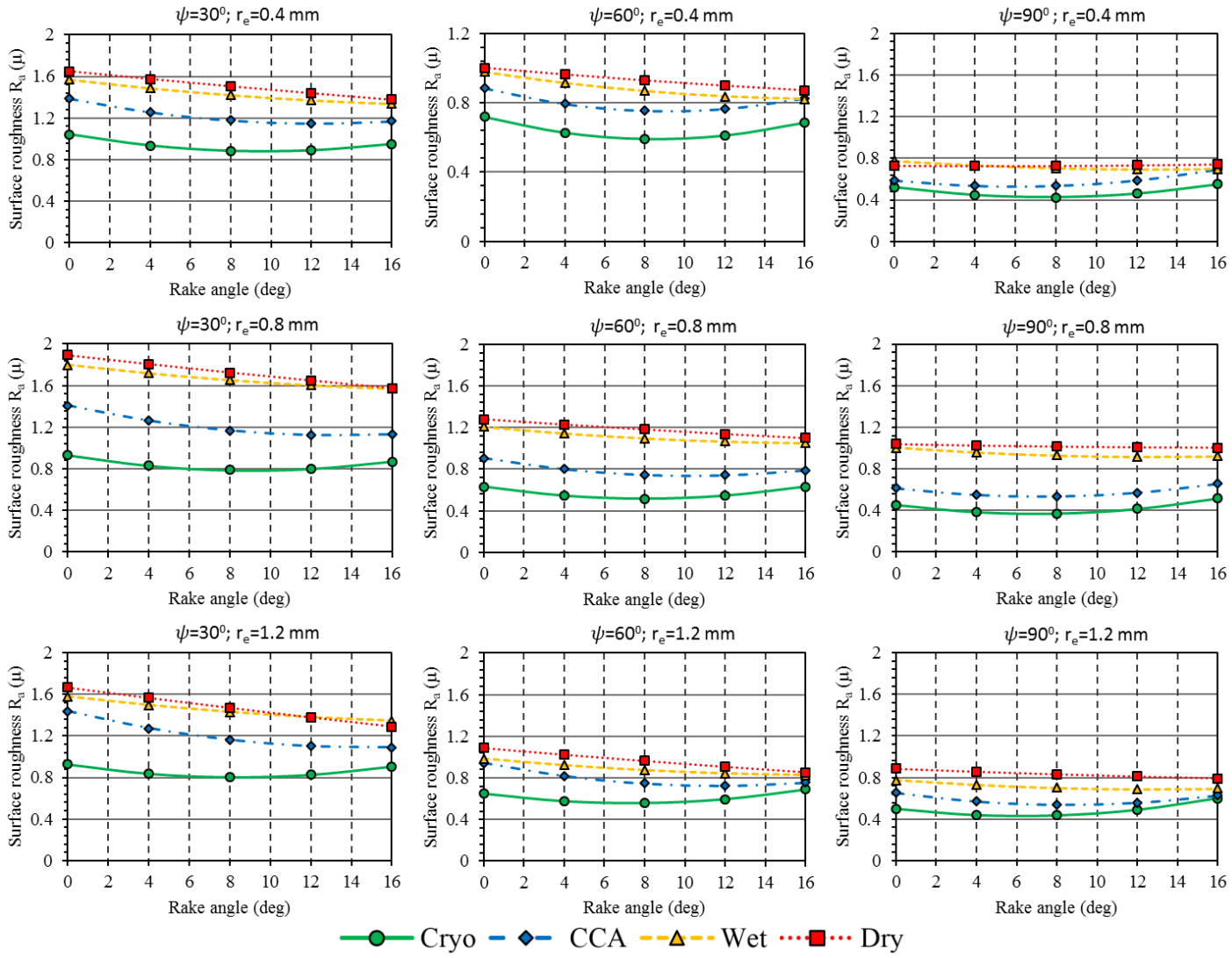

Fig. A.14. Variation of Surface roughness at cutting speed of 100 m/min and feed of 0.15 mm/rev for different rake angle with various levels of nose radii and approach angles under dry, wet, CCA gas and ALN spray assisted machining conditions (cryo).

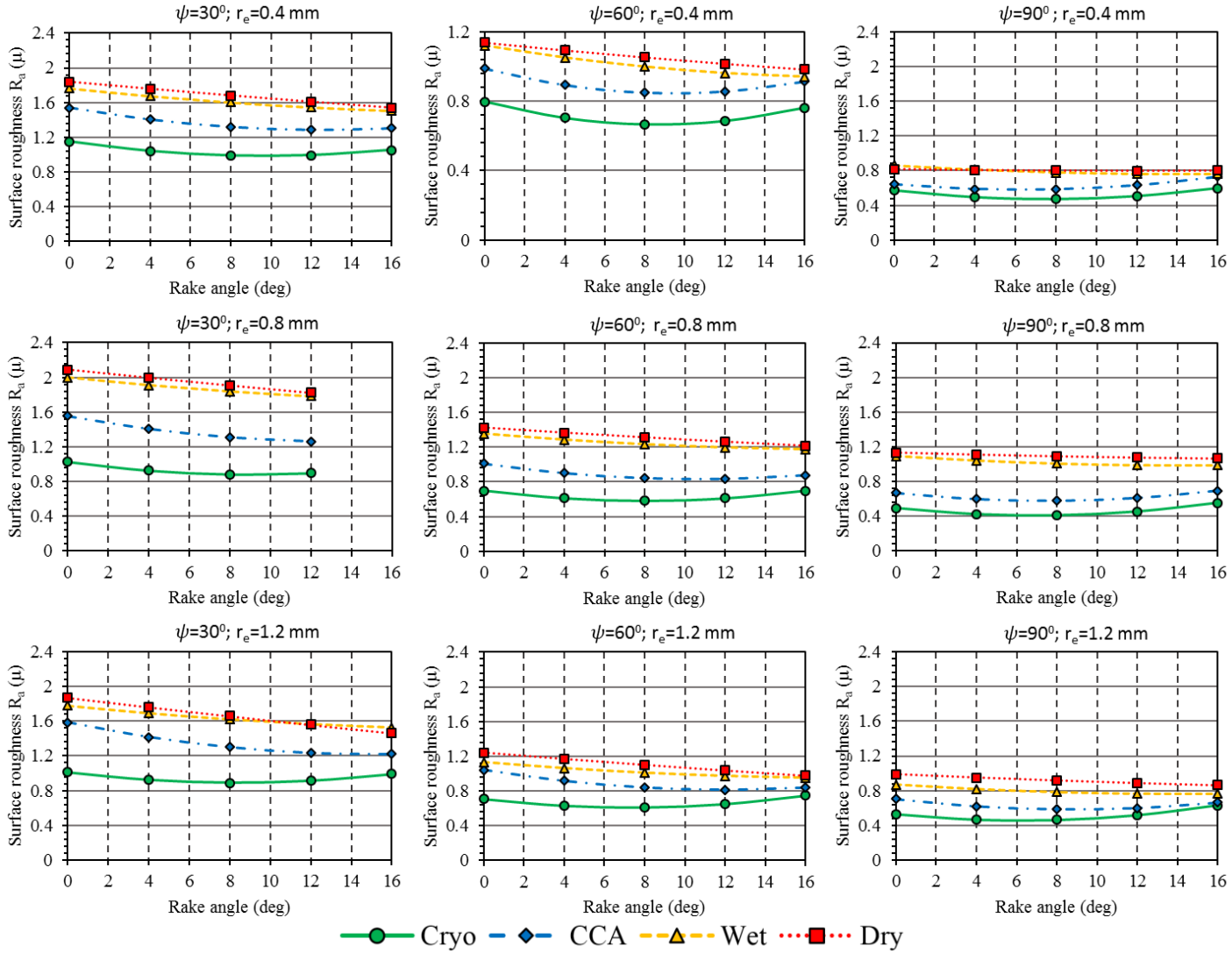

Fig. A.15. Variation of Surface roughness at cutting speed of 100 m/min and feed of 0.2 mm/rev for different rake angle with various levels of nose radii and approach angles under dry, wet, CCA gas and ALN spray assisted machining conditions (cryo).

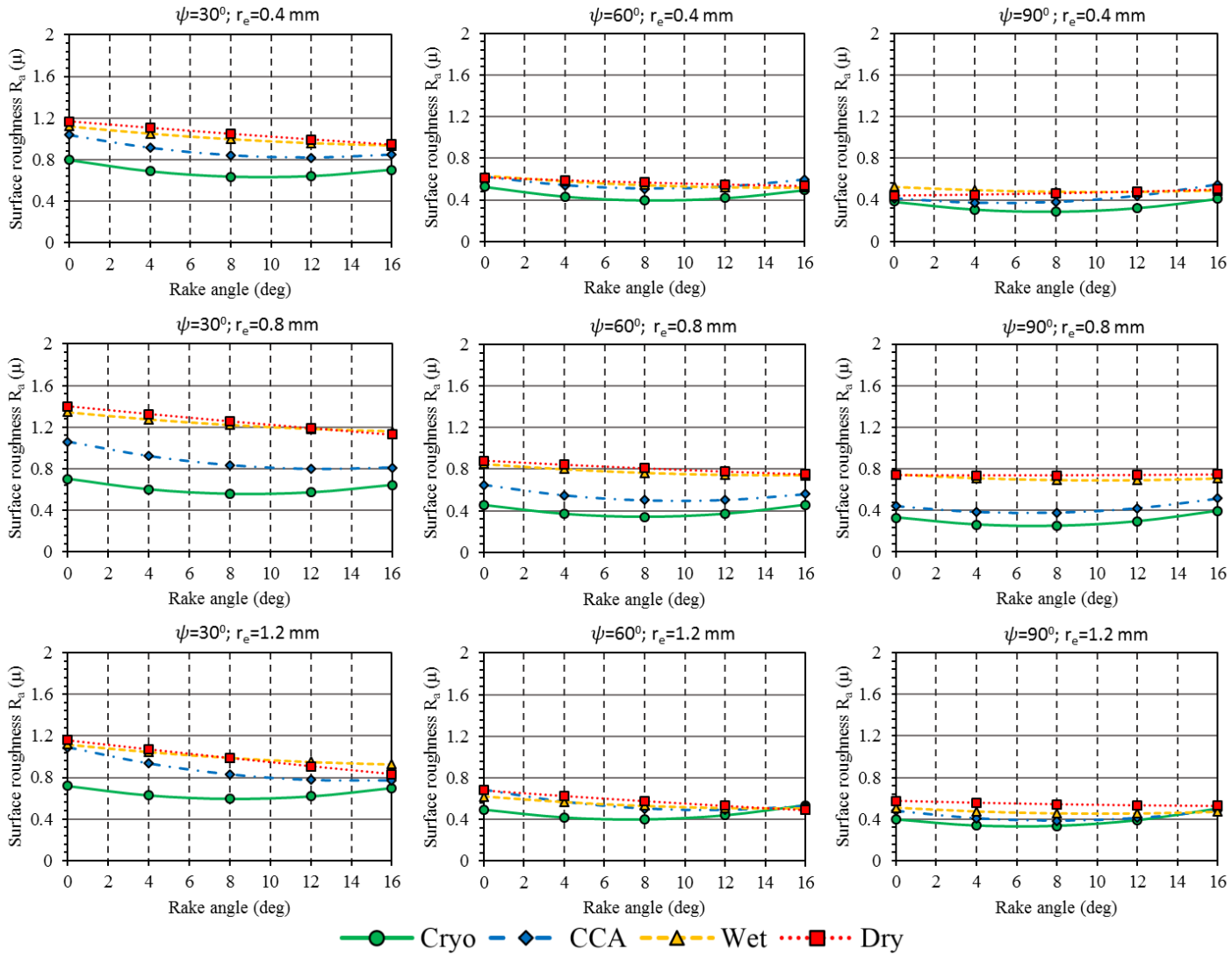

Fig. A.16. Variation of Surface roughness at cutting speed of 150 m/min and feed of 0.1 mm/rev for different rake angle with various levels of nose radii and approach angles under dry, wet, CCA gas and ALN spray assisted machining conditions (cryo).

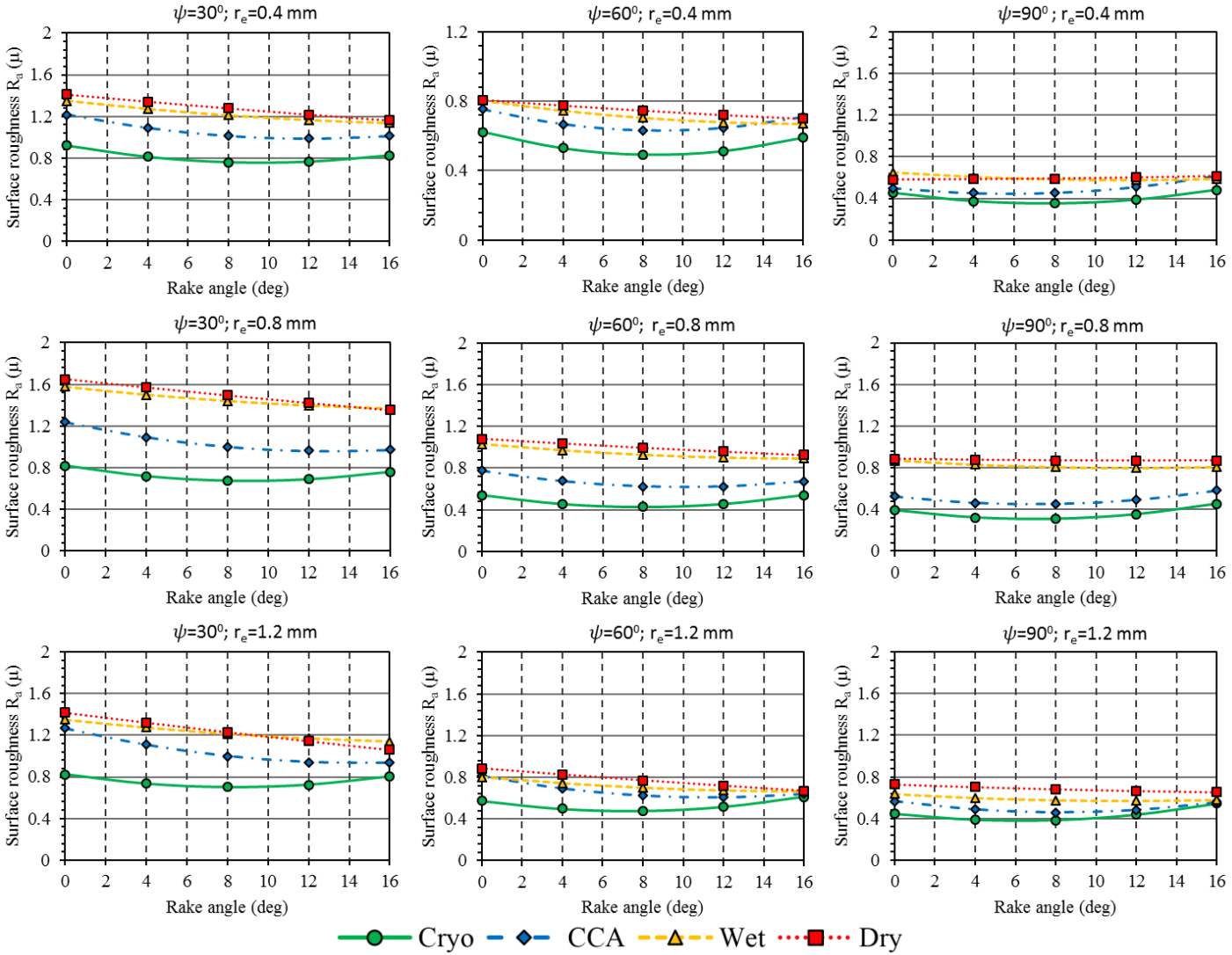

Fig. A.17. Variation of Surface roughness at cutting speed of 150 m/min and feed of 0.15 mm/rev for different rake angle with various levels of nose radii and approach angles under dry, wet, CCA gas and ALN spray assisted machining conditions (cryo).

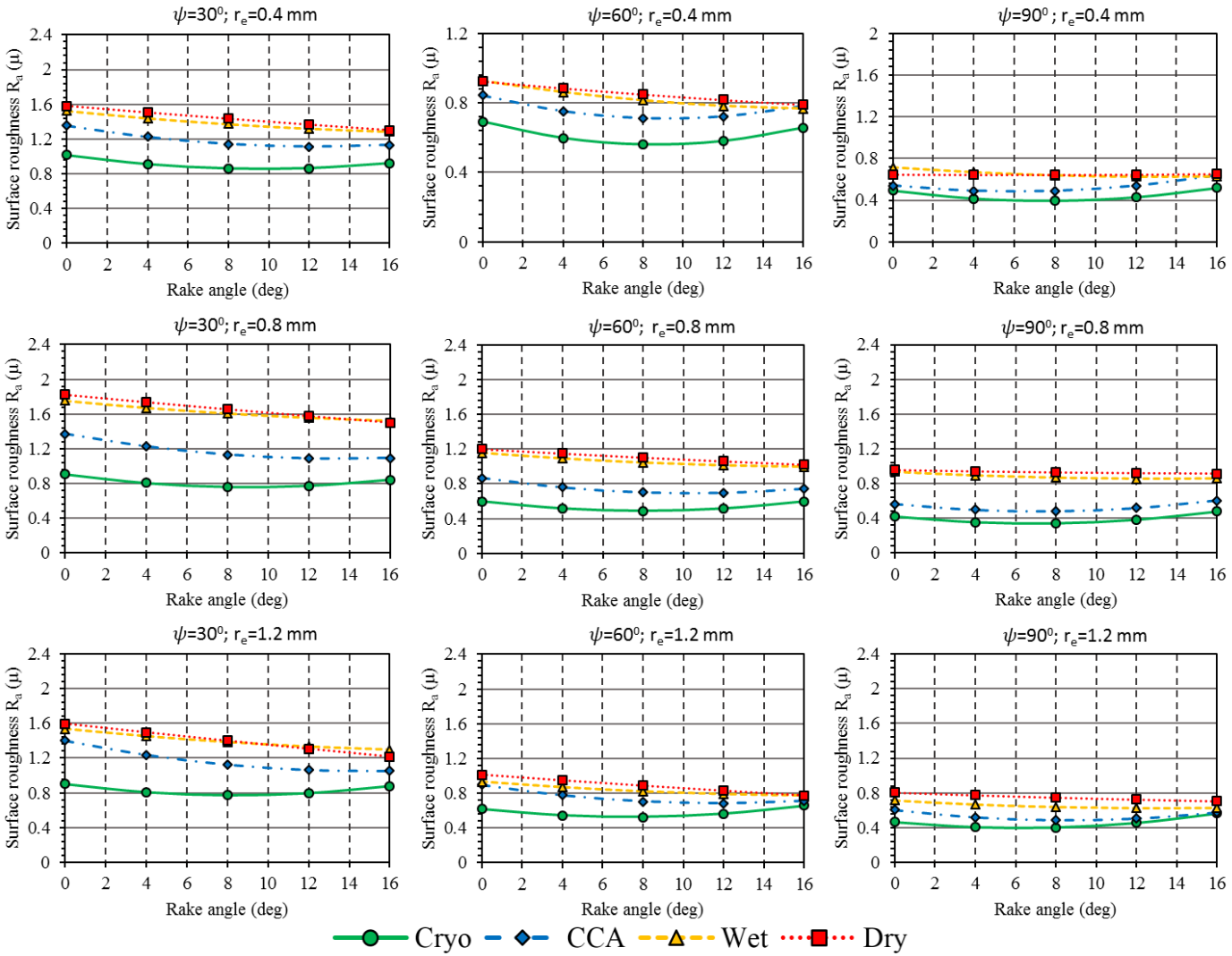

Fig. A.18. Variation of Surface roughness at cutting speed of 150 m/min and feed of 0.2 mm/rev for different rake angle with various levels of nose radii and approach angles under dry, wet, CCA gas and ALN spray assisted machining conditions (cryo)

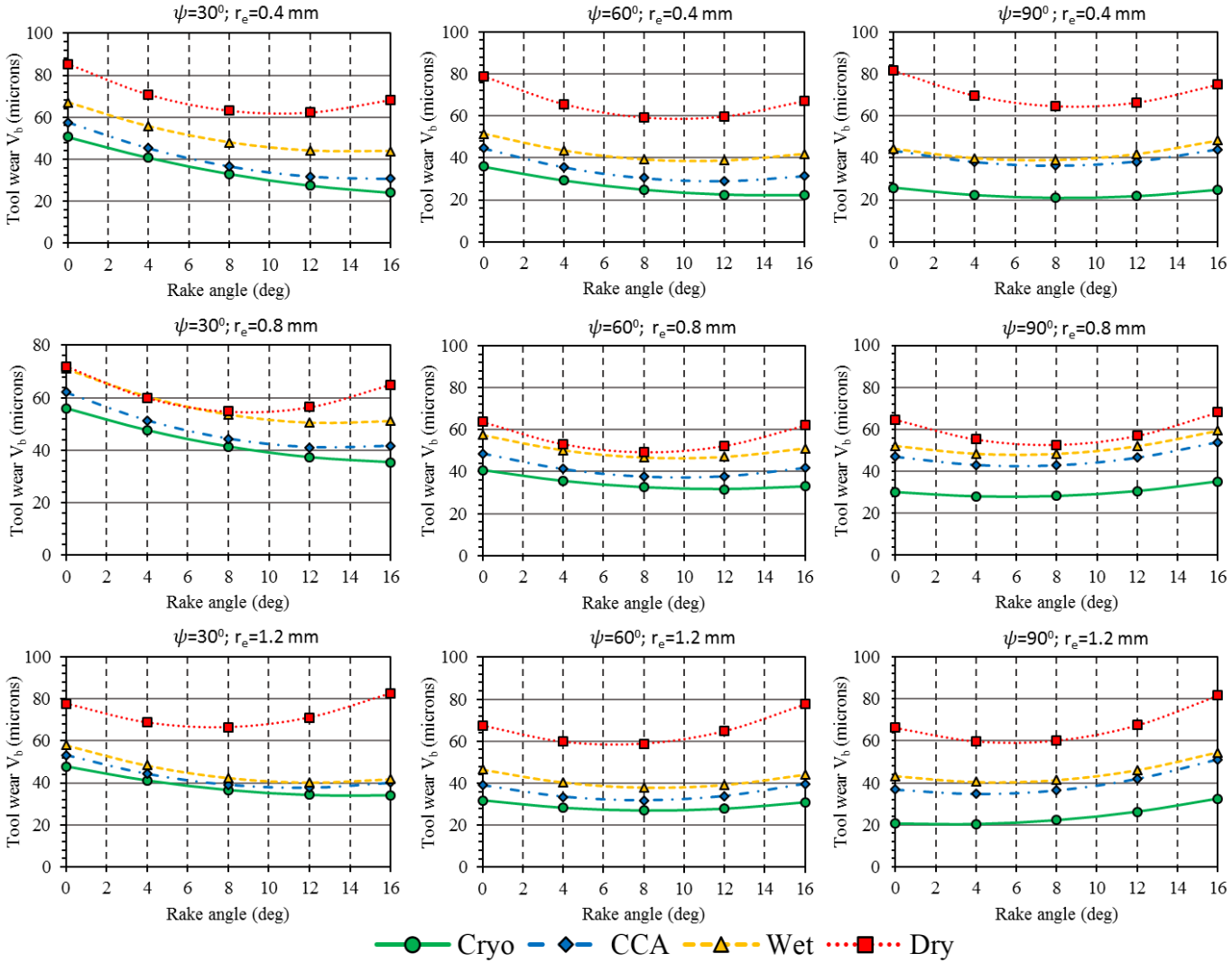

Fig. A.19. Variation of tool wear at cutting speed of 50 m/min and feed of 0.1 mm/rev for different rake angle with various levels of nose radii and approach angles under dry, wet, CCA gas and ALN spray assisted machining conditions (cryo).

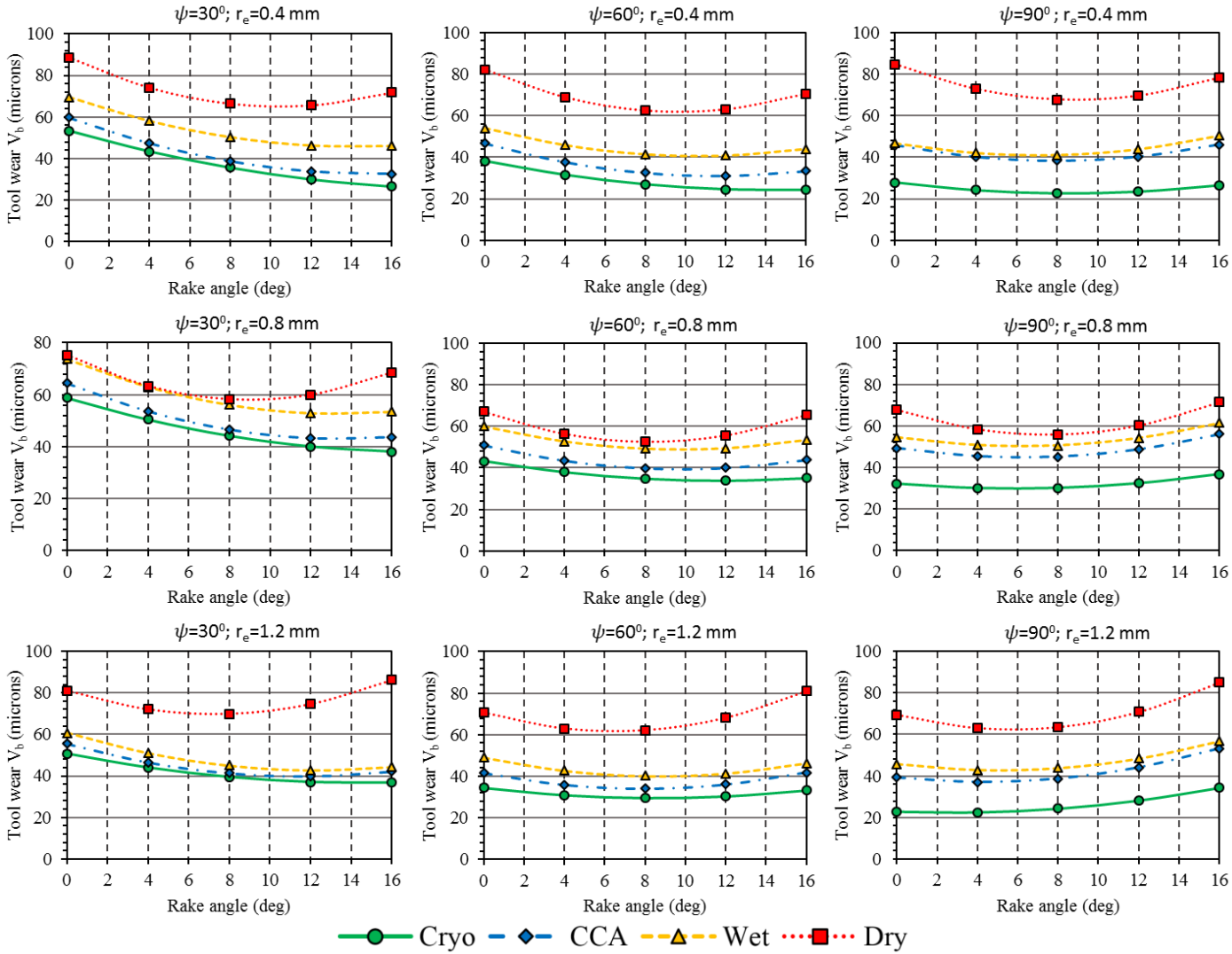

Fig. A.20. Variation of tool wear at cutting speed of 50 m/min and feed of 0.15 mm/rev for different rake angle with various levels of nose radii and approach angles under dry, wet, CCA gas and ALN spray assisted machining conditions (cryo).

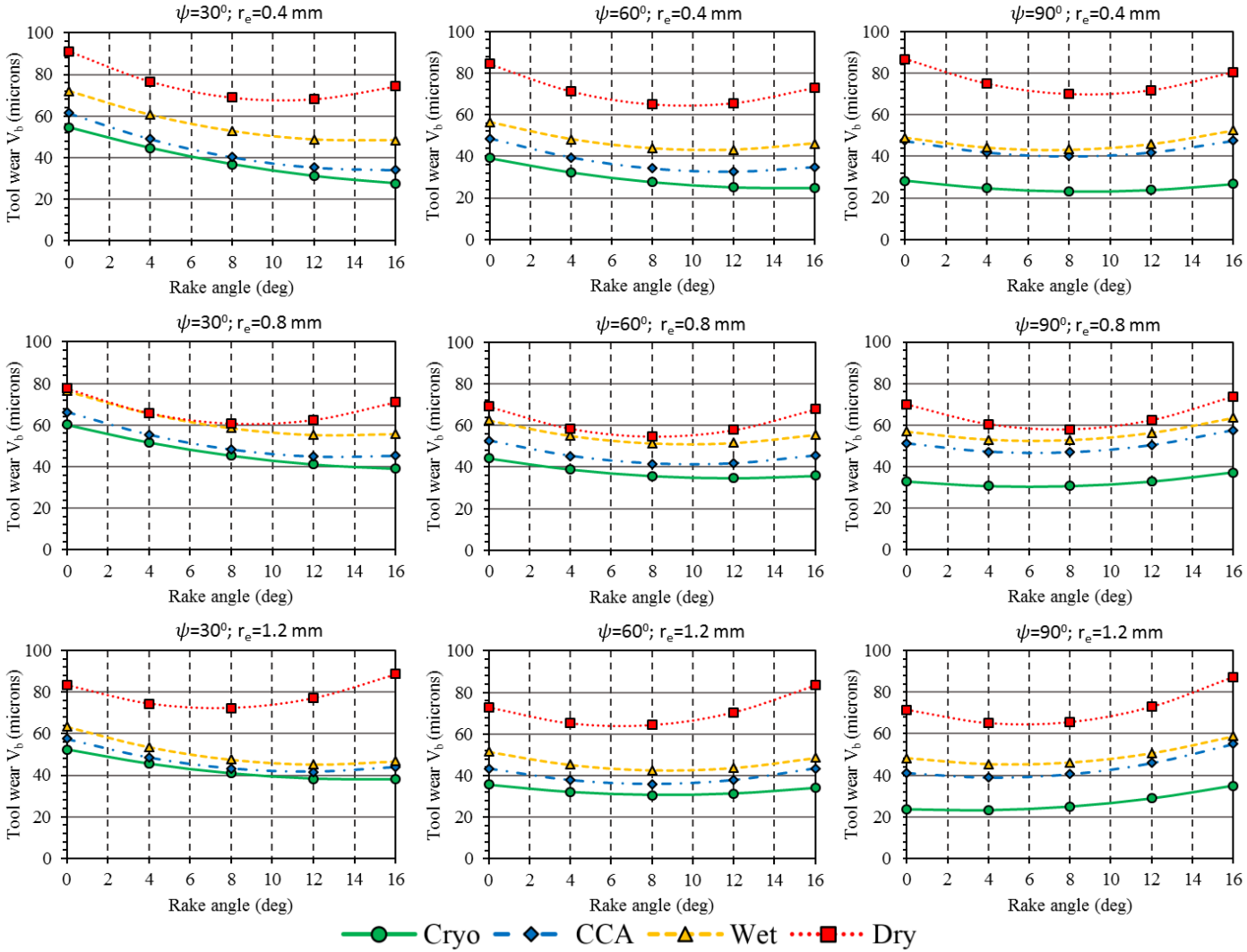

Fig. A.21. Variation of tool wear at cutting speed of 50 m/min and feed of 0.2 mm/rev for different rake angle with various levels of nose radii and approach angles under dry, wet, CCA gas and ALN spray assisted machining conditions (cryo).

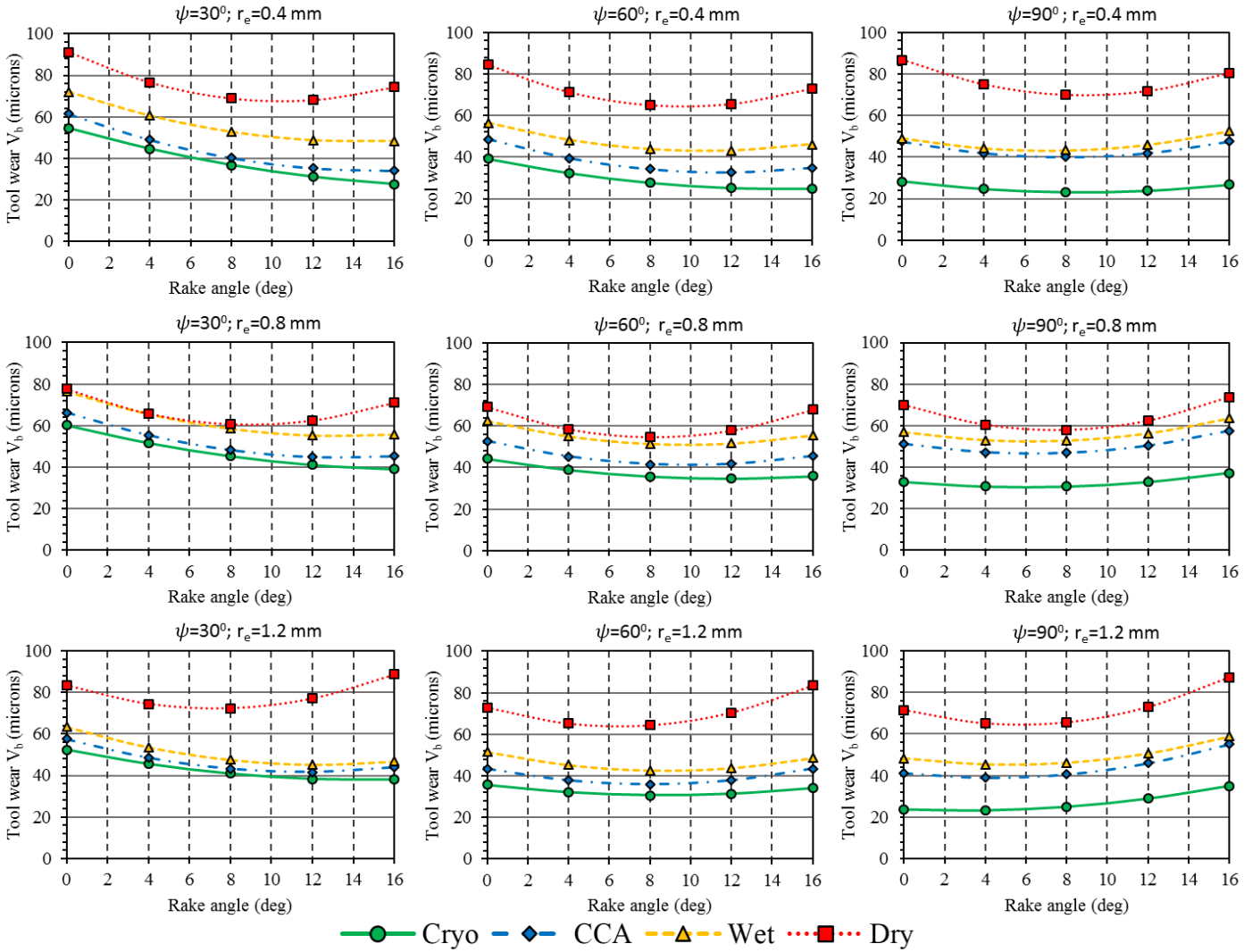

Fig. A.22. Variation of tool wear at cutting speed of 100 m/min and feed of 0.1 mm/rev for different rake angle with various levels of nose radii and approach angles under dry, wet, CCA gas and ALN spray assisted machining conditions (cryo).

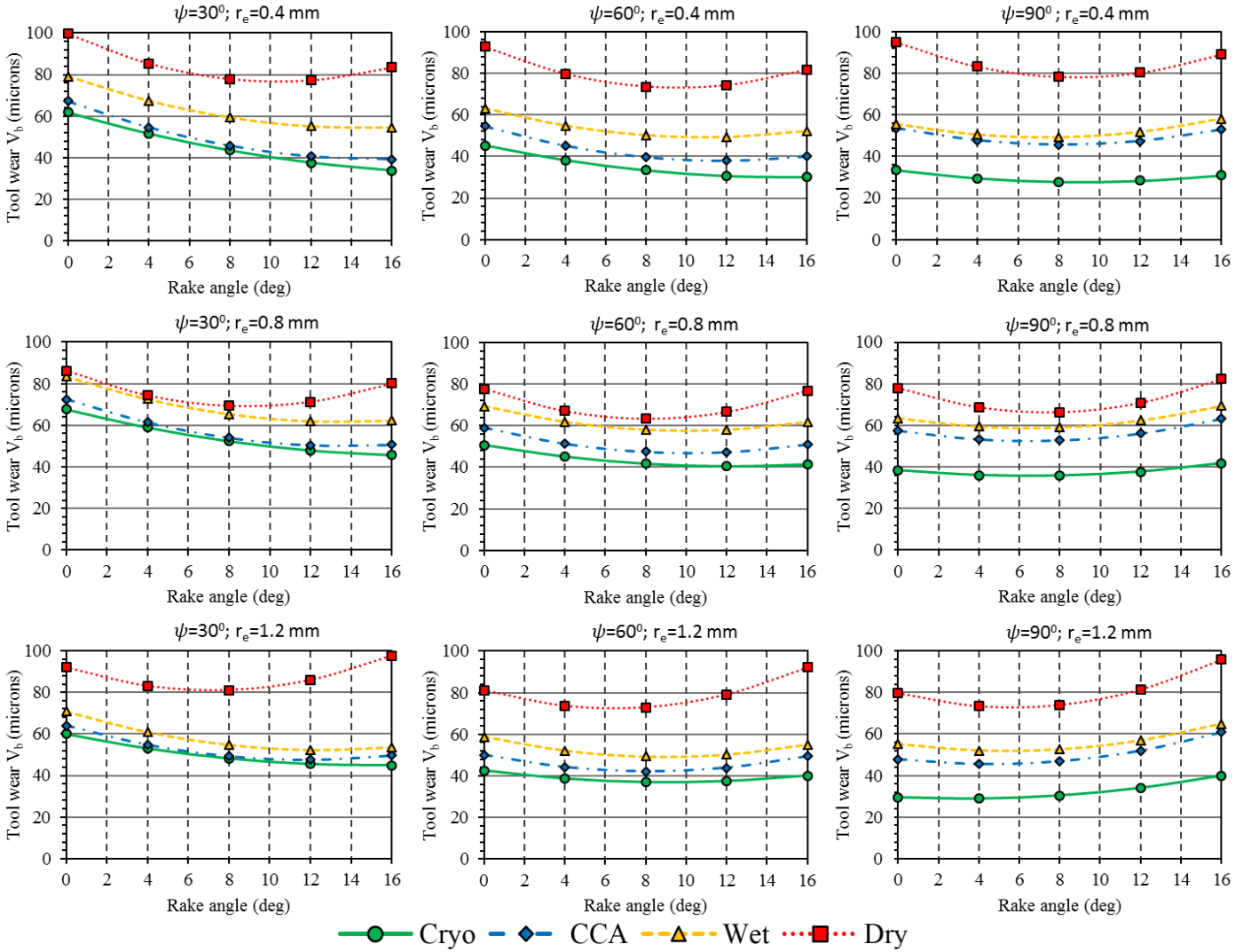

Fig. A.23. Variation of tool wear at cutting speed of 100 m/min and feed of 0.15 mm/rev for different rake angle with various levels of nose radii and approach angles under dry, wet, CCA gas and ALN spray assisted machining conditions (cryo).

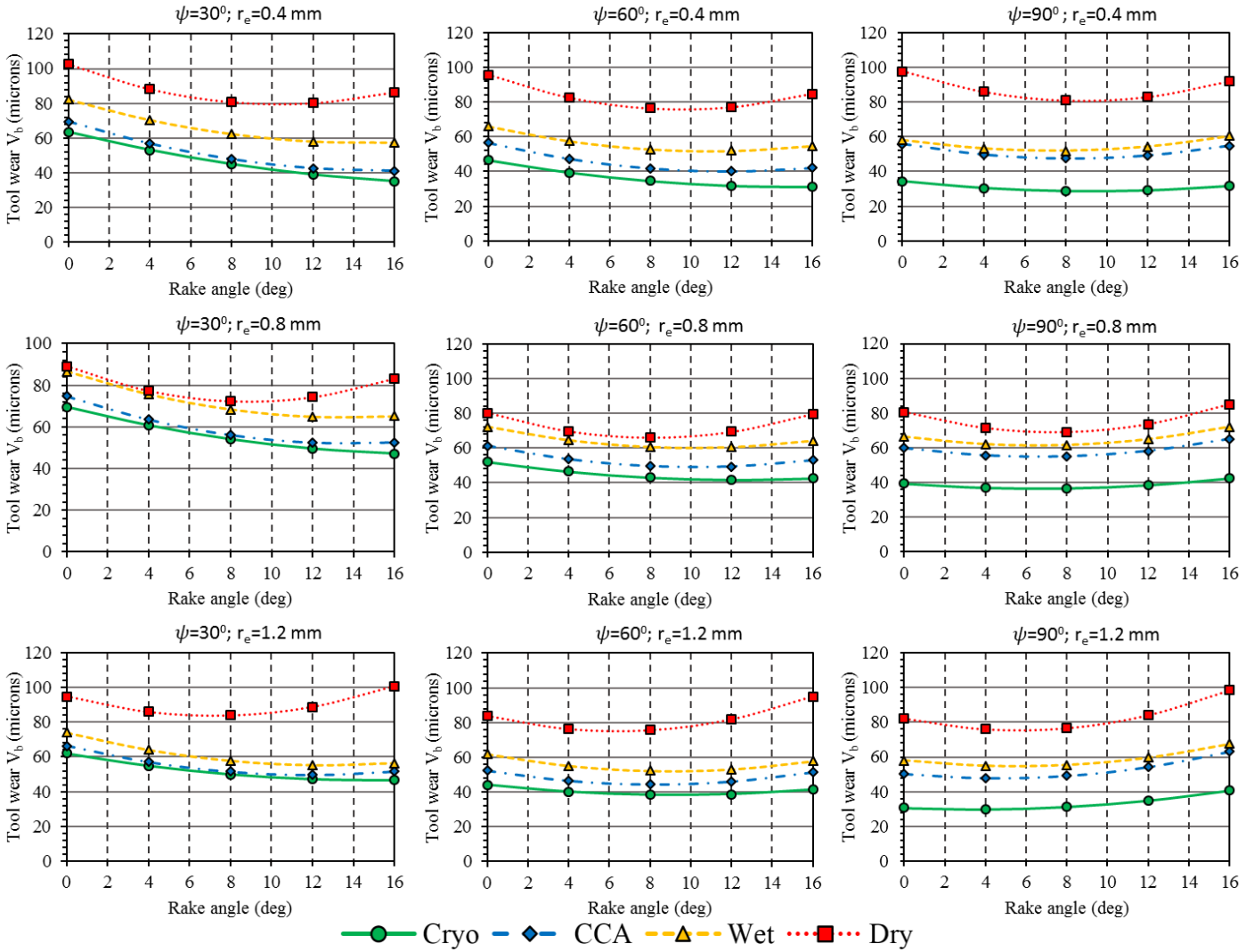

Fig. A.24. Variation of tool wear at cutting speed of 100 m/min and feed of 0.2 mm/rev for different rake angle with various levels of nose radii and approach angles under dry, wet, CCA gas and ALN spray assisted machining conditions (cryo).

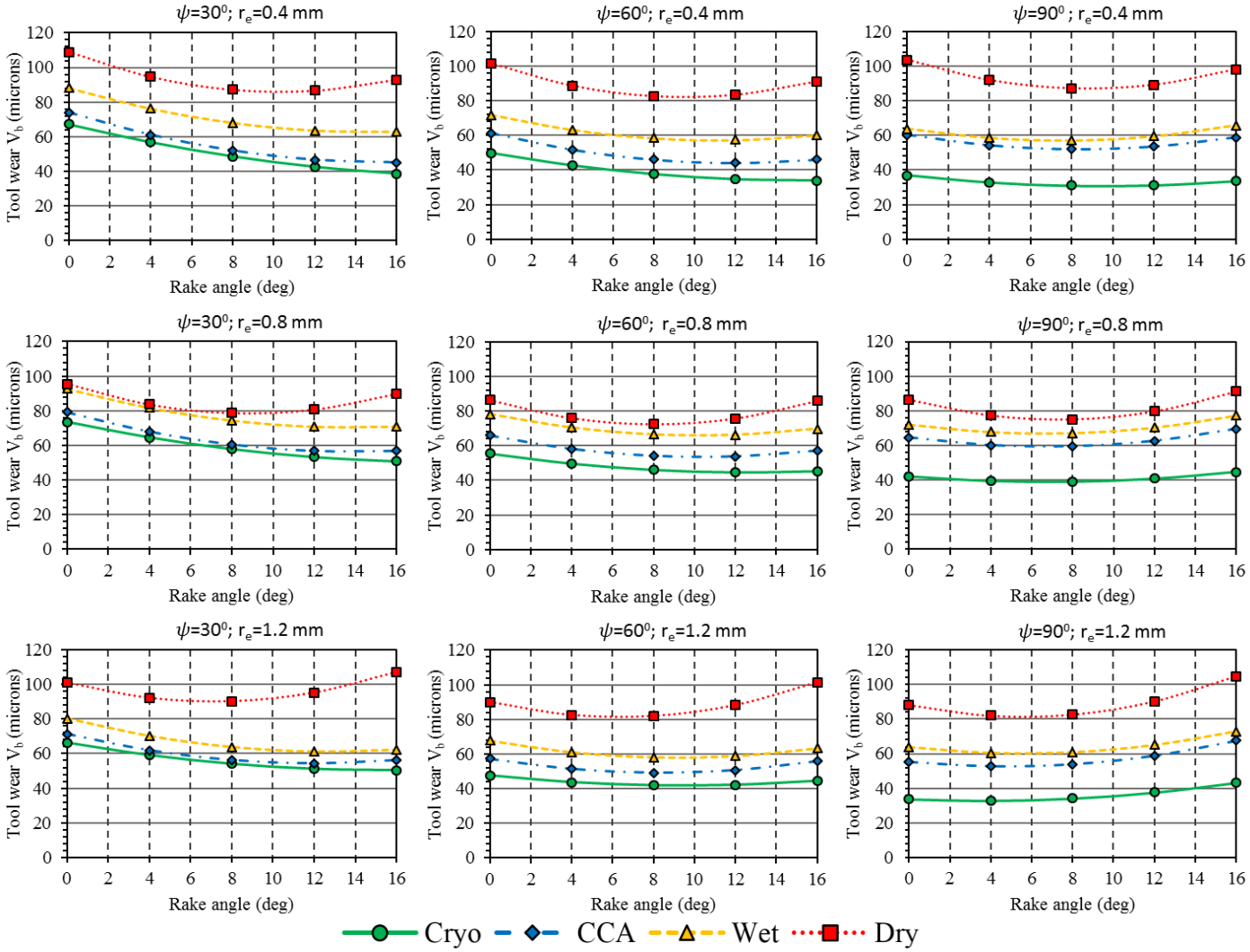

Fig. A.25. Variation of tool wear at cutting speed of 150 m/min and feed of 0.1 mm/rev for different rake angle with various levels of nose radii and approach angles under dry, wet, CCA gas and ALN spray assisted machining conditions (cryo).

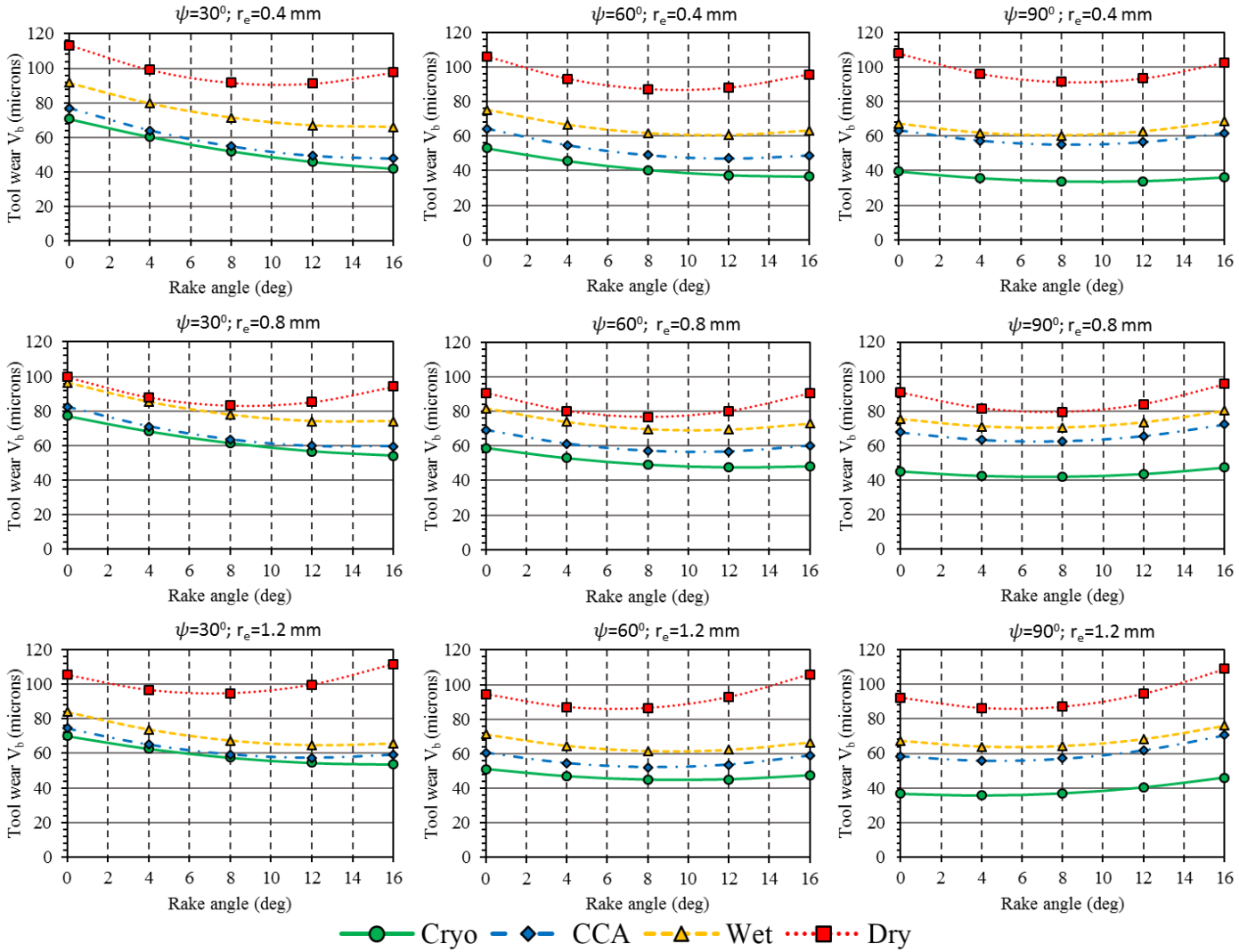

Fig. A.26. Variation of tool wear at cutting speed of 150 m/min and feed of 0.15 mm/rev for different rake angle with various levels of nose radii and approach angles under dry, wet, CCA gas and ALN spray assisted machining conditions (cryo).

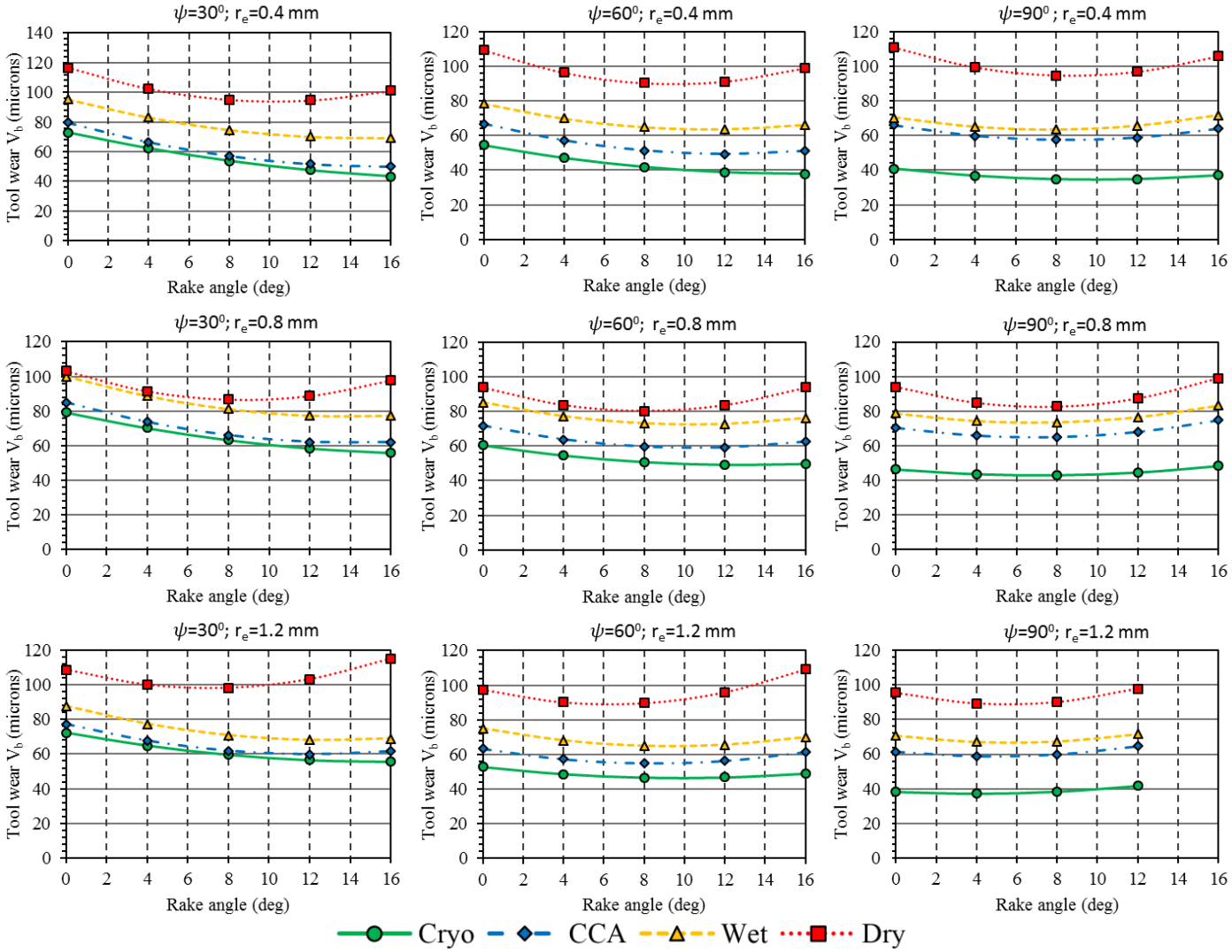

Fig. A.27. Variation of tool wear at cutting speed of 150 m/min and feed of 0.2 mm/rev for different rake angle with various levels of nose radii and approach angles under dry, wet, CCA gas and ALN spray assisted machining conditions (cryo).

APPENDIX - B.

Table B.1. Sequential of adequate model sum of squares for cutting force.

(a) Atomized liquid nitrogen spray machining condition						
Source	Sum of Squares	df	Mean Square	F Value	p-value Prob > F	
Mean vs Total	3.68E+05	1	3.68E+05			
Linear vs Mean	8311.22	5	1662.24	5.5	0.0006	
2FI vs Linear	168.2	10	16.82	0.042	1	
Quadratic vs 2FI	11024.17	5	2204.83	61.03	< 0.0001	Suggested
Cubic vs Quadratic	276.69	15	18.45	0.29	0.9837	Aliased
(b) Cryogenically chilled argon gas condition						
Mean vs Total	6.55E+05	1	6.55E+05			
Linear vs Mean	13147.85	5	2629.57	7.44	< 0.0001	
2FI vs Linear	250.88	10	25.09	0.054	1	
Quadratic vs 2FI	12366.65	5	2473.33	40.43	< 0.0001	Suggested
Cubic vs Quadratic	495.35	15	33.02	0.32	0.9772	Aliased
Residual	1033.95	10	103.4			
Total	6.82E+05	46	14823.47			
(c) Wet Machining						
Mean vs Total	9.12E+05	1	9.12E+05			
Linear vs Mean	18515.29	5	3703.06	10.37	< 0.0001	
2FI vs Linear	527.25	10	52.73	0.11	0.9995	
Quadratic vs 2FI	12360.57	5	2472.11	44.19	< 0.0001	Suggested
Cubic vs Quadratic	353.11	15	23.54	0.23	0.9951	Aliased
Residual	1045.38	10	104.54			
Total	9.45E+05	46	20542.21			
(d) Dry Machining						
Mean vs Total	1.26E+06	1	1.26E+06			
Linear vs Mean	27591.59	5	5518.32	12.35	< 0.0001	
2FI vs Linear	1031.54	10	103.15	0.18	0.9962	
Quadratic vs 2FI	13189.25	5	2637.85	18.07	< 0.0001	Suggested
Cubic vs Quadratic	750.13	15	50.01	0.17	0.9987	Aliased
Residual	2900.02	10	290			
Total	1.31E+06	46	28447.6			

Note: “Sequential model sum of squares”: Select the highest order polynomial value where the additional terms are significant and model is not aliased.

Table B.2. Lack of fit tests for cutting force.

(a) Atomized liquid nitrogen spray machining condition						
Source	Sum of Squares	df	Mean Square	F Value	p-value Prob > F	
Linear	12024.4	35	343.55	24.13	0.0011	
2FI	11856.2	25	474.25	33.31	0.0005	
Quadratic	832.01	20	41.6	2.92	0.1189	Suggested
Cubic	555.31	5	111.06	7.8	0.0208	Aliased
Pure Error	71.19	5	14.24			
(b) Cryogenically chilled argon gas condition						
Linear	13736.1	35	392.46	4.78	0.0437	
2FI	13485.2	25	539.41	6.57	0.0226	
Quadratic	1118.58	20	55.93	0.68	0.756	Suggested
Cubic	623.24	5	124.65	1.52	0.3292	Aliased
Pure Error	410.71	5	82.14			
(c) Wet Machining						
Linear	13938	35	398.23	5.72	0.0298	
2FI	13410.7	25	536.43	7.7	0.0159	
Quadratic	1050.16	20	52.51	0.75	0.7069	Suggested
Cubic	697.05	5	139.41	2	0.2323	Aliased
Pure Error	348.33	5	69.67			
(d) Dry Machining						
Linear	17192.2	35	491.2	3.62	0.077	
2FI	16160.6	25	646.42	4.76	0.0449	
Quadratic	2971.38	20	148.57	1.09	0.508	Suggested
Cubic	2221.24	5	444.25	3.27	0.1096	Aliased
Pure Error	678.78	5	135.76			

Note: “Lack of Fit Tests”: Want the selected model to have insignificant lack of fit.

Table B.3. Model summary statistics for cutting force.

(a) Atomized liquid nitrogen spray machining condition						
Source	Sum of Squares	df	Mean Square	F Value	p-value Prob > F	
Linear	17.39	0.4073	0.3332	0.2069	16184.48	
2FI	19.94	0.4155	0.1233	-0.4971	30550.71	
Quadratic	6.01	0.9557	0.9203	0.8319	3430.53	Suggested
Cubic	7.92	0.9693	0.8618	-0.7466	35642.44	Aliased
(b) Cryogenically chilled argon gas condition						
Linear	18.81	0.4817	0.4169	0.3048	18974.98	
2FI	21.52	0.4909	0.2363	-0.3124	35820.28	
Quadratic	7.82	0.944	0.8991	0.8144	5065.76	Suggested
Cubic	10.17	0.9621	0.8295	-0.483	40478.64	Aliased
(c) Wet Machining						
Linear	18.9	0.5645	0.51	0.412	19287.57	
2FI	21.42	0.5805	0.3708	-0.0997	36071.35	
Quadratic	7.48	0.9574	0.9233	0.8566	4702.22	Suggested
Cubic	10.22	0.9681	0.8566	-0.3753	45112.82	Aliased
(d) Dry Machining						
Linear	21.14	0.6069	0.5578	0.4734	23940.89	
2FI	23.69	0.6296	0.4444	0.0512	43134.91	
Quadratic	12.08	0.9197	0.8555	0.7171	12862.94	Suggested
Cubic	17.03	0.9362	0.7129	-2.1485	1.43E+05	Aliased

Note: “Model Summary Statistics” Focus on the model maximizing the Adjusted R-Squared and “Predicted R-Squared”.

Table B.4. Sequential of adequate model sum of squares for surface roughness.

(a) Atomized liquid nitrogen spray machining condition						
Source	Sum of Squares	df	Mean Square	F Value	p-value Prob > F	
Mean vs Total	15.74	1	15.74			
Linear vs Mean	0.89	5	0.18	31.11	< 0.0001	
2FI vs Linear	0.013	10	1.33E-03	0.19	0.9961	
Quadratic vs 2FI	0.17	5	0.034	19.78	< 0.0001	Suggested
Cubic vs Quadratic	0.032	15	2.11E-03	1.79	0.1782	Aliased
Residual	0.012	10	1.18E-03			
Total	16.86	46	0.37			
(b) Cryogenically chilled argon gas condition						
Mean vs Total	29.61	1	29.61			
Linear vs Mean	2.02	5	0.4	52.78	< 0.0001	
2FI vs Linear	0.046	10	4.64E-03	0.54	0.8502	
Quadratic vs 2FI	0.23	5	0.046	40.64	< 0.0001	Suggested
Cubic vs Quadratic	8.24E-03	15	5.50E-04	0.27	0.9882	Aliased
Residual	0.02	10	2.02E-03			
Total	31.93	46	0.69			
(c) Wet Machining						
Mean vs Total	55	1	55			
Linear vs Mean	2.92	5	0.58	23.77	< 0.0001	
2FI vs Linear	0.027	10	2.67E-03	0.084	0.9999	
Quadratic vs 2FI	0.92	5	0.18	154.31	< 0.0001	Suggested
Cubic vs Quadratic	0.02	15	1.31E-03	1.27	0.36	Aliased
Residual	0.01	10	1.03E-03			
Total	58.9	46	1.28			
(d) Dry Machining						
Mean vs Total	61.09	1	61.09			
Linear vs Mean	2.98	5	0.6	23.23	< 0.0001	
2FI vs Linear	0.048	10	4.83E-03	0.15	0.9985	
Quadratic vs 2FI	0.95	5	0.19	151.94	< 0.0001	Suggested
Cubic vs Quadratic	0.016	15	1.09E-03	0.73	0.7148	Aliased
Residual	0.015	10	1.49E-03			
Total	65.1	46	1.42			

Note: “Sequential model sum of squares”: Select the highest order polynomial value where the additional terms are significant and model is not aliased.

Table B.5. Lack of fit tests for surface roughness.

(a) Atomized liquid nitrogen spray machining condition						
Source	Sum of Squares	df	Mean Square	F Value	p-value Prob > F	
Linear	0.22	35	6.39E-03	6.41	0.0232	
2FI	0.21	25	8.42E-03	8.44	0.0129	
Quadratic	0.038	20	1.92E-03	1.93	0.2408	Suggested
Cubic	6.82E-03	5	1.36E-03	1.37	0.37	Aliased
Pure Error	4.99E-03	5	9.98E-04			
(b) Cryogenically chilled argon gas condition						
Linear	0.3	35	8.64E-03	13.26	0.0044	
2FI	0.26	25	0.01	15.72	0.0031	
Quadratic	0.025	20	1.26E-03	1.93	0.2404	Suggested
Cubic	0.017	5	3.38E-03	5.19	0.0475	Aliased
Pure Error	3.26E-03	5	6.51E-04			
(c) Wet Machining						
Linear	0.97	35	0.028	21	0.0015	
2FI	0.95	25	0.038	28.6	0.0007	
Quadratic	0.023	20	1.17E-03	0.88	0.6264	Suggested
Cubic	3.70E-03	5	7.41E-04	0.56	0.731	Aliased
Pure Error	6.63E-03	5	1.33E-03			
(d) Dry Machining						
Linear	1.03	35	0.029	62.89	0.0001	
2FI	0.98	25	0.039	83.9	< 0.0001	
Quadratic	0.029	20	1.44E-03	3.1	0.1066	Suggested
Cubic	0.013	5	2.50E-03	5.38	0.0443	Aliased
Pure Error	2.33E-03	5	4.66E-04			

Note: “Lack of Fit Tests”: Want the selected model to have insignificant lack of fit.

Table B.6. Model summary statistics for surface roughness.

(a) Atomized liquid nitrogen spray machining condition						
Source	Sum of Squares	df	Mean Square	F Value	p-value Prob > F	
Linear	0.076	0.7955	0.7699	0.727	0.31	
2FI	0.085	0.8074	0.711	0.5119	0.55	
Quadratic	0.042	0.9611	0.93	0.856	0.16	Suggested
Cubic	0.034	0.9894	0.9525	0.6034	0.44	Aliased
(b) Cryogenically chilled argon gas condition						
Linear	0.087	0.8684	0.8519	0.8234	0.41	
2FI	0.093	0.8883	0.8325	0.7147	0.66	
Quadratic	0.034	0.9878	0.978	0.9547	0.11	Suggested
Cubic	0.045	0.9913	0.9609	0.5322	1.09	Aliased
(c) Wet Machining						
Linear	0.16	0.7482	0.7167	0.655	1.34	
2FI	0.18	0.755	0.6326	0.3312	2.61	
Quadratic	0.035	0.9923	0.9862	0.9736	0.1	Suggested
Cubic	0.032	0.9973	0.9881	0.9367	0.25	Aliased
(d) Dry Machining						
Linear	0.16	0.7438	0.7118	0.6491	1.41	
2FI	0.18	0.7558	0.6337	0.3341	2.67	
Quadratic	0.035	0.9922	0.986	0.9704	0.12	Suggested
Cubic	0.039	0.9963	0.9833	0.7994	0.8	Aliased

Note: “Model Summary Statistics” Focus on the model maximizing the Adjusted R-Squared and “Predicted R-Squared”.

Table B.7. Sequential of adequate model sum of squares for tool wear.

(a) Atomized liquid nitrogen spray machining condition						
Source	Sum of Squares	df	Mean Square	F Value	p-value Prob > F	
Mean vs Total	82316.87	1	82316.87			
Linear vs Mean	2298.26	5	459.65	18.77	< 0.0001	
2FI vs Linear	264.46	10	26.45	1.11	0.3873	
Quadratic vs 2FI	608.2	5	121.64	28.41	< 0.0001	Suggested
Cubic vs Quadratic	23.99	15	1.6	0.19	0.9977	Aliased
Residual	83.04	10	8.3			
Total	85594.83	46	1860.76			
(b) Cryogenically chilled argon gas condition						
Mean vs Total	1.19E+05	1	1.19E+05			
Linear vs Mean	1667.3	5	333.46	8.63	< 0.0001	
2FI vs Linear	181.77	10	18.18	0.4	0.9362	
Quadratic vs 2FI	1316.36	5	263.27	138.63	< 0.0001	Suggested
Cubic vs Quadratic	27.39	15	1.83	0.91	0.5796	Aliased
Residual	20.08	10	2.01			
Total	1.22E+05	46	2648.21			
(c) Wet Machining						
Mean vs Total	1.77E+05	1	1.77E+05			
Linear vs Mean	3006.1	5	601.22	19.47	< 0.0001	
2FI vs Linear	224.74	10	22.47	0.67	0.745	
Quadratic vs 2FI	855.24	5	171.05	27.57	< 0.0001	Suggested
Cubic vs Quadratic	87.66	15	5.84	0.87	0.6117	Aliased
Residual	67.47	10	6.75			
Total	1.82E+05	46	3948.14			
(d) Dry Machining						
Mean vs Total	2.49E+05	1	2.49E+05			
Linear vs Mean	2867.78	5	573.56	7.84	< 0.0001	
2FI vs Linear	148.51	10	14.85	0.16	0.9979	
Quadratic vs 2FI	2391.35	5	478.27	30.84	< 0.0001	Suggested
Cubic vs Quadratic	306.71	15	20.45	2.53	0.0716	Aliased
Residual	80.97	10	8.1			
Total	2.55E+05	46	5548.2			

Note: “Sequential model sum of squares”: Select the highest order polynomial value where the additional terms are significant and model is not aliased.

Table B.8. Lack of fit tests for tool wear.

Source	Sum of Squares	df	Mean Square	F Value	p-value Prob > F	
(a) Atomized liquid nitrogen spray machining condition						
Linear	956.84	35	27.34	5.98	0.027	
2FI	692.38	25	27.7	6.06	0.0269	
Quadratic	84.18	20	4.21	0.92	0.6018	Suggested
Cubic	60.19	5	12.04	2.63	0.1558	Aliased
Pure Error	22.85	5	4.57			
(b) Cryogenically chilled argon gas condition						
Linear	1529.14	35	43.69	13.26	0.0044	
2FI	1347.37	25	53.89	16.36	0.0028	
Quadratic	31	20	1.55	0.47	0.8957	Suggested
Cubic	3.61	5	0.72	0.22	0.9394	Aliased
Pure Error	16.47	5	3.29			
(c) Wet Machining						
Linear	1178.13	35	33.66	2.95	0.114	
2FI	953.39	25	38.14	3.35	0.0911	
Quadratic	98.15	20	4.91	0.43	0.9188	Suggested
Cubic	10.49	5	2.1	0.18	0.9566	Aliased
Pure Error	56.98	5	11.4			
(d) Dry Machining						
Linear	2869.24	35	81.98	7.03	0.0189	
2FI	2720.73	25	108.83	9.33	0.0103	
Quadratic	329.38	20	16.47	1.41	0.3757	Suggested
Cubic	22.66	5	4.53	0.39	0.8385	Aliased
Pure Error	58.31	5	11.66			

Note: “Lack of Fit Tests”: Want the selected model to have insignificant lack of fit.

Table B.9. Model summary statistics for tool wear.

(a) Atomized liquid nitrogen spray machining condition						
Source	Sum of Squares	df	Mean Square	F Value	p-value Prob > F	
Linear	4.95	0.7011	0.6638	0.5919	1337.85	
2FI	4.88	0.7818	0.6727	0.4127	1924.99	
Quadratic	2.07	0.9673	0.9412	0.8872	369.63	Suggested
Cubic	2.88	0.9747	0.886	-0.1851	3884.86	Aliased
(b) Cryogenically chilled argon gas condition						
Linear	6.22	0.5189	0.4588	0.3497	2089.24	
2FI	6.74	0.5755	0.3633	-0.1121	3573	
Quadratic	1.38	0.9852	0.9734	0.954	147.73	Suggested
Cubic	1.42	0.9937	0.9719	0.9207	254.81	Aliased
(c) Wet Machining						
Linear	5.56	0.7088	0.6724	0.6116	1647.39	
2FI	5.8	0.7618	0.6427	0.4053	2522.09	
Quadratic	2.49	0.9634	0.9342	0.8881	474.64	Suggested
Cubic	2.6	0.9841	0.9284	0.8224	753.36	Aliased
(d) Dry Machining						
Linear	8.56	0.4948	0.4317	0.3535	3746.91	
2FI	9.62	0.5205	0.2807	-0.0725	6215.54	
Quadratic	3.94	0.9331	0.8796	0.7582	1401.46	Suggested
Cubic	2.85	0.986	0.9371	0.7352	1534.5	Aliased

Note: “Model Summary Statistics” Focus on the model maximizing the Adjusted R-Squared and “Predicted R-Squared”.

Table B.10. ANOVA for cutting force under ALN spray assisted machining condition.

Source	Sum of Squares	df	Mean Square	F Value	p-value Prob > F	observed	PC%
Model	19503.58	20	975.18	26.99	< 0.0001	significant	
A- cutting speed	2593.93	1	2593.93	71.8	< 0.0001		14.02
B-Feed	1916.99	1	1916.99	53.06	< 0.0001		10.32
C-Rake angle	3302.5	1	3302.5	91.41	< 0.0001		17.86
D-Nose radius	411.87	1	411.87	11.4	0.0024		2.234
E-Approach angle	85.92	1	85.92	2.38	0.1356		0.465
AB	9.14	1	9.14	0.25	0.6193		0.049
AC	11.55	1	11.55	0.32	0.5769		0.062
AD	1.11	1	1.11	0.031	0.8624		0.0060
AE	0.6	1	0.6	0.017	0.8983		0.0032
BC	8.73	1	8.73	0.24	0.6273		0.0472
BD	0.84	1	0.84	0.023	0.8802		0.0045
BE	0.46	1	0.46	0.013	0.9115		0.0024
CD	0.03	1	0.03	8.24E-04	0.9773		0.00016
CE	121.77	1	121.77	3.37	0.0783		0.659
DE	13.97	1	13.97	0.39	0.5397		0.0756
A2	345.18	1	345.18	9.55	0.0048		1.8684
B2	32.11	1	32.11	0.89	0.3548		0.173
C2	7732.01	1	7732.01	214.02	< 0.0001		41.8
D2	412.23	1	412.23	11.41	0.0024		2.23
E2	1432.16	1	1432.16	39.64	< 0.0001		7.75
Residual	903.19	25	36.13				0.19
Lack of Fit	832.01	20	41.6	2.92	0.1189	not significant	
Pure Error	71.19	5	14.24				
Cor Total	20406.78	45					100
Std. Dev.	6.01		R-Squared		0.9557		
Mean	89.39		Adj R-Squared		0.9203		
C.V. %	6.72		Pred R-Squared		0.8319		
PRESS	3430.53		Adeq Precision		23.429		

Table B.11. ANOVA for cutting force under CCA gas assisted machining condition.

Source	Sum of Squares	df	Mean Square	F Value	p-value Prob > F	observed	PC%
Model	25765.38	20	1288.27	21.06	< 0.0001	significant	
A- cutting speed	4868.73	1	4868.73	79.59	< 0.0001		20.298033
B-Feed	3594.78	1	3594.78	58.77	< 0.0001		14.986857
C-Rake angle	2889.17	1	2889.17	47.23	< 0.0001		12.045126
D-Nose radius	1443.48	1	1443.48	23.6	< 0.0001		6.0179563
E-Approach angle	351.7	1	351.7	5.75	0.0243		1.4662588
AB	18.58	1	18.58	0.3	0.5864		0.0774612
AC	19.2	1	19.2	0.31	0.5803		0.080046
AD	8.1	1	8.1	0.13	0.719		0.0337694
AE	0.015	1	0.015	2.38E-04	0.9878		6.254E-05
BC	14.52	1	14.52	0.24	0.6304		0.0605348
BD	6.13	1	6.13	0.1	0.7543		0.0255563
BE	0.011	1	0.011	1.80E-04	0.9894		4.586E-05
CD	100.1	1	100.1	1.64	0.2126		0.417323
CE	83.59	1	83.59	1.37	0.2535		0.3484918
DE	0.65	1	0.65	0.011	0.9188		0.0027099
A2	423.04	1	423.04	6.92	0.0144		1.7636796
B2	9.54	1	9.54	0.16	0.6963		0.0397728
C2	8981.58	1	8981.58	146.83	< 0.0001		37.444756
D2	17.56	1	17.56	0.29	0.5969		0.0732087
E2	1094.57	1	1094.57	17.89	0.0003		4.5633292
Residual	1529.3	25	61.17				0.2550215
Lack of Fit	1118.58	20	55.93	0.68	0.756	not significant	
Pure Error	410.71	5	82.14				
Cor Total	27294.68	45					100
Std. Dev.	7.82		R-Squared		0.944		
Mean	119.29		Adj R-Squared		0.8991		
C.V. %	6.56		Pred R-Squared		0.8144		
PRESS	5065.76		Adeq Precision		19.73		

Table B.12. ANOVA for cutting force under wet machining condition.

Source	Sum of Squares	df	Mean Square	F Value	p-value Prob > F	observed	PC%
Model	31403.11	20	1570.16	28.07	< 0.0001	significant	
A- cutting speed	6865.84	1	6865.84	122.74	< 0.0001		23.561096
B-Feed	5065.99	1	5065.99	90.56	< 0.0001		17.384657
C-Rake angle	2064.74	1	2064.74	36.91	< 0.0001		7.0854458
D-Nose radius	3504.54	1	3504.54	62.65	< 0.0001		12.026322
E-Approach angle	1014.19	1	1014.19	18.13	0.0003		3.4803357
AB	27.67	1	27.67	0.49	0.4883		0.0949535
AC	8.1	1	8.1	0.14	0.7067		0.0277963
AD	21.53	1	21.53	0.38	0.5406		0.0738832
AE	2.57	1	2.57	0.046	0.8319		0.0088193
BC	6.13	1	6.13	0.11	0.7435		0.021036
BD	16.28	1	16.28	0.29	0.5943		0.0558671
BE	1.95	1	1.95	0.035	0.8535		0.0066917
CD	63.88	1	63.88	1.14	0.2955		0.2192132
CE	237.47	1	237.47	4.25	0.0499		0.8149117
DE	141.67	1	141.67	2.53	0.1241		0.4861605
A2	685.22	1	685.22	12.25	0.0018		2.3514288
B2	31.33	1	31.33	0.56	0.4612		0.1075133
C2	7897.53	1	7897.53	141.18	< 0.0001		27.101485
D2	22.57	1	22.57	0.4	0.5311		0.0774521
E2	1405.44	1	1405.44	25.12	< 0.0001		4.8229651
Residual	1398.48	25	55.94				0.191966
Lack of Fit	1050.16	20	52.51	0.75	0.7069	not significant	
Pure Error	348.33	5	69.67				
Cor Total	32801.59	45					100
Std. Dev.	7.48		R-Squared	0.9574			
Mean	140.82		Adj R-Squared	0.9233			
C.V. %	5.31		Pred R-Squared	0.8566			
PRESS	4702.22		Adeq Precision	23.04			

Table B.13. ANOVA for cutting force under dry machining condition.

Source	Sum of Squares	df	Mean Square	F Value	p-value Prob > F	observed	PC%
Model	41812.38	20	2090.62	14.32	< 0.0001	significant	
A- cutting speed	9698.36	1	9698.36	66.42	< 0.0001		24.133913
B-Feed	7146.12	1	7146.12	48.94	< 0.0001		17.782783
C-Rake angle	9.23	1	9.23	0.063	0.8035		0.0229684
D-Nose radius	8886.53	1	8886.53	60.86	< 0.0001		22.113712
E-Approach angle	1851.34	1	1851.34	12.68	0.0015		4.6069725
AB	43.58	1	43.58	0.3	0.5897		0.1084468
AC	3.16	1	3.16	0.022	0.8843		0.0078635
AD	47.85	1	47.85	0.33	0.5721		0.1190725
AE	4.58	1	4.58	0.031	0.8609		0.0113971
BC	2.39	1	2.39	0.016	0.8993		0.0059474
BD	36.18	1	36.18	0.25	0.623		0.0900322
BE	3.46	1	3.46	0.024	0.8789		0.00861
CD	727.25	1	727.25	4.98	0.0348		1.8097274
CE	0.16	1	0.16	0.00111	0.9737		0.0003982
DE	162.95	1	162.95	1.12	0.3009		0.4054934
A2	533.72	1	533.72	3.66	0.0674		1.3281371
B2	0.84	1	0.84	0.005754	0.9401		0.0020903
C2	8140.33	1	8140.33	55.75	< 0.0001		20.256828
D2	4.38	1	4.38	0.03	0.8639		0.0108994
E2	2737.19	1	2737.19	18.75	0.0002		6.8113685
Residual	3650.15	25	146.01				0.363339
Lack of Fit	2971.38	20	148.57	1.09	0.508	not significant	
Pure Error	678.78	5	135.76				
Cor Total	45462.53	45					100
Std. Dev.	12.08			R-Squared	0.9197		
Mean	165.71			Adj R-Squared	0.8555		
C.V. %	7.29			Pred R-Squared	0.7171		
PRESS	12862.94			Adeq Precision	14.622		

Table B.14. ANOVA for surface roughness under ALN spray assisted machining condition.

Source	Sum of Squares	df	Mean Square	F Value	p-value Prob > F	observed	PC%
Model	1.07	20	0.054	30.91	< 0.0001	significant	
A- cutting speed	0.08	1	0.08	46.08	< 0.0001	significant	7.54
B-Feed	0.11	1	0.11	62.56	< 0.0001	significant	10.37
C-Rake angle	5.625E-07	1	5.625E-07	0.0003236	0.9858		0.00
D-Nose radius	0.69	1	0.69	398.02	< 0.0001	significant	65.05
E-Approach angle	0.008789	1	0.008789	5.06	0.0336		0.83
AB	0.000361	1	0.000361	0.21	0.6525		0.03
AC	0.00000025	1	0.00000025	0.0001438	0.9905		0.00
AD	0.00245	1	0.00245	1.41	0.2463		0.23
AE	0.000256	1	0.000256	0.15	0.7044		0.02
BC	0.00000225	1	0.00000225	0.001294	0.9716		0.00
BD	0.003306	1	0.003306	1.9	0.18		0.31
BE	0.0003423	1	0.0003423	0.2	0.661		0.03
CD	0.00366	1	0.00366	2.11	0.1592		0.35
CE	0.001156	1	0.001156	0.67	0.4225		0.11
DE	0.001764	1	0.001764	1.01	0.3234		0.17
A2	0.003879	1	0.003879	2.23	0.1477		0.37
B2	0.003096	1	0.003096	1.78	0.1941		0.29
C2	0.1	1	0.1	59.47	< 0.0001	significant	9.43
D2	0.031	1	0.031	17.68	0.0003		2.92
E2	0.019	1	0.019	10.7	0.0031		1.79
Residual	0.043	25	0.001738				0.16
Lack of Fit	0.038	20	0.001923	1.93	0.2408	not significant	
Pure Error	0.004987	5	0.0009975				
Cor Total	1.12	45					100
Std. Dev.	0.042		R-Squared		0.9611		
Mean	0.59		Adj R-Squared		0.93		
C.V. %	7.13		Pred R-Squared		0.856		
PRESS	0.16		Adeq Precision		22.269		

Table B.15. ANOVA for surface roughness under CCA gas assisted machining condition.

Source	Sum of Squares	df	Mean Square	F Value	p-value Prob > F	observed	PC%
Model	2.29	20	0.11	100.95	< 0.0001	significant	
A- cutting speed	0.16	1	0.16	137	< 0.0001	significant	7.06
B-Feed	0.21	1	0.21	186.27	< 0.0001	significant	9.26
C-Rake angle	0.055	1	0.055	48.41	< 0.0001	significant	2.43
D-Nose radius	1.59	1	1.59	1403.14	< 0.0001	significant	70.12
E-Approach angle	2.25E-04	1	2.25E-04	0.2	0.6601		0.01
AB	7.56E-04	1	7.56E-04	0.67	0.4222		0.03
AC	1.82E-04	1	1.82E-04	0.16	0.6922		0.01
AD	6.56E-03	1	6.56E-03	5.78	0.024		0.29
AE	4.00E-06	1	4.00E-06	3.52E-03	0.9532		0.00
BC	2.72E-04	1	2.72E-04	0.24	0.6287		0.01
BD	9.12E-03	1	9.12E-03	8.03	0.009		0.40
BE	6.25E-06	1	6.25E-06	5.50E-03	0.9415		0.00
CD	0.026	1	0.026	22.82	< 0.0001	significant	1.15
CE	3.48E-03	1	3.48E-03	3.06	0.0923		0.15
DE	7.23E-05	1	7.23E-05	0.064	0.803		0.00
A2	3.10E-03	1	3.10E-03	2.73	0.1111		0.14
B2	2.14E-03	1	2.14E-03	1.89	0.1817		0.09
C2	0.099	1	0.099	87.4	< 0.0001	significant	4.37
D2	0.1	1	0.1	91.26	< 0.0001	significant	4.41
E2	6.29E-04	1	6.29E-04	0.55	0.4636		0.03
Residual	0.028	25	1.14E-03				0.05
Lack of Fit	0.025	20	1.26E-03	1.93	0.2404	not significant	
Pure Error	3.26E-03	5	6.51E-04				
Cor Total	2.32	45					100
Std. Dev.	0.034		R-Squared		0.9878		
Mean	0.8		Adj R-Squared		0.978		
C.V. %	4.2		Pred R-Squared		0.9547		
PRESS	0.11		Adeq Precision		42.154		

Table B.16. ANOVA for surface roughness under wet machining condition.

Source	Sum of Squares	df	Mean Square	F Value	p-value Prob > F	observed	PC%
Model	3.87	20	0.19	161.34	< 0.0001	significant	
A- cutting speed	0.28	1	0.28	229.93	< 0.0001	significant	7.70
B-Feed	0.44	1	0.44	363.66	< 0.0001	significant	12.11
C-Rake angle	0.097	1	0.097	80.95	< 0.0001	significant	2.67
D-Nose radius	2.09	1	2.09	1742.48	< 0.0001	significant	57.51
E-Approach angle	0.019	1	0.019	16	0.0005		0.52
AB	2.25E-04	1	2.25E-04	0.19	0.6686		0.01
AC	4.00E-04	1	4.00E-04	0.33	0.5687		0.01
AD	8.28E-03	1	8.28E-03	6.91	0.0145		0.23
AE	4.90E-05	1	4.90E-05	0.041	0.8414		0.00
BC	5.52E-04	1	5.52E-04	0.46	0.5035		0.02
BD	0.011	1	0.011	9.37	0.0052		0.30
BE	6.40E-05	1	6.40E-05	0.053	0.8191		0.00
CD	5.85E-03	1	5.85E-03	4.88	0.0365		0.16
CE	0	1	0	0	1		0.00
DE	2.50E-05	1	2.50E-05	0.021	0.8863		0.00
A2	9.83E-03	1	9.83E-03	8.2	0.0084		0.27
B2	7.24E-03	1	7.24E-03	6.04	0.0212		0.20
C2	3.59E-03	1	3.59E-03	2.99	0.096		0.10
D2	0.29	1	0.29	238.58	< 0.0001	significant	7.98
E2	0.37	1	0.37	309.63	< 0.0001	significant	10.18
Residual	0.03	25	1.20E-03				0.03
Lack of Fit	0.023	20	1.17E-03	0.88	0.6264	not significant	
Pure Error	6.63E-03	5	1.33E-03				
Cor Total	3.9	45					100
Std. Dev.	0.035		R-Squared		0.9923		
Mean	1.09		Adj R-Squared		0.9862		
C.V. %	3.17		Pred R-Squared		0.9736		
PRESS	0.1		Adeq Precision		49.686		

Table B.17. ANOVA for surface roughness under dry machining condition.

Source	Sum of Squares	df	Mean Square	F Value	p-value Prob > F	observed	PC%
Model	3.98	20	0.2	159.43	< 0.0001	significant	
A- cutting speed	0.33	1	0.33	268.1	< 0.0001	significant	8.83
B-Feed	0.45	1	0.45	363.38	< 0.0001	significant	12.04
C-Rake angle	0.13	1	0.13	102.67	< 0.0001	significant	3.48
D-Nose radius	2.03	1	2.03	1624.46	< 0.0001	significant	54.34
E-Approach angle	0.04	1	0.04	31.72	< 0.0001	significant	1.07
AB	1.85E-03	1	1.85E-03	1.48	0.2349		0.05
AC	5.06E-04	1	5.06E-04	0.41	0.53		0.01
AD	7.83E-03	1	7.83E-03	6.27	0.0191		0.21
AE	1.00E-04	1	1.00E-04	0.08	0.7795		0.00
BC	7.29E-04	1	7.29E-04	0.58	0.4519		0.02
BD	0.011	1	0.011	8.5	0.0074		0.29
BE	1.44E-04	1	1.44E-04	0.12	0.737		0.00
CD	0.02	1	0.02	15.93	0.0005		0.54
CE	2.45E-03	1	2.45E-03	1.96	0.1735		0.07
DE	4.16E-03	1	4.16E-03	3.33	0.0799		0.11
A2	0.02	1	0.02	16	0.0005		0.54
B2	0.016	1	0.016	13.03	0.0013		0.43
C2	4.75E-05	1	4.75E-05	0.038	0.8469		0.00
D2	0.29	1	0.29	232.01	< 0.0001	significant	7.76
E2	0.38	1	0.38	303.45	< 0.0001	significant	10.17
Residual	0.031	25	1.25E-03				0.03
Lack of Fit	0.029	20	1.44E-03	3.1	0.1066	not significant	
Pure Error	2.33E-03	5	4.66E-04				
Cor Total	4.01	45					100
Std. Dev.	0.035		R-Squared		0.9922		
Mean	1.15		Adj R-Squared		0.986		
C.V. %	3.07		Pred R-Squared		0.9704		
PRESS	0.12		Adeq Precision		49.391		

Table B.18. ANOVA for tool wear under ALN spray assisted machining condition.

(a) Atomized liquid nitrogen spray machining condition

Source	Sum of Squares	df	Mean Square	F Value	p-value Prob > F	observed	PC%
Model	3170.92	20	158.55	37.03	< 0.0001	significant	
A- cutting speed	836.52	1	836.52	195.38	< 0.0001	significant	27.78
B-Feed	139.45	1	139.45	32.57	< 0.0001	significant	4.63
C-Rake angle	216.95	1	216.95	50.67	< 0.0001	significant	7.21
D-Nose radius	970.57	1	970.57	226.7	< 0.0001	significant	32.24
E-Approach angle	134.78	1	134.78	31.48	< 0.0001	significant	4.48
AB	1.09	1	1.09	0.25	0.6183		0.04
AC	1.37	1	1.37	0.32	0.5772		0.05
AD	7.68	1	7.68	1.79	0.1926		0.26
AE	0.71	1	0.71	0.16	0.6883		0.02
BC	0.23	1	0.23	0.053	0.8196		0.01
BD	1.28	1	1.28	0.3	0.5895		0.04
BE	0.12	1	0.12	0.027	0.8698		0.00
CD	148.99	1	148.99	34.8	< 0.0001	significant	4.95
CE	102.03	1	102.03	23.83	< 0.0001	significant	3.39
DE	0.97	1	0.97	0.23	0.6375		0.03
A2	0.37	1	0.37	0.086	0.7714		0.01
B2	0.22	1	0.22	0.05	0.8244		0.01
C2	161.91	1	161.91	37.82	< 0.0001	significant	5.38
D2	28.14	1	28.14	6.57	0.0168		0.93
E2	253.03	1	253.03	59.1	< 0.0001	significant	8.40
Residual	107.03	25	4.28				0.14
Lack of Fit	84.18	20	4.21	0.92	0.6018	not significant	
Pure Error	22.85	5	4.57				
Cor Total	3277.96	45					100
Std. Dev.	2.07		R-Squared		0.9673		
Mean	42.3		Adj R-Squared		0.9412		
C.V. %	4.89		Pred R-Squared		0.8872		
PRESS	369.63		Adeq Precision		27.588		

Table B.19. ANOVA for tool wear under CCA gas assisted machining condition.

Source	Sum of Squares	df	Mean Square	F Value	p-value Prob > F	observed	PC%
Model	3165.43	20	158.27	83.34	< 0.0001	significant	
A- cutting speed	1198.03	1	1198.03	630.86	< 0.0001	significant	40.70
B-Feed	199.7	1	199.7	105.16	< 0.0001	significant	6.78
C-Rake angle	214.5	1	214.5	112.95	< 0.0001	significant	7.29
D-Nose radius	3.28	1	3.28	1.73	0.2007		0.11
E-Approach angle	51.79	1	51.79	27.27	< 0.0001	significant	1.76
AB	1.41	1	1.41	0.74	0.3969		0.05
AC	1	1	1	0.53	0.475		0.03
AD	0.03	1	0.03	0.016	0.9002		0.00
AE	0.58	1	0.58	0.31	0.5849		0.02
BC	0.17	1	0.17	0.088	0.7696		0.01
BD	5.08E-03	1	5.08E-03	2.67E-03	0.9592		0.00
BE	0.097	1	0.097	0.051	0.8231		0.00
CD	137.1	1	137.1	72.19	< 0.0001	significant	4.66
CE	40.22	1	40.22	21.18	0.0001		1.37
DE	1.16	1	1.16	0.61	0.4421		0.04
A2	14.6	1	14.6	7.69	0.0103		0.50
B2	13.3	1	13.3	7	0.0139		0.45
C2	514.42	1	514.42	270.89	< 0.0001	significant	17.48
D2	308.38	1	308.38	162.39	< 0.0001	significant	10.48
E2	241.6	1	241.6	127.22	< 0.0001	significant	8.21
Residual	47.48	25	1.9				0.06
Lack of Fit	31	20	1.55	0.47	0.8957	not significant	
Pure Error	16.47	5	3.29				
Cor Total	3212.91	45					100
Std. Dev.	1.38		R-Squared		0.9852		
Mean	50.78		Adj R-Squared		0.9734		
C.V. %	2.71		Pred R-Squared		0.954		
PRESS	147.73		Adeq Precision		39.441		

Table B.20. ANOVA for tool wear under wet machining condition.

Source	Sum of Squares	df	Mean Square	F Value	p-value Prob > F	observed	PC%
Model	4086.07	20	204.3	32.93	< 0.0001	significant	
A- cutting speed	1793.74	1	1793.74	289.08	< 0.0001	significant	44.80
B-Feed	299	1	299	48.19	< 0.0001	significant	7.47
C-Rake angle	334.1	1	334.1	53.84	< 0.0001	significant	8.34
D-Nose radius	220.63	1	220.63	35.56	< 0.0001	significant	5.51
E-Approach angle	358.62	1	358.62	57.8	< 0.0001	significant	8.96
AB	2.1	1	2.1	0.34	0.5656		0.05
AC	1.08	1	1.08	0.17	0.6804		0.03
AD	0.87	1	0.87	0.14	0.7116		0.02
AE	3.63	1	3.63	0.59	0.4515		0.09
BC	0.18	1	0.18	0.029	0.8663		0.00
BD	0.14	1	0.14	0.023	0.8799		0.00
BE	0.6	1	0.6	0.097	0.7575		0.01
CD	185.18	1	185.18	29.84	< 0.0001	significant	4.63
CE	14.05	1	14.05	2.26	0.1449		0.35
DE	16.9	1	16.9	2.72	0.1114		0.42
A2	16.25	1	16.25	2.62	0.1182		0.41
B2	14.57	1	14.57	2.35	0.138		0.36
C2	515.13	1	515.13	83.02	< 0.0001	significant	12.87
D2	139.27	1	139.27	22.44	< 0.0001	significant	3.48
E2	81.55	1	81.55	13.14	0.0013		2.04
Residual	155.13	25	6.21				0.16
Lack of Fit	98.15	20	4.91	0.43	0.9188	not significant	
Pure Error	56.98	5	11.4				
Cor Total	4241.2	45					100
Std. Dev.	2.49		R-Squared		0.9634		
Mean	62.1		Adj R-Squared		0.9342		
C.V. %	4.01		Pred R-Squared		0.8881		
PRESS	474.64		Adeq Precision		25.445		

Table B.21. ANOVA for tool wear under dry machining condition.

Source	Sum of Squares	df	Mean Square	F Value	p-value Prob > F	observed	PC%
Model	5407.65	20	270.38	17.44	< 0.0001	significant	
A- cutting speed	2390.58	1	2390.58	154.16	< 0.0001	significant	39.92
B-Feed	398.48	1	398.48	25.7	< 0.0001	significant	6.65
C-Rake angle	41.44	1	41.44	2.67	0.1146		0.69
D-Nose radius	7.91	1	7.91	0.51	0.4818		0.13
E-Approach angle	29.38	1	29.38	1.89	0.1809		0.49
AB	2.51	1	2.51	0.16	0.6908		0.04
AC	0.38	1	0.38	0.024	0.877		0.01
AD	0.55	1	0.55	0.036	0.852		0.01
AE	0.012	1	0.012	7.58E-04	0.9783		0.00
BC	0.063	1	0.063	4.07E-03	0.9496		0.00
BD	0.092	1	0.092	5.92E-03	0.9393		0.00
BE	1.96E-03	1	1.96E-03	1.26E-04	0.9911		0.00
CD	0.55	1	0.55	0.035	0.8526		0.01
CE	114.03	1	114.03	7.35	0.0119		1.90
DE	30.33	1	30.33	1.96	0.1743		0.51
A2	20.77	1	20.77	1.34	0.2581		0.35
B2	18.54	1	18.54	1.2	0.2846		0.31
C2	1898.79	1	1898.79	122.45	< 0.0001	significant	31.71
D2	303.67	1	303.67	19.58	0.0002		5.07
E2	714.34	1	714.34	46.07	< 0.0001	significant	11.93
Residual	387.68	25	15.51				0.26
Lack of Fit	329.38	20	16.47	1.41	0.3757	not significant	
Pure Error	58.31	5	11.66				
Cor Total	5795.33	45					100
Std. Dev.	3.94		R-Squared		0.9331		
Mean	73.64		Adj R-Squared		0.8796		
C.V. %	5.35		Pred R-Squared		0.7582		
PRESS	1401.46		Adeq Precision		17.109		

Multiple regression equation

The final regression equation in terms of real factor as a function of input process variables is given below:

Cutting force:

$$\boldsymbol{ALN - CF} = +176.30994 + 0.20662 \times v_c + 218.91750 \times f - 10.74727 \times \gamma - 61.27431 \times r_e - 2.03894 \times \psi + 0.022990 \times \gamma \times \psi - 2.30636E - 003 \times {v_f}^2 + 0.47325 \times \gamma^2 + 46.22403 \times {r_e}^2 + 0.014815 \times \psi^2 \quad \text{(B.1)}$$

$$\boldsymbol{R^2 = 0.9519; Adj\ R^2 = 0.9381; Pred\ R^2 = 0.8908}$$

$$\boldsymbol{CCA - CF} = +148.78853 + 0.21449 \times v_f + 299.78250 \times f - 9.67980 \times \gamma + 23.74570 \times r_e - 1.63884 \times \psi - 2.81687E - 003 \times {v_f}^2 + 0.50001 \times \gamma^2 + 0.012355 \times \psi^2 \quad \text{(B.2)}$$

$$\boldsymbol{R^2 = 0.9334;\ Adj\ R^2 = 0.9190;\ Pred\ R^2 = 0.8966}$$

$$\boldsymbol{Wet - CF} = +157.72905 + 0.23452 \times v_f + 355.87875 \times f - 11.05438 \times \gamma + 66.75570 \times r_e - 1.91757 \times \psi + 0.032104 \times \gamma \times \psi - 0.49594 \times r_e \times \psi - 3.24409E - 003 \times {v_f}^2 + 0.48176 \times \gamma^2 + 0.014934 \times \psi^2 \quad \text{(B.3)}$$

$$\boldsymbol{R^2 = 0.9516;\ Adj\ R^2 = 0.9377;\ Pred\ R^2 = 0.9083}$$

$$\boldsymbol{Dry - CF} = +210.36932 + 0.12639 \times v_f + 422.67375 \times f - 11.12246 \times \gamma + 25.20836 \times r_e - 2.73124 \times \psi + 4.21367 \times \gamma \times \psi - 3.09396E - 003 \times {v_f}^2 + 0.47853 \times \gamma^2 + 0.019772 \times \psi^2 \quad \text{(B.4)}$$

$$\boldsymbol{R^2 = 0.9129;\ Adj\ R^2 = 0.8911;\ Pred\ R^2 = 0.8621}$$

Surface roughness:

$$\boldsymbol{ALN - SR} = +1.46609 - 1.41500E-003 \times v_c + 1.64875 \times f - 0.029323 \times \gamma - 1.19871 \times r_e - 8.07728E-003 \times \psi + 1.83417E-003 \times \gamma^2 + 0.42429 \times {r_e}^2 + 6.08003E-005 \times \psi^2 \quad \text{(B.5)}$$

$$\boldsymbol{R^2 = 0.9443; Adj\ R^2 = 0.9323; Pred\ R^2 = 0.9110}$$

$$\boldsymbol{CCA - SR} = +1.55415 - 1.89989E-003 \times v_f + 6.36891 \times f - 0.046164 \times \gamma - 1.90145 \times r_e + 8.58333E-004 \times \psi + 2.02500E-003 \times v_f \times r_e - 2.38750 \times f \times r_e + 0.025156 \times \gamma \times r_e - 1.22917E-004 \times \gamma \times \psi - 8.46303E-006 \times {v_f}^2 - 7.19636 \times f^2 + 1.63035E-003\gamma^2 + 0.66672 \times {r_e}^2 \quad \text{(B.6)}$$

$$\boldsymbol{R^2 = 0.9869;\ Adj\ R^2 = 0.9816;\ Pred\ R^2 = 0.9654}$$

$$\boldsymbol{Wet - SR} = +1.08190 - 1.76033E-003 \times v_f + 8.87825 \times f - 0.024366 \times \gamma - 2.63916 \times r_e + 0.028651 \times \psi + 2.27500E-003 \times v_f \times r_e - 2.65000 \times f \times r_e + 0.011953 \times \gamma \times r_e - 1.34233E-005 \times {v_f}^2 - 11.52333 \times f^2 + 3.16797E-004 \times \gamma^2 + 1.13141 \times {r_e}^2 - 2.29139E-004 \times \psi^2 \quad \text{(B.7)}$$

$$\boldsymbol{R^2 = 0.9920;\ Adj\ R^2 = 0.9887;\ Pred\ R^2 = 0.9822}$$

$$\boldsymbol{Dry - SR} = +1.12029 - 7.84924E-004 \times v_f + 10.68386 \times f - 0.028813 \times \gamma - 2.87780 \times r_e + 0.027371 \times \psi + 2.21250E-003 v_f \times r_e - 2.57500 \times f \times r_e + 0.022031 \times \gamma \times r_e + 2.68750E-003 \times r_e \times \psi - 1.93879E-005 \times {v_f}^2 - 17.52121 \times f^2 + 1.13456 \times {r_e}^2 - 2.32189E-004 \times \psi^2 \quad \text{(B.8)}$$

$$\boldsymbol{R^2 = 0.9908;\ Adj\ R^2 = 0.9870;\ Pred\ R^2 = 0.9776}$$

Tool wear

$$\boldsymbol{ALN - TW} = +43.83004 + 0.14461 \times v_f + 59.04347 \times f - 4.30606 \times \gamma - 51.90842 \times r_e + 0.65669 \times \psi + 1.90723 \times \gamma \times r_e + 0.021044 \times \gamma \times \psi + 0.066085 \times \gamma^2 + 10.73708 \times {r_e}^2 - 6.06914E - 003 \times \psi^2 \quad \text{(B.9)}$$

$$\boldsymbol{R^2 = 0.9631; Adj\ R^2 = 0.9526; Pred\ R^2 = 0.9157}$$

$$\boldsymbol{CCA - TW} = +62.98600 + 0.069582 \times v_f - 77.46059 \times f - 4.63344 \times \gamma - 72.94812 \times r_e + 0.65581 \times \psi + 1.82953 \times \gamma \times r_e + 0.013212 \times \gamma \times \psi + 5.17402E - 004 \times {v_f}^2 + 493.72854 \times f^2 + 0.11996 \times \gamma^2 + 37.15243 \times {r_e}^2 - 5.84613E - 003 \times \psi^2 \quad \text{(B.10)}$$

$$\boldsymbol{R^2 = 0.9838; Adj\ R^2 = 0.9780; Pred\ R^2 = 0.9672}$$

$$\boldsymbol{Wet - TW} = +56.21556 + 0.21176 \times v_f + 86.45859 \times f - 4.05060 \times \gamma - 70.82567 \times r_e + 0.50425 \times \psi + 2.12625 \times \gamma \times r_e + 0.17128 \times r_e \times \psi + 0.11115 \times \gamma^2 + 21.40958 \times {r_e}^2 - 4.02886E - 003 \times \psi^2 \quad \text{(B.11)}$$

$$\boldsymbol{R^2 = 0.9524;\ Adj\ R^2 = 0.9388;\ Pred\ R^2 = 0.9032}$$

$$\boldsymbol{Dry - TW} = +109.71139 + 0.24447 \times v_f + 99.80962 \times f - 5.06283 \times \gamma - 54.31664 \times r_e - 1.34372 \times \psi + 0.022247 \times \gamma \times \psi + 0.22043 \times \gamma^2 + 32.84945 \times {r_e}^2 + 9.33812E - 003 \times \psi^2 \quad \text{(B.12)}$$

$$\boldsymbol{R^2 = 0.9218;\ Adj\ R^2 = 0.9023;\ Pred\ R^2 = 0.8296}$$

Normal probability plot of residuals

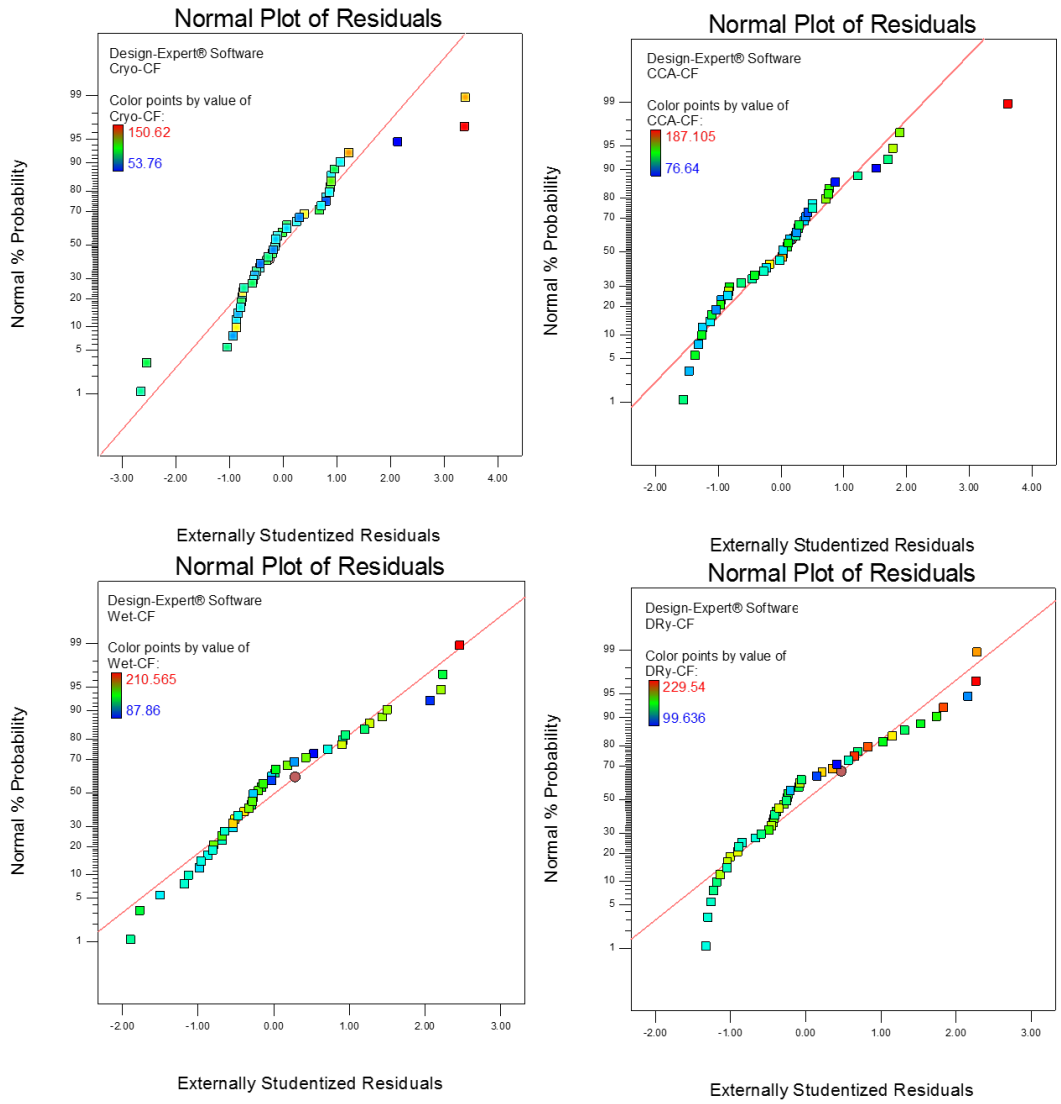

Fig. B.1. Normal probability plot of residuals for cutting force under different machining conditions.

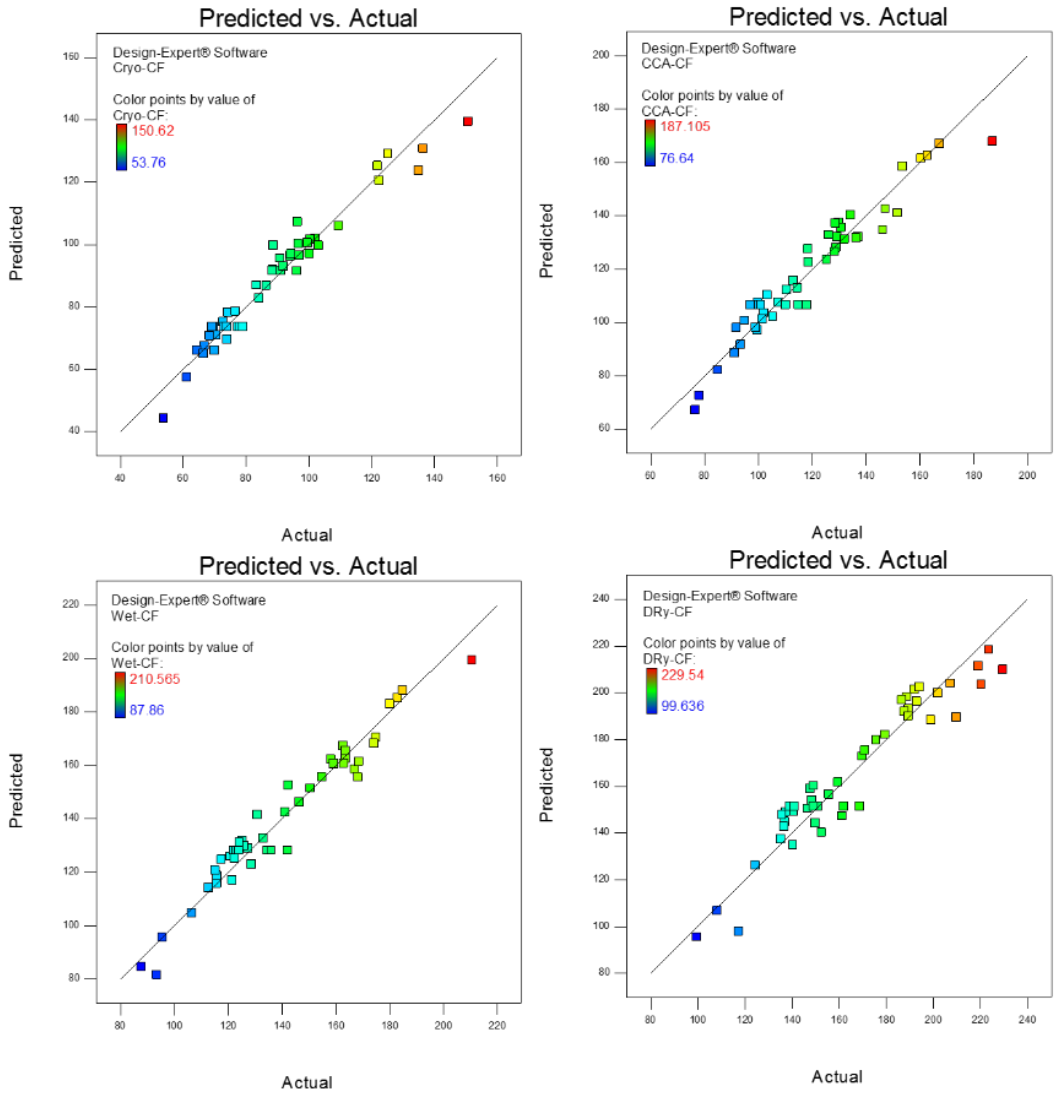

Fig. B.2. Predicted vs. actual values for cutting force under different machining conditions.

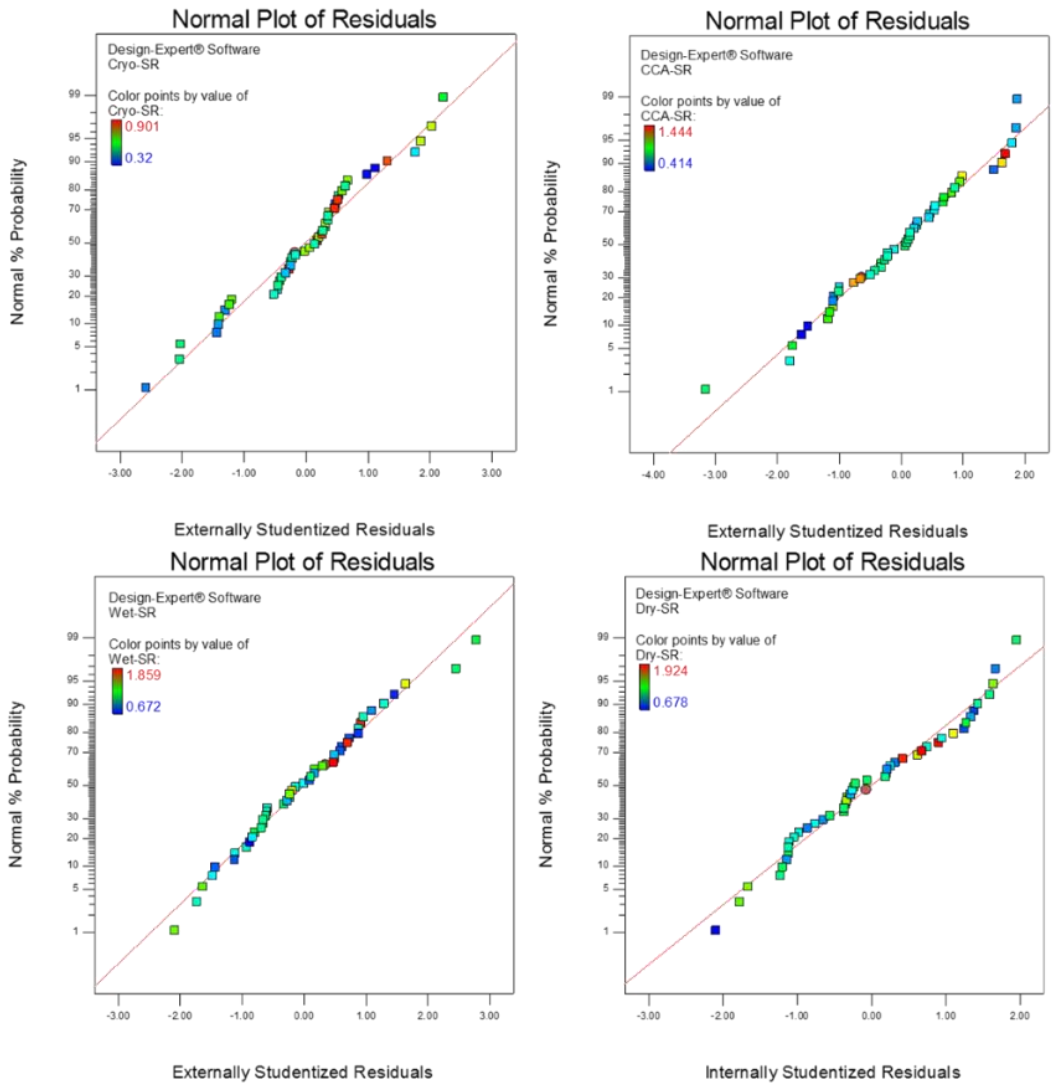

Fig. B.3. Normal probability plot of residuals for surface roughness under different machining conditions.

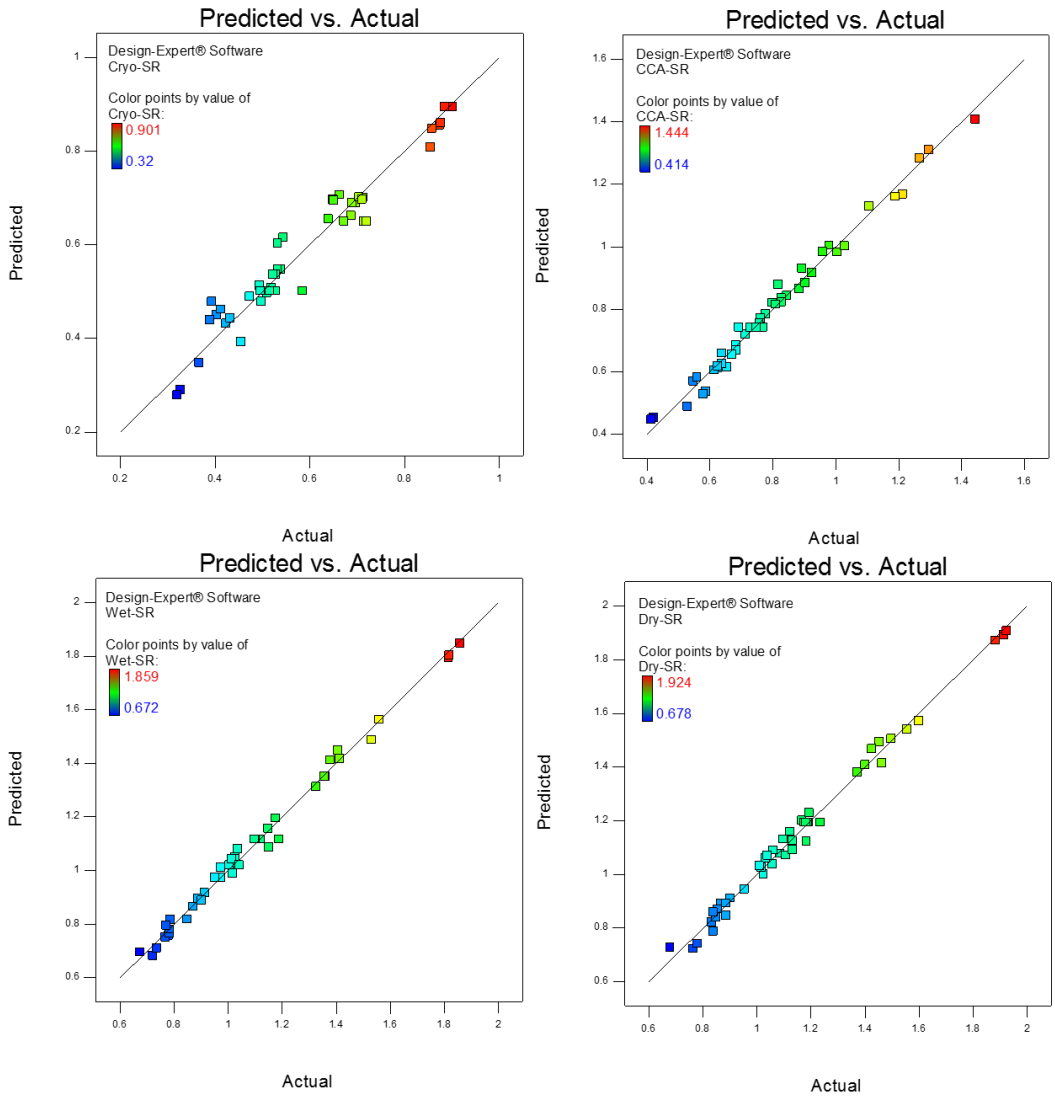

Fig. B.4. Predicted vs. actual values for surface roughness under different machining conditions.

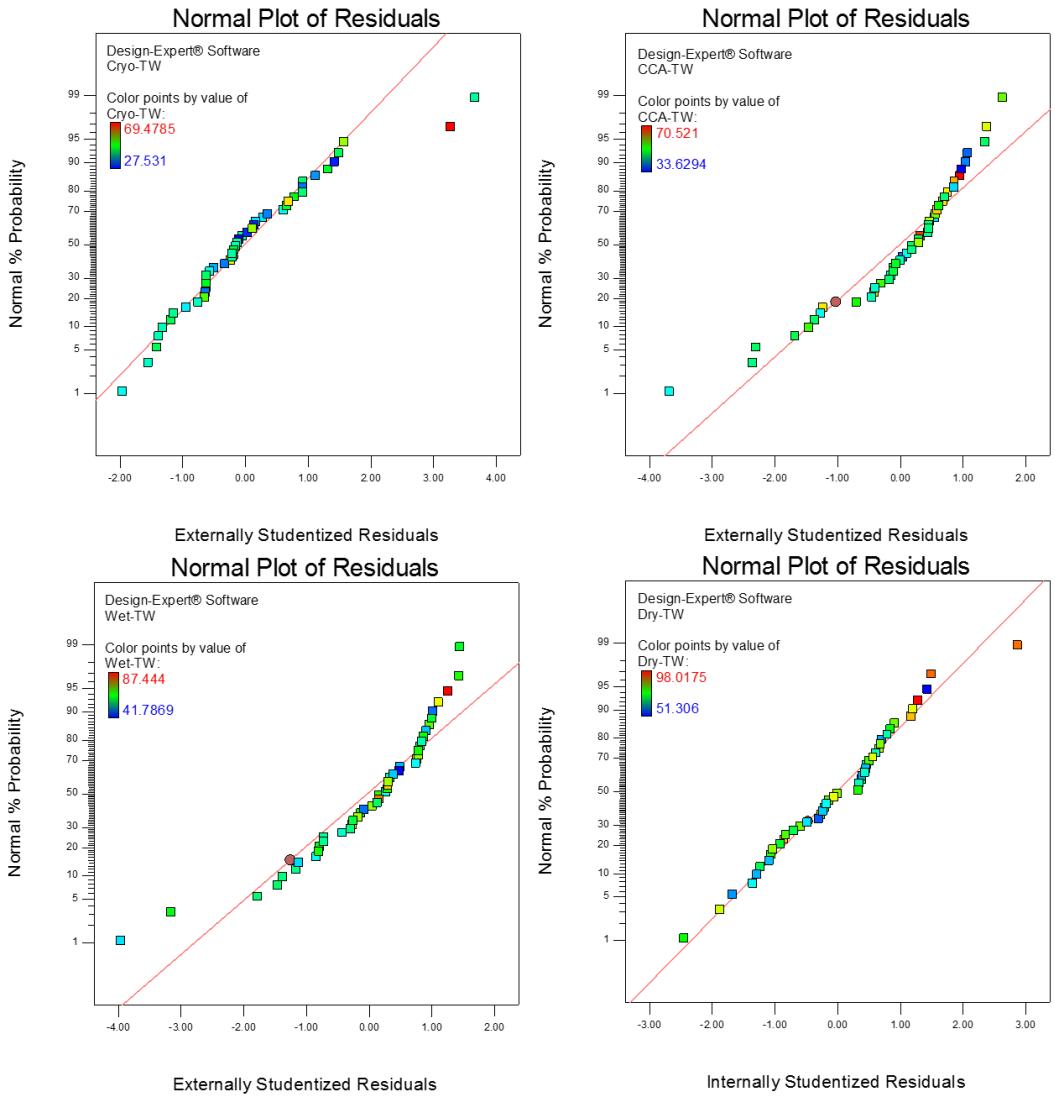

Fig. B.5. Normal probability plot of residuals for tool wear under different machining conditions.

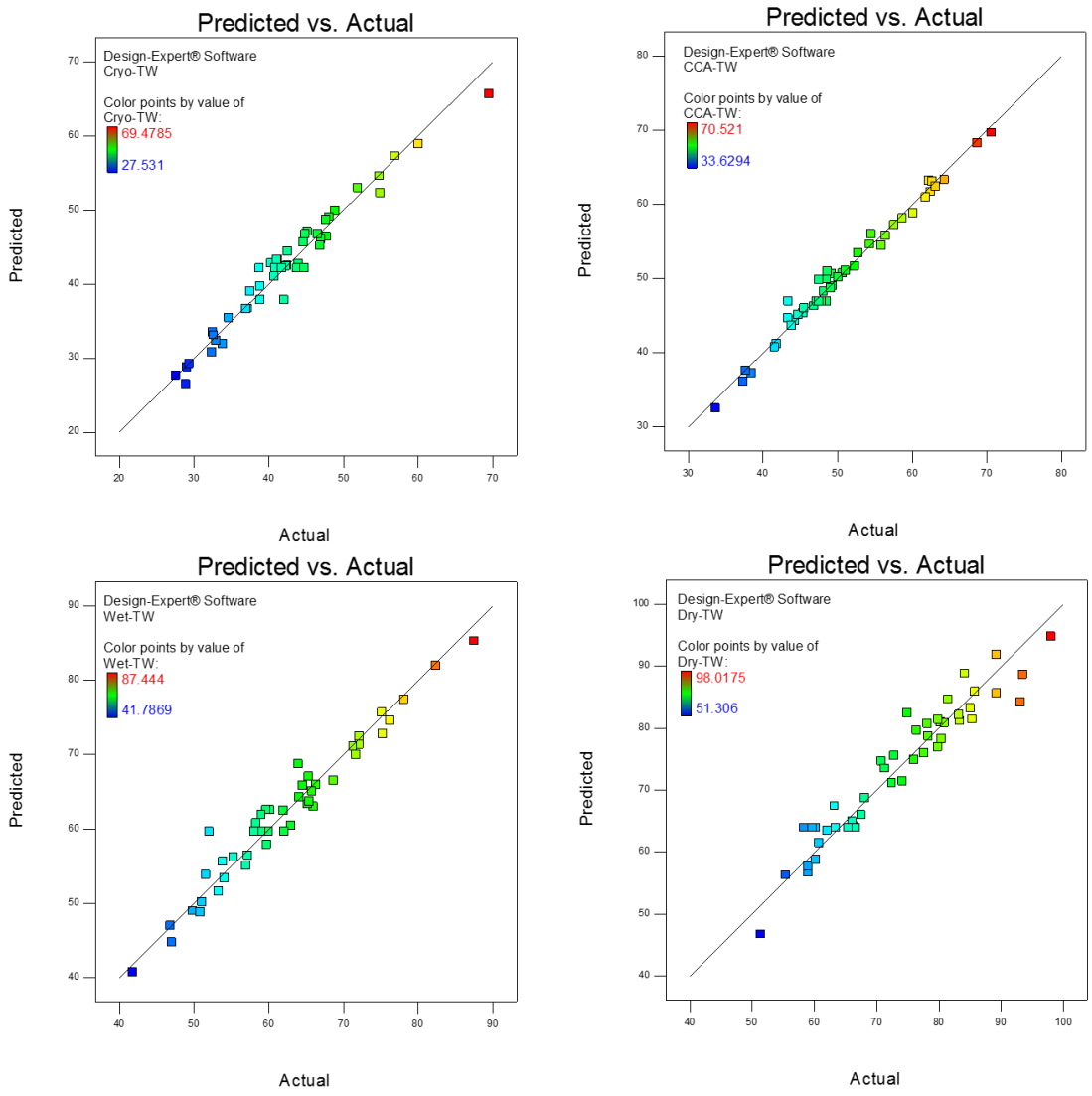

Fig. B.6. Predicted vs actual values for tool wear under different machining conditions.

Table B.22. Optimum values of machining conditions predicted by GA for corresponding minimum value of cutting force under ALN spray and CCA gas assisted machining.

Runs	Atomized liquid nitrogen spray-CF						CCA-CF					
	Min-CF	v_c	f	γ	r_e	ψ	Min-CF	v_c	f	γ	r_e	ψ
	N	m/min	mm/rev	deg	mm	deg	N	m/min	mm/rev	deg	mm	deg
1	61.84	100	0.10	8.00	0.66	60.00	82.26	100	0.10	8.00	0.4	60
2	61.74	100	0.10	8.00	0.66	62.61	81.76	100	0.10	8.00	0.4	66.32
3	62.71	100	0.10	8.00	0.80	60.00	91.75	100	0.10	8.00	0.8	60
4	62.61	100	0.10	8.00	0.80	62.61	91.26	100	0.10	8.00	0.8	66.32
5	60.13	100	0.10	9.90	0.66	60.00	80.84	100	0.10	9.68	0.4	60
6	60.11	100	0.10	9.87	0.66	61.16	80.35	100	0.10	9.68	0.4	66.32
7	61.00	100	0.10	9.90	0.80	60.00	90.34	100	0.10	9.68	0.8	60
8	60.99	100	0.10	9.87	0.80	61.16	89.85	100	0.10	9.68	0.8	66.32
9	72.78	100	0.15	8.00	0.66	60.00	97.24	100	0.15	8.00	0.4	60
10	72.68	100	0.15	8.00	0.66	62.61	96.75	100	0.15	8.00	0.4	66.32
11	73.65	100	0.15	8.00	0.80	60.00	106.74	100	0.15	8.00	0.8	60.00
12	73.56	100	0.15	8.00	0.80	62.61	106.25	100	0.15	8.00	0.8	66.32
13	71.08	100	0.15	9.90	0.66	60.00	95.83	100	0.15	9.68	0.4	60
14	71.06	100	0.15	9.87	0.66	61.16	95.34	100	0.15	9.68	0.4	66.32
15	71.95	100	0.15	9.90	0.80	60.00	105.33	100	0.15	9.68	0.8	60
16	71.93	100	0.15	9.87	0.80	61.16	104.84	100	0.15	9.68	0.8	66.32
17	43.34	150	0.10	8.00	0.66	60.00	57.77	150	0.10	8.00	0.4	60
18	43.24	150	0.10	8.00	0.66	62.61	57.27	150	0.10	8.00	0.4	66.32
19	44.21	150	0.10	8.00	0.80	60.00	67.27	150	0.10	8.00	0.8	60
20	44.11	150	0.10	8.00	0.80	62.61	66.77	150	0.10	8.00	0.8	66.32
21	41.64	150	0.10	9.90	0.66	60.00	56.36	150	0.10	9.68	0.4	60
22	41.62	150	0.10	9.87	0.66	61.16	55.86	150	0.10	9.68	0.4	66.32
23	42.50	150	0.10	9.90	0.80	60.00	65.86	150	0.10	9.68	0.8	60
24	42.49	150	0.10	9.87	0.80	61.16	65.36	150	0.10	9.68	0.8	66.32
25	54.28	150	0.15	8.00	0.66	60.00	72.76	150	0.15	8.00	0.4	60
26	54.18	150	0.15	8.00	0.66	62.61	72.26	150	0.15	8.00	0.4	66.32
27	55.16	150	0.15	8.00	0.80	60.00	82.26	150	0.15	8.00	0.8	60
28	55.06	150	0.15	8.00	0.80	62.61	81.76	150	0.15	8.00	0.8	66.32
29	52.58	150	0.15	9.90	0.66	60.00	71.35	150	0.15	9.68	0.4	60
30	52.56	150	0.15	9.87	0.66	61.16	70.85	150	0.15	9.68	0.4	66.29
31	53.45	150	0.15	9.90	0.80	60.00	80.85	150	0.15	9.68	0.8	60
32	53.43	150	0.15	9.87	0.80	61.16	80.35	150	0.15	9.68	0.8	66.32

Table B.23. Optimum values of machining conditions predicted by GA for corresponding minimum value of cutting force under wet and dry machining.

Runs	Wet -CF						Dry-CF					
	Min-CF	v_c	f	γ	r_e	ψ	Min-CF	v_c	f	γ	r_e	ψ
	N	m/min	mm/rev	deg	mm	deg	N	m/min	mm/rev	°	mm	deg
1	95.64	100.00	0.10	8.00	0.40	60.00	106.85	100.00	0.10	8.00	0.40	60.00
2	95.57	100.00	0.10	8.00	0.40	62.25	105.23	100.00	0.10	8.00	0.40	69.07
3	110.44	100.00	0.10	8.00	0.80	60.00	130.42	100.00	0.10	8.00	0.80	60.00
4	109.26	100.00	0.10	8.00	0.80	68.89	128.80	100.00	0.10	8.00	0.80	69.07
5	94.60	100.00	0.10	9.47	0.40	60.00	105.20	100.00	0.10	9.86	0.40	60.00
6	94.59	100.00	0.10	9.45	0.40	60.72	103.57	100.00	0.10	9.86	0.40	69.07
7	109.40	100.00	0.10	9.47	0.80	60.00	130.42	100.00	0.10	8.10	0.80	60.00
8	108.57	100.00	0.10	9.22	0.80	67.54	128.80	100.00	0.10	8.10	0.80	69.03
9	113.44	100.00	0.15	8.00	0.40	60.00	127.99	100.00	0.15	8.00	0.40	60.00
10	113.36	100.00	0.15	8.00	0.40	62.25	126.36	100.00	0.15	8.00	0.40	69.07
11	128.24	100.00	0.15	8.00	0.80	60.00	151.56	100.00	0.15	8.00	0.80	60.00
12	127.06	100.00	0.15	8.00	0.80	68.89	149.93	100.00	0.15	8.00	0.80	69.07
13	112.39	100.00	0.15	9.47	0.40	60.00	126.33	100.00	0.15	9.86	0.40	60.00
14	112.38	100.00	0.15	9.45	0.40	60.68	124.71	100.00	0.15	9.86	0.40	69.07
15	127.19	100.00	0.15	9.47	0.80	60.00	151.55	100.00	0.15	8.10	0.80	60.00
16	126.37	100.00	0.15	9.22	0.80	67.57	149.92	100.00	0.15	8.10	0.80	69.07
17	66.82	150.00	0.10	8.00	0.40	60.00	74.50	150.00	0.10	8.00	0.40	60.00
18	66.74	150.00	0.10	8.00	0.40	62.24	72.87	150.00	0.10	8.00	0.40	69.07
19	81.62	150.00	0.10	8.00	0.80	60.00	98.07	150.00	0.10	8.00	0.80	60.00
20	80.44	150.00	0.10	8.00	0.80	68.89	96.44	150.00	0.10	8.00	0.80	69.07
21	65.77	150.00	0.10	9.47	0.40	60.00	72.84	150.00	0.10	9.86	0.40	60.00
22	65.77	150.00	0.10	9.45	0.40	60.69	71.22	150.00	0.10	9.86	0.40	69.09
23	80.57	150.00	0.10	9.47	0.80	60.00	98.06	150.00	0.10	8.10	0.80	60.00
24	79.75	150.00	0.10	9.22	0.80	67.58	96.44	150.00	0.10	8.10	0.80	69.07
25	84.61	150.00	0.15	8.00	0.40	60.00	95.63	150.00	0.15	8.00	0.40	60.00
26	84.54	150.00	0.15	8.00	0.40	62.24	94.01	150.00	0.15	8.00	0.40	69.07
27	99.41	150.00	0.15	8.00	0.80	60.00	119.20	150.00	0.15	8.00	0.80	60.00
28	98.23	150.00	0.15	8.00	0.80	68.90	117.57	150.00	0.15	8.00	0.80	69.07
29	83.57	150.00	0.15	9.47	0.40	60.00	93.98	150.00	0.15	9.86	0.40	60.00
30	83.56	150.00	0.15	9.45	0.40	60.69	92.36	150.00	0.15	9.86	0.40	69.07
31	98.37	150.00	0.15	9.47	0.80	60.00	119.20	150.00	0.15	8.10	0.80	60.00
32	97.54	150.00	0.15	9.22	0.80	67.57	117.57	150.00	0.15	8.10	0.80	69.08

Table B.24. Optimum values of machining conditions predicted by GA for corresponding minimum value of surface roughness under ALN spray and CCA gas assisted machining.

Runs	Atomized liquid nitrogen spray - SR						CCA-SR					
	Min-SR	v_c	f	γ	r_e	ψ	Min-SR	v_c	f	γ	r_e	ψ
	microns	m/min	mm/rev	deg	mm	deg	microns	m/min	mm/rev	deg	mm	deg
1	0.4191	100	0.1	8	0.8	60	0.5995	100	0.1	8	0.8	60
2	0.4166	100	0.1	8	0.8	66.42	0.5958	100	0.1	8	0.8	90
3	0.2791	100	0.1	8	1.2	60	0.4358	100	0.1	6.03	1.2	30
4	0.2766	100	0.1	8	1.2	66.42	0.4346	100	0.1	8	1.2	90
5	0.4191	100	0.1	8	0.8	60	0.5913	100	0.1	10.25	0.8	60
6	0.4166	100	0.1	8	0.8	66.42	0.5772	100	0.1	11.38	0.8	90
7	0.2791	100	0.1	8	1.2	60	0.4383	100	0.1	8	1.2	60
8	0.2766	100	0.1	8	1.2	66.42	0.4344	100	0.1	8.29	1.2	90
9	0.5015	100	0.15	8	0.8	60	0.7325	100	0.15	8	0.8	60
10	0.4990	100	0.15	8	0.8	66.42	0.7288	100	0.15	8	0.8	90
11	0.3615	100	0.15	8	1.2	60	0.5210	100	0.15	6.03	1.2	30
12	0.3590	100	0.15	8	1.2	66.42	0.5198	100	0.15	8	1.2	90
13	0.5015	100	0.15	8	0.8	60	0.7243	100	0.15	10.25	0.8	60
14	0.4990	100	0.15	8	0.8	66.42	0.7102	100	0.15	11.38	0.8	90
15	0.3615	100	0.15	8	1.2	59.99	0.5236	100	0.15	8	1.2	90
16	0.3590	100	0.15	8	1.2	66.42	0.5197	100	0.15	8.29	1.2	90
17	0.3484	150	0.1	8	0.8	60	0.4797	150	0.1	8	0.8	60
18	0.3459	150	0.1	8	0.8	66.42	0.4760	150	0.1	8	0.8	90
19	0.2083	150	0.1	8	1.2	60	0.3565	150	0.1	6.03	1.2	30
20	0.2058	150	0.1	8	1.2	66.42	0.3553	150	0.1	8	1.2	90
21	0.3484	150	0.1	8	0.8	60	0.4715	150	0.1	10.25	0.8	60
22	0.3458	150	0.1	8	0.8	66.42	0.4574	150	0.1	11.38	0.8	90
23	0.2083	150	0.1	8	1.2	60	0.3590	150	0.1	8	1.2	60
24	0.2058	150	0.1	8	1.2	66.42	0.3552	150	0.1	8.294	1.2	90
25	0.4308	150	0.15	8	0.8	60	0.6127	150	0.15	8	0.8	60
26	0.4283	150	0.15	8	0.8	66.42	0.6090	150	0.15	8	0.8	90
27	0.2907	150	0.15	8	1.2	60	0.4417	150	0.15	6.03	1.2	30
28	0.2882	150	0.15	8	1.2	66.42	0.4405	150	0.15	8	1.2	90
29	0.4308	150	0.15	8	0.8	60	0.6045	150	0.15	10.25	0.8	60
30	0.4283	150	0.15	8	0.8	66.42	0.5904	150	0.15	11.38	0.8	90
31	0.2907	150	0.15	8	1.2	60	0.4443	150	0.15	8	1.2	60
32	0.2882	150	0.15	8	1.2	66.42	0.4404	150	0.15	8.29	1.2	90

Table B.25. Optimum values of machining conditions predicted by GA for corresponding minimum value of surface roughness under wet and dry machining.

Runs	Wet-SR						Dry-SR					
	Min-SR	v_c	f	γ	r_e	ψ	Min-SR	v_c	f	γ	r_e	ψ
	microns	m/min	mm/rev	deg	mm	deg	microns	m/min	mm/rev	deg	mm	deg
1	0.6822	100	0.1	8	0.8	30	0.7231	100	0.1	8	0.8	30
2	0.7514	100	0.1	8	0.8	90	0.8226	100	0.1	8	0.8	90
3	0.5509	100	0.1	8	1.141	30	0.5669	100	0.1	8	1.171	30
4	0.6201	100	0.1	8	1.141	90	0.7205	100	0.1	8	1.1003	90
5	0.6246	100	0.1	16	0.8	30	0.6336	100	0.1	16	0.8	30
6	0.6938	100	0.1	16	0.8	90	0.7331	100	0.1	16	0.8	90
7	0.5238	100	0.1	16	1.098	30	0.5360	100	0.1	16	1.0932	30
8	0.5931	100	0.1	16	1.098	90	0.6771	100	0.1	16	1.0222	90
9	0.8760	100	0.15	8	0.8	30	0.9353	100	0.15	8	0.8	30
10	0.9453	100	0.15	8	0.8	90	1.0348	100	0.15	8	0.8	90
11	0.6957	100	0.15	8	1.199	30	0.7286	100	0.15	8	1.2	30
12	0.7650	100	0.15	8	1.199	90	0.8905	100	0.15	8	1.1558	90
13	0.8184	100	0.15	16	0.8	30	0.8458	100	0.15	16	0.8	30
14	0.8877	100	0.15	16	0.8	90	0.9453	100	0.15	16	0.8	90
15	0.6743	100	0.15	16	1.157	30	0.7068	100	0.15	16	1.15	30
16	0.7435	100	0.15	16	1.157	90	0.8570	100	0.15	16	1.0792	90
17	0.5173	150	0.1	8	0.8	30	0.5300	150	0.1	8	0.8	30
18	0.5866	150	0.1	8	0.8	90	0.6295	150	0.1	8	0.8	90
19	0.4220	150	0.1	8	1.09	30	0.4122	150	0.1	8	1.1229	30
20	0.4912	150	0.1	8	1.09	90	0.5579	150	0.1	8	1.0514	90
21	0.4598	150	0.1	16	0.8	30	0.4405	150	0.1	16	0.8	30
22	0.5290	150	0.1	16	0.8	90	0.5400	150	0.1	16	0.8	90
23	0.3901	150	0.1	16	1.048	30	0.3726	150	0.1	16	1.0446	30
24	0.4594	150	0.1	16	1.048	90	0.5059	150	0.1	16	0.9735	90
25	0.7112	150	0.15	8	0.8	30	0.7422	150	0.15	8	0.8	30
26	0.7805	150	0.15	8	0.8	90	0.8417	150	0.15	8	0.8	90
27	0.5735	150	0.15	8	1.149	30	0.5792	150	0.15	8	1.1794	30
28	0.6427	150	0.15	8	1.149	90	0.7341	150	0.15	8	1.1078	90
29	0.6536	150	0.15	16	0.8	30	0.6527	150	0.15	16	0.8	30
30	0.7229	150	0.15	16	0.8	90	0.7522	150	0.15	16	0.8	90
31	0.5472	150	0.15	16	1.107	30	0.5497	150	0.15	16	1.1018	30
32	0.6165	150	0.15	16	1.107	90	0.6920	150	0.15	16	1.0302	90

Table B.26. Optimum values of machining conditions predicted by GA for corresponding minimum value of tool wear under ALN spray and CCA gas assisted machining.

Runs	Atomized liquid nitrogen spray -TW						CCA-TW					
	Min-SR	v_c	f	γ	r_e	ψ	Min-SR	v_c	f	γ	r_e	ψ
	microns	m/min	mm/rev	deg	mm	deg	microns	m/min	mm/rev	deg	mm	deg
1	23.587	50	0.1	8	0.8	30	30.263	50	0.1	8	0.785	30
2	29.28	50	0.1	6.71	0.8	90	33.861	50	0.1	8	0.785	90
3	17.516	50	0.1	8	1.2	30	30.271	50	0.1	8	0.8	30
4	20.021	50	0.1	0.93	1.2	90	33.87	50	0.1	8	0.8	90
5	19.086	50	0.1	16	0.8	30	28.269	50	0.1	12.52	0.673	30
6	29.392	50	0.1	8	0.8	90	33.841	50	0.1	8.459	0.773	90
7	17.108	50	0.1	10.6	1.2	30	28.754	50	0.1	11.47	0.8	30
8	25.88	50	0.1	8	1.2	60	33.862	50	0.1	8.267	0.8	90
9	26.539	50	0.15	8	0.8	30	32.564	50	0.15	8	0.785	30
10	32.232	50	0.15	6.71	0.8	90	36.16	50	0.15	8	0.785	90
11	20.469	50	0.15	8	1.2	30	32.571	50	0.15	8	0.8	30
12	22.973	50	0.15	0.93	1.2	90	36.168	50	0.15	8	0.8	90
13	22.035	50	0.15	16	0.8	30	30.571	50	0.15	12.54	0.673	30
14	32.344	50	0.15	8	0.8	90	36.139	50	0.15	8.458	0.774	90
15	20.06	50	0.15	10.5	1.2	30	31.054	50	0.15	11.53	0.8	30
16	26.273	50	0.15	8	1.2	90	36.16	50	0.15	8.257	0.8	90
17	30.817	100	0.1	8	0.8	30	37.623	100	0.1	8	0.785	30
18	36.511	100	0.1	6.71	0.8	90	41.221	100	0.1	8	0.785	90
19	24.747	100	0.1	8	1.2	30	37.631	100	0.1	8	0.8	30
20	27.251	100	0.1	0.94	1.2	90	41.231	100	0.1	8	0.8	90
21	26.313	100	0.1	16	0.8	30	35.633	100	0.1	12.73	0.668	30
22	36.622	100	0.1	8	0.8	90	41.2	100	0.1	8.455	0.773	90
23	24.337	100	0.1	10.5	1.2	30	36.112	100	0.1	11.51	0.8	30
24	30.551	100	0.1	8	1.2	90	41.222	100	0.1	8.254	0.8	90
25	33.769	100	0.15	8	0.8	30	39.921	100	0.15	8	0.785	30
26	39.463	100	0.15	6.71	0.8	90	43.519	100	0.15	8	0.785	90
27	27.699	100	0.15	8	1.2	30	39.931	100	0.15	8	0.8	30
28	30.203	100	0.15	0.93	1.2	90	43.53	100	0.15	8	0.8	90
29	29.266	100	0.15	16	0.8	30	37.925	100	0.15	12.53	0.674	30
30	39.574	100	0.15	8	0.8	90	43.499	100	0.15	8.466	0.773	90
31	27.292	100	0.15	10.5	1.2	30	38.412	100	0.15	11.6	0.8	30
32	33.503	100	0.15	8	1.2	90	43.52	100	0.15	8.256	0.8	90

Table B.27. Optimum values of machining conditions predicted by GA for corresponding minimum value of tool wear under wet and dry machining.

Runs	Wet-TW						Dry-TW					
	Min-SR	v_c	f	γ	r_e	ψ	Min-SR	v_c	f	γ	r_e	ψ
	microns	m/min	mm/rev	deg	mm	deg	microns	m/min	mm/rev	deg	mm	deg
1	36.42	50	0.1	8	0.8	30	46.76	50	0.1	8	0.8	60
2	44.78	50	0.1	8	0.8	60	46.71	50	0.1	8	0.8	62.42
3	33.90	50	0.1	6.76	1.2	30	46.74	50	0.1	8	0.827	60
4	43.77	50	0.1	8	1.02	60	46.69	50	0.1	8	0.827	62.42
5	35.69	50	0.1	10.6	0.8	30	46.72	50	0.1	8.45	0.8	60
6	44.05	50	0.1	10.8	0.8	60	46.68	50	0.1	8.35	0.8	62
7	33.99	50	0.1	8	1.14	30	46.69	50	0.1	8.45	0.827	60
8	43.73	50	0.1	8.6	0.99	60	46.66	50	0.1	8.35	0.827	62
9	40.74	50	0.15	8	0.8	30	51.75	50	0.15	8	0.8	60
10	49.10	50	0.15	8	0.8	60	51.70	50	0.15	8	0.8	62.42
11	38.23	50	0.15	6.76	1.2	30	51.73	50	0.15	8	0.827	60
12	48.10	50	0.15	8	1.02	60	51.68	50	0.15	8	0.827	62.42
13	40.01	50	0.15	10.6	0.8	30	51.71	50	0.15	8.45	0.8	60
14	48.37	50	0.15	10.6	0.8	60	51.67	50	0.15	8.35	0.8	62.04
15	38.32	50	0.15	8	1.15	30	51.69	50	0.15	8.45	0.827	60
16	48.05	50	0.15	9.03	0.97	60	51.65	50	0.15	8.37	0.827	61.57
17	47.01	100	0.1	8	0.8	30	58.99	100	0.1	8	0.8	60
18	55.37	100	0.1	8	0.8	60	58.93	100	0.1	8	0.8	62.42
19	44.49	100	0.1	6.83	1.2	30	58.96	100	0.1	8	0.827	60
20	54.36	100	0.1	8	1.02	60	58.91	100	0.1	8	0.827	62.42
21	46.27	100	0.1	10.5	0.8	30	58.94	100	0.1	8.45	0.8	60
22	54.64	100	0.1	10.6	0.8	60	58.91	100	0.1	8.36	0.8	61.76
23	44.59	100	0.1	8.04	1.13	30	58.92	100	0.1	8.45	0.827	60
24	54.31	100	0.1	8.94	0.97	60	58.88	100	0.1	8.35	0.827	62
25	51.33	100	0.15	8	0.8	30	63.98	100	0.15	8	0.8	60
26	59.69	100	0.15	8	0.8	60	63.92	100	0.15	8	0.8	62.42
27	48.81	100	0.15	6.86	1.19	30	63.95	100	0.15	8	0.827	60
28	58.69	100	0.15	7.94	1.02	60	63.90	100	0.15	8	0.827	62.42
29	50.60	100	0.15	10.6	0.8	30	63.93	100	0.15	8.45	0.8	60
30	58.96	100	0.15	10.6	0.8	60	63.90	100	0.15	8.35	0.8	61.99
31	48.91	100	0.15	8	1.14	30	63.91	100	0.15	8.46	0.827	59.96
32	58.63	100	0.15	8.97	0.97	60	63.87	100	0.15	8.35	0.827	61.99

APPENDIX - C.

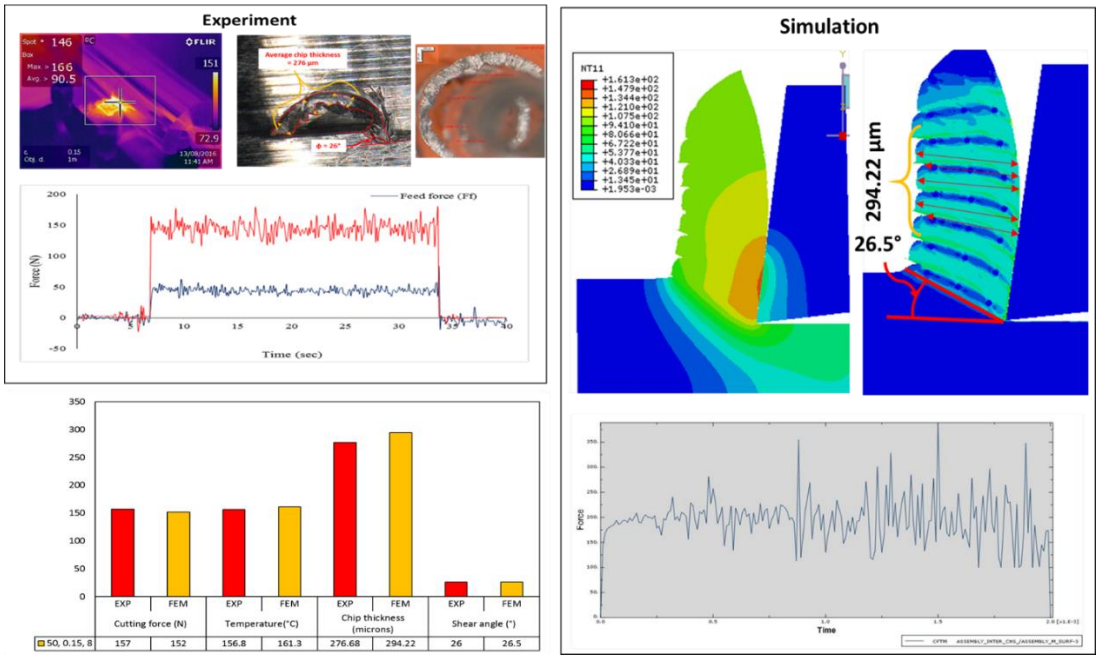

Fig. C.1. Comparison of simulated with experiment at Test-II.

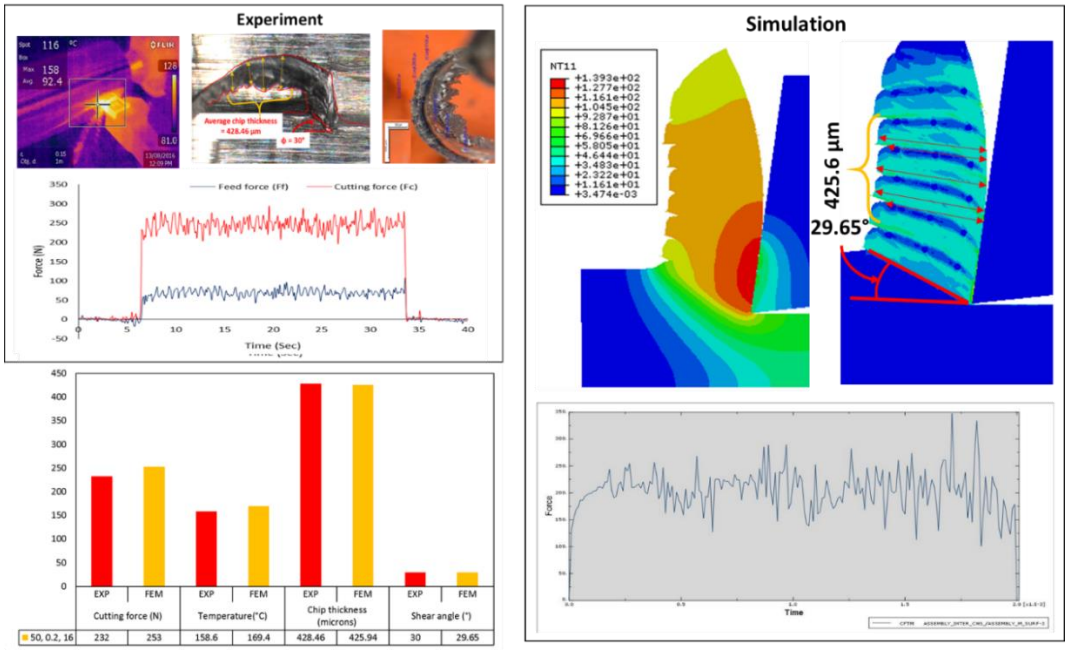

Fig. C.2. Comparison of simulated with experiment at Test-III.

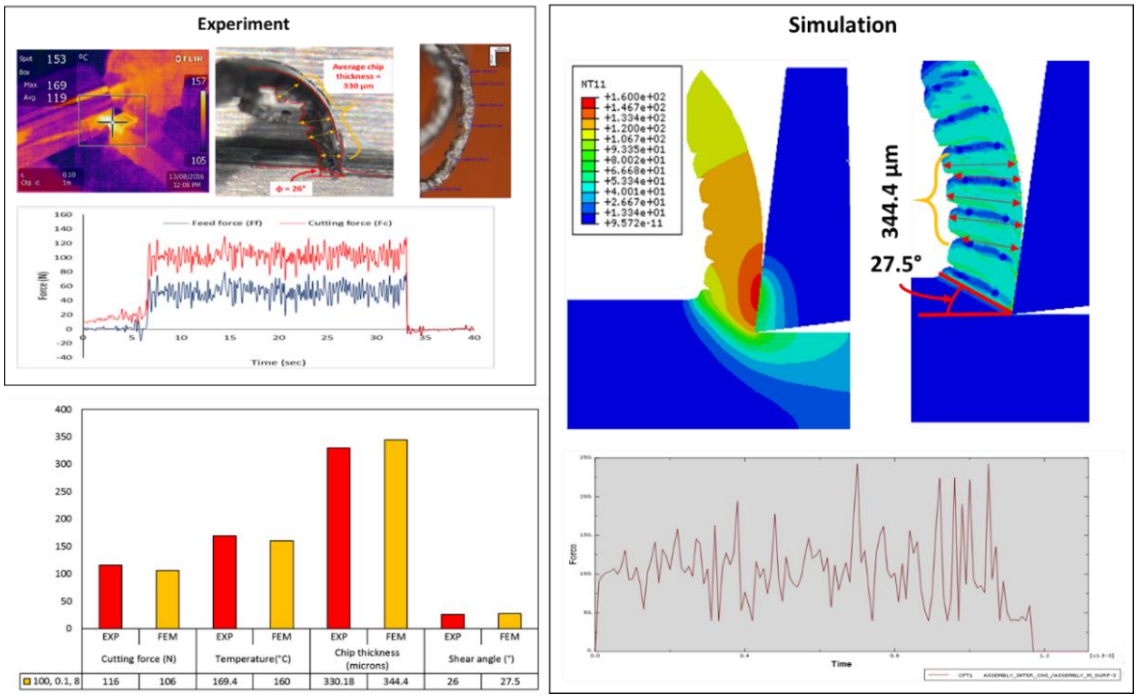

Fig. C.3. Comparison of simulated with experiment at Test-IV.

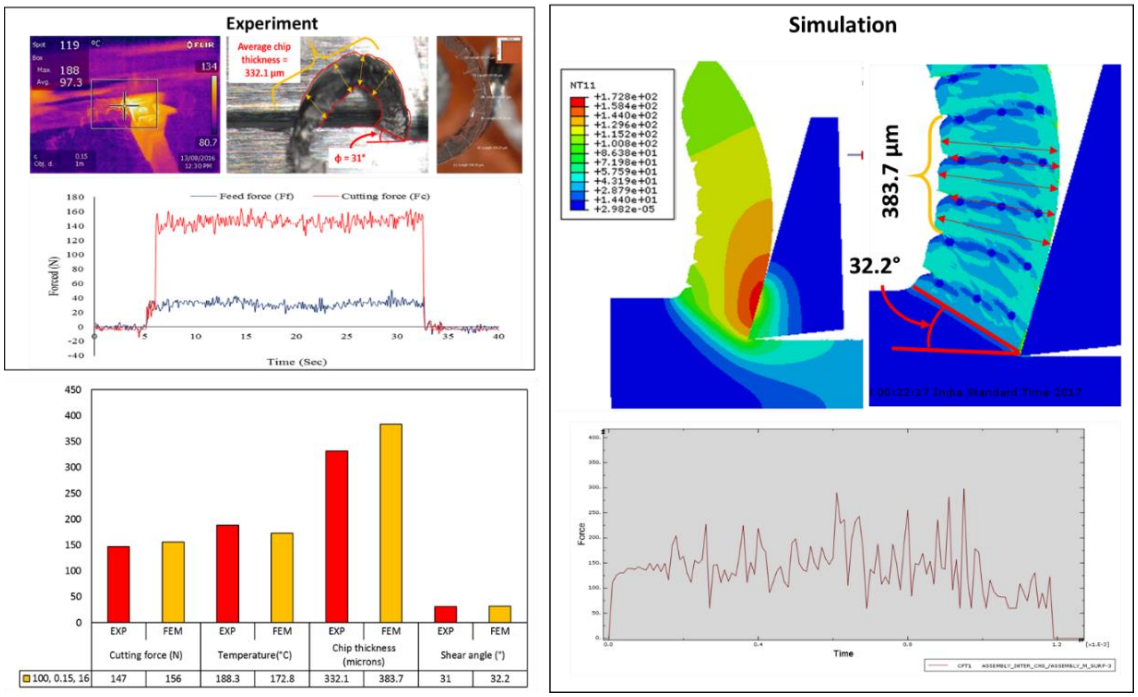

Fig. C.4. Comparison of simulated with experiment at Test-V.

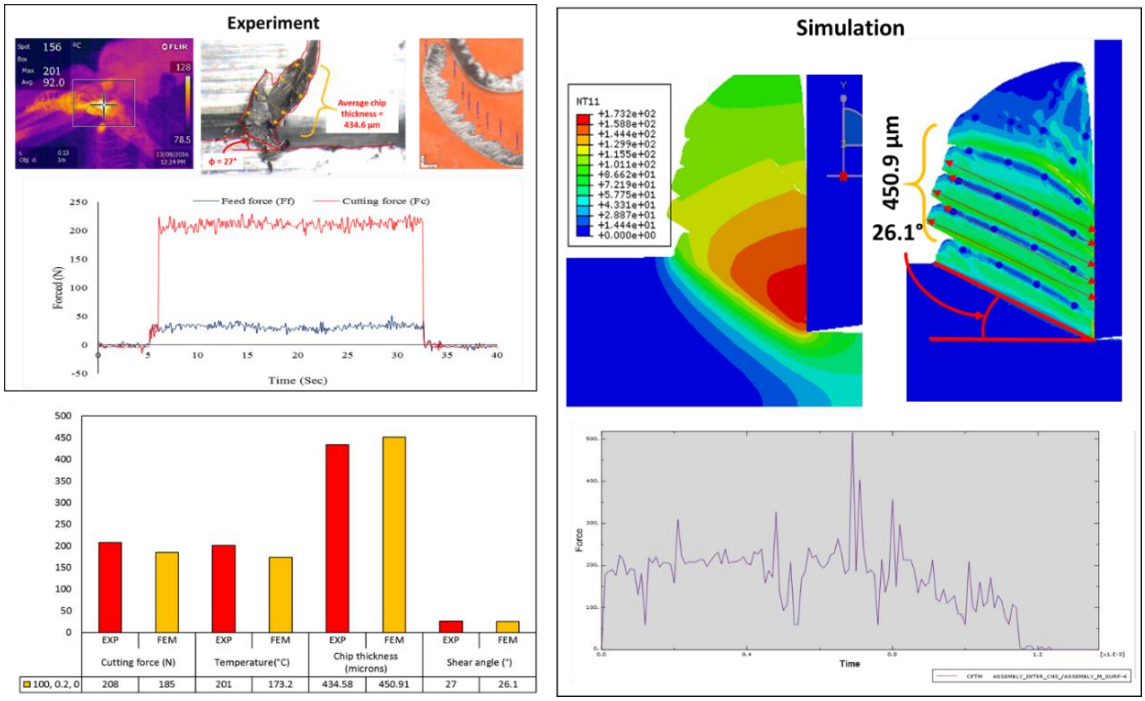

Fig. C.5. Comparison of simulated with experiment at Test-VI.

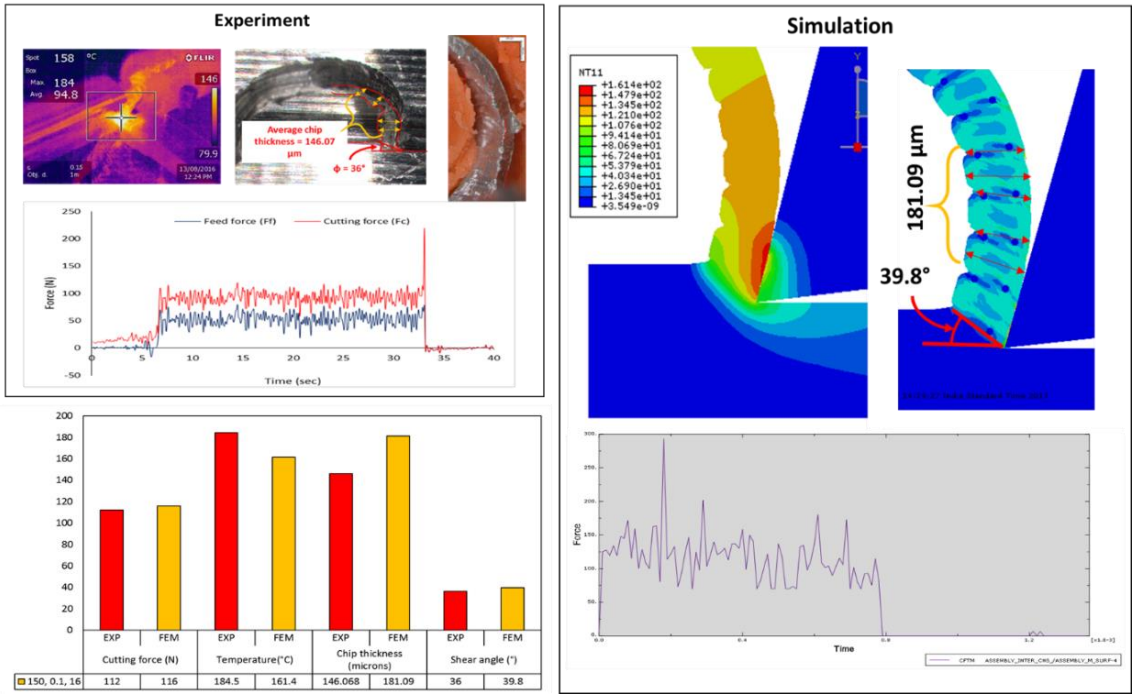

Fig. C.6. Comparison of simulated data with experimental data at Test-VII.

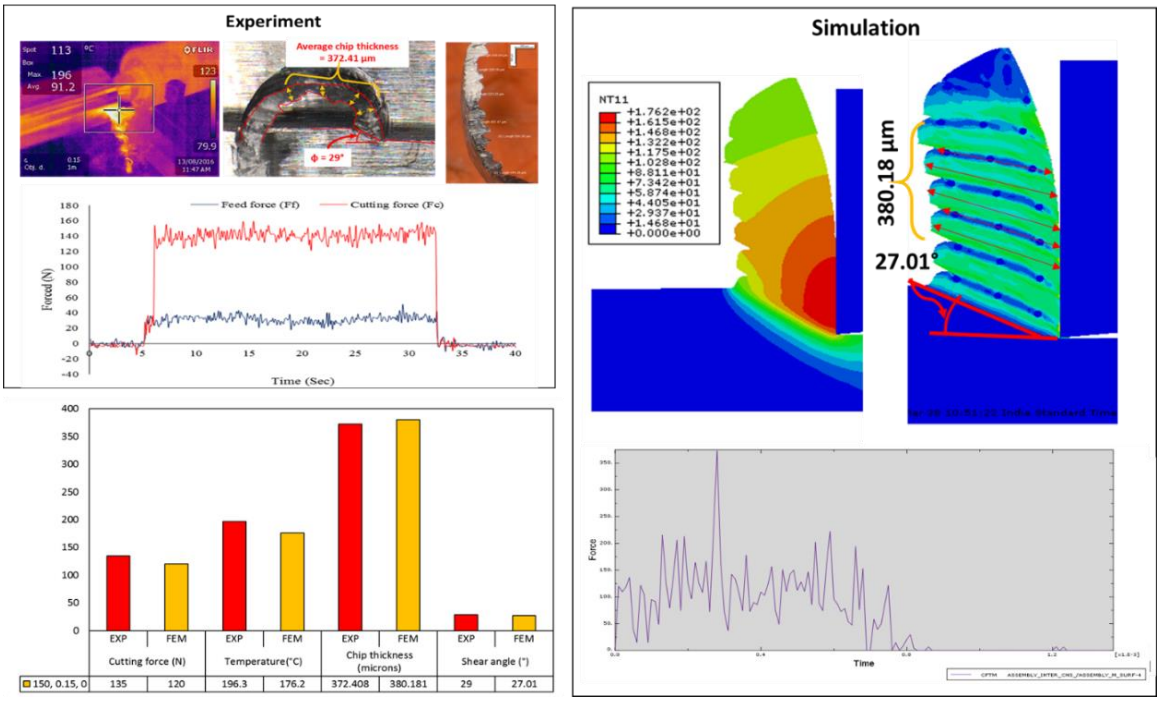

Fig. C.7. Comparison of simulated with experiment at Test-VIII.

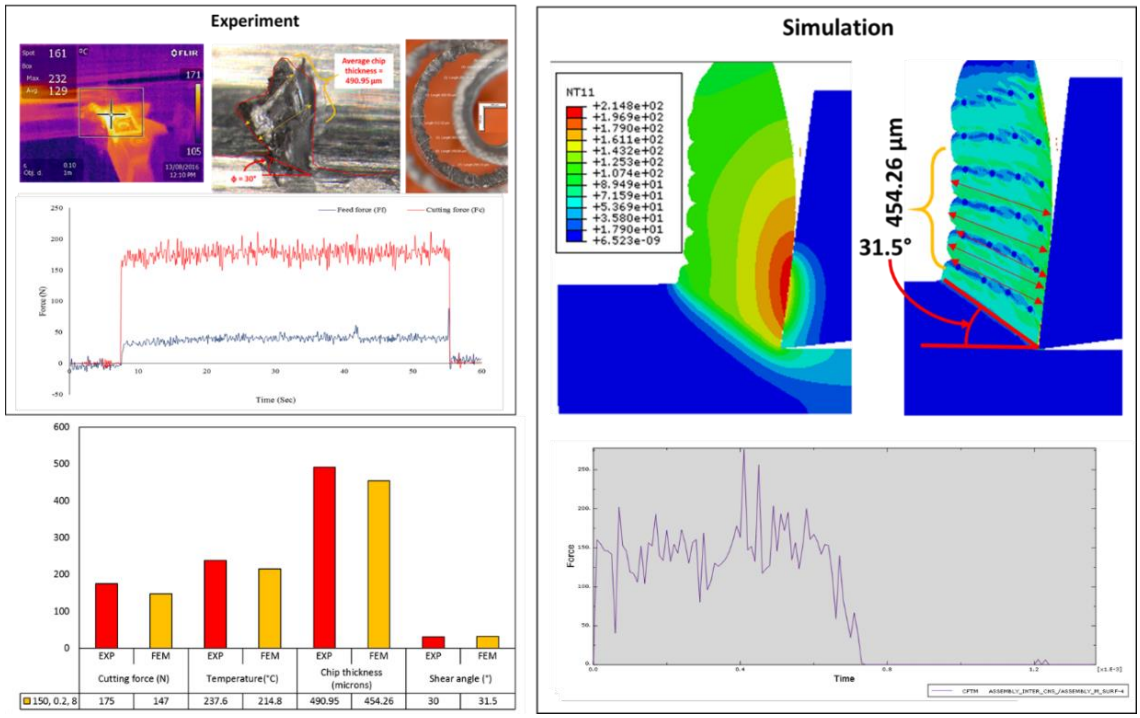

Fig. C.8. Comparison of simulated with experiment at Test-XI.

LIST OF PUBLICATIONS AND CONFERENCES

International journals

1. **Josyula Sravan Kumar**, Narala Suresh Kumar Reddy, Performance enhancement of cryogenic machining and its effects on tool wear during turning of Al-TiCp composite, Machining Science and Technology (Taylor & Francis), (Accepted for publication), (IF =1.053).
2. **Josyula Sravan Kumar**, Narala Suresh Kumar Reddy, Machinability Enhancement of Stir Cast Al-TiCp Composites under Cryogenic Condition, Journal of Materials and Manufacturing Processes (Taylor & Francis), Volume 40, 2017, 568-573, (IF = 1.419).
3. **Josyula Sravan Kumar**, Narala Suresh Kumar Reddy, Sustainable Machining of Metal Matrix Composites Using Liquid Nitrogen, Procedia CIRP (Elsevier), 40, 568-573, 2015.
4. **Josyula Sravan Kumar,** Narala Suresh Kumar Reddy**,** Experimental investigation on tribological behaviour of Al-TiCp composite under sliding wear conditions, Journal of Engineering Tribology (SAGE), 230 (8), 919-929, 2015, (IF = 1.320).
5. **Josyula Sravan Kumar**, and Narala Suresh Kumar Reddy, A Brief Review on Manufacturing of Al-TiC MMC, In Advanced Materials Research (Scientific.net), 980, 62-68, 2014.
6. A Marques, Suresh Kumar Reddy Narala**,** AR Machado, Rakesh Kumar Gunda, **Sravan Kumar Josyula**, RB Da Silva, MB Da Silva, Performance assessment of MQSL: Minimum quantity solid lubricant during turning of Inconel 718, Journal of Engineering Manufacture (SAGE), 1-10, 2014. (IF = 1.366)

7. **Josyula Sravan Kumar**, Narala Suresh Kumar Reddy, Study of TiC Particle Distribution in Al-MMCs using Finite Element Modelling, International Journal of Mechanical Science (Elsevier) [*under review*].

International Conferences

1. **Sravan Kumar Josyula** and Suresh Kumar Reddy Narala, Enhancement of Cryo Assisted Machining Performance during Turning of Al-5% TiCp Metal Matrix Composite,2016, 6th International and 27th All India Manufacturing Technology, Design and Research Conference, College of Engineering., Pune, Maharashtra, India.
2. **J. Sravan Kumar**, G. Rakesh Kumar and N. Suresh Kumar Reddy, A Study for Selection of Cutting Parameters in Turning Process using Decision Making Method, 2014, ICARIM, Warangal, India.

National Conferences

1. E. Gurucharan, **Sravan Kumar Josyula**, Sanchay Bapat, Meghana Maddala, Suresh Kumar Reddy Narala, V.Kalyan Chakravarty, Evaluating the Performance of End Milling of Hybrid Laminates under Dry And Cryo Milling Environments Through Experimental Analysis, Proceedings of 2nd DPLC Conference, BITS-Pilani Hyderabad Campus, Hyderabad, India.
2. **Sravan Kumar Josyula**, Narala Suresh Kumar Reddy, Tribological behaviour of Al-TiCp Composite under Cryogenic Environment, Proceedings of 2nd DPLC Conference, BITS-Pilani Hyderabad Campus, Hyderabad, India.

BIOGRAPHY OF THE CANDIDATE

Name of the candidate	Sravan Kumar Josyula
ID. No.	2012PHXF504H
Academic credentials	Ph.D. (pursuing at BITS-Pilani, Hyderabad Campus)
	M.E in Computer Aided Design (SVCE, Chennai)
	B.E in Mechanical Engineering (HCE, Chennai)
	Intermediate in M.P.C (Vignan Jr College, Hyderabad)
	SSC, (Sree Sree Educational society, Eluru)
Personal details	Residential address: D No: 4-14-1, Ooka Sandhu,
	Agraharam, Eluru – 534001,
	W.G Dist, Andhra Pradesh.
	Contact Number: +91-9542553908
	Email address: sravanjosyula@gmail.com

BIOGRAPHY OF THE SUPERVISOR

Name of the Supervisor	Dr. Suresh Kumar Reddy Narala
Designation and address	Associate Professor, Department of Mechanical Engineering, BITS, Pilani, Hyderabad Campus
Experience (years)	17
Number of publications	Journals – 25 International Conferences – 14
Number of citations	590
Sponsored projects	1. Performance evaluation of various coated drills based on wear and hole quality in dry drilling (Sponsor: Oerlikon Balzers) (Jan 2008 to Nov 2008) 2. BITS-SG Project on "Development of novel coated tools for green machining", Rs.11.8 Lakhs (2011-2013). 3. CSIR project on "Development of ES nano-solid lubricant coated tools for sustainable machining", Rs.18.52 Lakhs. (2012-15). 4. DST project on "Novel minimal application method for performance improvement in turning", Rs.40.16 Lakhs. (2013-17). 5. ISR project on "Studies related to control of porosity in casting", Rs. 8.03 Lakhs (2016-2019). 6. DRDL project on "Novel Casting Approach to Improve Quality of Aluminum Alloy Casting: Hybrid Ultrasonic Assisted Bottom Pour Stir Casting Process", Rs. 9.84 Lakhs (2017-2020)
No. of PhD students completed	1
No. of Ph.D. students under in-progress	5